

RESEARCH AND TECHNOLOGY



Langley Research Center
NASA Technical Memorandum 4331

1991

N92-30733

Unclass

HL/99 0109337

(NASA-TM-4331) RESEARCH AND
TECHNOLOGY, 1991. LANGLEY RESEARCH
CENTER (NASA) 283 p

RESEARCH AND TECHNOLOGY



1991



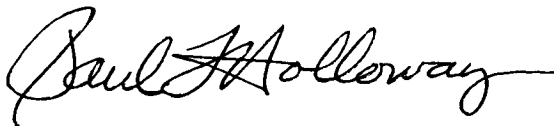
National Aeronautics and
Space Administration

Langley Research Center
Hampton, Virginia 23665-5225

Langley Research Center
NASA Technical Memorandum 4331

FOREWORD

The mission of the NASA Langley Research Center is to increase the knowledge and capability of the United States in a full range of aeronautics disciplines and in selected space disciplines. This mission will be accomplished by performing innovative research relevant to national needs and Agency goals, transferring technology to users in a timely manner, and providing development support to other United States Government agencies, industry, and other NASA centers. This report contains highlights of the major accomplishments and applications that have been made during the past year. The highlights illustrate both the broad range of the research and technology (R&T) activities at NASA Langley Research Center and the contributions of this work toward maintaining United States leadership in aeronautics and space research. For further information concerning the report, contact Dr. Michael F. Card, Chief Scientist, Mail Stop 105-A, NASA Langley Research Center, Hampton, Virginia 23665, (804) 864-6062.



Paul F. Holloway
Director

AVAILABILITY INFORMATION

The NASA program office and the corresponding Agency-wide Research and Technology Objectives and Plans (RTOP's) work breakdown structures are listed in the Contents for each research and technology accomplishment. OAST designates the Office of Aeronautics and Space Technology; OSSA designates the Office of Space Science and Applications; AA designates the Associate Administrator; OCE designates the Office of the Chief Engineer; OCP designates the Office of Commercial Programs; OSF designates the Office of Space Flight; and OSMQ designates the Office of Safety and Mission Quality.

The accomplishments are grouped in 12 strategic thrusts including contributions in Fundamental Knowledge, Subsonic Aircraft, High-Speed Civil Transport, High-Performance Military Aircraft, Hypersonic and Transatmospheric Vehicles, Space Transportation, Space Station, Space Technology, Exploration, Global Change, Facilities, and Technology Utilization.

For additional information on any summary, contact the individual identified with the highlight. This individual is generally either a member or a leader of the research group submitting the highlight. Commercial telephone users may dial the listed extension preceded by (804) 86. Telephone users with access to the Federal Telecommunications System (FTS) may dial the extension preceded by 928.

CONTENTS

Foreword	iii
Availability Information	iv

Fundamental Knowledge

Ferroelectric Liquid-Crystal Thin-Film Boundary-Layer Sensor (AA 307-50-11): Devendra S. Parmar and Harlan K. Holmes	1
Analysis of Flight-Measured Boundary-Layer Transition Data (OAST 505-59-10): Clifford J. Obara, Cynthia C. Lee, and Paul Vijgen	1
Compressible Large-Eddy Simulation of Isotropic Turbulence (OAST 505-59-40): Thomas A. Zang, Russell B. Dahlburg, and Jill P. Dahlburg	2
Development of High-Order Shock-Capturing Methods (OAST 505-59-50): H. L. Atkins	2
Compressible Boundary-Layer Transition Using PSE (OAST 505-59-50): C. L. Chang and M. R. Malik	3
Numerical Simulation of Laminar Breakdown in Supersonic Transition (OAST 505-59-50): C. David Pruett and Thomas A. Zang	4
Wind-Tunnel Interference and Assessment Code Development (OAST 505-59-53): Perry A. Newman, Javier A. Garriz, Veer N. Vatsa, and Kara J. Haigler	5
Advanced CFD Design Methods for Supersonic Flow (OAST 505-59-53): Richard L. Campbell	6
Numerical Simulation of Schlieren Image (OAST 505-59-53): Robert P. Weston and Beyung S. Kim	6
Sensitivity Analysis for Viscous Flows (OAST 505-59-53): Arthur Taylor and Gene Hou	7
Three-Dimensional Unstructured Adaptive Grid (OAST 505-59-53): Dimitri Mavriplis	8
Effect of Turbulence on Flow Over Delta Wing (OAST 505-59-53): Anthony Washburn	8
Investigation of Zoom Lenses for Digital Photogrammetry (OAST 505-59-54): A. W. Burner	9
Calibration Tests of Scientific CCD Cameras (OAST 505-59-54): W. L. Snow, A. W. Burner, and W. K. Goad	10

Grid Convergence for Adaptive Methods	10
(OAST 505-59-60): Gary P. Warren, W. Kyle Anderson, James L. Thomas, and Sherrie L. Krist	
Method for Internal Nozzle Performance Prediction	11
(OAST 505-62-30): J. R. Carlson	
Computational Analysis of Fixed-Geometry Slotted Nozzle	12
(OAST 505-62-30): K. S. Abdol-Hamid, J. R. Carlson, and S. P. Pao	
Accurate Prediction of Strain in Stiffened Composite Wing Panel by Nonlinear Finite-Element Analysis	12
(OAST 505-63-01): D. Dale Davis, Jr., T. Krishnamurthy, and W. Jefferson Stroud	
New Eigensolver Reduces Supersonic-Hypersonic Flutter Analysis Time by Two Orders of Magnitude	13
(OAST 505-63-01): O. O. Storaasli, C. Gray, J. Qin, D. T. Nguyen, and C. Mei	
Demonstration of Adaptive Analysis Procedure on Nonlinear Response of Composite Panel	14
(OAST 505-63-01): Susan L. McCleary, Jonathan B. Ransom, and Norman F. Knight, Jr.	
Cornering Properties of Bias-Ply, H-Type, and Radial Aircraft Tires	15
(OAST 505-63-10): Pamela A. Davis, Sandy M. Stubbs, and Thomas J. Yager	
Acoustic Radiation Damping in Subsonic Flows	16
(OAST 505-63-36): Karen H. Lyle	
Frequency-Based Approach to Dynamic Stress Intensity Analysis	17
(OAST 505-63-50): Stephen A. Rizzi	
Spatial Adaption Procedures for Accurate Unsteady Flow Analysis	18
(OAST 505-63-50): Russ D. Rausch and John T. Batina	
CFD Simulates Active Control of Delta Wing Rocking Motion	19
(OAST 505-63-50): Elizabeth M. Lee and John T. Batina	
Finite-Difference Meshes for Solution of Transonic Small Disturbance Equation	20
(OAST 505-63-50): Samuel R. Bland	
Optimization Scheme To Obtain Maximized Gust Loads for Nonlinear Aircraft	21
(OAST 505-63-50): Robert C. Scott, Anthony S. Pototzky, and Boyd Perry III	
Active Suppression of Flutter Using Piezoelectric Ceramic Actuators	22
(OAST 505-63-50): Jennifer Heeg	
Effect of Floor Location on Response of Composite Fuselage Frame	23
(OAST 505-63-09): Lisa E. Jones and Huey D. Carden	
Application of Optimal Input Design to Parameter Estimation Flight Experiments	24
(OAST 505-64-52): Eugene A. Morelli and Brent R. Cobleigh	
State Reduction for Aeroelastic Simulation	24
(OAST 505-64-52): Carey S. Buttrill and Barton J. Bacon	
Head Movement Correction Algorithm for Stereo 3-D Flight Displays	25
(OAST 505-64-13): Russell V. Parrish and Steven P. Williams	
Design for Full-Color Conversion of Monochrome Helmet-Mounted Display	26
(OAST 505-64-13): William S. Beamon, Russell V. Parrish, and Steven P. Williams	

Design for Laser-Scanned, Full-Color Helmet-Mounted Display	27
(OAST 505-64-13): William S. Beamon, Russell V. Parrish, and Steven P. Williams	
Brainmap Analysis Identifies States of Awareness for System Monitoring Tasks	28
(OAST 505-64-53): Alan T. Pope and Edward H. Bogart	
Task Battery for Pilot Strategic Behavior, Work Load, and Complacency Research	29
(OAST 505-64-53): J. Raymond Comstock, Jr., and Ruth J. Arnegard	
FLEX: A Programming Language for Real-Time Systems	30
(OAST 505-64-10): Kathryn A. Smith	
APPROXIMATE: A Query Processor That Returns Monotonically Improving Approximate Answers	31
(OAST 505-64-50): Kathryn A. Smith	
DEPEND Environment	32
(OAST 505-64-50): Kathryn A. Smith	
Navier-Stokes Solution About F/A-18 Aircraft	33
(OAST 505-68-30): F. Ghaffari	
Aerodynamic Surface Parameterization and Grid Sensitivity	34
(OAST 505-90-53): Robert E. Smith	
Efficient Multitasking of Choleski Matrix Factorization on CRAY Supercomputers	35
(OAST 505-90-53): Andrea L. Overman	
Neural Networks for NDE	36
(OAST 506-43-11): D. R. Prabhu and William P. Winfree	
Free Volume Model for Molecular Weights of Polymers	37
(OAST 506-43-21): Jag J. Singh and Abe Eftekhari	
EZDESIT—A Computer Program for Structural Element Sizing and Structural Weight Prediction	38
(OAST 506-43-31): Jeffrey A. Cerro, Lynn M. Bowman, and Charles P. Shore	
Advanced Reduced-Basis Methods Decrease Computational Requirements for Linear, Transient Structural Analysis	38
(OAST 506-43-71): David M. McGowan and Susan W. Bostic	
Modeling of Nonlinear Aerodynamic Responses for Aeroservoelastic Analysis and Design	39
(OAST 509-10-02): Walter A. Silva	
Prediction of HiSAIR Vehicle Air Loads Using CAP—TSD Code	40
(OAST 509-10-02): James T. Howlett	
Shape Sensitivity Analysis of Aeroelastic Response	41
(OAST 509-10-02): R. K. Kapania, L. B. Eldred, and J.-F. M. Barthelemy	
Continuous Production Method for Manufacturing High-Temperature Thermoplastic Prepreg	42
(OAST 510-02-11): Gary Johnson	
Transition Prediction in 3-D Flows Over Axisymmetric Bodies at Incidence	42
(OAST 537-03-23): Robert E. Spall, Venkit Iyer, and Mujeeb R. Malik	

Analytical Evaluation of Convective Heat-Transfer Correlations	43
(OAST 763-23-61): Dennis Petley and Bill Dziedzic	

Subsonic Aircraft

Hybrid Laminar-Flow Control Flight Research	47
(OAST 505-59-10): Dal V. Maddalon	
Hybrid Laminar-Flow Control Nacelle Concept	48
(OAST 505-59-10): Richard D. Wagner and F. S. Collier, Jr.	
Porous Transonic Airfoils for Multipoint Design	48
(OAST 505-59-10): Peter M. Hartwich and James M. Luckring	
Airborne Laser Diode Illumination System	49
(OAST 505-59-30): B. D. Taylor and F. Fitzpatrick	
Study on Use of Sulfur Hexafluoride for High-Lift Testing	50
(OAST 505-59-53): Daryl L. Bonhaus	
Smart Compass Upgrade	51
(OAST 505-61-77): Doug Garner	
Failure Modes of Composite Laminates With Hole and Subjected to Four-Point Bending	52
(OAST 505-63-01): M. J. Shuart and C. B. Prasad	
Structural Efficiency Determined for Optimized Graphite-Thermoplastic Panels	52
(OAST 505-63-01): Dawn C. Jegley	
Fracture Mechanics Analyses of Cracks Extending From Rivets	53
(OAST 505-63-10): J. C. Newman, Jr., K. N. Shivakumar, and D. S. Dawicke	
BVI Noise Prediction Validation	55
(OAST 505-63-36): Casey L. Burley and Michael A. Marcolini	
Government and Industry Assessment of DAMVIBS Program	55
(OAST 505-63-36): Raymond G. Kvaternik	
Demonstration of Extension-Twist Coupling Concept	56
(OAST 505-63-36): Renee C. Lake, Mark W. Nixon, Matthew Wilbur, Jeffrey Singleton, and Paul Mirick	
XV-15 Advanced Technology Blade Tilt-Rotor Hover Flight Test	57
(OAST 505-63-46): David Conner, Ken Rutledge, and Dan Hoad	
Evaluation of Toughened Matrix Composite Materials	58
(OAST 505-63-50): R. J. Cano and M. B. Dow	
Analysis of Local Delamination From Matrix Cracks in Laminated Composites	59
(OAST 505-63-50): S. A. Salpekar and T. K. O'Brien	
Differences Between Standard Impact Tests	60
(OAST 505-63-50): C. C. Poe, Jr., Wade C. Jackson, and M. A. Portanova	
Trail-Rotor Model Flutter Characteristics	61
(OAST 505-63-50): David L. Soistmann	

NACA 0012 Benchmark Model Test	62
(OAST 505-63-50): José A. Rivera, Jr., Bryan E. Dansberry, Moses G. Farmer, Clinton V. Eckstrom, Robert M. Bennett, and David A. Seidel	
Transonic Shock-Induced Dynamics of Flexible Wing	63
(OAST 505-63-50): Robert M. Bennett, Bryan A. Dansberry, Moses G. Farmer, Clinton V. Eckstrom, and José A. Rivera, Jr.	
Takeoff Performance Monitoring Systems Display Options	64
(OAST 505-64-13): David B. Middleton, Raghavachari Srivatsan, and Lee H. Person, Jr.	
Airborne Doppler Radar Detection of Microburst Wind Shear	65
(OAST 505-64-12): E. M. Bracalente	
RECORS Concept for Aircraft Applications	66
(OAST 505-64-13): Kathy Abbott, Eva Hudlicka, Kevin Corker, and Dawn MacLaughlin	
Decision-Aiding Concept and Pilot-Vehicle Interface (PVI) for In-Flight Diversions	67
(OAST 505-64-13): Michael T. Palmer	
Knowledge-Based Systems Concept for Primary Flight Display Information Management	68
(OAST 505-64-13): Wendell R. Ricks	
Estimation of Heavy Rain Effect on Airplane Performance	69
(OAST 505-64-13): Dan D. Vicroy	
Data Link for Air Traffic Control and Weather Information Exchange	70
(OAST 505-64-13): Charles E. Knox and Charles H. Scanlon	
Aging Aircraft Lap Joint Bond Nondestructive Evaluation	71
(OAST 505-63-10): William P. Winfree and K. Elliott Cramer	
Optical NDT for Aging Aircraft	72
(OAST 505-63-10): Leland D. Melvin and David S. Dawicke	
Detection of Cracks by Vibrational Mode Analysis in Thin Metal Plates	73
(OAST 505-63-10): B. Wincheski and M. Namkung	
Effect of Heavy Rain on Airfoil Performance at Large Scale	74
(OAST 505-68-01): Gaudy H. Bezos and Bryan A. Campbell	
Intelligent, Compact, Modular Aircraft Data Acquisition System	75
(OAST 505-68-30): Carroll Lytle, Dan Norfolk, and Keith Harris	
Application of Acoustic Plate Waves to Structural Integrity Assessment	76
(OAST 506-43-11): Keun J. Sun	
Tough, High-Modulus, Semicrystalline Amide Polyimides	77
(OAST 506-43-11): James F. Dezern and Carol R. Gautreaux	
Mechanics Models for Textile Preform Composites	77
(OAST 510-02-1): John E. Masters and Ray L. Foye	
Improved Damage Tolerance With Knitted/Stitched Composites	78
(OAST 510-02-11): H. Benson Dexter	

Blade-Web Intersection Critical for Graphite/Epoxy Y-Stiffened Panels	79
(OAST 510-02-12): P. D. Sydow and M. J. Shuart	
Curved Beams Made From Long Discontinuous Fiber (LDF) Material	80
(OAST 510-02-12): Dawn C. Jegley and Michael H. Santare	
Design-Build-Team Approach Provides Benefits in Composite Fuselage Structural Design	80
(OAST 510-02-13): John G. Davis, Jr., and W. T. Freeman	
Influence of Load and Component Interaction on Technology Integration Box Beam Test	81
(OAST 510-02-13): John G. Davis, Jr., and Randall C. Davis	
Global Stitching Paves Way for Low-Cost Composite Wing Structure	82
(OAST 510-02-21): John G. Davis, Jr.	
Directivity of Rotor Impulsive Noise Reduction Using Higher Harmonic Control	82
(OAST 532-06-37): Thomas F. Brooks and Earl R. Booth, Jr.	
Periodic Blade Loads and Performance of Inclined High-Speed Propeller	84
(OAST 535-03-10): M. A. Takallu and V. R. Lessard	
Transport Pylon Geometries for Reducing Nacelle Installation Drag	85
(OAST 535-03-10): A. M. Ingraldi, D. A. Naik, and O. C. Pendergraft, Jr.	
Interior Noise Control Using Piezoceramic Actuators	86
(OAST 535-03-11): Richard J. Silcox	
Active Adaptive Control of Axial Flow Turbofan Engine Noise	87
(OAST 535-03-11): Carl H. Gerhold and Shelby J. Morris	
Effect of Nonaxial Inflow on Propeller Noise	87
(OAST 535-03-11): F. Farassat, Mark H. Dunn, and Peter L. Spence	

High-Speed Civil Transport

HSCT Navier-Stokes Computations	91
(OAST 505-59-53): Veer N. Vatsa	
Multielement, Thin-Film Heat-Transfer Array Fabrication	91
(OAST 505-59-53): J. Bartlett	
Application of Knowledge-Based Tool To Understand HiSAIR Data Flow	92
(OAST 509-10-02): James L. Rogers	
Langley-Fabricated Powder-Metallurgy, Aluminum-Alloy Sheet Demonstrates Useful Stability at 600°F	93
(OAST 505-63-50): D. M. Royster and O. R. Singleton	
Supersonic Elliptic Nozzle	93
(OAST 537-02-22): Michael K. Ponton and John M. Seiner	
Aircraft Noise Prediction Program Jet Noise Calculations for HSCT	94
(OAST 537-03-11): Robert A. Golub	
Prediction of Subjective Response to Sonic Booms	95
(OAST 537-02-31): David A. McCurdy	

Sonic Boom Shaping for Reduced Loudness	96
(OAST 537-03-21): Jack D. Leatherwood and Brenda M. Sullivan	
Atmospheric Turbulence Increases Sonic Boom Rise Time	96
(OAST 537-03-21): Gerry L. McAninch	
Sonic Boom Shaping	97
(OAST 537-03-21): Robert J. Mack, Christine M. Darden, Kathy E. Needleman, and Daniel G. Baize	
Design System for Low Sonic Boom Configurations	97
(OAST 537-03-21): Raymond L. Barger and Mary S. Adams	
Jet Plume Effects on Sonic Boom Signature	98
(OAST 537-03-21): N. Duane Melson and Raymond L. Barger	
Effect of Fuselage Forebody Length on High-Lift Stability and Control of HSCT Conceptual Designs	99
(OAST 537-03-22): E. Richard White	
Computational Predictions of HSCT-Type Configuration	100
(OAST 537-03-22): Victor R. Lessard and Bryan A. Campbell	
HCST Leading-Edge Boundary-Layer Control Porous Skin Fabrication	100
(OAST 537-03-31): Barry Gibbens	

High-Performance Military Aircraft

Demonstration of Multi-Input/Multi-Output, Multiple Function Digital Control	103
(OAST 505-63-50): Boyd Perry III and Stanley R. Cole	
Flutter Suppression During Steady and Maneuvering Flight	104
(OAST 505-64-30): W. M. Adams, M. R. Waszak, and D. M. Christhilf	
Control Design for Future Agile Fighters	104
(OAST 505-64-30): Patrick C. Murphy and John B. Davidson	
Reliability Analysis of Integrated Airframe/Propulsion Control System Architecture	106
(OAST 505-64-10): Daniel L. Palumbo	
Vortex-Fin Interaction Research	106
(OAST 505-68-30): Anthony Washburn	
F-18 High-Angle-of-Attack Aerodynamics	107
(OAST 505-68-30): Daniel W. Banks, Robert M. Hall, William G. Sewall, and Gary E. Erickson	
Forebody Suction for High-Angle-of-Attack Directional Control	109
(OAST 505-68-71): E. Richard White	
Validation of Navier-Stokes Solutions for F-18 Forebody Control Strake	110
(OAST 535-02-35): Robert T. Biedron	

Hypersonic and Transatmospheric Vehicles

Advanced Aero-Propulsion Performance Design Tool (PEMACH)	113
(OAST 505-59-40): Suresh L. Goradia and Abel O. Torres	
Prediction of Hypersonic, Airbreathing Vehicle Aftbody Flow Field Under Simulated Powered Conditions	114
(OAST 505-59-40): Lawrence D. Huebner	
Multigrid Algorithm for Hypersonic Flow	115
(OAST 505-59-53): James L. Thomas and David H. Rudy	
CFD Code Validation for Supersonic Combustor Flow Fields	115
(OAST 505-62-31): Dean R. Eklund and G. Burton Northam	
Effect of Oxygen Dissociation on Hypersonic Combustion	116
(OAST 505-62-40): G. Y. Anderson, R. C. Rogers, and R. W. Guy	
Numerical Modeling of Strongly Coupled Fluid-Combustion Phenomenon	117
(OAST 505-62-40): Jeffery A. White	
CFD-Based Aerodynamic Design of Hypersonic Wind-Tunnel Nozzles	118
(OAST 505-62-40): John J. Korte	
Fuel-Air Mixing Enhancement by Jet-Shock Interactions	118
(OAST 505-62-40): J. Philip Drummond	
Scramjet Combustor Loss Evaluation	120
(OAST 505-62-40): David W. Riggins and Charles R. McClinton	
Instantaneous Planar Visualization of Reacting Supersonic Flow Using Silane Seeding	121
(OAST 505-63-40): Michael W. Smith and G. Burton Northam	
Effects of Thermal Gradients on Structural Vibration Frequencies	122
(OAST 505-63-50): Charles V. Spain and Kathleen A. Conley	
Aileron Buzz Characteristics for Several NASP Wing Configurations	123
(OAST 505-63-50): Ellen P. Bullock, Charles V. Spain, and David L. Soistmann	
Dynamic Response of Initially Deformed Composite Plates Using Finite Elements	124
(OAST 505-63-50): Stephen A. Rizzi	
Influence of Post-Forming Processing on Tensile Properties of Superplastic Al-Li Alloys	125
(OAST 505-63-50): Stephen J. Hales and John A. Wagner	
Analysis of Thermomechanical Fatigue of Unidirectional Titanium Metal-Matrix Composites	126
(OAST 505-63-59): W. S. Johnson, M. Mirdamadi, and Y. A. Bahei-El-Din	
Minimum Performance Requirements for Unpowered Landings of Lifting-Body Vehicles	127
(OAST 505-64-52): Bruce Jackson	
Guidance and Control System for Maneuvering in Hypersonic Flight	128
(OAST 505-64-40): David L. Raney and Frederick J. Lallman	
Visualization of Supersonic Mixing of Helium Into Air	129
(OAST 505-65-31): Behrooz Shirinzadeh, R. Jeffrey Balla, Mervin E. Hillard, John B. Anders, and Reginald J. Exton	

Large-Amplitude Finite-Element Flutter Analysis of Composite Panels in Hypersonic Flow 129
(OAST 505-80-31): Carl E. Gray, Jr.

Aerothermal Study of Axial Compression Corner With Shock Impingement at Mach 6 130
(OAST 506-40-21): S. Venkateswaran, L. Roane Hunt, and David Witte

No Draft, Unique Slip-Cast Wind-Tunnel Models 131
(OAST 506-40-41): P. Vasquez

Application of Efficient Direct Simulation Monte Carlo Algorithm to Delta Wing 131
(OAST 506-40-91): D. F. G. Rault, R. G. Wilmoth, and G. Bird

Development of Three-Dimensional Nonlinear Flux-Based Thermal Finite-Element Capability 132
(OAST 506-43-71): Sandra P. Polesky, Pramote Dechaumphai, Christopher E. Glass, and A. K. Pandey

Effect of Processing on Strength of EDB Honeycomb Sandwich Structure 133
(OAST 506-43-71): Eric K. Hoffman and R. Keith Bird

Atmospheric Disturbance Model for NASP Applications 134
(OAST 763-01-51): John D. McMinn and John D. Shaughnessy

Wind-Tunnel Blockage Tests of Scramjet Inlet at Mach 10 135
(OAST 763-23-21): Scott D. Holland

Numerical Study of External Burning Flow Fields 136
(OAST 763-23-21): Robert D. Bittner

Computational Analysis of Hypersonic Scramjet Combustor Flows 137
(OAST 763-23-21): Robert D. Bittner, Glenn J. Bobskill, David W. Riggins, and R. Clayton Rogers

Lightweight Coatings Protect Titanium Alloys From Oxidation in Hypersonic Environments 138
(OAST 763-23-41): R. K. Clark and K. E. Wiedemann

NASP Forebody Contour Trade Study Benchmark 139
(OAST 763-23-61): Arthur D. Dilley and Richard W. Hawkins

Scramjet Module-to-Module Interaction Study 140
(OAST 763-23-61): Thomas N. Jentink and Arthur D. Dilley

Space Transportation

Measurement of Acoustic Property Temperature Derivative at Adhesive Bondline for Determination
of Bond Integrity 143
(QSRMQ 323-51-66): Al Smith

OSEE—Analysis of Surface Contamination Monitor 144
(QSRMQ 323-51-66): William T. Yost

Aerobrake Pressure Port Vacuum Adapter 144
(OAST 505-59-50): H. G. Walthall

Global Heat-Transfer Measurements Using Relative-Intensity Two-Color Phosphor Thermography 145
(OAST 505-59-50): N. Ronald Merski

Wear Performance of Modified Space Shuttle Main-Gear Tire	146
(OAST 505-63-10): Robert H. Daugherty and Sandy M. Stubbs	
Resistance Spot Welding of Advanced Aluminum Alloys	146
(OAST 505-63-50): R. Hafley and J. Wagner	
Aerothermodynamic Measurement and Prediction for Modified Orbiter at Mach 6 and 10 in Air	147
(OAST 506-40-41): J. R. Micol	
Aerodynamic Characteristics of HL-20/HL-20A Lifting-Body Configurations	148
(OAST 506-40-41): George M. Ware and B. Spencer, Jr.	
Energetics of Gas-Surface Interactions in Transitional Flows at Entry Velocities	150
(OAST 506-40-91): R. G. Wilmoth, V. K. Dogra, and J. N. Moss	
Asynchronous, Macrotasked Relaxation Strategies for Solution of Viscous, Hypersonic Flows	150
(OAST 506-40-91): P. A. Gnoffo	
Comparison of Heating Rate Calculations With Experimental Data on Space Shuttle Orbiter at Mach 6	151
(OAST 506-40-91): H. H. Hamilton II, F. A. Greene, and K. J. Weilmuenster	
Advanced Information Processing System for Advanced Launch System	152
(OAST 506-59-61): Felix L. Pitts	
Analytic Redundancy Management for Large Flexible Structures	153
(OAST 506-59-61): Joram Shenhar and Raymond Montgomery	
Radiation Exposure Analysis for High-Altitude Aircraft	154
(OSF 906-11-01): John E. Nealy and John W. Wilson	

Space Station

Preintegrated Structures for Space Station <i>Freedom</i>	157
(OSF 476-14-07): Patrick A. Troutman and Phil Mutton	
Restructured Space Station <i>Freedom</i> Controllability	158
(OSF 476-14-07): Patrick A. Troutman, Michael L. Heck, and Renjith R. Kumar	
Power Optimal Single-Axis Articulating Strategies	159
(OSF 476-14-07): Renjith R. Kumar and Michael L. Heck	
Utilization of Common Modules on Space Station <i>Freedom</i>	160
(OSF 476-14-07): Marston Gould and Dan Mazanek	
Space Station Module Pattern Evolution	161
(OSF 476-14-07): Marston Gould	
Growth Capability of Solar Alpha Rotary Joint	162
(OSF 476-14-07): Donald W. Monell	
Real-Time Optimized Resolved Rate Control of Laboratory Telerobotic Manipulator	163
(OAST 505-11-22): L. Keith Barker	
Multidisciplinary Optimization of Space Structures	164
(OAST 506-43-41): Sharon L. Padula	

Analytical Simulation Confirms Feasibility of Space Station Modal Identification Experiment	165
(OAST 585-01-31): Paul A. Cooper, Tae Lim, and Zoran Martinovic	
Middeck 0-Gravity Dynamics Experiment	166
(OAST 589-01-31): Sherwin M. Beck	
Automated Assembly of Space Structures	167
(OAST 590-11-12): Marvin D. Rhodes and Ralph W. Will	
Machine Vision for Automated Structural Assembly	168
(OAST 590-11-12): Eric G. Cooper and P. Daniel Sydow	
Kinematics Equations for Control of Redundant ARMII Manipulator	169
(OAST 590-11-22): Robert L. Williams II	
Optical Measurement System for Large-Gap Magnetic Suspension System	170
(OAST 590-14-11): Sharon S. Welch	
Dynamic Scale Model Technology for Large Space Truss Structures	171
(OAST 590-14-31): Paul E. McGowan	
Robust Alpha Joint Controller Design	172
(OAST 590-14-31): Renjith R. Kumar, Paul A. Cooper, and Tae W. Lim	
Linear Proof Mass Actuator	173
(OAST 590-14-61): S. E. Holloway III	
Solar Flare Radiation Exposure Analysis for Space Station <i>Freedom</i> Using CAD Techniques	173
(OAST 594-83-30): J. E. Nealy, G. D. Qualls, and R. M. Boykin	

Space Technology

Visual Communication	177
(AA 307-50-10): Carl L. Fales and Friedrich O. Huck	
Hyperthermal Atomic Oxygen Generator	177
(AA 307-51-10): R. A. Outlaw	
Laser Velocimetry Measurements in Nonisothermal Chemical Vapor Deposition Systems	178
(OSSA 412-20-14): Ivan O. Clark	
Design and Analysis of SAFIRE Instrument	179
(OSSA 426-42-01): Robert D. Averill, Robert W. Moses, and William A. Roettker	
Smart Structures Research	180
(OAST 506-43-11): Claudio O. Egalon and Robert S. Rogowski	
Effects of LDEF Exposure on Polymeric Matrix Composites	181
(OAST 506-43-21): W. S. Slemph	
Prediction of Thermally Induced Damage in Composites for Spacecraft Applications	181
(OAST 506-43-21): D. E. Bowles	
PAEI High-Quality Film for Precision Segmented Reflectors	182
(OAST 506-43-21): John W. Connell and Tim W. Towell	

Vibration of Axially Loaded Column With Piecewise Constant Cross Section	183
(OAST 506-43-41): Mark Lake	
Photogrammetric Surveys Verify PSR Test-Bed Truss Surface Accuracy and Coefficient of Thermal Expansion	183
(OAST 506-43-41): Timothy J. Collins and W. B. Fichter	
New Method Controls Thermal Distortion of Space Antenna	184
(OAST 506-43-41): Robert H. Tolson	
Spaceflight Application of Erasable Programmable Logic Devices	185
(OAST 506-48-01): D. Rosenbaum	
Demonstration of Self-Correcting Techniques for Large Antennas	186
(OAST 506-59-41): L. C. Schroeder and M. C. Bailey	
High-Power Semiconductor Diode Laser for Optical Communication Applications	187
(OAST 506-59-41): Herbert Hendricks	
High-Activity CO-Oxidation Catalyst for Air Purification	188
(OAST 506-59-51): David R. Schryer and Billy T. Upchurch	
Integrated Structural/Thermal Model of SUNLITE Optical Bench	189
(OAST 589-01-11): Kelly D. Smith and Ruth M. Amundsen	
Verification of Integrated Controls-Structures Design of CSI Evolutionary Model	190
(OAST 590-14-51): Peiman G. Maghami	
Comparison of Controller Designs for CSI Evolutionary Model	191
(OAST 590-14-11): Kyong Lim	
Solar Array Vibration Parameters of Hubble Space Telescope Identified From Flight Data	192
(OAST 590-14-21): Jer-Nan Juang, Lucas G. Horta, Keith W. Belvin, and John Sharkey	
Control Experiments of CSI Evolutionary Model Test-Bed	193
(OAST 590-14-61): Lucas G. Horta, Anne Bruner, Jeff Sulla, Keith W. Belvin, Kenny Elliott, and Jer-Nan Juang	
Results of Phase I CSI Guest Investigator Program	194
(OAST 590-14-91): R. Smith-Taylor	
Application of Titanium-Doped Sapphire Laser Technology to LASE Project	194
(OAST 590-31-31): James C. Barnes	
High-Speed Fiber Optic Transceiver Description	195
(OAST 590-32-11): Herbert Hendricks	
Advanced Multiprocessing Strategy	196
(OAST 590-32-31): Paul J. Hayes	
Modeling of Spaceflight Optical Disk Recorder	197
(OAST 590-32-21): Glenn Hines	
Solar Dynamic Concentrator Support Truss Enables Replacement of Collector Panels	198
(OAST 590-33-31): Walter L. Heard, Jr., Harold G. Bush, and Catherine L. Herstrom	
Aerobrake Panel Support Concept Results in Zero Slope Along Panel Edge	198
(OAST 591-22-21): John T. Dorsey	

Science Data Interface to Space Shuttle Payload Data Interleaver System	199
(OSSA 618-22-31): M. Grant	
Diode Laser Injection Seeding of LASE Laser	200
(OSSA 618-32-33): L. G. Wang, W. C. Edwards, G. W. Sachse, J. C. Barnes, and R. V. Hess	
Data Acquisition for Lidar Applications	201
(OSSA 618-32-33): J. Williams	
Effects of Long-Duration Exposure on UV Optical Components	202
(OSSA 678-12-04): Gale A. Harvey	
Organic Contamination of LDEF	202
(OSSA 678-12-04): Gale A. Harvey	
Determination of Temperature Anomalies in Space Shuttle Furnace Calibration	203
(OSSA 694-80-70): Archibald L. Fripp	

Exploration

Contribution of Galactic Cosmic Ray Ion Fragmentation to Radiation Risk	207
(OSSA 199-04-16): L. W. Townsend, J. Wilson, F. A. Cucinotta, and J. L. Shinn	
Nonequilibrium Radiative Heating and Influence of Energy Exchange Models	207
(OAST 506-40-91): L. C. Hartung, R. A. Mitcheltree, and P. A. Gnoffo	
Adaptive Guidance Algorithm for Manned Mars Aerobraking Vehicles	208
(OAST 506-49-11): Richard W. Powell and Robert D. Braun	
Design Considerations Enabling Low Lift-to-Drag Ratio Aerobrakes for Manned Mars Missions	209
(OAST 506-49-11): Robert D. Braun, Scott A. Striepe, and Richard W. Powell	
Experimental Aerothermodynamic Characteristics of AFE Engine/Ballute Concept	210
(OAST 592-01-11): Scott A. Berry	
Viscous Shock-Layer Analysis for Mars Aerobraking Entry	211
(OAST 593-11-21): R. N. Gupta, J. N. Moss, K. Sutton, and K. P. Lee	
Exploration Mission Radiation Exposure: Analysis of October 1989 Solar Proton Event	212
(OAST 593-42-31): Lisa C. Simonsen and John E. Nealy	
Aerobrake/SSF Minimum Accommodation Study—Phase II	213
(OAST 594-81-21): Stephen Katzberg and Dave Haynes	
Aerobrake Concept Selection and Integration for Lunar Transportation System	214
(OAST 594-81-21): Dave Haynes and Joe Rehder	
Manned Lunar Habitat Concepts	214
(OAST 594-84-20): Warren D. Hypes, Robert L. Wright, and Marston J. Gould	

Global Change

Radiation Budget of Atmosphere in Thermal Infrared Wavelengths	217
(OSSA 146-74-04 and OSSA 672-22-26): Thomas P. Charlock and G. Louis Smith	
Biomass Burning and Production of Nitrous Oxide	218
(OSSA 199-30-76): Wesley R. Cofer III, Joel S. Levine, and Edward L. Winstead	
Gaseous and Particulate Emissions From Kuwaiti Oil Fires	218
OSSA 199-30-76): Joel S. Levine, Donald R. Cahoon, Jr., and Wesley R. Cofer III	
Cloud-Pumping Theory and Global Simulation of Pollution	219
(OSSA 199-30-76): Robert C. Costen, Geoffrey M. Tennille, and Joel S. Levine	
Long-Term Monitoring of Clouds by Lidar	220
(OSSA 460-42-08): David Winker	
Spectroscopic Measurement of HO ₂ , H ₂ O ₂ , and OH in Stratosphere	221
(OSSA 464-12-03): Jae H. Park	
Diurnal Variation of Ozone in Middle Atmosphere	222
(OSSA 464-13-19): Brian J. Connor	
Simple Method for In Situ Production of High-Purity Ozone	223
(OSSA 464-23-08): M. D. Venkataraman, C. T. Solomon, and M. A. H. Smith	
Long-Term Trends of Hydrogen Fluoride and Hydrogen Chloride	224
(OSSA 464-44-02): Curtis P. Rinsland	
Effects of African Fires on Southern Hemisphere	225
(OSSA 464-51-01): Jack Fishman	
Airborne Lidar Investigation of Ozone and Aerosols Over Canada	226
(OSSA 464-54-16): Edward V. Browell	
Accuracy of Nimbus 7 LIMS Temperatures in Arctic Stratosphere	227
(OSSA 579-21-44): Ellis E. Remsberg	
Efficiency of Solar Heating in Middle Atmosphere	228
(OSSA 579-21-44): Martin G. Mlynczak	
Polar Stratospheric Cloud Climatology From SAM II	228
(OSSA 665-10-40): Lamont R. Poole	
Stability of ERBE Scanner Measurements	229
(OSSA 665-45-30): W. Frank Staylor	
ERBE Observations of 1987 El Niño Event	230
(OSSA 665-45-30): Edwin F. Harrison	
Systematic Variability in Total Solar Irradiance	231
(OSSA 665-45-30): Robert B. Lee III	
Mass Loading of Stratospheric Aerosols	231
(OSSA 665-45-30): Glenn K. Yue	

Observation of Stratospheric Response to Solar Proton Events	232
(OSSA 665-54-30): Joseph M. Zawodny	
Global Ozone Trends From SAGE I and SAGE II Measurements	233
(OSSA 665-45-30): William P. Chu	
Measurement of Tropospheric Aerosols From Space Using Solar Occultation Techniques	234
(OSSA 665-45-30): M. P. McCormick	
Anthropogenic Trends and Solar Effects on Total Column Ozone	235
(OSSA 673-56-05): Gerald M. Keating, G. Brasseur, L. S. Chiou, and N. C. Hsu	

Facilities

Reduction of Tire Characterization Test Time by Variable Yaw System	239
(OAST 505-63-10): Robert H. Daugherty	
Statically Unstable Model on Cable Mount System	239
(OAST 505-63-50): Michael H. Durham and Donald F. Keller	
TDT Data Acquisition System Improvements	241
(OAST 505-63-51): David C. Rosser, Jr.	
Compressible Turbulent Boundary-Layer Predictions Use Langley 8-Foot HTT Data	241
(OAST 506-40-21): Cindy W. Albertson and Richard W. Barnwell	
Improved Fuel Injector for Langley 8-Foot HTT Developed	242
(OAST 506-42-31): Richard L. Puster	
Convective Temperatures and Heat-Transfer Coefficients on Spray Bar of Langley 8-Foot HTT	243
(OAST 506-43-31): Marco A. Egoavil	
Langley Jet Noise Laboratory Forward Flight Simulator	244
(OAST 537-02-22): John M. Seiner and James C. Manning	
Space Structures Research Laboratory Placed Into Operation	245
(OAST 590-14-61): Robert Miserentino, Keith Belvin, and Paul McGowan	

Technology Utilization

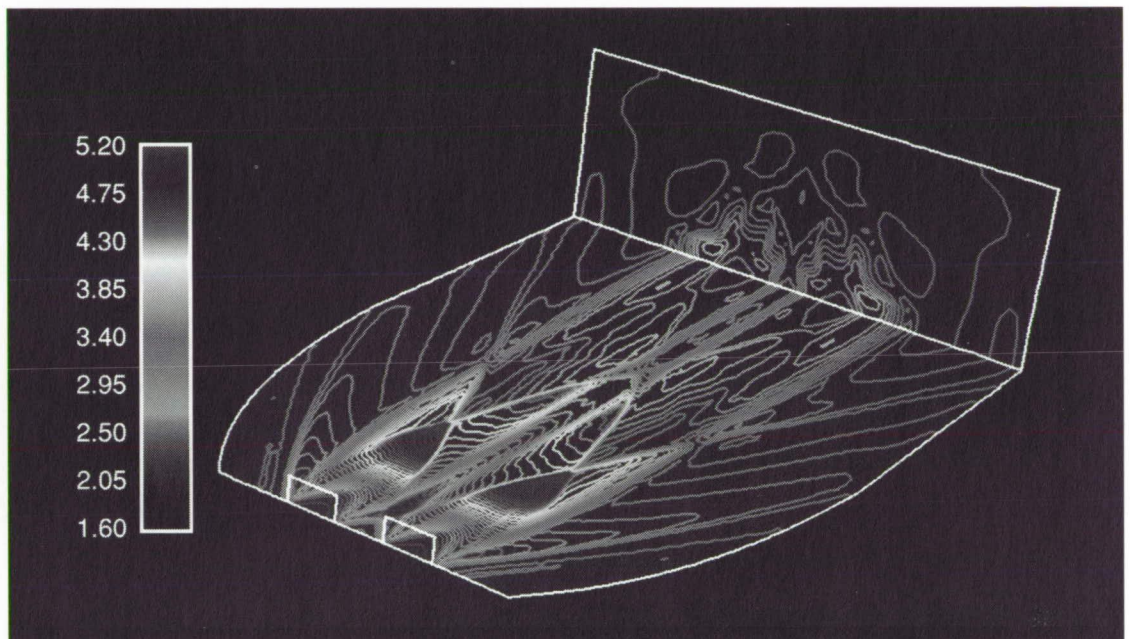
X-Ray Spectroscopy of Contact Lens Polymers	247
(OCP 141-20-10): Jag J. Singh and Chih-Ping Shen	
Carbon-Carbon Piston Development	247
(OCP 141-20-10): Mark P. Gorton and John L. Shideler	
Ultrasonic Dosimetry	248
(OCP 141-20-40): William T. Yost and John H. Cantrell	
Surgical Force Detection Probe	249
(OCP 141-20-40): P. Tcheng, Charles Scott, and Paul Roberts	

Remote Semicontinuous Flow Rate Logging Seepage Meter	250
(OCP 141-30-10): H. G. Walthall	
Ceramic Susceptor for Induction Bonding of Metals, Ceramics, and Plastics	250
(OCP 141-30-10): R. L. Fox	
Benchmark Active Controls Model Actuator	251
(OAST 505-63-50): Michael R. Sorokach, Jr.	
CAD Interface Programming to Aid Model Fabrication	251
(OAST 535-03-01): Christopher M. Cagle and Melinda F. Cagle	

Contributing Organizations

Aeronautics Directorate	255
Electronics Directorate	255
Flight Systems Directorate	256
Space Directorate	256
Structures Directorate	257
Systems Engineering and Operations Directorate	259
Technology Utilization	260

■ FUNDAMENTAL KNOWLEDGE



*Provide understanding of
physical phenomena and
verified computational
techniques important to the
design and operation of
advanced aeronautical systems*

Ferroelectric Liquid-Crystal Thin-Film Boundary-Layer Sensor

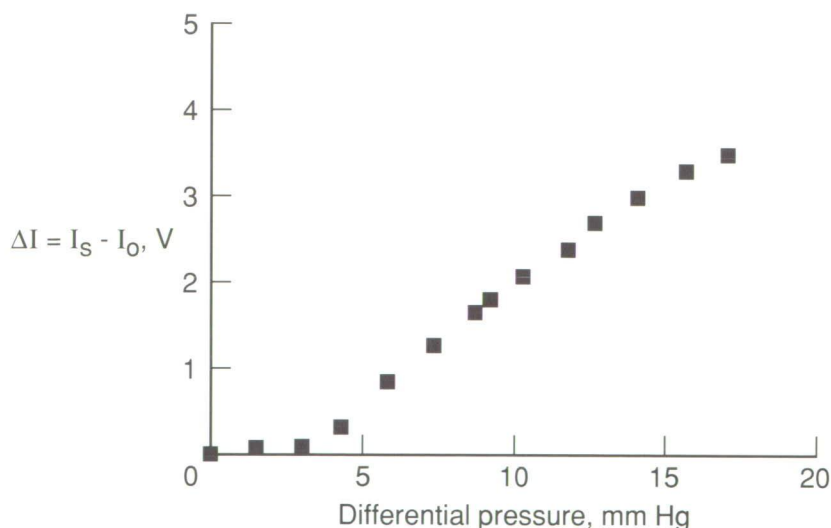
A new boundary-layer sensor for quantitative measurement of the flow field has been developed with shear-induced optical switching in ferroelectric liquid-crystal thin ($\sim 1\text{-}\mu\text{m}$) films. Shear stresses caused by wind flow on the model surface, placed under crossed polarizers, reorient the molecules of the system and switch them (within microseconds) to a new optical state that can be detected from the intensity of the transmitted or reflected light from the boundary layer. Measurement of the intensity of the transmitted or reflected light from the model surface as a function of the

wind flow provides direct quantitative measurement of the boundary-layer shear stress field. For an applied airflow differential pressure Δp , the change ΔI in the transmitted light intensity follows the relation $\Delta I \sim \sin^2(\Gamma/2)$, where $\Gamma = (\Delta n + \delta\Delta n) k_0 d$ is the amplitude of the phase retardation for an incident light of wave vector k_0 propagating through a film of thickness d and the birefringence Δn , and $\delta\Delta n$ is the Δp induced change in birefringence. (Devendra S. Parmar, 44744, and Harlan K. Holmes) Electronics Directorate

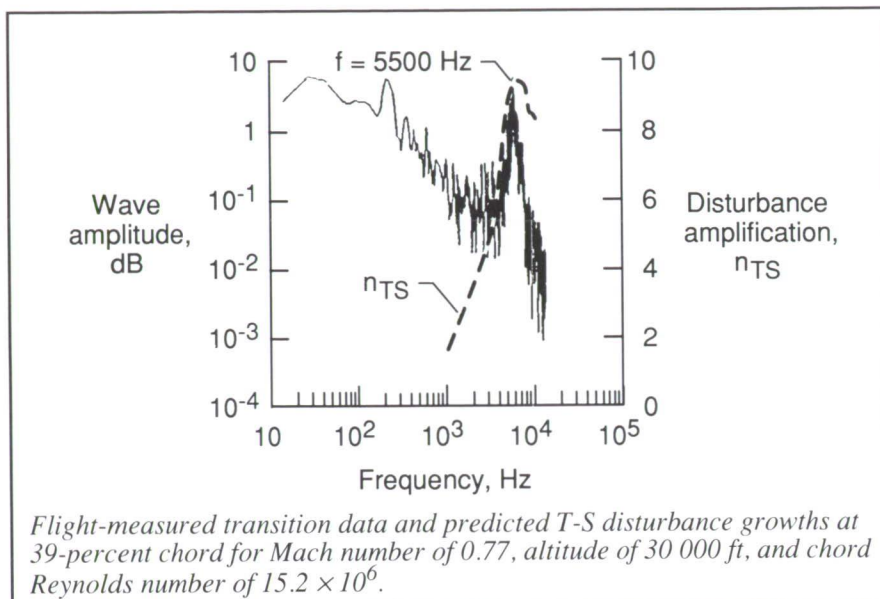
Analysis of Flight-Measured Boundary-Layer Transition Data

Current laminar-flow research conducted by NASA is focused on understanding the dominant instability modes responsible for initiating the transition process from laminar to turbulent flow. Recent flight experiments were conducted to study, in detail, the growth of Tollmien-Schlichting (T-S) and crossflow instabilities in the laminar boundary layer on a gloved surface of a Lear Model 28/29 airplane.

The purpose of these experiments was to help validate computational fluid dynamics (CFD) compressible linear stability theory through measurement of the instability mechanisms. Results have shown the ability to detect T-S and crossflow wave frequencies from detailed analysis of the measured hot-film signals. Power spectral density analyses were made of the hot-film signals to determine the dominant frequencies. These frequencies are shown in the figure where a spike in the measured wave amplitude occurs at a frequency of 5500 Hz. This signal was obtained at a chord location of 39 percent, just ahead of the measured transition location of 40-percent chord. The CFD analysis of the boundary layer using compressible linear stability theory predicted a comparable frequency for the maximum disturbance amplification of the T-S waves, which is also shown in the figure. This research has provided information on the disturbance growth and transition



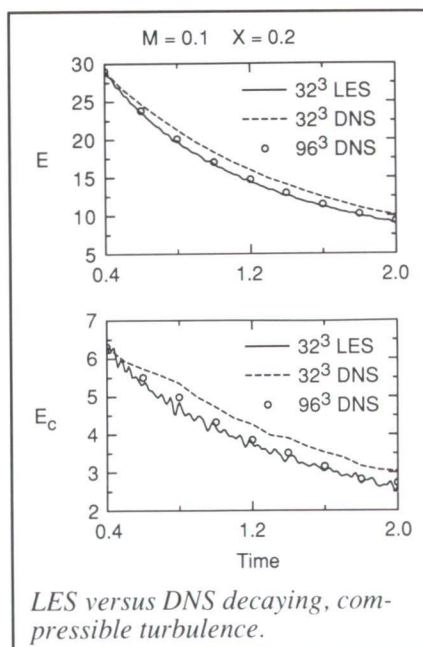
Variation of transmitted light intensity with shear stress. I_s is light intensity in presence of shear stress and I_0 is light intensity in absence of shear stress.



mode that is essential to the understanding of design limits for applications of laminar-flow technology. (Clifford J. Obara, Cynthia C. Lee, and Paul Vijgen, 43941) Aeronautics Directorate

Compressible Large-Eddy Simulation of Isotropic Turbulence

Extensive testing has been conducted on a subgrid-scale (SGS) model proposed for compressible large-eddy simulation (LES) by Speziale, Erlebacher, Zang, and Hussaini. The first step consisted of generating an extensive new set of direct numerical simulation (DNS) data on 96^3 grids. These data covered a range of fluctuating Mach numbers M and fraction of compressible energy χ , the key parameters in compressible turbulence according to a recent theory developed at the Institute for Computer Applications in Science and Engineering. The proposed SGS model was utilized in LES for all of these cases.



The figure compares the time evolution of the kinetic energy of decaying, isotropic turbulence from three different runs (a fine-grid (96^3) DNS, a coarse-grid (32^3) DNS, and a coarse-grid (32^3) LES). As shown in the figure, the coarse-grid LES does quite well on the total kinetic energy E , but it is somewhat less accurate for the compressible component of the kinetic energy E_c . Moreover, the coarse-grid

LES does substantially better than a coarse-grid DNS. The model constants were adjusted slightly from those proposed originally in order to achieve better agreement with DNS for the specific parameters M and χ of this case. The agreement of the LES results with the DNS data for other values of these two parameters is less good, but definite trends exist as the M and χ are changed. Subtle changes in the model itself appear necessary to obtain more consistent predictions throughout the compressible regime.

Previous tests of this SGS model were based solely on DNS data and did not include actual large-eddy simulations. The results show that this first-cut SGS model for compressible turbulence performs better than anticipated. Moreover, they contain some hints about what improvements need to be incorporated.

(Thomas A. Zang, Russell B. Dahlburg, and Jill P. Dahlburg, 42307) Aeronautics Directorate

Development of High-Order Shock-Capturing Methods

Research in the fields of aeroacoustics, transition physics, and turbulence demands extreme precision. For this reason, spectral-based methods have been the primary tool for numerical investigations. Unfortunately, several large classes of problems exist for which a spectral approach is not feasible. One of these areas is flow that contains complex shock structures.

Shock-capturing methods that are commonly used in applied aerodynamics are usually low-order methods and are not suitable as a research tool in the areas just mentioned. Direct

extension of these tools to a higher order approach usually results in numerical oscillations that destroy the solution. The recent development of essentially nonoscillatory (ENO) methods has provided a means to implement a high-order shock-capturing method.

The ENO techniques, which are inherently one-dimensional, have been extended to multidimensional domains and applied to the solution

accurate methods. However, at later times, the disturbances interact nonlinearly and, in the particular case shown, form a shock within the flow. Grid refinement studies have verified that the fundamental and important harmonics are well-resolved on a 64 by 128 grid.

When compared to low-order shock-capturing methods, the ENO methods are more expensive in terms of cost per point; however, the

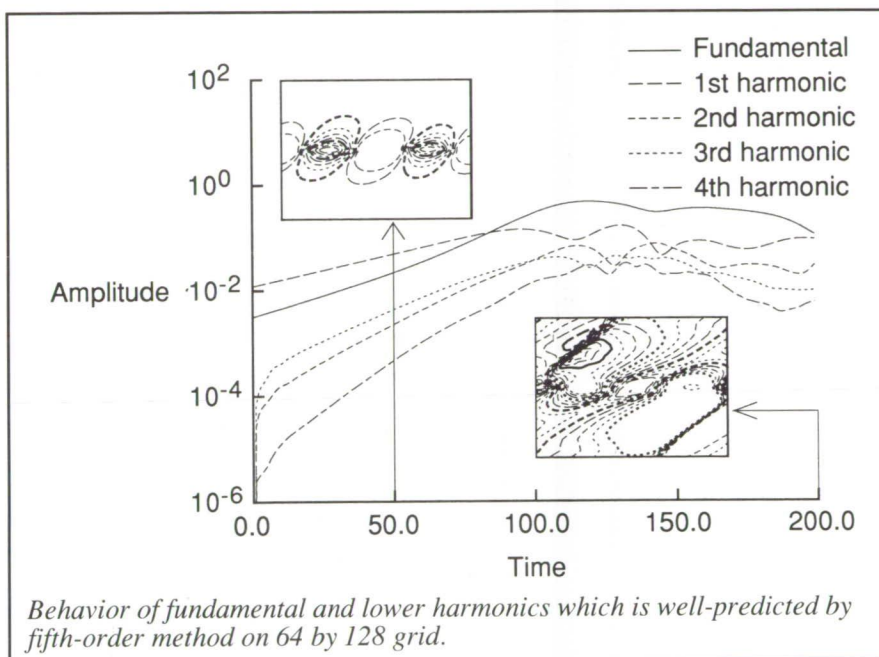
Compressible Boundary-Layer Transition Using PSE

The objective of this research is to study and understand the mechanisms involved in compressible boundary-layer transition. The ultimate goal is to provide a capability for boundary-layer transition prediction in both quiet and disturbed environments. This study employs parabolized stability equations (PSE) for linear and nonlinear development of disturbances in growing boundary layers.

In the PSE approach, the partial differential equations for the evolution of disturbances in compressible boundary layers are simplified with a parabolizing assumption. The resulting parabolized stability equations are solved numerically by a marching procedure in the streamwise direction.

As a consequence, the PSE method provides a much more efficient procedure than direct numerical simulations using the full Navier-Stokes equations. The PSE method can be used to study the nonparallel and nonlinear evolutions of disturbances in compressible boundary layers, starting from the linear stage up to transition. Coupled with receptivity phenomena (i.e., the initiation of disturbances in the boundary layer), the present approach offers a computationally viable means to study and predict the complex and intricate phenomenon of compressible boundary-layer transition.

The PSE code developed in this study can handle both two-dimensional and three-dimensional disturbances for flat-plate geometries. Nonlinear PSE results for a Mach 1.6 boundary layer indicate that secondary instability mechanisms, such as subharmonic or fundamental breakdown procedures similar to those in compressible flows, may occur for supersonic flows,



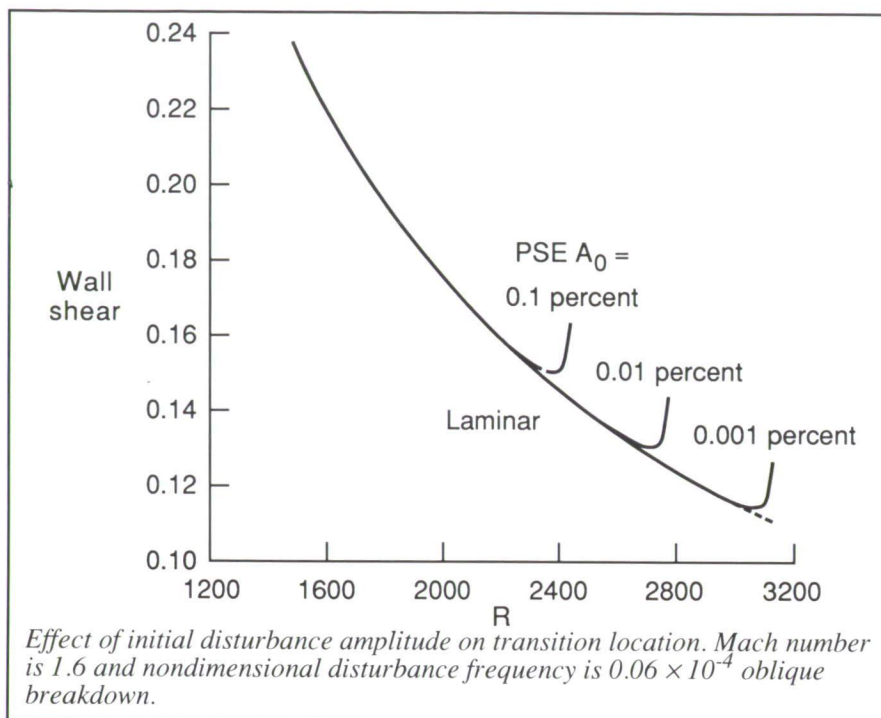
of the unsteady compressible Navier-Stokes equations. The finite-difference approach was chosen for its efficiency of computation and economy of storage. The ENO methods as high as sixth-order have been validated on a variety of basic two- and three-dimensional flows.

A test case, which is of relevance to transition physics, is illustrated by the temporally growing shear layer. In this flow, a steady-state mean flow is agitated by a very small disturbance. The initial behavior of the disturbance is well-known from other, more

improved accuracy reduces the number of points required to the degree that the overall cost is less. The payoff of the high-order approach will be more pronounced in three-dimensional simulation.

Development is continuing in the areas of inflow/outflow and wall boundary conditions that preserve the high-order properties. Such methods are expected to be a useful research tool in all areas in which a high degree of precision is needed.

(H. L. Atkins, 42308)
Aeronautics Directorate



Numerical Simulation of Laminar Breakdown in Supersonic Transition

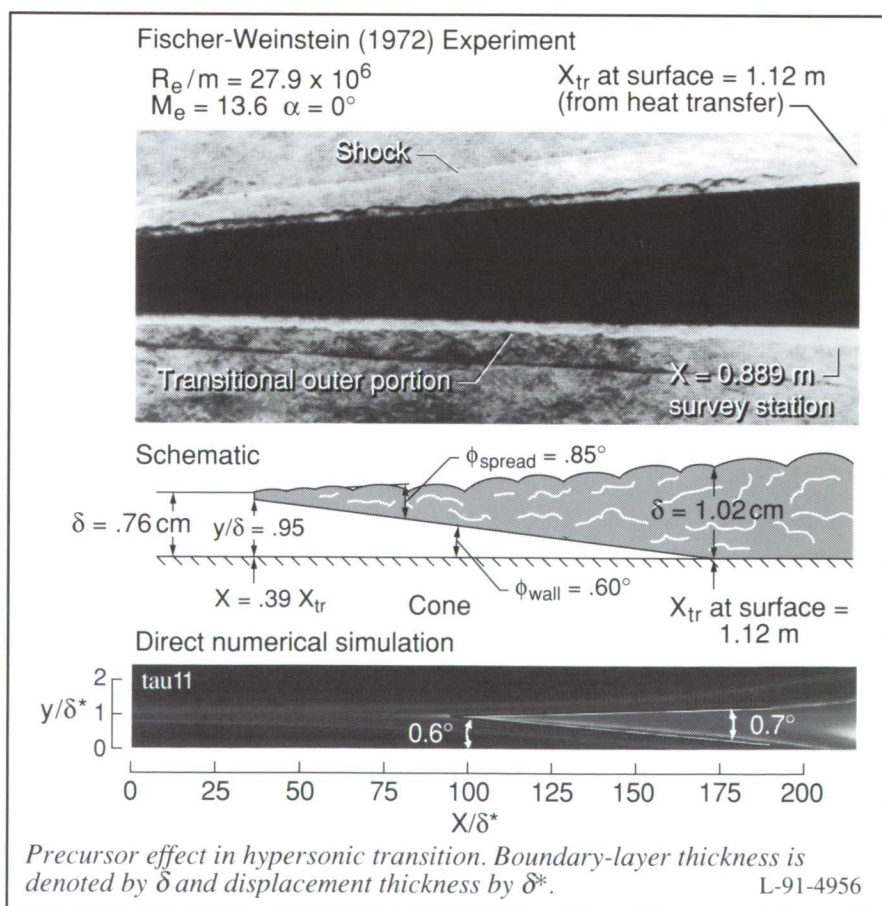
Numerical simulation has been utilized to study the rope-like structures and the precursor transition effect that have been observed experimentally in supersonic transition since the 1960's. The rope-like structures refer to the braided patterns that are visible near the boundary-layer edge in schlieren photographs. The precursor transition effect refers to the origination of transitional disturbances near the boundary-layer edge a considerable distance upstream of the first detection of transition by surface measurements.

Two high-resolution numerical simulations of the strongly nonlinear,

provided the initial amplitude of the two-dimensional primary wave is sufficiently high. Because three-dimensional waves are the most amplified modes for supersonic boundary layers, a more likely route to transition may consist of two oblique primary waves interacting with each other. The PSE results show that the initial amplitude required for this oblique breakdown to occur is significantly lower compared with that for the secondary mechanisms. The figure shows the wall shear versus Reynolds number $R = \sqrt{RE_x}$ for the oblique breakdown procedure for three different initial amplitudes at the given frequency. Transition location is clearly indicated by the rise of wall shear.

(C. L. Chang and M. R. Malik, 45563)

Aeronautics Directorate



laminar breakdown stage of supersonic transition to turbulence were conducted (for Mach 4.5 flow past a cylinder and for Mach 6.8 flow past a cone). The top frame of the figure shows a schlieren photograph that is typical of experimental results for transition on a cone in hypersonic flow. (The measurements were performed for a cone at angle of attack $\alpha = 0$, for a Mach number at the boundary-layer edge M_e , and a Reynolds number per meter R_e/m , as noted on the figure. Distance along the surface of the cone is denoted by X , and X_{tr} denotes the location on the surface at which transition was detected.) The essential features are displayed in the middle of the figure. The angle that the disturbed region makes with respect to the wall is denoted in the figure by ϕ_{wall} , and the spreading angle of the entire disturbed region is denoted by ϕ_{spread} . The turbulence intensities extracted from the computation for the Mach 6.8 cone case (bottom frame) display these key features. In particular, the precursor transition effect has been captured, with even the spreading angles of the disturbance regions in good agreement with the experimental range (between 0.5° and 1°). Moreover, numerical schlieren flow-field visualizations from the simulation display rope-like structures remarkably similar to those that have been observed experimentally.

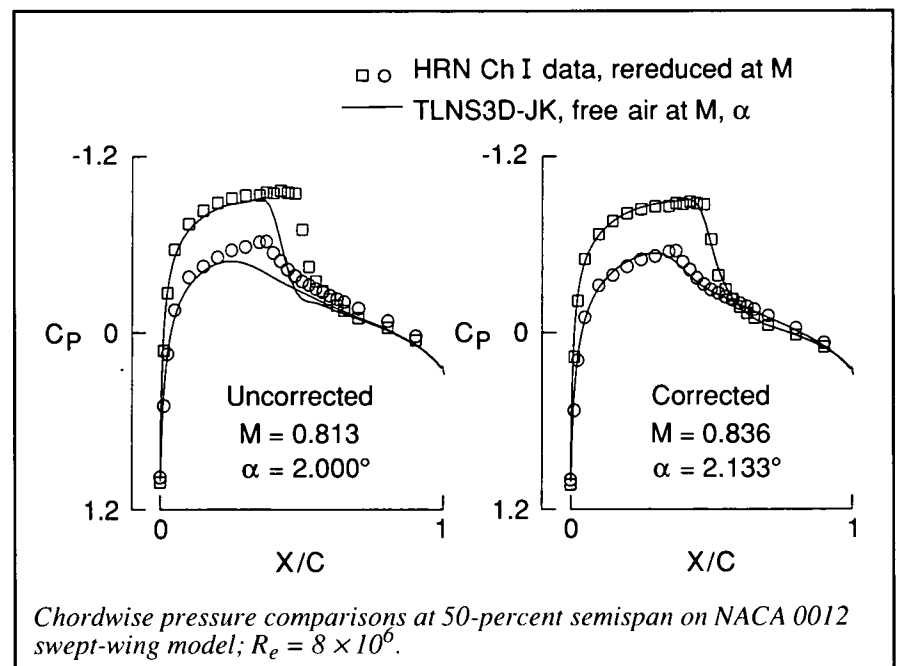
A comparison of linear stability theory, secondary instability theory, and numerical simulation results for the spreading angle of the disturbances indicates that the spreading rate cannot be attributed to linear instability alone (as has long been believed), nor even to secondary instability, but is, indeed, a strongly nonlinear effect. (C. David Pruett and Thomas A. Zang, 42307) Aeronautics Directorate

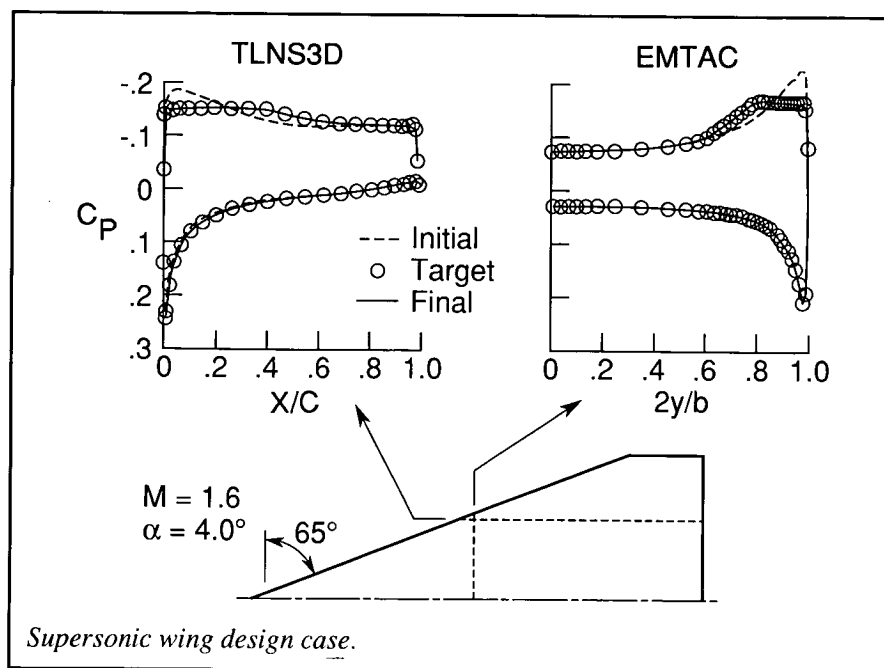
Wind-Tunnel Interference and Assessment Code Development

Transonic test data from wind tunnels, such as the National Transonic Facility (NTF), generally contain wall interference that must be assessed and, if significant, corrected. Over the past several years, both linear and nonlinear computational fluid dynamics (CFD) codes have been developed for the NTF. These codes are applied after the test, using pressure data measured at the test section wall in lieu of classical wall boundary conditions. The latest nonlinear code, WIACX, was jointly developed with Vigyan, Incorporated, by incorporating wall interference correction concepts into the CAP-TSD (Computational Aeroelasticity Program—Transonic Small Disturbance) unsteady analysis code at Langley Research Center.

Several sets of published semispan wing data have been used to evaluate the WIACX results. In addition to comparisons of WIACX results with

those from other correction codes, an independent CFD evaluation is made as follows. The thin-layer Navier-Stokes code TLNS3D is used to generate free-air solutions at both uncorrected and corrected flow conditions; these solutions then are compared with original test data and test data rereduced at the corrected Mach number, respectively. A sample of such comparison between TLNS3D-JK (Johnson-King turbulence model) results and data from the Ames Research Center High-Reynolds-Number (HRN) Channel I for an NACA 0012 swept-wing model is shown in the figure. These chordwise X/C pressure C_p distribution data are at the 50-percent semispan wing location. The agreement at the corrected conditions is better, thus indicating reasonable corrections for Mach number and angle of attack. (Perry A. Newman, Javier A. Garriz, Veer N. Vatsa, and Kara J. Haigler, 42247) Aeronautics Directorate





only 3 to 5 design cycles were required. Because the methods converge the flow solution and design changes in parallel, the cost of a design run was approximately the same as that required for an analysis only.

(Richard L. Campbell, 42872)
Aeronautics Directorate

Numerical Simulation of Schlieren Image

The purpose of the research was to develop software to simulate schlieren images of CFD computations for comparison with schlieren images from experiment.

Advanced CFD Design Methods for Supersonic Flow

As part of the renewed research on high-speed civil transports, Euler and Navier-Stokes codes are being used in the analysis of these configurations. These advanced computational fluid dynamics (CFD) codes have been shown to be more accurate than the linear potential flow methods used in the earlier supersonic transport research. Unfortunately, most of the automated aerodynamic design capability for supersonic flows still utilizes linear potential flow methods. To help address this need, two iterative design methods have been coupled with advanced CFD codes to provide the capability of designing to a specified surface pressure distribution. The first method is the Direct-Iterative Surface Curvature (DISC) approach, originally developed for subsonic and transonic design applications. This method has been coupled with TLNS3D, a time-marching, multigrid Euler/Navier-Stokes code. A variation of the DISC approach, known as the

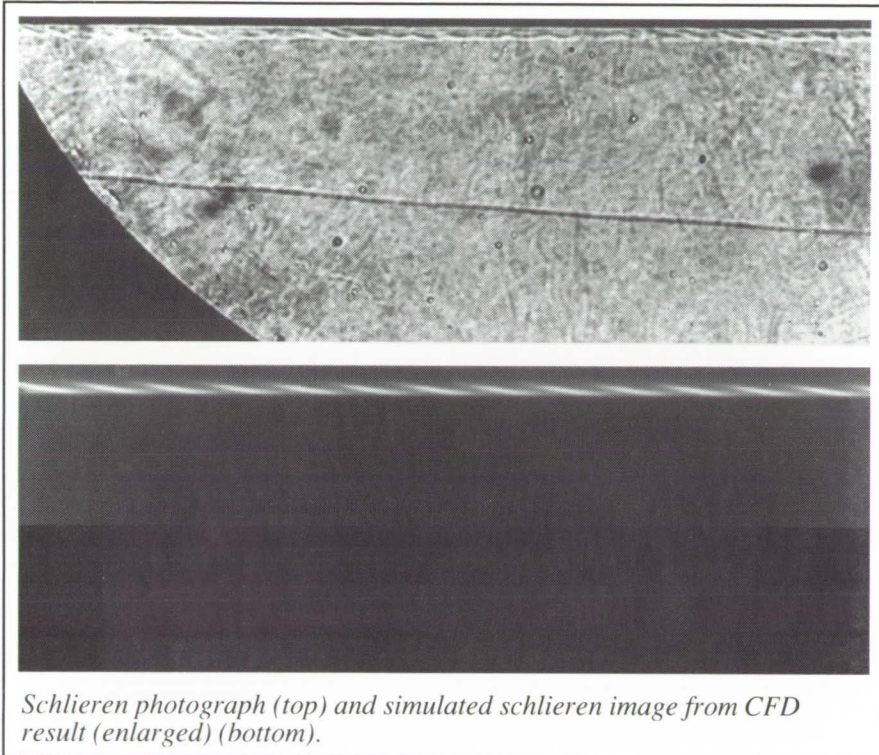
Direct-Iterative Surface Slope (DISS) method, was developed for space-marching codes and has been coupled with the EMTAC Euler code.

The figure shows design results from both codes for a cropped-delta wing at a Mach number of 1.6 and an angle of attack of 4.0° . The initial geometry had NACA 0004 airfoils in the streamwise direction. As shown by the dashed line on the pressure distribution plots, this configuration had a leading-edge peak followed by an adverse gradient over the first half of the chord for TLNS3D and over the outer half of the semispan for EMTAC. Target pressure distributions were developed by prescribing a neutral pressure gradient over the first 40 percent of the chord for TLNS3D and over the outer 20 percent of the semispan for EMTAC and then fairing into the initial pressure distributions so that the section lift coefficients were held constant. The solid line in the plots shows that the pressure coefficients for the final design cycles very closely matched the target pressure distributions. For each code,

A numerical method was developed to simulate a schlieren image in a computationally efficient manner. This method provides an effective way for CFD code validation by simulating and displaying simulated schlieren images of CFD results for direct comparison with experimental schlieren images on a workstation. The figures demonstrate the comparison of a simulated schlieren image with an experimental schlieren photograph for a laminar breakdown in a high-speed axisymmetric boundary-layer flow. In high-speed transition experiments, an unexplained rope-like wave effect is often observed near the edge of the boundary layer. The simulated schlieren image confirms that the CFD solution replicates this phenomenon. Conventional density contour plots of the CFD solution fail to reveal the rope-like wave effect; the numerically simulated schlieren image was essential to detect this feature (because of lambda vortices) in the CFD solution.

The software allows more meaningful comparisons between CFD computations and schlieren images from

ORIGINAL PAGE
BLACK AND WHITE PHOTOGRAPH



Schlieren photograph (top) and simulated schlieren image from CFD result (enlarged) (bottom).

with respect to the design variables. The ability to efficiently and accurately compute these aerodynamic sensitivity derivatives will greatly enhance the power of CFD codes as design tools.

Sensitivity derivatives have many important applications that are useful to the design engineer, including use in design optimization. These derivatives may also be used in approximate analysis (see the first figure), where changes in the response of a system are estimated as a consequence of changes in the design variables.

General procedures have recently been developed and successfully tested for computing aerodynamic shape sensitivity derivatives for compressible viscous flow using the 2-D thin-layer Navier-Stokes equations. The second figure shows the computed steady-state solution, a plot of the Mach contours,

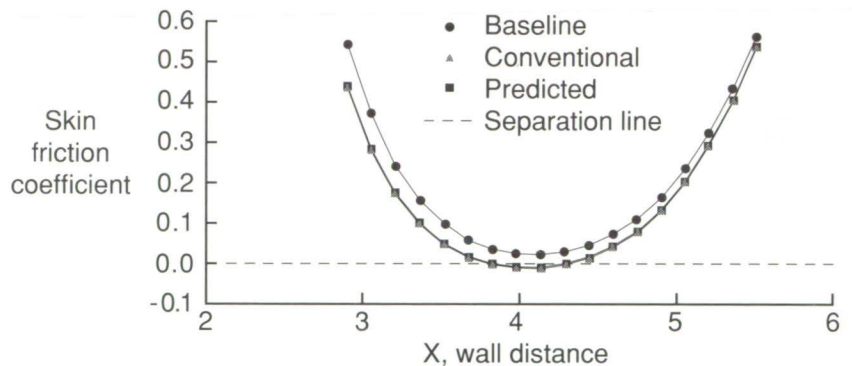
experiments, and it provides an important tool for CFD code validation.

Further research is under way to extend the capability of this software package to handle more general grid topologies.

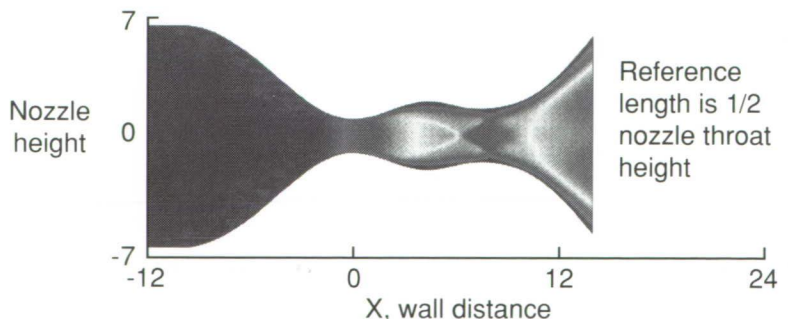
(Robert P. Weston and Beyung S. Kim, 42151)
Aeronautics Directorate

Sensitivity Analysis for Viscous Flows

For the engineer who is applying modern computational fluid dynamics (CFD) software to practical multi-disciplinary problems in a design environment, a critical need exists for the development of efficient procedures for calculating slopes (known as sensitivity derivatives). Sensitivity derivatives are defined as the derivatives of the responses of a system taken



Lower wall skin friction prediction versus conventional numerical solution. (All distances are measured in reference lengths.)



Mach contours for baseline solution; $Re_L = 100$. (All distances are measured in reference lengths.)

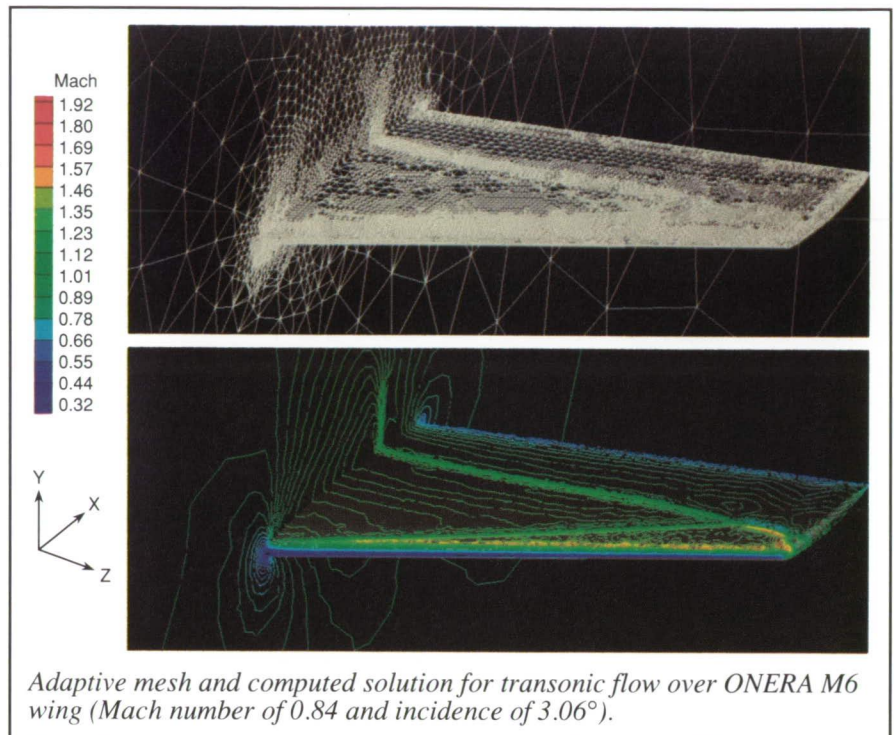
for a low Reynolds number laminar transonic flow through a double-throat nozzle. Also shown is the accurate prediction of flow separation in the nozzle through the use of sensitivity derivatives in response to a 10-percent increase in the cross-sectional area everywhere in the nozzle, where the prediction using sensitivity analysis is far less computationally expensive than the corresponding conventional CFD solution.

(Arthur Taylor and Gene Hou,
42158)
Aeronautics Directorate

Three-Dimensional Unstructured Adaptive Grid

The purpose of this research is to provide accurate and efficient solutions of inviscid compressible flow over complex three-dimensional (3-D) configurations. This effort included the development of a 3-D Euler solver in order to enable the solution of the Euler equations on arbitrary 3-D unstructured meshes and the development of a multigrid procedure to accelerate the convergence to a steady state, thus resulting in an efficient solution algorithm. An adaptive meshing strategy was also developed and implemented in conjunction with the multigrid algorithm, thus enabling the highly accurate resolution of localized flow phenomena with a relatively small number of grid points. The multigrid Euler solver was implemented on the Intel iPSC860 hypercube parallel computer.

Preliminary calculations on a simple geometry (ONERA M6 wing) have demonstrated the accuracy and efficiency of the present methodology. Solutions can be obtained in under 1 hour on a single CRAY-YMP processor or on 64 Intel iPSC860 processors.



The ability to predict flow over complex geometries is important to the aircraft industry. Work is currently under way to apply the present methodology to more complex geometries with a larger number of grid points.

(Dimitri Mavriplis, 42213)
Aeronautics Directorate

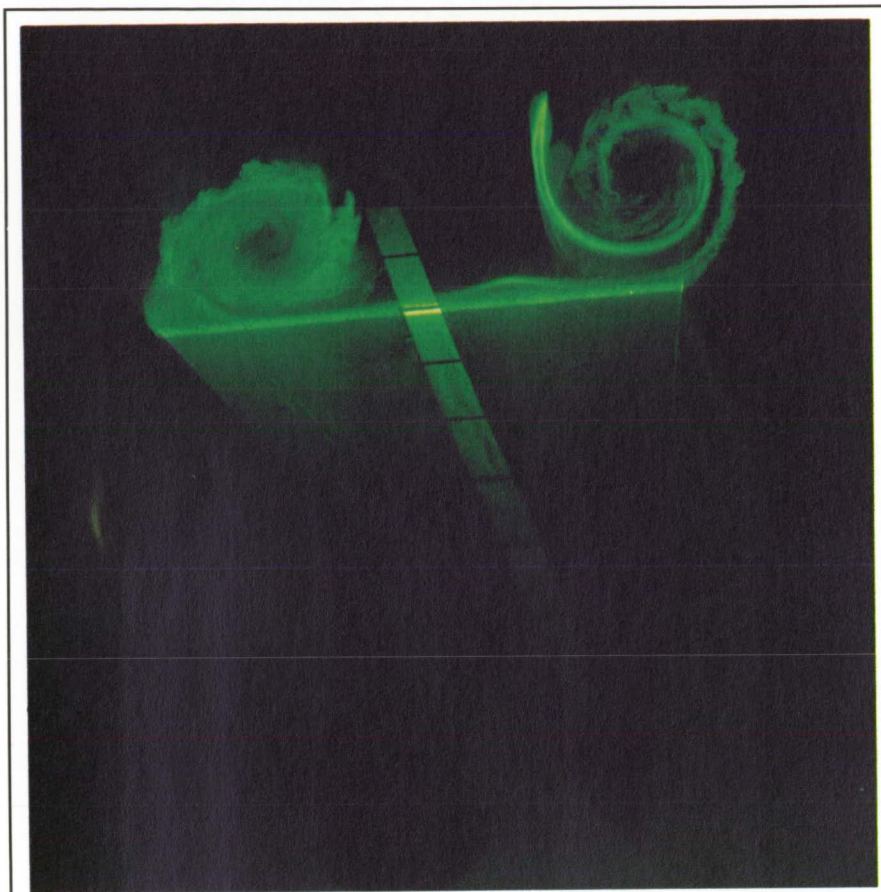
Effect of Turbulence on Flow Over Delta Wing

The existing data base for vortex flows over delta wings exhibits a considerable amount of scatter. This investigation was conducted to determine if the free-stream turbulence level can significantly influence the vortical flow field over a sharp-edged delta wing of 76° . The empty tunnel free-stream turbulence level was increased from less than 0.1-percent intensity to greater than 7-percent

intensity by placement of a grid upstream of the model. The model was tested at Reynolds numbers between 500 000 and 1 000 000 for angles of attack up to 40° and sideslip angles to 20° . Off-body and surface flow visualizations were used to examine the effect of turbulence on the vortex topology, burst position, and boundary-layer transition. In addition, force and moment data were acquired to quantify the free-stream turbulence and Reynolds number effects on the aerodynamic loads. Laser light sheet flow visualization was used to characterize the flow field. When the light sheet was pulsed, small-scale structures in the vortex shear layer were "frozen" as shown in the figure.

The increase in turbulence had a large influence on the flow field characteristics. In the case of highly turbulent flow, the boundary layer was found to be primarily turbulent at all speeds. The measured lift decreased near the angle of maximum lift for sideslip angles of less than 10° .

ORIGINAL PAGE
COLOR PHOTOGRAPH



Small-scale structures in vortices over yawed delta wing.

L-90-9929

The results indicate that the effect of free-stream turbulence levels on the leading-edge vortical flow field can be significant. Future studies will consider intermediate levels of intensity, such as those commonly encountered in a wind-tunnel environment.

(Anthony Washburn, 41290)
Aeronautics Directorate

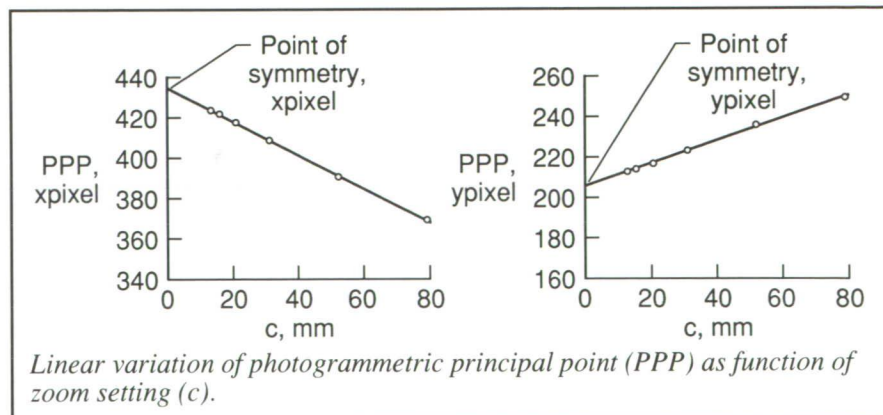
Investigation of Zoom Lenses for Digital Photogrammetry

Zoom lenses have a variable field of view that can be advantageous in

wind-tunnel applications using area array solid-state video cameras. However, a varying field of view is an additional complication in photogrammetric measurements, so zoom lenses are not normally used.

Measurements of the photogrammetric principal point and distortion as a function of the principal distance (zoom setting) of several zoom lenses have been made. The linear variation of the principal point and the variation in distortion as a function of zoom setting are in agreement with studies made at the University of Illinois at Urbana-Champaign. Personnel at Langley Research Center have postulated that the linear variation of principal point is because of misalignment of the axis of symmetry of the zoom lens to the sensor image plane and that the proper point of symmetry to be used for distortion computations can be found as the intercept at zero principal distance. If this postulation is correct, then a common point of symmetry should be used for distortion computations at all zoom settings, but a linearly varying (with zoom setting) principal point should be used in photogrammetric computations. In addition, it follows that the angle of misalignment of the zoom lens axis of symmetry can be computed from the principal point versus principal distance data. The mean image plane misalignment angle of seven solid-state cameras measured with this technique was 0.36° .

It has been further postulated that the asymmetrical component of distortion caused by the misalignment of the zoom lens is directly proportional to the symmetrical radial



distortion component, the principal distance, and the angle of misalignment. Simulations support this theory of zoom lens behavior but show that for typical misalignment angles and for reasonably large values of radial distortion, the additional error introduced by ignoring the zoom lens misalignment may be only of the order of a few hundredths of a pixel, which at the current levels of accuracy is almost insignificant. The implications of this study are that special measures to properly align the zoom lens to the sensor image plane are probably not necessary, but that as the accuracy obtainable in digital photogrammetry approaches the 0.01 pixel level, the use of a separate point of symmetry for distortion computations should be considered.

(A. W. Burner, 44635)
Electronics Directorate

Calibration Tests of Scientific CCD Cameras

Commercially available Charge-Coupled Device (CCD) television cameras are gaining increasing acceptance for metrology applications. These cameras, which have small active areas and operate at video framing rates (30 Hz), typically require resampling of the video waveform to transform the temporal information into the digital format required for subsequent computer analysis. The discrete nature of the photo sites can be compromised in the course of making the data stream compatible with standard video display equipment. Large format, high-resolution CCD cameras, on the other hand, are slow scan (e.g., 0.1 Hz), usually cooled to reduce dark current, and they often use sophisticated readout schemes to increase available dynamic range.



Scientific slow-scan CCD camera.

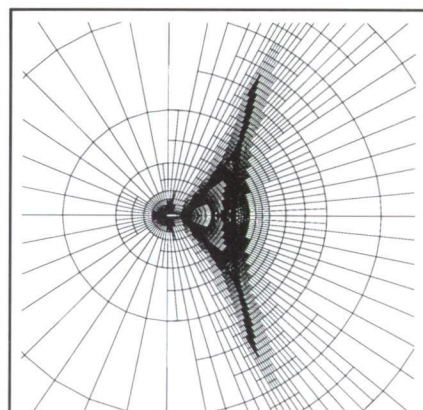
A commercially marketed scientific CCD camera is shown attached to its Peltier cooler control module. Its active sensor array is comprised of 1024 by 1024 19- μ m square pixels.

Slow-scan CCD cameras are routinely used in astronomical observatories for radiometry and astrometry. To our knowledge, this is the first evaluation of such a device for close-range photogrammetry applications. The calibration, which was done using eight views of a retroreflective target test field, was reduced with sophisticated photogrammetric algorithms. A zoomed image of a single retro target is displayed on the accompanying monitor along with an irradiance profile through its diameter. The dynamic range for this camera is 14 bits (16 384) versus 8 bits (256) for conventional video. The measured proportional accuracy was 100 000:1 for the test configuration. By comparison, a typical commercial camera usually tests between 10 000:1 and 20 000:1 under ideal conditions.

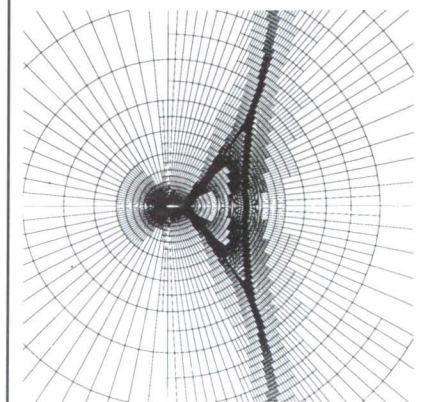
(W. L. Snow, A. W. Burner, and W. K. Goad, 44636)
Electronics Directorate

Grid Convergence for Adaptive Methods

The ability of adaptive methods to obtain accurate results has been examined using two different adaptive Euler solvers for a near-sonic flow containing several important flow features. The accuracy obtained has been shown to be greatly affected by the lack of resolution of smooth portions of the flow caused by adapting only to the more prevalent flow features (such as discontinuities). The accuracy of several adaptive methods has been evaluated by comparing adaptive calculations to the results from a grid convergence study.



Grid produced by adapting to undivided velocity differences.



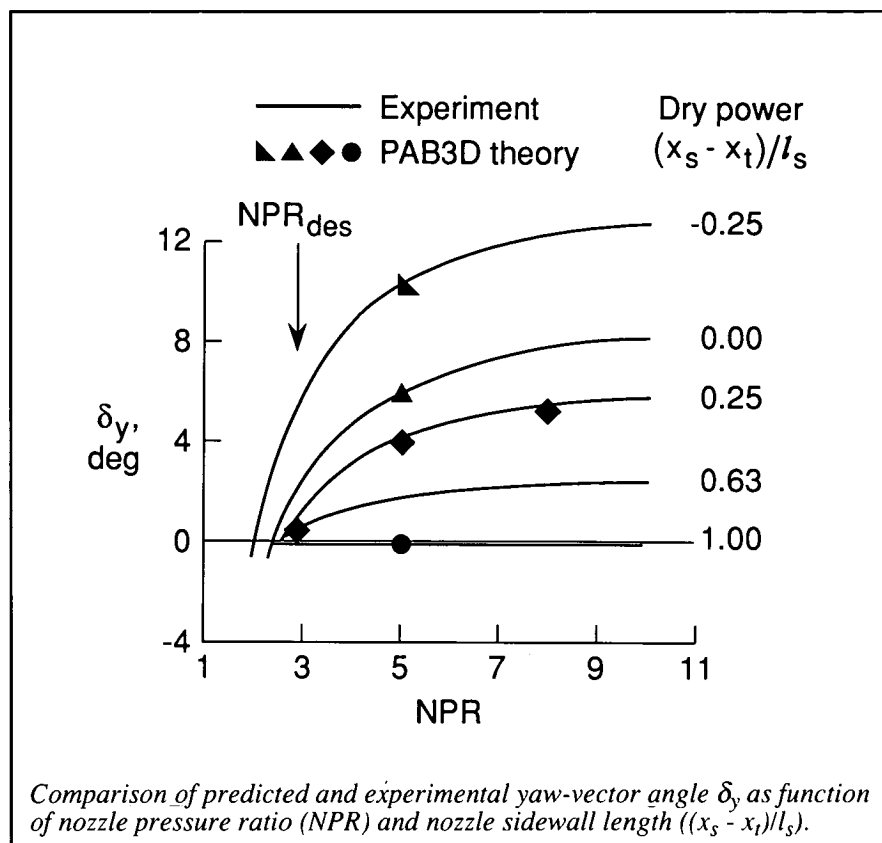
Grid produced by adapting to undivided velocity differences multiplied by local length scale.

The grid convergence study was conducted by running a series of finer grids with a structured Euler solver.

Results are shown for an NACA 0012 airfoil at a free-stream Mach number of 0.95. The first adaptive grid (shown in the first figure) was obtained by refining cells based on the undivided difference of total velocity, which is a very common weighting function used in computational fluid dynamics. As shown, the normal shock in the wake has been resolved, but the location of the shock shows a 15-percent error when compared with the grid-converged result. The inability of an adaptive method to obtain the grid-converged result is caused by the weighting function (or error indicator) not behaving as the actual error as the cells are refined. The second adaptive grid (shown in the second figure) was obtained by making the weighting function approach zero in all cells (even at discontinuities) as they are refined. This property is enforced by multiplying the undivided velocity difference by a local length scale, and the corresponding result is shown. This correction to the weighting function produces shocks in the same locations as those in the grid convergence study. (Gary P. Warren, W. Kyle Anderson, James L. Thomas, and Sherrie L. Krist, 42162) Aeronautics Directorate

Method for Internal Nozzle Performance Prediction

The capability of determining the forces and moments generated by the internal flow field of a nozzle has been added to a current technology computation method. The flow field solution is supplied by a three-dimensional,



multiblock/multizone Navier-Stokes solver. This approach involves calculation of a nine-component stress tensor from that solution and integrating these forces over defined boundaries surrounding the nozzle geometry for the resultant forces and moments. The performance module has no restrictions as to the geometry and flow field conditions that can be handled.

The performance module has been successfully applied to several different nozzle configurations involving under- and overexpanded nozzle flows exhausting into static, subsonic, transonic, and supersonic external flow conditions. Unvectored and vectored axisymmetric and nonaxisymmetric geometries have been calculated. Analysis times are highly dependent upon geometry and flow field. An unvectored rectangular nozzle exhausting into static conditions would

typically require 200 000 grid points utilizing approximately 4 megabytes of memory on a CRAY-2 computer. Converged solutions can be obtained using approximately 1 hour of central processing unit time.

The present capability of the module is prediction of nozzle discharge coefficient typically to within experimental accuracy (highly separated flows are the exception). The thrust ratio is typically 1 to 2 percent high for laminar-flow solutions. A representative comparison, as indicated in the figure, shows predicted versus experimentally determined effective yaw-vector angles generated by a translating sidewall yaw-vector concept that operates at different conditions and sidewall positions. Predicted effective vectoring angles are within 0.5° of the experimental data. Off-axis forces and moments are

typically predicted to within 1 to 2 percent of the experimental data. This analysis greatly enhances the preliminary design, selection, and modification capability for nozzle investigations.

(J. R. Carlson, 43047)
Aeronautics Directorate

Computational Analysis of Fixed-Geometry Slotted Nozzle

A series of axisymmetric, supersonic cruise exhaust nozzle concepts were tested in the Langley 16-Foot Transonic Tunnel and the Unitary Plan Wind Tunnel. These nozzles were designed with fixed divergent flaps for mechanical simplicity and optimized for achieving peak performance at a nozzle pressure ratio (NPR) of approximately 20. However, at subsonic speeds where the NPR is typically less than 5, the propulsion performance of these nozzles was severely degraded. In order to improve off-design performance, divergent flap venting was

incorporated into the nozzle design. Both annular and longitudinal slots were investigated. Wind-tunnel results indicated that longitudinal slots were effective in alleviating performance problems at low NPR while retaining good performance at high NPR.

In the present investigation, a three-dimensional, multiblock/multizone Navier-Stokes code (PAB3D) was utilized to analyze the longitudinally slotted nozzles. The objectives were to validate the PAB3D code for nozzle flow analysis and to gain in-depth understanding of flow details that would lead to better design concepts. The nozzle configuration, which was geometrically complex and fully three dimensional, included an annular inflow channel, an internal centerbody, and eight longitudinal slots positioned around the divergent section of the nozzle. A six-component performance code module and a special grid generation package were developed for this study.

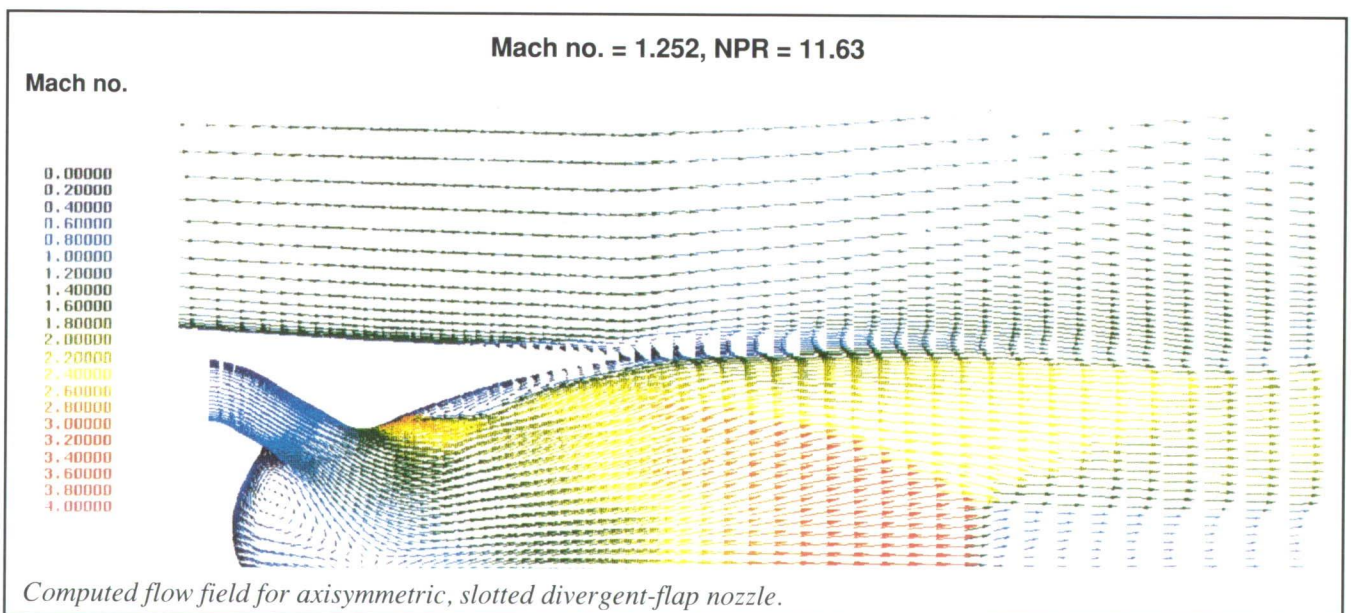
As shown in the figure, important flow features (such as flow separations within the nozzle, embedded shock systems, and flow interactions resulting

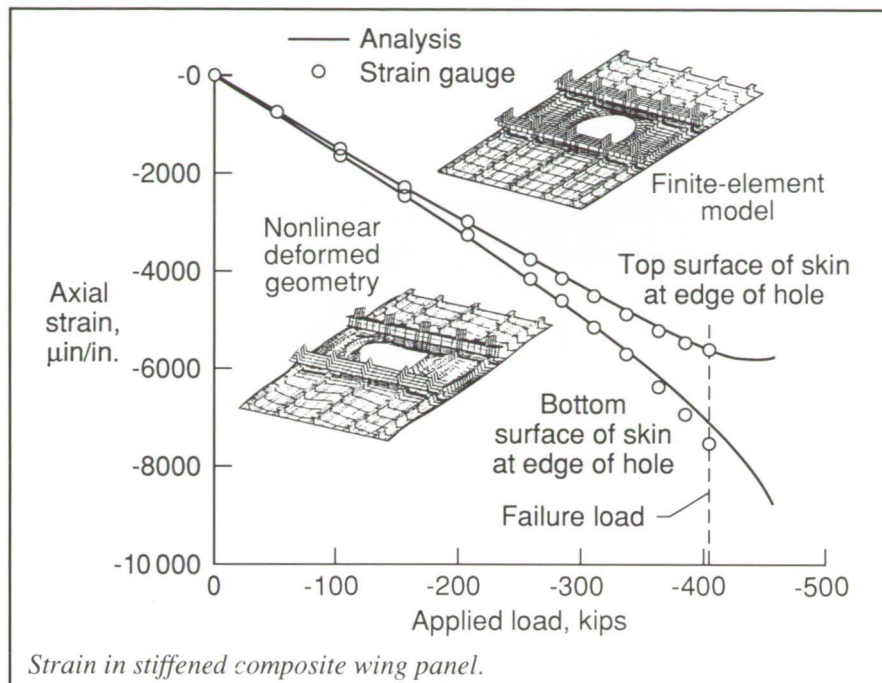
from pressure differences across the slots) were clearly captured in the computational analysis. However, the most important result was the accuracy of the predicted nozzle performance. Mass flow predictions were within 0.5 percent of the measured values for all cases in which data were available. Thrust predictions were generally within 2 percent of measured values. For the NPR = 5 case in which severe performance degradation existed, the error was 4 percent. Improvements in turbulence modeling will be needed for better predictions for such cases.

**(K. S. Abdol-Hamid, 43049,
J. R. Carlson, and S. P. Pao)**
Aeronautics Directorate

Accurate Prediction of Strain in Stiffened Composite Wing Panel by Nonlinear Finite-Element Analysis

Accurate calculation of stresses and strains is critical to predict failure modes and improve composite aircraft design, but sometimes comparisons





of analytical and experimental data are made on configurations that are simplified for ease of analysis or experiment to the point that the structure is not representative of an actual aircraft component. The purpose of this study was to validate and demonstrate the accuracy of nonlinear analysis methods on a realistic aircraft structural composite component for which there are experimental results.

Nonlinear structural analysis techniques were applied to a panel from the lower wing skin of the V-22 tilt-rotor aircraft. The graphite/epoxy composite panel contained design features such as ply drops, ply interleaves, axial stiffeners, transverse ribs, clips, brackets, and a large central elliptical access hole that greatly complicated modeling and analysis. Bell Helicopter Textron Corporation provided blueprints, drawings, and experimental data. Linear and nonlinear stress analyses were performed using a state-of-the-art finite-element formulation and nonlinear solution strategy. First-ply failure

techniques were applied to the results of the stress analyses and linear and nonlinear buckling analyses were performed to gain insight into the failure mechanism of the panel.

Excellent correlation between the nonlinear stress analysis and the experimental strain-gauge data was obtained (see the figure). The nonlinear analysis accurately predicted the nonlinear response of the panel, but a traditional linear stress analysis did not. Even with the relatively coarse mesh surrounding the access hole, the finite-element formulation (nine-node assumed natural-coordinate strain element) accurately predicted the strains in the region. Traditional finite elements would have required a much higher mesh density to achieve a comparable level of accuracy. When a first-ply failure technique was applied to the stresses from the linear and nonlinear analyses, the nonlinear results predicted considerably more damage in the vicinity of the hole. The buckling load was only slightly decreased by including the nonlinear

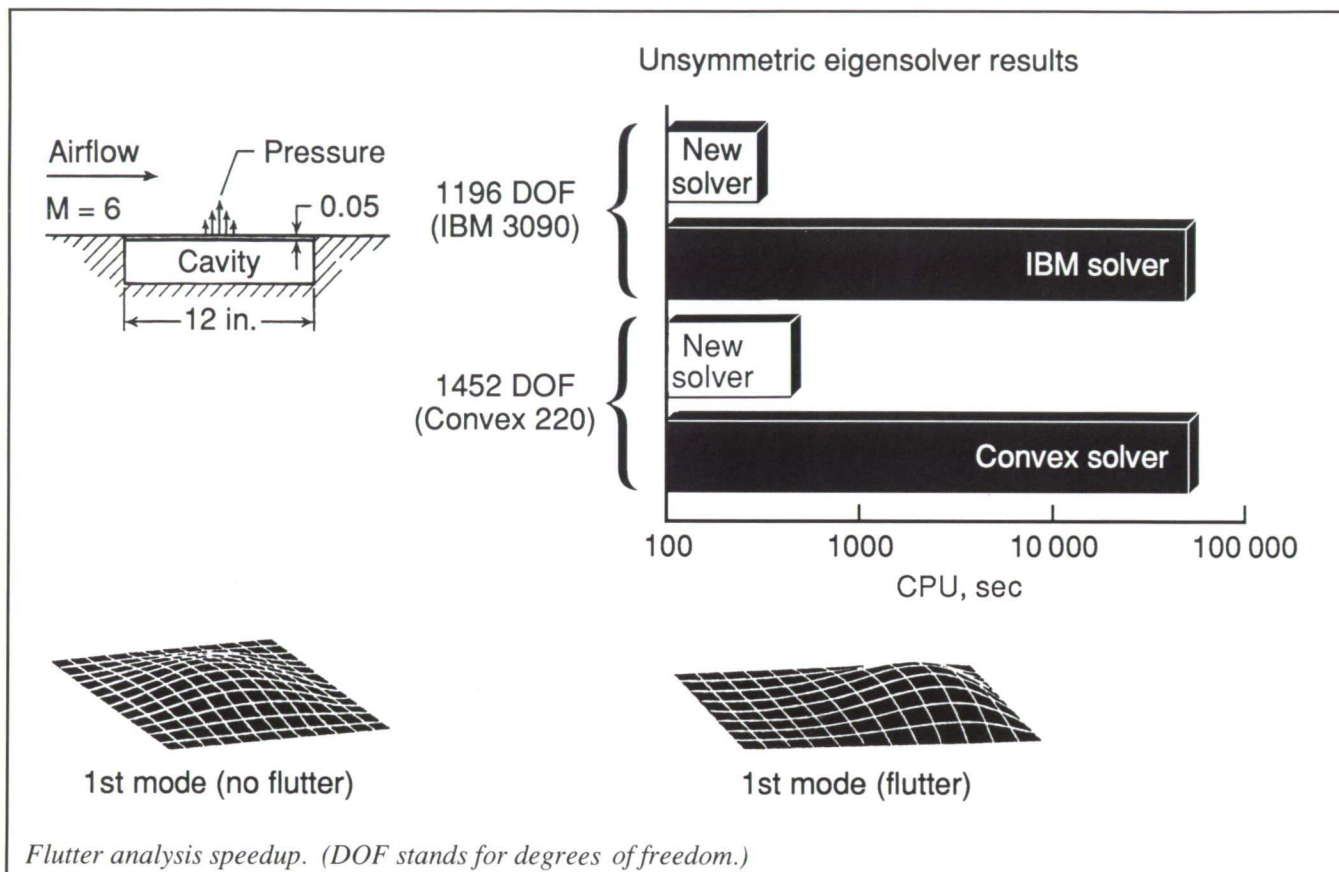
effects because the panel response is globally linear through failure. The local nonlinearities around the cutout had little effect on the global buckling load of the panel.

(D. Dale Davis, Jr., 42916, T. Krishnamurthy, and W. Jefferson Stroud)
Structures Directorate

New Eigensolver Reduces Supersonic-Hypersonic Flutter Analysis Time by Two Orders of Magnitude

Proposed flight vehicles such as the High-Speed Civil Transport (HSCT), the National Aero-Space Plane (NASP), and the Advanced Tactical Fighter (ATF) are to operate not only at high supersonic Mach numbers, but also far into the hypersonic regime. The accurate and rapid prediction of panel flutter at these super/hypersonic speeds is needed. Finite-element formulations for determining the large deflection flutter characteristics of panels using unsteady, third-order aerodynamic piston theory have been developed. The computations involved are extensive and time-consuming using conventional unsymmetric matrix solvers; therefore, a new eigensolver that exploits the vector capability of a high-performance computer was developed.

The parallel-vector unsymmetric eigensolver was developed and tested on a panel flutter example on both Convex and IBM high-performance computers. The new eigensolver, based on the extension of pvsolve (a new Langley-developed parallel-vector solver), was optimized for vector performance and was several orders of magnitude faster than the existing unsymmetric eigensolvers in IBM and Convex mathematical libraries.



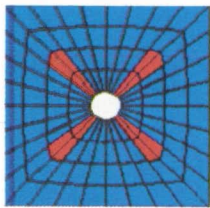
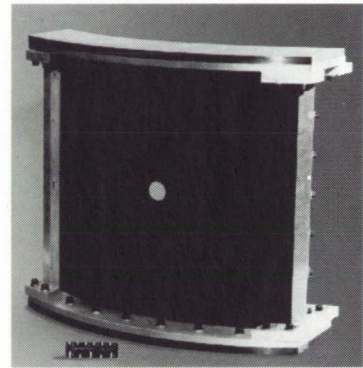
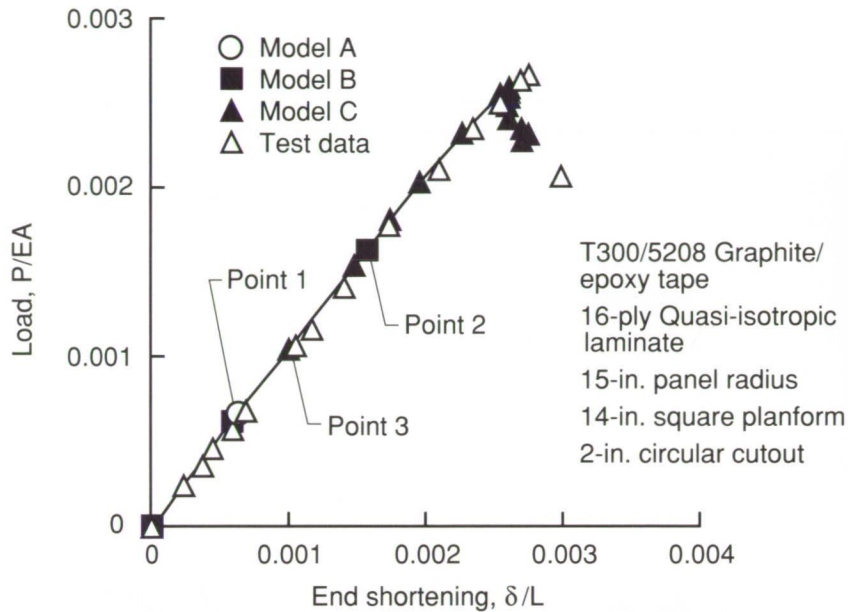
The new finite-element formulation, including the new solution procedure, yields the displayed nonlinear panel flutter results. Furthermore, existing unsymmetric eigensolvers contain excessive computations that prohibit and make impractical the accurate solution of the nonlinear panel flutter problem. The newly developed unsymmetric eigensolver is 134 times faster than existing unsymmetric eigensolvers and permits the efficient performance of parameter and design studies. (O. O. Storaasli, 42927, C. Gray, J. Qin, D. T. Nguyen, and C. Mei) Structures Directorate

Demonstration of Adaptive Analysis Procedure on Nonlinear Response of Composite Panel

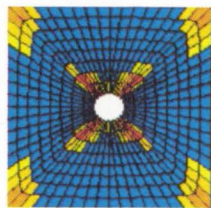
Frequently, finite-element models are developed for various components, and only limited convergence studies are performed on the finite-element mesh. The approach is typically one of comparing the finite-element model to the physical structure and refining the mesh in areas suspected of containing high-stress gradients. For nonlinear stress analysis, this approach may break down entirely because the locations of stress gradients may change with the nonlinear response. In many cases, performing multiple nonlinear analyses in order to determine the adequacy of the mesh is not feasible because even one nonlinear

analysis is expensive. An adaptive nonlinear analysis procedure has been developed to establish the reliability of a computed geometrically nonlinear response.

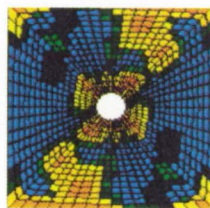
The problem of discretization error detection and control is addressed through an adaptive nonlinear solution procedure that incorporates a semiautomatic mesh refinement strategy for controlling the discretization error and provides a means of automatically controlling the nonlinear solution procedure. An iterative solution recovery procedure provides a mechanism for making the transition from one finite-element mesh at a given load step to another more refined mesh at the same load step, thereby enhancing solution efficiency. The computational strategy is implemented with the computational mechanics test-bed (COMET).



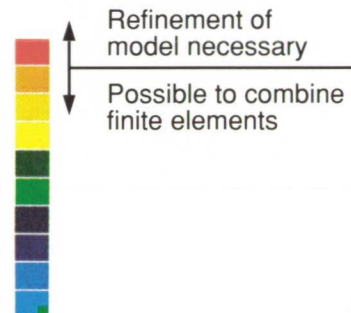
Model A



Model B



Model C



Composite panel nonlinear response to load.

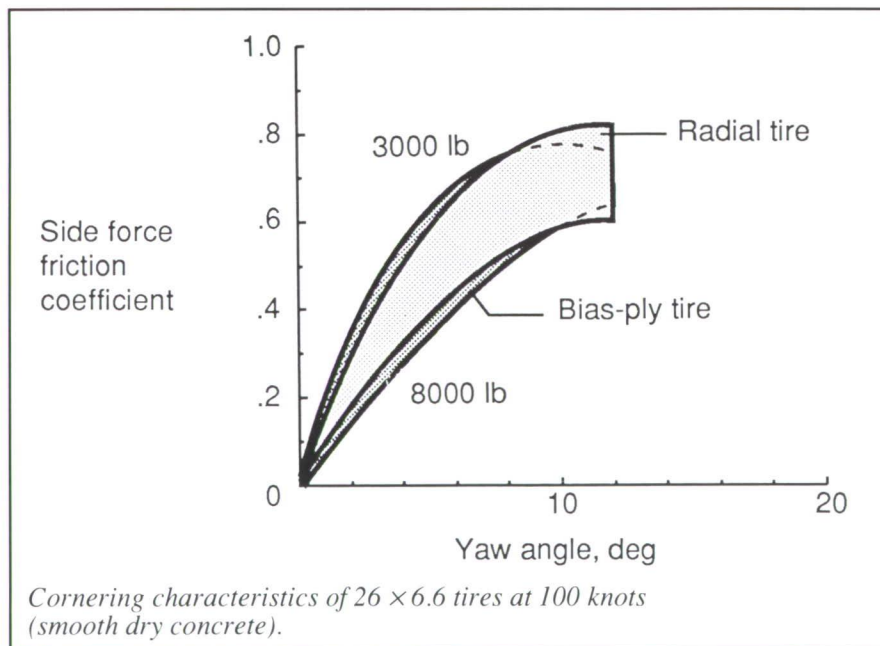
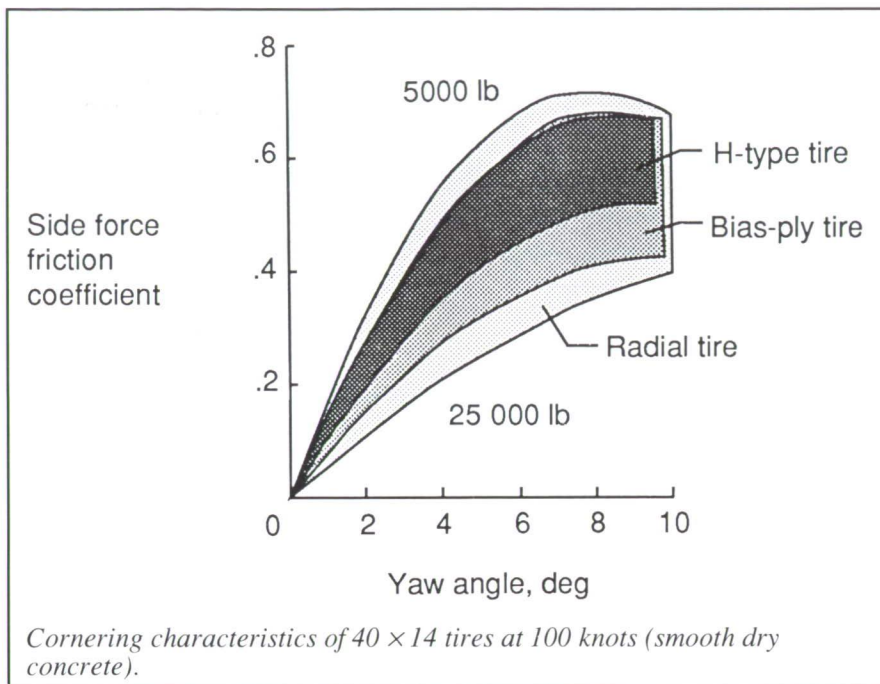
An adaptive nonlinear analysis was performed on the curved graphite/epoxy panel with a central circular hole loaded in axial compression (upper right of the figure). The longitudinal load P normalized by the experimentally determined extensional stiffness EA as a function of the applied end-shortening δ normalized by the panel length L is shown in the upper left of the figure. The solution is initiated with model A. The model with the shaded refinement indicator based on the standard deviation in stress resultants (the scale is shown at the lower right of the figure) at the first load step is shown at the lower left of the figure. At point 1, model A is found to be inadequate, and a more refined model B is generated. At point 2, model B is

found to be inadequate, and a final finite-element model C is generated. This final model begins the analysis at point 3, and it is sufficient for the analysis through buckling with excellent experiment correlation providing confidence in the final solution as refinements to the finite-element model are performed automatically.

(Susan L. McCleary, 42912,
 Jonathan B. Ransom, and
 Norman F. Knight, Jr.)
 Structures Directorate

Cornering Properties of Bias-Ply, H-Type, and Radial Aircraft Tires

A variety of studies have been completed at the Aircraft Landing Dynamics Facility (ALDF) using 40×14 and 26×6.6 size tires to define the mechanical properties and friction characteristics of bias-ply, radial-belted, and H-type designs. The 40×14 tire, which is a main-gear tire on aircraft such as the Boeing B-737 and the McDonnell-Douglas DC-9, was tested in a bias-ply, radial-belted, and H-type bias-ply design. Static load-deflection tests, braking tests, and cornering tests were conducted. The



cornering characteristics of this size tire on a dry runway at 100 knots are shown in the first figure for a range of vertical loads. The variation of vertical load affects the cornering characteristics of the radial tire to a greater extent than the cornering behavior of bias-ply or H-type tires. These results indicate

that the ground-handling properties of aircraft equipped with radial tires may be more sensitive to aircraft weight variations than aircraft equipped with bias-ply or H-type tires. The 26 × 6.6 tire size, which is the nose-gear tire for the McDonnell-Douglas MD-80, has been tested in a bias-ply and radial-

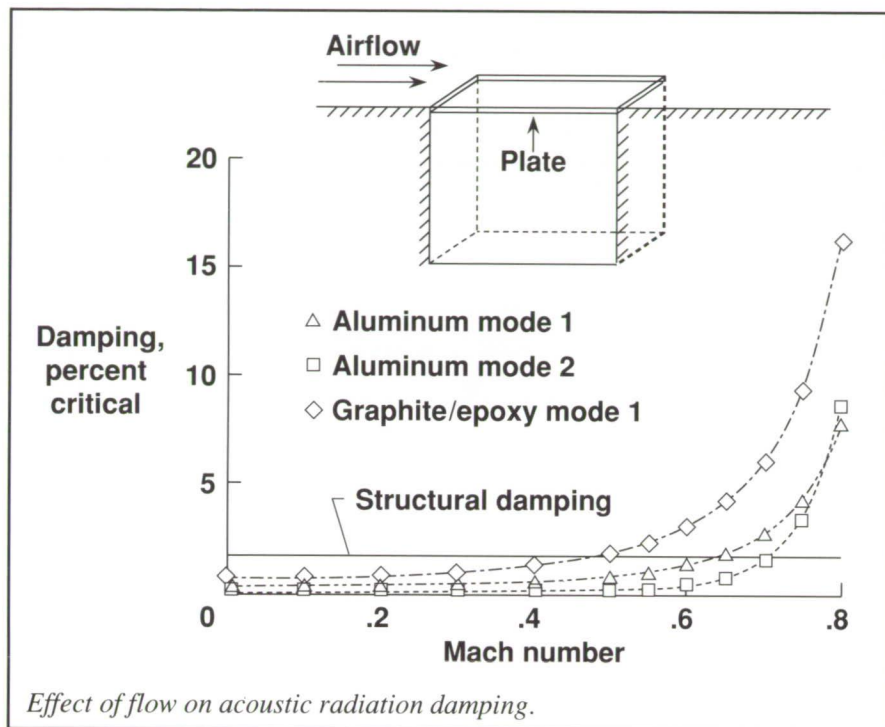
belted design. The cornering results for these tires are shown in the second figure. At the lower yaw angles, the radial tire cornering behavior is affected less by vertical load variations than the cornering behavior of the bias-ply tire. In general, however, the 26 × 6.6 radial and bias-ply tires have comparable cornering properties.

Data such as those shown in the figures will contribute significantly to the establishment of a national data base for radial-belted and H-type aircraft tires that will be used to compare their mechanical property and friction characteristics with those of bias-ply tires. These data will also enhance aircraft safety during ground operations under adverse weather conditions.

(Pamela A. Davis, Sandy M. Stubbs, and Thomas J. Yager, 41308) Structures Directorate

Acoustic Radiation Damping in Subsonic Flows

Structural vibration response is largest in magnitude near the system natural frequencies. The magnitude in this region is approximately inversely proportional to the system damping; therefore, accurate predictions for structural dynamic response require equally accurate knowledge of system damping. The system damping may be separated into two components: structural, primarily resulting from motion at the structural junctions, and acoustic radiation, resulting from the fluid/structure interaction. The acoustic radiation is known to depend on flow over the vibrating surface, but analytical models have been developed, thus far, for very low-speed and supersonic flows. An analytical study has recently been completed to evaluate the



acoustic radiation (or aerodynamic) damping of panels in a wider range of subsonic flows to determine its importance relative to structural damping. The emphasis of this project is the acoustic radiation damping prediction for simple isotropic and composite panels.

The analysis is based on the linear vibration differential equation for a flat plate. A perturbation pressure derived from the linearized Bernoulli and continuity equations is used to characterize the air loading on the panel. The acoustic radiation damping prediction computer program for simple isotropic and composite panels has been completed. Existing limiting-case analyses have verified the predictions. Parameters varied in the analysis include Mach number, mode number, panel size, aspect ratio, and material property. Examples of the effects of Mach number, mode number, and material property are seen in the figure for panels typical of the size used in aircraft (12 in. by 18 in. by 0.04 in.).

For Mach numbers greater than 0.5, the damping increases exponentially. In addition, material property and mode number can cause a factor-of-2 difference in damping. The acoustic radiation damping of aircraft-like panels in subsonic flows can be equal to or greater than the structural damping (frequently assumed as 1.5 to 2.0 percent). Appropriate conditions for simplifying the analysis and thus decreasing the computation time have been determined, and many cases allow simplification to reduce the computation time from hours to minutes. The perturbation approximation gives a good estimate in a few minutes.

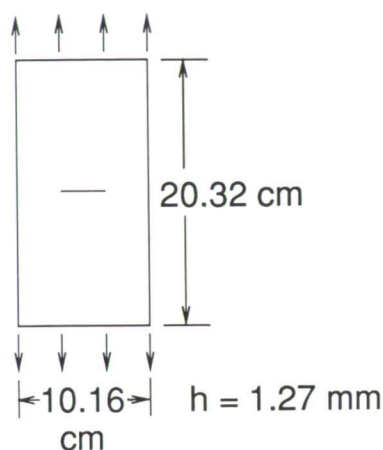
(Karen H. Lyle, 43588)
Structures Directorate

Frequency-Based Approach to Dynamic Stress Intensity Analysis

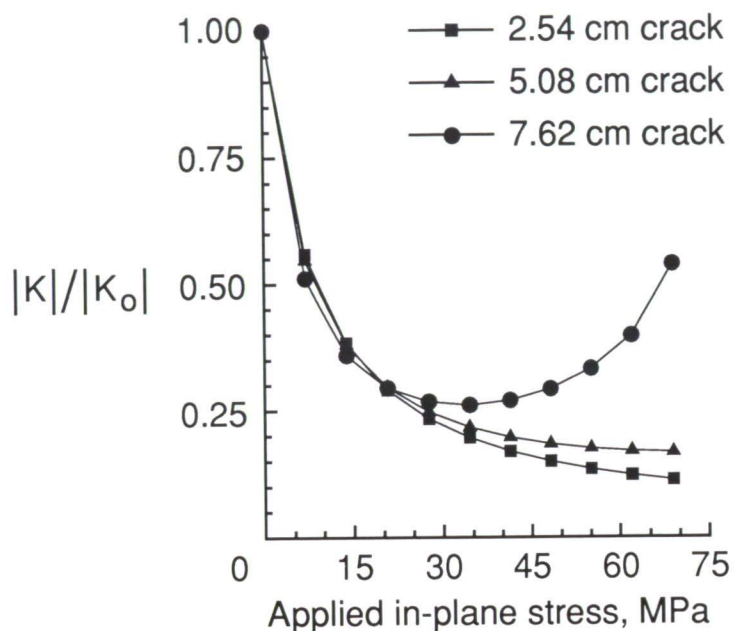
Dynamic fracture mechanics analyses have been used extensively to obtain the time dependence of quantities such as the strain energy release rate G and stress intensity factor K . The information is particularly useful in this form when the response of the structure is deterministic. However, when the response is nondeterministic, as would be the case for a random excitation, the frequency dependence is of greater interest. Recasting the system in the frequency domain so that these quantities may be computed directly would therefore be beneficial.

This work is motivated by the need to characterize the fatigue crack growth in aircraft structures subjected to the combined action of an in-plane tensile load and a random acoustic loading. Fatigue crack growth in aircraft fuselage structures resulting from low-cycle, high-stress cabin pressurizations has been successfully modeled using linear elastic fracture mechanics principles. The addition of acoustic loading, having a high-frequency content but low-stress level, has been shown to dramatically increase this fatigue crack growth rate. Yet, while the dynamics of the system have been successfully modeled using a finite-element analysis, little effort has been expended to obtain frequency-dependent crack quantities. This work combines a finite-element/modal analysis/spectral analysis method for the determination of these quantities.

A finite-element analysis is first used to obtain the stiffness, initial stress, mass, and damping matrices of the structure. Because these can be quite large for a structure containing cracks, the modal analysis method is then used to reduce the system of



Test panel
2024-T3 aluminum
 $E = 72.4 \text{ GPa}$, $\nu = 0.33$



Variation of stress intensity magnitude with applied in-plane stress for first out-of-plane vibration mode.

equations. The solution of this system is then obtained in the frequency domain, and the strain energy release rate and stress intensity are extracted with a spectral form of the crack closure technique.

Studies were carried out on a center-cracked 10.16-cm by 20.32-cm by 1.27-mm 2024-T3 aluminum panel subject to the combined action of in-plane stress on the two short sides and out-of-plane acoustic loading. The figure shows the variation of normalized stress intensity magnitude with applied in-plane stress for the first out-of-plane vibration mode. This rise in the 7.64-cm crack case is because of the onset of local crack buckling and is consistent with observations of increased crack growth at this condition. Future work includes the incorporation of the dynamic stress intensity into a frequency-based crack growth law.

(Stephen A. Rizzi, 43599)
Structures Directorate

Spatial Adaption Procedures for Accurate Unsteady Flow Analysis

Many of the flow fields determined using numerical methods have been obtained without the grid resolution that is required for high spatial accuracy. To improve this accuracy, much finer meshes are generally required. A globally fine mesh, however, is not practical because the calculations would require an enormous amount of computer resources. What is required for efficiency is an adaptive mesh procedure whereby the grid is refined locally according to some measure of the quality of the solution. Consequently, modifications were made to a two-dimensional unstructured-grid upwind-type Euler code to include procedures for mesh enrichment and mesh coarsening to either add points in high gradient regions of the flow or remove points where they are not needed, respectively, to produce

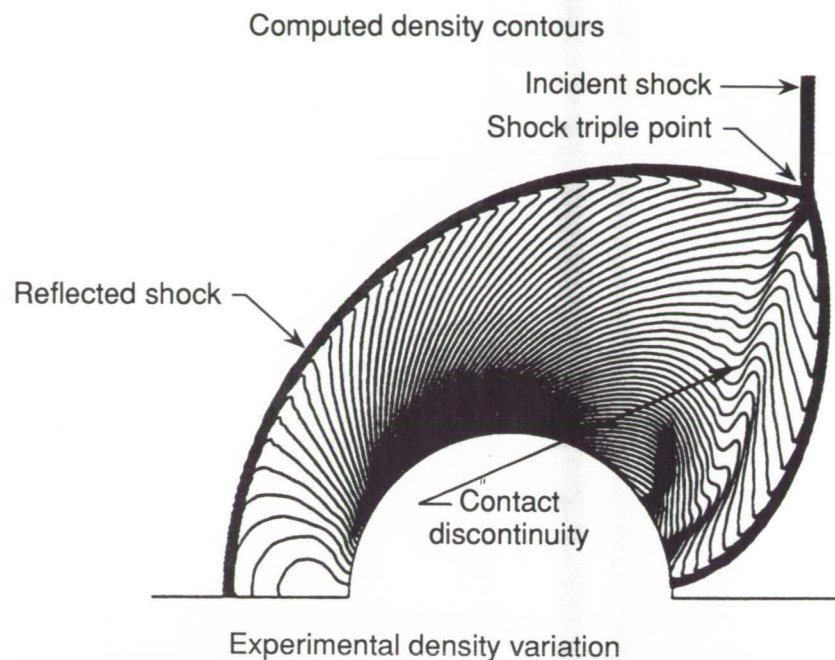
solutions of high spatial accuracy at minimal computational cost. The advantage of using a spatial adaption procedure is that the solution dictates the mesh topology for an efficient computation.

Calculations were performed for a normal shock moving from left to right at a supersonic Mach number that impinges on a half cylinder. The problem was selected to test the adaption procedures by studying the resulting transient shock wave diffraction phenomena and comparing computed time-dependent solutions with experimental data. Computed density contours are shown in the top part of the figure, and the experiment data, at the same instant in time, are shown in the bottom part of the figure. The density contours give a reasonable representation of the flow and the subsequent development of the diffraction process that covers regular reflection, transition to Mach reflection, and shock-on-shock interaction.

CFD Simulates Active Control of Delta Wing Rocking Motion

Recently, a growing interest has existed in high angle-of-attack fighter capability for increased maneuverability. Typically, these high-performance aircraft have thin, highly swept lifting surfaces that produce a vortical flow over the leeward side of the vehicle at high angle of attack. However, in addition to its beneficial effects on performance, this vortical flow may also have adverse effects including structural fatigue due to tail buffet and also stability and control problems due to wing rock, wing drop, nose slice, and pitch-up. In order to gain a more complete understanding of these types of vortical flows and to research the problems that they create, a conical Euler methodology has been developed to efficiently investigate unsteady vortical flows about highly swept delta wings undergoing free-to-roll motions including roll suppression. This conical Euler methodology is used to demonstrate that the limit-cycle wing-rocking motion of a highly swept delta wing can be actively suppressed through the use of a rate-feedback control law and antisymmetrically deflected leading-edge flaps.

Modifications were made to an unstructured grid conical Euler code to allow for the application of a rate-feedback control law to leading-edge flaps on the delta wing. The modifications included the addition of a control law to the simultaneous time integration of the rigid-body roll equation with the governing flow equations. A deforming mesh algorithm was also included to deform the mesh about the deflected leading-edge flaps. Unstructured grid methods are well suited for this type of problem because the deforming mesh algorithm can be easily and efficiently applied to these types of meshes.



Comparison of experimental and computed densities for transient shock wave that impinges on half cylinder.

The incident shock, shock triple point, reflected shock, and contact discontinuity are identified.

The calculated results using spatial adaption were obtained with a fraction of the computer resources that would be required by using a globally fine

mesh, and they compare well with the experimental data. The results demonstrate the ability of the automated adaption procedures to accurately and efficiently resolve transient flow features. (Russ D. Rausch and John T. Batina, 42268) Structures Directorate

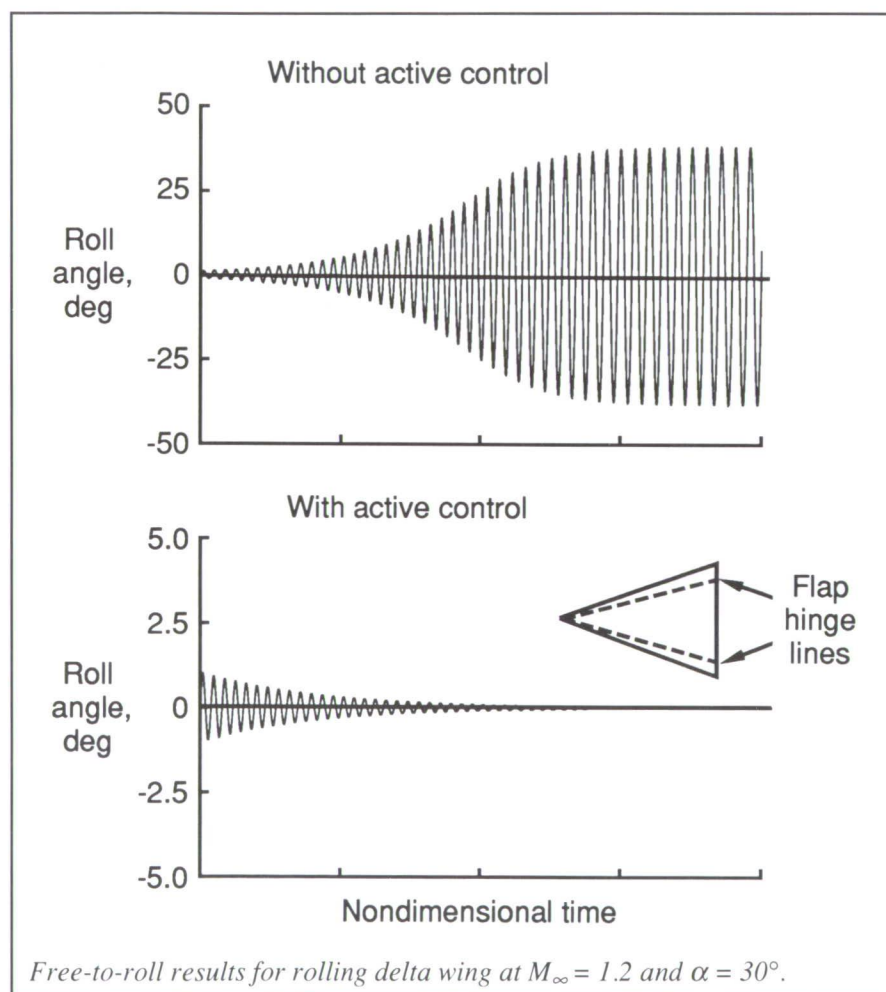
Calculations were performed for the sharp-leading-edge delta wing swept 75° at a free-stream Mach number $M_\infty = 1.2$ and an angle of attack $\alpha = 30^\circ$. The leading-edge flaps are approximately 28 percent of the local semispan (see the figure). The rolling-moment coefficient transfer function due to the motion of the flaps was determined for these flow conditions from the aerodynamic response

without active control. Plots of the free response time history for both cases are shown in the figure. Note the different scaling on the vertical axes. Without active control, the roll response diverges initially at the small roll angles, but as the amplitude of motion grows with time, the response undergoes a transition to a wing-rock type of limit-cycle oscillation. With active control included, the roll response

Finite-Difference Meshes for Solution of Transonic Small Disturbance Equation

Time accurate solutions of the Transonic Small Disturbance (TSD) equation play a key role in the analysis of aircraft operating in the flutter critical transonic speed range. Numerical errors arise from inadequate treatment of waves propagating outward from the vehicle through the finite-difference mesh. The simple wave equation is used to study these errors, employing the same algorithm as that in the well-known CAP-TSD code. Analysis predicts numerical wave reflections that arise from both the stretching of the mesh away from the vehicle and the simulated far boundary.

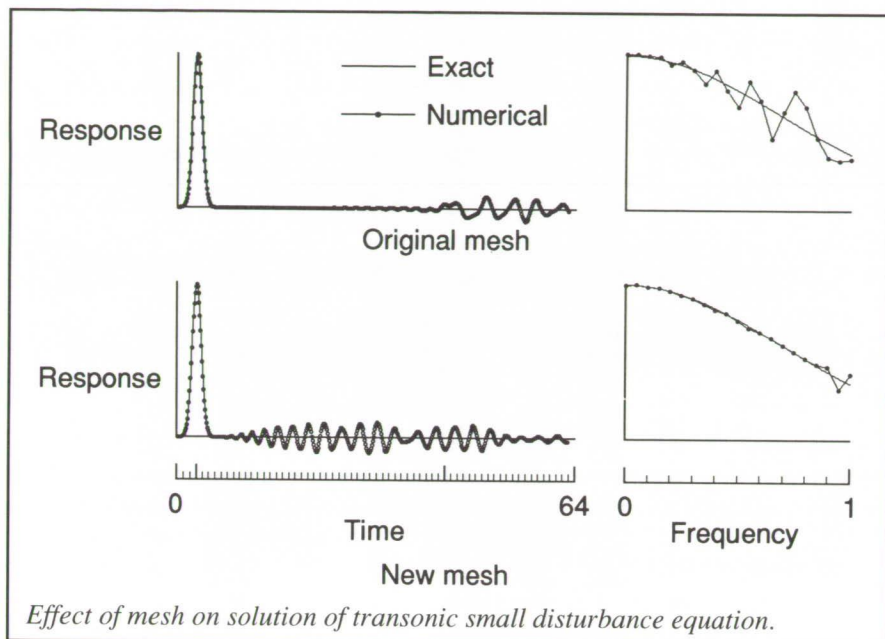
These effects are demonstrated in the figure. On the left is shown the time history of the response at the wing to a pulse in angle of attack. On the right the Fourier transform of this response as a function of frequency is shown. The top part of the figure is for a mesh that has good properties for minimizing internal reflections but that is not fine enough in the far field to eliminate the boundary reflection. This reflection occurs during the last third of the time history, at the time required for the pulse to travel to the boundary and return. This error contaminates the solution at the flutter critical low frequencies. The bottom part of the figure is for a new mesh designed during this study. Fine spacing in the far field eliminates the low-frequency boundary reflection error. Although the time history for the new mesh looks worse, the errors occur at frequencies above those of interest for flutter. Both meshes have the same minimum spacing at the wing, a maximum spacing of approximately one, and they contain 40 and 37 points, respectively.



of the delta wing because of a forced motion of the flaps. This transfer function was then used to predict the control gain necessary to suppress the limit-cycle motion of the delta wing. The free-to-roll response due to an initial small angular velocity perturbation was then computed both with and

converges to its initial steady-state value after the same small perturbation, and thus the wing rocking motion is suppressed.

(Elizabeth M. Lee and John T. Batina, 42269)
Structures Directorate



This study has produced improved meshes and has led to a mesh design code for use with the CAP-TSD aeroelastic analysis code. (Samuel R. Bland, 42272) Structures Directorate

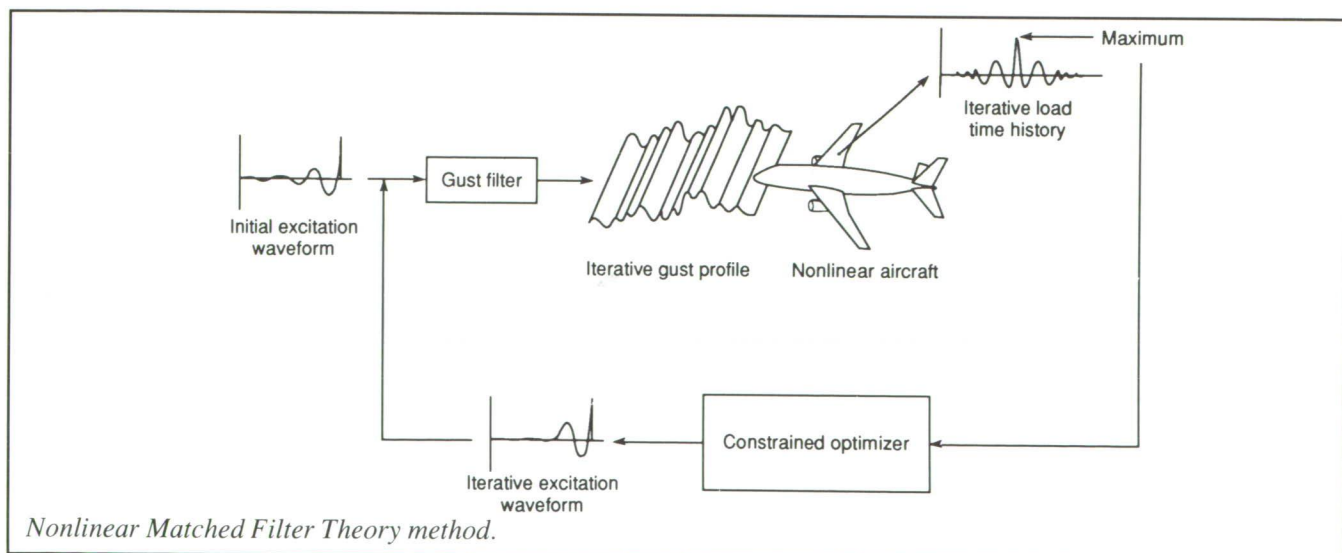
Optimization Scheme To Obtain Maximized Gust Loads for Nonlinear Aircraft

Modern transport aircraft employ active control systems that almost always contain significant hardware nonlinearities (such as actuator rate and deflection limits and deadbands) and software nonlinearities. While most of the established methods used

to calculate aircraft gust loads are applicable to linear systems only, the current method offers a novel approach to obtain the maximized and time-correlated gust loads for aircraft with nonlinear systems. This method utilizes Matched Filter Theory (MFT) and constrained optimization to obtain its answers.

The MFT method, which alone offers a means of computing maximized and time-correlated gust loads for linear systems, has been applied to and successfully demonstrated on a number of linear airplanes. The MFT method may be applied to a nonlinear system, but because the system is nonlinear, obtaining a maximized load is not guaranteed. To aid in the search for the maximized load for a nonlinear system, a constrained optimization scheme has been combined with the MFT method, as illustrated in the figure.

Beginning at the upper left of the figure, the quantity labeled initial excitation waveform is an intermediate result from the MFT method, and it is used as the starting point in the optimization scheme. The remainder of the figure describes the looping process that maximizes the maximum value of



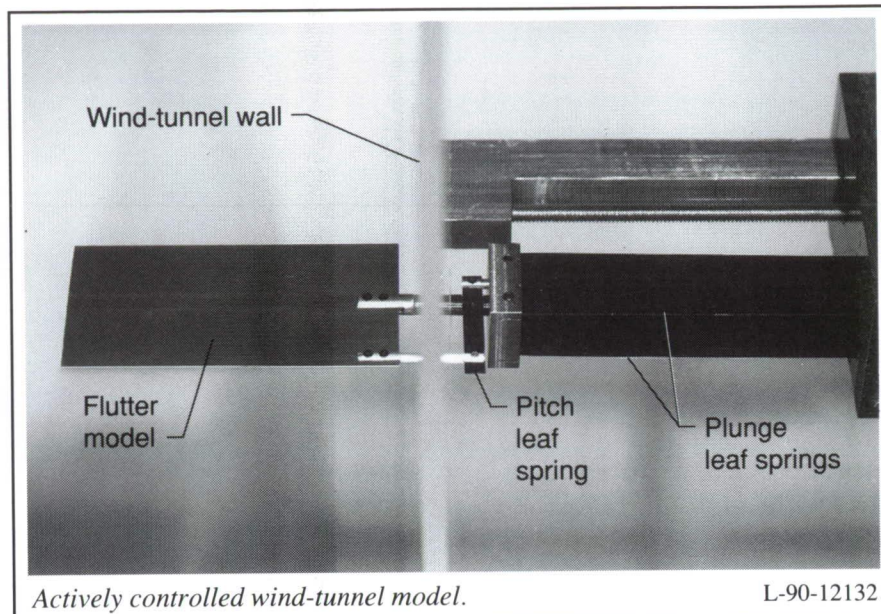
the load. Within each loop, the following steps are performed. The iterative excitation waveform is passed through a gust filter to obtain the iterative gust profile. A simulation of the nonlinear aircraft model is performed to obtain, in response to the iterative gust profile, an iterative load time history, which contains some maximum value. The constrained optimizer chooses a new search direction, chosen to increase the maximum value of the iterative load time history; this results in a new excitation waveform (which is constrained to have the same root mean square value as the initial excitation waveform) and completes the cycle through the loop. Looping continues until the maximum value of the iterative load time history no longer increases. The resulting optimized excitation waveform then can be used to obtain the maximized and time-correlated gust loads for a particular flight condition.

(Robert C. Scott, 42838, Anthony S. Pototzky, and Boyd Perry III)
Structures Directorate

Active Suppression of Flutter Using Piezoelectric Ceramic Actuators

The objective of this research was to study the capabilities of adaptive material plate actuators for suppressing flutter experimentally and analytically and to correlate results from the two. The validity of analytical modeling techniques for adaptive material also was to be investigated.

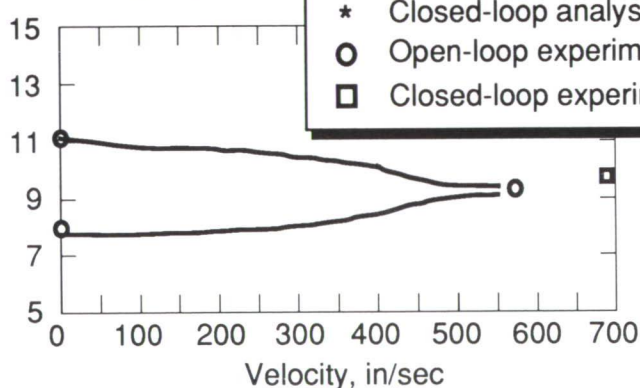
A two-degree-of-freedom mount system was designed, constructed, and fitted with a rigid wing as shown in the first figure such that the wing flutters within the wind-tunnel operating



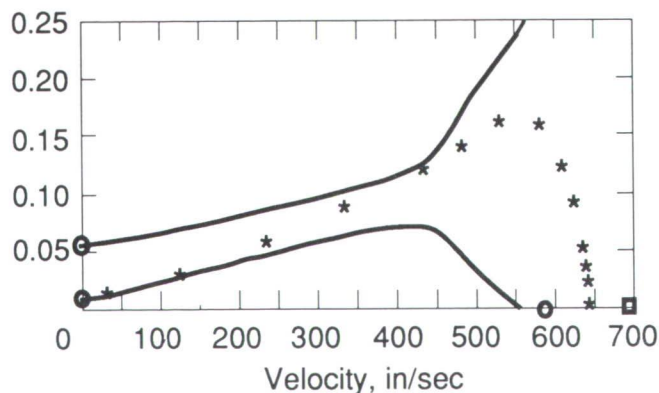
Actively controlled wind-tunnel model.

L-90-12132

Frequency, Hz



Damping ratio



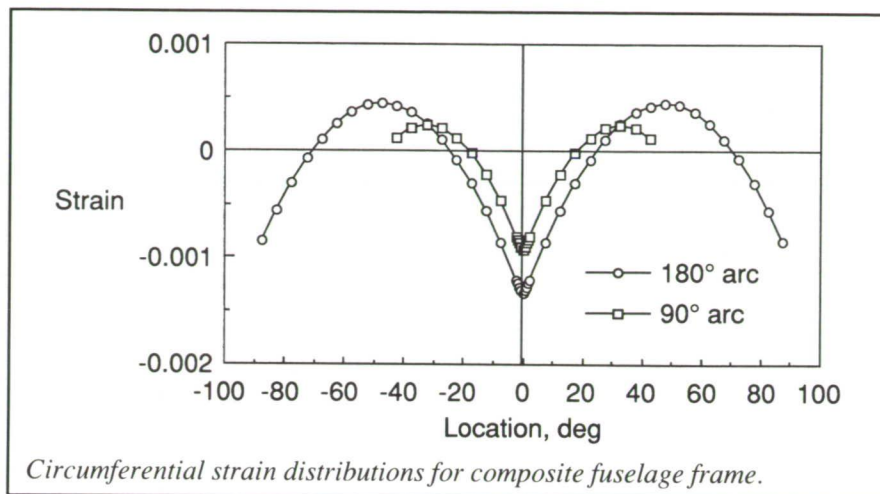
Predicted and measured frequencies and damping ratios.

envelope. Each degree of freedom was controlled by a separate leaf spring. Actuators, made of piezoelectric material (which is a subcategory of adaptive material), were affixed to leaf springs of the mount system. Command signals, applied to the piezoelectric actuators, exert control over the damping and stiffness properties of each degree of freedom. A mathematical aeroservoelastic model was constructed using finite-element methods, laminated plate theory, and aeroelastic analysis tools. Plant characteristics were determined from this model and verified by open-loop experimental tests. A flutter suppression control law was designed and digitally implemented. Closed-loop flutter testing was conducted.

The results shown in the second figure are comparisons of the predicted and measured frequencies and damping ratios as a function of flow velocity. Analysis of the open-loop aeroelastic equations of motion produced a flutter condition at 560 in/sec and a frequency of 9.1 Hz. The experimental flutter point obtained was 580 in/sec at 9.4 Hz. A gain feedback control law that utilized the intrinsic dynamics of the digital computer to simulate derivative feedback of strain was designed. Only one actuator, consisting of plates measuring 1.5 in. by 1 in. and 0.0075 in. thick, was required to suppress flutter. The analytical closed-loop flutter prediction was 648 in/sec. Experimentally, flutter was inhibited up to 697 in/sec, an increase of more than 20 percent. The experimental results, which represent the first time that adaptive materials have been used to actively suppress flutter, demonstrate that carefully placed small actuating plates can be used effectively to control aeroelastic response.

(Jennifer Heeg, 42795)

Structures Directorate



Effect of Floor Location on Response of Composite Fuselage Frame

Experimental and analytical studies are part of the composite impact dynamics research to generate a data base on the behavior of composite structures under crash loads. Part of the effort has been the determination of the effect of the floor vertical attachment position on the response and failure of generic composite fuselage frame concepts. Nonlinear finite-element models of a 6-ft diameter composite fuselage frame concept were formulated. Static loads were applied to the frame/floor simulation to determine the response of the composite frames. Strain distributions were determined using the models in which the location of the simulated floor was moved to several locations on the circumference of the frame.

As shown in the figure, typical circumferential strain distributions (at a 1000-lbf load) for the composite fuselage frame for a frame arc of 90° were similar to the distributions for the floor located at the diameter (180° arc). Although the strain distributions associated with the lower floor locations were compressed horizon-

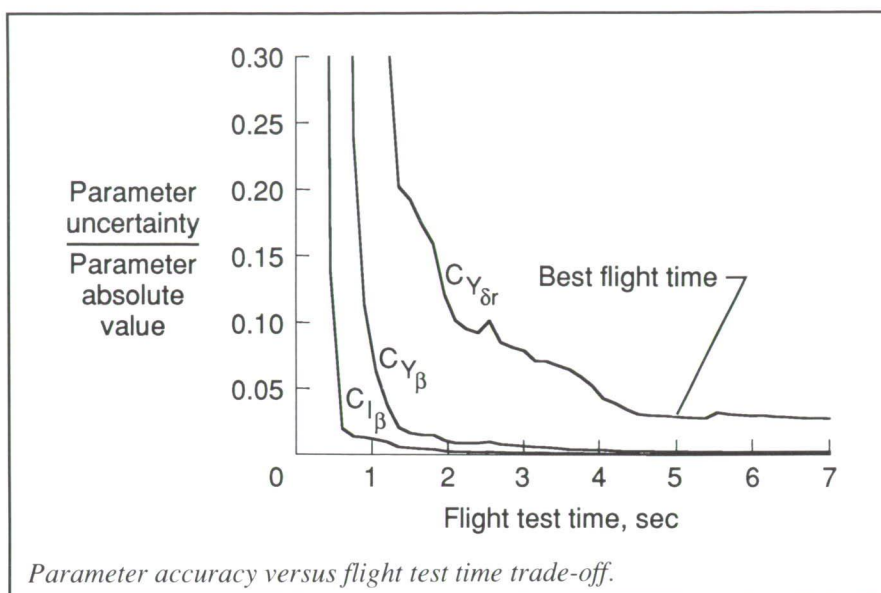
tally between the ends of the floor attachment points, maximums in strain still occurred at the point of ground contact and at plus or minus positions up the frame from the point of ground contact.

Failure loads (not shown) were also determined using the analytical models with the simulated floor placed at the different locations on the circumference of the frame. The load with the finite-element model that produced failure of a composite I-frame varies essentially linearly as a function of 1/arc length of the loaded lower portion of the frame. The linear variation with 1/arc length of the ring or arch is also predicted by closed-form solutions for loaded rings/arches. Further, the shorter frame segments produced the highest failure loads. Data such as those shown here are fundamental to the understanding of crash dynamics and to the design of more crash-resistant structures.

(Lisa E. Jones and Huey D.

Carden, 44148)

Structures Directorate



Application of Optimal Input Design to Parameter Estimation Flight Experiments

Determining accurate mathematical models of aircraft dynamics from flight test data requires careful design of the flight test maneuvers. These maneuvers can be implemented by a pilot or by a computerized system that may directly move either pilot controls or the aircraft control surfaces. In either case, the choice of input for the maneuver is crucial because it determines the accuracy achievable when estimating parameters in the mathematical model during postflight data analysis. A technique recently developed at Langley Research Center can be used to design globally optimal square wave inputs for parameter estimation flight experiments. The method computes inputs that maximize the achievable accuracy of model parameter estimates using a priori information about the aircraft dynamics, control system, and the practical constraints of the flight test. The goals of this research were to examine the benefits of the optimal input method by

designing optimal flight test inputs for the X-31 drop model and to investigate related trade-off and robustness issues.

A nonlinear six-degree-of-freedom computer simulation of the X-31 drop model was used to evaluate the optimal input method relative to conventional doublet inputs. Results showed that model parameters could be determined more accurately using optimal inputs and that computer-driven optimal inputs produced significant additional increases in achievable parameter accuracy. The robustness of the optimal input technique to errors in the a priori mathematical model was investigated by introducing moderate (15 percent) errors in the a priori model parameters and again optimizing the input. Less than 3-percent degradation in achievable parameter accuracy was found as a result of the modeling errors. Because flight time is always limited, achievable accuracy for the parameter estimates using optimal inputs was investigated as a function of flight test time. The figure shows that uncertainty in the estimates of model parameters $C_{Y_{\delta r}}$, $C_{Y_{\beta}}$, and $C_{l_{\beta}}$ decreases as flight test time increases. In this case, a 5-sec maneuver was chosen because the slow rate of

decrease in the uncertainty of the model parameter estimates would not warrant additional flight test time. This information can be used to maximize the return on expensive and limited flight test time. The investigations included the design of a complete parameter estimation flight test program for the X-31 drop model using optimal inputs.

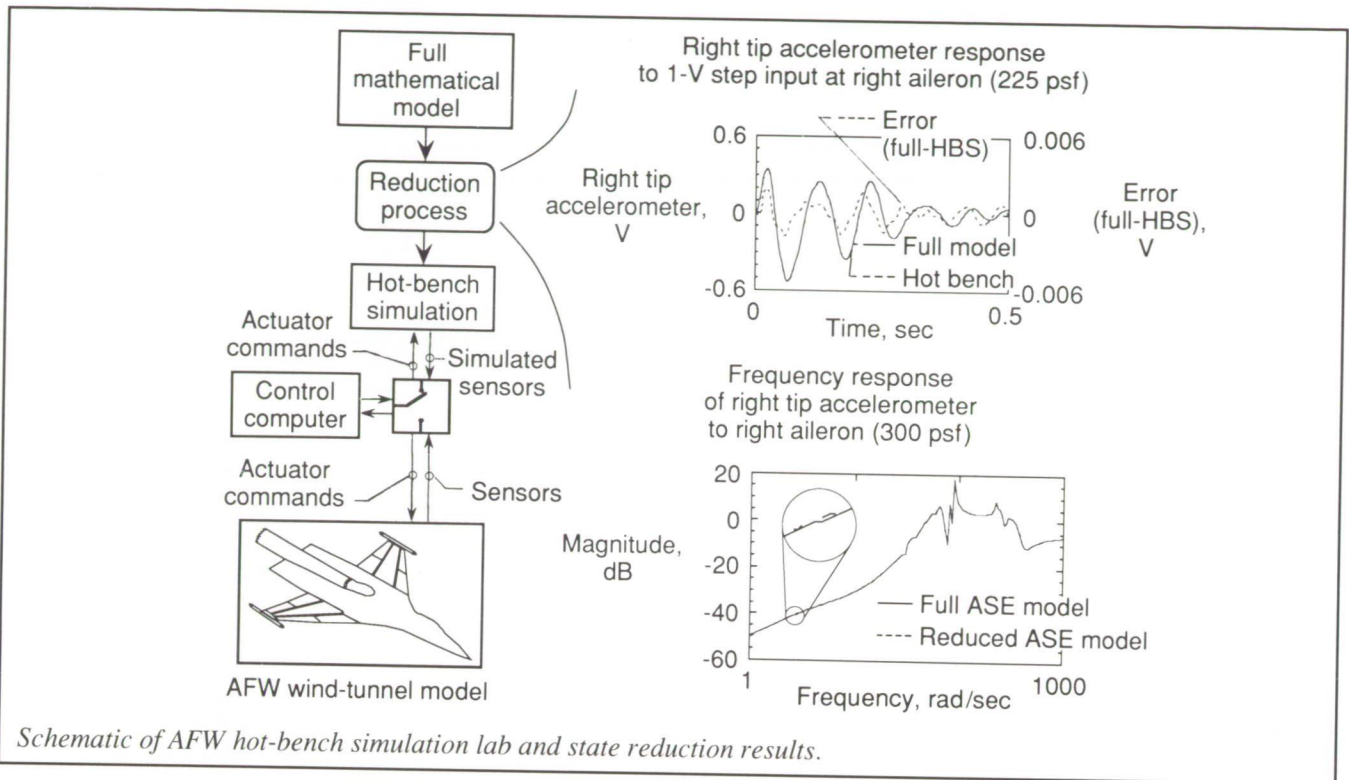
(Eugene A. Morelli and Brent R. Cobleigh, 44078)
Flight Systems Directorate

State Reduction for Aeroelastic Simulation

The Active Flexible Wing (AFW) Test Program was a joint Langley Research Center/Rockwell International Corporation effort investigating digital active control of flutter and roll-induced loads. A hot-bench simulation capability (see the figure) was developed to test high-risk controller hardware and software prior to wind-tunnel tests.

An aeroservoelastic (ASE) system forms the largest part of the total simulation mathematical model. Direct implementation of the full, 172-state, ASE mathematical model would cause the hot-bench simulation to run too slow. The goal of this research was to reduce the state dimension of the ASE system while preserving response accuracy for all combinations of 10 inputs and 56 outputs (considered a true multi-input/multi-output problem).

The reduction process first decomposes the 172-state ASE model into stable and unstable subsystems. The stable subsystem then is mathematically transformed into an internally balanced (IB) coordinate form, wherein states are ordered in their



importance to system frequency response. Therefore, the last n IB states of the stable system can be removed, thus creating a reduced system. The maximum difference in frequency response between the full system and the reduced system (over all input/output pairs and frequencies) is bounded by a well-known expression that can be viewed as a function of n . Given a selected level of accuracy, one solves for the number of states to remove. For the AFW problem, an accuracy bound was chosen that was equivalent to 10 bits of precision. The reduced stable subsystem is recombined with the unstable portion of the original ASE model to form a complete reduced ASE model.

The reduction process was repeated at a variety of simulated operating points, thus spanning anticipated test conditions. At all operating points, the ASE systems state dimension was reduced by more than 50 percent, which allowed hot-bench timing goals

to be met. Example frequency and time responses at two operating points are shown in the figure. The agreement between full and reduced models was excellent. Detectable differences in frequency response magnitude do not occur until 60 dB below peak response (a factor of 1000 or approximately 2^{10}).

Numerical problems may arise when attempting IB decompositions of large systems. Initial efforts with available software (which worked for smaller problems) failed when applied to the AFW problem. A new algorithm was subsequently developed which employed singular value decompositions (well known for numerical robustness) to achieve an IB transformation matrix that worked without difficulty.

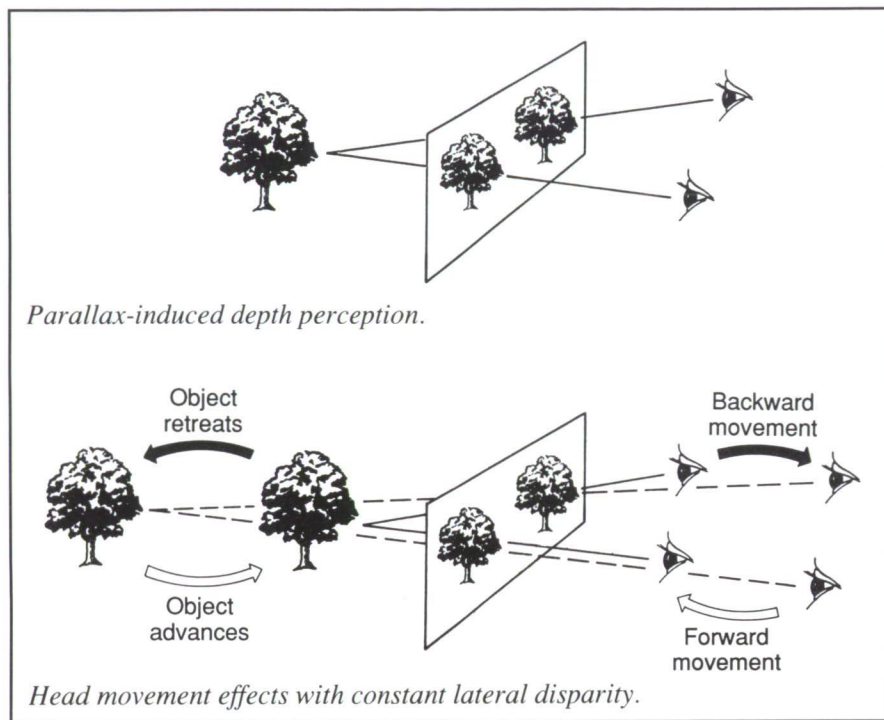
Advanced multi-input, multi-output state reduction methods must both preserve the salient features of the full mathematical model and work for problems of practical dimension. This

research contributes to the development of reliable state reduction methods and aeroelastic simulation technologies.

(Carey S. Buttrill and Barton J. Bacon, 44016)
Flight Systems Directorate

Head Movement Correction Algorithm for Stereo 3-D Flight Displays

Real-world, three-dimensional pictorial displays incorporating true depth cues via stereopsis techniques have proved to be an effective means of displaying complex information in a natural way to enhance situation awareness and provide increases in pilot/vehicle performance. However, head movements can seriously distort the depth information embedded in stereo three-dimensional (3-D) displays



because the transformations used in mapping the visual scene to the depth-viewing volume depend intrinsically on the viewer location. The goal of this effort has been to provide parallax corrections for head movements, based on head-movement sensor input data, to the lateral disparity calculations used to generate stereo displays and to verify their accuracy.

The top portion of the figure illustrates the parallax concept that is employed to produce objects behind a flight display monitor screen via stereo pairs (lateral disparity). If the subject viewing a stereo display moves away from the display screen and the lateral disparity remains constant (i.e., is not corrected for this movement), the perceived object will appear to retreat farther from the screen (illustrated in the bottom portion of the figure). Conversely, if the subject moves forward toward the screen the object appears to also move toward the screen. Thus, any head movement effect is exaggerated by the accompa-

nying object movement. To further confuse the viewer, objects presented in front of the screen perversely move in directions opposite to those of objects located behind the screen. An algorithm was developed and implemented that corrects the lateral disparity calculations, based on head-movement sensor input data, to eliminate these exaggerated and confusing object movements. A verification experiment was conducted in the Crew Station Systems Research Laboratory.

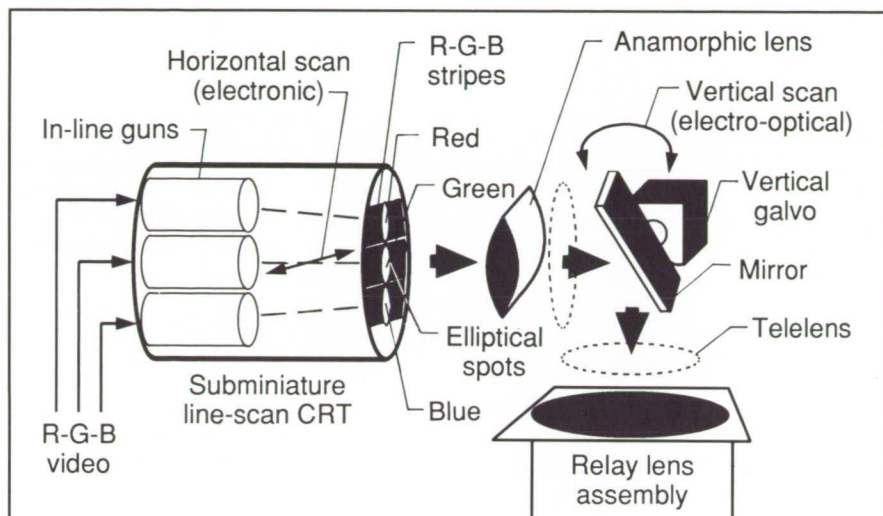
**(Russell V. Parrish and Steven P. Williams, 46649)
Flight Systems Directorate**

Design for Full-Color Conversion of Monochrome Helmet-Mounted Display

Helmet-Mounted Displays (HMD's) are used in flight vehicles for

target acquisition tasks and for the presentation of flight symbologies analogous to the use of Head-Up Displays (HUD's). The display formats have been primitive in terms of graphic capabilities because they were confined by the stroke technology employed. In flight simulation, rastergraphic HMD's have found application as conveyers of the outside visual scene (as dome replacement systems) and have provided a realistic, wide field-of-view (WFOV) visual environment for the pilot. However, in order to maintain the high resolution desired in such applications, color capability has been sacrificed, and monochrome raster HMD's are being used. One color system, which employs fiber-optic cables to convey the visual scene to the helmet, is available, but its application to the flight regime is impractical. The goal of this effort has been to provide an inexpensive and practical design for a color upgrade to an existing WFOV, monochrome HMD.

Traditional methods of producing color on a cathode-ray tube (CRT) by using a shadow mask or grill with red, green, and blue (R-G-B) phosphor triads or stripes cannot be properly scaled-down in size for use with the subminiature CRT's employed in HMD's without significant loss in resolution. However, a subminiature color CRT of sufficient resolution with only one horizontal scan line of R-G-B phosphors can be produced. This horizontal line is generated repetitively, and a galvanometer-driven mirror can then be used to supply vertical scanning (see the figure). This color raster subsystem invention, which was jointly developed by Langley Research Center and General Electric Company researchers, is designed to replace the existing monochrome CRT assemblies on an existing Langley HMD. An in-line, three-beam electron gun is used to



Simplified color generation principle for HMD upgrade.

To achieve the high luminance and high resolution (up to 2000 lines) desired, a laser-scanned, fiber-coupled system (based on enhancements of a feasibility prototype) was designed. The fundamental approach is outlined in the figure. Full-color pixel data for eight simultaneous scan lines per eye are generated by lasers (either gas or, if available, solid-state) and acousto-optic modulators off-helmet. The separately modulated beams (generated from red-green-blue (R-G-B) single sources via beamsplitter/mirror combinations) are combined and input to very small (9- μm core) optical fibers with suitable optical components. This luminance information is conveyed to

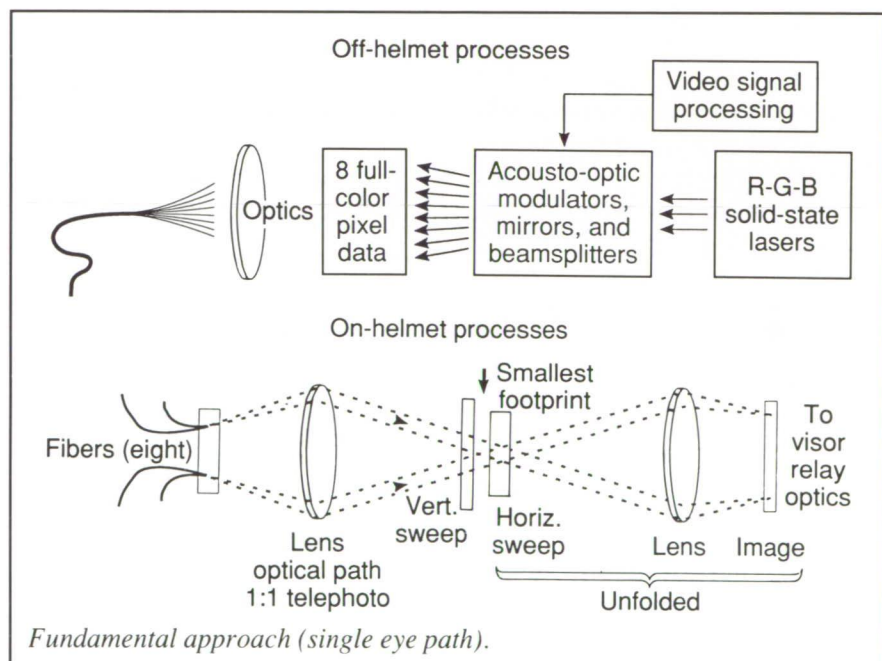
activate the three parallel R-G-B phosphor stripes (with very fast decay times) to produce repetitively a single R-G-B horizontal scan line.

(William S. Beamon, Russell V. Parrish, and Steven P. Williams, 46649)

Flight Systems Directorate

Design for Laser-Scanned, Full-Color Helmet-Mounted Display

Many of the emerging concepts for advanced pictorial flight displays to be used in Helmet-Mounted Displays (HMD's) are predicated on raster formats, with full-color, high-resolution images. These formats are to be presented with stereoscopic cueing in wide field-of-view (FOV) displays, fused with sensor imagery or sensor-based information. To provide stereopsis, binocular HMD systems must trade some of the total FOV available from their two monocular fields to obtain a partial overlap region. The visual field then provides a mixture of cues, with monocular regions on both peripheries



Fundamental approach (single eye path).

and a stereo region in the overlapped center. The addition of color cueing capability is more difficult and it requires a costly trade-off in resolution. The goal of this joint Langley Research Center, U.S. Army, and General Electric Company effort was to design a stereo-capable, wide FOV HMD that provides full color without sacrificing high resolution.

on-helmet scanning processes through a small umbilical cord. Thus, the bulky, heavy, heat-producing components are located off-helmet. The on-helmet ends of the fibers are systematically angled outward from the center such that the images of each pixel cross in the center of the telephoto lens path, thus forming a small "waist" suitable for use by very small mirrors. A 4-kHz horizontal scan

mirror and a linear, 60-Hz vertical galvanometer scanner convert the eight pixels into a complete raster image. (William S. Beamon, Russell V. Parrish, and Steven P. Williams, 46649)
Flight Systems Directorate

Brainmap Analysis Identifies States of Awareness for System Monitoring Tasks

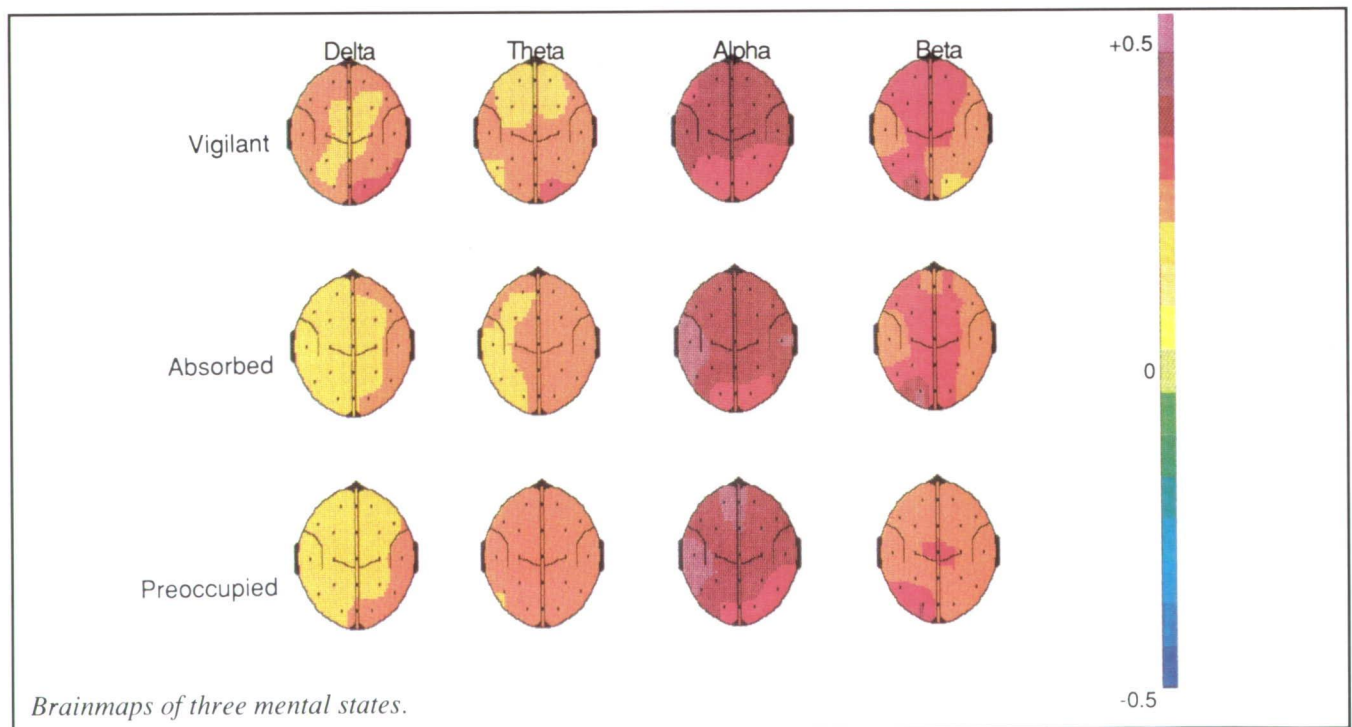
Analysis of the Aviation Safety Reporting System (ASRS) data base reveals that flight crew members often relate their mistakes to their experience of certain states of awareness. The crew members, whose responsibility it is to monitor and manage the progress of highly complex systems, lapse into states that are incompatible with the demands of that task. These states can

be characterized as hazardous. As automated systems become more capable, conditions that induce hazardous states are more likely to occur. The objective of this research has been to determine the physiological correlates of hazardous and effective states experienced during a monitoring task.

The brainmaps in the first figure reveal that certain electrode sites exhibit activity in the alpha and beta frequency bands which is different across the three states. The second figure summarizes one individual's discriminant results in a trial of the procedure for a subset of electrode sites for the alpha and beta bands. The rows represent the states that subjects were instructed to assume. Each of the underlined numbers on the diagonals represents the percentage of the data which is correctly identified by the discriminant function. Each of the off-diagonal entries represents the propor-

tion of the data which is incorrectly identified. In the second figure, each of the underlined diagonal terms under the "subsequent identification" heading represents an estimate of the likelihood that a single 2 1/2-sec epoch of electroencephalograph (EEG) could be correctly identified as a sample of brain activity observed during the corresponding state.

Discriminant functions have correctly assigned better than 90 percent of the initial data and averaged better than 60 percent correct in the identification of the retest data across six individual cases. The state identification procedure, then, represents a technology for objectively indexing mental-state experiences within individuals, and this procedure can be used to subsequently identify these states when they occur in these same individuals under operational conditions. This technology provides the capability to evaluate the design of



ORIGINAL PAGE
COLOR PHOTOGRAPH

Mental state	n	Classification, percent, as:				
		I	II	III	IV	V
Initial discriminant (test)						
I Eyes open	40	<u>95.0</u>	0.0	2.5	0.0	2.5
II Eyes closed	28	3.6	<u>96.4</u>	0.0	0.0	0.0
III Vigilant	40	0.0	0.0	<u>100.0</u>	0.0	0.0
IV Absorbed	37	5.4	0.0	0.0	<u>89.2</u>	5.4
V Preoccupied	40	0.0	0.0	0.0	2.5	<u>97.5</u>
Subsequent identification (retest)						
I Eyes open	33	<u>69.9</u>	2.7	5.5	4.1	17.8
II Eyes closed	40	1.5	<u>98.5</u>	0.0	0.0	0.0
III Vigilant	39	6.3	0.0	<u>92.4</u>	0.0	1.3
IV Absorbed	40	3.9	0.0	6.5	<u>62.3</u>	27.3
V Preoccupied	40	0.0	23.8	6.3	2.5	<u>67.5</u>

Computer classification of mental states for one subject using EEG power spectra.

flight management aids, including automation and information transfer technologies, based on their capacity to promote effective performance states. (Alan T. Pope and Edward H. Bogart, 46642)
Flight Systems Directorate

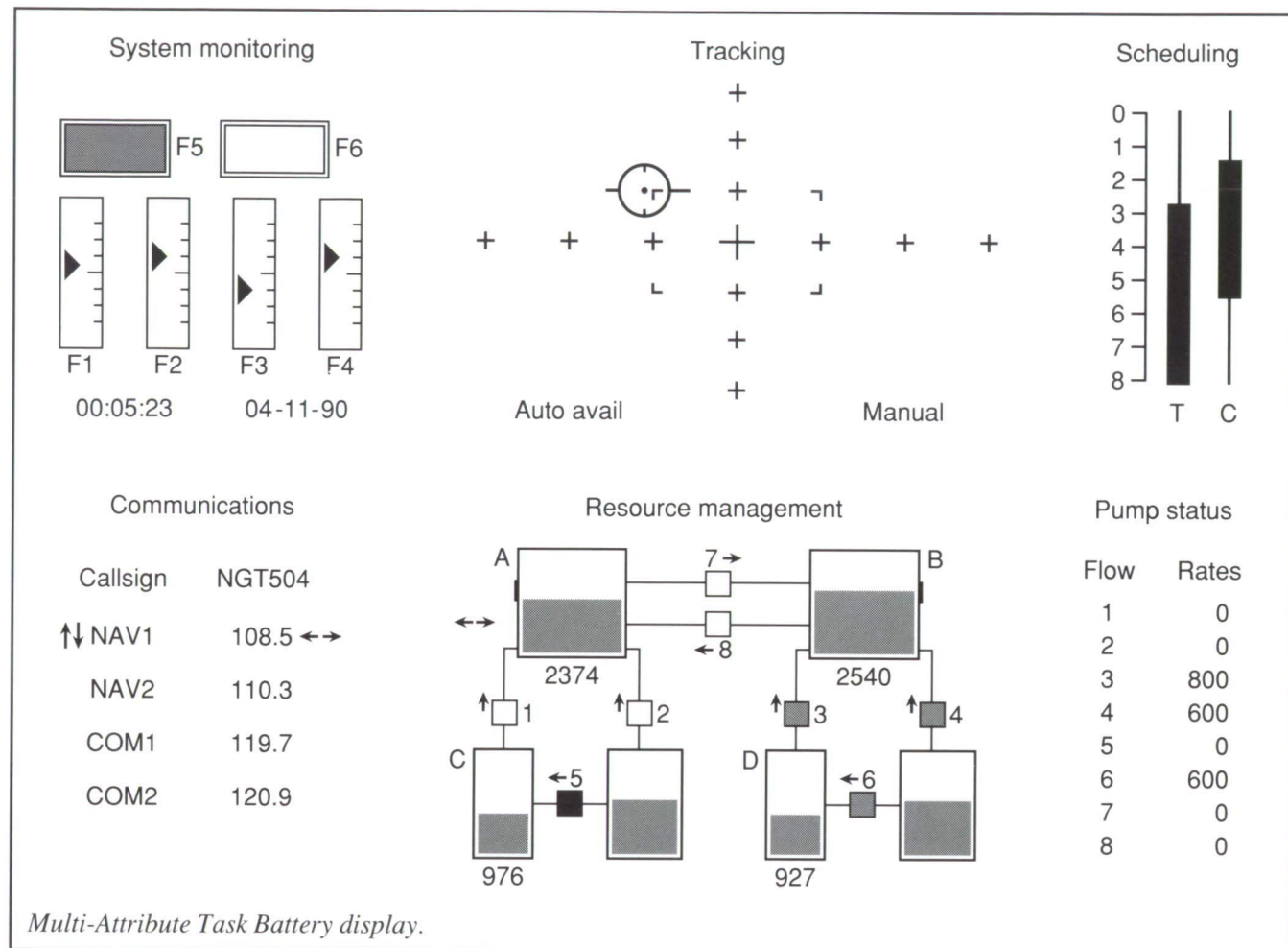
Task Battery for Pilot Strategic Behavior, Work Load, and Complacency Research

The definition and measurement of strategic behavior in a complex environment are crucial to understanding pilot performance, work load, and complacency. Strategic behavior is defined as the action (or inaction) that an operator takes in order to change the task structure, sequence of responding,

or allocation of mental resources with the purpose of dealing with an unexpected change in the environment, achieving a more manageable work load, and/or achieving one's goal safely and efficiently. The objective of this effort was the development of a real-time, interactive Task Battery to facilitate studies on strategic behavior, work load, and complacency. The approach used was to develop a flexible Multi-Attribute Task (MAT) Battery, utilizing desktop computer technology, for broad application in laboratory environments. The design incorporates tasks analogous to activities that crew members perform in flight, while providing a high degree of experimenter control of task activities, automatic collection of behavioral response data, and freedom to use nonpilot test subjects. Features not found in existing computer-based tasks include an auditory communica-

tion task (to simulate air traffic control (ATC) communications) and a resource management task permitting many strategies for maintaining target performance. In addition, the MAT Battery was designed so that the task can be paused and on-screen work load rating scales presented to the subject.

The MAT Battery display, shown in the figure, presents up to four different tasks to the operator (monitoring, tracking, communications, and resource management) and allows the operator many different strategies for achieving good performance, including the use of automation. The type and timing of task events and stimuli presented to the operator are controlled by a script that can be edited to manipulate work load. In an initial study, which served to validate the effectiveness of task-activity-level manipulation and to demonstrate the



readiness of the MAT Battery, 92-min test sessions were employed with task activity levels patterned after a flight profile (high-low-high). Timing signals sent from the MAT Battery permitted simultaneous recording of the topographic electroencephalograph, eye movement/lookpoint, pupil diameter, heart rate and heart rate variability, and subjective work load ratings. (J. Raymond Comstock, Jr., and Ruth J. Arnegard, 46643) Flight Systems Directorate

FLEX: A Programming Language for Real-Time Systems

The Concord project at the University of Illinois has built a programming environment for large real-time systems, supporting explicit timing constraints, imprecise computations, and multiple versions of computations. This project developed a means to implement predictable real-time programs that have their timing constraints expressed as Boolean expressions. Programming tools were built which can analyze the performance information and propagate the timing constraints so that the programs have a high probability of meeting

their deadlines. This environment was built around FLEX, an object-oriented real-time language. The research was supported in part by the Illinois Computer Laboratory for Aerospace Systems and Software (ICLASS) block grant in coordination with the Langley Research Center, the Office of Naval Research, and the National Science Foundation.

In FLEX, the programmer specifies the limits on time and resources via the constraint block, which identifies a set of constraints on time and resources that must be satisfied when a given section of the program is in execution. A constraint may be either a Boolean expression, which is treated as an assertion to be maintained throughout

the lifetime of the block, or a timing constraint, which describes a constraint on the time at which the block may begin or end its execution. The timing constraint can be expressed using four attributes: start and finish times of the block; interval, which refers to the difference between the start times of two successive executions of the block; and duration, which refers to the difference between the start and finish times of the block.

FLEX also provides the ability to measure the performance of a block of code. Any sequence of statements may be instrumented by a special directive. This directive requests that the usage of a particular resource be measured at run-time, and it provides a model for

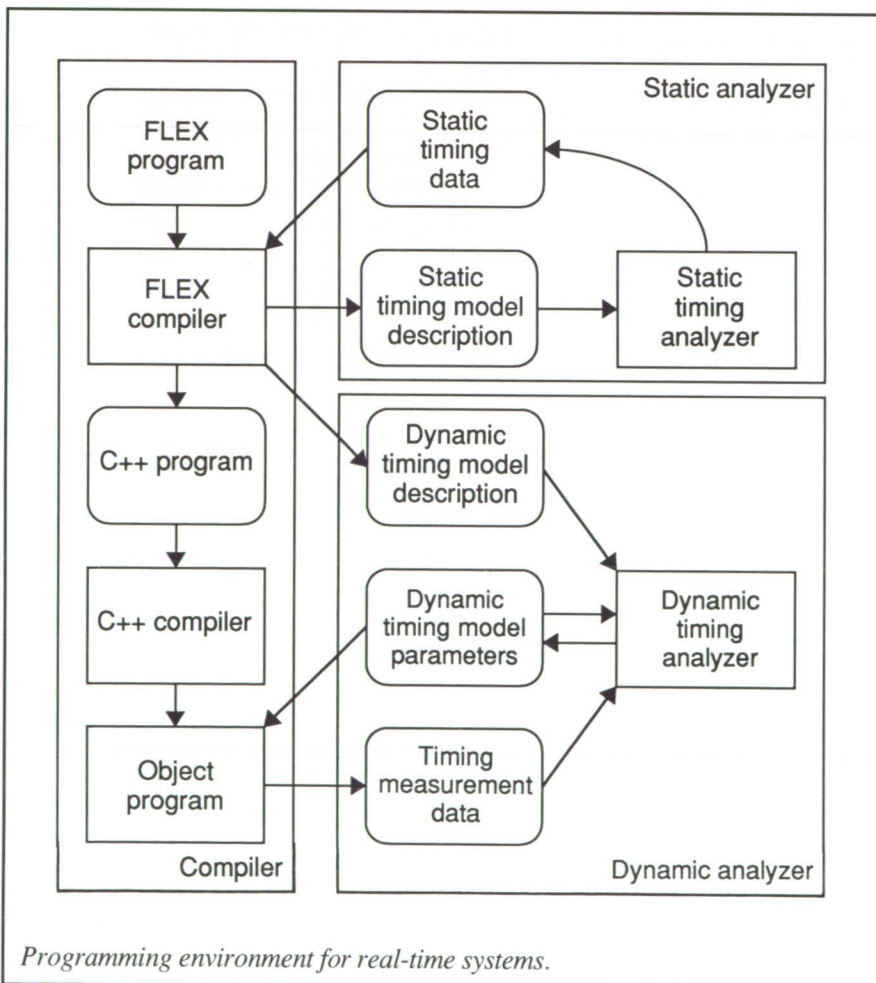
the amount of the resource that the programmer expects the block to consume. The parameters of the model are determined from the measured performance data by a timing analyzer.

The overall architecture of the programming environment for the FLEX language is shown in the figure. The FLEX compiler is based on a C++ compiler. The executable program writes the observed performance data for the performance measurement directives into a file. A separate program, the dynamic timing analyzer, reads these data and the performance model and determines the performance parameters. These parameters are recorded in a file that is read by the executable program at initialization

time, giving it the information needed to do more accurate binding and allocation. The portions of the system relating to the static analyzer, which determines the performance of a program by examining it at the instruction level and using some model of the underlying hardware, are now being implemented.

In the future, analysis tools for scheduling will be added to this environment so that programmers can easily verify the ability of the system to schedule.

(Kathryn A. Smith, 41699)
Flight Systems Directorate

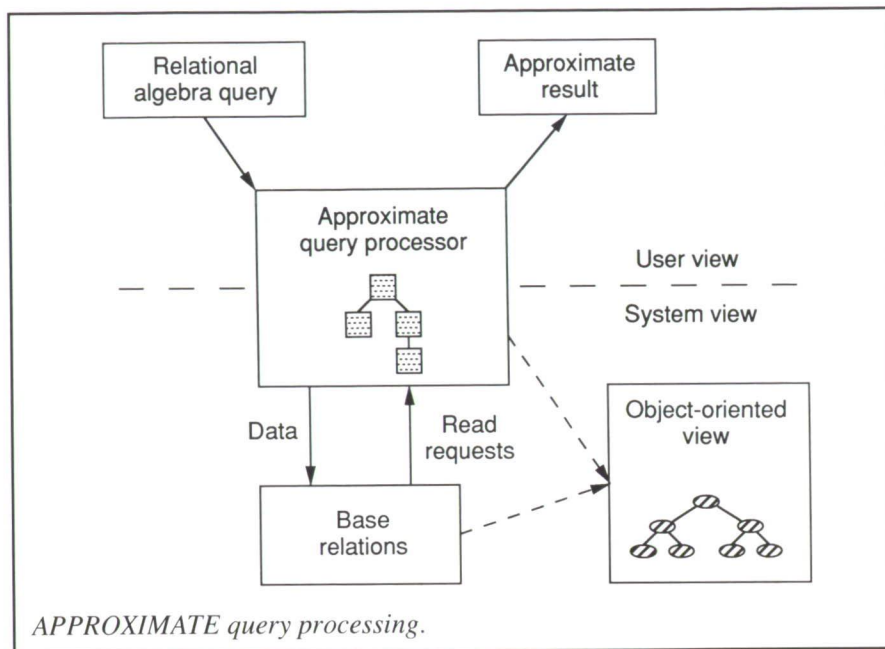


Programming environment for real-time systems.

APPROXIMATE: A Query Processor That Returns Monotonically Improving Approximate Answers

APPROXIMATE is a query processor designed to produce approximate answers to data base queries. Approximate answers are needed if part of the data base is inaccessible or not enough time exists to retrieve and process all the data to answer the queries. This type of data base scheme is applicable to hard real-time applications such as machine vision, multiple robots, and collision avoidance systems. The work was performed at the University of Illinois Urbana-Champaign and was partially supported by the Illinois Computer Laboratory for Aerospace Systems and Software block grant with Langley Research Center.

APPROXIMATE uses the imprecise computation approach of making a usable approximate result available whenever the exact one cannot be produced in time, and it produces approximate answers that have



nondecreasing accuracy as more data are retrieved and processed. The data base is assumed to be complete and the query precise. The imprecision in the answer occurs because time constraints or failures prevent all the data required to answer any query from being retrieved and processed. When all the data are retrieved and processed, the final answer is the exact answer.

Each approximate answer consists of two parts: a certain subset of the data objects that are known to be in the exact answer and a possible subset of data objects whose membership in the exact answer is yet unknown. The union of these two subsets contains the exact answer. The certain subset is produced from the data processed thus far. As the query processing progresses, an approximate answer improves when some data objects are moved from the possible subset to the certain subset because either their membership in the exact answer becomes certain or because they are discarded when their not being in the exact answer becomes known.

The APPROXIMATE query processor maintains an object-oriented view of the data base. APPROXIMATE relies on this view for the semantic support needed to identify an initial approximation to compute the attributes of data objects in the possible subset and to monotonically improve the approximation during query processing.

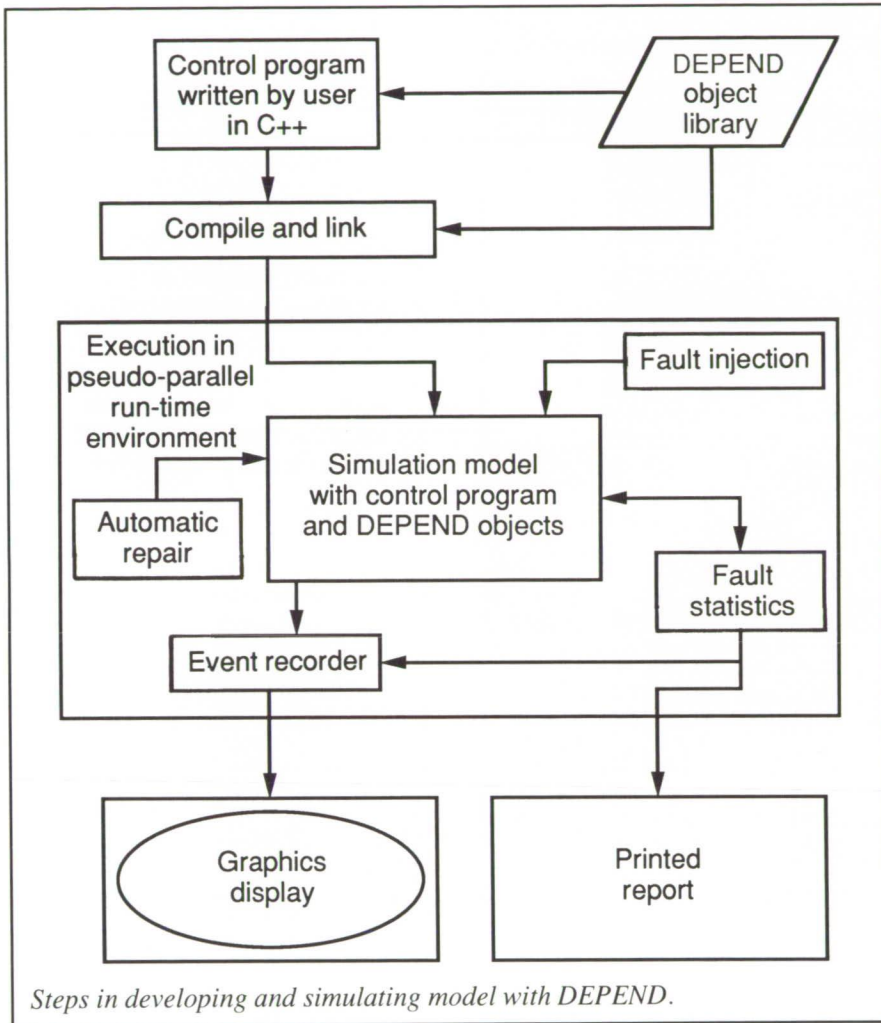
An object-oriented prototype, APPROXIMATE has been implemented at the University of Illinois Urbana-Champaign. This prototype produces approximate answers to relational algebra queries and displays the approximate answers as they are produced during processing. Its interactive interface allows the user to stop the processor when an approximate answer produced is good enough and to request query processing be continued if the approximate answer produced thus far is not yet useful. APPROXIMATE can be implemented in a relational data base system with little or no change required to the underlying relational architecture. (Kathryn A. Smith, 41699)
Flight Systems Directorate

DEPEND Environment

DEPEND is a joint performability and dependability analysis tool that facilitates the modeling and analysis of fault-tolerant architectures at the system level. DEPEND provides a library of objects that simulate the functional behavior of components commonly used in fault-tolerant systems. These objects also inject faults, initiate repairs, compile fault statistics, and generate detailed reports. To model a system, the user writes a control program that declares instances of these objects, initializes them, and coordinates their actions in a way that mimics the system being simulated. The bulk of the simulation work is performed by the DEPEND objects.

The steps required to develop and execute a model are shown in the figure. The user writes a control program in C++ with the objects provided by DEPEND. Once it is written, a command is used to compile and link the program with the DEPEND objects and the run-time environment. The model is then executed in a simulated parallel environment created by the run-time environment. Here, the assortment of objects (including the fault injectors, servers, and links) executes simultaneously to simulate the functional behavior of the architecture. Faults are injected and repairs are initiated, all according to the user's specifications. When the simulation is complete, the user can opt to play back the results with the graphical display or produce a report containing the essential statistics of the simulation.

DEPEND has been used to model and analyze the Tandem S2 UNIX-based fault-tolerant system. The entire system was simulated from a dependability perspective. Facets of the machine that have a bearing on its



A high-fidelity surface grid definition for the F/A-18 aircraft, suitable for Navier-Stokes computation, has been generated from a computer-aided design (CAD) surface patch description. The geometrical simplifications made to the configuration include fairing over the inlet, splitter plate, diverter, and leading-edge-extension slots. The empennage has also been neglected in the present effort. A multiblock structured volume grid has been generated using a transfinite interpolation technique. The entire domain is represented by approximately 1.25×10^6 grid points that are contained within 20 blocks using combinations of topologies. The flow field was computed with a version of CFL3D (developed at Langley) which has been recently extended for a generalized surface patching. The CFL3D code solves the compressible full Navier-Stokes equations by a finite volume technique that incorporates an upwind-biased, flux-difference-splitting approach.

The thin-layer Navier-Stokes results, with turbulent flow assumption, have been obtained at flight test conditions for the NASA F/A-18 High Alpha Research Vehicle (HARV) flown recently at the Hugh L. Dryden Flight Research Facility. The crossflow total pressure contours at various planes along the length of the configuration, with undeflected leading-edge flaps, as well as the leading-edge extension (LEX) vortex-core streamlines are shown in the figure. The magnitudes associated with contour quantities are displayed with a color bar. The results indicate that the wing upper surface is experiencing a considerable viscous loss because of a massive leading-edge flow separation. The present numerical results correspond to a two-orders-of-magnitude reduction of the residuals, requiring 3000 cycles and approximately 20 hours of CRAY-2 time. Solutions with

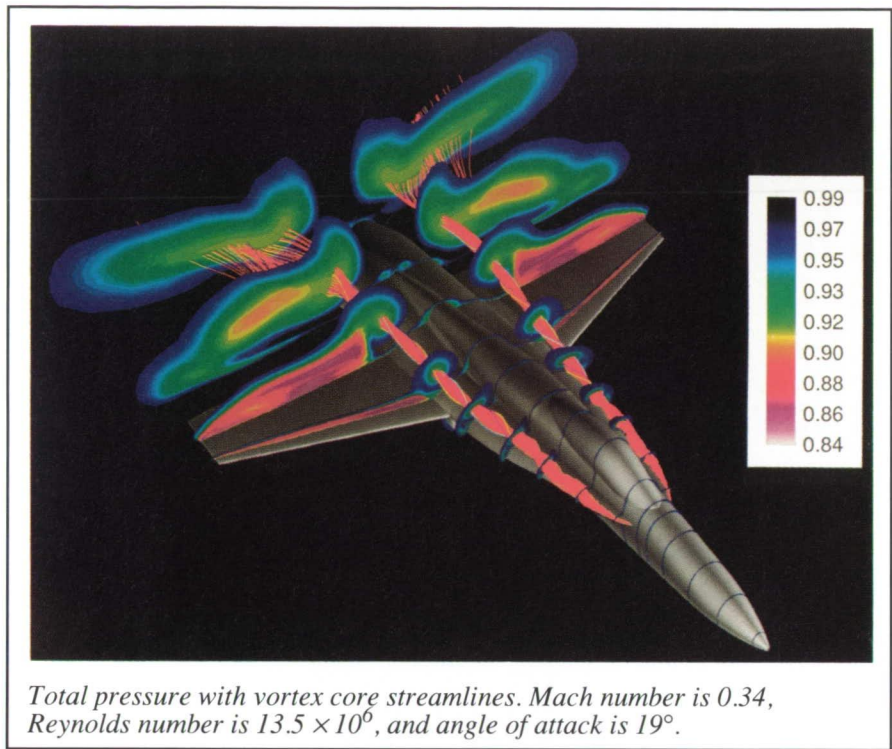
dependability, such as memory scrubbing, reintegration policies, and work-load-dependent repair times, are analyzed to determine their effect on the failure characteristics of the system. The simulated system was analyzed by injecting correlated errors, latent errors, and a combination of the two.

This work was performed at the University of Illinois Urbana-Champaign and was funded in part by the Illinois Computer Laboratory for Aerospace Systems and Software block grant with Langley Research Center.

(Kathryn A. Smith, 41699)
Flight Systems Directorate

Navier-Stokes Solution About F/A-18 Aircraft

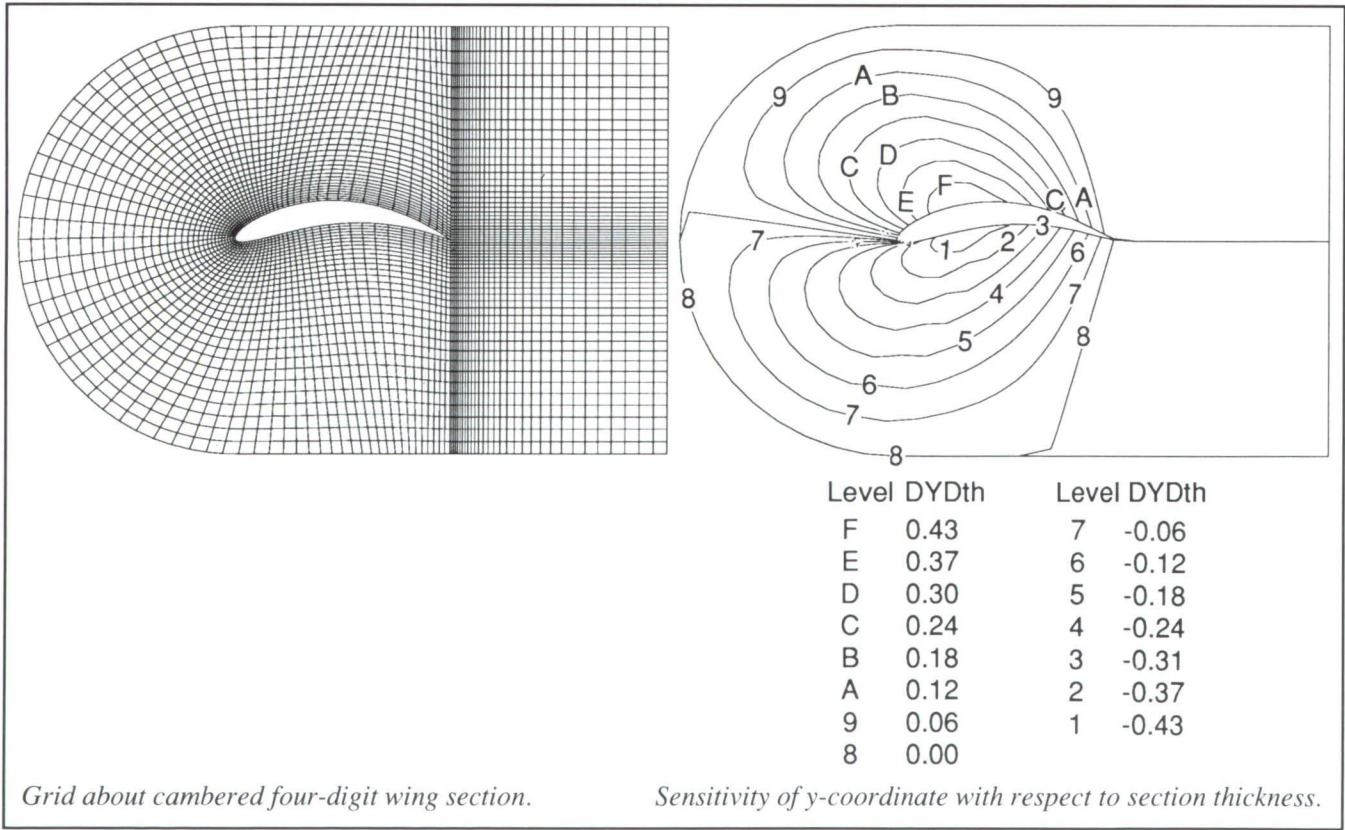
The High-Angle-of-Attack Technology Program (HATP) is specifically designed to provide an understanding of and a means to explore high-angle-of-attack aerodynamics about the F/A-18 aircraft. This intercenter cooperative effort among the Langley, Ames, and Lewis Research Centers includes data from a wide range of resources such as flight tests, wind-tunnel experiments, and computational fluid dynamics (CFD) simulations. The present effort is focused on applying an advanced Navier-Stokes method to an accurate numerical representation of the F/A-18 aircraft.



the leading-edge flap deflected have also been achieved.
(F. Ghaffari, 42856)
Aeronautics Directorate

Aerodynamic Surface Parameterization and Grid Sensitivity

An algebraic grid generation technique called the Two-Boundary Grid Generation (TBGG) is being used in conjunction with analytic representations of four- and five-digit NACA wing sections to investigate surface parameterization and grid sensitivity. With a minimum of three design parameters per section and three or more sections located in the spanwise direction, a reasonably complex wing



surface can be specified. A surface grid is obtained by interpolating the section-design variables in the spanwise direction, distributing points along the chord line, and evaluating surface grid coordinates. A different distribution of computational points along the chord line produces a different grid, but the underlying surface shape is fixed by the design parameters. The volume grid is computed with the TBGG algorithm. Chain rule differentiation of the algebraic volume-grid equations and surface-grid equations with respect to the design parameters yields the grid sensitivity derivatives.

A two-dimensional example grid using the four-digit section equations and three design parameters is shown in the left figure. The grid has concentrations at the leading and trailing points of the section and an exponential concentration from the wing section to the outer boundary. The sensitivity of the y-coordinate with respect to the section-thickness parameter is shown as a contour plot in the right figure.

(Robert E. Smith, 45774)
Electronics Directorate

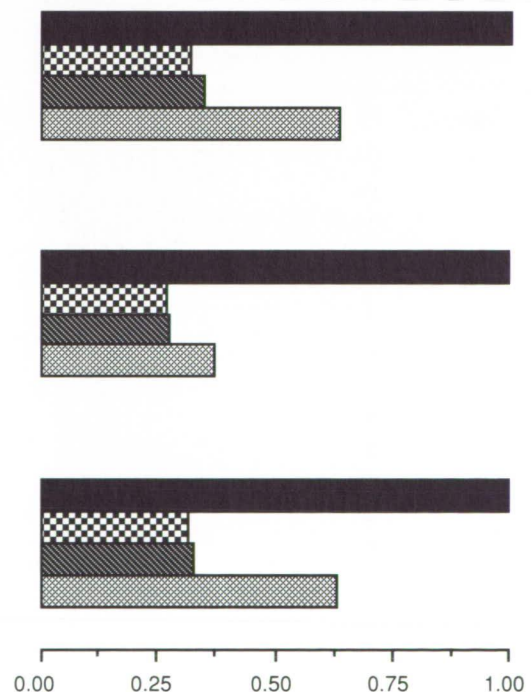
Efficient Multitasking of Choleski Matrix Factorization on CRAY Supercomputers

The computational cost of computerized structural analysis is often dominated by the cost of solving a very large system of algebraic equations associated with a finite-element model. Described here is a Choleski method used to solve linear systems of equations that arise in large-scale structural analyses.

The most efficient implementation of the Choleski method for a class of problems depends both on the structure

Method	CPU time, sec	Wall time, timef	Rate, MFLOPS	Speedup
High-Speed Civil Transport Aircraft, 16,146 equations Max. Semibandwidth = 594, Avg. Semibandwidth = 319				
VECTOR	6.20	6.22	216	-
AUTO	7.77	1.96	687	3.17
MICRO	7.85	2.15	626	2.89
FORCE	11.42	3.94	342	1.58
Composite cross-ply laminate with hole, 11,929 equations Max. Semibandwidth = 1,597, Avg. Semibandwidth = 1,081				
VECTOR	47.92	48.07	272	-
AUTO	50.52	12.84	1020	3.74
MICRO	51.22	13.04	1004	3.69
FORCE	55.34	17.57	746	2.74
Space Shuttle Solid Rocket Booster, 54,780 equations Max. Semibandwidth = 558, Avg. Semibandwidth = 355				
VECTOR	24.83	24.91	218	-
AUTO	30.25	7.78	698	3.20
MICRO	31.07	8.01	678	3.11
FORCE	43.87	15.74	345	1.58

VECTOR - no parallelization
 AUTO - autotasking
 MICRO - microtasking
 FORCE - FORCE using macrotasking



CRAY-2 factorization times in dedicated mode using four CPU's. Comparison of vector and parallel implementations of Choleski factorization for three example problems (left) and comparison of wall clock time (normalized) (right).

of the linear systems and the architectural features of the computer used for the analysis. A version of the Choleski method was designed to exploit key architectural features of CRAY supercomputers which have multiple parallel high-speed vector CPU's (central processing units). It uses a novel variable-band storage scheme and is structured to exploit fast local memory caches while minimizing data access delays between main memory and vector registers. Several parallel implementations of this version were developed for the CRAY-2 and CRAY YMP that compared the use of microtasking and autotasking directives. FORCE, a portable parallel language that uses macrotasking subroutines, was used for comparison with the microtasked and autotasked implementations.

Three structural analysis example problems were used to compare the parallel implementations of the Choleski method. The example problems were all generated using the computational mechanics test-bed (COMET) finite-element software system. The matrix factorization for each problem was timed in both dedicated and multiuser modes on both the CRAY-2 at Langley Research Center and the CRAY YMP at Ames Research Center. The CPU and wall clock timings for the parallel implementations were compared to single processor timings of the same algorithm. The autotasked and microtasked implementations were shown to be more efficient than the FORCE implementations. Computation rates over 1 gigaflop (1 billion floating-point operations per second) on a four-processor CRAY-2 and over 2 gigaflops on an eight-processor CRAY YMP were demonstrated as measured by wall clock time in a dedicated environment. The figure shows the CRAY-2 dedicated environment results. Reduced wall clock

timings for the parallel implementations relative to the single processor implementation of the same Choleski algorithm were also demonstrated for runs made in a multiuser environment.

(Andrea L. Overman, 45790)

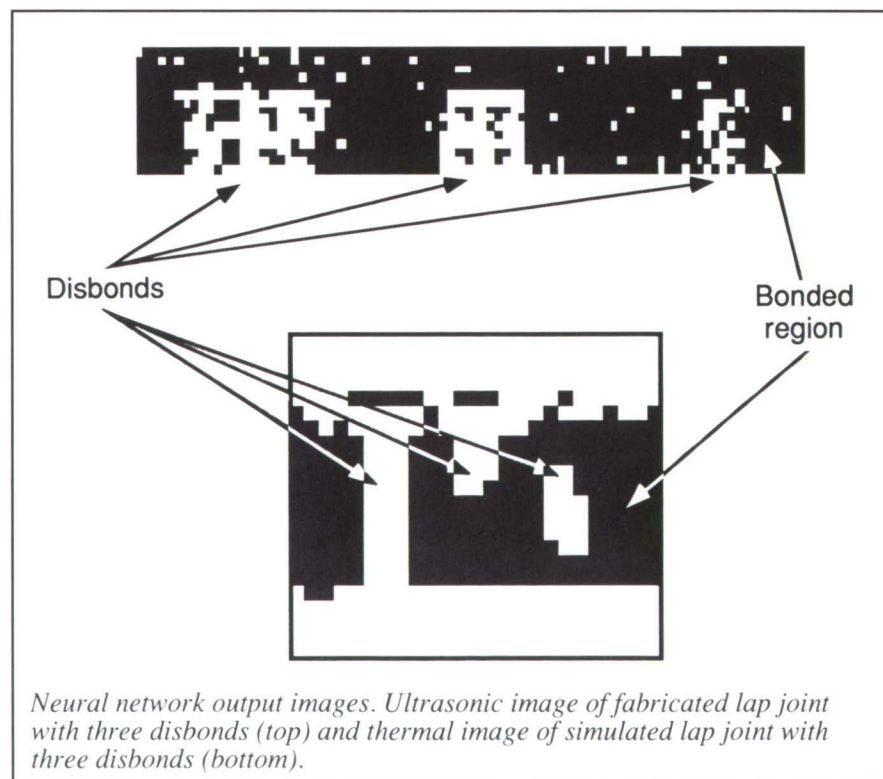
Electronics Directorate

Neural Networks for NDE

Thermal and ultrasonic nondestructive evaluation (NDE) techniques are currently proving to be effective methods to detect disbonds in the lap joints and doubler joints of aging aircraft. During thermal testing of aircraft, data are acquired in the form of thermal images, which are images of the temperature distribution in the test region. During ultrasonic testing, data are obtained in the form of ultrasonic signals that are a result of repeated reflections of an input

ultrasonic pulse at the bond interfaces. The thermal images and ultrasonic signals characterize the test location as being bonded or disbonded, and manual interpretation of these is a tedious, time-consuming process, especially in the presence of noise. With the aim of reducing human subjectivity and monotony associated with data interpretation and with the goal of speeding up aircraft inspection, a neural network-based NDE data analysis and interpretation has been pursued.

A neural network consists of a set of highly interconnected nonlinear processing elements called neurons. Each interconnection has an associated weight that can be adjusted to achieve a desired network behavior. The neural network can be trained to classify good signals from bad, by passing it through a learning phase. The network typically has an input layer of neurons to which are fed the input signals directly or a preprocessed version, and the classifi-



cation is obtained at an output layer of neurons. The advantages of using neural networks for signal classification are their high-classification accuracy, low sensitivity to noise, and high-classification speed.

Neural networks were successfully trained to classify data from both thermal and ultrasonic NDE. A very good classification accuracy of 99 percent was achieved with both experimental and simulation signals as part of the training set. The networks were trained to yield an output neuron value of 0.0 ("off" state) for a bonded location and an output value of 1.0 ("on" state) for a disbonded location. The output neuron value is rendered in the form of an image of pixels corresponding to various test locations and is thresholded at a value of 0.5 to obtain a binary image, clearly showing the extent of bond in the test region. The result of an ultrasonic testing of a fabricated panel with three disbands, with signals classified using a neural network, is presented at the top of the figure. The result of classifying thermal heating and postheating curves obtained through simulation of a lap joint with three disbands of various types and sizes is shown at the bottom of the figure. This technique has been successfully used to classify data acquired during on-site testing of aircraft. A hardware implementation of the neural network will considerably speed up data classification.

(D. R. Prabhu, 47530, and William P. Winfree)

Electronics Directorate

Polymer sample	Sample molecular weight	
	M*	M†
<u>Para-PAEK</u>	<u>X10³</u>	<u>X10³</u>
Whole polymer	19.0	21.3 ± 1.5
Fraction A	47.0	51.3 ± 2.4
Fraction B1	44.5	43.2 ± 1.9
Fraction C	17.6	17.5 ± 1.9
Fraction D	16.3	15.5 ± 2.0
<u>Meta-PAEK</u>		
Whole polymer	20.8	22.8 ± 0.2
Fraction AB1	60.8	60.3 ± 0.3
Fraction C	19.8	20.4 ± 0.3

* Gel permeation chromatography values: all ±10%

† Free volume model values: $V_f = A M^B$

Comparison between experimental and calculated values of molecular weights.

Free Volume Model for Molecular Weights of Polymers

One of the outstanding problems in aerospace polymer chemistry relates to the determination of molecular weights of processed polymers. Molecular weight, which is the most important property of polymers, determines their processability, structural integrity, and mechanical performance. No technique is currently available for accurately measuring the molecular weights of polymer films or moldings. A unique technique has been developed for measuring molecular weights of linear polymers. This technique is based on a predictive relationship between the average free volume cell size V_f and

the molecular weight M of the processed polymer, quite analogously to the Mark-Houwink relation between the intrinsic viscosity η and the molecular weights of the polymers in solution. Thus, V_f of the solid phase polymer becomes the counterpart of η of the polymer in solution. The V_f value can be measured accurately by positron lifetime spectroscopy.

The model has been tested on two geometries of poly[arylene ether ketone]s (PAEK). The molecular weights computed using the free volume model are in good agreement with the values measured by gel permeation chromatography. The results are summarized in the table. (Jag J. Singh, 44760, and Abe Eftekhari)
Electronics Directorate

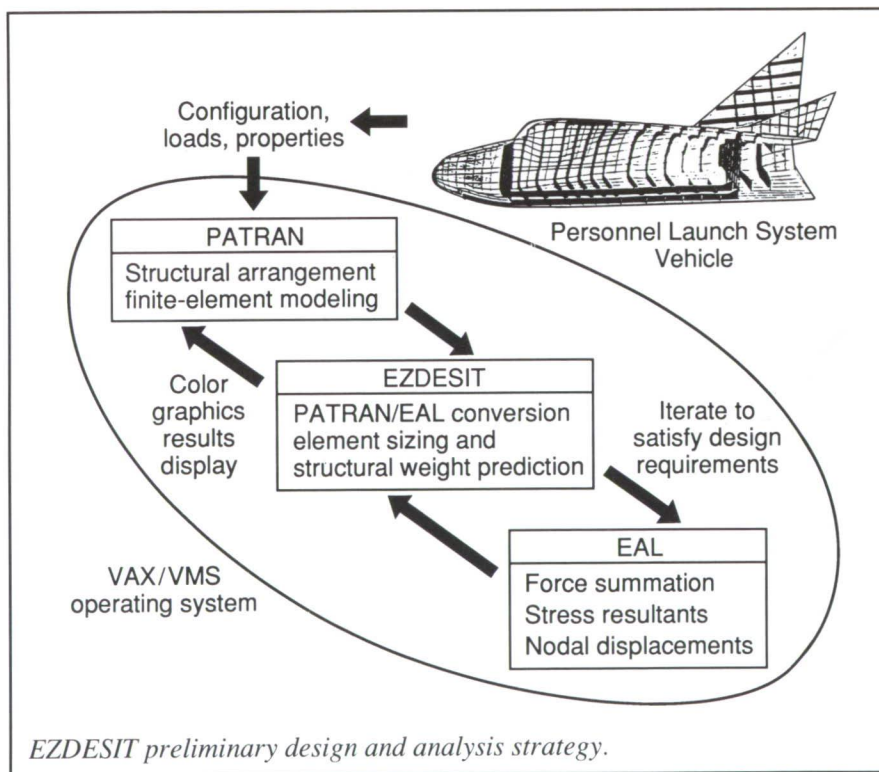
EZDESIT— A Computer Program for Structural Element Sizing and Structural Weight Prediction

Traditionally in flight vehicle design, early structural weight assessments are based on historical data. For advanced vehicles such as supersonic or hypersonic transports, virtually no historical weight data exist, and design studies rely heavily on preliminary structural analyses. A computer code for structural element sizing and structural weight prediction has been developed for preliminary analysis and design.

structural analyses of vehicle components. Configuration data are input into PATRAN to generate component structural arrangements and corresponding finite-element models compatible with EAL input requirements to calculate element stress resultants that are used within EZDESIT to evaluate and satisfy design requirements by resizing element dimensions. Ultimate and yield strengths, buckling loads, and minimum-gauge constraints are typical failure criteria that are satisfied by EZDESIT. Automatic iteration occurs between EZDESIT and EAL until all design requirements are satisfied for all design load cases. Final dimensions are

By performing structural analyses early in the design phase of PLS, it was recognized that using tension ties to support crew compartment pressurization loads resulted in a 576-lb (20-percent) weight savings over a design without such ties. This technique permits vehicle designers to consider effects of various structural arrangements, flight loads, assumed design criteria, material selections, and other important parameters on vehicle performance early in the design phase. (Jeffrey A. Cerro, Lynn M. Bowman, 45425, and Charles P. Shore)

Structures Directorate

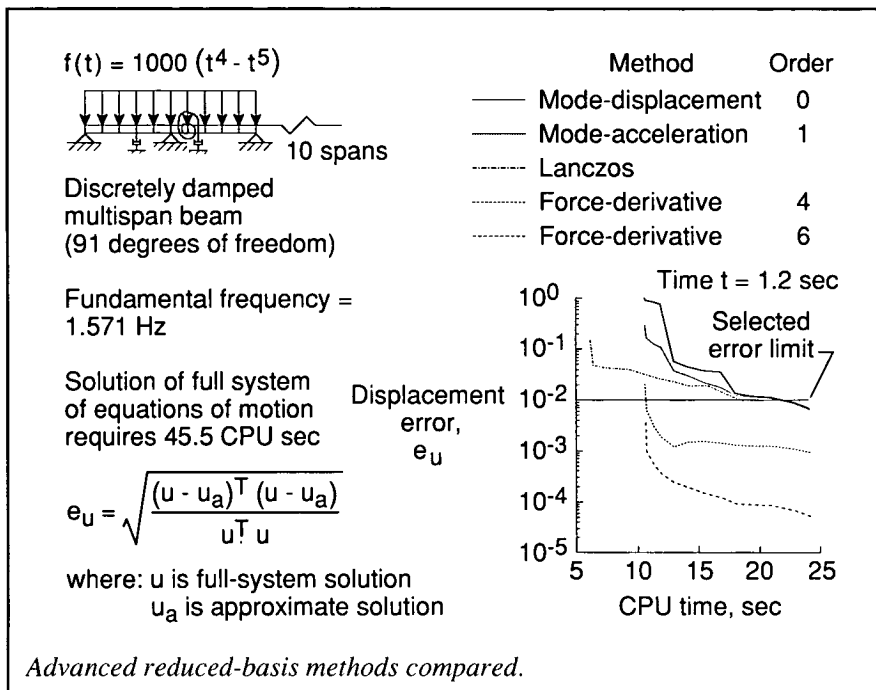


With the EZDESIT program on the VAX/VMS operating system, a graphical data manipulation program (PATRAN) was combined with a finite-element analysis program (EAL). As suggested in the figure, this combination creates a design tool that can be used for preliminary parametric

selected on a worst load case basis and are used with user-specified nonoptimum factors to estimate structural weights for various vehicle components. PATRAN is then used to graphically display pertinent sizing and weight-prediction results.

Advanced Reduced-Basis Methods Decrease Computational Requirements for Linear, Transient Structural Analysis

The transient analysis of complex structures that are modeled as discrete, multidegree-of-freedom systems often requires the solution of very large, coupled systems of equations. Calculation of the transient structural response for such large systems is computationally expensive and, hence, methods that can significantly reduce the problem size and computational cost and still retain solution accuracy are highly desirable. Reduced-basis methods can be used to approximate the solution of the complete system of equations with a much smaller or reduced set of generalized basis vectors. The purpose of the present study is to compare two advanced reduced-basis methods, the force-derivative method (FDM) and the Lanczos method, as well as two widely used methods, the mode-displacement method (MDM) and the mode-acceleration method (MAM), for



solving linear, transient structural analysis problems.

These four reduced-basis methods have been implemented on a Convex C220 high-performance computer using the computational mechanics test-bed (COMET) as a general purpose finite-element code, and results from these methods have been compared for solutions to linear, transient structural analysis problems. The comparison includes the number of basis vectors required to attain a desired level of accuracy and the associated computational time requirements. The approximate solutions obtained with the reduced-basis methods are also compared to a full-system solution obtained by directly integrating the full system of equations of motion of the system.

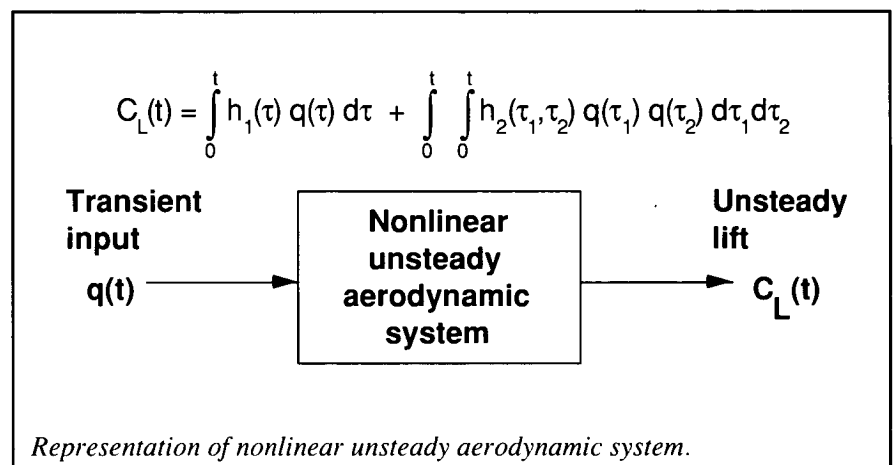
A typical example problem (simply supported beam) studied is shown in the figure. The higher order modal methods converge in approximately one-fourth of the time required for the full-system solution and approximately

one-half of the time required for the Lanczos method and the lower order modal methods. For the structural problems studied so far, the FDM has been shown to be the most efficient method.

(David M. McGowan, 44916,
and Susan W. Bostic)
Structures Directorate

Modeling of Nonlinear Aerodynamic Responses for Aeroservoelastic Analysis and Design

Because unsteady transonic aerodynamics are nonlinear and cannot be approximated accurately using traditional linear methods, the present research was undertaken to develop a methodology for modeling unsteady, nonlinear aerodynamic responses using the Volterra-Wiener theory of nonlinear systems for subsequent use in aeroservoelastic analysis and design. The basic premise of the Volterra-Wiener theory is that any nonlinear system can be modeled by an infinite sum of multidimensional convolution integrals as indicated by the equation at the top of the figure. These convolution integrals contain a kernel that describes the behavior of the system at a given order. The first-order kernel h_1 is simply the linear unit impulse response of the system. The second-order kernel h_2 is the second-order, nonlinear unit impulse response of the system. The second-order term is a measure of the relative influence of a previous input on the current response, which is a measure of nonlinearity. Similar definitions apply to higher order kernels although the present analysis is limited to a second-order formulation. For a linear system,



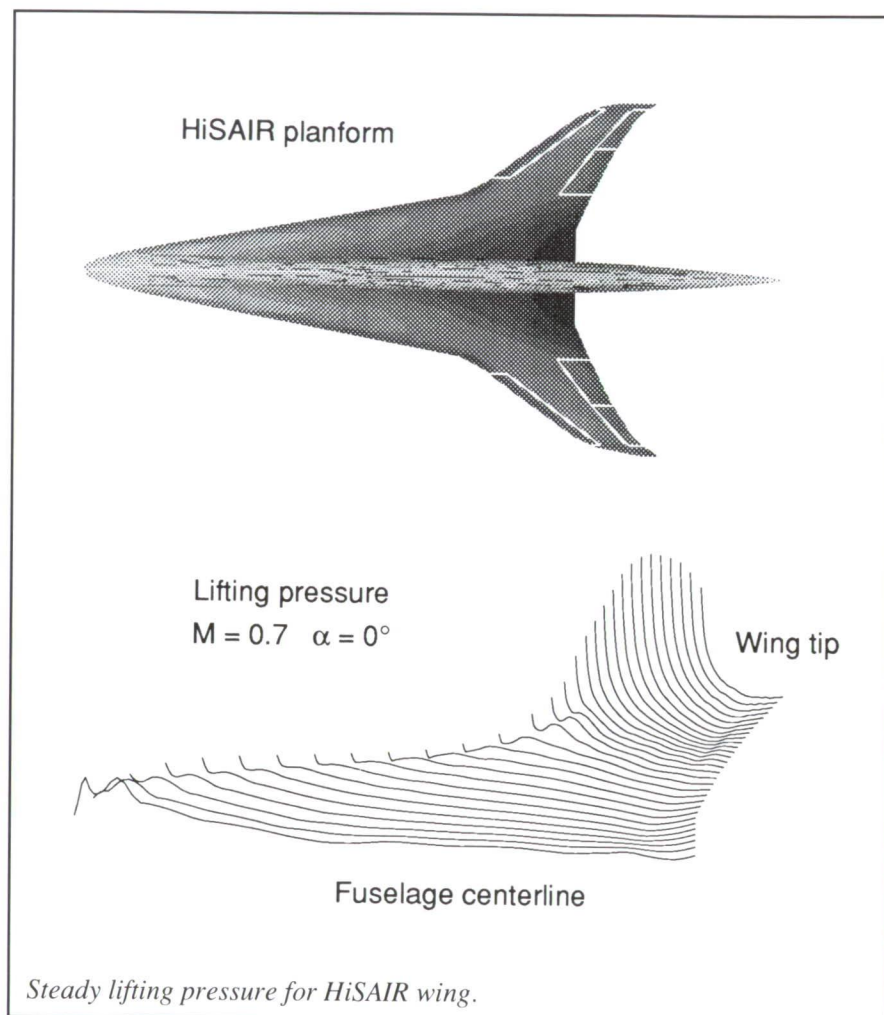
the second-order kernel and higher order kernels are identically zero.

Once the kernels of a given nonlinear aeroelastic system are identified, the nonlinear response of the system to an arbitrary input can be predicted. For a given aeroelastic configuration, the first- and second-order kernels can be generated using the advanced CAP-TSD (Computational Aeroelasticity Program-Transonic Small Disturbance) code. For example, as shown schematically in the figure, the nonlinear unsteady lift C_L because of some arbitrary aeroelastic transient input q can be determined. Once the kernels have been calculated for a given flow condition, the CAP-TSD code does not need to be reexecuted. The ability to provide nonlinear, unsteady aerodynamic information without having to continually execute a costly CFD (computational fluid dynamics) code is a significant advantage of this methodology. This characteristic feature of the approach makes it highly suitable for aeroservoelastic analyses and designs that can account for nonlinearities in the unsteady aerodynamics. Although the results are not shown here, the method has been successfully applied to practical applications.

(Walter A. Silva, 42834)
Structures Directorate

Prediction of HiSAIR Vehicle Air Loads Using CAP-TSD Code

The CAP-TSD (Computational Aeroelasticity Program-Transonic Small Disturbance) computer code is being used to investigate the capabilities of nonlinear CFD theories to provide improved unsteady aerodynamics analyses for complex, blended



wing/body configurations, including the modeling of highly swept wing planforms, multiple control surfaces, and wing/body interference effects. As part of this study, a fully three-dimensional analytical model of the HiSAIR vehicle is being developed for unsteady transonic aeroelastic analysis. The analytical model will include the vehicle body, wing thickness, twist, dihedral, and control surfaces. Aeroelastic calculations will be performed using mode shapes supplied by the structural analysts in order to determine a flutter boundary.

The initial model of the HiSAIR vehicle consists of a swept and tapered wing with thickness, twist, dihedral,

and control surfaces. The plot on the lower part of the figure shows the steady lifting pressure distributions for the thick wing model at $M = 0.7$ and $\alpha = 0^\circ$. As the plot indicates, the lifting pressure is low over the highly swept inboard section of the wing and increases significantly on the outboard section. Although not shown on the figure, the effect on the lift and moment coefficients of individually deflecting the flaps 1° has also been calculated. The inboard trailing-edge flap has the largest effect on both the lift and the moment coefficients, and the effect of the leading-edge flap is minimal. The incremental forces because of control surface deflection agree very well with flat plate calcula-

tions, thus verifying known results for control surface effects and validating the analytical model.

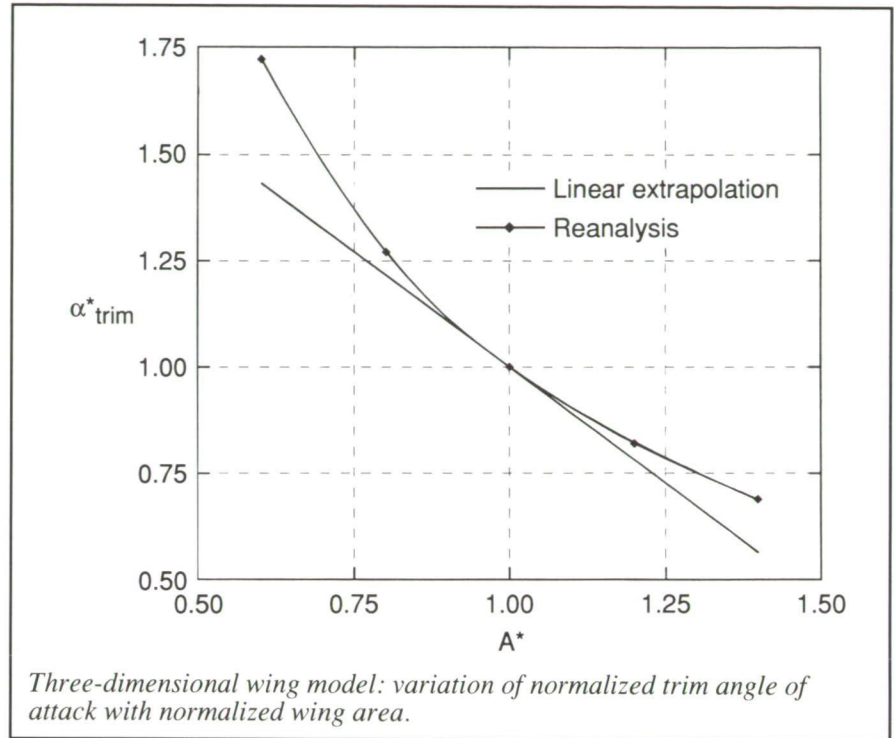
The results indicate that the CAP-TSD computer code can be used to calculate the aerodynamic loads on the highly swept wing planform of the HiSAIR vehicle. In addition, the effect on these loads of control surface deflections can be investigated. These results suggest that the method can be applied to investigate aeroelastic effects that may be significant for the HiSAIR vehicle.

(James T. Howlett, 42280)
Structures Directorate

Shape Sensitivity Analysis of Aeroelastic Response

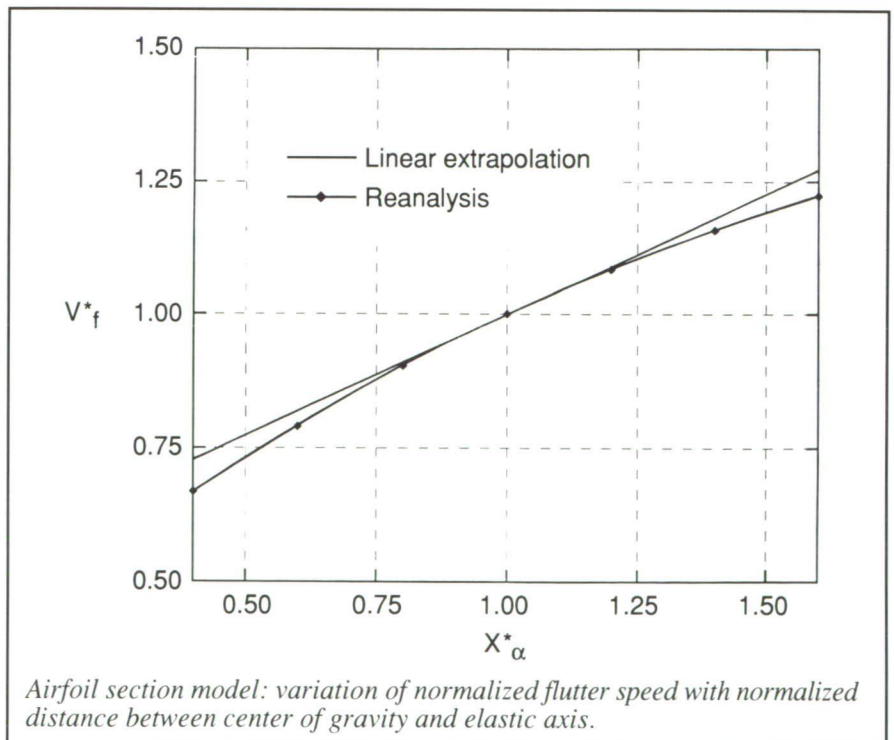
Sensitivity analysis is a technique that predicts changes in the response of an engineering system to changes in its design parameters. Shape sensitivity analysis of aeroelastic responses is a critical tool in the design and optimization of flexible aircraft.

A variation of Sobieski's Global Sensitivity Equations approach has been implemented to perform shape sensitivity analysis of the static aeroelastic response of a three-dimensional wing model. The formulation is general and accepts any aerodynamic and structural analysis capability. In its current implementation, the aerodynamic package FAST, based on lifting surface theory, and the structural package ELAPS, based on equivalent plate theory, are used. The first figure shows the sensitivity of the normalized trim angle of attack α^*_{trim} to changes in normalized wing area A^* for a forward-swept trapezoidal wing. A linear extrapolation based on the sensitivity derivative of the trim angle of attack to wing area is exactly



tangent to a sensitivity curve obtained by recalculating the angle of attack for different wing areas. In addition, the linear extrapolation proves to be a

good predictor of the actual changes in angle of attack for wide (40 percent) variations in the wing area.



The sensitivity of the flutter response of a two-dimensional wing section was also obtained using a first-order state space form for the unsteady aerodynamic forces. The second figure shows the sensitivity of the normalized flutter speed V_f^* to changes in the normalized distance between the center of gravity of the section and its elastic axis X^*_α . Observations similar to those from the previous example can be made.

(R. K. Kapania, L. B. Eldred, and J.-F. M. Barthelemy, 42809) Structures Directorate

Continuous Production Method for Manufacturing High-Temperature Thermoplastic Prepreg

LaRC-TPI (Langley Research Center-Thermoplastic Polyimide) is a linear aromatic polyimide that was discovered by NASA in the late 1970's. This material possesses physical properties desirable in an engineering thermoplastic, such as elevated temperature resistance as well as superior stiffness and impact strength. A primary method of fabricating advanced thermoplastic-matrix parts involves the use of prefabricated stock materials, such as "prepreg" (preimpregnated tape). However, the production of LaRC-TPI prepreg, using traditional hot-melt methods, has been hindered by the relatively poor melt flow characteristics of this polymer.

An improved manufacturing method is currently under development that will allow the production of LaRC-TPI prepreg suitable for postfabrication into high-performance composite structural profiles. This processing method is a pultrusion-

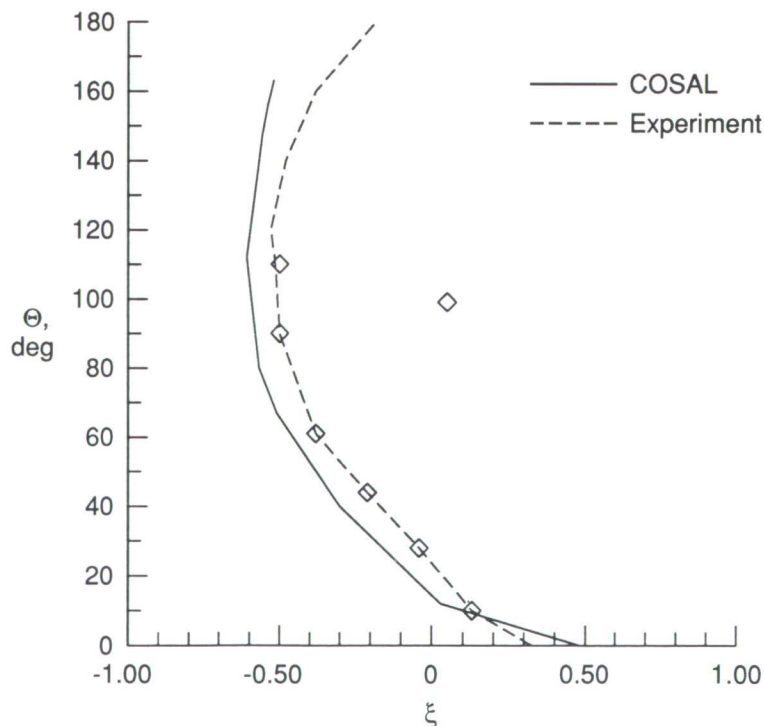
based technique currently utilizing LaRC-TPI powder impregnated graphite reinforcement to produce 0.250-in.-wide by 0.006-in.-thick prepreg tape. In the process, the impregnated reinforcement is spread to the desired width and pulled through a preheating station, where consolidation is initiated. It then passes into a specially designed die, which applies heat and pressure to form the composite material to specified dimensions. The final stage involves cooling the prepreg under containment to preserve these dimensions. This process should be adaptable to produce prepreg (using a variety of thermoplastic polymers) of any width up to 12 in.

(Gary Johnson, 44526) Systems Engineering and Operations Directorate

Transition Prediction in 3-D Flows Over Axisymmetric Bodies at Incidence

The purpose of this research effort was to develop a design tool for transition prediction, based on linear stability analysis, in fully three-dimensional (3-D) boundary-layer flows. This effort was accomplished by modifying an existing linear stability code. The modified stability code was validated for several cases, including forebody and swept-wing configurations, at both high and low speeds. The final code should provide designers with a useful tool for laminar-flow control applications.

The existing compressible stability code, COSAL, was developed for transition prediction on swept wings with straight isobars. In order to extend



Computed versus experimental transition location for flow over prolate spheroid at incidence.

the prediction capability to general 3-D bodies, COSAL has been modified to accept 3-D boundary-layer profiles from boundary-layer and Navier-Stokes solvers. A filtering routine was developed to convert the Navier-Stokes profiles from nonorthogonal grids into a format acceptable for the stability calculations.

Results have been obtained for forebody and swept-wing configurations. As shown in the figure, calculations are compared with experimental results for the case of a prolate spheroid at an angle of attack of 10° . Here, ξ represents the axial distance along the spheroid centerline, and θ represents the circumferential location. The mean flow was computed using a boundary-layer code. Results for the transition front agree well with the experimental results of Meier and Kreplin.

In summary, the linear stability code, COSAL, was modified to accept fully 3-D mean flow profiles. The code has been verified for several different configurations and is expected to provide designers with a useful tool in

the development of laminar-flow control applications.

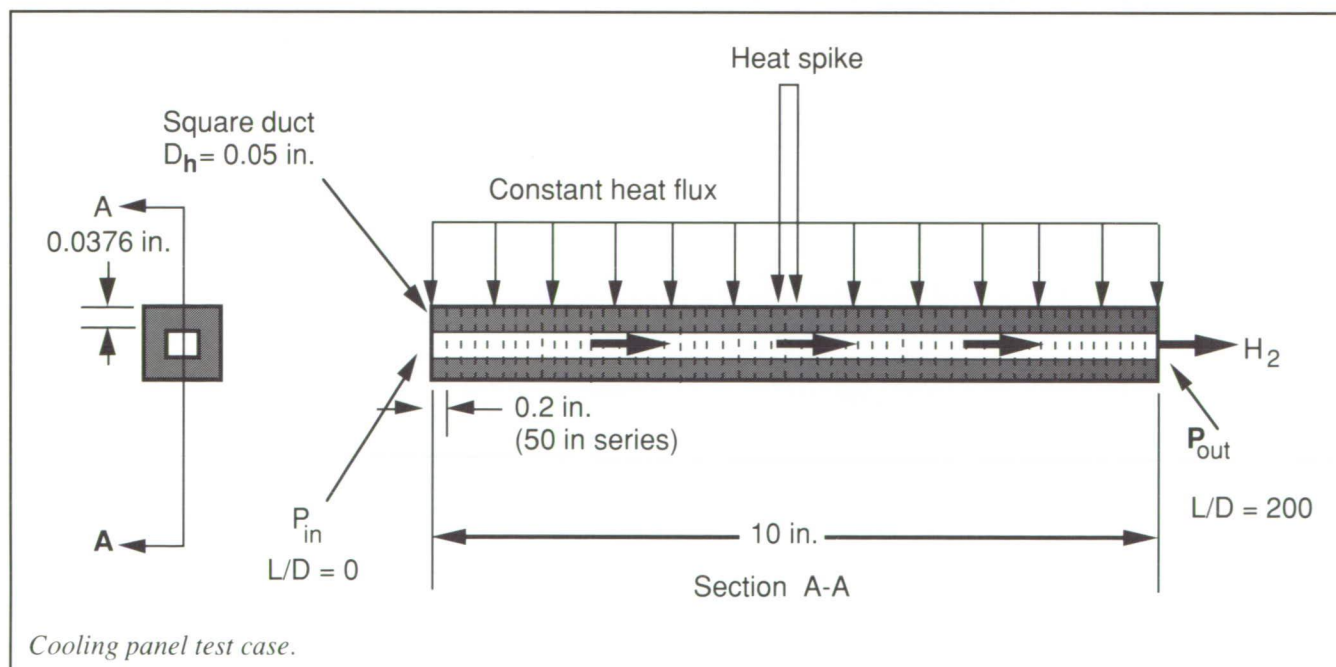
**(Robert E. Spall, Venkit Iyer, and Mujeeb R. Malik, 45561)
Aeronautics Directorate**

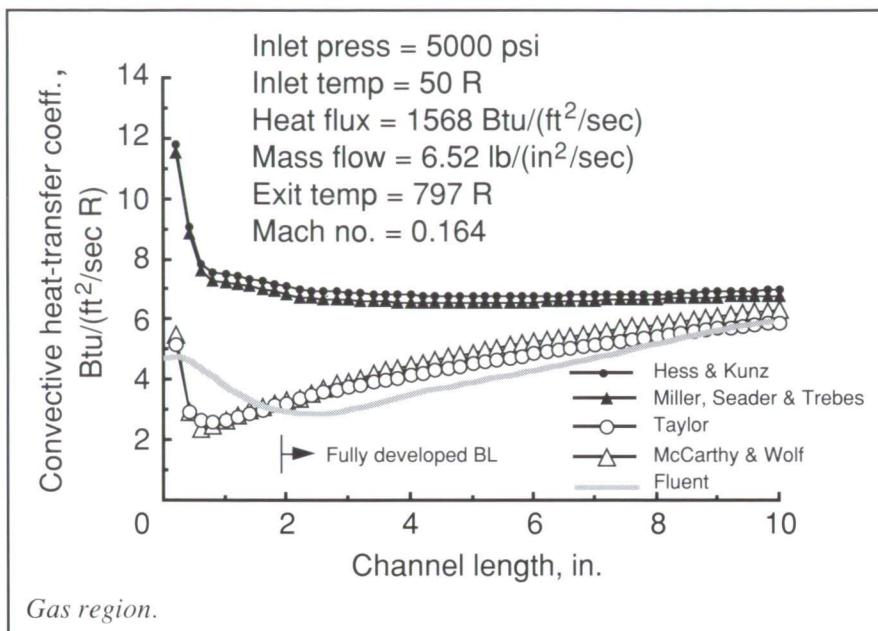
Analytical Evaluation of Convective Heat-Transfer Correlations

Active cooling systems for hypersonic aircraft often must be designed to conditions that are outside the range of existing convective heat-transfer correlations. One way to extend the applicability range of existing correlations is to compare them with a more accurate analytical result. Convective heat-transfer correlations for supercritical hydrogen are in wide disagreement for some of the high heat-flux design conditions that are needed in the National Aero-Space Plane (NASP) Program. To help resolve this problem, four correlations were compared with computational fluid

dynamics (CFD) analysis. The main differences in the correlations are in the terms accounting for fluid property variation at the wall. The correlation of Hess and Kunz and the correlation of Miller, Seader, and Trebes use a wall-to-bulk viscosity ratio term for the wall effect. In contrast, the correlations of Taylor and McCarthy and Wolf use a wall-to-bulk temperature ratio term for the wall effect. For high heat-flux conditions, the properties of the fluid near the wall in both the laminar sublayer and turbulent region have a significant effect on convective heat transfer, and the type of wall correction term that is used in a correlation may depend on whether the laminar or the turbulent effect is stronger. Also, the NASP design conditions for supercritical hydrogen cover the liquid-like to gas-like range. In the liquid-like range, viscosity goes down with increasing temperature, while in the gas-like range, viscosity goes up with increasing temperature.

The configuration analyzed was convection in a 10-in.-long square duct with internal dimensions of 0.05 in. by



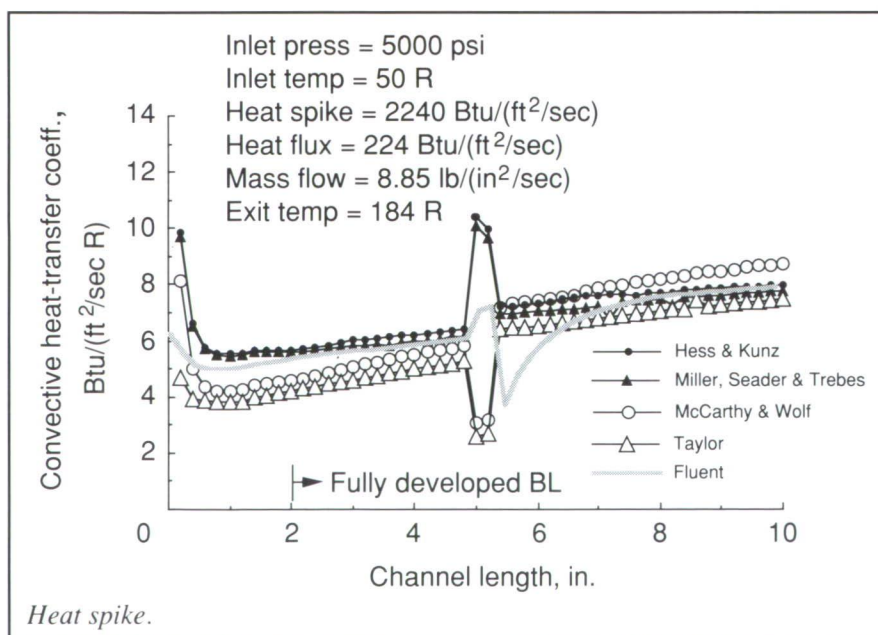


boundary layer. The correlation by Taylor showed the best agreement with CFD results for the high uniform heat-flux cases. All four of the correlations disagreed with CFD results for a heating spike case. Although the CFD results cannot be viewed as being definitive, these results are believed to be more accurate than the correlations and, therefore, useful for choosing a best correlation. A more accurate answer must be obtained by testing, which is planned under a NASP work package.

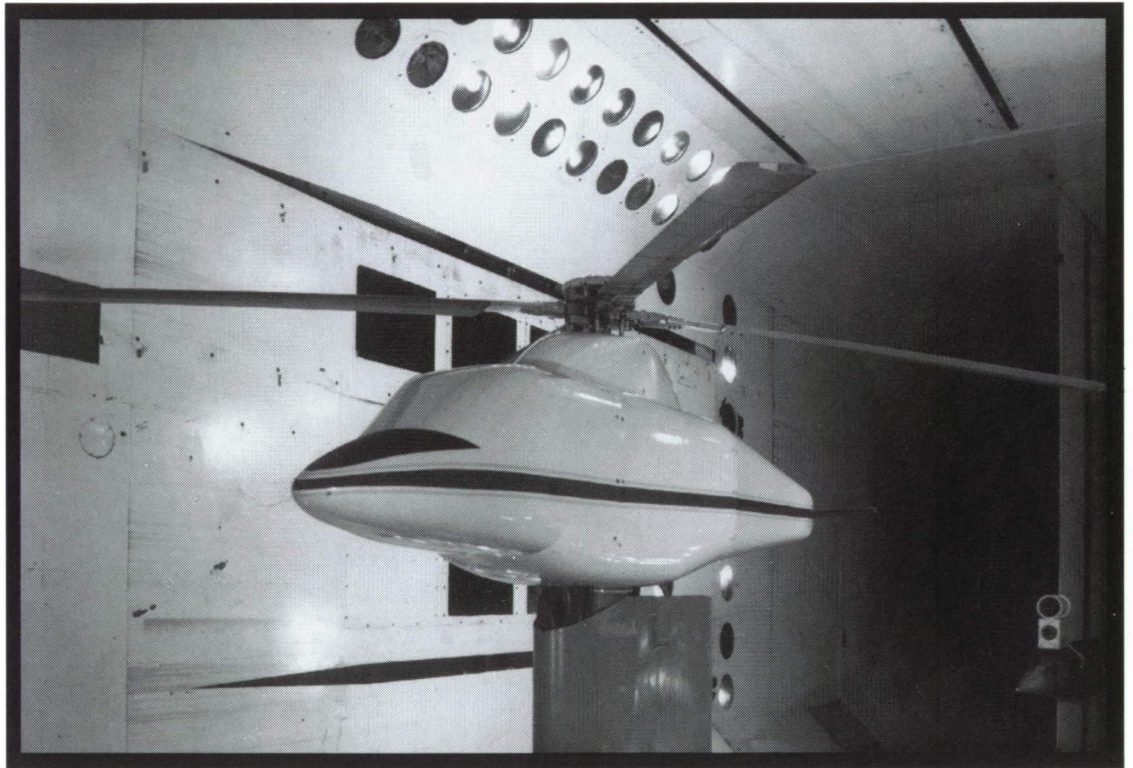
(Dennis Petley and Bill Dziedzic, 43759)
Aeronautics Directorate

0.05 in. The analysis was done first using the four correlations in the NASP/SINDA thermal management code. The NASP/SINDA is a FORTRAN code developed by Langley Research Center to adapt the general SINDA-85 code for thermal management analysis. Forty-eight different combinations of pressure, temperature, and heat flux were analyzed using

NASP/SINDA, and five combinations were chosen for comparison with CFD. The Fluent code was used for the CFD analysis. Typical results of a uniform heat-flux case and a heating spike case are shown in the figures. In the figures, D_h is the hydraulic diameter, P_{in} is pressure in, P_{out} is pressure out, L/D is the length of the duct divided by the diameter of the duct, and BL is



■ SUBSONIC AIRCRAFT

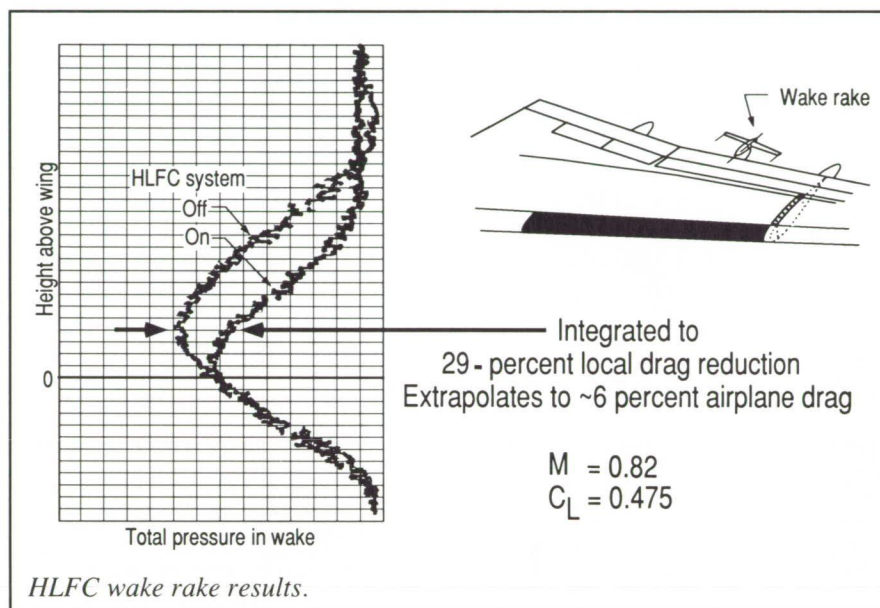


ORIGINAL PAGE
BLACK AND WHITE PHOTOGRAPH

*Develop technologies to ensure
the competitiveness of U.S.
subsonic aircraft and to enhance
the safety and capacity of our
national airspace system*

Hybrid Laminar-Flow Control Flight Research

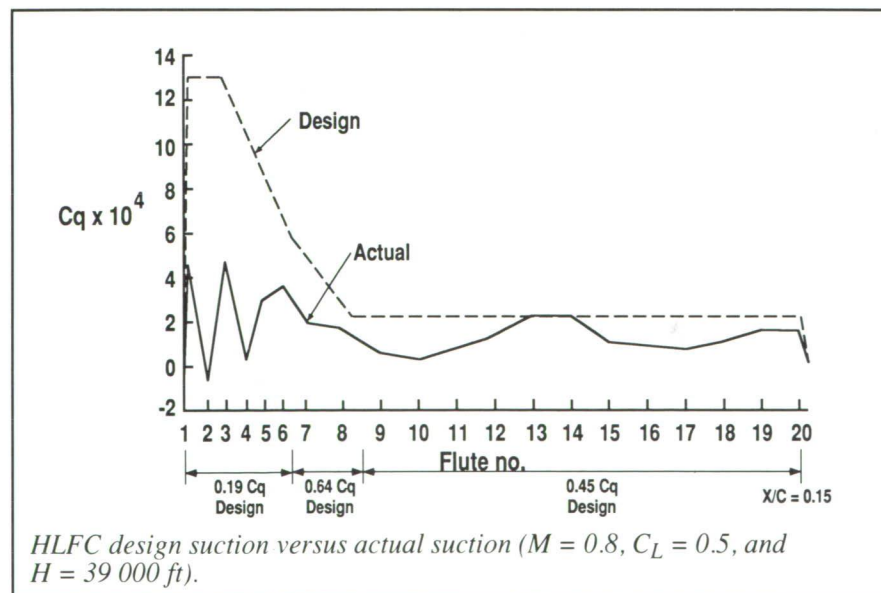
During the past year, flight research experiments with the Hybrid Laminar-Flow Control (HLFC) system installed in the Boeing 757 flight research aircraft have yielded results that could significantly advance the application of this technology into the commercial transport fleet. An HLFC system provides suction boundary-layer control in the leading edge (to the front spar) to control the highly three-dimensional laminar boundary layer. Downstream of the front spar, the surface pressure distribution is used to stabilize the boundary-layer flow and maintain laminar flow to the wing shock or aft pressure rise. The suction surface in the leading edge is a microperforated titanium skin with over 19×10^6 tiny laser-drilled, closely spaced holes.

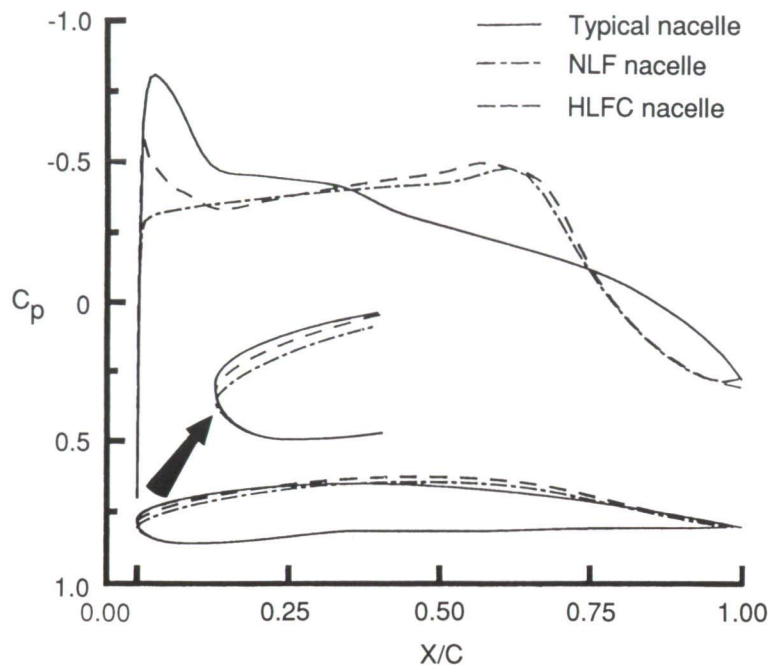


The experiments of the past year demonstrated that the suction required to obtain large amounts of laminar flow over the wing chord (as much as 65 percent chord) is much less than

had been previously believed and amounts to only one-third of that indicated by the early design calculations (shown in the first figure). In addition, pressure measurements made in the wake behind the trailing edge of the wing in the center of the 17-ft test span (shown in the second figure) confirmed a major reduction in wing drag over a wide variety of test conditions and showed that large amounts of laminar flow over the wing box area of the aircraft had been achieved as indicated by the early hot-film data.

The program is jointly funded by NASA, the U.S. Air Force, and Boeing Commercial Airplanes.
(Dal V. Maddalon, 41909)
Aeronautics Directorate





Pressure distribution and nacelle geometry.

Hybrid Laminar-Flow Control Nacelle Concept

Research has led a concept of combined suction and natural laminar flow (NLF) control to achieve extensive laminar boundary-layer flow on the nacelle of an aircraft engine and thereby greatly reduce the surface friction drag. The engine specific fuel consumption might be reduced by as much as 2 percent.

Current engine nacelles have high skin friction, turbulent boundary-layer flows. Two methods to achieve laminar flow on the engine exterior surfaces have been previously proposed. In one method, referred to as NLF, the nacelle is shaped to give favorable pressure gradients that delay boundary-layer transition and extend the length of laminar-boundary-layer flow. The other method uses suction at the surface to stabilize the boundary

layer and delay transition to turbulent flow; this technique is referred to as laminar-flow control (LFC).

The primary disadvantage of NLF is that the required nacelle shapes have very small inlet lip radii that result in flow separation in the inlet at low-speed conditions, such as landing approach; the engine performance is severely degraded under these conditions. With LFC, laminar boundary-layer flow can be achieved with a turbulent nacelle geometry and pressure distribution, but the suction is required for the full length of laminar flow.

The new hybrid LFC nacelle combines these two methods to minimize the requirement for suction. First, a pressure coefficient C_p distribution is selected which produces an inlet lip that is as blunt as a typical turbulent nacelle inlet lip. This design process results in a very strong initial accelera-

tion to a pressure peak very far forward on the nacelle (approximately 2 percent of the nacelle length). This acceleration is illustrated in the figure, which also shows typical turbulent and NLF nacelle contours and pressure coefficient versus percent chord X/C distributions. The flow deceleration on the downstream side of the pressure peak is shaped to avoid shock development by a continuous reduction in deceleration of the flow to about 20 percent of the nacelle length. Just ahead of the initial pressure peak and downstream to approximately 20-percent chord, surface suction is used to control the boundary layer and maintain laminar flow. At 20 percent of the nacelle length, the flow is reaccelerated by proper contour shaping to produce favorable pressure gradients and to maintain NLF as far downstream as a second pressure peak (about 65 percent of the nacelle length). Inverse aerodynamic design codes have been applied for defining the precise geometry to produce these pressure distributions (see the figure), and stability analyses indicate that extensive laminar flow can be maintained at flight conditions typical of large turbofan engines.

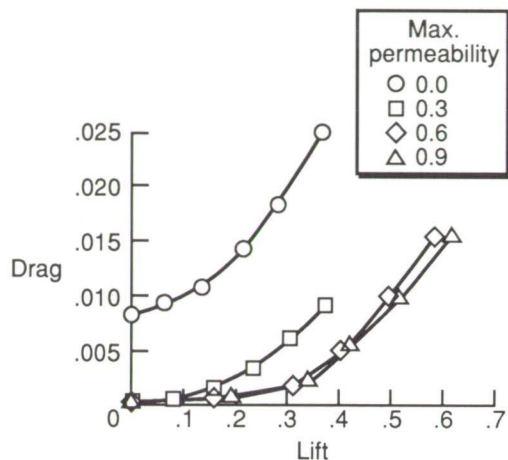
(Richard D. Wagner, 41903, and F. S. Collier, Jr.)
Aeronautics Directorate

Porous Transonic Airfoils for Multipoint Design

The objective of this investigation was to determine the feasibility of using a passive venting technique for restructuring the flow past airfoils such that they become self-adaptive to very dissimilar flow conditions. This property would open an alternate route to achieve multipoint design, that is, the design of airfoils which satisfies several, oftentimes conflicting, constraints.

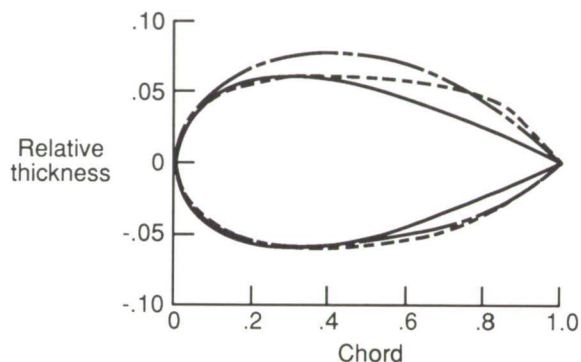
Drag polars for solid and porous NACA 0012 airfoils

$M_\infty = 0.80$



Self-adaptive airfoil through porosity

— Porous NACA 0012
 - - - $M_\infty = 0.80, \alpha = 1.25^\circ$ } Solid
 — $M_\infty = 0.63, \alpha = 2.00^\circ$ } equivalent



Porosity for transonic airfoils with view toward multipoint design.

A computational pilot study was conducted with an in-house-developed time-implicit upwind method for the nonconservative Euler equations using floating shock fitting for accurate representations of shocks. The computational approach allowed a faster and less expensive assessment of influencing parameters (such as profile geometry, arrangement of porous surface patches, and degree of porosity) than an experimental study.

Solutions were computed for steady transonic flow over NACA 0012 and supercritical airfoils with solid as well as porous surfaces. The porous surfaces were applied to both upper and lower profile surfaces, and they extended over the nominal chord. Either connected or separated cavities were assumed to lie beneath the upper and lower surfaces. The porosity distribution is described by a modified sine wave with several amplitudes. The sinusoidal porosity distribution was chosen to facilitate the numerical approximation of flow through permeable surfaces.

Applied to an NACA 0012 airfoil, porosity generally increases lift for a given angle of attack, in some instances by up to 65 percent. As indicated by the figure, the wave drag taken at constant lift for supercritical flow past a porous NACA 0012 airfoil with separated cavities is up to one order of magnitude lower than that for its solid counterpart.

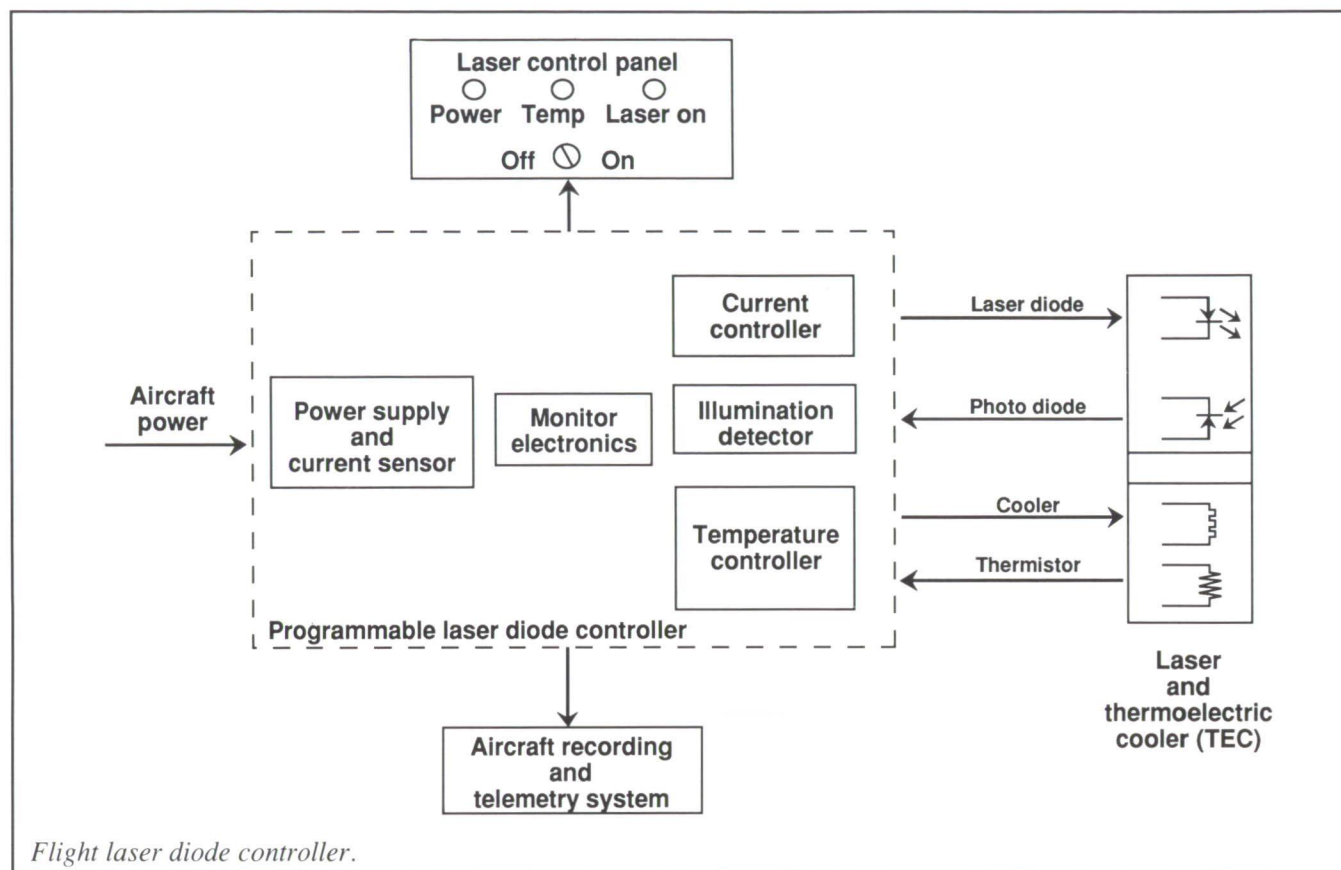
The figure also illustrates that the ability to be self-adaptive to dissimilar flow conditions is a new quality of a porous NACA 0012 airfoil. Using the calculated porous surface pressure distributions as target pressures, equivalent solid airfoil shapes were constructed using a computational design tool. While the subcritical equivalent airfoil basically retains the teardrop shape of the NACA 0012 profile, the supercritical companion piece reveals a distinct flattening of the upper surface combined with a hump-shaped closure toward the trailing edge.

Making the surfaces of an already optimized supercritical airfoil permeable also broadens its operational speed and incidence range.

(Peter M. Hartwich and James M. Luckring, 42881)
Aeronautics Directorate

Airborne Laser Diode Illumination System

The need for an improved light sheet illumination system was recognized during the flow visualization phase of the F-106 vortex flap flight tests. The previous system utilized an incandescent lamp that has been prone to breakage in the harsh flight environment and required only dark-night flights to eliminate background ultraviolet light. Commercial high-power laser diodes (1 W and 3 W), operating at a wavelength of 820 nm, were selected as alternative flight light sources to increase reliability. An electronic



controller was developed to control the laser diode current and temperature and provide transient protection throughout the full range of aircraft environmental conditions and meet flight safety requirements. In conjunction with an ultraviolet filter on the flow visualization video camera, the new illumination system will allow experimenters to conduct future flow visualization flight tests during daylight hours.

The controller provides programmable constant current to the laser diode and maintains its operating temperature at 25°C ($\pm 1.5^{\circ}\text{C}$) over the full range of aircraft operating temperatures by using an integral laser diode thermoelectric cooler (TEC). The laser diode is protected from thermal overload by an electronics comparator that automatically shuts down the laser if preset programmable limits are exceeded. Cockpit indicators, controls, and

monitor signals are provided to an onboard observer or pilot as well as to the aircraft's flight data recording and real-time telemetry system. The new system has been environmentally tested to flight qualification levels and has been successfully demonstrated in wind-tunnel flow visualization tests.

(B. D. Taylor and F. Fitzpatrick, 41666)

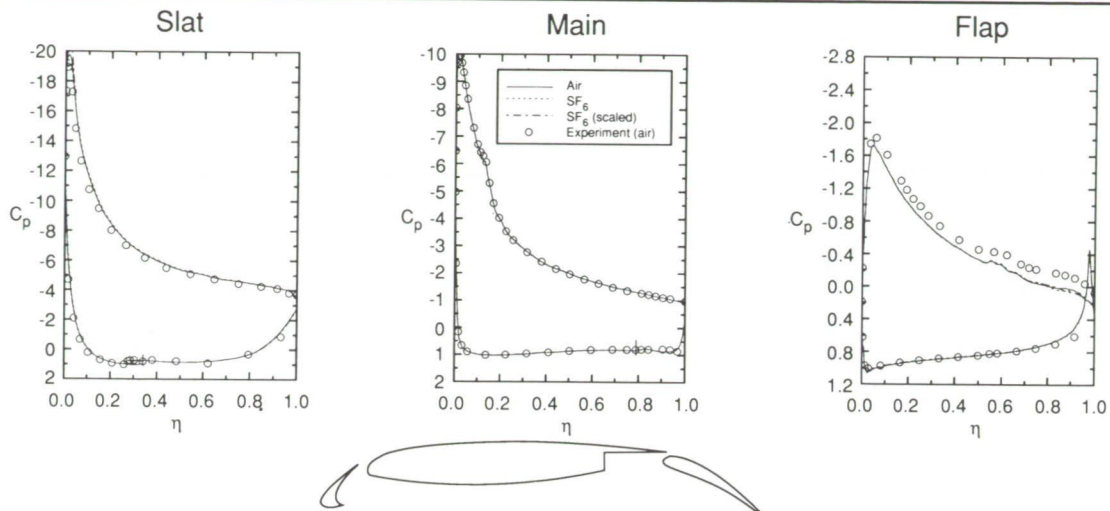
Electronics Directorate

Study on Use of Sulfur Hexafluoride for High-Lift Testing

Recently, heavy gases such as sulfur hexafluoride (SF_6) have become attractive as alternate test gases for wind

tunnels because of their high molecular weights, which result in a significant increase in available Reynolds number. Difficulties arise, however, because of thermodynamic imperfections in heavy gases, particularly for flows in which compressibility effects are important.

The emphasis for the current study is on flows over multielement airfoil configurations that may exhibit local regions of transonic flow even though the free-stream Mach number may be very low. These flows are highly viscous in nature, with the potential for merging boundary layers, flow separation, and complex wake profiles. The purpose of the current work is to investigate possible aerodynamic effects attributable to the use of heavy gas by utilizing a two-dimensional Navier-Stokes code that has been modified to include SF_6 thermodynamics.

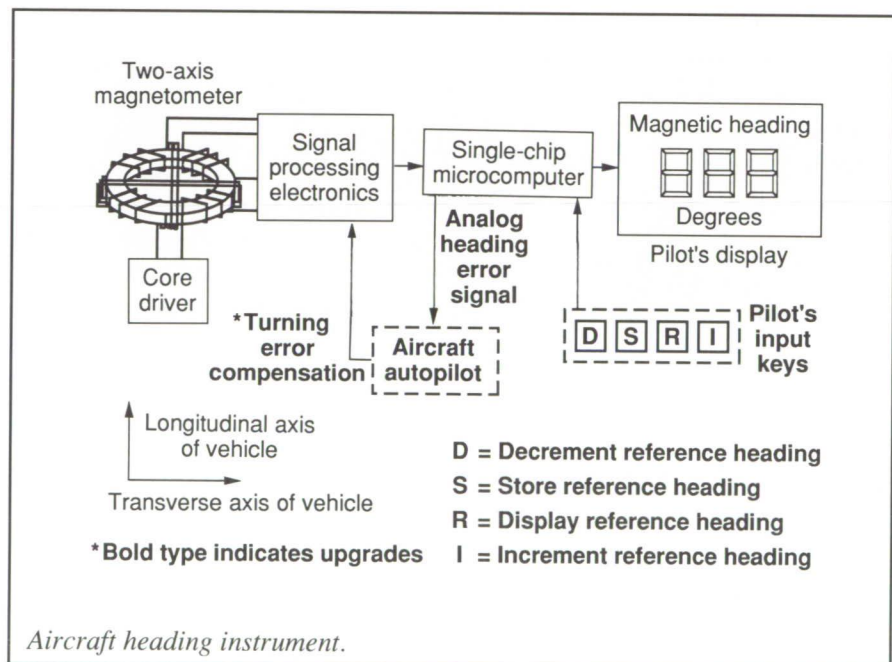


Surface pressure distribution for three-element airfoil at an angle of attack of 23.39° and free-stream Mach number of 0.2 (η is longitudinal coordinate nondimensionalized by airfoil chord length).

Results are shown for a three-element high-lift system in a typical landing configuration (with slat and flap deflected 30°). The figure shows the computed surface pressure distributions for each element including air results and SF₆ results with and without a Mach number scaling. The case shown is near the maximum lift condition as determined by experiments. The calculations agree well with the experimental data, and heavy-gas effects appear to be negligible even on the slat, where a significant region of supersonic flow exists.

(Daryl L. Bonhaus, 42293)

Aeronautics Directorate



Aircraft heading instrument.

Smart Compass Upgrade

The Smart Compass was developed as a simple, low-cost substitute for the mechanical-compass/directional gyroscope combination that has been in use as a pilot's heading reference since the mid-1930's. Both the flux gate magnetometer and its attendant circuitry and microcontroller program were specifically designed for maximum

simplicity, cost-effectiveness, and the expected greatly enhanced reliability over the gyroscopic instrument it replaces. The system has been used on general-aviation aircraft as well as on NASA aircraft flight models and military remotely piloted vehicle (RPV) models.

The Smart Compass has been upgraded to provide a heading error

reference for use with autopilots on low-end general-aviation aircraft. This upgrade allows the Smart Compass to be used as an ideal substitute for the more expensive directional gyro conventionally used with autopilots. To achieve this, the resident microcontroller software program was rewritten and hardware additions were made to allow the pilot to enter a heading reference that is compared

with the current heading of the aircraft at any instant; the heading error was computed and output as an analog error signal compatible with current autopilot usage.

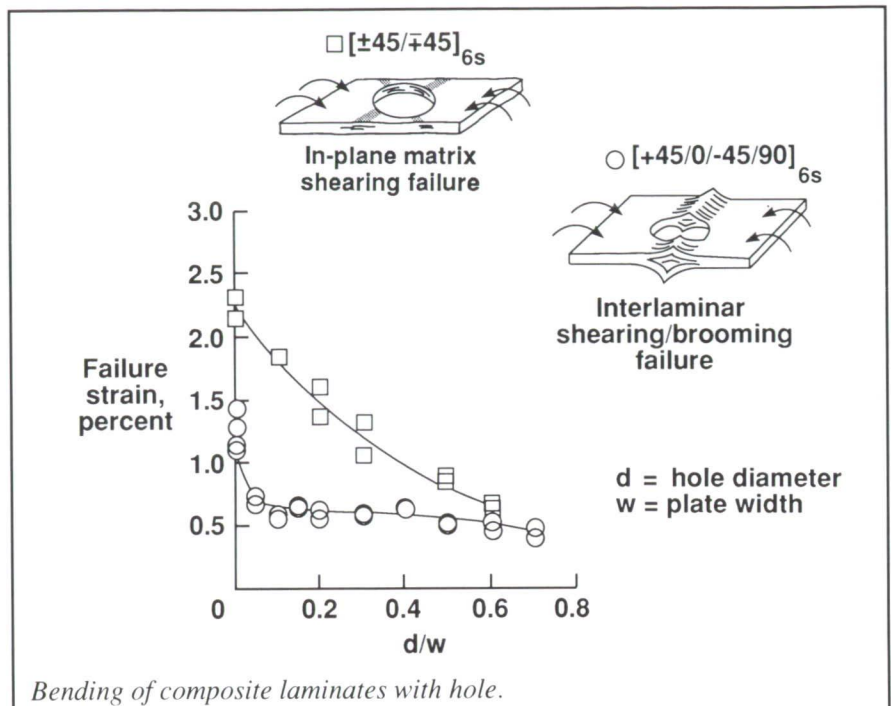
Other improvements that enhance the overall utility of the compass include compensation for turning error, data averaging to avoid display flicker encountered with the original program in the presence of magnetic noise, a facility to use the display as a voltmeter in the calibration procedure, and the capability of driving several optional heading displays as identified in the figure.

(Doug Garner, 41683)
Electronics Directorate

Failure Modes of Composite Laminates With Hole and Subjected to Four-Point Bending

The response and failure of laminates with holes and subjected to bending loads is a fundamental design consideration for composite aircraft structures because of the need for maintenance access, wiring and tubing passageways, and windows. To identify the failure characteristics of a composite laminate with a circular hole, quasi-isotropic and $\pm 45^\circ$ laminates were tested to failure in four-point bending. The IM7/8551-7A graphite/epoxy laminates were 48 plies thick, had test sections that were 6 in. long by 5 in. wide, and had hole diameters ranging from 0 in. to 3.5 in.

Both laminates failed progressively through the laminate thickness. The quasi-isotropic laminates failed in the 0° plies, initiating at the compressive side and continuing through the thickness with an interlaminar shearing/brooming effect. The $\pm 45^\circ$ laminates showed no visual evidence that



the failure consistently initiated on either the compression or tension side of the specimen. In this group the failure was characterized by in-plane matrix shearing. These laminate failure modes are illustrated in the figure, and the failure strain is plotted as a function of the hole-diameter-to-plate-width ratio d/w . The quasi-isotropic laminates show a sudden decrease followed by a more gradual decrease in failure strain with increasing hole diameter, while failure strains for the $\pm 45^\circ$ laminates decrease almost linearly with increasing hole diameter.

These tests established that the initial failure mechanisms for laminates with circular holes subjected to four-point bending are similar to those for corresponding laminates subjected to uniaxial in-plane loadings; however, failure progresses through the laminate thickness rather than failing all plies in the cross section simultaneously, as is the case with uniaxial loading.

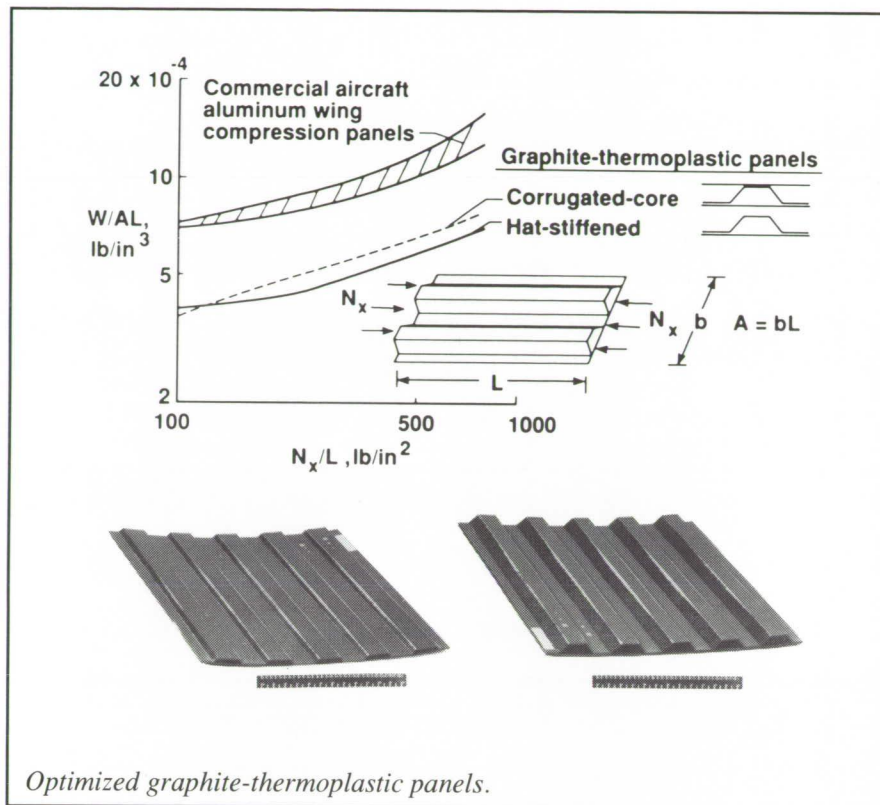
(M. J. Shuart, 43170, and
C. B. Prasad)

Structures Directorate

Structural Efficiency Determined for Optimized Graphite-Thermoplastic Panels

Graphite-thermoplastic structures are being considered for many aircraft applications. As in all aircraft structural considerations, structurally efficient (least-weight) designs must be identified for economic reasons. With the PASCO computer code, the most structurally efficient designs for AS4/PEEK graphite-thermoplastic panels subjected to axial compressive loading were determined to be the corrugated-core and hat-stiffened panels.

The panels were 30 in. long and 24 in. wide and were simply supported on all sides during loading. They were not allowed either to buckle prior to the design load level or to exceed an allowable compressive strain of 0.006 in/in. in the load index N_x/L range from 100 lb/in² to 800 lb/in². Minimum overall axial and shear stiffnesses and



minimum laminate-thickness requirements were also included. For the hat-stiffened and corrugated-core panels, weight index W/AL as a function of N_x/L is shown in the figure along with the range for typical commercial aircraft aluminum wing panels. The corrugated-core and hat-stiffened panels are significantly more structurally efficient (lower W/AL) than the aluminum wing panels. For all but the lowest load level, the hat-stiffened panel is more structurally efficient than the corrugated-core panel because the second skin for a corrugated-core panel adds unnecessary weight.

Optimum designs of each panel contained five stiffeners and were used to fabricate test specimens. Typical hat-stiffened test specimens are shown in the photographs at the bottom of the figure. The specimen on the left is designed for a low compressive load level, and the specimen on the right is designed for a high load level.

This study identified two graphite-thermoplastic panel designs that are more structurally efficient than currently used aluminum wing panels for a broad range of compressive loading conditions.

(Dawn C. Jegley, 43185)
Structures Directorate

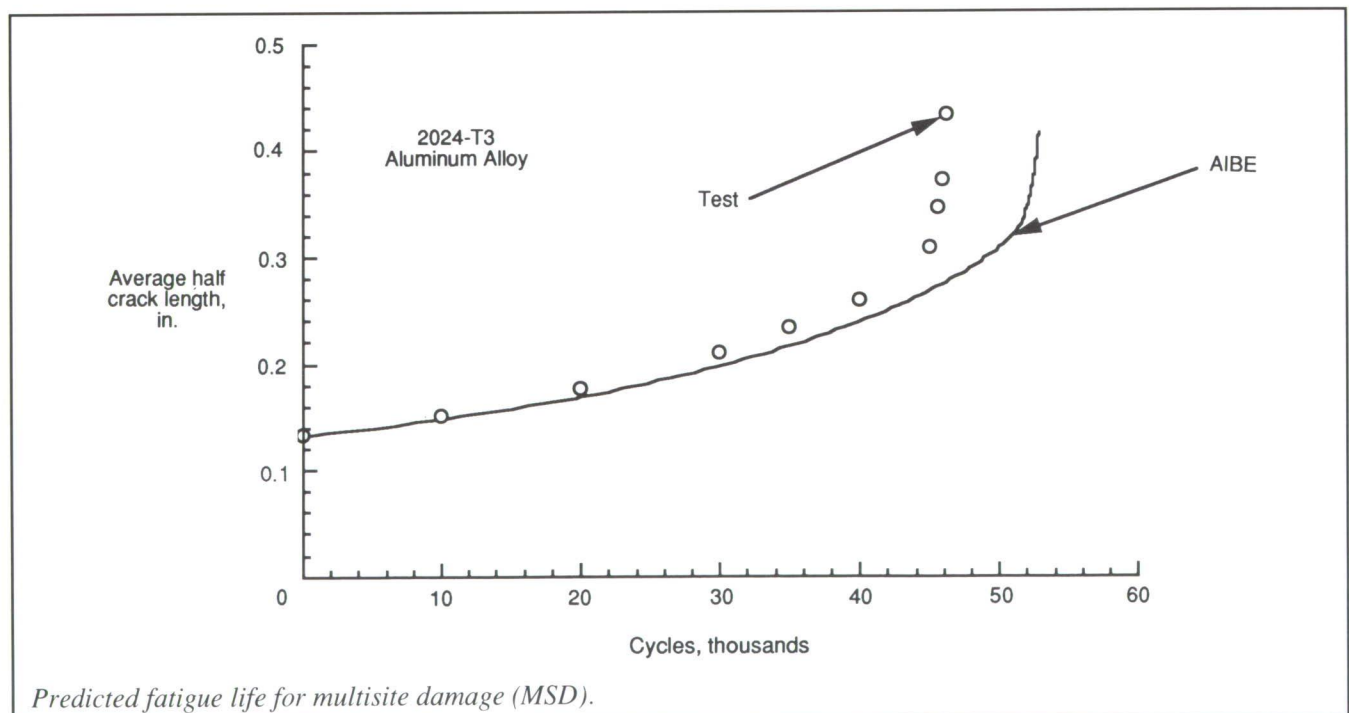
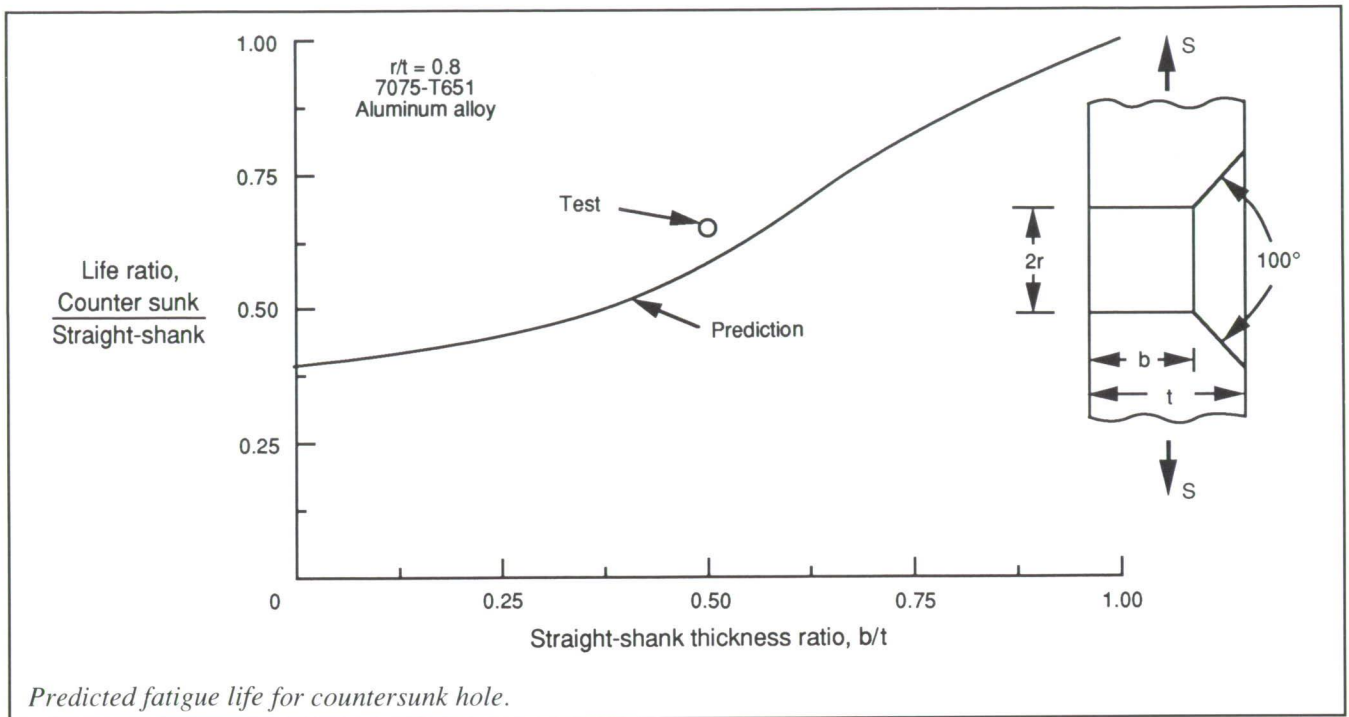
Fracture Mechanics Analyses of Cracks Extending From Rivets

Several recent incidents involving fatigue cracking in the aging commercial transport aircraft fleet have raised concerns about their structural integrity. The development of multiple site damage (MSD) in lap-splice joints and other structural components is of great concern to the aerospace community. MSD is the formation of a row of

cracks, such as along the top row of rivets in a lap-splice joint, which interact with each other. NASA has undertaken an Aircraft Structural Integrity Program to address some of these issues. The fracture mechanics approach has been divided into three distinct categories based on crack size: small cracks emanating from rivet holes (crack size below damage-tolerance level, 0.05 in.), multiple interacting cracks at the damage-tolerance level, and post-linkup of multiple cracks that interact with structural details, such as stiffeners and frames. The program is focused on the first two categories. Fracture mechanics analyses and tests are being conducted on surface and corner cracks emanating from countersunk rivet holes under simulated joint loading. For damage-tolerant crack sizes and greater, tests are being conducted and analysis methods are being developed to study crack interactions. Results from these analyses will be used to predict total fatigue life of lap-splice joints and damage-tolerant lives to establish inspection intervals.

With the stress-intensity factor solutions for small surface and corner cracks at holes, a comparison of total fatigue life for a countersunk hole to that for a straight-shank portion to sheet thickness b/t ratio (solid curve) is given in the first figure. The experimental data are for 7075-T6 aluminum alloy plate (symbol) in this figure. These results show that the countersunk hole can cause as much as a factor-of-2 reduction in total fatigue life.

To establish inspection intervals for lap-splice joints, analysis methods are being developed to analyze MSD cracking in aircraft components. An alternating-indirect-boundary-element (AIBE) method has recently been developed to analyze any number of straight cracks at any orientation.



Stress-intensity factors at each crack tip are calculated and used to calculate crack growth rate. A comparison of average crack length against cycles

to failure from test (symbols in the second figure) and an AIBE analysis of a panel subjected to remote tension

with ten unequal cracks show good agreement.

(J. C. Newman, Jr., 43487, K. N. Shivakumar, and D. S. Dawicke)
Structures Directorate

BVI Noise Prediction Validation

Blade-vortex interaction (BVI) noise is a highly impulsive helicopter noise source that occurs when rotor blades strike, or pass very close to, tip vortices previously shed into the wake of the rotor. This occurs most often when the rotor is in descent.

Far-field noise and blade pressure data obtained from a model rotor test were employed to validate the rotor noise prediction code WOPWOP for BVI noise. The test was done as part

pressures as input into the noise prediction code WOPWOP. This code is based on Farassat's Formulation 1A, which is a time domain solution to the Ffowcs Williams and Hawkings equation.

Measured and predicted acoustic time histories have been compared for a number of rotor operating conditions and measurement locations. A comparison for a BVI case at a moderate advance ratio of 0.20 is presented in the figure. The measured acoustic time history is shown on the left, and the predicted time history with measured blade pressures is shown on the right.

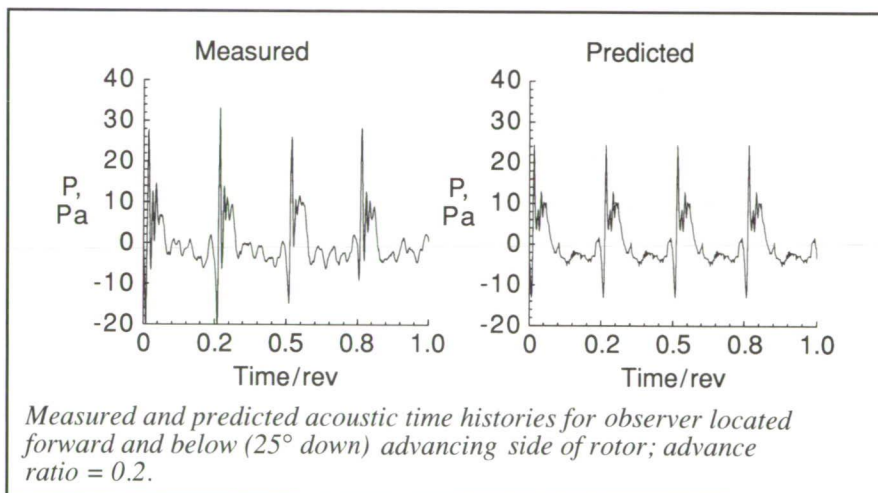
made with predicted air loads are not in good agreement with measured noise data. The data base of both acoustics and aerodynamic loads will add immensely to the understanding and development of predictions for both rotor acoustics and blade loads.

**(Casey L. Burley, 43659, and Michael A. Marcolini)
Structures Directorate**

Government and Industry Assessment of DAMVIBS Program

Excessive vibration is the most common technical problem to arise in the development of a new rotorcraft. With only a few exceptions, vibration problems have not been identified until the flight test. Solutions at that stage of development are usually add-on fixes that adversely impact the cost, schedule, and vehicle performance. Vibration predictions have not been relied on by the rotorcraft industry during design because of the deficiencies in current vibration analysis methods. Langley Research Center has under way a program, designated DAMVIBS (Design Analysis Methods for Vibrations), to establish the technology base needed by the industry for developing a superior finite-element-based dynamics design analysis capability for vibrations.

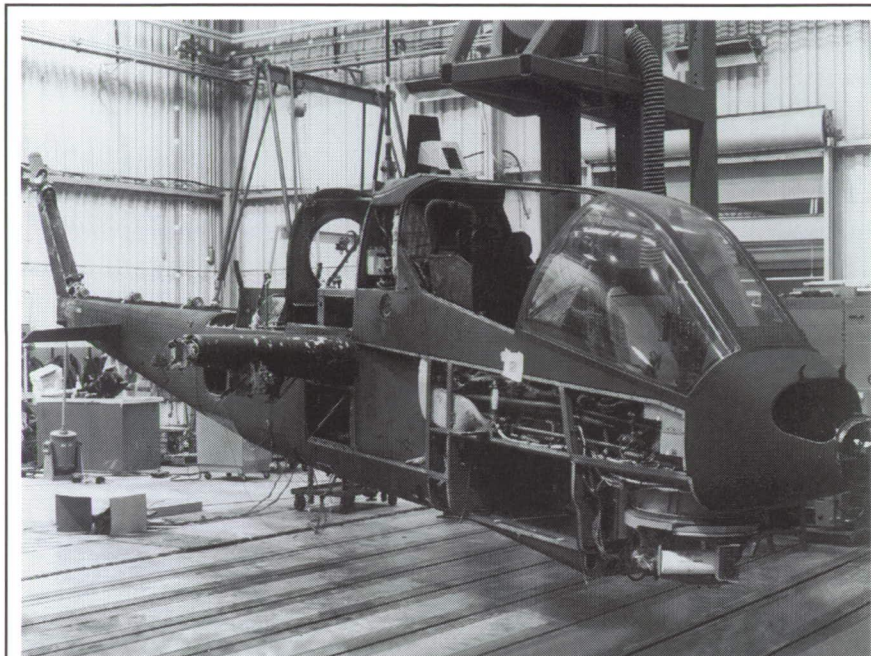
Industry teams conduct modeling, analysis, testing, and correlation studies on both metal and composite airframes. The finite-element models developed in these studies are then used in follow-on studies to identify difficult components that require refined finite-element representation, to improve analyses for computing coupled rotor-airframe vibrations, and to develop techniques for airframe



of a cooperative effort between the Army Aeroflightdynamics Directorate, United Technologies Research Center, Sikorsky Aircraft, and NASA Ames and Langley Research Centers. The test was performed in the Duits-Nederlandse Wind Tunnel (DNW), which is a large acoustic wind tunnel in the Netherlands. The model rotor was a 1/6-scale, four-bladed, swept-tip design. The rotor blades were instrumented on both the upper and lower surfaces with a total of 176 pressure transducers. The blade pressure resolution was sufficiently high to capture BVI events. Noise predictions were made with the measured blade

Both the measured and predicted acoustic time histories are for an observer that is forward and down 25° from the rotor tip path plane. The major features of the measured acoustic data are reproduced well in both shape and magnitude, with the peak-to-peak amplitude in the predicted time history being bracketed by the blade-to-blade variability in the measured time history.

The results show that the rotor noise prediction code predicts BVI noise given accurate high-resolution blade loading data as input. This is significant because noise predictions



Stripped-down configuration of AH-1G metal airframe tested as part of DAMVIBS difficult component studies. L-89-7126

techniques have the potential to play a major role in vibrations design work. (Raymond G. Kvaternik, 41228) Structures Directorate

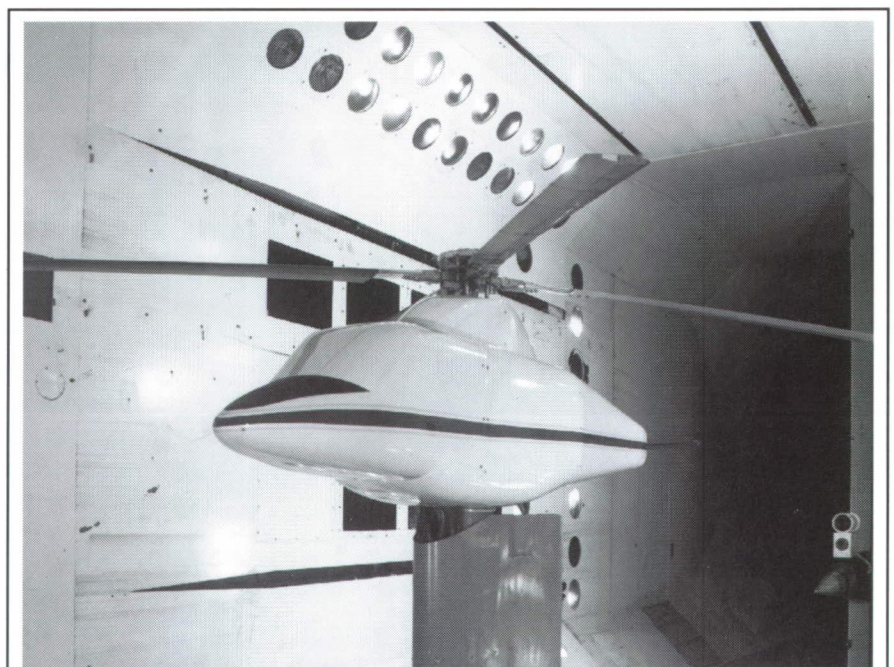
Demonstration of Extension-Twist Coupling Concept

Tilt-rotor aircraft are designed to operate in helicopter and airplane flight modes. This operational flexibility results in several conflicting design requirements. One such design requirement, which has significant effects on aerodynamic performance, is blade twist. Typically, the twist employed is a compromise between that required in the two modes of flight. Performance could be improved if it were possible to vary the blade twist between the two flight modes. Tilt-rotor aircraft typically vary rotor speed by approximately 20 percent between the two flight modes. This

structural dynamics optimization. DAMVIBS, which was initiated in 1984 with the award of task contracts to the four major helicopter airframe manufacturers, was the initial phase of a new and broader scope in-house rotorcraft structural dynamics program initiated at Langley.

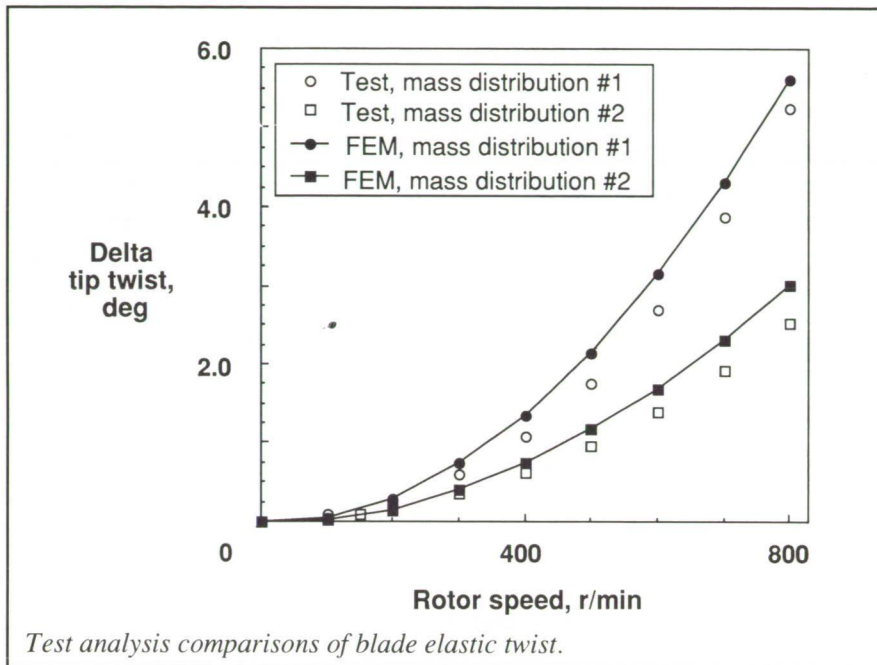
vibrations has spurred industry to reexamine their codes and make them more reliable. Preliminary studies have shown that structural optimization

Industry teams have formed finite-element models (FEM), conducted ground vibration tests (GVT), and made test/analysis comparisons of six airframes (three metal and three composite). Difficult components studies of two airframes (metal and composite) such as that shown in the figure have identified several important structural contributors to airframe vibrations. The finite-element modeling and difficult components studies have led to significant improvements in both FEM techniques and GVT methods throughout industry. For the first time, FEM's are being relied on by industry for airframe vibrations design work. The evaluation of industry codes for analysis of coupled rotor-airframe



ETC composite rotor blades in TDT.

L-90-2352



change in rotor speed induces a substantial change in the centrifugal force along the blade, which could be used to passively change the twist of an extension-twist-coupled (ETC) composite blade.

Analytical and experimental studies have been designed to demonstrate the improvements in tilt-rotor blade performance. These studies include whirl tests and wind-tunnel tests conducted on a set of model-scale blades, with the primary goal of measuring blade twist as a function of rotor speed. Results from this experimental phase will be compared with those obtained from analytical studies using companion finite-element analysis (FEA) models of the rotor blade.

Wind-tunnel testing of the set of ETC rotor blades was recently completed in the Transonic Dynamics Tunnel, following an abbreviated initial entry in the hover test facility. Data were obtained in hover for a ballasted (mass distribution 1) and for an unballasted (mass distribution 2)

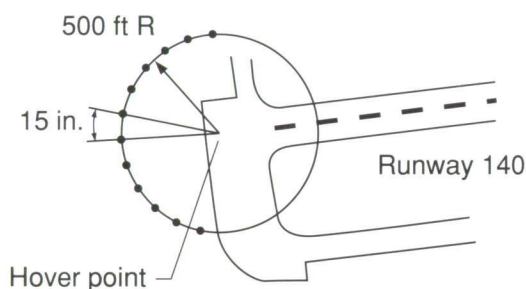
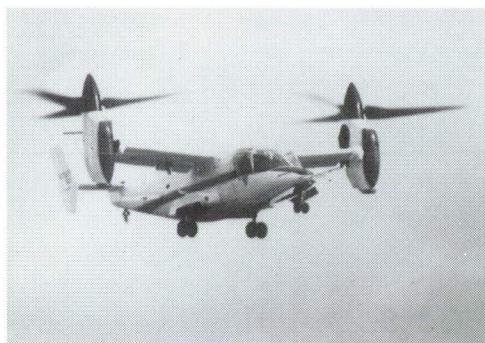
configuration in ambient air conditions and for a ballasted configuration (only) in near-vacuum conditions. The blades were mounted on the Aeroelastic Rotor Experimental System (ARES) helicopter model (shown in the first figure) and were spun through the 100-to-800-r/min range, with a corresponding sweep of collective pitch at 100 r/min intervals. Test results presented in the second figure showed maximum twists of 2.54° and 5.24° in the ambient air condition for the unballasted and ballasted blade configurations, respectively. These results were compared with those from a detailed nonlinear FEA of the rotor blade, which yielded maximum twists of 3.02° for the unballasted blade configuration and 5.61° for the ballasted blade configuration. The maximum twist obtained experimentally from the ballasted blade configuration in the near-vacuum condition (not shown) was nearly unchanged from that of the corresponding ambient result.

(Renee C. Lake, 41226, Mark W. Nixon, Matthew Wilbur, Jeffrey Singleton, and Paul Mirick)
Structures Directorate

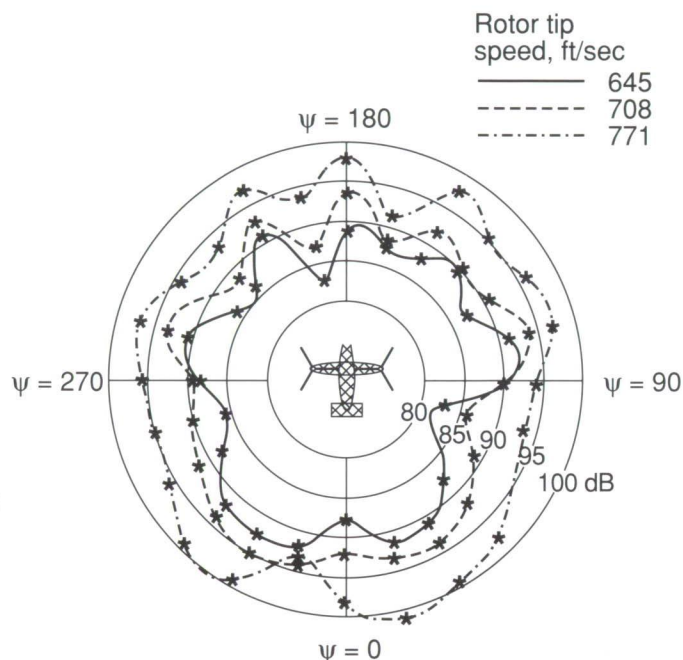
XV-15 Advanced Technology Blade Tilt-Rotor Hover Flight Test

The tilt-rotor aircraft with its unique flight characteristics has been identified as a possible solution to the civil air capacity problem by the year 2000, with projected market potential of over 2600 aircraft. The external and internal noise exposure to the community was identified as one of the most critical items for research. A series of acoustic programs with the original-blade XV-15 have been conducted over the years, and a new set of advanced technology blades (ATB's) have recently been acoustically tested in hover at Ames Research Center in a cooperative program with Langley Research Center. The purpose of the latest test program was to identify the acoustic benefit of the advanced technology blade configuration and to study the effect of rotor tip speed variation on the hovering acoustic directivity characteristics of the XV-15 ATB.

In order to develop the data base needed to assess these purposes, this hover test program was conducted at the Moffett Field Naval Air Station in December 1990. Acoustic data were obtained for a range of rotor tip speeds (645 ft/sec to 771 ft/sec) and aircraft wheel heights (2 ft to 500 ft). The flight experiment consisted of hovering the aircraft over a 500-ft radius semicircular array of 12 ground plane microphones, in which each flight condition was repeated for two reciprocal aircraft headings to provide a full 360° acoustic coverage. The results of this program and comparison with the past acoustic efforts on the XV-15 have provided valuable information about the unique characteristics of the tilt-rotor aircraft and developed a limited data base for validation of developing acoustic analytical methods. In particular, the tip speed reduc-



Effect of rotor tip speed on overall sound pressure level



XV-15 advanced technology blades far-field hover acoustics test.

L-91-6754

tion capability of this research vehicle has been utilized to show the benefits for noise reduction that can be obtained; however, more sophisticated methods are ready for application in the noise reduction arena for the future. Utilization of valuable resources like the XV-15 and the U.S. Navy's V-22 over the next several years, in more comprehensive acoustic test programs, will provide a valuable data base for development of the civil tilt-rotor vehicles to meet the perceived needs into the year 2000.

(David Conner, Ken Rutledge, and Dan Hoad, 45060)
Structures Directorate

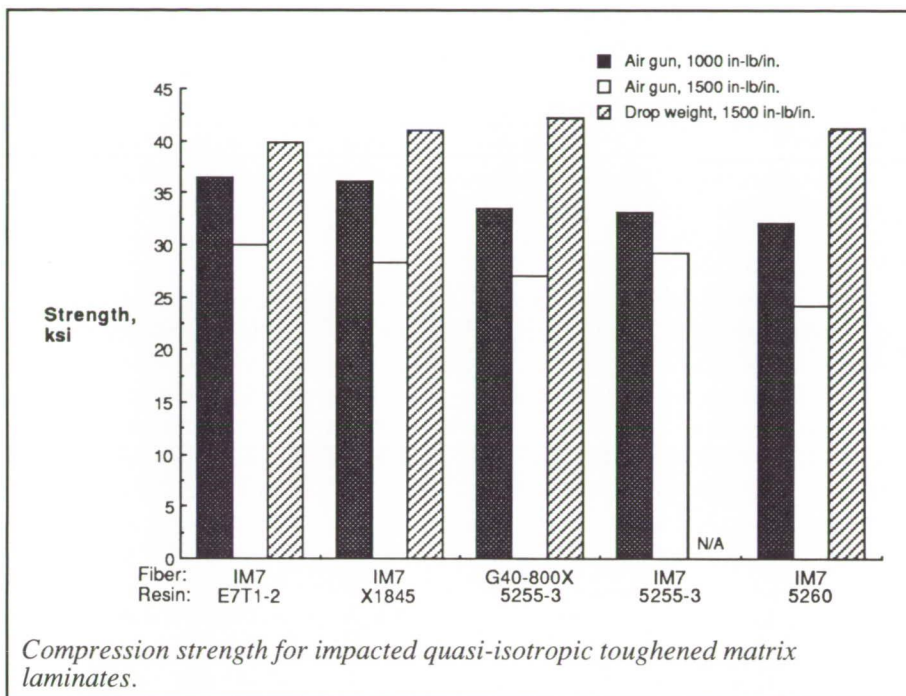
Evaluation of Toughened Matrix Composite Materials

The use of composite materials in primary aircraft applications has been limited by poor damage tolerance. The

use of toughened matrix composites (thermoset/thermoplastic blends) offers an attractive solution to the problem by providing the mechanical properties of a thermoset with the toughness of a thermoplastic. In this study, five high-strain graphite fiber/toughened matrix materials were studied. Four materials had an epoxy matrix: IM7/E7T1-2, IM7/X1845, G40-800X/5255-3, and IM7/5255-3. The fifth material, IM7/5260, had a bismaleimide (BMI) matrix. A measure of the ability of a material to resist impact damage is its compression after impact (CAI) strength. The five toughened matrix materials were impacted at 1000 in-lb/in. and 1500 in-lb/in. with the Langley Research Center air gun (high-velocity impact, 440 ft/sec and 540 ft/sec) and then tested to failure in compression. A limited number of CAI tests were also performed with a drop-weight apparatus (1500 in-lb/in. at low-velocity impact, 14 ft/sec).

As shown in the figure, drop-weight CAI strengths are higher than air gun CAI strengths. Because the 1000 in-lb/in. air gun impact resulted in a lower CAI strength than the 1500 in-lb/in. drop-weight impact, the materials demonstrate less damage tolerance when struck by a fast moving projectile. The epoxy materials had similar drop-weight CAI strengths and their air gun CAI strengths were also similar (values are within 10 percent for each impact energy level). The IM7/5260, a BMI, had the lowest air gun CAI strengths, but did exhibit a comparable drop-weight CAI strength to the epoxy matrix laminates.

The undamaged mechanical properties (not shown) of the materials evaluated in this investigation are comparable with properties for previously evaluated toughened resin systems (T800/F3900, IM7/8551-7, and IM6/1808I, materials that incorporate a compliant interleaf layer for added



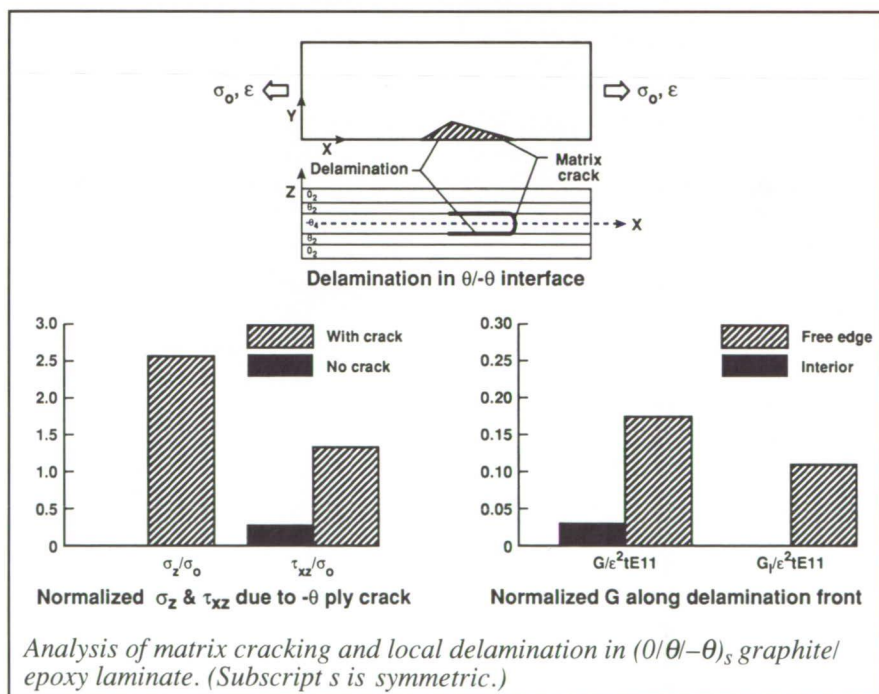
the off-axis ($-\theta$) plies and to analyze the local delaminations that form in the $\theta/-\theta$ interface of $(0/\theta/-\theta)_s$ graphite/epoxy laminates. (See the top portion of the figure.) The interlaminar normal stress σ_z near the free edge in the $\theta/-\theta$ interface increases from a very small compressive stress in an uncracked laminate to a very high tensile stress because of cracking in the $-\theta$ ply. Thus, the matrix cracking of $-\theta$ ply causes a high tensile stress in the corner of the matrix crack and the free edge, where a delamination in the $\theta/-\theta$ interface will initiate. (See the bottom left figure.)

A uniform delamination was modeled initiating at the $-\theta$ ply crack and growing between the $\theta/-\theta$ interface. The highest values of G and

toughness), but their damage tolerance is not as good. However, all five materials evaluated in this study were stronger and more damage tolerant (by 15 to 43 percent) than brittle composite materials, such as T300/5208, which are currently in use in aircraft structures. (R. J. Cano, 43951, and M. B. Dow) Structures Directorate

Analysis of Local Delamination From Matrix Cracks in Laminated Composites

Matrix cracks may exist in composite laminates because of manufacturing defects, residual thermal stresses following manufacture, low-velocity impact during production, or service loads. These matrix cracks may initiate delaminations locally, which may lead to structural failures. The present study was conducted to determine the interlaminar stresses and strain-energy-



release rates G responsible for localized delaminations.

Three-dimensional finite-element analyses were developed to model and analyze the effect of matrix cracks in

its opening mode component occurred near the free edge, thereby indicating the corner between the free edge and matrix crack to be the site for delamination onset. These values of G and its components are compared with the

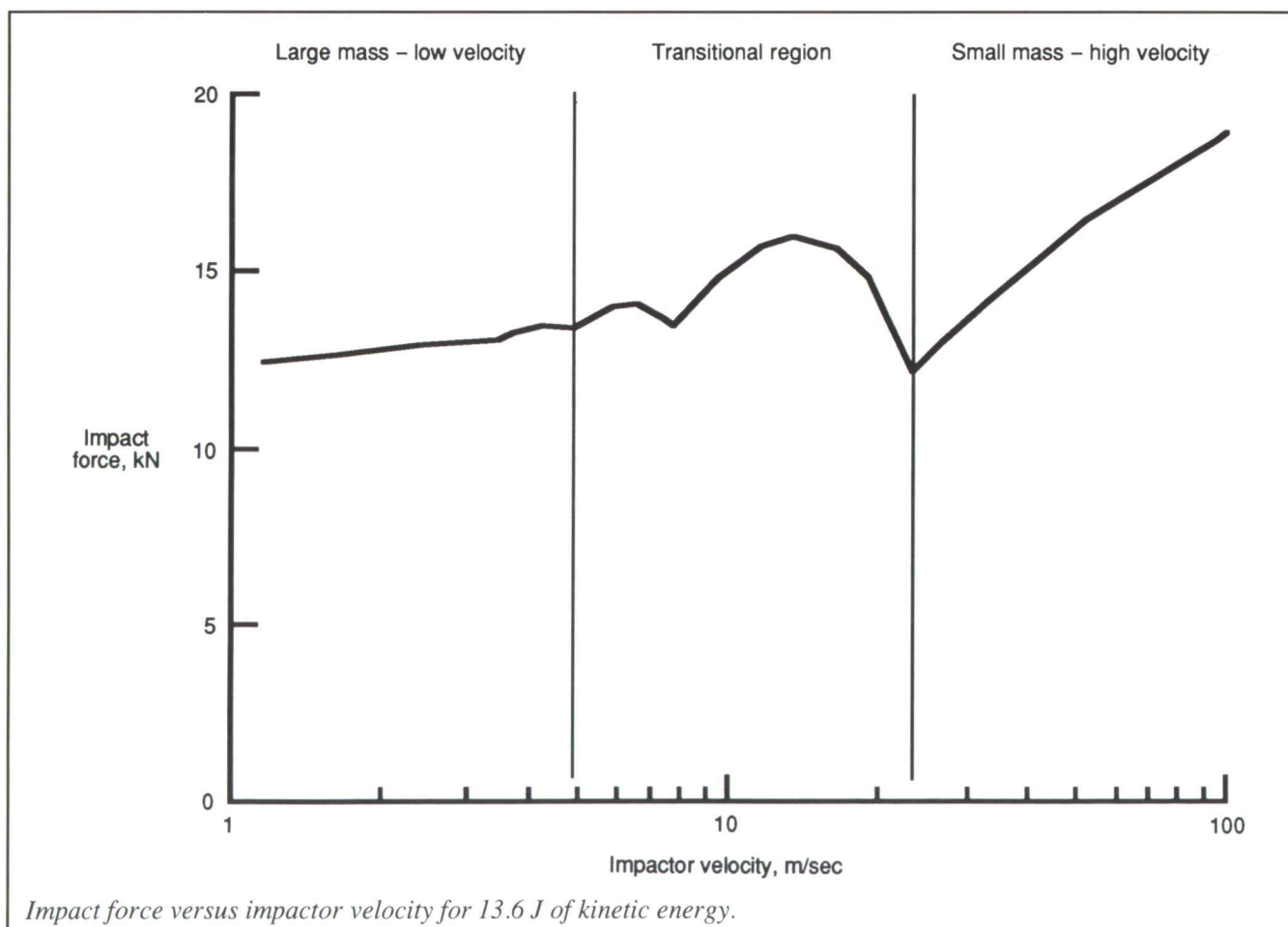
material fracture toughness to predict local delamination onset from matrix cracks. (See the bottom right figure.)
(S. A. Salpekar, 43464, and T. K. O'Brien)
Structures Directorate

Differences Between Standard Impact Tests

Composite structures are currently designed and certified using a building block approach. Composite materials tend to be susceptible to damage from out-of-plane impact loads. Standard impact tests are typically used to evaluate the impact resistance. In these

tests, a small specimen in a frame is impacted by an object with a certain kinetic energy, then residual strength is measured. Two methods are currently being used to impact a test specimen: a falling weight (large mass/low velocity) or a spherical projectile shot out of an air gun (small mass/high velocity). However, the damage generated from these two methods, and hence the residual strength, can be quite different for a given value of kinetic energy. These differences were investigated analytically with a finite-element method. The results from this study will aid in the establishment of a standard impact test to support the design of damage-tolerant composite structures.

Damage in laminated composites has been shown to be a function of the force that an impactor exerts on the laminate. Consequently, the variation of impact force with the impactor mass and velocity was analytically investigated. Curves of the impact force versus velocity (see the figure) were created by varying the impactor mass and velocity such that kinetic energy remained constant. Each point on the line represents the maximum contact force for an impact at a kinetic energy of 13.6 J with the velocity given on the horizontal axis. When the velocity was increased (mass was decreased), the impact duration decreased. The impact response could then be divided into three regions (see the figure) depending on contact duration and bending wave speed. Deflection of the plate



under the impactor is associated mainly with propagation of the bending wave. When the contact duration was long, relative to the time required for a bending wave to be reflected from the boundary (left side, large mass/low velocity), the plate deformed in a static manner and the impact force was relatively independent of the velocity for a given value of kinetic energy. However, when the contact duration was shorter than the time required for a bending wave to reflect from the boundaries (right side, small mass/high velocity), the impact force increased smoothly with the velocity.

A transitional region can be seen in the center of the figure, indicating the point at which the impact force fluctuated up and down with the velocity. Because the maximum contact force can be different for a large-mass/low-velocity and a small-mass/high-velocity impact, the damage and hence the residual strength can be different. Because the specimen boundaries come into play for large-mass/low-velocity impacts but not for low-mass/high-velocity impacts, damage and residual strength may depend upon plate size in the one case but not in the other. Thus, results from a large-mass/low-velocity test will be difficult to use as a design allowable. (C. C. Poe, Jr., 43467, Wade C. Jackson, and M. A. Portanova) Structures Directorate

Trail-Rotor Model Flutter Characteristics

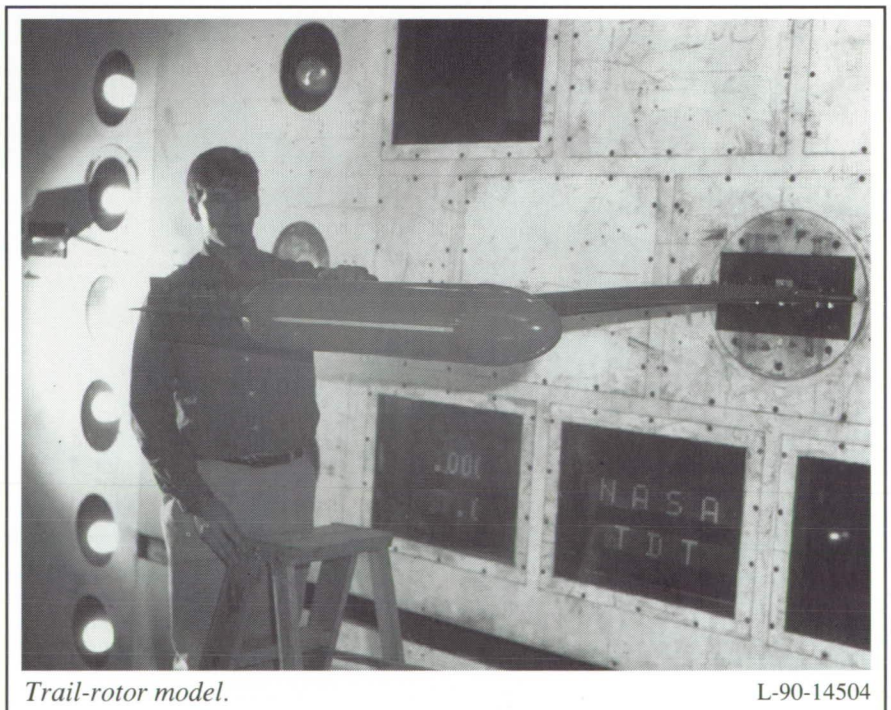
The trail-rotor vehicle is one possible design for a future generation high-speed rotorcraft. This vehicle uses a tilt-rotor concept that includes a fixed wing with gear-box nacelle and rotor

blades at each wing tip. In takeoff, landing, and hover conditions, the gear-box nacelles are in the vertical position with the blades extended. During conversion to the forward flight mode, the blades are feathered as the nacelles tilt aft 90° , after which the blades are folded back into a trailing position. This study was to investigate the flutter behavior of a simple trail-rotor model in the forward flight mode.

Four different configurations of the trail-rotor concept were tested for flutter in the Transonic Dynamics Tunnel (TDT). All four were cantilevered wing models mounted on the tunnel sidewall. The wing consisted of an aluminum flat plate with an NACA 65A010 foam airfoil bonded to it. The first configuration was the wing only. The second configuration consisted of the wing plus a tip pod (representing the gear-box nacelle). The third configuration consisted of the wing plus the tip pod and four rigid trailing rotor blades as shown in the first figure. The fourth configuration consisted of the wing plus the tip pod

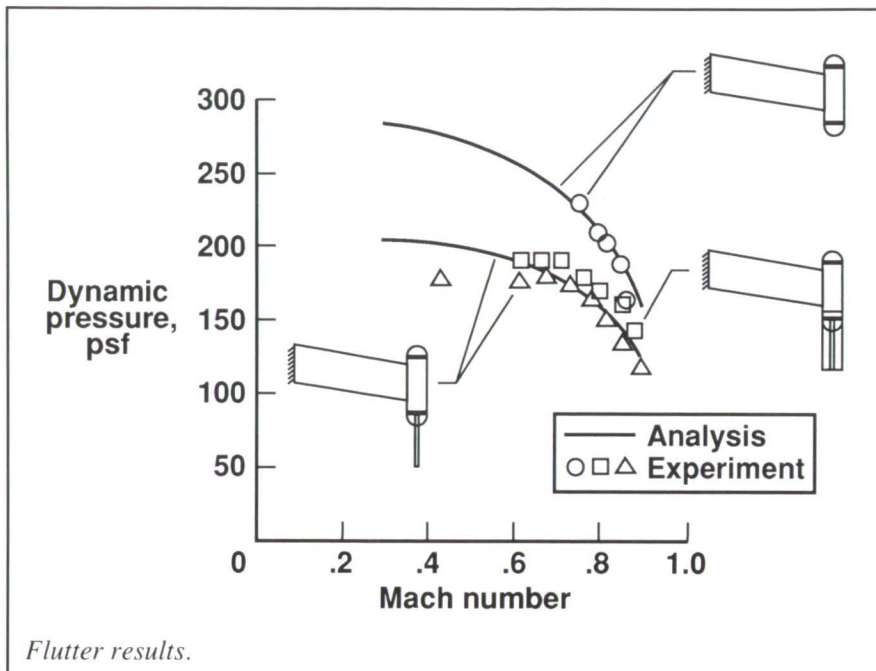
and a steel bar representing the mass and inertia of the blades but not their longitudinal aerodynamics. For the flutter analysis, mode shapes and frequencies were generated with a finite-element model, and generalized aerodynamic forces were obtained with a subsonic kernel function code.

No flutter points were obtained for the wing-only configuration within the TDT air operating envelope. Experimental and analytical results for the three remaining configurations are shown in the second figure as the variation of flutter dynamic pressure with Mach number. A large reduction in measured and calculated flutter dynamic pressure was experienced when the four rigid trailing blades were added to the wing/pod configuration. A further slight reduction in the flutter boundary occurred when the four trailing blades were replaced by the steel bar. The results indicate a possible beneficial aerodynamic damping effect when the blades are present. The experimental data were predicted accurately by the analysis



Trail-rotor model.

L-90-14504



results that are also shown in the second figure. This study defined the basic flutter characteristics for a conceptual trail-rotor vehicle in the forward flight mode and showed that current flutter analysis procedures will be adequate as an aid in the design of this type of vehicle.

(David L. Soistmann, 41073)
Structures Directorate

NACA 0012 Benchmark Model Test

A Benchmark Models Program has been initiated at Langley Research Center with the primary objective of obtaining aeroelastic data for computational fluid dynamics (CFD) code development, evaluation, and validation. The first model in the series, a rigid wing supported on a flexible mount system, was tested to define the conventional flutter boundary, the angle-of-attack flutter boundary, and other transonic instability boundaries

with simultaneous measurements of surface pressures.

The rigid rectangular wing model shown in the first figure had an NACA 0012 airfoil with a panel aspect ratio of 2.0. The model was tested in the

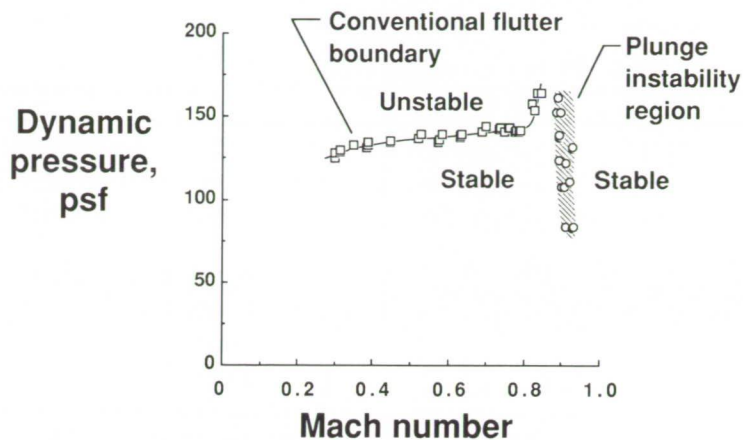
Transonic Dynamics Tunnel (TDT) on the flexible Pitch and Plunge Apparatus (PAPA). This model was equipped with in situ pressure transducers to measure wing upper- and lower-surface steady and unsteady pressures along chord lines at the 60-percent span station and the 95-percent span station. The model and support system were also instrumented with accelerometers and strain-gauge bridges for the measurement of model frequencies, displacements, and forces. A ground vibration test was performed to define the wind-off structural dynamic characteristics of the model system. Wind-on data were obtained in the Mach number range from 0.3 through 0.97.

The Mach number effects on the conventional flutter boundary (coupling of pitch and plunge models) for the model at an angle of attack of 0° are shown as a function of dynamic pressure and Mach number in the second figure. Also shown is a narrow instability region near Mach number 0.90 in which the mode of oscillations was primarily plunge motion.



NACA 0012 model mounted on PAPA system in tunnel.

L-90-8987



Mach number effects for model at angle of attack of 0°.

Although not shown here, angle-of-attack effects on flutter were also determined at several Mach number test conditions. Instrumentation time history records were recorded at most instability points as well as at some subcritical test conditions. Flow studies were also performed using both tufts and liquid crystals to define shock locations and lines of flow separation. (José A. Rivera, Jr., Bryan E. Dansberry, Moses G. Farmer, Clinton V. Eckstrom, Robert M. Bennett, and David A. Seidel, 41270) Structures Directorate

Transonic Shock-Induced Dynamics of Flexible Wing

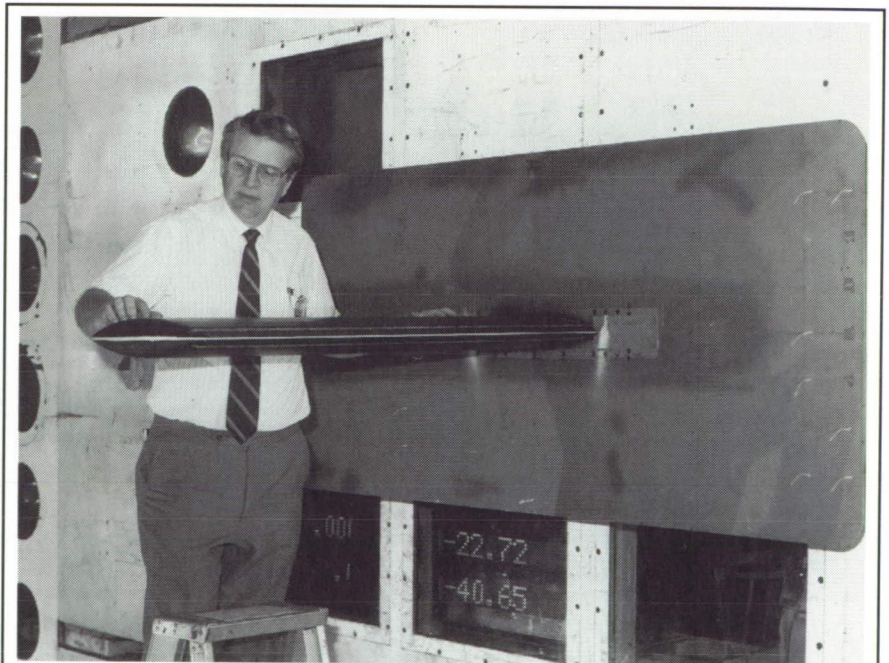
Periodic transonic shock-boundary-layer oscillations are known to occur over a narrow range of Mach numbers on thick rigid circular-arc airfoils. The objective of this research was to determine the dynamic response of a flexible wing under these conditions. This investigation is intended to aid in the physical understanding of complex unsteady transonic aerodynamics, and the model is an element

of the Structural Dynamics Division Benchmark Models Program.

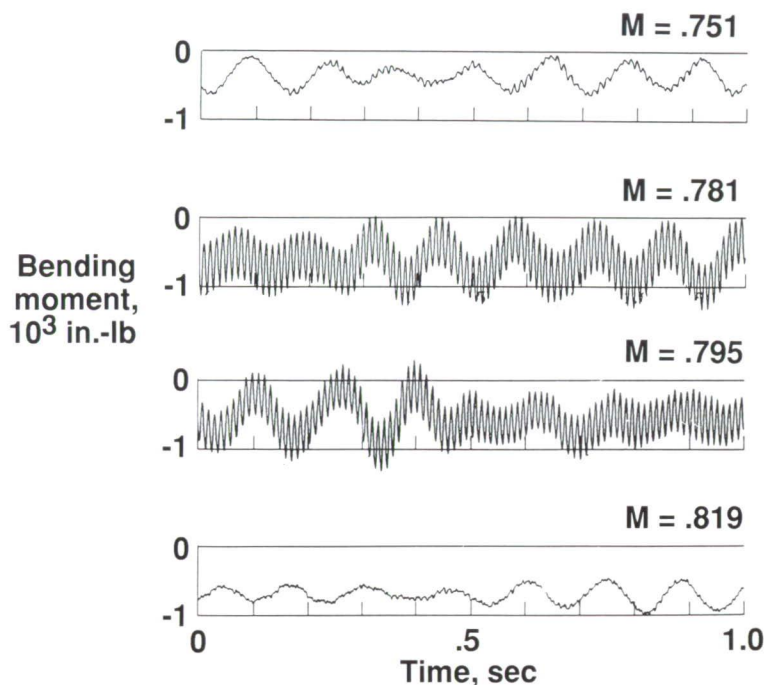
A simple flexible wing was designed and built at Langley Research Center and tested in the Transonic Dynamics Tunnel (TDT) to determine the shock-boundary-layer-induced dynamics. The wing was rectangular in planform with an 18-in. chord and

45-in. span. The wing consisted of an aluminum plate with balsa wood forming an 18-percent circular-arc airfoil section. The first figure shows the model mounted in the TDT. The model was instrumented with bending and torsion strain gauges at the root and accelerometers on the outer portion of the wing.

Some illustrative bending-moment response time histories are shown in the second figure. In the region of shock-boundary-layer oscillations, an increased random buffeting level was found for the first bending mode which was at a much lower frequency than the frequency of the shock-boundary-layer oscillations. A limit-cycle oscillation was found for a third-bending-like mode that involved splitter plate motion and had a natural frequency that was near the frequency of the shock-boundary-layer oscillations. These results are illustrated in the second figure. For $M = 0.751$, random amplitude buffeting response in the first bending mode is shown in the bending-moment time history.



Flexible wing with 18-percent circular-arc airfoil tested in TDT. L-90-11579



Sample time histories of bending-moment response.

At $M = 0.781$ and 0.795 , the first bending buffeting response is larger, and a nearly constant amplitude high-frequency response is evident. With a further increase in M to 0.819 , the high-frequency response disappears, and the first mode buffeting is again of lesser magnitude. A small spanwise strip and wishbone-type vortex generators were used to alleviate the limit-cycle oscillations, but they resulted in either increased buffeting of the first mode or induced flutter.

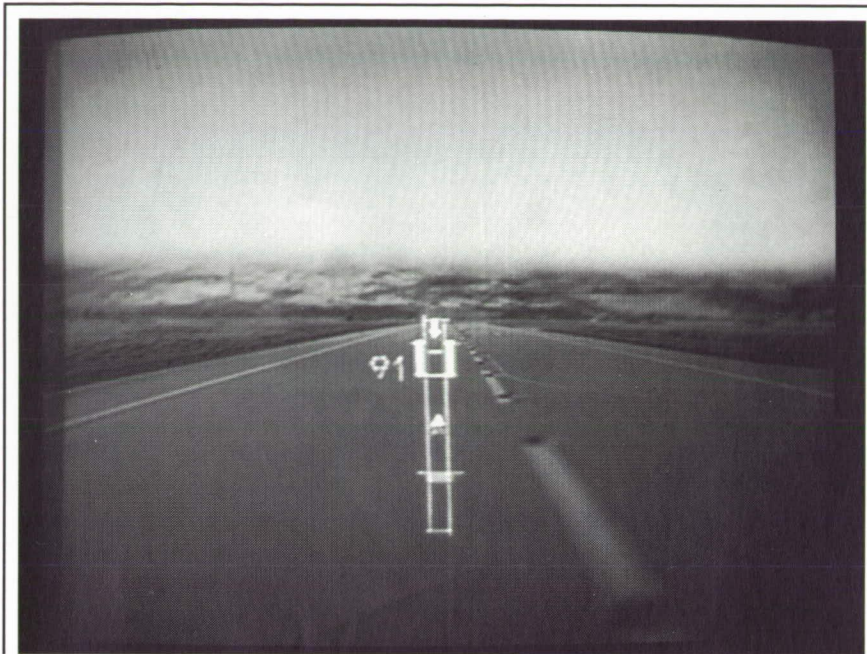
(Robert M. Bennett, 42274,
Bryan A. Dansberry, Moses G.
Farmer, Clinton V. Eckstrom,
and José A. Rivera, Jr.)
Structures Directorate

Takeoff Performance Monitoring Systems Display Options

Over the past decade, approximately 10 percent of all aircraft accidents occurred during takeoff. Transport aircraft takeoff/abort procedures currently rely heavily on the perceptions and judgments of pilots rather than precise knowledge of how well the airplane is achieving a desired performance. To aid pilots in making critical "Go/No-Go" decisions, a Takeoff Performance Monitoring System (TOPMS) has been developed and evaluated in simulation and flight using the Langley Research Center Transport Systems Research Vehicle (TSRV), a highly modified B-737 airplane. The TOPMS provides elemental, predictive, and summary information on acceleration performance and engine status.

Baseline heads-down and head-up displays (HUD's) for TOPMS were developed and evaluated by more than 40 government, airline, and other industry pilots. Both displays were judged easy to monitor and highly appropriate for the takeoff/abort task. Airline operators, airframe and avionics manufacturers, and Federal Aviation Administration officials have expressed interest in the system; however, concern has been expressed that it may provide more information than is actually needed or desired. In an attempt to resolve some of these concerns, several reduced-feature display options were implemented on the TSRV/TOPMS simulator and evaluated by several NASA research pilots. Most of the options involved simplifications and/or relaxation of conditions that activate the abort-advisory flag ("Stop" sign). For example, the TOPMS HUD shown in the figure indicates that the airplane has accelerated to 91 knots, but it is experiencing a significant acceleration deficiency (shown by the arrow at the far end of the runway). In the baseline option, if the arrow extends over the tick mark between the two white engine-pressure-ratio (EPR) bars, the "Stop" sign will appear and advise an abort. However, in the most basic of the new options, no such advisory symbol appears; therefore, the pilot must make his "Go/No-Go" decision after mentally processing several bits of elemental information, including the length of the arrow. Similarly, this option does not provide the "Stop" sign when an engine fails; however, the pilot can still quickly detect the failure by observing that the associated EPR bar has diminished in length and turned red. This option does contain a "Go" advisory flag, which appears whenever the TOPMS algorithm determines that the remaining runway distance is inadequate for stopping.

ORIGINAL PAGE
BLACK AND WHITE PHOTOGRAPH



TOPMS HUD showing deficient along-track acceleration.

L-89-07029

All options, including the most basic one just described, were judged to be adequate and suitable for the task. These options provide potential users with a choice of valuable, easy-to-monitor takeoff/abort performance information coupled with a selected amount of higher level advisory information.

(David B. Middleton,
Raghavachari Srivatsan, and
Lee H. Person, Jr., 44034)
Flight Systems Directorate

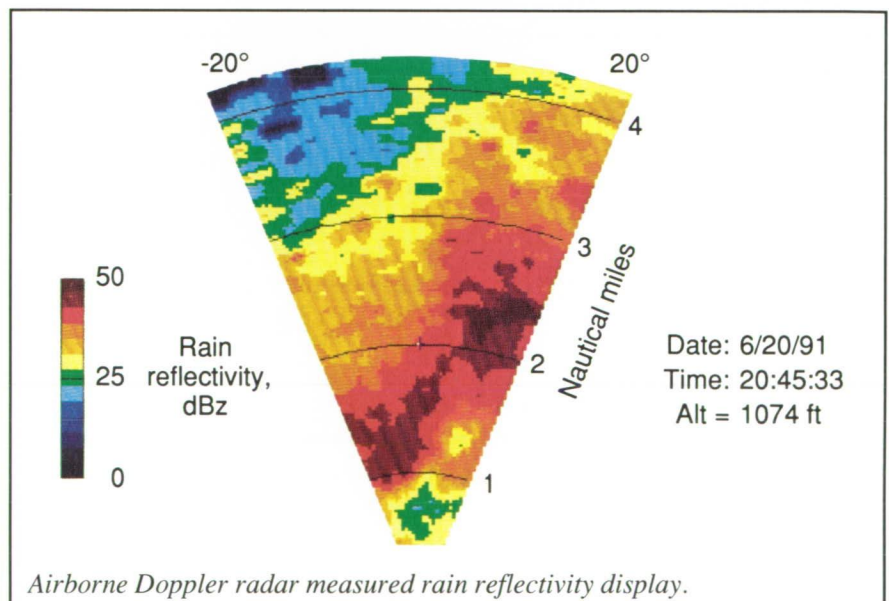
Airborne Doppler Radar Detection of Microburst Wind Shear

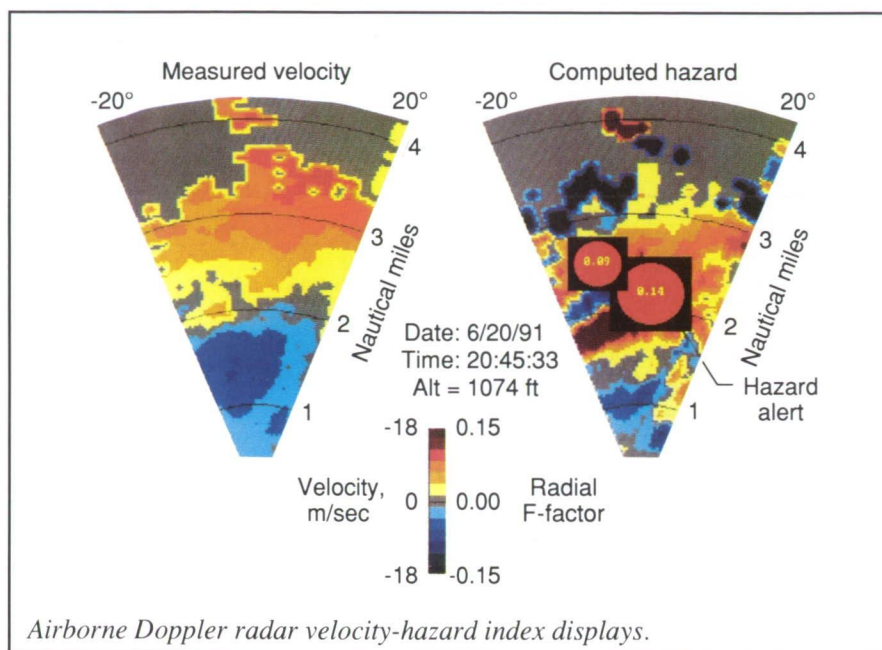
The purpose of this research is to develop airborne Doppler radar technology for the detection of low-altitude microburst wind shear and to assess the capabilities and limitations of the Doppler radar as a forward-looking sensor for detecting wind shear during aircraft landing or takeoff.

One specific goal of the research has been the development of a Doppler radar simulation program that accurately calculates the expected output of an airborne pulse-Doppler radar system viewing a microburst wind shear along or near the approach path of the aircraft in the presence of a background clutter environment. This goal has been

achieved. The simulation program has been used to assess the performance of an airborne Doppler radar to detect hazardous microburst wind shear and to aid in the development of processing algorithms that can suppress the effects of severe ground clutter.

A second goal is to conduct flight test experiments using an experimental airborne Doppler radar installed on the NASA 515 aircraft. An experimental airborne Doppler radar for the detection of wind shear has been developed and is installed on the NASA 515 Boeing 737 aircraft. The objectives of these flight experiments are threefold: to gather ground clutter data to help validate the clutter models presently utilized in the radar simulation program, to gather weather and wind shear data to aid in the development of wind shear detection and clutter suppression algorithms, and to evaluate the performance of candidate wind shear detection and clutter suppression algorithms in a real-time wind shear environment. A number of local checkout and clutter flight experiments, including the Philadelphia airport, have been conducted. Preliminary analysis of the Philadelphia clutter





data indicates that the simulation clutter model used for that airport compares well with the data.

Severe weather flight experiments were also conducted in June 1991 in the Orlando area in which a number of microburst events were approached, and in some cases penetrated, at safe altitudes and aircraft speeds. Preliminary analysis of the recorded radar data from these approaches and penetrations indicates that the Doppler radar was able to detect the various weather parameters, including hazardous wind shear areas, prior to penetrating the microburst events. The first and second figures provide representative range azimuth displays of reflectivity, measured velocity, and the computed hazard index resulting from Orlando Doppler radar test data. The red hazard alert circles shown on the right side of the second figure identify the location of wind shear hazards of the indicated intensity. In the preliminary analysis, the data compared well with weather products obtained from the ground Terminal Doppler Weather Radar (TDWR), which was supporting the flight experiment.

A similar set of flight experiments are being conducted in Denver in July 1991. Detailed analyses will be conducted of the Orlando and Denver clutter and microburst data to aid in the validation of the radar simulation clutter modeling and to evaluate the performance and efficiency of wind shear hazard detection and clutter suppression algorithms. A real-time signal and data processing system is being developed that will be incorporated, along with candidate algorithms, in the experimental airborne radar. Flight experiments will be conducted in the summer of 1992 to demonstrate in real time the performance of Doppler radar to detect hazardous wind shear.

**(E. M. Bracalente, 41810)
Flight Systems Directorate**

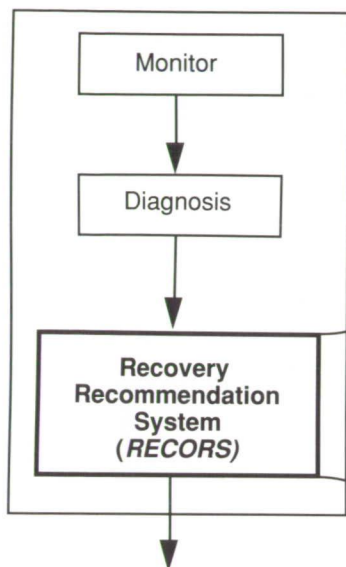
RECORS Concept for Aircraft Applications

Aircraft accident and incident analyses reveal that many disastrous

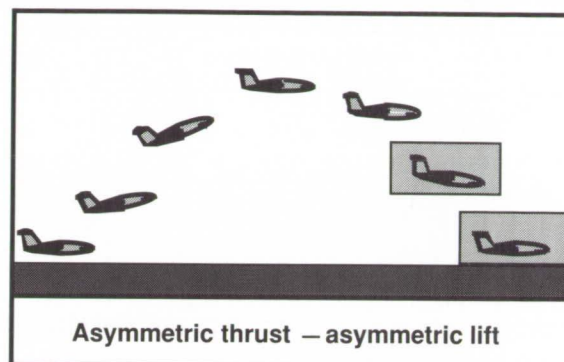
aircraft accidents involve multiple subsystems failures. The primary objective of this research effort was to design and implement a knowledge-based system concept to recommend responses to failures involving multiple subsystems. A second objective was to perform a preliminary evaluation of pilot interaction with the Automated Recovery Recommendation System (RECORS) concept.

The input to the recovery recommendation process is a set of fault hypotheses; its output is a description of fault effects and a set of recommended crew responses. The knowledge for the RECORS concept was acquired by interviewing pilots, reviewing airline training tapes and training and operations manuals, and observing pilots in a flight simulator. The primary knowledge base of RECORS consists of qualitative causal models of aircraft subsystems (electrical, fuel, and hydraulic), effectors (engines, control surfaces, and gear), forces acting on the aircraft (drag, thrust, gravity, and lift), and the current flight profiles (airspeed, altitude, and attitude). As shown in the figure, the knowledge encoded in the models is used for assessing fault effects on flight phases and goals, generation of recovery procedures, and explanation of the reasoning. A preliminary engineering evaluation of the concept was done by having four airline pilots interact with the workstation implementation of RECORS for fault scenarios based on actual accidents and incidents.

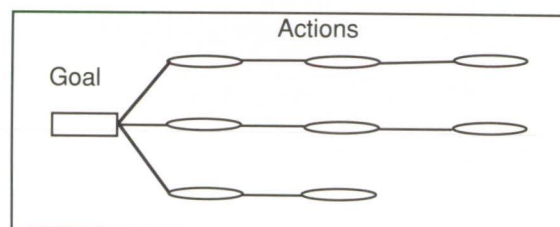
Among the preliminary results of the engineering evaluation, data showed that pilots seem to use different mental models of the aircraft systems for situational assessment rather than for response. The use of differing mental models implies that different information is required to support reasoning with those models.

Faultfinder**What RECORS Does:**

- Assesses fault effects on flight phases/goals



- Generates recovery procedures for
 - Novel faults
 - Multiple independent faults
 - Multiple subsystems



Recovery recommendations for fault management.

For situational assessments, pilots liked having information about the whole aircraft and its individual components. For response, the pilots preferred information concerning the controls as a single unit rather than divided into individual components. Pilots liked the integrated display because it showed multiple subsystems, and they commented that the RECORS concept also had significant potential utility for training.

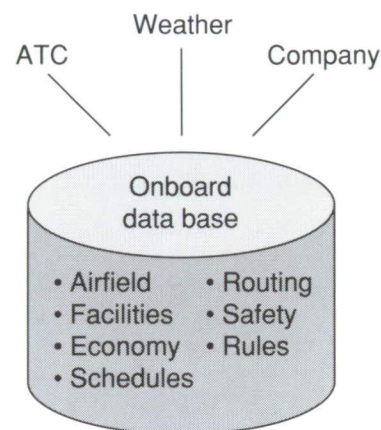
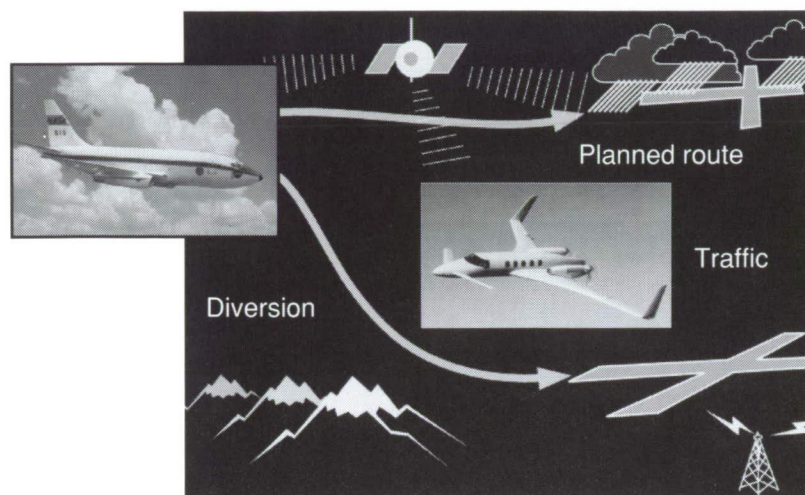
(Kathy Abbott, Eva Hudlicka, Kevin Corker, and Dawn MacLaughlin, 48262)
Flight Systems Directorate

Decision-Aiding Concept and Pilot-Vehicle Interface (PVI) for In-Flight Diversions

A current problem in flight operations is the high pilot work load required while responding to flight plan diversions, especially during critical flight phases. The overall objective of this research effort, called DIVERTER, was to develop concepts, based on artificial intelligence (AI) techniques, to reduce this pilot work load, and to provide guidelines for the integration of these concepts into current and future flight management systems. This work has been performed under contract to Langley

Research Center by Lockheed Aeronautical Systems Company. The objective of the currently completed Phase III task was to develop concepts for the pilot-vehicle interface.

The information flow between DIVERTER (the expert system developed for this effort), the pilot, the onboard systems, and external sources (such as air traffic control) was assessed. The pilot-vehicle interface requirements were then determined, and a rigorous specification of an interface concept and the design process that produced this concept were completed. The specification of the design process included the alternatives that were considered and the reasoning behind each design



Provides decision-aiding information during unexpected in-flight diversions:

- Integrates data from many sources
- Provides pertinent information for contingency management
- Improves situation awareness

Elements

- Onboard data base
- AI processor
- Pilot-vehicle interface
- Real-time data link

DIVERTER decision aiding for diversions.

decision made. The functionality of the DIVERTER prototype software was improved by integrating the selection process for airfields and routes, dynamically predicting movement of weather cells, and modularizing the code so that the demonstration drivers for the aircraft simulation and map display can be easily replaced by links to a research simulator such as Langley Research Center's Advanced Concepts Simulator (ACS).

A presentation of the interface design and a demonstration of the improved DIVERTER prototype software have both been accomplished. The pilot-vehicle interface concept and accompanying design process specification will provide a solid foundation as well as flexibility during definition

of simulator cockpit displays. The DIVERTER demonstration software package incorporates all specified enhancements, and it has many improved features for highlighting the capabilities of the decision-aiding concept.

(Michael T. Palmer, 42044)

Flight Systems Directorate

Knowledge-Based Systems Concept for Primary Flight Display Information Management

The amount of information already in today's civil transport cockpit, the

difficulties experienced in managing the large amount of information, and the trend to increase the amount of information in future cockpits have made information management a primary concern. An overall research objective, therefore, has been established to develop concepts that will help flight crews manage the extensive amount of available information. As an initial step toward this overall objective, managing information on the primary flight display (PFD) is being explored using a task-tailoring approach. This task-tailored approach requires complex logic that led to difficult-to-manage software when traditional programming techniques were used. As a result, a knowledge-based system (KBS) approach was chosen over the traditional program-

ming approach, based on an earlier study that found KBS architectures easier to manage, given complex applications. Because this effort would involve the first study with integrated KBS's running in LISP in real time on a civil transport aircraft, a preliminary study to validate the KBS concept was necessary. The objective of this particular study was to test the KBS's, collectively called the Task-Tailored Flight Information Manager (TTFIM), in flight on Langley Research Center's Transport Systems Research Vehicle (TSRV) to validate their implementation and integration and to confirm the software engineering advantages of the KBS approach in an operational environment.

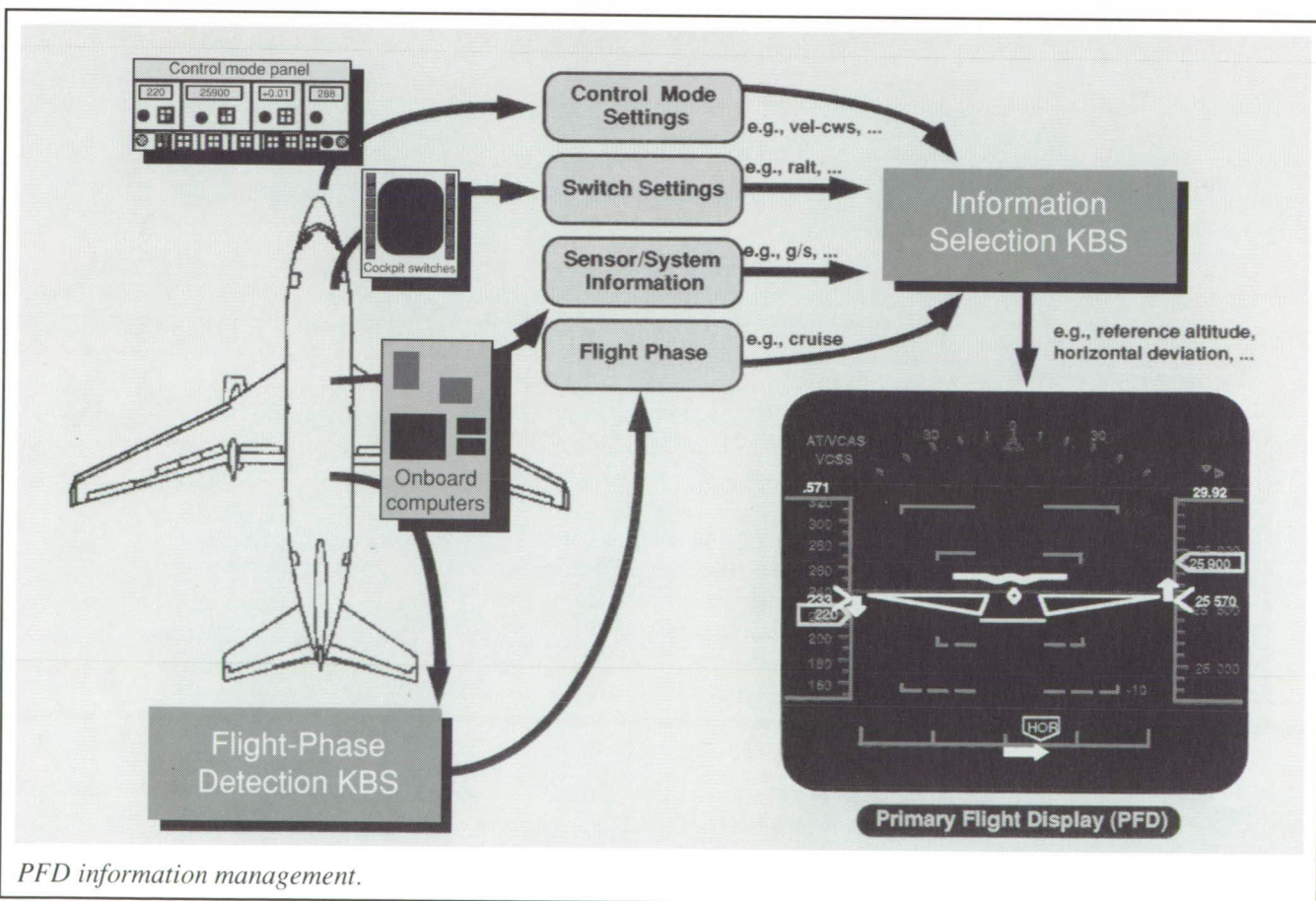
The flight tests successfully validated the KBS concept for PFD information management. Correct

presentation of information on the PFD during all flight tests validated the implementation of the information selection KBS and the integration of the two KBS's with each other and with the existing TSRV systems. As expected, the KBS for information selection was not as computationally fast as its equivalent traditional system when selecting some information, but this aspect did not interfere with cockpit operations. The flight-phase detection KBS was successful for all elements within the flight test envelope except one, with the one logic error causing the problem being easily isolated (on-line), given the KBS environment. The flight tests demonstrated the feasibility of the KBS concept with actual sensor data and confirmed the software engineering advantages of using KBS architectures. The flight tests were the first in a civil

transport aircraft involving integrated KBS's running in LISP in real time.
(Wendell R. Ricks, 46733)
Flight Systems Directorate

Estimation of Heavy Rain Effect on Airplane Performance

A series of tests were conducted at Langley Research Center to measure the effect of heavy rain on airfoil aerodynamics. The tests were part of the Wind Shear Program being conducted in conjunction with the Federal Aviation Administration. The results of the tests showed that heavy rain significantly degrades airfoil performance; however, the

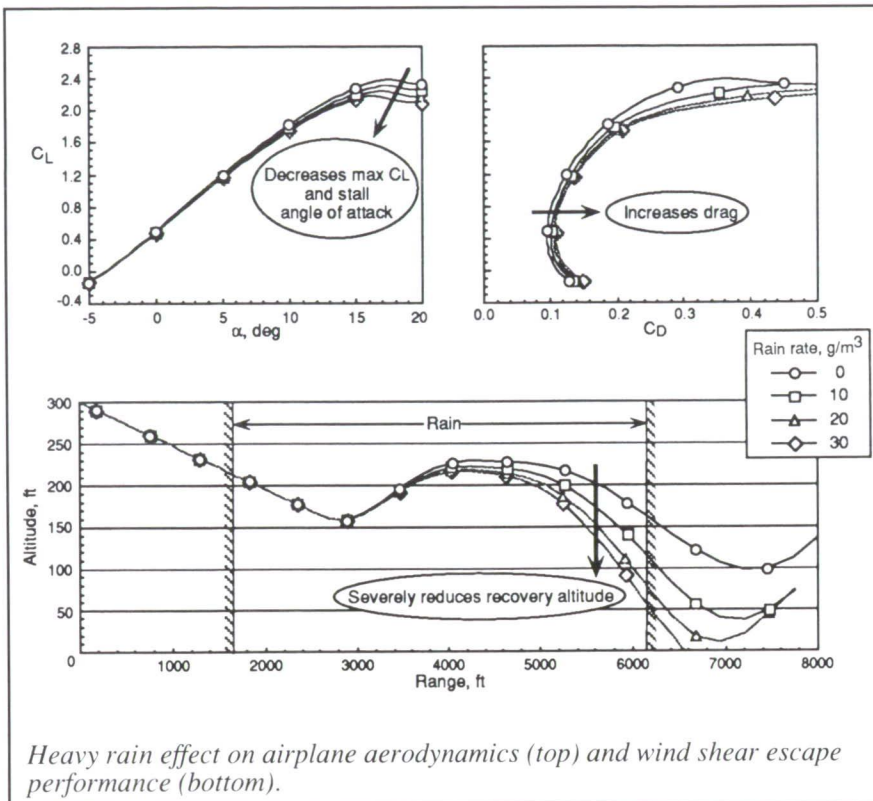


Data Link for Air Traffic Control and Weather Information Exchange

Message exchange for air traffic control (ATC) purposes, via data link, offers potential benefits of increasing airspace system safety and efficiency by reducing communications errors and relieving the overloaded ATC radio frequencies. The objective of this study was to evaluate the use of data link as the primary communications source for ATC strategic and tactical clearances, for weather information, and for company messages during a typical commercial airline flight. A menu-driven, touch-panel display, illustrated on the left side of the figure, was developed to provide the pilots' interface to the data-link system. By touching appropriate buttons on the display, for example, the crew may accept or reject clearances from the ATC controller, or may even accept a clearance and simultaneously enter it into the flight management system for execution by simply touching the "Roger/Enter" button.

Analysis of the data shows an almost total elimination of confusion, errors, and voice-communications repeats (shown on the right side of the figure) with the flights conducted with data link as the primary communications device. Generally, the test crews found the use of data link, with voice backup, acceptable for ATC tactical clearances. The majority of the test crews believed that data link would reduce the nonflying pilot's work load and mistakes. All of the test crews indicated that the menu/window format concept was very user friendly and required little training to use.

The results of these tests indicate that the use of data link as the primary communications source for ATC clearances and communications, with



corresponding effect on the total airplane aerodynamics and aircraft performance was unknown. The objective of this research effort was to estimate the heavy rain performance of a conventional commercial twin-jet based on the airfoil test results.

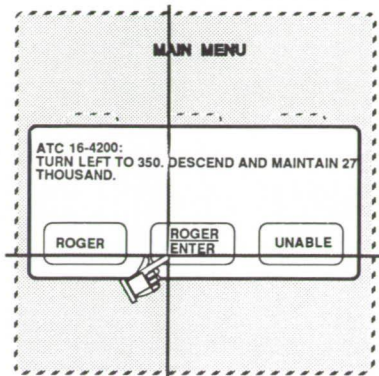
The airfoil test results were integrated across the planform of a conventional commercial twin-jet to determine the heavy rain aerodynamic effect on the airplane. An aerodynamic model of the airplane was then developed which included the heavy rain effect. This model was included in a point-mass numerical simulation of the airplane flying in a wet microburst environment. The simulation incorporates a variety of wind shear escape procedures for both takeoff and approach conditions.

The heavy rain aerodynamic model, presented in the figure, shows the loss of lift and increased drag associated with heavy rain rates. The effect of this

aerodynamic performance degradation on the ability of the airplane to escape a wet microburst encounter is demonstrated in the corresponding altitude profiles shown in the bottom part of the figure. For rain rates greater than 8 in/hour, the airplane was unable to recover from this microburst encounter. Low-altitude wind shear (such as that associated with a microburst) is often accompanied by rain. A performance-limiting wind shear may be fatal when combined with heavy rain. The numerical simulation of a wet microburst encounter provides a tool to evaluate the effect of heavy rain on wind shear escape procedures and hazard alerting criteria.

(Dan D. Vicroy, 42022)
Flight Systems Directorate

DATA LINK MENU / WINDOW FORMAT CONCEPT



ATC / AIRPLANE COMMUNICATION CONFUSION, ERRORS, & REPEATS

	VOICE	DATA LINK
CONFUSION	5	0
DIDN'T KNOW IF CLEARED TO LAND	1	--
WENT TO WRONG WAYPOINT	1	--
DIDN'T KNOW HEADING FOR VECTOR	1	--
DIDN'T KNOW ALTITUDE ASSIGNMENT	1	--
ERRORS	7	4
WENT TO WRONG WAYPOINT	1	--
FREQ SEL / RADIO OPS INCORRECT	2	3
MISSED CROSSING ALTITUDE	1	--
CLEARANCE READ BACK INCORRECT	3	--
DIDN'T CONTACT ATC	--	1
REPEATS	46	6
MISSED ALL/PART OF CALL	34	2
DUE TO ERRORS OR CONFUSION	12	4

Langley Research Center data link flight test.

voice radio as a backup, was acceptable and desired by the majority of the test flight crews. The use of data link was shown to reduce communications errors, which could improve system safety and efficiency.

(Charles E. Knox and Charles H. Scanlon, 42038)
Flight Systems Directorate

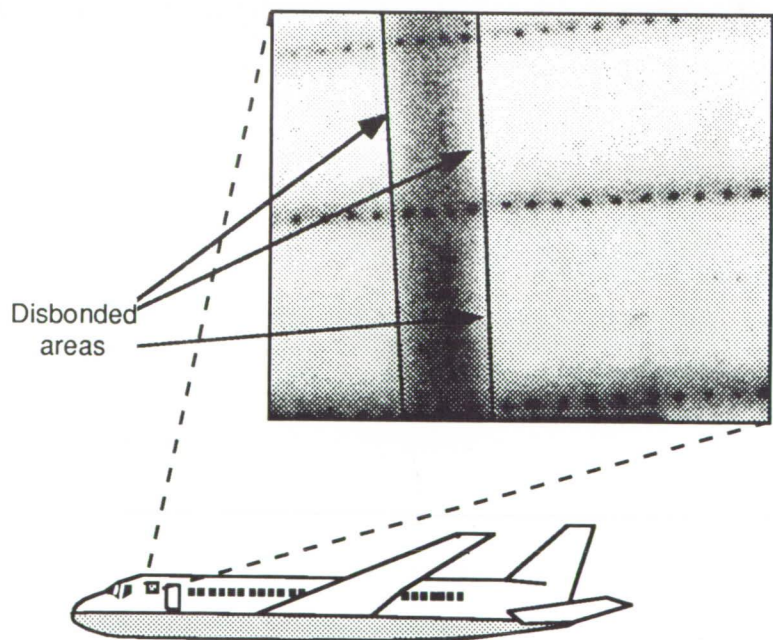
approximately 1 m^2 in size are analyzed in each data set. The structure is evenly heated to no greater than 10°C above ambient, while the time evolution of the temperature of the structure is recorded to the image processor, averaged, and archived both during and

after the application of heat for subsequent analysis.

The analysis of the images is based on computational modeling of the heat diffusion in the lap joint geometry. The result of such an analysis technique

Aging Aircraft Lap Joint Bond Nondestructive Evaluation

A technique has been developed for assessing the condition of lap joint bonds of large airframes. The technique involves large area, non-contacting inspection of the aircraft fuselage using infrared detection of the response of the structure to a thermal input. The measurement is taken at a distance ranging from 4 ft to 10 ft from the aircraft and is completely one-sided. (The heating and detection are both from the exterior of the aircraft, eliminating the need for access to the interior of the fuselage.) At this distance from the aircraft, areas



Results of thermal nondestructive evaluation of typical aircraft structure. Solid lines in image indicate original extent of bond.

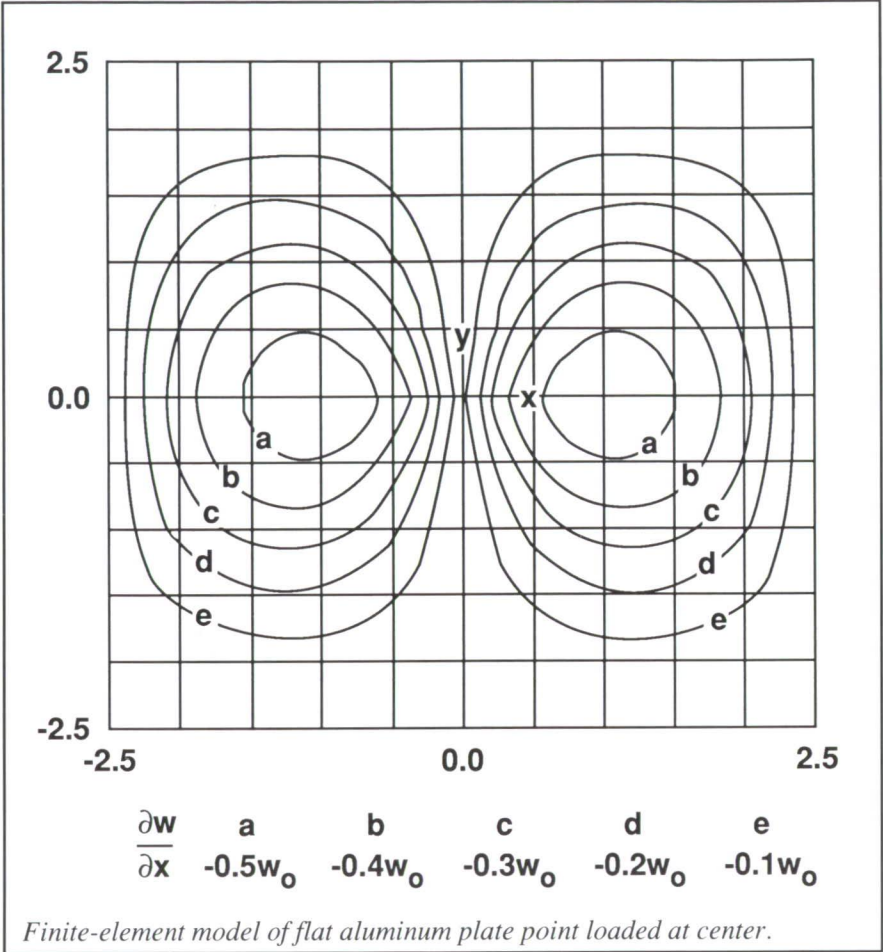
leads to an image of optimum contrast where the areas of disbond are clearly delineated. This technique involves the computation of an instantaneous time derivative at the moment of removal of heat. A processed image of the subsurface structure of an actual aircraft is shown in the figure, in which the areas of disbond are clearly visible.

The characterization of the bond integrity of aircraft lap joints with this thermal bond inspection system is a safe, fast, and accurate means of determining the condition of the subsurface structure. This technique will have increasing value as the current aircraft fleet continues to age, and it could offer significant improvement in the safety of air travel. (William P. Winfree, 44963, and K. Elliott Cramer) Electronics Directorate

Optical NDT for Aging Aircraft

Optical interferometry is a technique used to measure small surface displacements of materials subjected to mechanical, acoustic, and thermal excitation. The application of this technique to field inspection for nondestructive testing (NDT) has been impeded because of the inherent sensitivity to mechanical instabilities. However, one optical interferometry technique, electronic shearography, is less sensitive to mechanical instabilities and thus is a candidate for field-quantitative NDT.

The electronic shearography technique illuminates an object with a laser, producing a speckle pattern that corresponds to the microroughness of the surface. Appropriate processing of the interference patterns captured

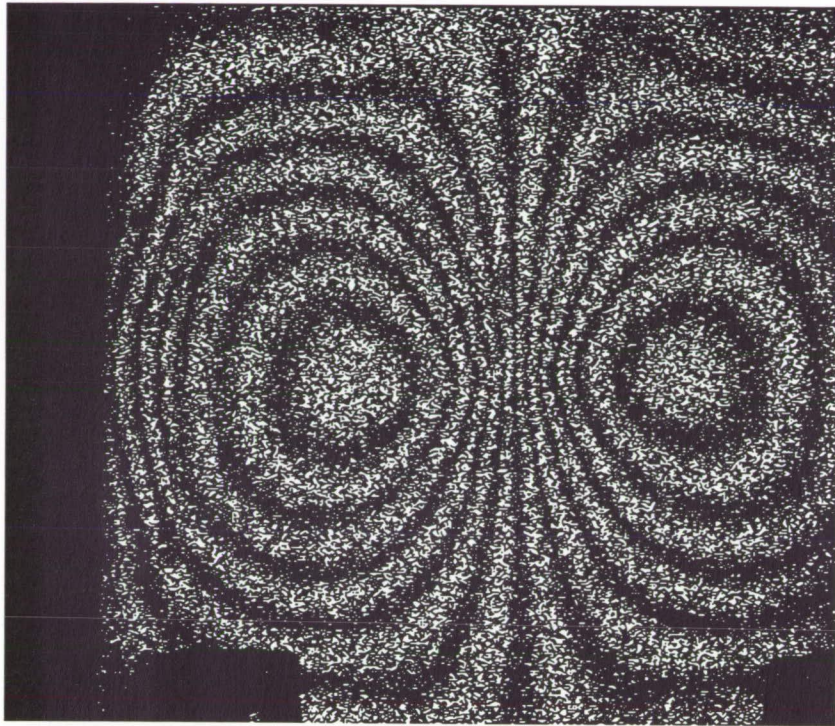


before and after object deformation generates a pattern of rings that are surface-displacement gradient contours. This technique has been used to measure out-of-plane surface-displacement gradients of flat aluminum plates. These preliminary tests serve as a demonstration of the technique and provide initial input for a data base that will allow for rapid and noncontacting detection of disbands and cracks in riveted lap joints in commercial airframes with shearography.

The initial tests consisted of a 5-in. by 5-in.-square by 0.04-in.-thick plate constrained along the edges and subjected to an imposed out-of-plane center point displacement w_0 . A finite-element simulation was conducted for comparison with the shearography

measurements. The out-of-plane displacements obtained from the finite-element analysis were normalized with respect to the imposed center displacement w_0 . The displacement gradients with respect to the x -direction are plotted in the first figure.

The shearography technique illuminated the test plate with a 35-mW helium-neon laser, and speckle patterns were captured before and after a center point displacement of 0.00043 in. was imposed. The unprocessed fringe pattern is shown in the second figure. A comparison of the first and second figures indicates a good correlation between theory and experiment. Additional experiments and analyses will be conducted on test plates with cracks and disbands prior



Shearogram of flat aluminum plate point loaded to 0.43 mil at center.

scan capability, the electromagnetic plate mode-generation method has been investigated.

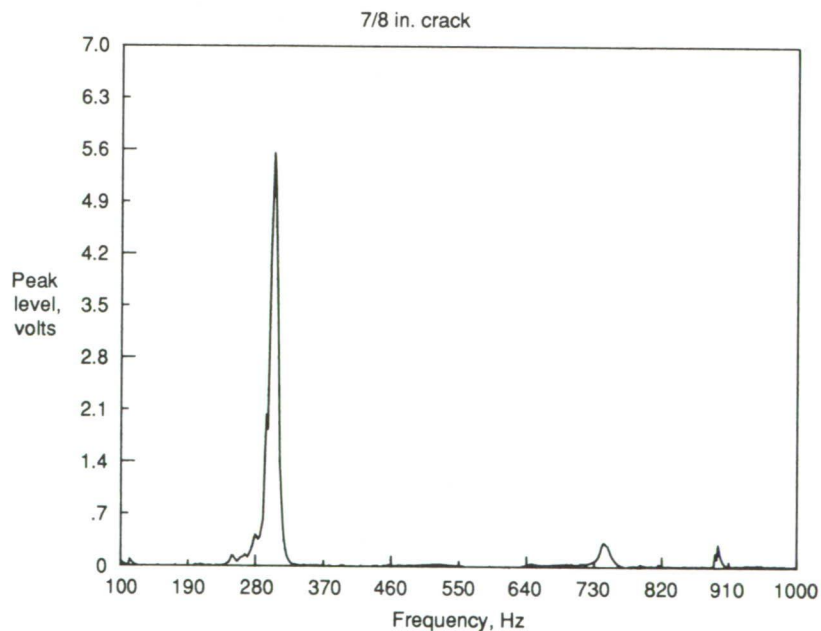
Plate vibrations are generated by applying alternating point loads in two adjacent locations separated by 3 cm. For actual laboratory experiments, the alternating point loads are simulated by using external a.c. magnetic fields and permanent magnets attached to the plate under investigation. The plate vibrations are detected by acoustic emission (AE) and polyvinylidene fluoride (PVDF) film transducers in contact with the plate. Both sensors provide suitable detectability. The first figure shows the typical experimental results that locate the resonance frequency of the plate vibrational mode by detecting the PVDF film transducer output as a function of the frequency of externally applied alternating loads. The location of the amplitude peak has been confirmed to be unique to a

to making measurements on riveted lap joints in commercial airframes.

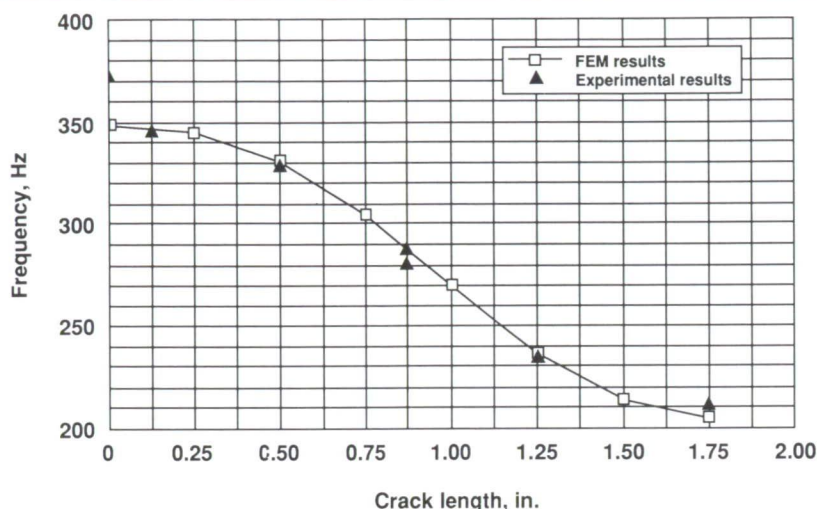
**(Leland D. Melvin, 47970,
and David S. Dawicke)
Electronics and Structures
Directorates**

Detection of Cracks by Vibrational Mode Analysis in Thin Metal Plates

Various eddy-current techniques are commonly used to detect very small cracks in thin metal plates and in bore holes. Because of the slow rate of testing, the application of these techniques to the assurance of aircraft structural integrity is a lengthy and laborious process. As a part of the effort to develop nondestructive evaluation (NDE) techniques capable of detecting fatigue cracks with rapid



Experimental data locating resonance frequency of cracked plate at 288 Hz.



Comparison between FEM simulation and experimental results on resonance frequency as function of fatigue crack length.

particular geometry of fatigue crack under given experimental conditions.

The characteristics of vibrational modes can be modeled by the finite-element method (FEM) technique. As a result, the resonance frequency of plate vibrations at a given length of fatigue crack can be determined computationally. The second figure shows the results of the experiments and FEM simulation. The results agree very well for the plates with fatigue cracks, but they show some discrepancy for an uncracked plate. This discrepancy is currently under further investigation.

(B. Wincheski, 44798, and M. Namkung)
Electronics Directorate

Effect of Heavy Rain on Airfoil Performance at Large Scale

Large-scale heavy rain effects testing at the Aircraft Landing Dynamics Facility (ALDF) ended in Decem-

ber of 1990 after a 2-year research effort. A large-scale ground test capability for acquiring aerodynamic data was developed to assess the actual effect of heavy rain on airfoil performance. A large-scale confirmation of wind-tunnel results was required to eliminate uncertainties with regard to the sensitivity of the experimental

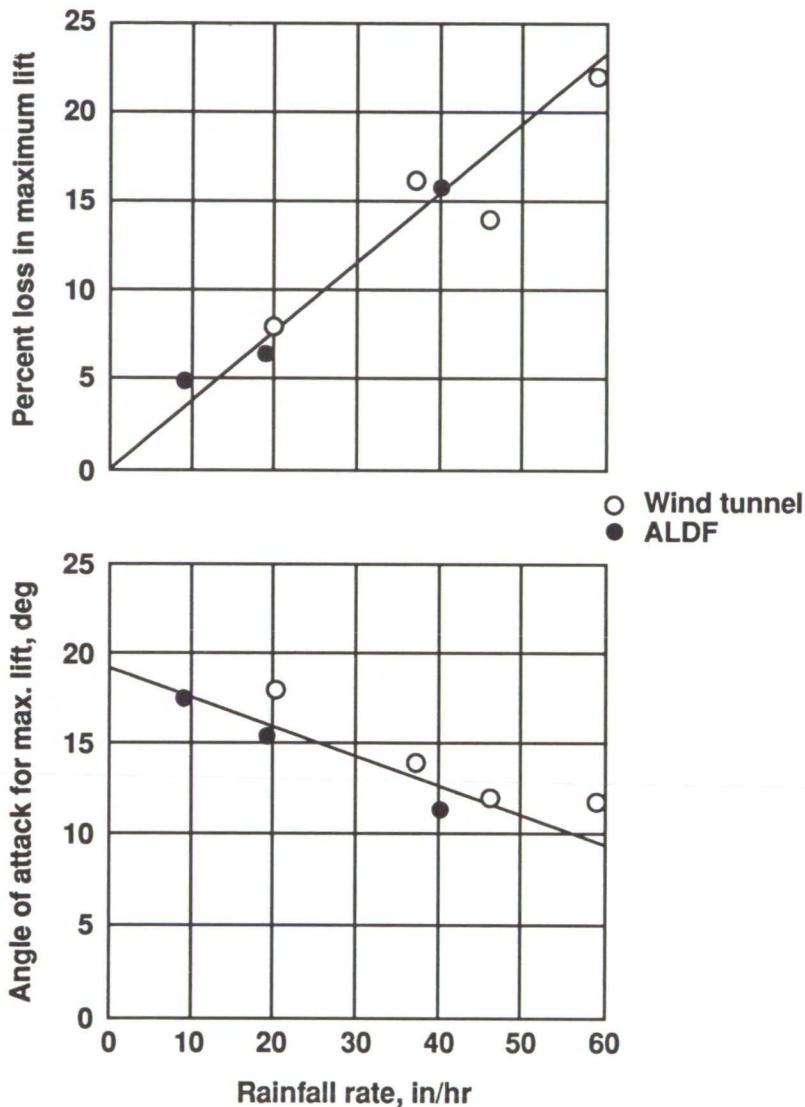
process to the rain scaling relationships involved. The ALDF test carriage was modified to transport a 10-ft chord NACA 64-210 wing section (which was representative of a commercial transport) along a 3000-ft track at full-scale airplane approach speeds. An overhead rain simulation system along a 500-ft section of the track test section produced rainfall rates of 9 in/hr, 19 in/hr, and 40 in/hr. The wing was tested with high-lift devices deployed to simulate landing conditions. Lift data were acquired, with and without the rain simulation system on, at a maximum speed of 160 knots and an angle-of-attack range from 7.5° to 19.5° for all three rainfall rates.

Preliminary large-scale test results indicate that the effect of rain on lift is significant for angles of attack near or at stall. The lift loss is a function of rainfall rate and angle of attack. The magnitude of the loss in maximum lift capability and the reduction in the stall angle of attack are a function of rainfall rate. A comparison between the wind-tunnel results, which were obtained on



Modified ALDF carriage exiting 19 in/hr rainfield.

L-90-14620



Effect of heavy rain on maximum lift capability and stall angle of attack.

a 2.5-ft chord NACA 64-210 airfoil, and the large-scale results shows a good correlation with respect to the behavior of the airfoil near or at stall. (Gaudy M. Bezos, 45083, and Bryan A. Campbell)
Aeronautics Directorate

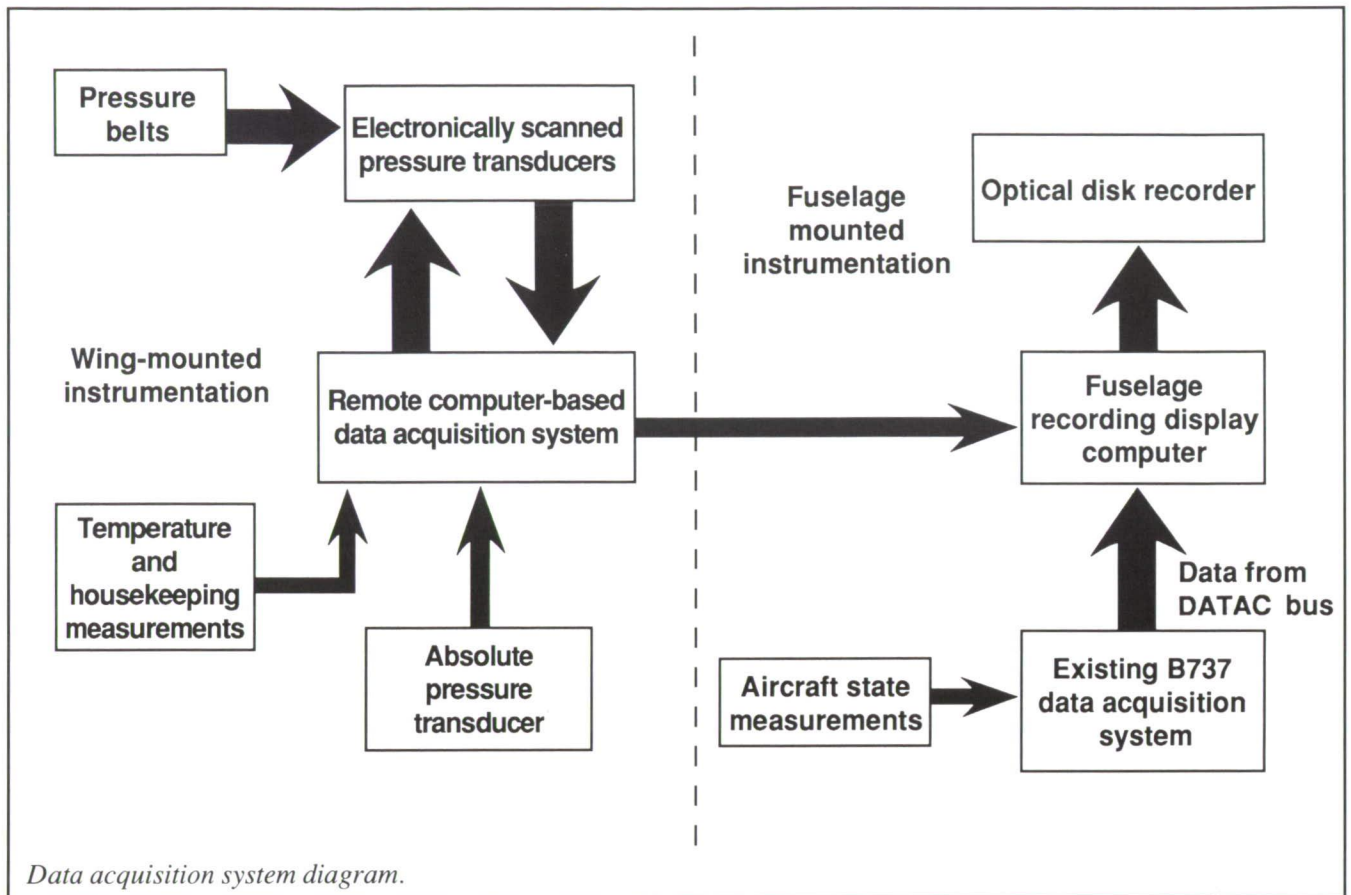
Intelligent, Compact, Modular Aircraft Data Acquisition System

Aircraft research flight projects are requiring intelligent, compact, modular data acquisition and recording systems. In many cases, the data must be acquired with sensors at remote measurement sites outside the fuselage and transferred to a recording station

within the fuselage. The data from multiple sensors must be consolidated and formatted into single data streams at the remote site to minimize the need to penetrate the pressure bulkhead with wires or to allow for wireless transmission. The recording station must provide high-rate and large-volume data storage in a small system, along with real-time computation and display to the experimenter.

A new data system comprised of a remote wing-mounted, single-board computer subsystem connected to a centrally located fuselage-mounted computer and optical disk recording system has been developed for use on the High Lift Flight Research Program as well as other future flight research aircraft. The new system, which was designed for quick installation, was successfully integrated and flown on the Advanced Transport Operating System (ATOPS) B737 aircraft to measure pressure profiles around the flap elements. Data from 160 pressure ports in six thin, multielement pressure belts were acquired from computer-driven, electronically scanned pressure multiplexers. The pressure data along with temperature and housekeeping data were digitized, formatted, and transferred by wire to the fuselage data system with a serial digital protocol. The remote system, which was mounted in the wing-flap-control housing canoe, can acquire and transfer data at rates up to 2 MB/sec.

The fuselage-mounted system used a flight-hardened 386 computer for merging the remote wing measurements with aircraft state measurements from the existing Boeing 737 data acquisition system DATAC bus, for recording data on the optical disk recorder, and for computing and displaying real-time experimental data in engineering units (EU). The optical disk flight recorder provided ample storage (600 MB per disk) and can



store data at rates up to 4 MB/sec. The computer-compatible optical disk recorder simplified the ground support equipment (GSE) required for post-flight data processing.

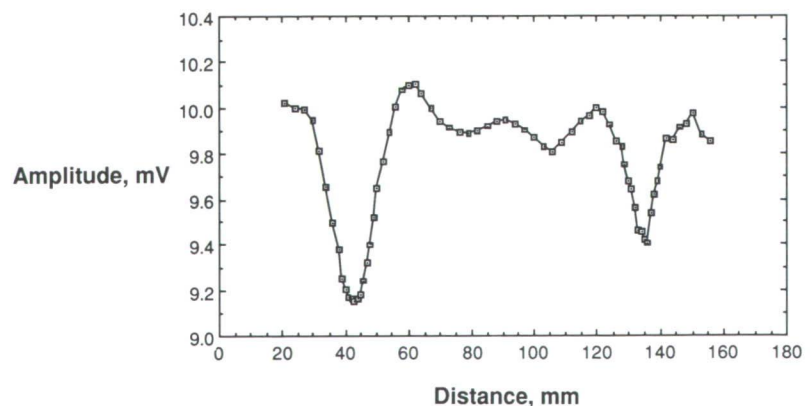
(Carroll Lytle, Dan Norfolk, and Keith Harris, 41675)
Electronics Directorate

Application of Acoustic Plate Waves to Structural Integrity Assessment

Acoustic plate waves are guided sound waves capable of propagating a relatively long distance in the plate configuration of materials. The magnitudes of particle displacements in the plate induced by these waves are

determined by the thickness, elastic properties, and boundary conditions of the plate as well as by the frequency of the imposed sound waves. A technique was developed to probe the optimum

out-of-plate displacement by locally changing the boundary condition of the plate and, in turn, locating the structural variations.



Two minima in amplitude at 43 mm and 137 mm which indicate occurrence of cracks with widths of 1.5 mm and 0.8 mm, respectively.

This technique was tested on an epoxy-bonded aluminum plate assembly. While the measurements were done on one surface of the first plate, the amplitude variations of the received plate waves revealed the locations of the disbands between the plates and the cracks that occurred in the second plate. With its relative high inspection rate, this technique has a potential application to large area, structural integrity nondestructive evaluation, such as that on an airframe surface.

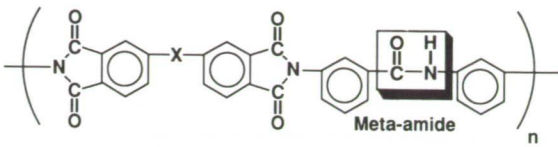
(Keun J. Sun, 44974)

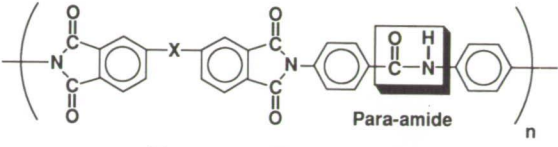
Electronics Directorate

Tough, High-Modulus, Semicrystalline Amide Polyimides

A series of novel polyimides were prepared from amide diamines. The structures, as shown in the figure, differ from other polyimides by the incorporation of a more flexible amide linkage. These polymers were characterized by a variety of methods, and the data were compared to state-of-the-art polyimides to evaluate the differences.

The amide polyimides exhibited high molecular weights and glass transition temperatures as high as 312°C. They were easily made into tough, flexible films that showed exceptional thermal stability and good resistance to organic solvents. Mechanical properties of the films, especially the para-amide-imides, were as good as or better than those of other state-of-the-art polyimides. The exceptionally high-modulus values of over 1×10^6 psi make these materials extremely attractive for composite applications. Films of the para-amide-imides were semicrystalline and also exhibited tough behavior during impact evaluation.

 Meta-amide					
X	η_{inh} , dL/g	T_g , °C	T_m , °C	Strength, ksi	Modulus, ksi
Nil	1.75	312	591	19.4	454
O	0.84	278	562	19.6	470
Carbonyl	0.96	287	525	17.2	556

 Para-amide					
X	η_{inh} , dL/g	T_g , °C	T_m , °C	Strength, ksi	Modulus, ksi
Nil	1.38	NO	625	29.4	1008
O	0.65	NO	600	20.1	760
Carbonyl	1.36	NO	580	25.5	1019

Amide polyimide film properties.

These amide polyimides would be useful as high-temperature films and coatings. The para-isomer polymers were determined to be semicrystalline, which resulted in improved thermal stability as well as enhanced solvent resistance. In addition, because of their excellent mechanical properties, these polymers exhibit strong potential as matrix resins in graphite-reinforced composite aerospace structures. (James F. Dezern, 44263, and Carol R. Gautreaux) Structures Directorate

Mechanics Models for Textile Preform Composites

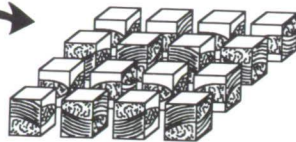
A prime inhibition to the wide-scale use of composite materials in aircraft is the cost of fabrication. Although the lay-up process has been automated, the cost of assembling a thick section with 0.005-in.-thick prepreg tape is restrictive. The use of composites reinforced

with textile fabric preforms offers an attractive materials alternative. Traditional textile operations have been modified to develop braided, woven, knit, and stitched graphite fiber preforms that, when impregnated with thermoset or thermoplastic resins, form net-shaped components.

The ability to manufacture these material forms has outpaced our ability to analyze them. Analytical models are needed to guide material development because the permutations of the preform manufacturing parameters lead to an infinite number of material forms. The objective of this work was to develop the analytical capability to predict the moduli, Poisson ratio, and coefficients of thermal expansion of textile-reinforced composite materials.

The analysis is based on a mechanical model that consists of a single rectangular unit cell that typically contains one repeating pattern of the fabric design. The unit cell is assumed to be divisible into smaller rectangular subcells in which the reinforced

Master subcell



Subcells – transformations of master subcell



Unit cell – assembly of subcells

Weave		E warp, ksi	G _{wf} , ksi	v _{wf}	α _w , in/in/°F
Plain	(Pred)	9.29	0.82	0.05	1.11
	(Exp)	9.13	--	0.10	--
5 Harness	(Pred)	9.62	0.84	0.05	1.11
	(Exp)	10.59	0.76	0.05	1.12

Prediction of woven fabric composite properties through subcell analysis.

Improved Damage Tolerance With Knitted/Stitched Composites

Composite materials researchers are currently striving to develop improved damage-tolerant materials at an affordable cost for primary aircraft structural applications. Textile-reinforced material forms, consolidated into composites via resin transfer molding (RTM), are candidate materials and processes to meet these goals. Two relatively new multi-axial warp knitting textile processes that produce carbon fabrics with (0°, 90°, 45°, -45°) fiber orientations have been developed by Hexcel Hi-Tech and Milliken. An experimental investigation was conducted to establish the performance of these fabric-reinforced composites when subjected to low-velocity impacts. Fabrics knitted with AS4 carbon fiber and knitted fabrics that were subsequently stitched together through-the-thickness with Kevlar 29 yarns were resin transfer molded with three different epoxy resins: Hercules 3501-6, British Petroleum E905L, and 3M PR500.

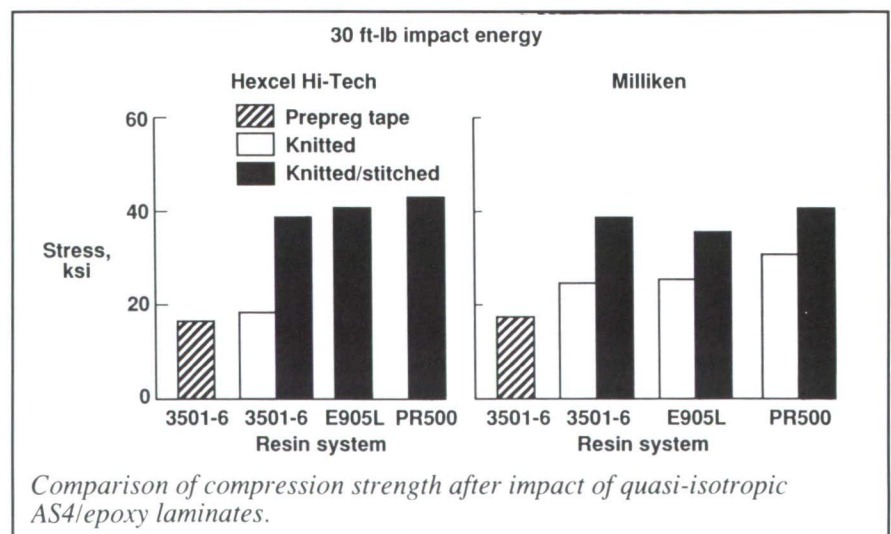
Test panels were impacted at an energy level of 30 ft-lb to simulate

geometries are easier to visualize, define, and analyze (see the figure). Finite-element computation schemes are applied to the subcells to define the unit cell performance.

A special-purpose computer program was written to perform the analysis just described because most general-purpose finite-element codes are awkward to use with the boundary conditions associated with moduli predictions. This method avoids some of the difficulties associated with matching finite-element node point locations and element boundaries to internal material boundaries. Partially reinforced elements are used, along with the general formula for their stiffness matrix. This formula partially accounts for material property variations within the element. A study was conducted to determine the sensitivity of the model to element size. General rules for sizing elements were developed for woven and braided textiles. The program was used to analyze a number of woven, braided, and knit textile preforms. A comparison of predicted and experimentally measured

properties of several types of two-dimensional woven textiles is given in the table in the figure.

(John E. Masters, 43460, and Ray L. Foye)
Structures Directorate

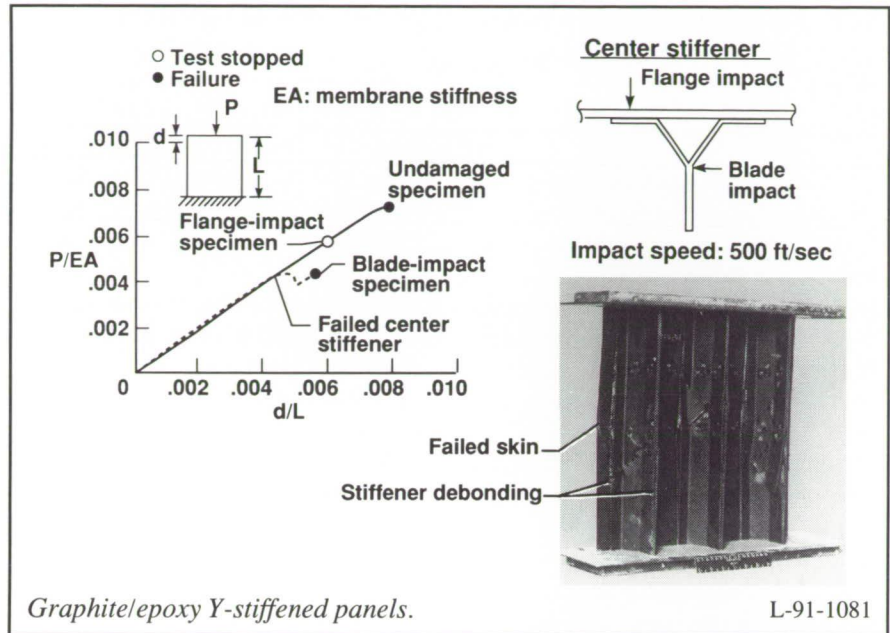


aircraft structural damage that could be induced by dropped tools or runway debris. The compression strength after impact (CAI) for 16-ply, 1/4-in.-thick (0° , 90° , 45° , -45°) quasi-isotropic laminates is shown in the figure. Test results for the knitted and knitted/stitched laminates are compared with state-of-the-art AS4/3501-6 prepreg tape laminates. Because of lack of material availability, the Hexcel Hi-Tech knitted fabric was evaluated only with the Hercules 3501-6 resin. The knitting process alone (i.e., without stitching) did not significantly increase the CAI strength for the Hexcel Hi-Tech fabric; however, a 75-percent increase in CAI strength was achieved with the PR500 Milliken laminates. The knitted/stitched composites, however, had CAI strengths that were up to 150 percent higher than the CAI strength of the laminated prepreg tape composites. These results substantiate the significant benefits achievable from stitching for damage tolerance enhancement. Continued development of knitting and stitching processes will result in materials with an optimum balance between in-plane and through-the-thickness properties.

(H. Benson Dexter, 43094)
Structures Directorate

Blade-Web Intersection Critical for Graphite/Epoxy Y-Stiffened Panels

The use of Y-stiffened composite structures is attractive because they are structurally efficient, highly tailorable, and potentially manufacturable with cost-effective material forms such as textiles. The objective of this study was to determine the response and failure characteristics of these advanced concept Y-stiffened composite structures.



Three-stringer panels, 20 in. long by 17.3 in. wide, were fabricated with IM7/8551-7 graphite/epoxy material. The panels were designed to be typical of upper skin cover panels for a high-aspect-ratio commercial transport wing. Undamaged and impact-damaged specimens were tested to failure under uniaxial compression. The damaged panel was impacted at both the flange-skin interface (flange impact) and at the web-blade interface (blade impact) with a 0.5-in.-diameter aluminum sphere as illustrated in the upper right corner of the figure. The sphere velocity at impact was approximately 550 ft/sec, which corresponds to an impact energy of approximately 27.5 ft-lb.

Normalized load-shortening results are shown on the left side of the figure. The undamaged specimen had a global axial strain d/L at failure of approximately 0.008 in/in. The damaged specimen with a flange impact only was loaded to a global axial strain of 0.006 in/in., and the test was stopped. This strain level represents the design ultimate strain for a heavily loaded

composite structure. Minimal damage growth was observed for this specimen, and it was subsequently unloaded and subjected to a blade impact. This multiple impact specimen was loaded until local failure of the center stiffener occurred at a global axial strain of 0.0045 in/in. The specimen loading redistributed to the outer stiffeners until specimen global failure occurred at an axial strain of 0.0057 in/in. Strain and deflection data indicate that blade rolling and web buckling initiated failure for the undamaged and damaged specimens. A failed specimen is shown in the lower right corner of the figure. The failure surface occurs in the test section of the specimen and is characterized by skin failure and stiffener debonding.

(P. D. Sydow, 43180, and M. J. Stuart)
Structures Directorate

Curved Beams Made From Long Discontinuous Fiber (LDF) Material

From a structural efficiency viewpoint (weight savings), the potential for fibrous composite materials in aircraft structures has been known for decades. Two deterrents to the use of these materials have been the lack of knowledge to predict their behavior and the cost of manufacturing complex structural elements. The objective of this University of Delaware work is to develop a constitutive relationship and analytical models to predict the behavior of long discontinuous fiber (LDF) composite structures and to investigate methods to fabricate LDF curved beams.

A finite-element analysis was conducted to develop models of the fabrication process and a constitutive relationship for LDF composite materials. An elasticity solution was developed to predict the struc-

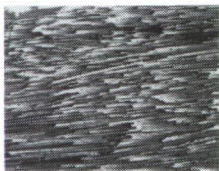
tural response of LDF composite curved beams. A sheet-forming procedure was used to fabricate LDF composite curved beams. The LDF composite material form typically has 2-in.-long graphite fibers and a thermoplastic resin matrix. These discontinuous fibers can slide relative to one another during the forming process of composite structures, enabling the forming of complex shapes with potentially improved structural performance by eliminating the current practice of prepreg cutting and piecing for curved components (which often causes local stress concentrations or stiffness discontinuities). Variation of material properties in the radial and tangential directions is predicted. A fluid flow analysis of the fabrication process indicates that resin viscosities differ dramatically in different directions and that fiber orientation is highly collimated in both the unformed and formed parts. A 200x magnification of a region of a formed sheet of LDF material is shown in the upper part of the figure to illustrate the orientation of the fibers within the matrix. The resulting fiber orientation indicated that 95 percent of the fibers were within ± 5 percent of 0° . Prototype curved beam parts have been successfully formed using metal molds and a sheet-forming process. A photograph of a curved C-channel frame section constructed from LDF material is shown in the lower part of the figure.

The LDF material form will enable structurally efficient cost-effective curved composite frames to be fabricated for transport aircraft fuselages. A comparison of experimental and analytical results for structural response is projected to show behavioral predictability. (Dawn C. Jegley, 43185, and Michael H. Santare) Structures Directorate

Design-Build-Team Approach Provides Benefits in Composite Fuselage Structural Design

The Advanced Composites Technology Program is developing an integrated technology data base to facilitate the introduction of composites into the fuselage structure of future commercial aircraft. Design-Build-Teams (DBT) at Boeing Commercial Airplanes are optimizing concurrent engineering principles to understand the trade-offs between cost and weight for the replacement of current aluminum structure with large composite equivalent structure. Boeing has divided the fuselage barrel into panel elements for crown (top), window belt (side), and keel (bottom) locations. The figure shows the DBT results for optimization of the crown panel for the fuselage section just aft of the wing and forward of the rear pressure bulkhead for a wide-body transport. The figure shows the ratio of cost (ordinate) and weight (abscissa) for a composite crown panel to its metallic equivalent for a 1995 wide-body transport. As the DBT considered a variety of issues and criteria, the final crown design was locally optimized to have an 18-percent cost savings and a 45-percent weight savings relative to the 1995 benchmark.

Following global evaluation, the tension damage tolerance criteria for failsafe conditions were modified to account for larger notches and severed frames. The original design (see point 1 on the figure) had a negative margin of safety for failsafe requirements, and the skin gauge was increased to achieve sufficient damage tolerance (point 2); this increased both cost and weight. Mechanical tests revealed that tow-placed laminates have improved tensile fracture characteristics compared to tape laminates, and they provide improved tension damage

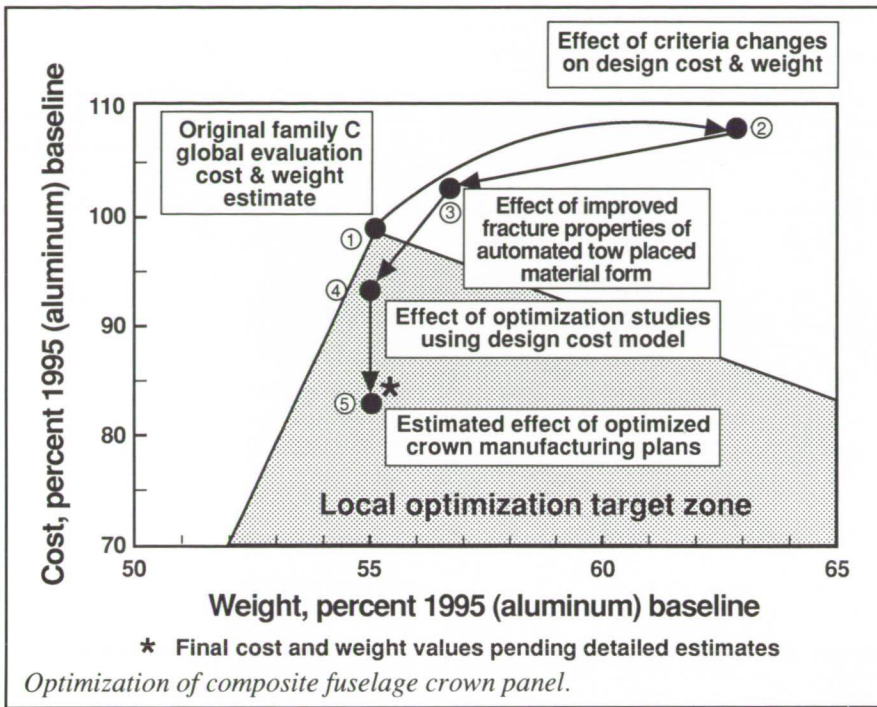


Cross section magnified 200 x



Finished curved beam

Long discontinuous fiber material and curved beam. L-90-15492

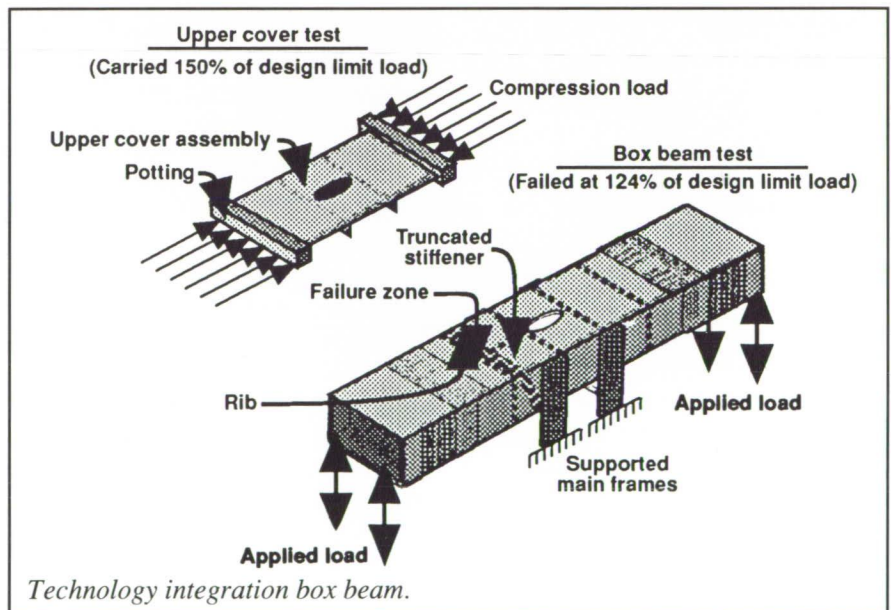


integrated technology data base to support the introduction of composites into the primary structure of future aircraft. Design and manufacturing integration studies are in progress at Lockheed Aeronautical Systems Company to simultaneously advance the material and fabrication technologies necessary to build low-cost, lightweight composite wing structures. The center wing box beam of the C-130 aircraft has been selected as the baseline to represent a typical piece of heavily loaded wing structure. Analyses and tests are used to substantiate the strength of the structure.

The figure in the upper left shows a separate upper cover assembly that was fabricated and tested prior to building the complete box beam. The cover specimen was successfully tested to ultimate load in compression. Subse-

tolerance that allows reduction in cost and weight (point 3). A prototype software design tool being developed to relate manufacturing cost to design parameters including stringer spacing, material costs, and number of skin plies was used to locally optimize panel design stiffener spacing and achieve further reductions in cost and weight (point 4). The final local optimization task included results of fabrication trials to further attack cost centers and optimize manufacturing methods. Reducing the number of tools for stringer and frame fabrication, increasing tow band width to obtain lower towpreg material cost, and using soft tooling concepts to minimize labor costs for panel bagging reduced the cost to point 5.

(John G. Davis, Jr., 42936, and W. T. Freeman)
Structures Directorate



Influence of Load and Component Interaction on Technology Integration Box Beam Test

The Advanced Composites Technology Program is developing an

sequently, the upper cover assembly was subjected to impact damage in two critical areas near the elliptical access hole. The damaged upper cover assembly also survived loading in compression to ultimate load. Fabrication of the box beam was then carried out, and tests were conducted to

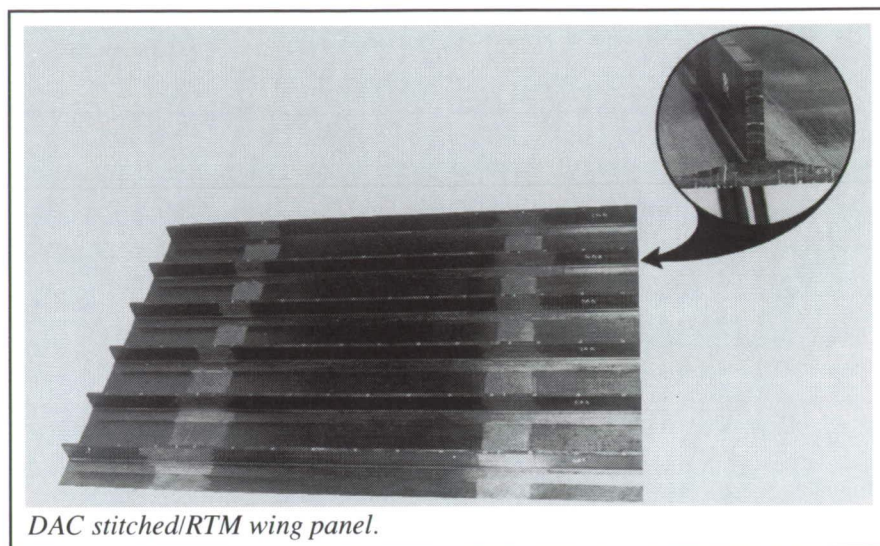
simulate wing loading. During testing (upbending and torsion to ultimate), failure occurred across the right side of the upper cover at 124 percent of the design limit load (83 percent of ultimate), causing catastrophic damage to the wing box. Because the cover panel alone survived ultimate load, component and load interaction played a significant role in causing a compression failure adjacent to a transverse rib on the upper skin near the end of a truncated hat stiffener (dashed lines in the figure).

Design and manufacturing integration is providing an understanding of load and component interaction for composite structures. This type of information will lead to the capability of designing cost-effective composite structures that offer improved performance over aluminum structure.

(John G. Davis, Jr., 42936, and Randall C. Davis)
Structures Directorate

Global Stitching Paves Way for Low-Cost Composite Wing Structure

Composite materials fabricated of graphite filaments embedded in an epoxy resin matrix and laminated into structural forms are attractive candidates for subsonic commercial transport aircraft structures. Major benefits of such structures are weight savings because of high strength/stiffness-to-weight properties, enhanced corrosion resistance, and improved fatigue life compared to conventional metallic structures. The Advanced Composites Technology (ACT) Program is developing technology to support introduction of composites into the primary structure of future U.S. transports. Studies at Douglas Aircraft



Company sponsored by ACT are developing composite wing structure for cost-effective manufacture.

A common mode of failure in composite structures is delamination. Methods were studied to supply through-the-thickness strength to composite panels typical of wing structure. Through-the-thickness stitching using graphite filaments was found to be an effective way to prevent delamination.

Recently, selections have been made for wing structural concepts and manufacturing methods that capitalize on the stitching method. Wing covers are dry preforms globally stitched throughout the planform area and which have stiffeners attached with stitching. The preforms are subsequently compacted, formed, and cured by resin transfer molding (RTM). RTM is a process by which a resin is infiltrated by either pressure or vacuum and then subjected to heat and pressure to form a precise, mold-line-contoured structural component. A wing cover panel that is 4 ft wide by 6 ft long has been fabricated by this process. A photograph of this panel is shown in the figure. The inset shows a close-up view of the end of one of six blade

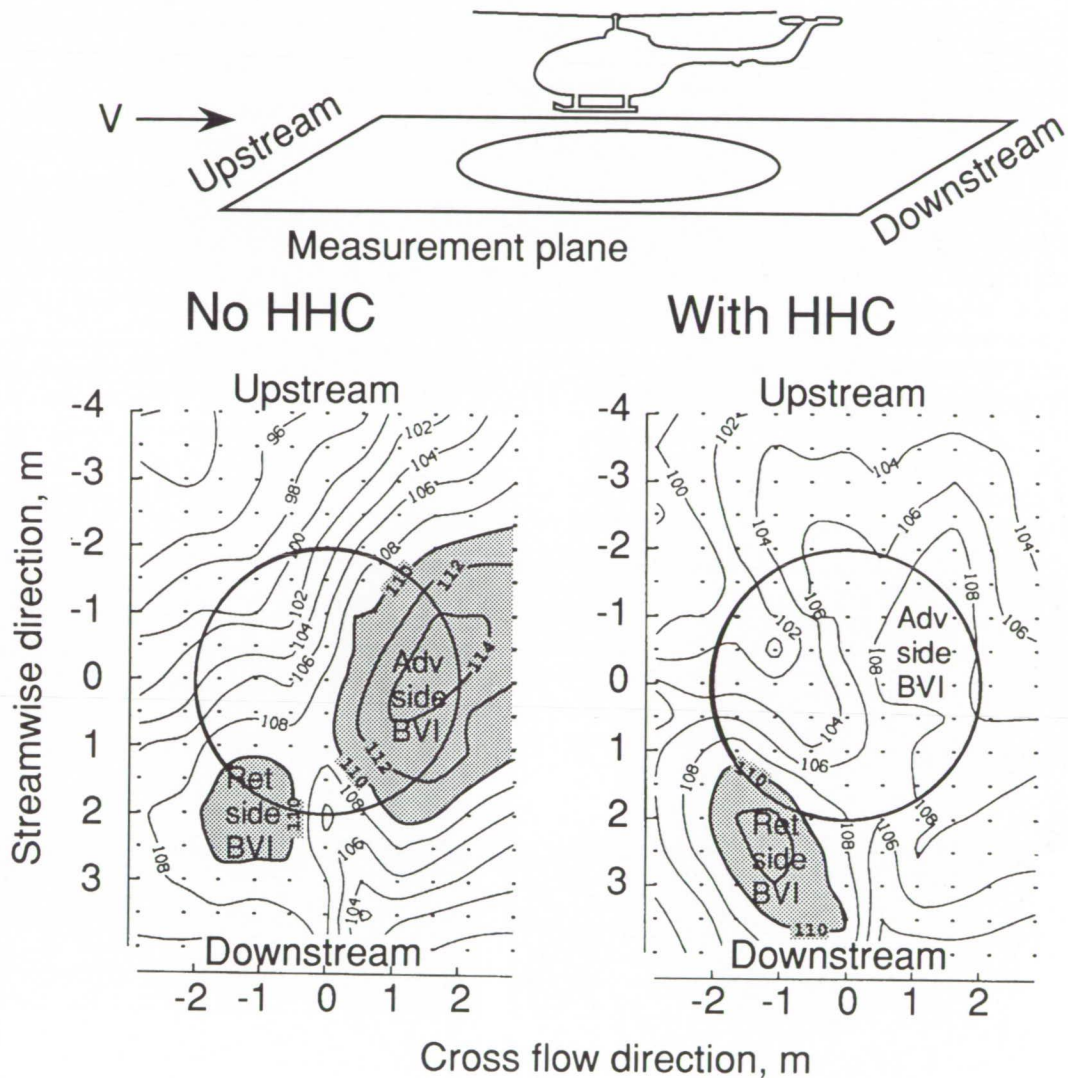
stiffeners stitched to the wing skin. Wing covers would probably be mechanically attached to ribs and spars to form a complete wing structure.

The stitching method gives through-the-thickness strength to laminates composed of relatively low-cost composite materials. The number of mechanical fasteners used in the assembly process is drastically reduced compared with conventional aluminum construction, and this fact leads potentially to substantial reductions in assembly cost relative to metal construction.

(John G. Davis, Jr., 42936)
Structures Directorate

Directivity of Rotor Impulsive Noise Reduction Using Higher Harmonic Control

Impulsive blade-vortex interaction (BVI) noise is caused by aerodynamic interaction of the rotor blades with previously shed blade-tip vortices. A previous rotor noise study performed at Langley Research Center proved that higher harmonic control (HHC) of



BVI noise directivity with use of HHC.

blade pitch could be used to reduce this noise. Conceptually the noise is reduced because of increases in blade-vortex miss distances and decreases in vortex strengths and mean lift at BVI locations.

The present study was undertaken to obtain, for the first time, a detailed noise directivity of BVI noise, while employing HHC on a 40-percent aeroelastically scaled BO-105 rotor. The test, conducted in the anechoic German/Dutch Wind Tunnel (DNW, Duits-Nederlandse Windtunnel/

Deutsch Niederlandischer Windkanal), was a cooperative effort among Langley, the German Aerospace Establishment Deutsche Forschungsanstalt für Luft- und Raumfahrt (DLR), and the European helicopter companies MMB and Aérospatiale. The noise was determined

over a large measurement plane underneath the rotor by the use of a traversing inflow microphone array. Noise and vibration measurements were made for a range of matched rotor operating conditions in which prescribed higher harmonic pitch was superimposed on normal (baseline) collective and cyclic trim pitch.

Presented in the figure are mid-frequency noise contour plots over the measurement plane for a particular flight descent condition that is considered rather typical for full-scale helicopters. On the left, a baseline case is shown in which no HHC is used. Indicated on the plot are the locations of the advancing side BVI directivity lobe and the retreating side BVI lobe. The plot to the right is the noise contour for an HHC pitch schedule (4 per rev at an amplitude of 1.2° and control phase of 32°), which causes a significant 6-dB reduction in the advancing side lobe levels, although the retreating side increases somewhat.

The relative levels and directivity can be modified by changing the control phase.

An interesting feature of the present data is the apparent strong role that rotor aeroelasticity plays in the BVI noise results. Earlier Langley tests with relatively rigid blades found similar noise reductions but with different HHC amplitudes and phases. (Thomas F. Brooks, 43634, and Earl R. Booth, Jr.)
Structures Directorate

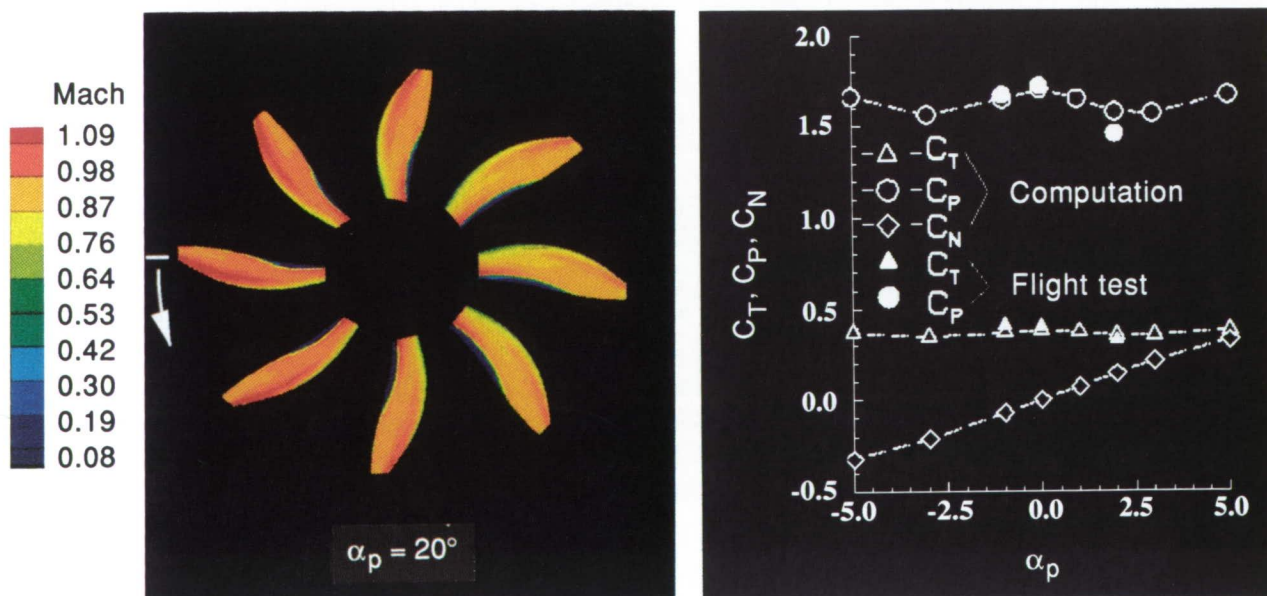
Periodic Blade Loads and Performance of Inclined High-Speed Propeller

The flow field around an inclined high-speed propeller is asymmetric and viscous. The locations of shocks and separation lines vary periodically as

the blades azimuthally experience different angles of attack and Mach numbers. These periodic blade loads can alter the blade aeroelastic behavior and the radiated noise.

A propeller analysis code has been developed based on strip theory and a relaxation method to efficiently compute periodic propeller loads and performance. This code, Unsteady Propeller Analysis (UPA), analytically represents the above azimuthal variations in terms of the angles of attack and flow Mach numbers of the sections. The code can utilize linear or nonlinear and viscous or inviscid solution modules at each blade section depending on the operating requirements.

The computational results, which were obtained for an eight-bladed Hamilton Standard SR-7L propeller at cruise operating conditions, are compared with flight test data obtained during the NASA Propfan Test Assessment Program. For the above



Periodic blade loads and performance of inclined SR-7L propeller. Operating conditions are $M_{cruise} = 0.813$, J_p (propeller advance ratio) = 3.14, $B_{75\%}$ (nominal blade angle at 0.75 R) = 58.1° , R is propeller radius, and H (altitude) = 35 000 ft.

ORIGINAL PAGE
BLACK AND WHITE PHOTOGRAPH

cruise operating conditions, the solution module implemented was based on the Reynolds averaged thin-layer Navier-Stokes equations. This module is a two-dimensional version of the CFL3D code. Computational results of time-averaged propeller thrust C_T , power C_P , and normal force C_N coefficients for small inclinations α_p are in excellent agreement with the flight test data. The results shown indicate the importance of inclusion of both periodicity and viscosity for proper simulation of a nonsymmetric propeller flow field.

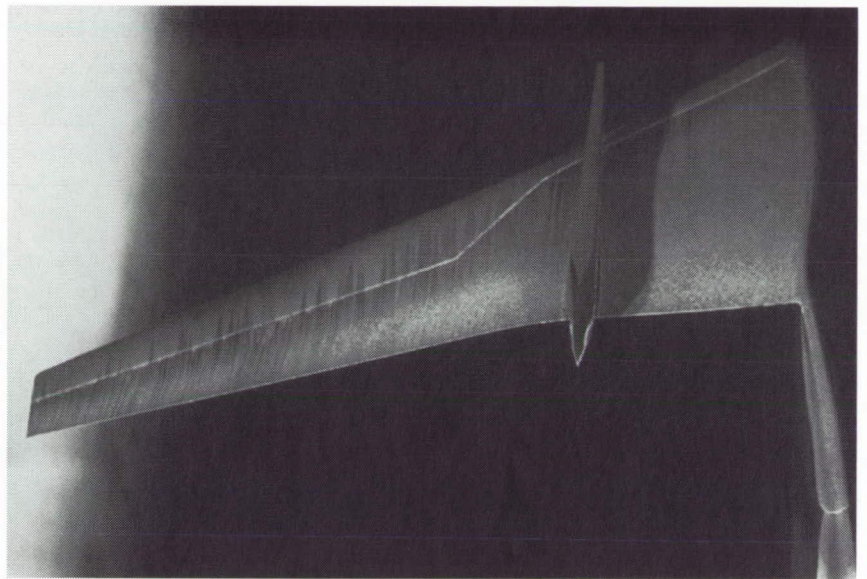
(M. A. Takallu, 47671, and
V. R. Lessard)

Aeronautics Directorate

Transport Pylon Geometries for Reducing Nacelle Installation Drag

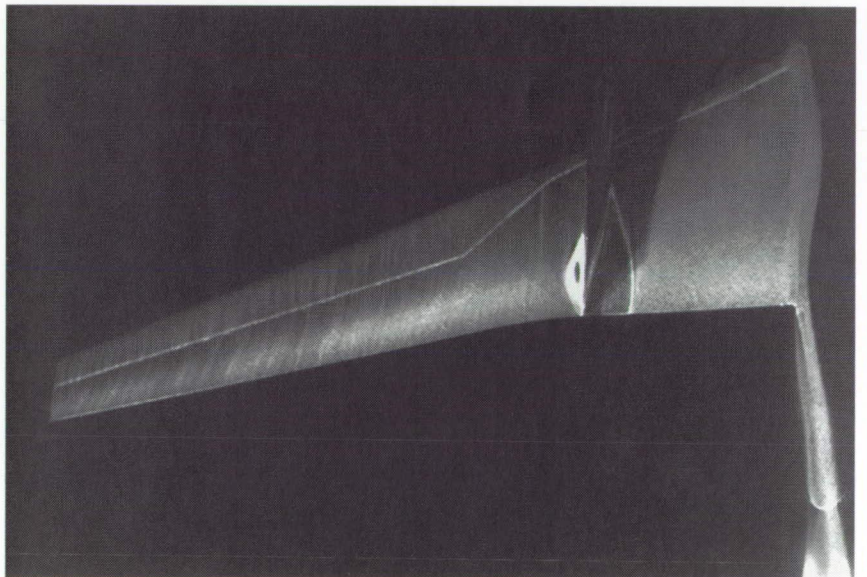
For transport aircraft, the wing-mounted engines are typically hung from pylons. Generally the pylon introduces friction drag and induced interference drag. Two primary sources of induced interference drag exist. First, the flow accelerating around the thickest portion of the pylon could give rise to a low-pressure region acting on the wing lower surface, thus resulting in lift loss and possibly wave drag from regions of supersonic flow. Second, the adverse pressure gradient arising from the pylon trailing-edge closure could encourage flow separation at the pylon-wing junction, thus resulting in form drag. Precisely ascertaining the individual contributions of these drag components is difficult. However, general inferences regarding pylon installation effects can be made from experimental force and pressure data.

Flow acceleration could be alleviated without introducing severe adverse pressure gradients with a



Compression pylon

L-91-7041



Full-chord pylon

Comparison of pylon-wing junction separated flow regions for compression versus full-chord pylons. Airplane at cruise conditions.

gradually diverging flat-sided pylon whose closure is moved aft of the wing trailing edge. In order to achieve maximum effect, this compression pylon would be widest at the wing trailing edge. This pylon concept would be expected to have higher skin

friction drag (because of larger wetted area) but much lower induced interference drag than conventional pylon designs. A computer code for the analysis of inviscid, compressible, three-dimensional flow was used to analyze the pressure peaks and

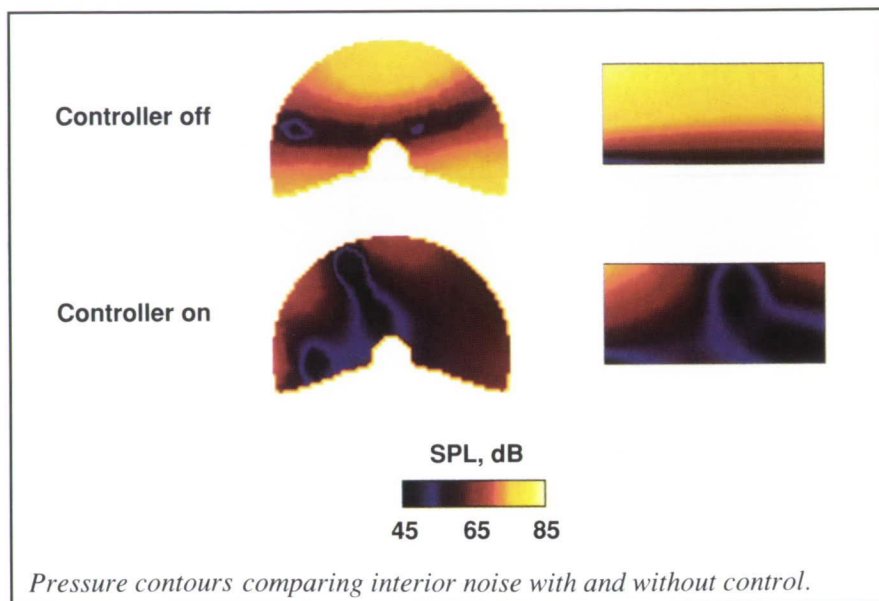
pressure gradients for various pylon cross-sectional shapes. Promising geometries were then investigated on a generic low-wing transport model in the Langley 16-Foot Transonic Tunnel.

The force, surface pressure, and surface flow visualization data obtained seem to substantiate the design philosophy. The compression pylon results in lower total airplane drag, over the entire lift range, than the full-chord pylons; at minimum lift, the drag coefficient is approximately 0.005 lower, and at cruise conditions (lift coefficient of 0.55 and Mach number of 0.77), the drag is 0.001 lower. The figure shows the significantly smaller separated flow region at the pylon-wing junction, thus resulting from the compression pylon concept.

(A. M. Ingraldi, 43039, D. A. Naik, and O. C. Pendergraft, Jr.)
Aeronautics Directorate

Interior Noise Control Using Piezoceramic Actuators

Recent work in interior noise control has demonstrated the potential of active techniques for low-frequency noise and vibration control in aerospace vehicles. Past work has centered on the use of acoustic sources for interior noise control. However, recent work at Langley Research Center has highlighted the potential for global noise reductions for the interior cabin with a limited number of piezoceramic actuators bonded directly to the cabin shell or frames. This approach generally requires significantly fewer actuators when compared to acoustic sources. Compared to conventional shakers used as force inputs, the piezoceramic actuators exhibit less extraneous excitation of the structure and require no inertial mass or auxiliary structural elements.



Pressure contours comparing interior noise with and without control.

This concept was evaluated on a large-scale composite fuselage model in the Acoustics Research Laboratory. This is a geometric model of a Fairchild Metro aircraft section 12 ft in length and 5.5 ft in diameter. The composite cylinder was comprised of nine layers of carbon fibers embedded in an epoxy resin with an overall thickness of 0.067 in. This shell was riveted and bonded to a framework of 12 ring frames and 22 stringers, and a floor was installed. The ends are sealed with 3.75-in.-thick wooden bulkheads. The model is excited by an external loudspeaker representing a propeller noise source.

Control actuators consisting of pairs of piezoceramic patches, 1.5 in. by 2.5 in. and 0.007 in. thick, were bonded on directly opposite surfaces of the inner and outer walls. This configuration allowed the structure to be driven either in-plane or in bending, and it confirmed predictions that a dominant in-plane force was advantageous for exciting the required low-order structural modes. The actuator excitation was optimized with a time domain least-mean-squares algorithm, such that the sum of the squared pressure

sensed at up to six interior microphones was minimized. The left plots of the figure illustrate the pressure field amplitude at the source cross section. In the right plots, the pressure for a vertical section from the centerline to the wall shows the variation for the same two contour conditions at 172 Hz. Noise reductions in each cross section averaged 12 dB to 14 dB with only two actuator pairs.

This experiment demonstrated the potential of piezoceramic transducers as actuators for the control of aircraft interior noise. They are significantly lighter in weight, require no special mounting, and may be integrated directly with the structure. Current analytical efforts suggest that they may be configured in their size and distribution to couple only into those structural modes contributing most significantly to the interior acoustic response. This versatility may be useful in minimizing structural response or local stress concentrations that could increase vibroacoustic fatigue life.

(Richard J. Silcox, 43590)
Structures Directorate

Active Adaptive Control of Axial Flow Turbofan Engine Noise

Propulsion systems for future subsonic aircraft are expected to incorporate ultra-high-bypass-ratio-ducted fan engines. The dominant noise source from these engines is expected to be the fan with a blade passage frequency less than 1000 Hz. This lower frequency, combined with the requirement of a short, thin nacelle, diminishes the effectiveness of conventional duct noise absorbing liners. The purpose of the present research is to evaluate active noise control as a viable fan-noise-reduction technique to supplement noise absorbers. Active noise control introduces sound to the noise field that is equal in intensity but opposite in phase to the primary sound, thereby producing a null of the sound intensity. The system is adaptive because the control sound

varies with changes in the character of the primary sound. Active noise control is most efficient at relatively low frequencies.

A small turbofan engine is the test-bed for development of an active adaptive noise control system. Noise drivers are distributed around the inlet duct and serve as control sound sources. A far-field microphone provides the error signal. A blade-passage sensor generates the reference signal to the controller. The control algorithm is a filtered-X adaptive least-mean-squares routine operating in the time domain.

Preliminary results demonstrate that the control system converges and is stable. Reduction of the blade passage frequency tone by an average of 7 dB is measured as shown in the figure. The scatter in the sound is primarily because of nonuniform inflow to the fan, which is a problem typically encountered in static engine

testing. Work is under way to improve the inflow to simulate flight inflow conditions more accurately, which is expected to improve the controller operation. This research was done by Virginia Polytechnic Institute and State University and was jointly funded by the Structures and Aeronautics Directorates.

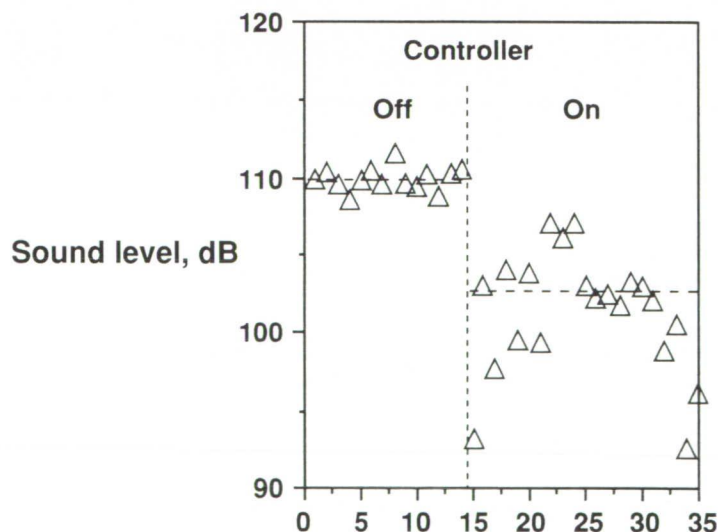
**(Carl H. Gerhold, 45279, and Shelby J. Morris)
Structures and Aeronautics Directorates**

Effect of Nonaxial Inflow on Propeller Noise

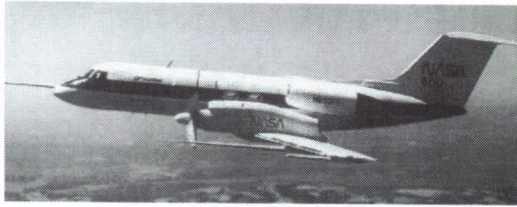
Propeller-driven aircraft take off at an angle such that the flow into the propeller disk is nonaxial. Tests in wind tunnels have shown that nonaxial inflow can influence the noise level of the propeller at some microphone positions. Concerns about community impact and meeting aircraft noise standards prompted the effort to predict the effect of nonaxial flow on the noise of propellers. Langley Research Center had developed an advanced propeller noise prediction code in the time domain. This code was originally written for axial flow into the propeller disk.

To incorporate nonaxial flow, new retarded time equations for the two acoustic formulations had to be derived and solved, which were more complex than the axial flow case. Because of the transcendental nature of these equations, a numerical approach was used for solution. The new advanced propeller noise prediction code is now called ASSPIN (advanced subsonic and supersonic propeller induced noise).

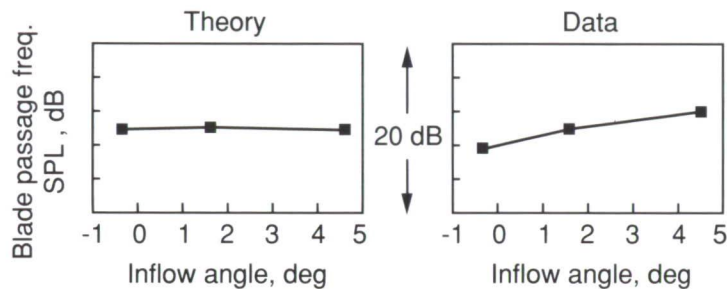
This research showed that while the noise below the aircraft increased, the noise above the aircraft decreased.



Blade passage frequency sound level in far field.



Flight Mach 0.8
boom mic in rotor plane



Measured and predicted effect of inflow angle for microphone in rotor plane.

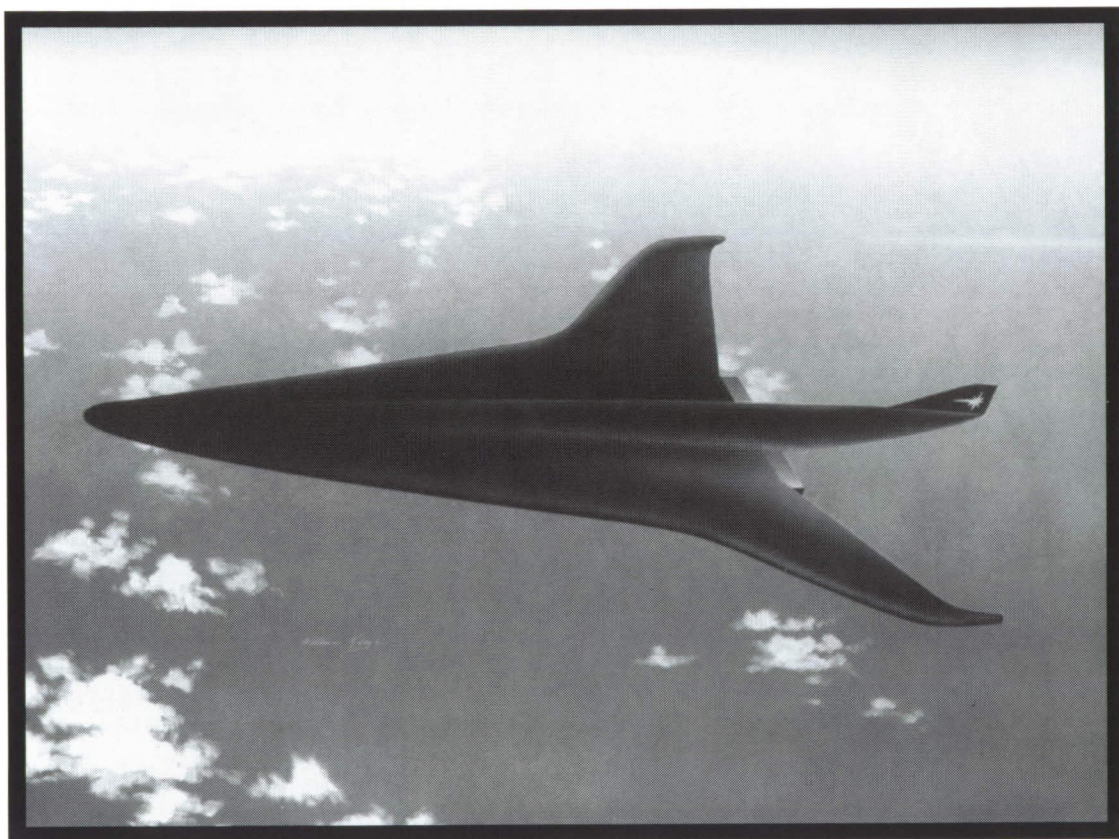
Thus, the noise footprint used for noise certification is adversely affected by nonaxial inflow into the propeller. This occurrence can be explained by noting that the acoustic field of the propeller is tilted up by an angle equal to the flight path angle. The ground surface thus intersects this field at a different section than for a horizontal flight path. However, the peak noise levels on the aircraft fuselage are largely unaffected by the nonaxial inflow. The figure shows the measured and predicted effect of inflow angle for a microphone in the rotor plane and on a boom at the wing tip. This microphone is at the same radial distance from the propeller axis as the nearest point on the fuselage in the rotor plane, corresponding to peak noise level on the fuselage. The propeller is a 9-ft-diameter propfan with SR-7L blades at flight Mach number of 0.8. The figure shows that the effect of inflow angle is small at this microphone position.

**(F. Farassat, Mark H. Dunn,
and Peter L. Spence, 43626)
Structures Directorate**



SUBSONIC AIRCRAFT

■ HIGH-SPEED CIVIL TRANSPORT



ORIGINAL PAGE
BLACK AND WHITE PHOTOGRAPH

*Resolve the critical
environmental issues and
provide the technology
base for future high-speed
air transportation*

RT

PRECEDING PAGE BLANK NOT FILMED

HSCT Navier-Stokes Computations

Considerable interest exists at present to design an economically feasible civil transport that can cruise at supersonic speeds in order to reduce the travel time over the Pacific routes. To expedite the development of such a complex vehicle, various conceptual designs must be analyzed in a timely manner. Thus, computational fluid dynamics (CFD) methods must be used to supplement and minimize wind-tunnel testing whenever possible. Of course, the CFD method selected for such a task has to be efficient, accurate, and reliable over the range of test conditions of interest. Recently, a very efficient numerical scheme that was originally developed for transonic flows over aircraft configurations (TLNS3D) has been extended to supersonic flows. The basic numerical scheme is a finite-volume central

differencing scheme, and it achieves its efficiency mainly through the use of a multigrid acceleration technique.

The computations for flow over a generic high-speed civil transport (HSCT) model (NASA TM-4058) have been performed at the design cruise Mach number ($M = 3$) using the Navier-Stokes code known as TLNS3D for the nacelles-off configuration. The angle of attack was varied from 0° to 8° in these computations to correspond to an in-house experimental investigation, and each test condition required approximately 2.5 hr of central processing unit time on a CRAY-2 computer. The computed lift and drag coefficients are compared with the experimental data in the figure. Obtaining such a good correlation with the data over the entire angle-of-attack range is encouraging, especially for the drag coefficient, which is dominated by the viscous component at lower values of lift.

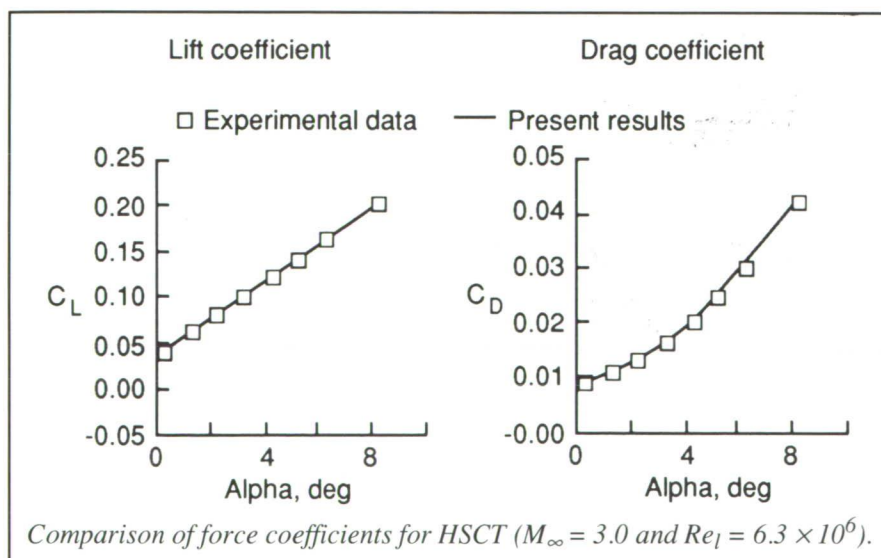
Future work will concentrate on simulating the effects of nacelles on the flow field and force coefficients for the HSCT configuration.

(Veer N. Vatsa, 42236)
Aeronautics Directorate

Multielement, Thin-Film Heat-Transfer Array Fabrication

Multielement, thin-film heat-transfer arrays are a powerful, nonintrusive flow diagnostic device that provides a simultaneous global method for studying complex steady- and unsteady-flow structures over aerodynamic surfaces in flight and in wind tunnels. The arrays have been used to measure a variety of boundary-layer phenomena including transition, separation, shock-boundary type interaction, crossflow, and Tollmien-Schlichting instabilities leading to transition.

Model size, test conditions, and the nature of the model surface curvature are considered when selecting which of two available fabrication techniques is to be used. In the first technique, which is suitable for 2-D surfaces, the sensors are fabricated on a thin, flexible dielectric substrate that is bonded to the model surface. In the second technique, which is suitable for 2-D or 3-D surfaces, a thin dielectric layer is either vacuum deposited or sprayed on the surface to electrically insulate the sensors from the model. The sensors are then vacuum deposited on the dielectric layer.



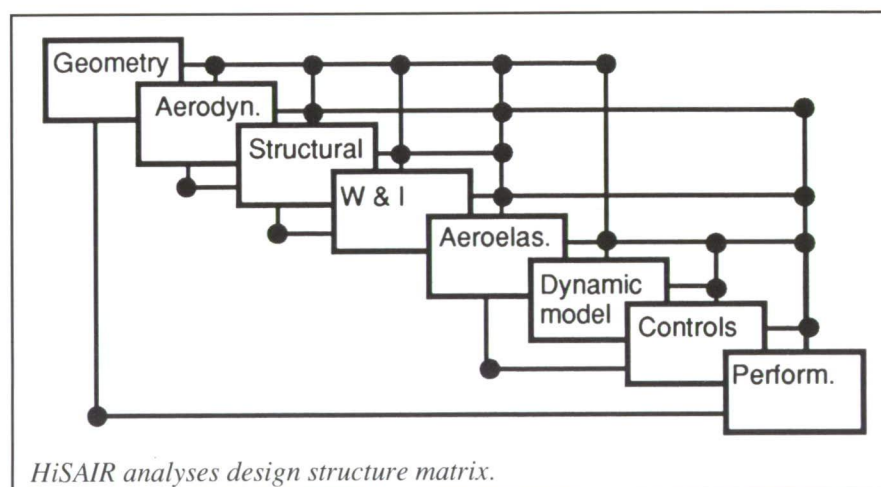
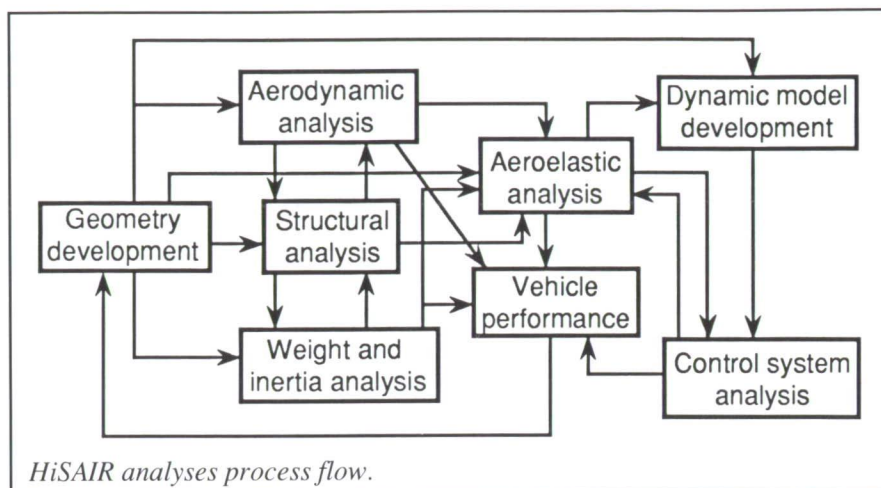
Recent improvements in fabrication processes and materials selection have significantly enlarged the test condition window of applicability. Sensors have been successfully tested at temperatures from -300°F to 400°F, pressures from 0.1 psi to 96 psi, and speeds up to Mach 15. Most recently, hypersonic transition has been detected as well as the interaction of elements in a multi-element wing. Two-dimensional arrays up to 80 in. long have been produced and larger sizes are practical.

An effort is under way to improve the fabrication processes and materials selection to increase the operating temperature to 2000°F. The increased operating temperature capability would enhance the usefulness of hot-film sensors for hypersonic applications as well as engine exhaust nozzle flow diagnostics.

(J. Bartlett, 45472)
Systems Engineering and
Operations Directorate

Application of Knowledge-Based Tool To Understand HiSAIR Data Flow

The HiSAIR design project requires data from numerous disciplines, and each discipline applies one or more computer programs to generate these design data. The responsible engineer for each discipline knows what data are used and generated by that discipline, but he or she does not necessarily know which other disciplines supply or use these data. DeMAID (Design Manager's Aide for Intelligent Decomposition) is a knowledge-based tool that was recently developed to aid a design manager in the design of a new concept such as the HiSAIR aircraft. DeMAID orders the data flow to minimize feedback. In addition, modules forming an iterative process

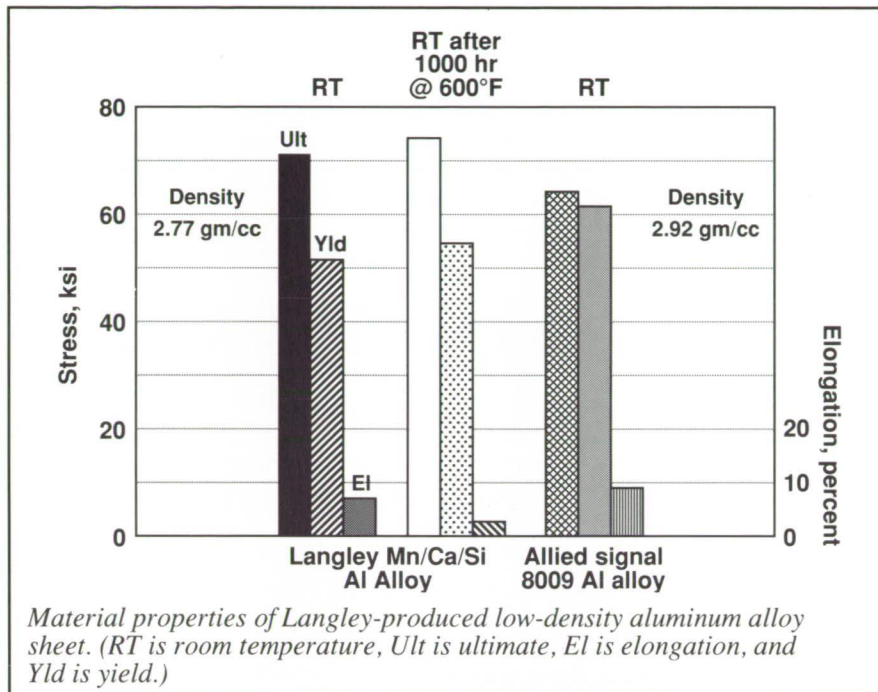


are grouped together. The result is an informative display of the modules in a design structure ($N \times N$ format) matrix, which indicates the order in which the modules should be processed and the major interfaces among the modules.

The HiSAIR design project needed a tool that would aid the design team in understanding all processes required to complete the design and the data flow among these processes. DeMAID allows the design manager to examine any level of detail. For simplicity, the first figure depicts the data flow among the eight major disciplines. No order exists to this flow, nor is there any indication as to which modules, if any, form an iterative process. The second figure depicts the design structure

matrix for these disciplines after DeMAID was executed. In this figure, discipline boxes are placed along the diagonal of the matrix. A vertical line entering a box indicates an input to that process, while a horizontal line exiting from a box indicates an output from that process. Lines below the diagonal indicate a feedback that means an iterative process exists. For example, in this figure, aeroelastic analysis, dynamic model development, and control system analysis form an iterative process. The design manager can now use this information to organize and optimize the design process for the HiSAIR aircraft.

(James L. Rogers, 42810)
Structures Directorate



Langley-Fabricated Powder-Metallurgy, Aluminum-Alloy Sheet Demonstrates Useful Stability at 600°F

Conventional precipitation-hardened aluminum alloys have only selected and limited usefulness over long times at temperatures above approximately 300°F (150°C). Hence, materials such as titanium alloys, which are more expensive and more difficult to fabricate than aluminum, are used to meet aerospace requirements at temperatures above that which aluminum alloys are stable. Aerospace needs for aluminum alloys useful at elevated temperatures are both current and growing.

Considerable research has existed over the last decade toward the development of dispersion-hardened aluminum alloys for elevated temperature use. The best emerging high-temperature commercial aluminum alloy is the 8009 alloy produced by

Allied Signal Corporation. Alloy 8009 is consolidated from ribbon-cast strip particulate and requires the very rapid solidification of ribbon casting. Consolidated strip particulate products seem to have some disadvantages compared to products made from more conventional (and less rapidly cooled) atomized powder. Langley Research Center recently began an in-house program to explore dispersion-hardened, powder-metallurgy alloys for use up to 600°F (315°C) with ultrasonic gas atomization.

Approximately 20 alloy compositions have been alloyed, atomized, consolidated, vacuum degassed, vacuum hot-pressed, forged, and rolled to sheet. One alloy of promise is a complex aluminum powder composition containing manganese, calcium, and silicon as its major elements.

As shown in the figure, sheet fabricated from this alloy is almost competitive in mechanical properties with 8009 alloy and is about 5 percent less dense. Lower density is important

because it relates linearly to lower-weight usage in aerospace structures. The Langley alloy shows good thermal stability after 1000 hr at 600°F (315°C) at this early stage of development. (Note that 8009 does not change its strength properties after 1000 hr at 600°F (315°C).) This study has demonstrated that the Langley in-house aluminum powder metallurgy research capability allows for fast and inexpensive screening of innovative alloy compositions and consolidation and fabricating practices that will contribute to the needs of the aerospace community.

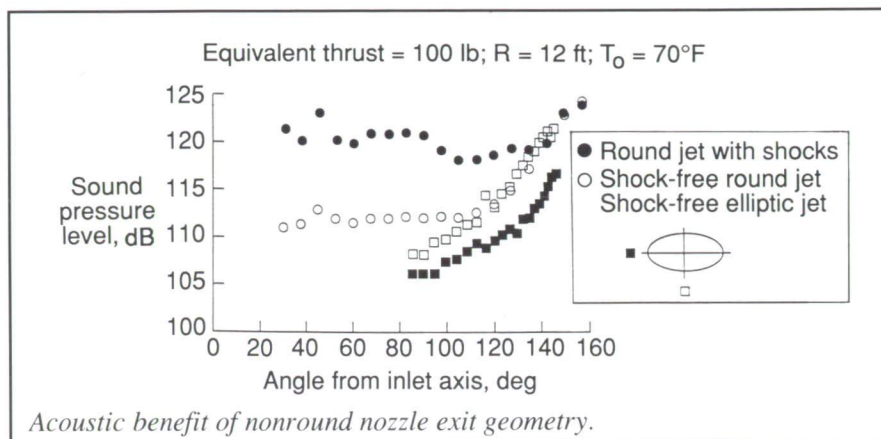
(D. M. Royster and O. R. Singleton, 43135)
Structures Directorate

Supersonic Elliptic Nozzle

The development of a High-Speed Civil Transport (HSCT) capable of Mach 2 to Mach 3 flight must address the challenge of meeting federally mandated community noise standards. Noise suppression techniques are practical only if they incur minimal thrust penalties. Nonround engine nozzle geometries may provide some of the needed acoustic reduction for an HSCT while minimally affecting aircraft performance.

Researchers at Langley Research Center and Pennsylvania State University formulated a nozzle design method that was applied in the development of a shock-free Mach 1.5 elliptic nozzle. The acoustic benefit of this nozzle, as compared to a round nozzle, was determined in the Langley Anechoic Noise Facility. These data are presented in the figure.

In general, the acoustic field at lower emission angles is dominated by shock-associated noise and at higher



angles is dominated by turbulent mixing noise. The acoustic benefit of reducing the strength of plume shocks, which lowers shock noise, is clearly evident even for round nozzle geometries. The reduction of shock noise because of the elliptic geometry (angles < 110°) is an indicator of not only the acoustic benefit of this nonround geometry but also the accuracy of the aforementioned nozzle design technique to produce shock-free flow. The data also show that the acoustic emission from the elliptic nozzle exhibits an azimuthal dependence in which the noise along the major axis is less than that along the minor axis. Thus, the potential for noise reduction for a commercial transport may exist not only in the application of nonround nozzle exit geometries but also in the orientation of such asymmetric designs to create a more favorable acoustic directivity. (Michael K. Ponton, 46278, and John M. Seiner)

Structures Directorate

Aircraft Noise Prediction Program Jet Noise Calculations for HSCT

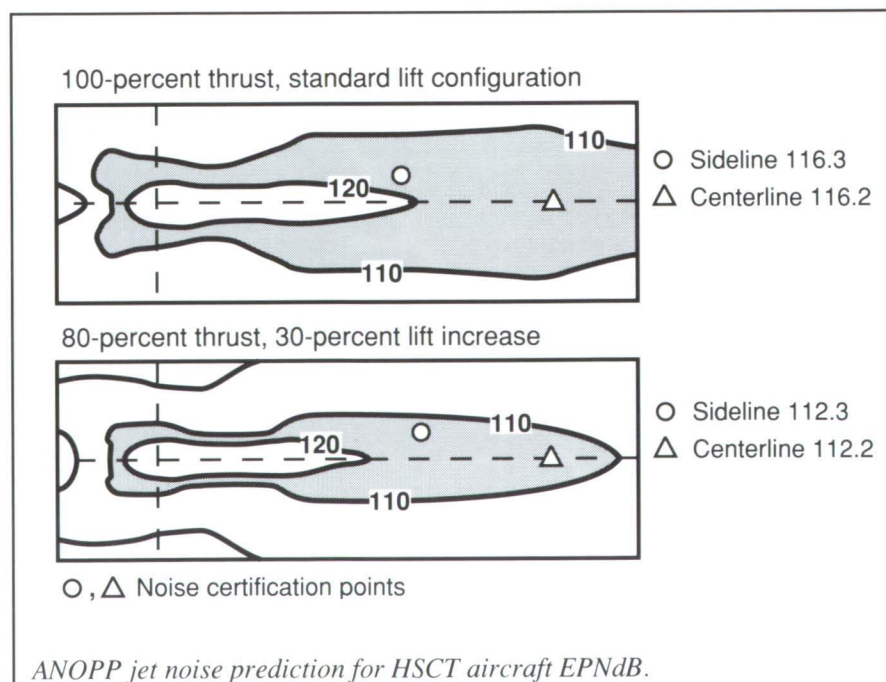
One of the major technological problems facing the High-Speed Civil

Transport is the challenge of reducing the sideline certification point jet noise. The ANOPP code was used to evaluate the effects of reduced jet thrust levels on the takeoff certification points and the resulting community noise levels. Because reducing jet thrust levels at takeoff increases the required ground roll, proposed advances in high lift technology were used in this study to offset the increased ground roll.

Predictions were made with the ANOPP dual-stream coannular jet noise module for the AST-205-1

aircraft powered by GE21/J11B14A scaled engines. A power setting of 100-percent thrust and a standard lift configuration were used as a baseline for this study. Aircraft power settings varied from 100-percent to 80-percent thrust, while lift was increased in increments of 15 percent, to a maximum of 60 percent. An angular rotation rate of 3°/sec and a constant climb angle of 8° were used. Effective perceived noise level (EPNL) values were calculated at the FAA noise measuring points as described in Part 36, Section C36.3 of the Federal Aviation Administration's Code of Federal Regulations. Noise levels were also calculated on a 1- by 6-mi grid consisting of 65 observer positions. Each observer was located at a height of 4 ft above the ground. Noise contours were generated from these observer positions.

Contours for both the baseline case and the 80-percent thrust/30-percent increased lift case are shown in the figure. The reduced thrust case decreases the necessary ground roll distance by 646 ft and lowers the sideline EPNL



ORIGINAL PAGE
BLACK AND WHITE PHOTOGRAPH

level by 4 EPNdB from the maximum thrust baseline case. Although the centerline noise level is not of major concern, it too benefits by 4 EPNdB from the reduction in thrust and increase in lift. Additionally, as the figure shows, reducing thrust and increasing lift alter the shapes of the contours. As thrust is decreased and lift is increased, the contours tend to shorten in length and become more compact.
(Robert A. Golub, 45281)
Structures Directorate

Prediction of Subjective Response to Sonic Booms

The impact of sonic booms on people is a major environmental concern associated with the development of a second-generation high-speed civil transport aircraft. A noise metric that adequately predicts the subjective loudness of sonic booms having different physical characteristics is needed for the assessment of sonic boom signatures predicted for candidate high-speed transport configurations. To address this need, the sonic boom simulator shown in the first figure was developed to study subjective response to sonic booms.

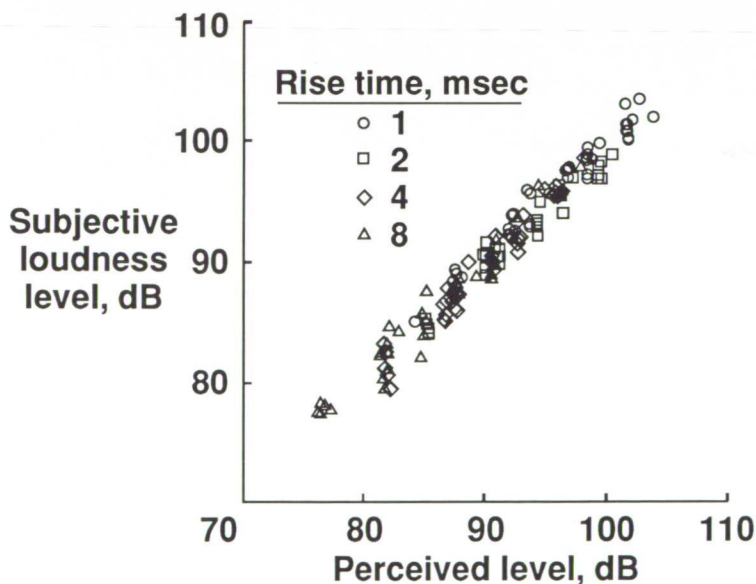
Thirty-six test subjects judged the loudness of each of 150 simulated sonic booms on a scale from 0 to 10. The sonic booms represented different combinations of overall duration, rise time, overpressure, and wave shape. The loudness judgments were averaged across test subjects and converted to subjective loudness levels for each of the 150 sonic booms.

Of several noise metrics considered, perceived level PL and A-weighted sound pressure level L_A were clearly the two best metrics for predicting the subjective response.



Sonic boom simulator.

L-90-5755



Subjective loudness of sonic booms as function of perceived level.

The second figure shows the subjective loudness levels plotted against PL for each of the four rise times. Analyses indicated that, of the two metrics L_A and PL , only PL completely accounted for the effects of rise time,

over-pressure, and wave shape. Neither metric fully accounted for the effect of duration, which was small. These results demonstrate that PL is a valid method for comparative assessment of the subjective acceptability of

sonic boom signatures predicted for candidate high-speed civil transport configurations.

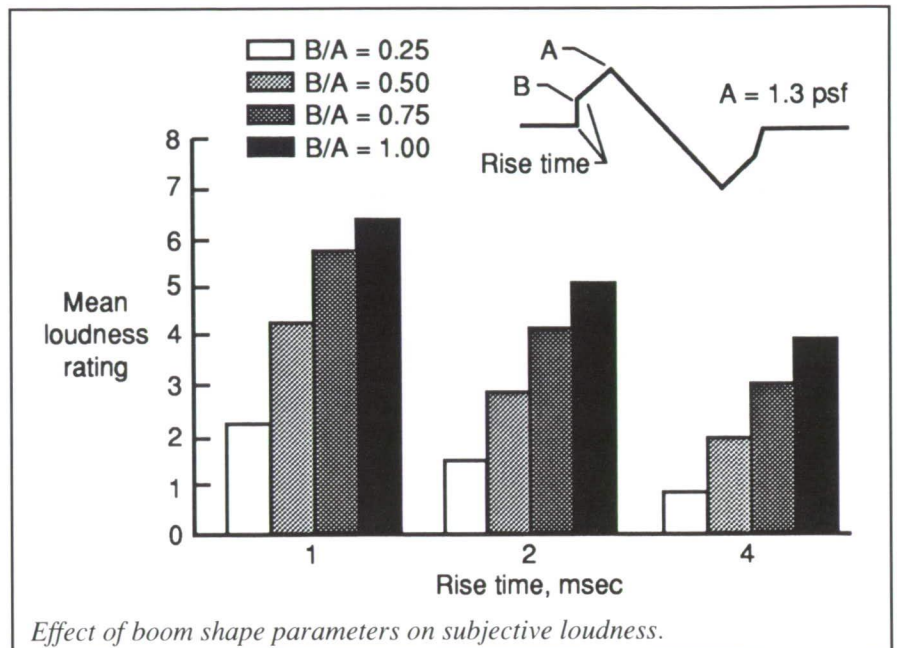
(David A. McCurdy, 43596)

Structures Directorate

Sonic Boom Shaping for Reduced Loudness

The economic viability of a second-generation supersonic transport would be enhanced if it were permitted to fly over land at supersonic speed. This issue is being addressed in ongoing research at Langley Research Center to determine the feasibility of designing low-boom aircraft that would minimize subjective sonic boom effects (loudness and startle, for example) at ground level. These studies have shown boom shaping to be a viable means of reducing boom loudness and improving public acceptance. However, the specific shapes and amplitudes that will be most acceptable to the public have not yet been identified.

The Sonic Boom Simulator at Langley was used to obtain subjective loudness judgments (from a group of local residents) of a wide range of candidate boom shapes. The range of shapes is shown at the top of the figure. These shapes were characterized by an initial rapid rise to an intermediate overpressure (level B) followed by a more gradual rise to peak positive overpressure (level A). Peak overpressure for the data presented in the figure was 1.3 psf. The bottom part of the figure shows mean loudness ratings as a function of initial rise time for four ratios of intermediate to peak overpressure. These data indicate that loudness, for a constant peak overpressure, decreased with increasing rise time and, for a specific rise time, decreased as the ratio of intermediate to peak overpressure decreased. These



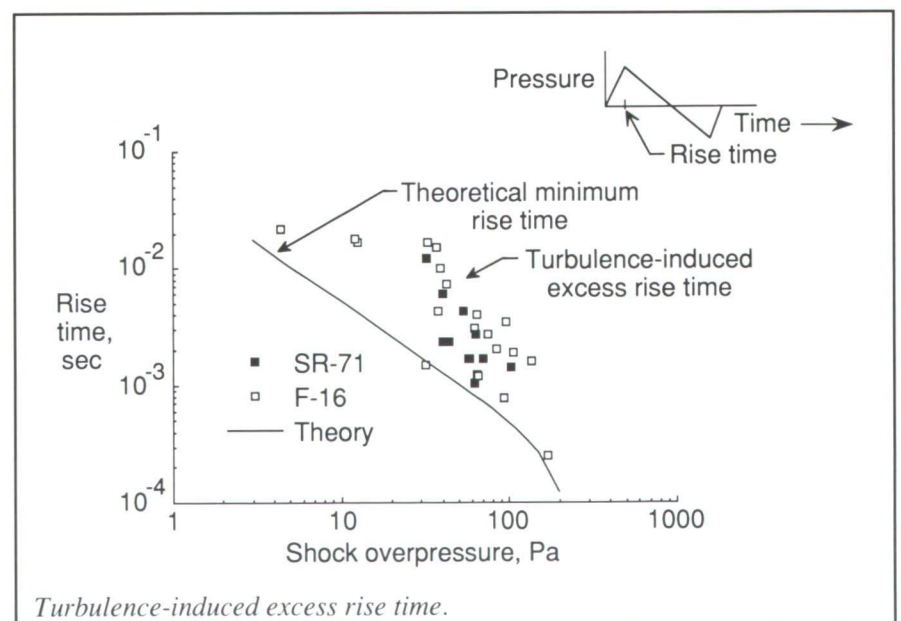
results show that significant reductions in subjective boom loudness can be achieved by detailed shaping of the boom signatures. The results also provide data that can be used to assist in the selection of a preferred boom shape.

(Jack D. Leatherwood, 43591, and Brenda M. Sullivan)

Structures Directorate

Atmospheric Turbulence Increases Sonic Boom Rise Time

Classical sonic boom theory predicts that the disturbance generated by a supersonic aircraft will be led by a very sharp rise in pressure from ambient to the peak overpressure. This



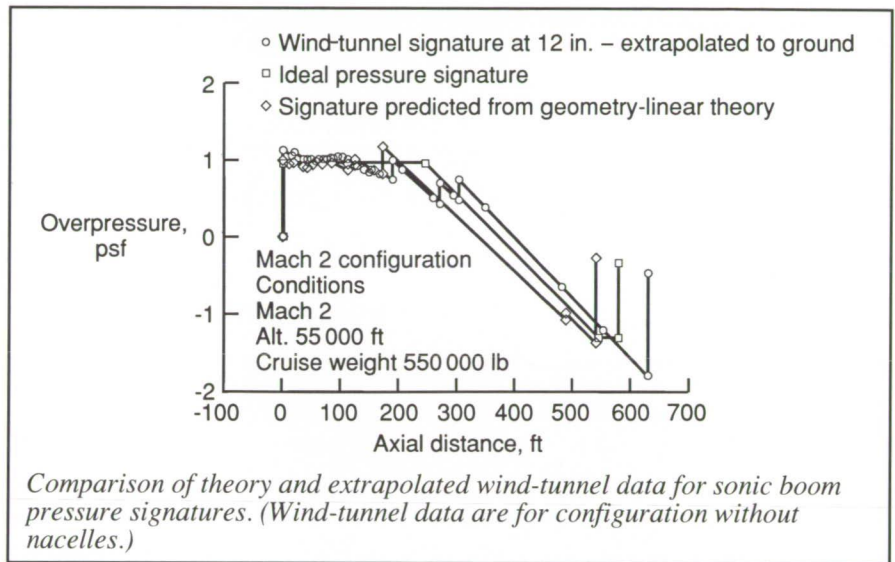
sharp pressure rise occurs over a time interval that is generally less than 1 percent of the time interval of the total disturbance. Yet this rapid pressure rise is probably the most disturbing part of the sonic boom. Although multiple definitions of rise time exist and are used, by any definition rise time is nothing more than a measure of this very short time period over which the sonic boom disturbance pressure rises to its peak value.

The objective of the current research is to determine the effects of the atmosphere on the sonic boom waveform, and because rise time is one of the characteristics of the waveform used to describe its disturbing properties, to determine the effects of the atmosphere on sonic boom rise time. At the simplest level, the overall shape of the sonic boom waveform may be thought of as determined by a balance between nonlinear steepening of the wave (which tends to decrease rise time), viscous dissipation, and molecular absorption effects (which tend to increase rise time). However, when these effects are fully accounted for and predicted rise times are compared with those determined from measured sonic boom waveforms, the measured rise times are generally larger than the predicted rise times. This increase may be attributed to the effects of the atmospheric turbulence that is neglected at the current level of the model. However, the fact that a minimum rise time may now be confidently predicted is important because increased rise time is associated with decreased annoyance. Thus, the current theory provides a conservative lower bound to rise time. This work was accomplished by A. Pierce at Pennsylvania State University, under grant. (Gerry L. McAninch, 45269) Structures Directorate

Sonic Boom Shaping

Current supersonic aircraft generate a pressure signature on the ground which is characterized by a bow shock, a middle expansion, and a rear shock. Flight tests in the 1960's indicated that

dicted using linear theory, and the extrapolated wind-tunnel data. The level of the bow shock and the excellent agreement of the forward parts of the pressure signature indicate that minimization through aircraft shaping is valid. The tests also indicated that further work on the proper integration



this N-wave for most transport-sized aircraft has a bow shock of 2 psf to 2.5 psf, which is a noise level that is totally unacceptable to the general population.

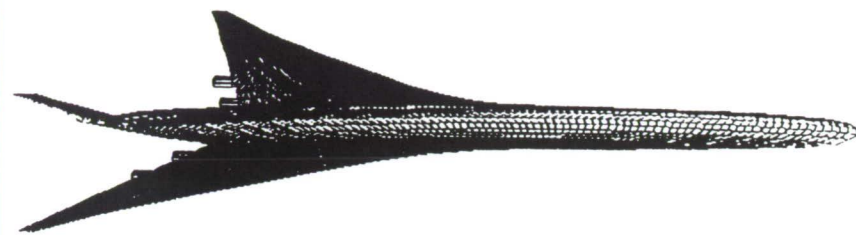
The current approach to sonic boom minimization is to shape the aircraft in such a way that the signature on the ground is not an N-wave and the level of the bow shock is much lower than that of existing airplanes. Tests at the Langley Unitary Plan Wind Tunnel on a 12-in. twisted and cambered low-boom concept indicate that this minimization approach is valid at a Mach number of 2 for the configuration without nacelles. Pressures measured at a radial distance of one body length from the model were extrapolated several hundred body lengths to simulate the distance that a full-scale signature would travel. A comparison is shown of the target flattop signature, the signature pre-

of the nacelles, the definition of the expansion area, and the location of the rear shock is indicated and will probably require the use of higher order methods.

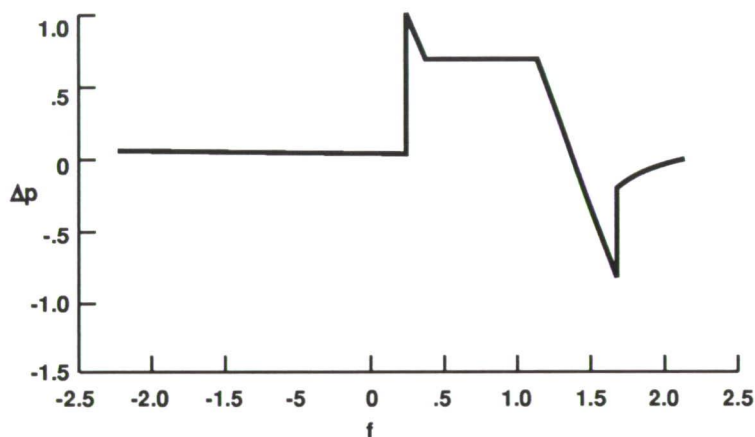
(Robert J. Mack, 45988, Christine M. Darden, Kathy E. Needleman, and Daniel G. Baize)
Aeronautics Directorate

Design System for Low Sonic Boom Configurations

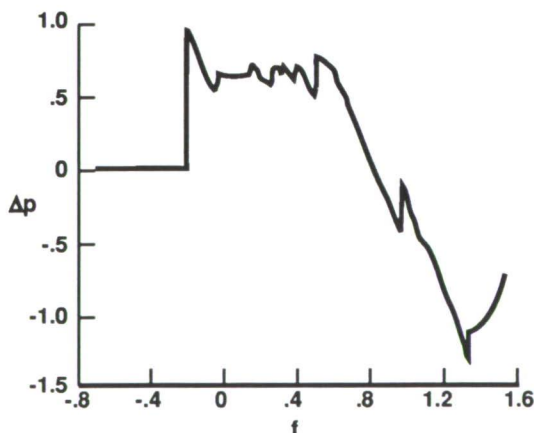
High-Speed Civil Transport (HSCT) milestones for assessment of the sonic boom problem can more easily be met if model design can be accelerated. Configurations with acceptable sonic boom characteristics would open the possibility of overland supersonic flight. The purpose of this



Blended wing-body configuration



Specified target signature



Signature actually obtained according to analysis codes

Computed signature results for low-boom configuration.

research was to facilitate and accelerate the design and analysis of low sonic boom blended wing-body configurations:

Existing codes were modified so that all input and output geometry and array formats were compatible, and

new codes were written and incorporated as required. (One new code automatically adjusts the thickness distribution to obtain the geometry required by low-boom constraints.) Computerized lofting was incorporated to reduce drawing board work. The

use of a blended wing-body concept eliminates the tedious problem of accounting for the wing-fuselage gap that occurs when these components are treated separately. Graphics codes were also incorporated for rapid display of relevant geometries and distributions.

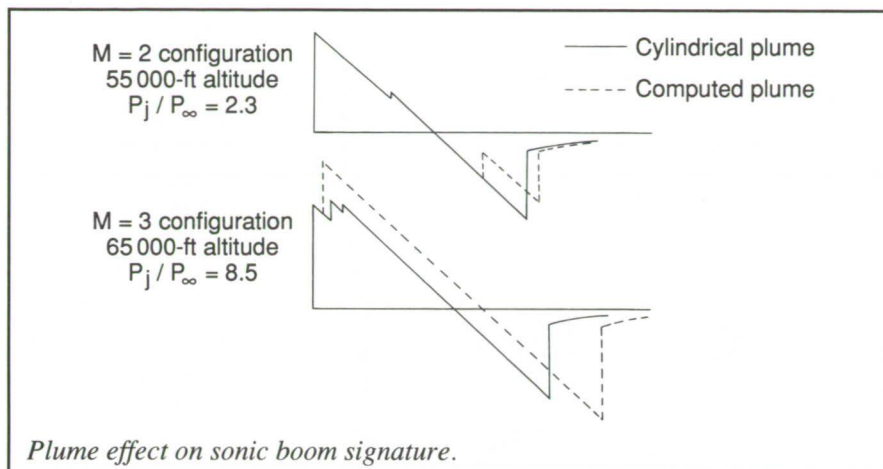
Some sample designs have been completed. Ground-level signature results for one case are shown in the figure. Experience in the use of the system is being gained, and some minor tailoring of the codes occurs as a result of this experience.

(Raymond L. Barger and Mary S. Adams, 42315)
Aeronautics Directorate

Jet Plume Effects on Sonic Boom Signature

Considerable ongoing research is taking place in the area of sonic boom reduction for potential supersonic civil transport configurations. To date, most predictions of sonic boom strength have either neglected or improperly modeled the effect of the jet exhaust plume. Previous attempts using a small perturbation method (NASA TND-279) and a method of characteristics solution with a conical nozzle flow model (NASA TND-5553) both failed to yield satisfactory predictions of experimentally determined plume shapes.

In the current work, an Euler shock-fitting space-marching code was used to predict the plume shape. This Euler method yields precise predictions of plume shapes for shock-free nozzle flow. For nozzle flow containing shocks, the accuracy is significantly better than previous techniques. The influence of the plume on the sonic boom signatures of some generic



configurations has been computed; a sample result showing ground-level pressure variations with time at a fixed observation position is shown in the figure. For small jet pressure ratios ($1 < p_j/p_\infty < 3$), the influence of the plume effects may be favorable, thus reducing the strength of the rear shock. For larger pressure ratios, the plume influence invades the forward positive part of the signature where the effect has always been found to be unfavorable.

Future research will include studies of the plume effects on the signature of current supersonic transport configurations and the effects of plumes on aerodynamic drag.

(N. Duane Melson and Raymond L. Barger, 42227)

Aeronautics Directorate

Effect of Fuselage Forebody Length on High-Lift Stability and Control of HSCT Conceptual Designs

The development of effective high-lift systems for High-Speed Civil Transport (HSCT) applications is a key factor in enabling such concepts to meet environmental goals related to sonic boom, atmospheric emissions,

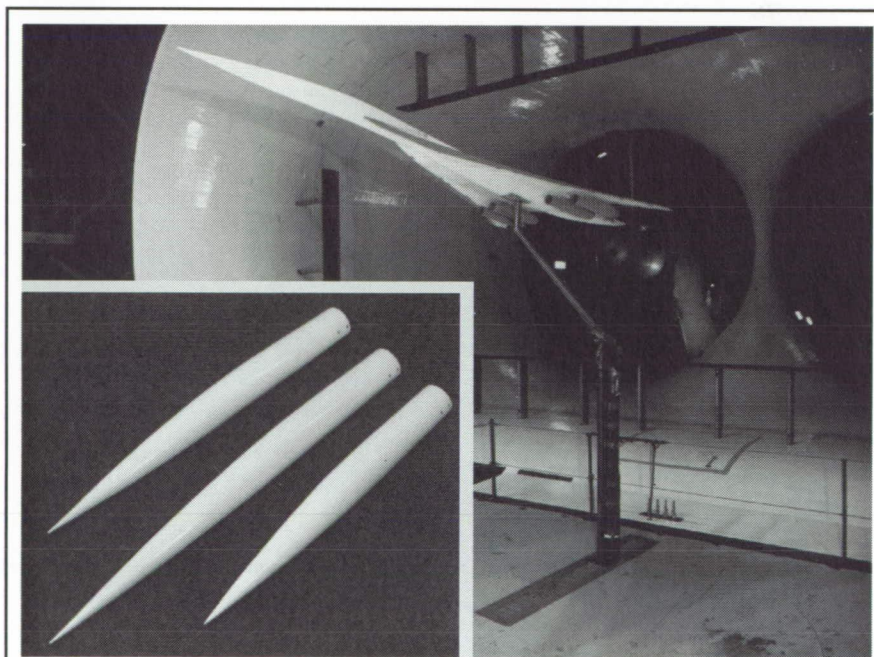
and airport and community noise. Typically, such high-lift concepts permit a desirable reduction in wing size. Because of passenger requirements, however, the vehicle fuselage remains relatively unaffected, which results in an increase in the forebody size relative to the wing. As an example, during 1970 supersonic transport studies, the concepts typically incorporated a forebody having a fineness ratio (length/diameter) on the

order of 5.0. In contrast, current HSCT concepts incorporate forebodies with fineness ratios approaching 8.0. As a result, there is concern about the effect of forebody fineness ratios on the vehicle directional stability at high-lift conditions.

To address this concern, an existing supersonic transport wind-tunnel model with a forebody fineness ratio of 5.0 was modified to permit testing with alternate forebodies with fineness ratios of 6.5 and 8.0. The tests were conducted in the Langley 30- by 60-Foot Tunnel and involved a number of high-lift configurations and control deflections in addition to the three forebodies. Initial results show only minor effects of forebody fineness ratio on configuration directional stability for the angle-of-attack range corresponding to normal operating conditions. For higher angles of attack, increasing fineness ratio is found to have a positive stabilizing effect on directional stability.

(E. Richard White, 41147)

Aeronautics Directorate



HSCT model mounted in Langley 30- by 60-Foot Tunnel. Insert shows forebodies with fineness ratios of 5.0, 6.5, and 8.0.

L-91-2961

Computational Predictions of HSCT-Type Configuration

A study has been conducted to investigate the capability of a computational method to predict the subsonic, high-lift aerodynamic performance of

a High-Speed Civil Transport (HSCT) configuration. Experimental results were obtained for this portion of the flight envelope in the Langley 14- by 22-Foot Subsonic Tunnel on the AST-210 model. The data include force and moment measurements, surface flow visualization, and off-body flow

visualization obtained via a laser light sheet. Theoretical results were obtained using the thin-layer, turbulent Navier-Stokes equations, computed on the Langley CRAY-2S supercomputer. The code used to obtain the solution was CFL3D. A two-block domain decomposition procedure was utilized to solve the entire flow domain of the AST-210 cruise configuration. Surface forces and pressures were calculated along with off-body flow variables.

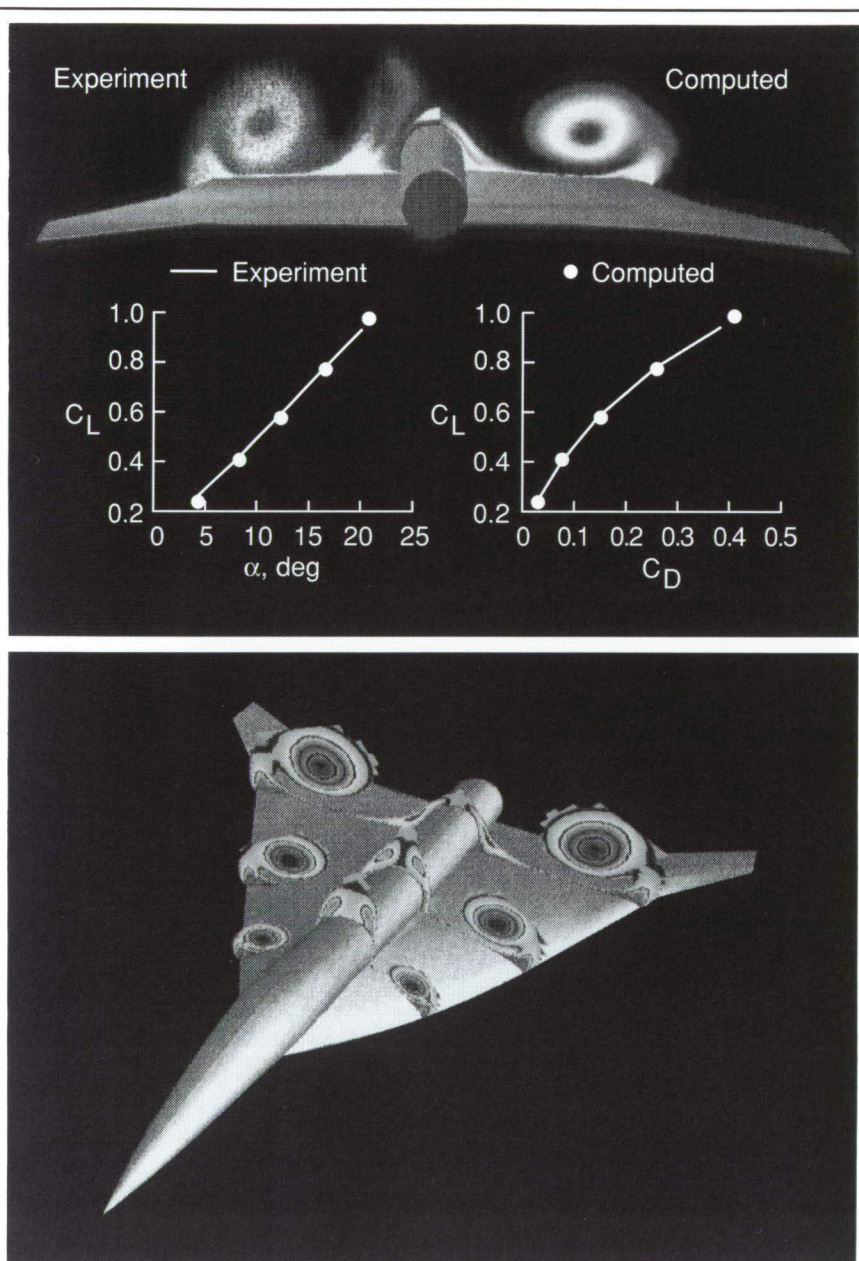
Computed lift and drag coefficients compare well with tunnel data at Mach 0.22 over an angle-of-attack range from 4° to 20° , with a corresponding Reynolds number of $1.45 \times 10^6 \text{ ft}^{-1}$. Additionally, the computed off-body total pressure contours agreed well with the resulting upper-surface vortices captured by the laser light sheet and, thus, provides an effective means of tracking the growth and development of vortices over the configuration length.

Although the comparisons thus far are for the baseline configuration, the good agreement between experimental and theoretical results, including the flow-field characteristics, demonstrate the potential of CFL3D to be an effective analysis tool for guiding engineers in the design and optimization of model configurations.

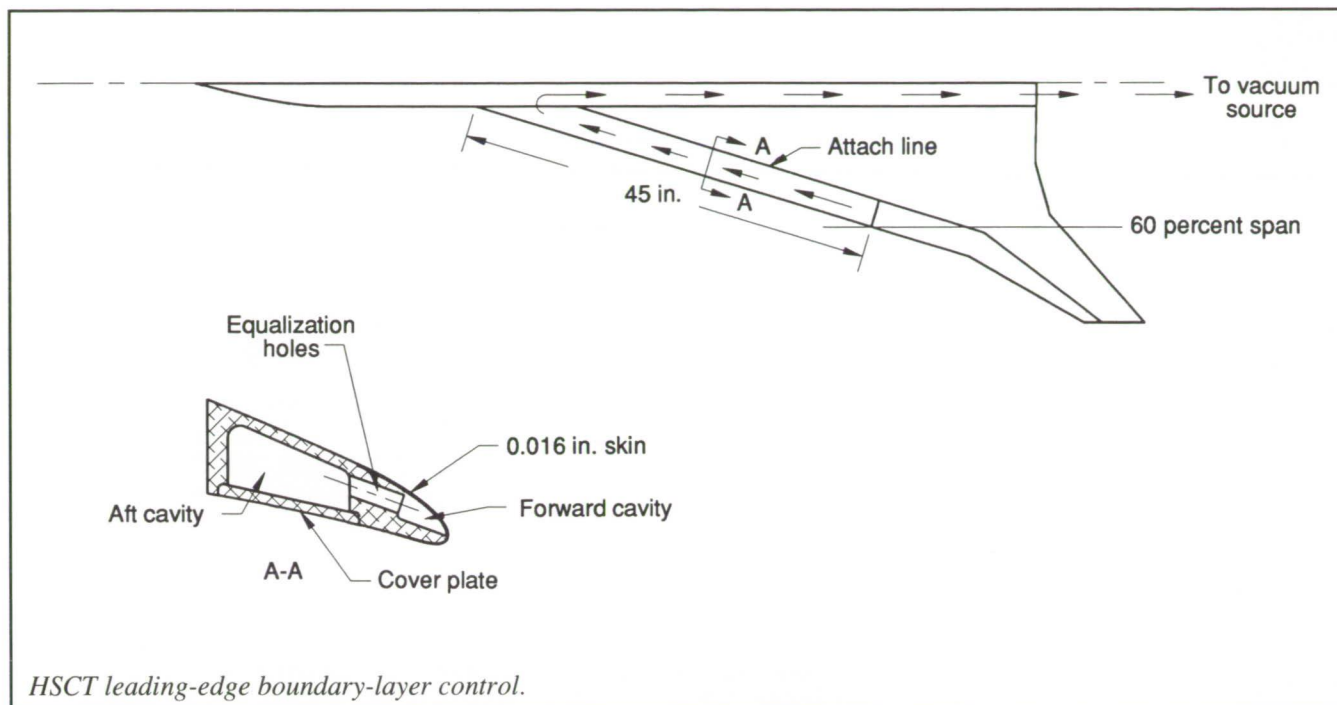
(Victor R. Lessard, 45072,
and Bryan A. Campbell)
Aeronautics Directorate

HSCT Leading-Edge Boundary-Layer Control Porous Skin Fabrication

Two sets of porous leading edges have been designed to replace the existing ones on the AST-210 High-Speed Civil Transport (HSCT) model.



Computational and experimental comparisons (top) and computational total pressure contours (bottom) of AST-210 model at $M = 0.22$ and $\alpha = 16^\circ$.



HSCT leading-edge boundary-layer control.

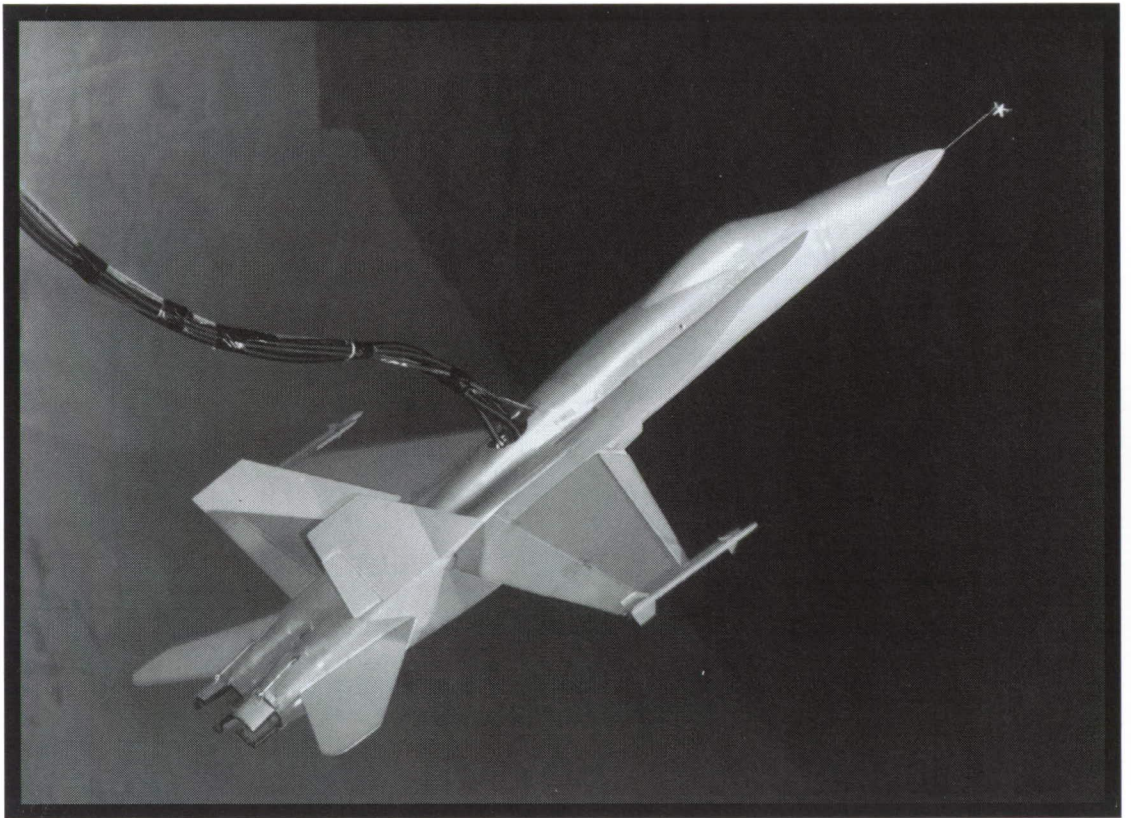
The new leading edges, along with an internal suction system, will allow for boundary-layer control, thus alleviating leading-edge flow separation typical of low aspect ratio, highly swept wing configurations. The porous leading-edge skins are to be fabricated from 0.016-in.-thick material, one set from commercially pure titanium sheet and the other from electroformed nickel. Pore (hole) spacing will vary from 0.010 in. to 0.020 in., using 0.002-in.-diameter holes, with a spacing pattern dictated by isobar lines predicted by computational fluid dynamics analysis.

The two sets of leading edges are to be fabricated simultaneously, using two different experimental fabrication techniques in order to determine the better technique for future applications. One set of leading-edge skins is to be laser drilled while flat, then heat-formed over a numerically controlled machined mandrel. The second set is to be fabricated by electroforming the nickel skin, then using a five-axis laser drilled to add the hole patterns.

Both sets are to be fabricated, wind tunnel tested, and evaluated and compared. Criteria for comparison will include time, cost, and ease of fabrication, structural integrity, hole and surface quality, and geometrical accuracy. Test and comparison results will be used to determine fabrication techniques to be used for future porous skin models and model components.

(Barry Gibbens, 47141)
Systems Engineering and
Operations Directorate

■ HIGH-PERFORMANCE MILITARY AIRCRAFT



ORIGINAL PAGE
BLACK AND WHITE PHOTOGRAPH

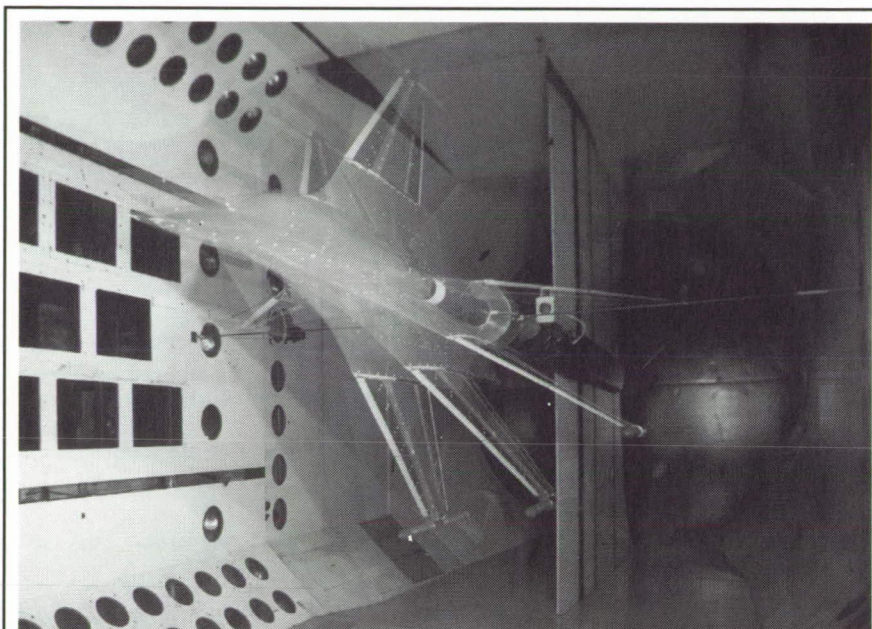
*Provide technology
options for revolutionary
new capabilities in
future high-performance
military aircraft*

ORIGINAL PAGE
BLACK AND WHITE PHOTOGRAPH

Demonstration of Multi-Input/Multi-Output, Multiple Function Digital Control

The Active Flexible Wing (AFW) Program is a joint Langley Research Center/Rockwell International effort with the overall program goal to demonstrate multi-input/multi-output (MIMO) multiple function digital control of a sophisticated aeroelastic wind-tunnel model. The AFW model, which has the capability of rolling on the sting support, is shown in the first figure. In the winter of 1991, the final test in a series of tests of the AFW wind-tunnel model was conducted in the Transonic Dynamics Tunnel (TDT). The MIMO multiple function digital control involved flutter suppression systems (FSS) in combination with one of three rolling control laws: a roll trim system (RTS), a rolling maneuver load alleviation (RMLA) system, and a roll rate tracking system (RRTS). The research objective of the program is to validate analysis, synthesis, simulation, and test methodologies necessary to perform such a demonstration.

The bar chart in the second figure illustrates the dynamic pressures attained during the MIMO multiple function testing. The ratio q/q_f is the ratio of dynamic pressure attained divided by the open-loop flutter dynamic pressure. Values of this ratio greater than 1.0 indicate that the model was tested above the open-loop flutter dynamic pressure. The first bar represents increases in dynamic pressure of 23 percent above the open-loop flutter dynamic pressure; these

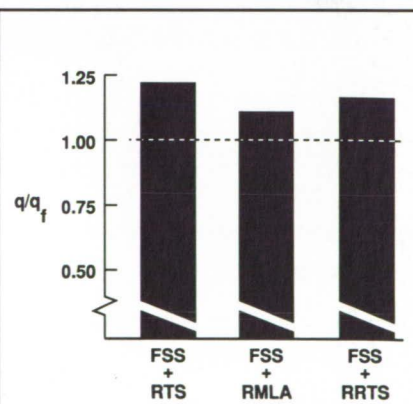


Multiple-exposure photograph of AFW model in TDT.

L-89-12446

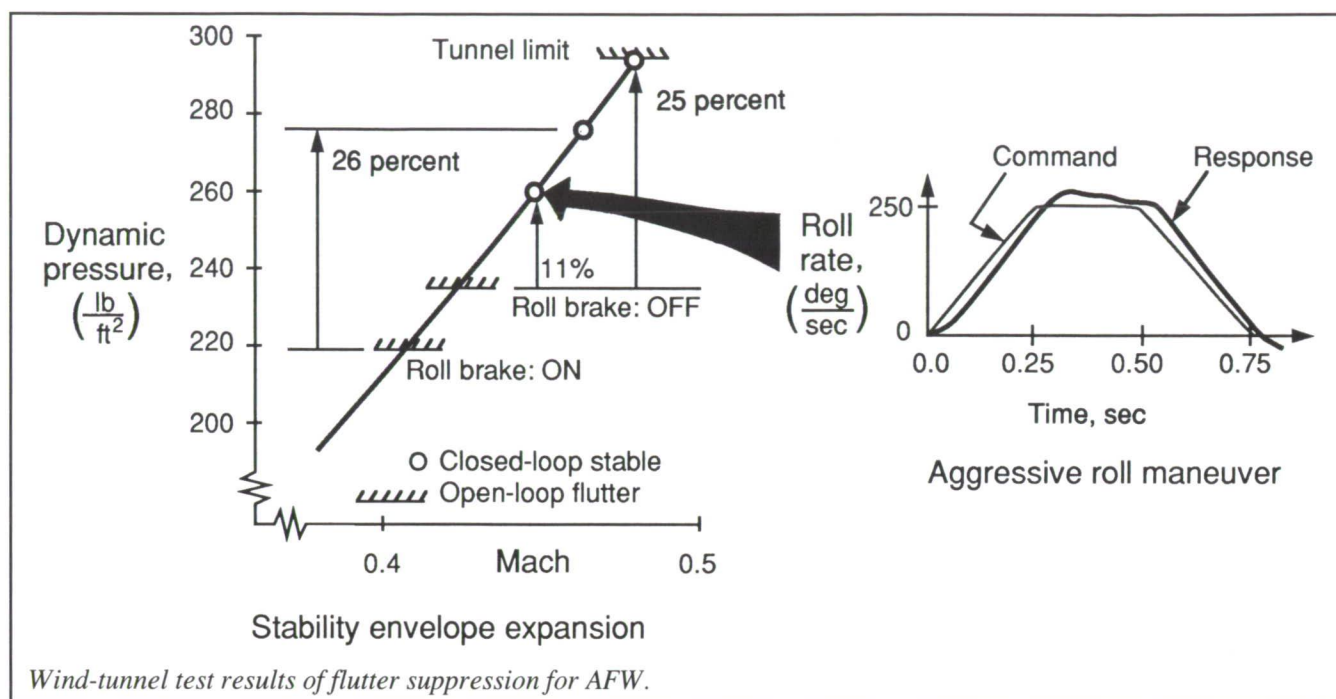
increases were attained by four separate FSS control laws operating one at a time, but each was in conjunction with the RTS. The second bar represents increases in dynamic pressure of 11 percent while simultaneously performing, via the RMLA, rolling maneuvers in which key wing loads were reduced. The second bar represents increases in dynamic pressure of 17 percent while simultaneously performing, via the RRTS, rolling maneuvers in which key wing loads were controlled.

As indicated by the preceding discussion, the AFW program was successful in demonstrating MIMO multiple function digital control of a complex aeroelastic wind-tunnel model. This demonstration served as a validation of the analysis, synthesis,



Bar chart of dynamic-pressure ratios.

simulation, and test methodologies utilized to conduct the wind-tunnel test. (Boyd Perry III, 42840, and Stanley R. Cole) Structures Directorate



Flutter Suppression During Steady and Maneuvering Flight

Active flutter suppression can permit utilization of more flexible aircraft structures with attendant weight savings and operational envelope expansion.

The objectives of this research were to design flutter suppression systems (FSS) and experimentally demonstrate their performance both in steady flight and during aggressive rolling maneuvers.

A full-span Active Flexible Wing (AFW) wind-tunnel model of an advanced fighter concept was used as a test-bed. Based upon mathematical models of the AFW, FSS control laws were developed using two approaches. The first design was a robust, low-complexity controller developed using classical (i.e., Nyquist and root locus) techniques. The poles and zeros of the controller were chosen to exploit predicted variations in the AFW dynamic properties with changes in

dynamic pressure. The second design was a multi-input/multi-output controller obtained using optimization techniques. The optimization maximized a performance measure that reflected the desire for robustness and insensitivity to variations between actual and mathematical models of the AFW.

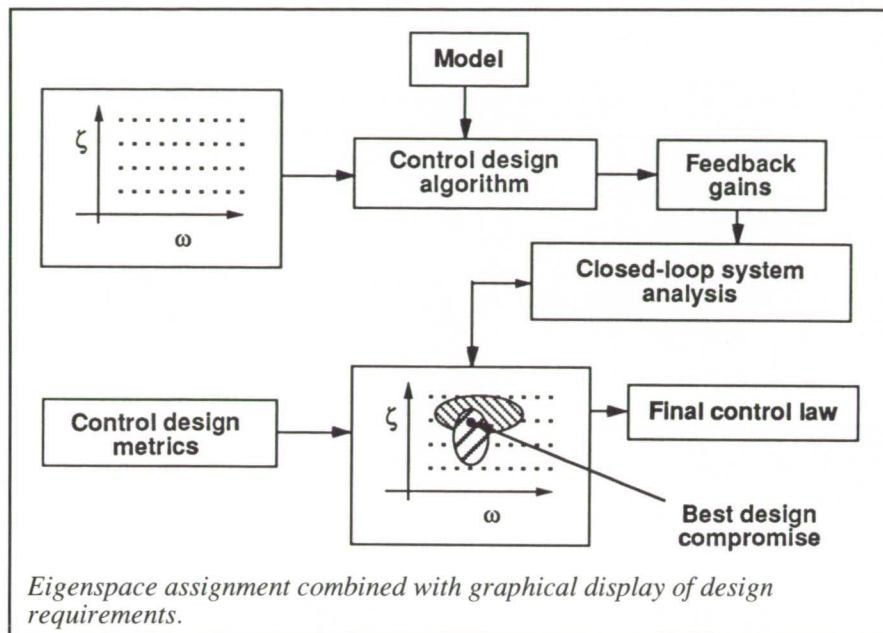
The AFW model was "flown" in the Transonic Dynamics Tunnel at Langley Research Center to evaluate the validity of the mathematical model, identify flutter boundaries, and test FSS performance. Despite inaccuracies in the mathematical model, particularly in predicted flutter frequencies, both FSS controllers performed well. Test results are summarized in the figure. Both controllers were shown to stabilize symmetric flutter to the tunnel limit (at a dynamic pressure 25 percent above the uncontrolled flutter boundary) during steady flight with the model free-to-roll. With the roll degree of freedom restrained (roll brake on), both symmetric and antisymmetric flutter were simultaneously suppressed, achieving a dynamic pressure 26

percent above the flutter boundary; wind-tunnel turbulence-induced loads that exceeded preset safety limits prevented attainment of the tunnel limit in this case.

Increasingly aggressive roll maneuvers were also performed which required simultaneous active flutter suppression and active roll control. On the right in the figure, commanded roll rate and response time histories are shown for the most aggressive of these (250°/sec commanded roll rate). This test was accomplished at a dynamic pressure 11 percent above the uncontrolled flutter boundary. (W. M. Adams, M. R. Waszak, and D. M. Christhilf, 44013) Flight Systems Directorate

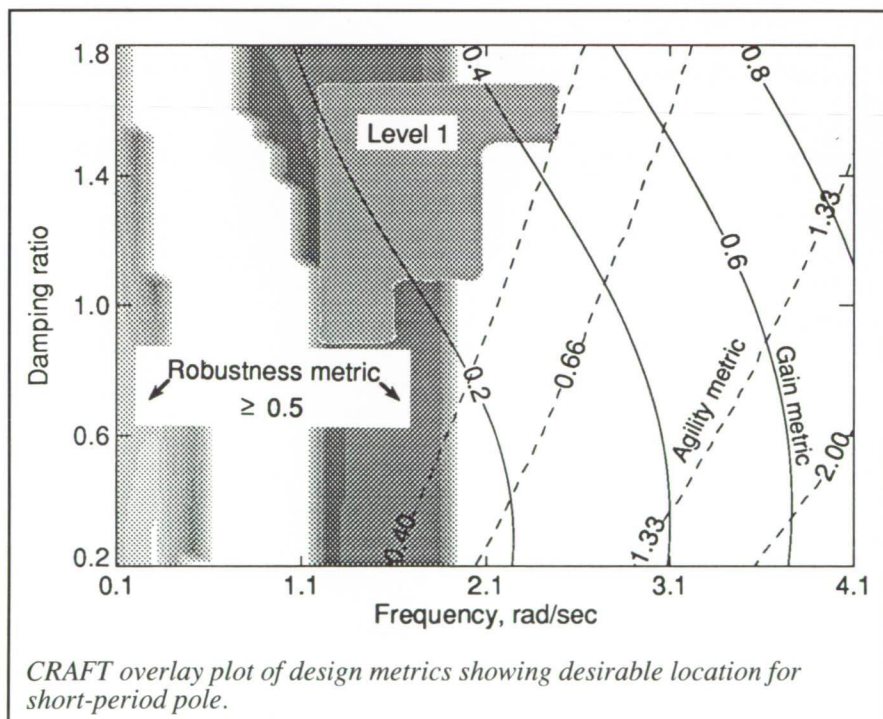
Control Design for Future Agile Fighters

One major requirement for success in the fighter combat arena of the



flying qualities, stability robustness, and control power. The objective of this research is to develop a flight control design methodology that makes use of all the metrics and allows trade-offs among the many competing design requirements.

The approach makes use of graphical overlays of metric surfaces that indicate desirable regions for specifying closed-loop frequency and damping. The procedure addresses Control Power, Robustness, Agility, and Flying Qualities Trade-offs (CRAFT) and is summarized in the block diagram. Using eigenspace assignment, systematic placement of closed-loop frequency and damping characteristics can be achieved. Each control design metric is evaluated and plotted over the frequency and damping space to find the most desirable region for the closed-loop dynamics. A final overlay plot of desirable regions from each metric surface can then be obtained. The intersection of desirable regions provides the best compromise for all the design criteria considered. An overlay plot for an advanced fighter is shown with one metric from each of the four design objective areas. For this example, desirable locations for the short-period pole are given by the intersection of gray regions indicating good robustness and Level 1 flying qualities. In addition, contour lines for control power (gain metric) and agility indicate desirable directions to move within the intersecting gray regions. Increasing values of the agility metric indicate greater pitch acceleration capability, and greater values of the gain metric indicate greater control power required.



future is enhanced maneuverability and controllability throughout a greatly expanded flight envelope. This enhancement is commonly referred to as agility, and designing control systems to provide it represents a serious challenge to engineers. Special-

ized design criteria, or metrics, capable of translating advanced air combat maneuvering requirements into terms for flight control system design are needed. Additionally, the control designer must consider metrics from other areas besides agility, namely,

CRAFT is a multivariable design technique that provides a graphical framework to trade-off multiple and often competing design requirements from diverse areas in a single efficient design process. The method allows

the designer to use a building block approach to select or emphasize a particular required capability. In particular, CRAFT should allow selection of dynamics that provide the greatest agility available while still satisfying appropriate levels of flying qualities, controlling system robustness, and respecting the available control power. The approach allows multi-input/multi-output (MIMO) design without requiring full-state feedback. By control of the closed-loop eigenspace, flying qualities specifications can be incorporated into the design.

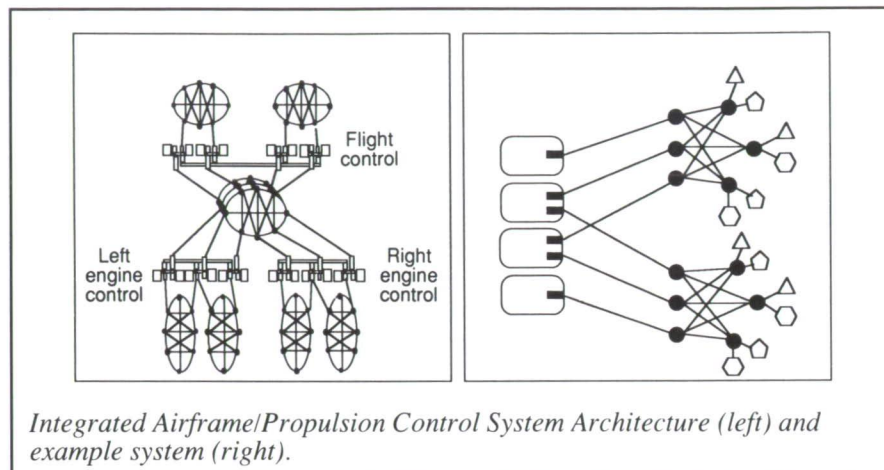
(Patrick C. Murphy and John B. Davidson, 44071)

Flight Systems Directorate

Reliability Analysis of Integrated Airframe/Propulsion Control System Architecture

The Integrated Airframe/Propulsion Control System Architecture (IAPSA) Program developed a design for a computer control system that could be used on an advanced fighter aircraft. The architecture is graphically represented on the left side of the first figure. A quad fault-tolerant computer controls the airframe, and two triplex fault-tolerant computers control the engines. A unique characteristic of the architecture is the use of reconfigurable mesh networks. Dual mesh networks connect the computers to sensors and actuators. A triplex mesh network forms an intercomputer data path.

The size of the IAPSA system created a challenge for the reliability analysis tools; including all input/output devices, the IAPSA system has over 500 components. Using the Abstract Semi-Markov Specification Interface to the SURE Tool/Semi-



Technique	SURE model size	Memory required	Run time
ASSIST/SURE	27 Mbyte	100 Mbyte	11.5 hr
Serial ASSURE	N/A	1 Mbyte	0.6 hr
Parallel ASSURE	N/A	1 Mbyte	0.01 hr

Example system performance data.

Markov Unreliability Range Evaluator (ASSIST/SURE) reliability analysis package, it was necessary to partition the architecture into several segments, thus potentially introducing error into the analysis.

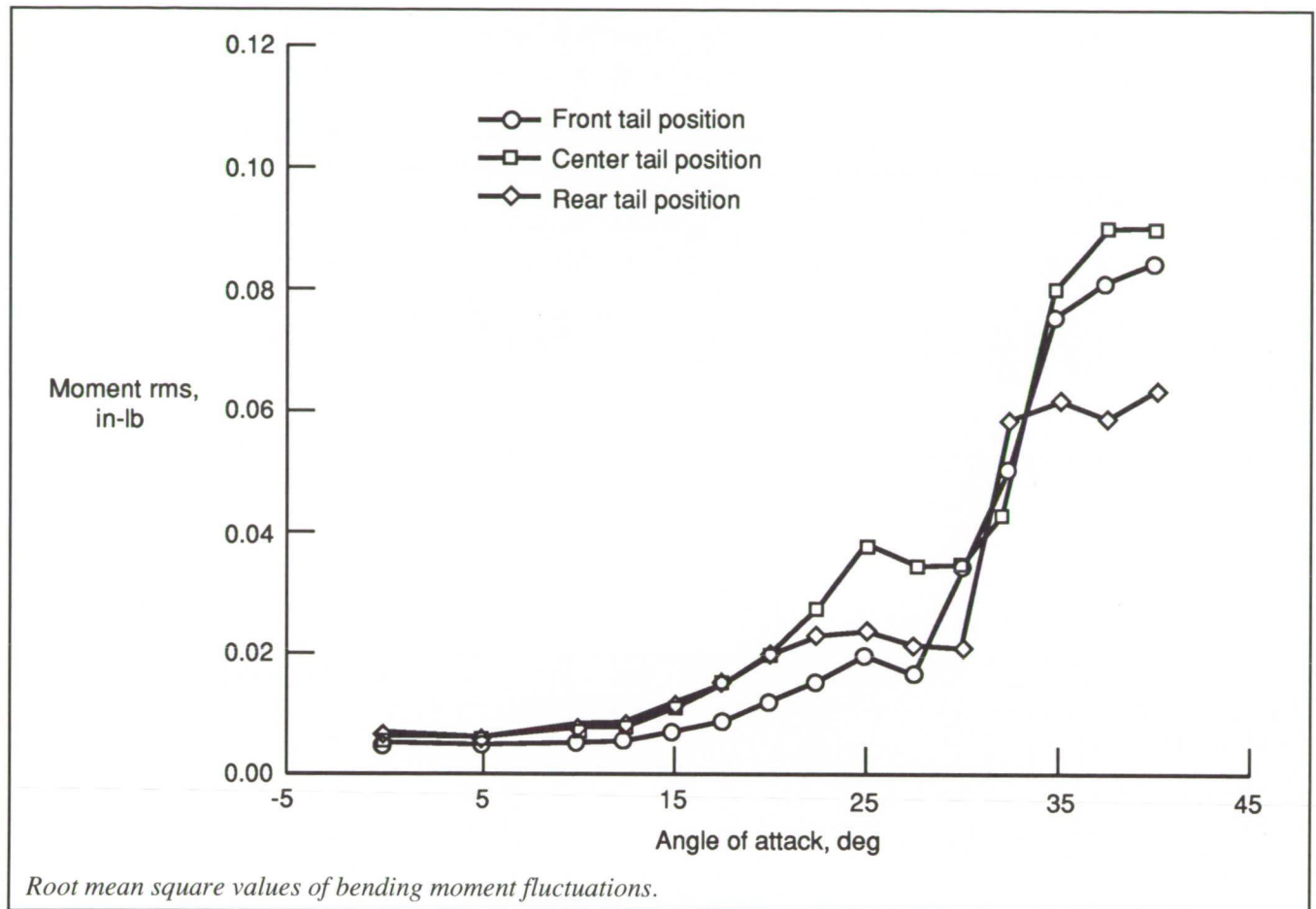
A two-phase approach was taken to increase the size of the model that the ASSIST/SURE analysis technique could process. In the first phase, the SURE solution technique was integrated with the ASSIST language processor. The resulting tool (ASSURE) improves performance in three ways. First, it was no longer necessary for ASSIST to construct an intermediate model file for SURE to read. Second, ASSURE, by taking advantage of the SURE technique of decomposing the model into independent paths, can discard a state after computing its probability. Third, because ASSURE computes the state probability as the model is grown, the model can be refined dynamically. These

three techniques reduce the memory requirements of a given analysis, thus allowing the tool to process larger models on any given host computer. In the second phase, ASSURE was parallelized to run on an iPSC/860 hypercube. This use of the parallelized ASSURE dramatically decreased processing times because the hypercube was typically over 90 percent utilized. The performance data in the second figure were obtained using a model of the example system shown on the right side of the first figure.

(Daniel L. Palumbo, 46185)
Flight Systems Directorate

Vortex-Fin Interaction Research

A cooperative research program between Langley Research Center and McDonnell Aircraft Company has



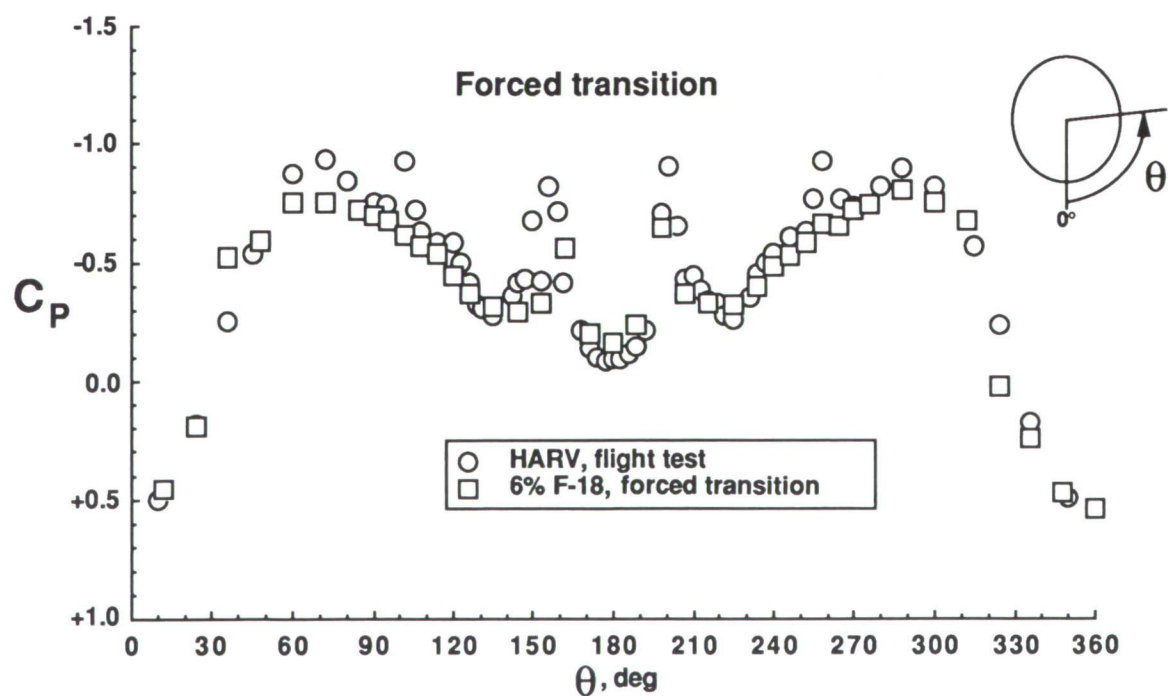
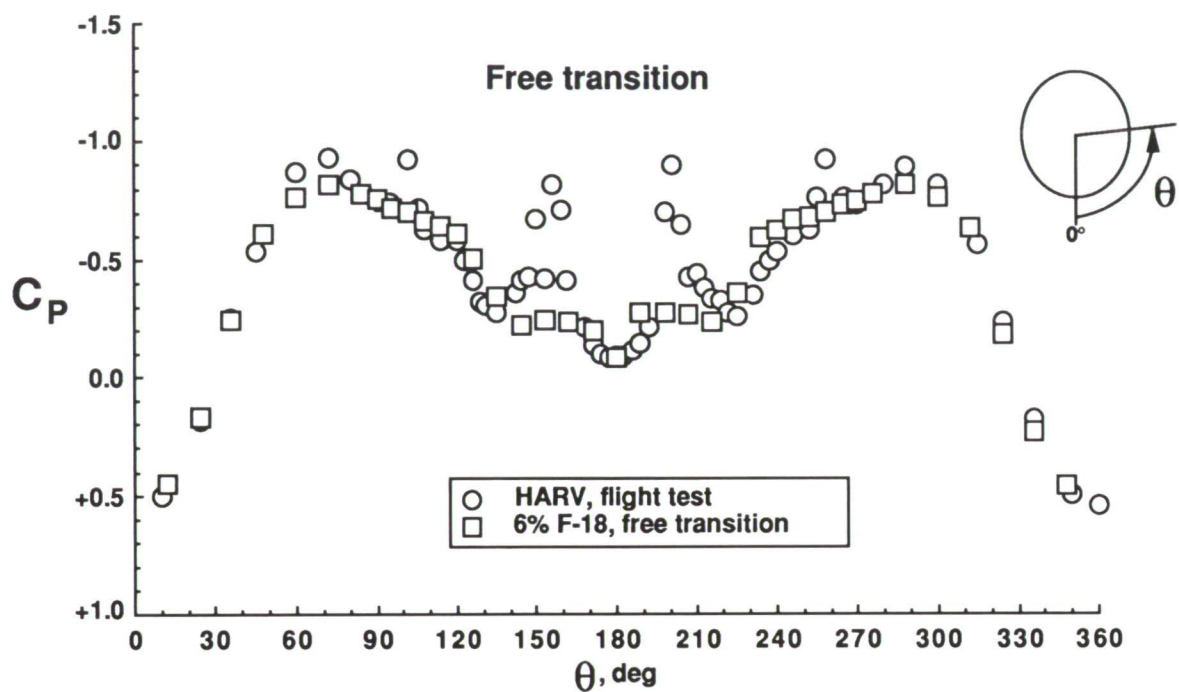
been established to provide a fundamental understanding of the interaction between vortical flows and vertical tails. This multidisciplinary program involving both aerodynamic and structural dynamic groups will provide a data base for developing improved tail-buffet criteria and determine the ability of computational fluid dynamics methods to predict the physics of the flow field. The configuration being investigated consists of a geometrically simple delta wing of 76° fitted with two vertical tails that can be positioned at three longitudinal and three lateral positions behind the wing. Three types of tails are used in this investigation: a noninstrumented rigid tail, a rigid tail instrumented with 10 unsteady pressure transducers, and a flexible tail instrumented with strain gauges located at the tail root.

The parametric study portion of this multiphase experiment has been concluded. The data obtained to date show the effect of tail position on the vortex trajectory and burst location, aerodynamic loads on the wing, aerodynamic moments on the flexible tail, and unsteady surface pressure fluctuations on the rigid tail. The figure presents the root mean square (rms) values of the bending moment fluctuations as measured on the flexible tail as a function of angle of attack for three tail positions. The sudden rise in the rms of the fluctuations at an angle of attack of approximately 30° is a result of the movement of the vortex burst to a location ahead of the vertical tails. (Anthony Washburn, 41290) Aeronautics Directorate

F-18 High-Angle-of-Attack Aerodynamics

To enhance maneuverability, fighter aircraft need to be designed with good high-angle-of-attack characteristics. Wind-tunnel investigations of the F-18 configuration have been closely correlated with flight tests, conducted at the Hugh L. Dryden Flight Research Facility, utilizing a highly instrumented F-18 aircraft called the High Alpha Research Vehicle (HARV).

During the initial high-angle-of-attack development of the F-18, discrepancies between wind-tunnel and flight test lateral stability were uncovered. These discrepancies appear to be



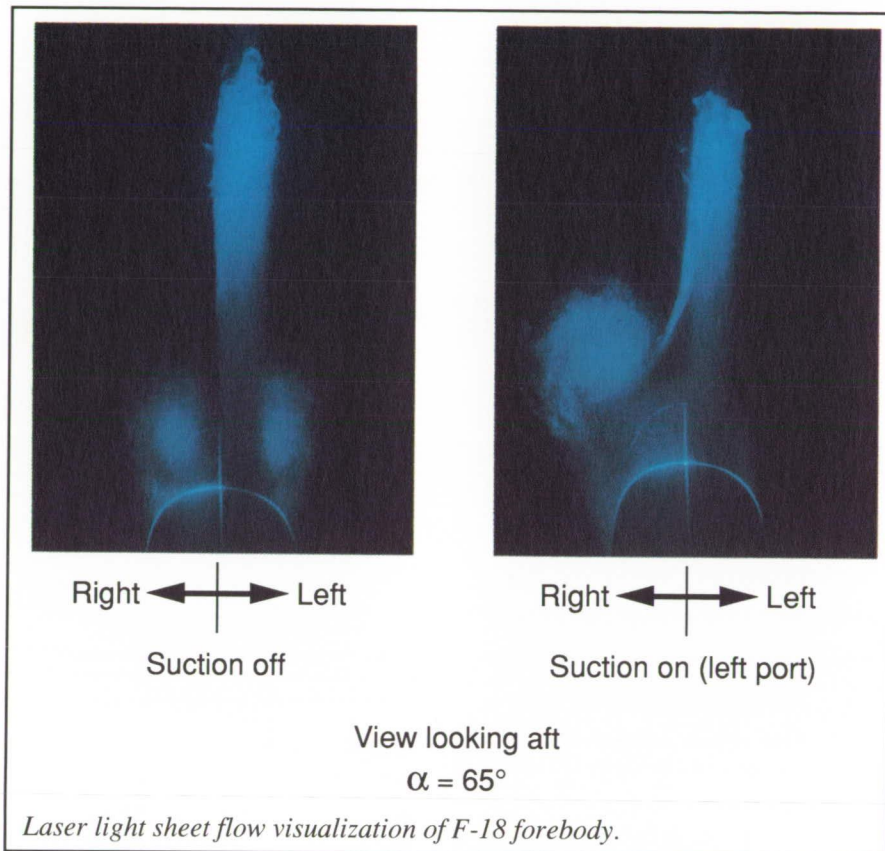
F-18 forebody pressure distribution (angle of attack is 40° , Mach number is 0.3, and fuselage station is 142).

ORIGINAL PAGE
COLOR PHOTOGRAPH

the result of interactions between the forebody and leading-edge extension (LEX) vortex flows. Investigations have been conducted both in the wind tunnel and in flight to define these flow fields. The results from these tests imply that, at the conditions tested, the forebody flow field is sensitive to boundary-layer state, while the LEX flow field is sensitive to compressibility effects even at relatively low Mach numbers. Recent results indicate that flight forebody crossflow Reynolds numbers, based on forebody diameter, can be simulated by fixed transition techniques. This fact suggests that an appropriate test technique for subscale high-angle-of-attack testing would be able to fix transition on the forebody while testing at the intended Mach number.

An F-18 shroud model (forebody section) with free and with fixed transition was tested at a Mach number of 0.3 and an angle of attack of 40° and compared to flight test data on the HARV. The case with free transition shows the forebody vortices are undeveloped; however, with the transition forced (gritted), the vortical flow develops (shown by the central suction peaks) much the same in location and strength to that of the HARV. The results of these investigations have indicated these transition characteristics are important to properly model the forebody flow field, which is necessary to obtain the correct high-angle-of-attack aerodynamics.

(Daniel W. Banks, 45067, Robert M. Hall, William G. Sewall, and Gary E. Erickson)
Aeronautics Directorate



Forebody Suction for High-Angle-of-Attack Directional Control

Modern fighter aircraft typically exhibit a degradation in directional control at high angles of attack, and this degradation limits their maneuvering capability. To alleviate this deficiency, exploratory tests are being conducted to evaluate the use of suction near the apex of a slender forebody as a potential method for augmenting high-angle-of-attack directional control. This concept involves controlling the forebody vortex development using varying levels of suction. The evaluation of suction control methods is based primarily on the level of side force and/or yawing moments that can be generated at the higher angles of attack where conventional yaw controls (such as rudders) become ineffective.

The present research has concentrated on exploratory studies in the Langley 12-Foot Low-Speed Tunnel using a generic tangent ogive forebody with a fineness ratio of 5.0 and a 0.16-scale F-18 having a forebody fineness ratio of 3.8. A number of suction port locations were evaluated using force and moment data, surface oil-flow studies, and laser light sheet flow visualization techniques. Suction was found to generate large yawing moments for the tangent ogive geometry; however, the F-18 forebody results show lower levels of control produced by suction. The flow visualization studies shown in the figure indicate that the suction mechanism involves the prolonged attachment of flow in proximity to the active suction port. For conditions with suction off, the flow visualization figures show separated vortices on either side of the forebody. However, for conditions

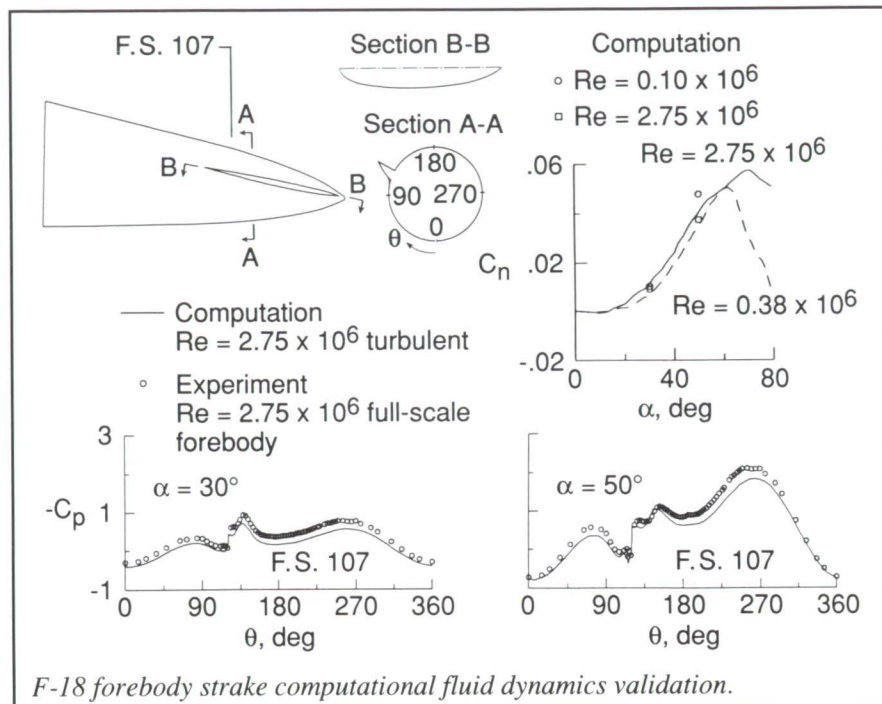
with suction on the left side, the left-side separated vortex has been eliminated, and the resulting asymmetric flow produces a nose right yawing moment. These results indicate that the effectiveness of suction as a yaw control concept is dependent on the forebody geometry. Further tests are planned to evaluate other forebody geometries and to study the use of apex suction using slots rather than discrete ports.

(E. Richard White, 41147)
Aeronautics Directorate

Validation of Navier-Stokes Solutions for F-18 Forebody Control Strake

Navier-Stokes solutions for the flow around an F-18 forebody with an actuated control strake have been obtained. The analysis was performed as part of a series of proof-of-concept studies conducted in advance of flight tests with the F-18 High Alpha Research Vehicle (HARV). The forebody strake concept has been developed to enhance yaw control at high angles of attack; the current work represents one of the first numerical analyses of a control device. The particular configuration analyzed in the computations is shown in the figure.

Computational results were obtained using the Navier-Stokes code CFL3D, with a seven-block grid, to represent the forebody, strake, and surrounding flow field. Interblock communication was provided by a patched-grid algorithm that allowed smooth passage of viscous layers through block boundaries. The computations were performed for both fully laminar flow and fully turbulent flow corresponding to $Re = 0.10 \times 10^6$ and $Re = 2.75 \times 10^6$, respectively. The



F-18 forebody strake computational fluid dynamics validation.

results were compared to wind-tunnel data for a strake mounted on a full-scale F-18 forebody as well as one mounted on a 16-percent-scale forebody.

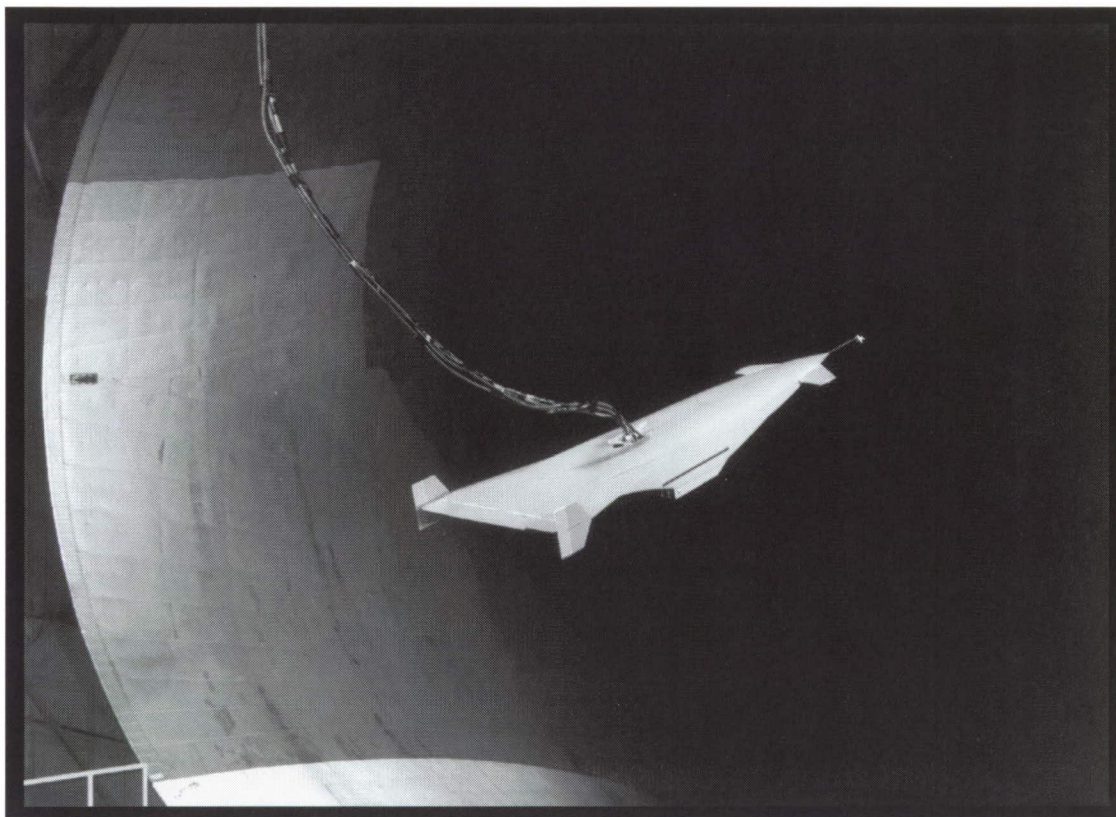
Surface pressure distributions corresponding to fuselage station 107 are shown for an angle of attack of both 30° and 50° . The agreement between the computation and the experimental data is generally good. A strong vortex is shed from the strake and is evident in the pressure distributions as a local minimum near $\theta = 135^\circ$. Also shown in the figure is the comparison between the yawing moment generated by the strake c_n as determined by experiment and computation. The computed moments are in agreement with experiment and show the correct trend with both angle of attack and Reynolds number.

The comparison with experiment indicates that the computational modeling of the complex vortical flow field is substantially correct. This validation process adds to the confi-

dence in the numerical algorithm, particularly with regard to future design applications.

(Robert T. Biedron, 42156)
Aeronautics Directorate

■ HYPERSONIC AND TRANSATMOSPHERIC VEHICLES



*Develop the critical technologies
for future hypersonic and
transatmospheric vehicles*

ORIGINAL PAGE
BLACK AND WHITE PHOTOGRAPH

PRECEDING PAGE BLANK NOT FILMED

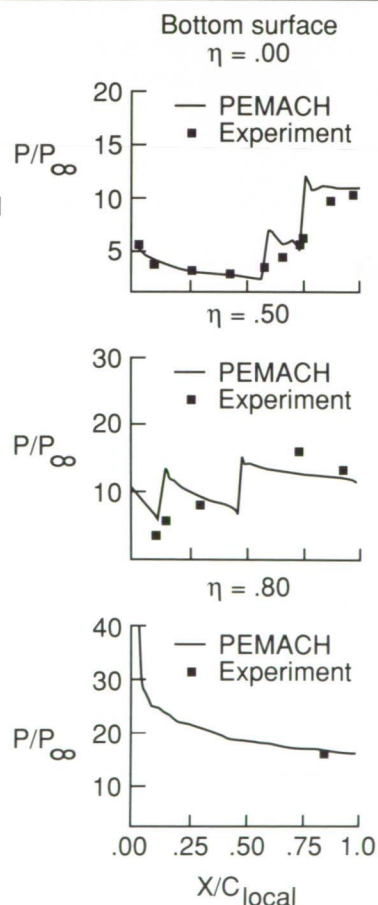
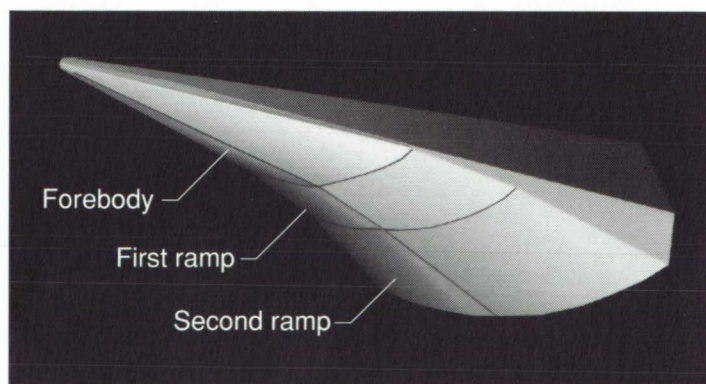
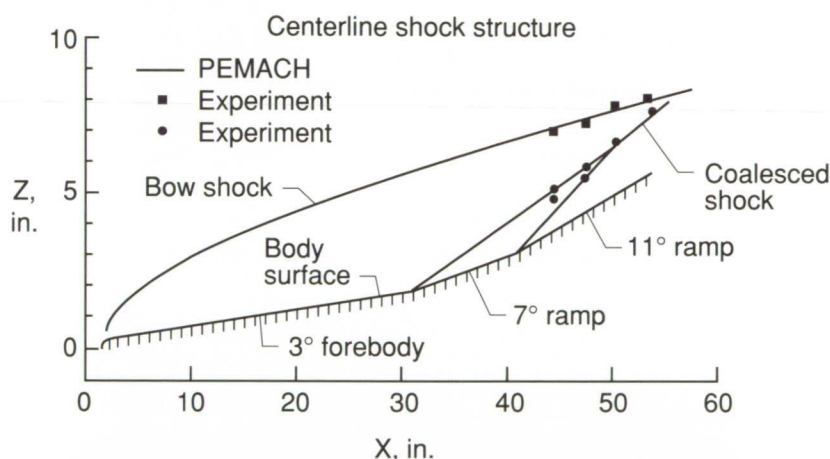
Advanced Aero-Propulsion Performance Design Tool (PEMACH)

Although great strides have been achieved in the application of computational fluid dynamics (CFD) to the evaluation and design of high-speed aerodynamic configurations, a requirement remains for rapid engineering design methods. This need is especially

required for advanced hypersonic airbreathing vehicles that have a limited design data base and which require a high degree of engine-airframe integration.

Current engineering methods for hypersonic aerodynamic analysis include Newtonian methods such as the Aerodynamic Preliminary Analysis System (APAS). These methods can accurately estimate lift and drag for

unpowered aerodynamic configurations. However, the methods do not accurately predict the aerodynamic moments nor do they have the capability to predict airbreathing powered configuration performance. Such predictions require as a minimum: blunt-body solutions, three-dimensional inviscid and viscous effects over the entire external body, inlet mass capture, inlet compression efficiency, combustor simulation, nozzle chemistry



PEMACH-computed pressure distributions and experimental data comparisons (Generic Option Number 2 inlet model, M_∞ of 12, and α of 0°).

and plume simulation, and complete wall heating analysis for actively cooled sections of the engine and vehicle.

An engineering method being developed at Langley Research Center will address all these issues. The code, PEMACH (a Practical Engineering Method for Aero-Propulsion Characteristics at Hypersonic Mach Numbers), is based on a two-dimensional method-of-characteristics. The method solves the flow over the fuselage and wings, including removal of engine mass flow, in a quasi-three-dimensional fashion. The code includes solution capabilities for either sharp or blunt leading and trailing edges and completely arbitrary planform.

Part of the method development was calibration to experimental results, as illustrated in the figure. The illustrated comparison used the experimental results from the NASP (National Aero-Space Plane) Generic Option Number 2 three-dimensional forebody-inlet model. Shown is a side view (Z versus X) of the model geometry and the shock structure at the centerline as experimentally measured and computed by PEMACH. Normalized pressure distributions (P/P_∞) along the lower surface (X/C_{local}) are compared at three different locations or η -stations: the centerline, midspan, and 80-percent span; $\eta = 0.0, 0.5$, and 0.8 , respectively. A comparison with CFD solutions verifies the accurate prediction of mass capture, and comparisons with unpowered aerodynamic test results from the NASP Test Technique Demonstrator (TTD) model verify the accurate prediction of pitching moment over a large variation in angle of attack.

A preliminary version of PEMACH has been released and is currently being used for aerodynamic design (lift, drag, and moment) and analysis of hypersonic vehicles. Work is continuing to efficiently model the inlet,

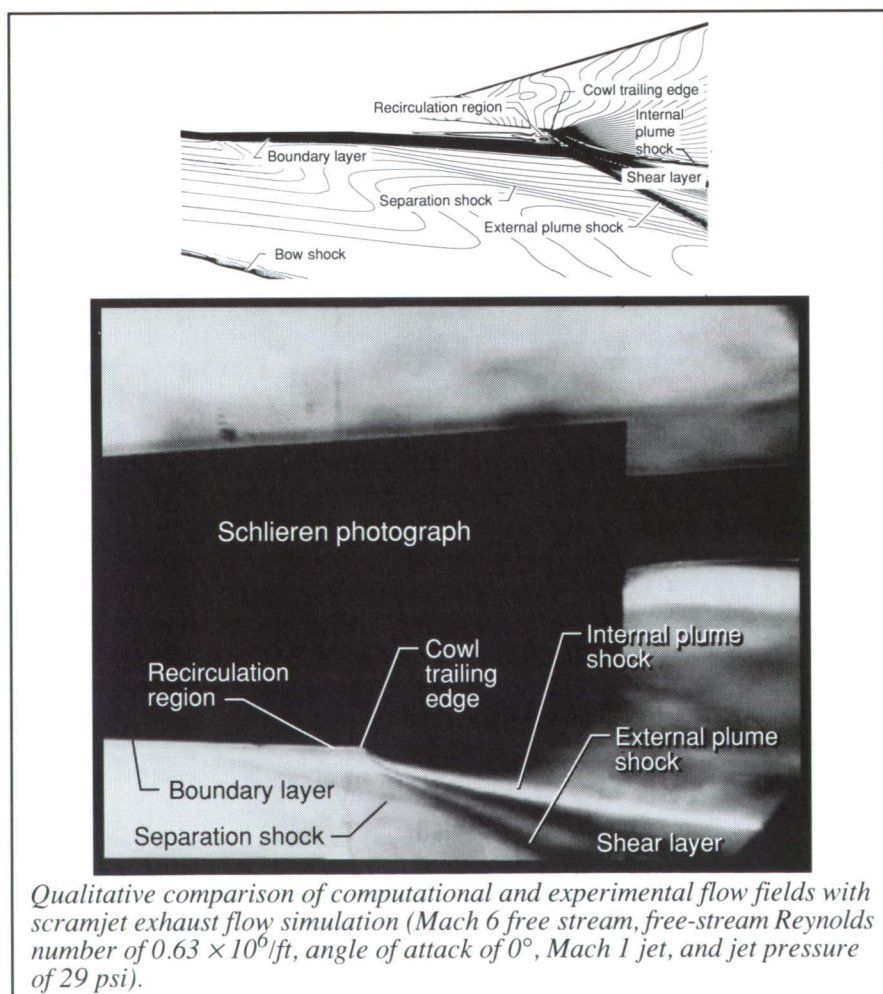
combustor, and nozzle flows to fully couple the boundary layer to the three-dimensional effects and to include boundary-layer transition prediction. (Suresh L. Goradia and Abel O. Torres, 43736) Aeronautics Directorate

Prediction of Hypersonic, Airbreathing Vehicle Aftbody Flow Field Under Simulated Powered Conditions

Because of restrictions associated with small-scale wind-tunnel tests of powered hypersonic airbreathing

(PHA) models (the word "powered" refers to simulated scramjet exhaust flow), CFD predictions for this type of problem are receiving much attention. However, code calibration for these types of flows is essential before CFD codes can be used as analysis tools.

An investigation was undertaken to qualitatively assess the General Aerodynamic Simulation Program (GASP) of Robert Walters, Virginia Polytechnic Institute and State University, for PHA model flow field prediction. During a test in the 20-Inch Mach 6 Tunnel on a PHA model, schlieren and video photographs of the aft region of the vehicle were obtained at two tunnel conditions and two simulant exhaust gas plenum pressures.



Initial two-dimensional Euler solutions obtained for all four cases using GASP did not accurately predict details of the external flow. Assuming that the flows were affected by viscous effects, parabolized Navier-Stokes (PNS) solutions for these cases were obtained.

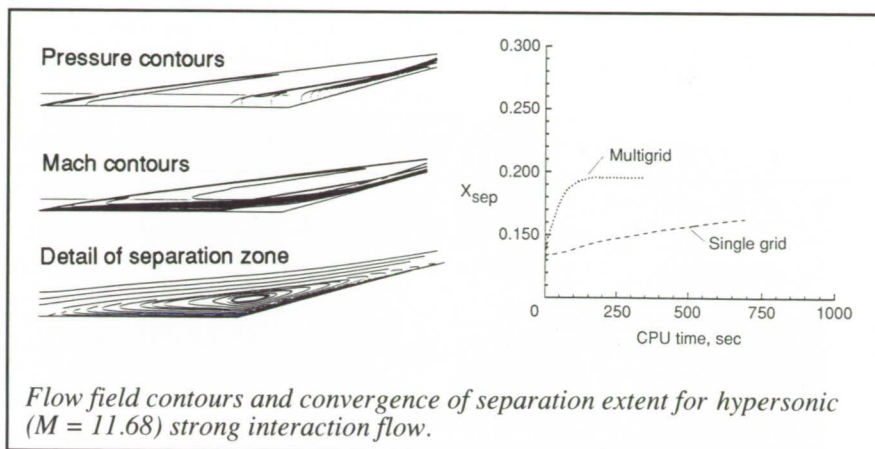
Comparisons of PNS solutions with schlieren photographs indicated improved agreement of the salient flow-feature locations over the Euler solutions. For one case, as shown in the figure, a shock emanates from the outside cowl boundary layer and feeds into the external plume shock. The high pressure inside the nozzle probably causes reverse flow in the boundary layer outside the cowl. This reverse flow subsequently causes vortex formation and a separation of the boundary layer, which is large enough to produce a shock. Because the PNS equations cannot predict streamwise separation, a thin-layer Navier-Stokes (TLNS) solution was obtained using GASP. As the figure shows, a recirculation region was predicted and was of sufficient size to cause a separation shock.

Based on these results, GASP was shown to be capable of simulating the afterbody flow associated with PHA models, thus lending credibility to the computational method for this class of problem.

(Lawrence D. Huebner, 45583)
Aeronautics Directorate

Multigrid Algorithm for Hypersonic Flow

A multigrid algorithm that is applicable to the simulation of viscous hypersonic flows has been developed for efficient solutions of the Navier-Stokes equations. The multigrid method uses a series of coarser meshes



Flow field contours and convergence of separation extent for hypersonic ($M = 11.68$) strong interaction flow.

to accelerate the solution on the fine mesh and enables the overall solution time to scale directly on the number of grid points in the mesh. The multigrid method has been used to improve the efficiency of viscous flow solutions for subsonic and transonic flows, but little progress has been made for hypersonic flows because of the presence of strong shocks and substantial regions of separated flow.

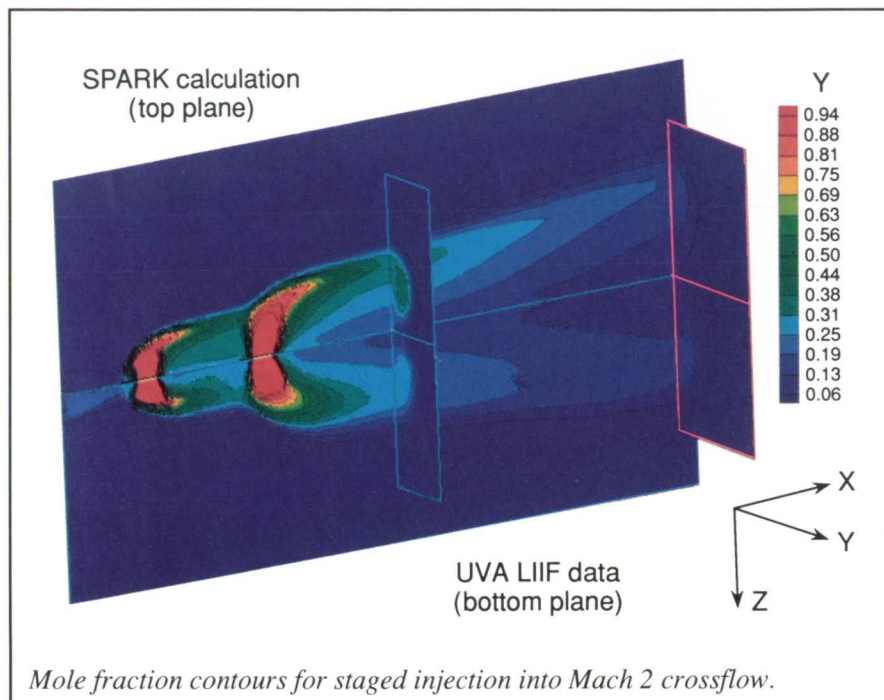
The present algorithm uses upwind-biased spatial differencing for the convective and pressure terms and central differencing for the shear stress and heat-transfer terms. An implicit spatially factored scheme is used to advance the solution in time on a given mesh. Special care is taken in both the time advancement and correction stages of the Full Approximation Scheme algorithm to maintain positivity of the thermodynamic variables.

An application of the algorithm to the laminar strong interaction flow over a compression ramp at a Mach number of 11.68 is shown. Contours of pressure and Mach number and streamlines in the vicinity of the separation zone are shown. The separation extent is determined by an upstream propagation of information through the subsonic part of the boundary layer. As shown in the variation of separation extent with

computer time for the multigrid and single grid schemes, an order of magnitude improvement in efficiency occurs with the multigrid scheme. (James L. Thomas and David H. Rudy, 42146)
Aeronautics Directorate

CFD Code Validation for Supersonic Combustor Flow Fields

Experiments of mixing in generic supersonic combustors were conducted in a nonreacting, room-temperature wind tunnel constructed under grant at the University of Virginia. Air, seeded with iodine molecules, was injected into a Mach 2 flow for several configurations. Laser-Induced Iodine Fluorescence (LIIF) techniques have been developed and calibrated for nonreacting, compressible flow fields at the University of Virginia. These nonintrusive optical techniques provide detailed data bases that can serve as benchmarks for computational fluid dynamics (CFD) codes. Two flow fields have been investigated experimentally using these techniques: Mach 2 flow over a rearward-facing step and staged injection behind a rearward-facing step into a Mach 2 free



stream. The LIIF techniques have been used to make detailed pointwise measurements of pressure, temperature, and two components of velocity. A LIIF technique has also been developed to make planar measurements of the mole fraction of the injectant. This data set has been selected by the Joint Army, Navy, NASA, Air Force (JANNAF) scramjet combustor modeling group as a benchmark case for CFD codes.

In a cooperative effort, numerical experiments have been conducted under support from the National Research Council with the SPARK Navier-Stokes code developed at Langley Research Center. Calculations performed with the SPARK code have been used to examine the sensitivity of the solution to grid resolution and turbulence modeling. Shown in the figure are calculated and measured mole fraction contours, respectively, along the centerline of the channel. The good overall agreement observed between the measurements and the calculations is a major milestone in

validating the SPARK computer code for transverse jet flow fields.
(Dean R. Eklund, 46248, and G. Burton Northam)
Aeronautics Directorate

Effect of Oxygen Dissociation on Hypersonic Combustion

To accomplish its single-stage-to-orbit mission, the National Aero-Space Plane (NASP) must employ the airbreathing supersonic combustion ramjet (scramjet) engine. Therefore, a knowledge of fuel-air mixing and combustion performance to near-orbital flight speeds is a critical issue for the NASP Program. Experimental data are required to anchor computational fluid dynamics (CFD) methods that will be used for scramjet design and performance prediction at the hypervelocity speeds.

Pulse facilities, such as reflected-shock tunnels and expansion tubes

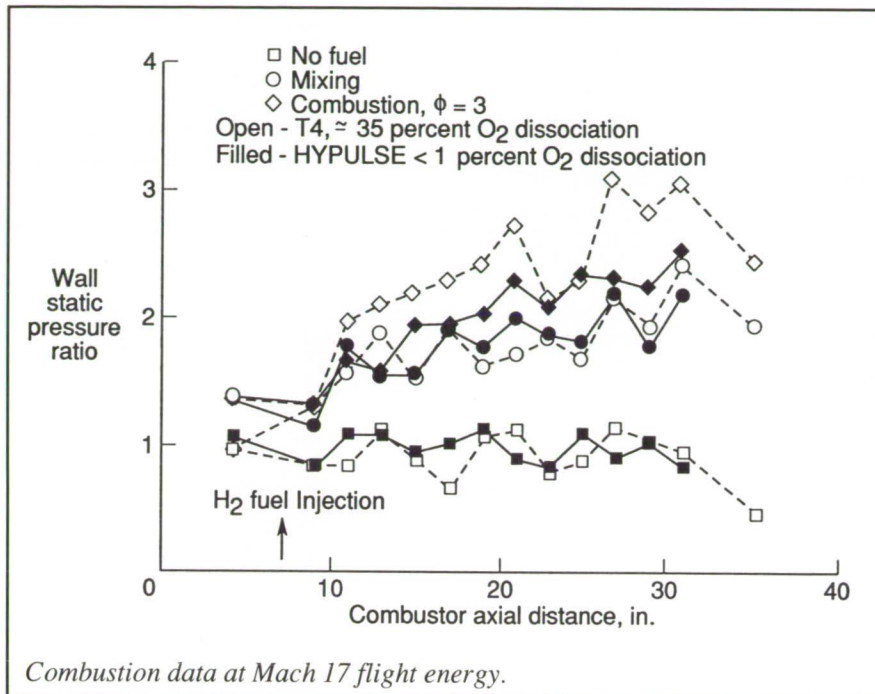
(which have useful test times on the order of a millisecond), represent the only practical means available to duplicate the energy (velocity) of flight beyond Mach 10 to 12. The free-piston-driven reflected shock tunnel T4, which has been operating at the University of Queensland in Australia since 1987, can easily produce flow at an energy level equal to Mach 17 flight. However, because energy is added to the test gas at rest, approximately 35 percent of the molecular oxygen is dissociated to atomic oxygen, and this composition is essentially constant as the test gas is expanded to the hypervelocity test condition. For comparison, no significant oxygen dissociation is expected to exist in the flow entering a scramjet at Mach 17 conditions in flight. An expansion tube, which can produce Mach 17 energy flow without dissociating the oxygen in air, provides an alternate means of simulating the same flight condition. In the expansion tube, much of the energy is added to the moving test gas in an unsteady expansion process. The former Expansion Tube at Langley Research Center has been reactivated at the General Applied Science Laboratories, Incorporated (GASL), Ronkonkoma, New York, under the name HYPULSE.

Preliminary hydrogen mixing and combustion data have been obtained in T4 and HYPULSE at simulated Mach 17 flight energy conditions using identical, cylindrical combustor models. The relative pressure data are shown in the figure. Data without hydrogen injection (filled and open square symbols) show nearly constant pressure over the length of the combustor. Mixing-only data, with injection of hydrogen into nitrogen (filled and open circular symbols), show a distinctly similar pressure rise in both facilities. Combustion data, with injection of hydrogen into air (filled and open

Numerical Modeling of Strongly Coupled Fluid-Combustion Phenomenon

In supersonic combustion ramjet engines, a strong interaction exists between the mean flow and the combustion processes. Of particular interest is the phenomenon of detonation as it pertains to detonation-wave engines. This class of engine has the potential to significantly reduce the length of time required to achieve complete combustion of fuel and air. Numerical simulations are used to provide insight into the mechanisms that control the strongly coupled combustion process.

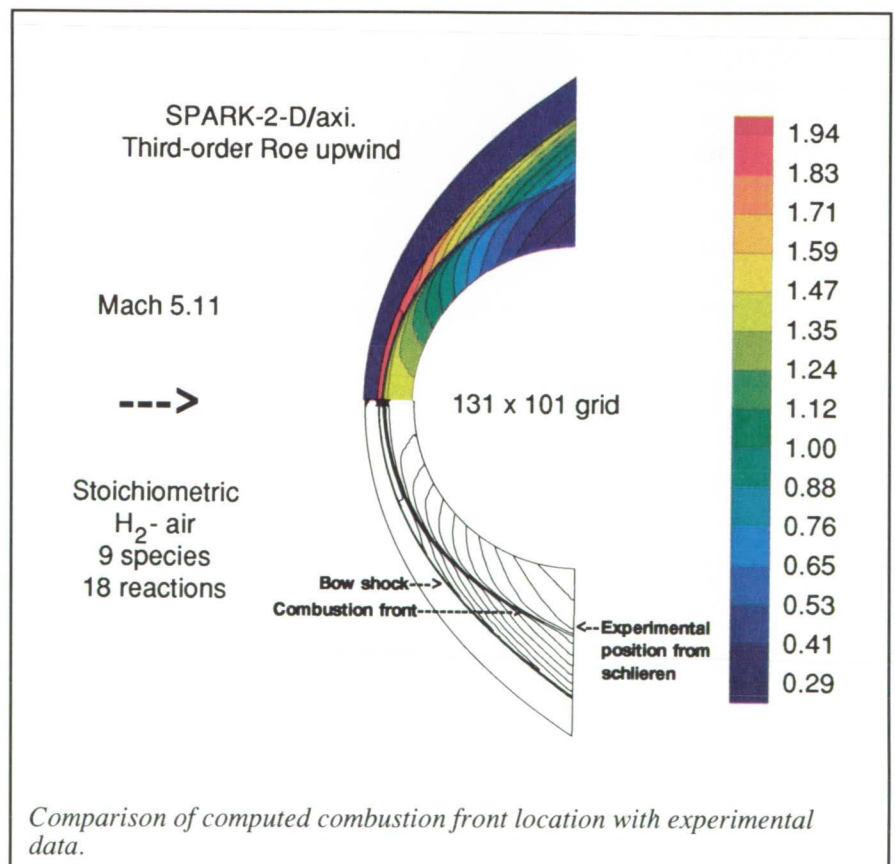
A computer program has been developed that solves the equations governing a multicomponent chemically reacting flow. This code employs



diamond symbols) at a fuel equivalence ratio of 3, show that the pressure rise obtained in the dissociated T4 flow was nearly twice that obtained in the undissociated HYPULSE flow (filled symbols of all shapes). The larger pressure rise in the T4 combustion data (open diamond symbols) is believed to be a result of the recovery as sensible energy of the energy tied up in dissociation during the reaction of the injected hydrogen with the atomic oxygen to form water. The effect is to increase the apparent heat release of the fuel compared with undissociated air leading to a larger-than-flight observed effect of combustion on pressure and thrust in the ground simulation using the reflected shock tunnel. The implications of these data on NASP performance remain to be determined from more extensive experimental investigations and from detailed comparisons with computational simulations.

(G. Y. Anderson, R. C. Rogers, and R. W. Guy, 46239)

Aeronautics Directorate



advanced numerical methods to improve resolution and decrease numerical smearing of the shock and combustion fronts. The numerical method is based on the Roe flux difference splitting procedure for multicomponent fluids. Higher order accuracy is obtained through the use of flux limiters.

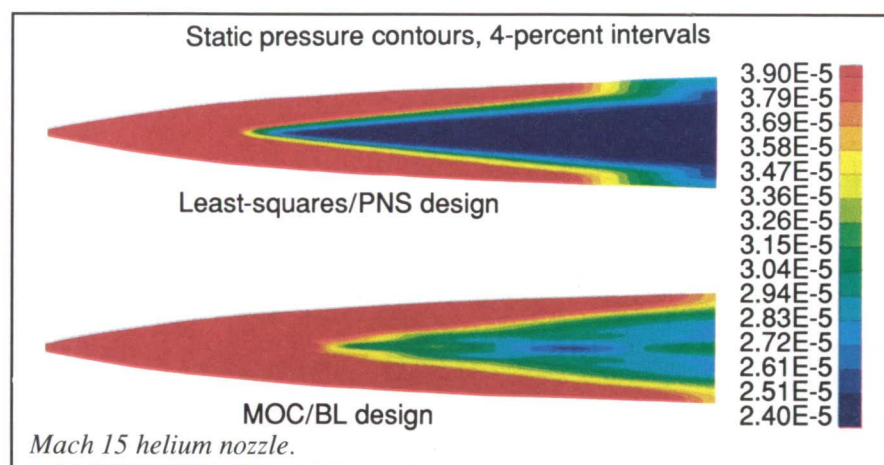
Validation of the numerical method is obtained through comparison with experimental data. The figure shows a comparison of computed density contours with an experimentally determined combustion front position. The experimental and computational results are for an axisymmetric body flow at Mach 5.11 in a ballistic range containing a premixed stoichiometric air-hydrogen gas. The bow shock created by the body causes a temperature rise that generates a combustion front downstream of the shock. The combustion front is coupled with the shock near the forward-most position of the body because of the subsonic flow caused by the normal shock. The locations of the shock and combustion fronts are very sensitive to grid resolution and to the amount of numerical dissipation. The agreement between experiment and data is very good and demonstrates that the computer code has the potential to be a useful tool in increasing the understanding of these types of flows. (Jeffery A. White, 47967) Aeronautics Directorate

CFD-Based Aerodynamic Design of Hypersonic Wind-Tunnel Nozzles

A new procedure, which unifies the best of current classical design practices, computational fluid dynamics (CFD), and optimization procedures,

has been demonstrated for designing the aerodynamic lines of hypersonic wind-tunnel nozzles. The new procedure can be used to design hypersonic wind-tunnel nozzles in which the classical procedure (based on the method-of-characteristics (MOC) and the boundary-layer (BL) correction) has been shown to break down. An efficient CFD code, which solves the parabolized Navier-Stokes (PNS) equations using an explicit upwind

This new procedure has been demonstrated by designing a Mach 15 helium nozzle. In the figure, this nozzle, designed using the new CFD-based procedure, is compared to a nozzle designed with the method-of-characteristics/boundary-layer correction method. The CFD-based nozzle design reduced the fluctuations of static pressure to less than ± 2 percent for the uniform core region. This reduction is a significant improvement

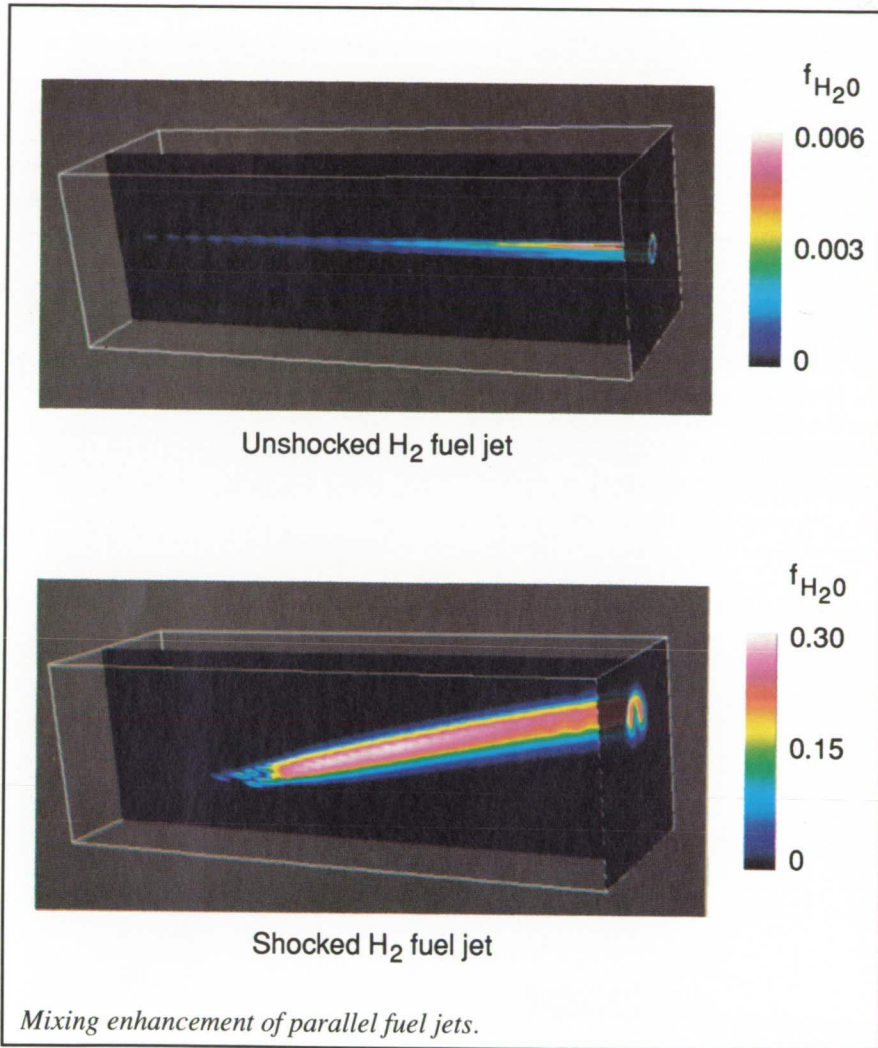


algorithm, is coupled to a least-squares (LS) optimization procedure. An LS problem is formulated to minimize the difference between the computed flow field and an objective function, consisting of the centerline Mach number distribution and the exit Mach number and crossflow velocity profiles. The aerodynamic lines of the nozzle are defined using cubic splines, the slopes of which are optimized with the design procedure. The advantages of the new procedure are that it eliminates the use of the method-of-characteristics for determining the nozzle contour and it automatically compensates the nozzle contour for viscous effects as part of the unified design procedure. Initial programming and validation have been completed on a computer code for implementing the new design procedure.

over the classically designed nozzle that had fluctuations of static pressure greater than ± 30 percent for the uniform core region. The computed flow field for the least-squares/parabolized Navier-Stokes (LS/PNS) designed nozzle demonstrates a significant improvement over the classically designed nozzle. (John J. Korte, 46920) Aeronautics Directorate

Fuel-Air Mixing Enhancement by Jet-Shock Interactions

High-speed propulsion devices, such as the supersonic combustion ramjet or scramjet, will require enhanced fuel-air mixing in order to



through an oblique shock of 10° produced by a wedge. When the low-density hydrogen jet passed through the shock, the pressure field and density field became misaligned, bifurcating the jet and producing a vortex pair. As a result, mixing was significantly enhanced, and large amounts of water were produced through reaction of the hydrogen and air.

The figure shows the resulting water mass fraction along the center plane downstream of the shock-jet interaction. The shocked fuel jet shows a large cross section of water with a peak mass fraction of 25 percent. The resulting vortex pair can also be seen at the outflow station in the figure. When the hydrogen jet is not processed by the shock, little mixing of fuel and air results. Only a narrow annular ring of water, also shown in the figure, is produced with a water peak of 0.6 percent. So, as can be seen, the fuel injector design results in a significantly larger amount of mixing and chemical reaction that produces a marked increase in combustion efficiency. The combustion efficiency of the unshocked fuel jet is only 0.4 percent, whereas the shocked fuel jet results in a combustion efficiency of 72 percent.

obtain the desired combustion efficiency. A computer program has been developed which solves, using an accurate numerical algorithm, the equations governing the mixing and chemical reaction of a multicomponent mixture in combination with physically realistic chemical kinetics models to describe combustion processes occurring in configurations of interest. The code was validated against experiments involving both nonreacting and reacting flow fields and then applied in studies of combustor high-speed engine flows.

Recent research has been directed toward the optimization of a scramjet

combustor and, in particular, the efficiency of fuel-air mixing and reaction in the engine. Mixing is significantly reduced in this engine as the combustor Mach number increases with flight Mach number, and mixing enhancement is required to achieve a sufficient degree of combustion efficiency. Because of this difficulty, alternate combustor fuel injector configurations were studied to evaluate their potential for producing an improved degree of mixing and reaction. A fuel injector configuration, using parallel injection, was considered to improve fuel-air mixing. In this configuration, a gaseous hydrogen fuel jet, coflowing with air, was processed

These numerical simulations provide an improved insight of the mechanisms controlling high-speed mixing and combustion in supersonic reacting flows. Using knowledge gained from these basic simulations, techniques can be developed for enhancing mixing and reaction in supersonic combustors, thus improving the overall level of combustion efficiency in these devices. Work is now under way to optimize the degree of enhancement that can be achieved from this and other fuel injector configurations.

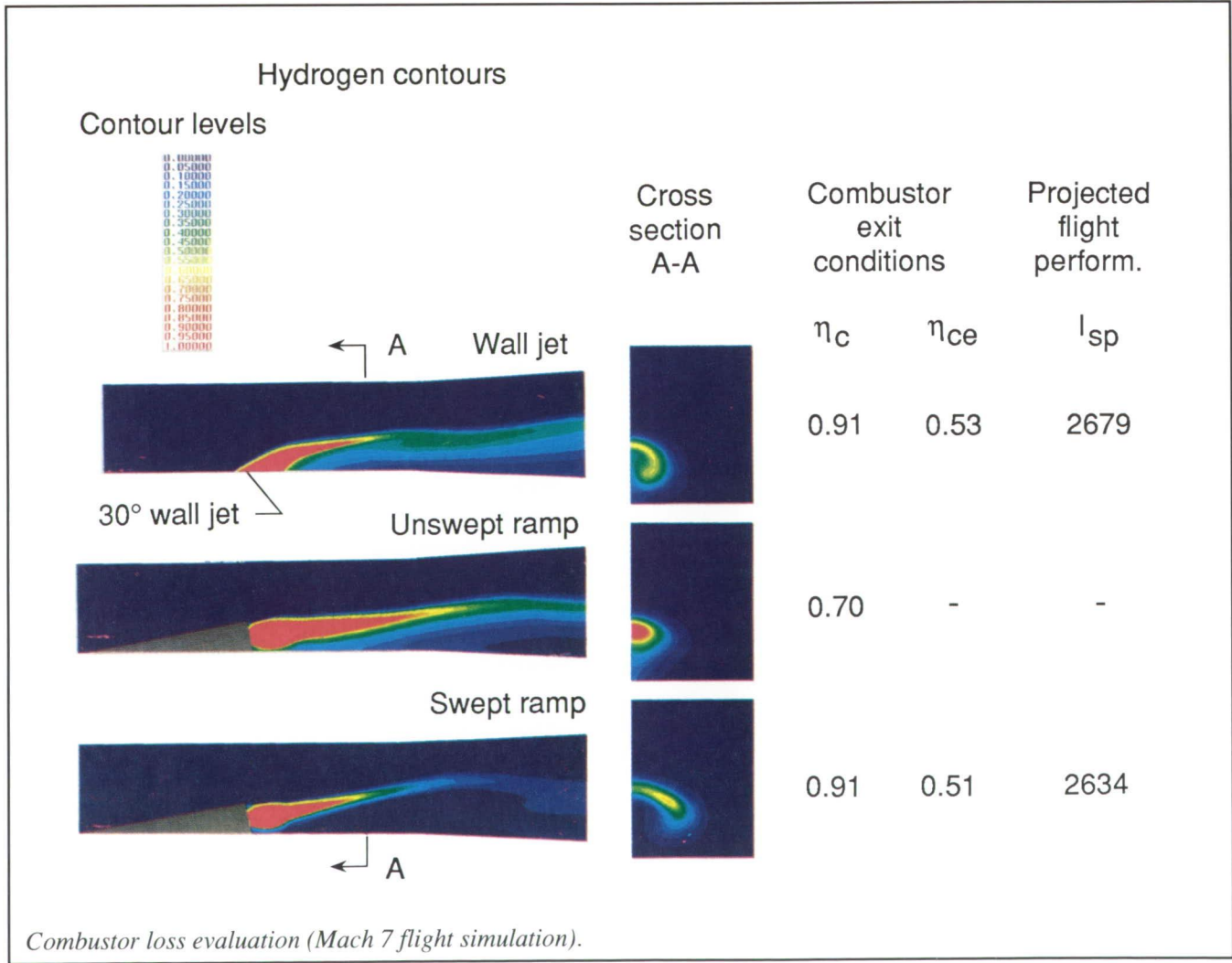
(J. Philip Drummond, 42298)
Aeronautics Directorate

Scramjet Combustor Loss Evaluation

Flow losses in supersonic mixing and reacting flows are caused by a combination of coupled complex physical phenomena including shocks, viscosity, mixing, Rayleigh losses, and wall pressure integrals. Although some of these losses are unavoidable, for efficient high-speed scramjet performance, a method of quantification of these losses is required. Flow losses are impacted by many combustor and fuel injector design parameters. Therefore, the method selected must be capable of evaluating the entire combustor flow

field and, hopefully, will include sufficient flexibility to evaluate individual contributors to the performance loss. The method selected for quantification of the scramjet combustor losses is the engine thrust potential expressed as the combustor effectiveness, which is a measure of the useful work potential based on the combustor inflow with ideal fuel injection, mixing, and combustion. Numerical procedures have been developed at Langley Research Center to perform this optimization evaluation using the excellent detail provided by three-dimensional computational fluid dynamics solutions of reacting combustor flows.

The method developed includes a complete and consistent one-dimensionalization of the three-dimensional flow field generated by the computational fluid dynamics solution, one-dimensional evaluation of ideal combustor thrust (no viscous, heat, shock wave, or Rayleigh losses), and evaluation of combustor work potential. This method is included as a separate subroutine for postprocessing of numerical results and can be utilized to provide both overall and axial distributions of combustor effectiveness, the latter being useful in identification of the causes of combustor losses.



The figure illustrates an application of this methodology to determine combustor effectiveness η_{ce} and resulting engine specific impulse I_{sp} for three fuel injectors, one flush wall injector, and a swept and unswept ramp injector. The combustor exit combustion efficiency η_c for the flush wall and swept ramp injectors was identical and significantly higher than that for the unswept ramps. This good performance is attributed to the large-scale axial vorticity induced by these two injector concepts; this vorticity is clearly visible by the swirl imparted to fuel jets in the near-field, cross section A-A. The combustor effectiveness (engine thrust potential) at the combustor exit is slightly higher for the flush wall injector. The analysis of the axial distribution of combustor effectiveness illustrated that much of the loss incurred by the ramp drag was overcome by rapid initial combustion, but at the combustor exit, the flush wall injectors provided higher thrust potential. In terms of engine specific impulse, the flush wall injector would provide approximately a 50-sec improvement over the swept ramp injector.

These results are presented as a demonstration of this enhanced numerical capability, not as a true assessment of competing fuel injector concepts. To assess competing concepts, each concept must first be optimized to a particular combustor configuration by performing trade studies. These optimized configurations then can be compared to select the best concept. This work was done on a grant with the University of Missouri-Rolla.

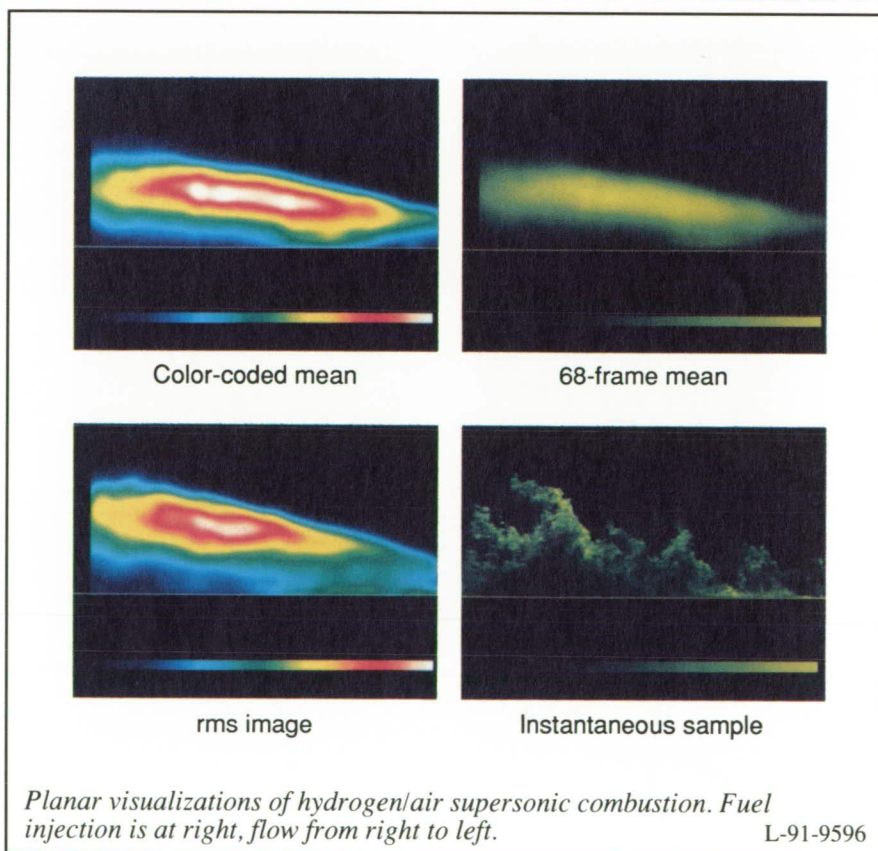
(David W. Riggins and Charles R. McClinton, 46253)
Aeronautics Directorate

Instantaneous Planar Visualization of Reacting Supersonic Flow Using Silane Seeding

A new flow visualization technique for supersonic reacting flow has been developed and demonstrated in a scramjet combustor model. The technique is based on Mie scattering of laser light off particles produced by the combustion of gaseous silane (SiH_4). One of the products of silane and oxygen combustion is solid phase silica (SiO_2). The silica particles that form in the flow are small enough (approximately 0.1 μm) to follow even high-speed supersonic flows. A frequency-doubled Nd:YAG pulsed laser sheet was used to illuminate the particles, and the Mie scattering from them was imaged on a Charged-Coupled Device (CCD) camera

through filters that rejected the natural luminosity of the flame.

The technique was demonstrated using a silane and hydrogen mixture as the fuel in a scramjet combustor model installed in the Direct-Connect Supersonic Combustion Test Facility. The figure shows four views of the same portion of the combustor (approximately a 4-in. field of view). In each view, the free-stream flow is from right to left at Mach 3 with a total temperature of approximately 1670 K. Fuel was injected just upstream of the right edge of each image. The top two images show the mean Mie scattering signal that is a measure of the combustion progress in a given fluid element. At the lower left is an rms (root mean square) image indicating where variations in signal occur, and at the lower right is a single sample from the series of images used to generate the



rms. This image shows that large-scale, organized turbulence structures dominate the fuel/air mixing flow and probably the combustion process.

(Michael W. Smith and G. Burton Northam, 46248)

Aeronautics Directorate

Effects of Thermal Gradients on Structural Vibration Frequencies

During flight, the National Aero-Space Plane (NASP) will be subjected to severe aerodynamic heating that will probably cause steep thermal gradients on the vehicle structure. Historically, very little research has been done to predict the effects that such large thermal gradients might have on aeroelastic characteristics. The objective of this work has been to correlate analysis predictions with experimental results for a wing-like built-up structure.

An aluminum wing-box model fabricated with spars, ribs, and curved skin panels was mounted cantilevered

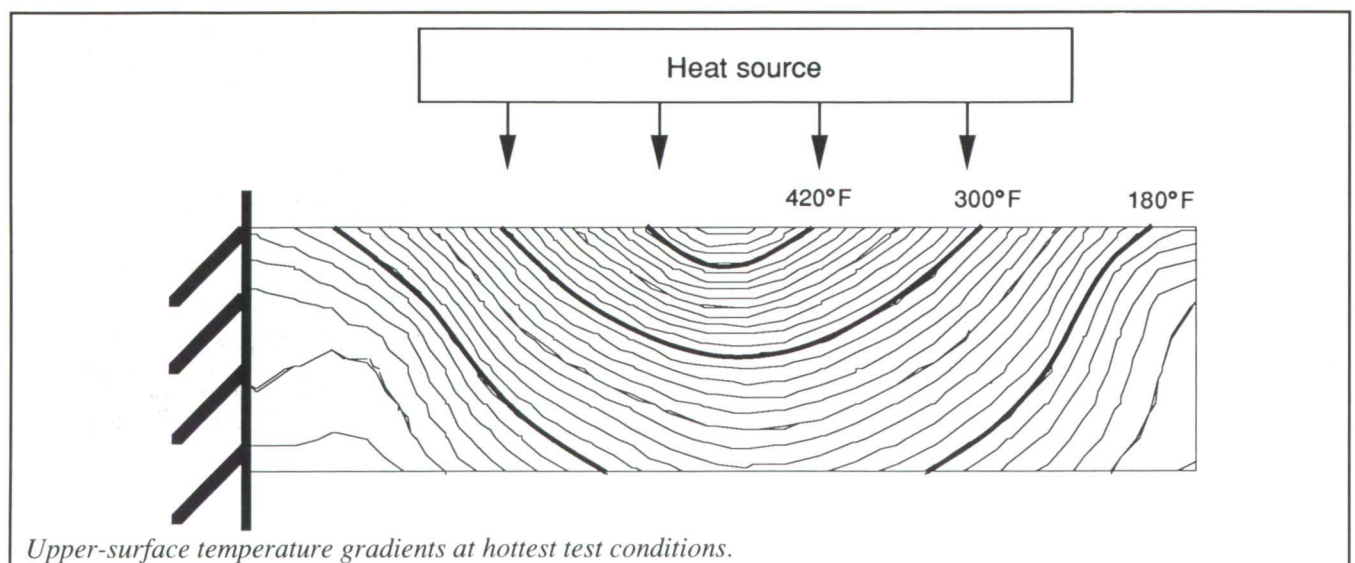


Test arrangement.

L-90-14613

from a rigid backstop as shown by the photograph presented in the first figure. A resistance rod heater was used to focus intense heating on the model leading edge. The temperature distribution on the model and the structural mode frequencies for the model were measured throughout a heat-up and cool-down cycle. The temperature gradients for the hottest

test condition are shown on the contour plot in the second figure. The measured temperature distribution data were incorporated into a thermoelastic analysis procedure and used to predict structural mode frequencies. The analysis procedures automatically account for the changes in material properties at elevated temperatures and the effects of internal stresses on

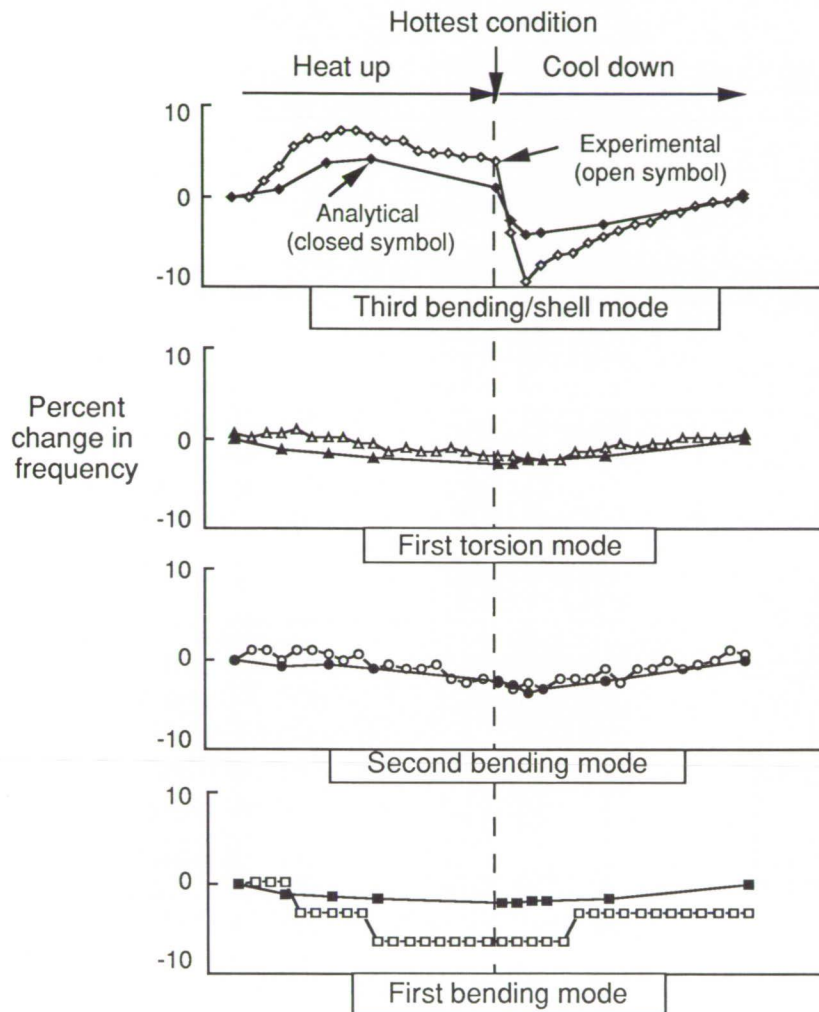


Upper-surface temperature gradients at hottest test conditions.

Aileron Buzz Characteristics for Several NASP Wing Configurations

Aileron buzz is a term used to describe potentially violent, single-degree-of-freedom aileron oscillations that occur primarily at transonic speeds. Earlier research suggests that this phenomenon may be related to the formation of shock waves on the wing surface. This study was performed to determine if aileron buzz would occur on generic National Aero-Space Plane (NASP) wing configurations and, if so, to observe how variations in geometry would affect the occurrence or behavior of buzz. Four delta-wing models with full-span ailerons were designed and built for testing in the Transonic Dynamics Tunnel (TDT). The delta-wing geometries selected were representative of NASP design concepts being studied. A photograph of one of these models, with a splitter plate, is shown mounted on the tunnel sidewall in the first figure. The four models consisted of two planform variations and two airfoil thicknesses for each planform. Each of the models was tested first for conventional flutter at an atmospheric tunnel stagnation pressure at subsonic speeds with dynamic pressures up to 200 psf. Several additional tests were then made at various subatmospheric stagnation pressures to determine aileron buzz boundaries in the transonic speed range.

Single-degree-of-freedom aileron oscillations, both stable and unstable, were observed at transonic speeds for each model. The Mach number and dynamic pressures at which divergent oscillations occurred are indicated in the second figure. Flutter produced by the coupling of the aileron pitch mode and the wing first bending mode occurred at Mach numbers below buzz



Effect of thermal gradients on vibration frequencies.

stiffness resulting from nonuniform thermal expansion.

The data presented in the third figure show how measured (experimental) and predicted (analytical) frequencies varied for four structural modes over the entire heat-up and cool-down cycle. The results indicate that the trends predicted analytically are correct, but the predicted frequency changes are often less than those measured. This experimental investigation provides confidence

that recently developed finite-element analysis procedures can provide reasonable predictions of aerothermoelastic characteristics of aircraft-type structures subjected to nonuniform heating.

(Charles V. Spain and Kathleen A. Conley, 41265)
Structures Directorate



Delta-wing model for aileron buzz testing.

L-89-11313

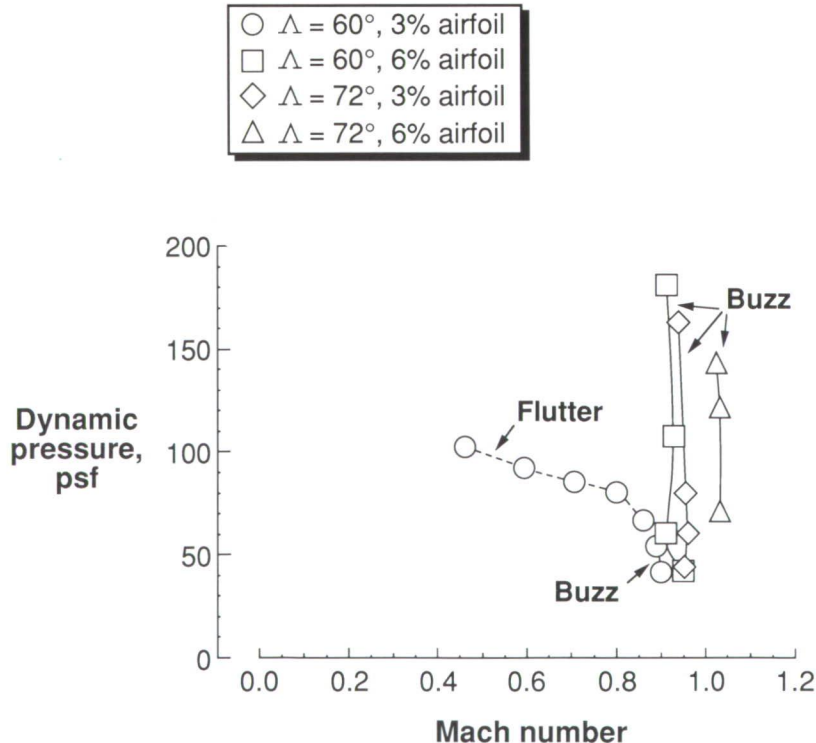
onset for one configuration. Increasing the wing leading-edge sweep appeared to increase the Mach number at which divergent aileron oscillations occurred. Increasing the airfoil thickness had a similar effect. At lower dynamic pressures, the onset of buzz occurred gradually with limited-amplitude oscillations observed prior to divergence. At higher dynamic pressures, the onset of buzz was more explosive and less predictable. In one instance, the aileron was lost. This study provides some experience for estimating the potential for buzz on the actual NASP flight vehicle.

(Ellen P. Bullock, Charles V. Spain, and David L. Soistmann, 41258)
Structures Directorate

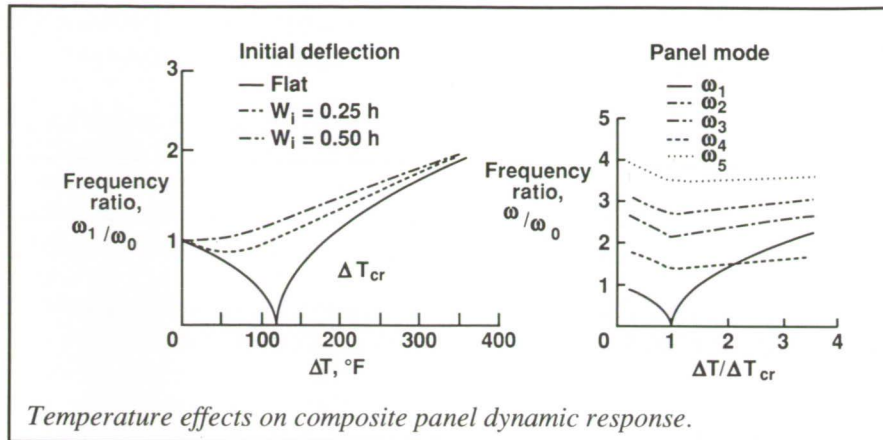
Dynamic Response of Initially Deformed Composite Plates Using Finite Elements

The recent push for the development of hypersonic aircraft has created a need for the analysis of structures at very high temperatures. The dynamic response of aircraft skin panels depends not only on the imposed thermal and mechanical loads but also on any initial deformations. The effect of these parameters on the response must be well understood in order to maximize the fatigue life. The purpose of this work is to investigate the simultaneous effect of large initial and thermal deformations and temperature-dependent material properties on the free vibration of composite panels.

A finite-element formulation has been developed to analyze the effects of moderately large initial deflections and large thermal deformations on the frequency response of these panels. The von Kármán nonlinear strain-displacement relations are used to



Measured buzz boundaries.



Temperature effects on composite panel dynamic response.

derive the stiffness matrices, and the principle of virtual work is applied to obtain the equations of motion. The resulting system is solved in a two-step procedure. First, a Newton-Raphson iterative technique is used to solve the incremental static system for the thermal deformation based on a given initial deflection and temperature distribution. This result is then used in the eigenvalue problem to solve for the natural frequencies and vibration modes of the panel. The ability exists for a completely arbitrary temperature distribution.

Studies were carried out on a 12-in.-square graphite/epoxy panel with an antisymmetric $(-30/30)_2$ lay-up having a length-to-thickness ratio of 100 (i.e., a thin plate). Simply supported boundary conditions were imposed on all sides with immovable in-plane conditions. The temperature distribution used in these studies was uniform.

The left figure compares the fundamental frequency ratios of the panel with various initial deflections. It shows that as the initial deflection increases, the decrease in frequency because of a temperature rise vanishes. This is because of the stiffening effect of the linear and first-order nonlinear terms with increasing initial deflections. The right figure presents the

frequency ratio of an initially flat panel in both the pre- and postbuckled configurations. The fundamental frequency goes to zero at the critical temperature because the stiffness of the panel vanishes. The other frequencies exhibit a similar behavior, but they are not as sensitive to the increasing temperature in the postbuckled range.

Future work includes modifications of the formulation to analyze the effect of acoustic loads. The forced vibration response of these panels from random acoustic loading can then be analyzed and compared with experimental data obtained from the Thermal Acoustic Fatigue Apparatus (TAFA) at Langley Research Center. The application of this analysis to hypersonic vehicle design will aid in maximizing the fatigue life.

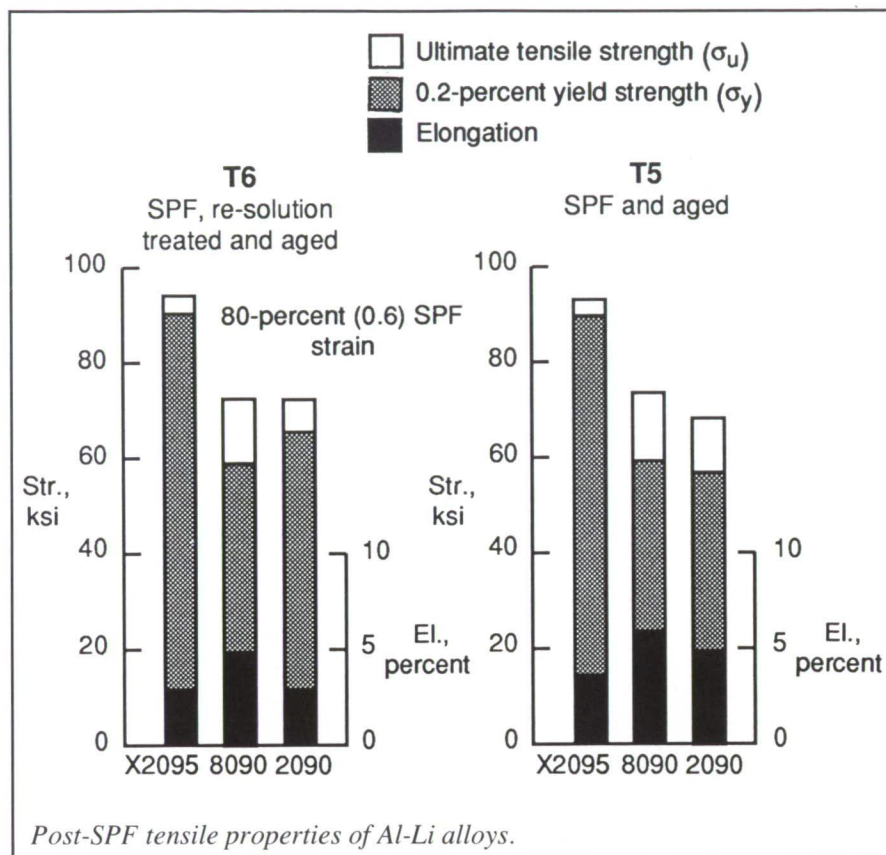
(Stephen A. Rizzi, 43599)
Structures Directorate

Influence of Post-Forming Processing on Tensile Properties of Superplastic Al-Li Alloys

The use of built-up structures for future cryogenic tank fabrication is an approach being considered in the

National Launch System Program. Among the activities, superplastic forming (SPF) of aluminum-lithium (Al-Li) alloys is being evaluated for manufacturing the stiffener components that impart structural stability to the tank skin. In this particular portion of the program, the effect of thermal processing on the tensile properties of typical SPF structural components is being addressed. Standard thermal processing practices for Al-Li SPF components normally include air cooling from the forming temperature, followed by heat treatment to place the material in a peak strength condition (T6). This usually involves solution treatment at a temperature the same as, or higher than, that employed for forming the components, followed by cold water quenching. A lower temperature age hardening treatment is subsequently used to place the material in the T6 temper.

The application of SPF technology to built-up structures will require cost-effective fabrication of structurally efficient skin stiffener components to close, reproducible tolerances. A reduction in fabrication costs may be realized if post-SPF thermal processing operations can be streamlined. Specifically, the potential to reduce the number of processing steps exists if placing the components in a T5 temper can be shown to be acceptable. This alternate thermal processing involves cold water quenching directly from the SPF die, followed by an age hardening treatment to maximize strength, thus eliminating the solution treatment stage for T6 processing. Additional benefits of this approach may be a reduction in the amount of component warpage associated with multiple cooling operations and a decrease in surface depletion of alloying elements associated with reduced exposure to high temperatures. However, the elimination of the solution treatment stage will be feasible only if it can be



demonstrated that the modified processing route is not detrimental to mechanical properties.

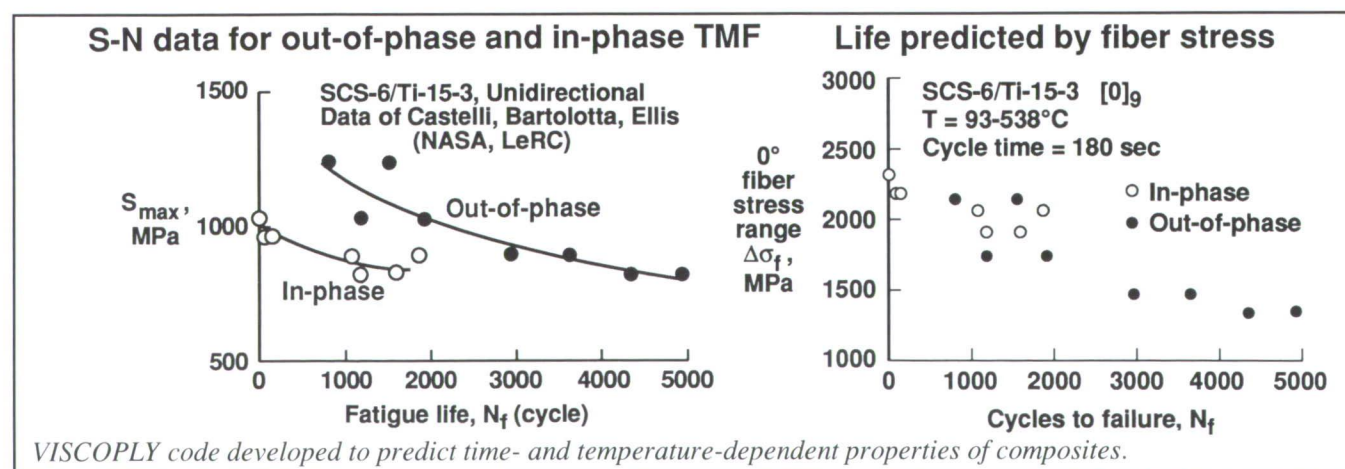
The figure represents a summary of an extensive test matrix designed to assess the differences in the tensile properties between a T5 and a T6 temper. The data compiled for the

three commercially available Al-Li alloys, X2095 (formerly Weldalite™ 049), 8090, and 2090, are presented as a function of temper. The tests were performed on material extracted from SPF components produced from sheet with a starting thickness of 0.090 in. The results are for material that had undergone a superplastic strain of

approximately 80 percent, which is representative of the upper level of forming strain required for a typical stiffener component. It is apparent from the ultimate tensile strength σ_u , yield strength σ_y , and tensile elongation El data presented that there is no significant degradation in the tensile properties of the materials on replacing the T6 with a T5 temper condition. When combined with the inherent reduced density of these alloys, these data represent a considerable improvement in specific properties compared with conventional Al alloys. Ongoing activities are concerned with microstructure/property correlations and also with addressing the effect of post-SPF thermal processing on other mechanical properties considered important for cryogenic tank applications. (Stephen J. Hales, 43128, and John A. Wagner) Structures Directorate

Analysis of Thermomechanical Fatigue of Unidirectional Titanium Metal-Matrix Composites

Titanium metal-matrix composites are prime candidates to be used in future supersonic and hypersonic



airframe structures and engines. These applications will require that the material retain structural integrity after many exposures to cyclic load and cyclic temperature. The objectives of this research were to develop an analytical method to evaluate thermomechanical fatigue (TMF) data of titanium metal-matrix composites SCS-6/Ti-15-3 under in-phase and out-of-phase loading conditions and to determine the critical constituent stresses (or strains) that control laminate fatigue behavior under TMF loading, taking into account the rate-dependent behavior of the matrix.

An analysis code named VISCOPLY was developed to predict matrix and fiber stresses and strains as a function of load, temperature, and time. The VISCOPLY code incorporates the vanishing fiber diameter (VFD) model, thermo-viscoplasticity theory, and laminated plate theory for two-dimensional laminate analysis. The analysis is based on the constituent properties. The fiber and matrix can both be viscoplastic with temperature dependency. The VISCOPLY code was used to analyze the TMF data generated at Lewis Research Center on unidirectional SCS-6/Ti-15-3 composites. The in-phase and out-of-phase TMF waveform had a cycle time of 180 sec with the temperature cycling from 93°C to 538°C. The TMF data were plotted based on the applied maximum stress as a function of cycles to failure (shown in the left figure). For a given applied stress, in-phase TMF loading resulted in a shorter fatigue life than the out-of-phase TMF loading. The in-phase TMF loading resulted in extensive fiber breakage and no matrix cracking, whereas out-of-phase TMF loadings resulted in extensive matrix cracking and loss of stiffness prior to failure.

The VISCOPLY code predicted the fiber and matrix stresses generated

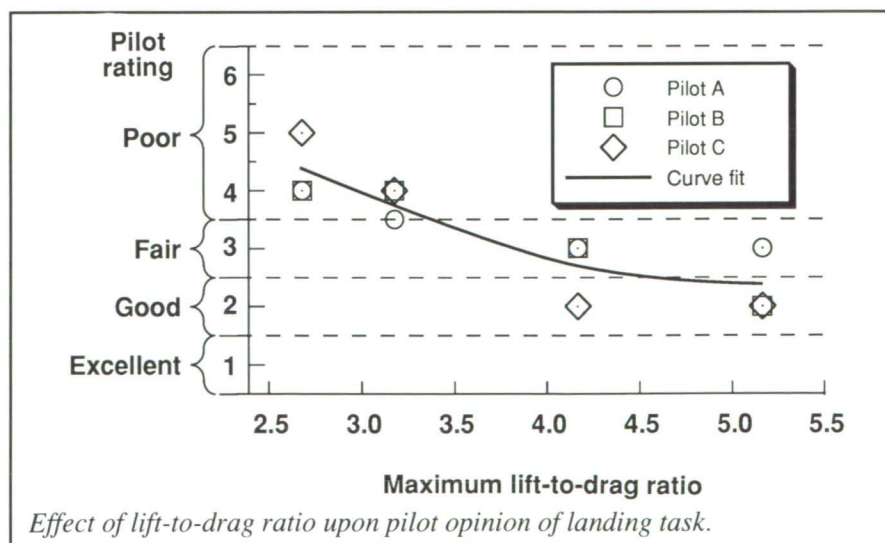
during the TMF cycle. Under in-phase TMF loading, the peak stress in the fiber was higher than for the out-of-phase TMF loading. In contrast, under out-of-phase loading, the matrix stress was higher than for the in-phase TMF loading. This is consistent with the experimental observations that specimens tested in out-of-phase TMF loading developed extensive matrix cracking prior to failure. Conversely, the in-phase loading resulted in no significant matrix cracking prior to failure. The predicted fiber stress range of 0° was plotted as a function of cycles to failure and resulted in the collapse of the in-phase and out-of-phase TMF data to a narrow band (shown in the right figure).

The study showed for a given set of conditions (temperature, loading frequency, and time at temperature), the fiber stress range of 0° controls the TMF response of unidirectional composite. Further, the VISCOPLY laminate analysis code has proved to be a powerful tool for future research in the area of thermomechanical fatigue of composite materials. (W. S. Johnson, 43463, M. Mirdamadi, and Y. A. Bahei-El-Din) Structures Directorate

Minimum Performance Requirements for Unpowered Landings of Lifting-Body Vehicles

In anticipation of future hypersonic and manned launch system requirements, an investigation of the relationship between pilot opinion and gliding capability (lift-to-drag ratio) of an unpowered lifting-body vehicle was conducted using the Langley Visual Motion Simulator. The simulation was based upon a preliminary version of the proposed HL-20 vehicle. A range of vehicle configurations with maximum lift-to-drag ratios between 2.7 and 5.2 were simulated by adding to or subtracting from the nominal drag coefficient. No other changes were made in the vehicle pitch dynamics or control system.

A three-part landing approach trajectory, consisting of a steep outer glideslope, a preflare portion, and a shallow inner glideslope, was defined. The outer glideslope was sufficiently inclined to allow a constant equivalent airspeed approach, while allowing enough energy to perform the preflare and final flare maneuvers. A final flare maneuver was performed at the end of



the inner glideslope. Outer glideslope angle, preflare load factor, and preflare initiation altitudes were predetermined for each lift-to-drag configuration to satisfy the energy requirements.

A computer-generated image of a typical runway, which included Precision Approach Path indicator lights as an outer glideslope aimpoint reference, was presented to the pilot for outside visual cues. Guidance information in the form of a "fly-to" box on the head-down electronic attitude indicator display was provided. No head-up display was provided.

Three different test pilots with appropriate experience were asked to evaluate a series of approaches and landings. Following a set of five familiarization approaches and landings for each configuration, each pilot repeated the task several times for each configuration and provided a numerical pilot opinion rating of the perceived difficulty of performing the landing. The results for each configuration were then averaged and plotted as shown in the figure. The figure clearly shows the trend of a reduction in perceived difficulty as maximum lift-to-drag ratio was increased. The data indicated that fair to good opinions

(pilot ratings of 3.5 or less) may be obtained for configurations with a lift-to-drag ratio above approximately 3.8. Subsequently, additional analysis of the data indicates a strong correlation between time available for the pilot to perform the landing maneuver and maximum lift to drag.

This result is significant in that it gives indication of a lower bound on maximum lift-to-drag ratio to achieve successful landings of an unpowered lifting-body vehicle.

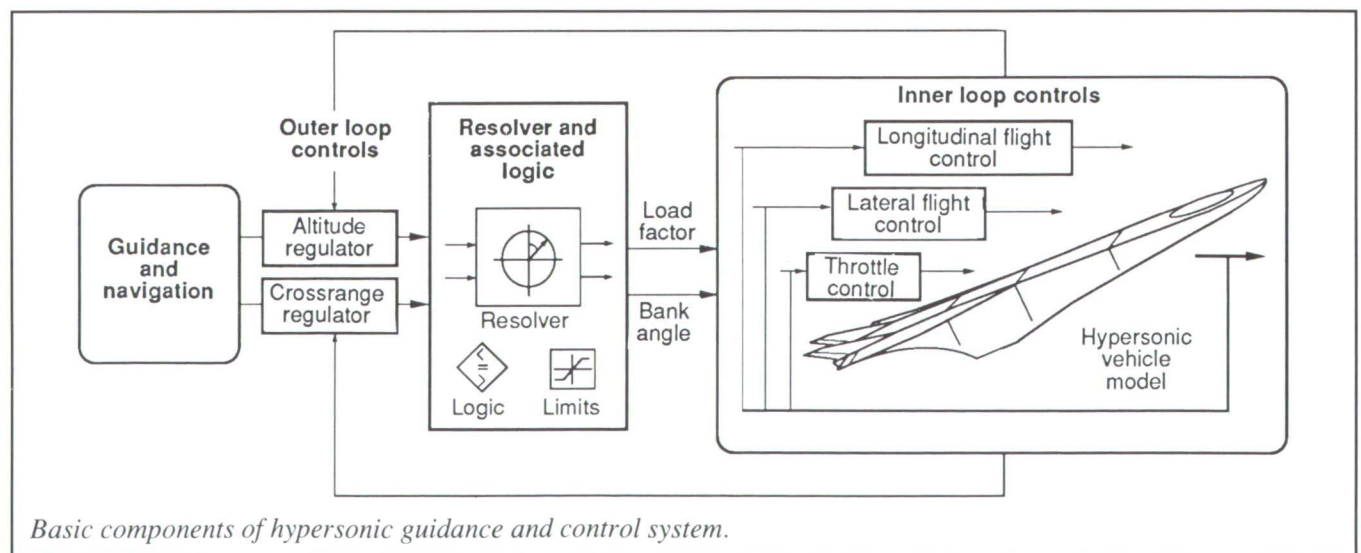
**(Bruce Jackson, 44060)
Flight Systems Directorate**

Stringent constraints are applied to angle-of-attack, sideslip, and dynamic pressure variations because hypersonic propulsion system performance will probably be dependent on flight condition and may suffer dramatically if excessive perturbations in these parameters are experienced. Lateral maneuvering in hypersonic flight is complicated by a high-speed effect caused by centripetal acceleration of the vehicle, which results in a noticeable reduction in load factor required to maintain constant altitude. This effect, referred to as centrifugal relief, causes the bank angle required to produce a given lateral acceleration to increase with velocity.

Guidance and Control System for Maneuvering in Hypersonic Flight

Several factors complicate manual maneuver control for airbreathing vehicles at hypersonic speeds. This manual control is particularly critical in the case of airbreathing single-stage-to-orbit vehicles that may follow a trajectory profile determined by a combination of engine performance, dynamic pressure, and heating criteria.

The objective of this research is to provide precise, coordinated guidance and control (G&C) during excursions from a hypersonic cruise flight path while regulating dynamic pressure and observing other necessary flight condition constraints. A system was developed to provide the desired guidance commands by resolving altitude and crossrange errors into load factor and bank angle commands that, in turn, drive automatic flight controls. The basic components of the system are shown in the figure. The interface between the outer loop guidance and



ORIGINAL PAGE
COLOR PHOTOGRAPH

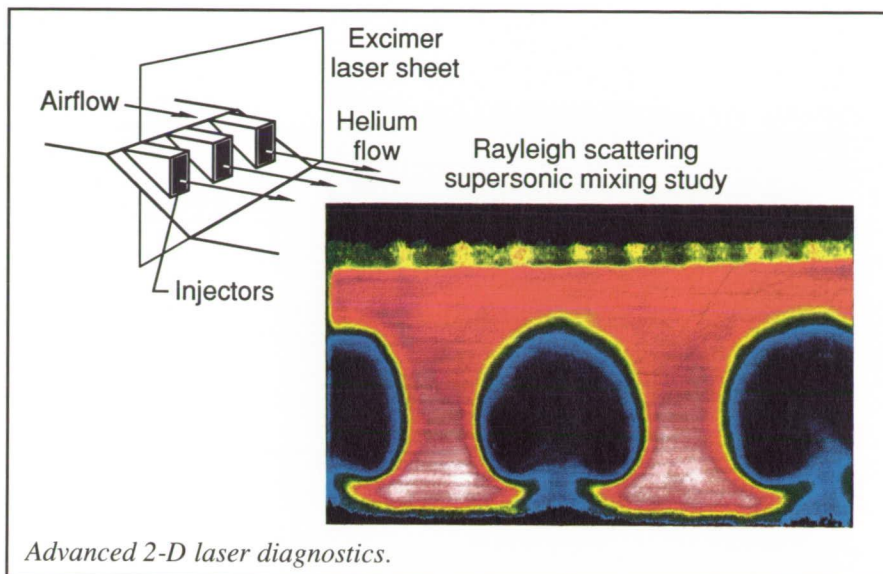
inner loop flight controls, referred to as a resolver, applies constraints on angle of attack and dynamic pressure perturbations and is designed to provide first priority to altitude regulation over crossrange. A throttle control law to regulate dynamic pressure during maneuvers was also provided in the inner loop.

Simulation test results for a generic hypersonic vehicle concept have shown that angle-of-attack constraints, combined with high-speed flight effects and the requirement to maintain nearly constant dynamic pressure, significantly impact the maneuver envelope of a hypersonic vehicle. For example, density variation with altitude strongly influences the climb and descent rate limits if dynamic pressure is to be maintained during vertical transitions between cruise flight conditions. The G&C system developed in this study was able to achieve altitude and crossrange commands while compensating for high-speed flight effects without violating constraints on angle of attack or dynamic pressure. This system can be used either to drive inner loop flight controls directly or to drive a cockpit flight director to assist the pilot in conducting hypersonic maneuvers.

(David L. Raney and Frederick J. Lallman, 44033)
Flight Systems Directorate

Visualization of Supersonic Mixing of Helium Into Air

As part of a mixing augmentation study in the Mach 6 High Reynolds Number facility, a high-power, pulsed excimer laser emitting a sheet of light at 193 nm was employed to visualize helium mixing into air. The helium (simulating H₂ fuel) was fed into a



Advanced 2-D laser diagnostics.

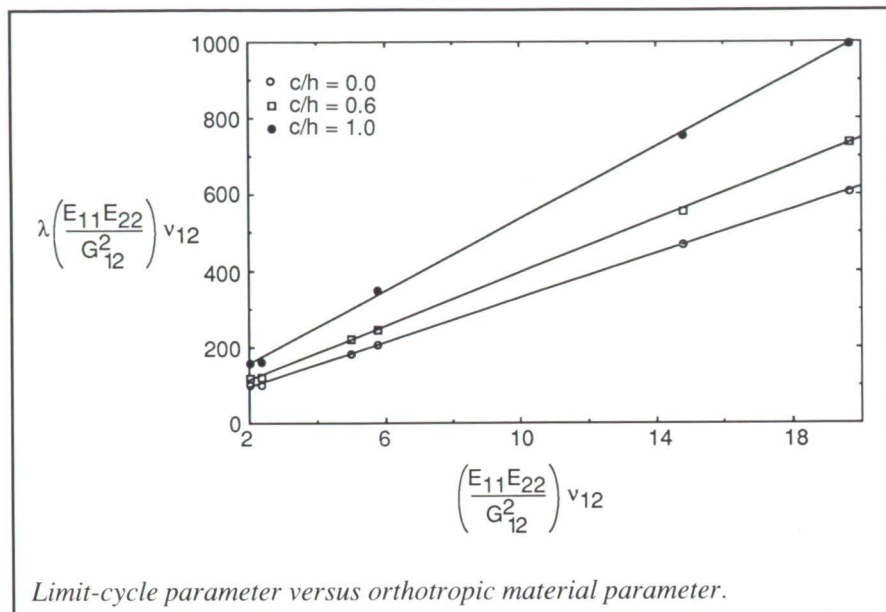
Mach 6 airflow through three fuel injectors on a model designed and built by the California Institute of Technology. The laser sheet was situated at several downstream locations and was viewed by a UV intensified Charged-Coupled Device (CCD) camera. The visualization was made possible by the low Rayleigh scattering cross section for helium relative to air (lower by a factor of 80). Thus, regions containing only helium appear dark relative to the surrounding air. This effect is further enhanced by Rayleigh-sized condensates that are also present in the supersonic airstream. The image shown is composed of an average of 22 individual snapshots of the flow looking upstream toward the three injectors. The helium flow is shown as dark blue, while the free-stream air appears red in the false color image. Analysis of the individual snapshots also provided useful aerodynamic information on the turbulent nature of the mixing environment.

(Behrooz Shirinzadeh, R. Jeffrey Balla, Mervin E. Hillard, John B. Anders, and Reginald J. Exton, 44605)

Electronics Directorate

Large-Amplitude Finite-Element Flutter Analysis of Composite Panels in Hypersonic Flow

The dawning of flight into the supersonic regime, during the 1950's, stressed the conflicting conditions of fabricating a structure strong enough to withstand large aerodynamic forces during supersonic flight, yet light enough to be economically efficient to allow for an increase in the payload capability of the flight vehicle. Because of the resurgent interest in flight vehicles such as the High-Speed Civil Transport (HSCT), the National Aero-Space Plane (NASP), and the Advanced Tactical Fighter (ATF) that will operate not only at high-supersonic Mach numbers but also well into the hypersonic regime, the additional requirement for energy-efficient, high-strength, and minimum-weight vehicles has become apparent. These requirements have generated an interest in the advanced composite materials to meet the high-strength, minimum-weight requirements.



In addition to the structural material concerns, the issue of the range of applicability of the most-used first-order piston aerodynamic theory into the hypersonic regime has been questioned. These questions have been generated in response to neglecting the higher order terms in the derivation of the first-order theory. It has been hypothesized that the higher order terms in the piston aerodynamic theory, at the large Mach numbers of interest, may be significant. Coupling these concerns with the realistic need for analytical tools to evaluate complex structures, the finite-element method presents itself as the most appropriate means that can conveniently and efficiently incorporate all the known complexities of the physical problem.

Thus, a finite-element approach has been developed for determining the nonlinear flutter characteristics of two-dimensional isotropic and three-dimensional composite-laminated thin panels using the third-order-piston, transverse loading aerodynamic theory. The unsteady, hypersonic aerodynamic theory and the von Kármán large deflection plate theory are used to formulate the aeroelastic problem.

Nonlinear flutter analyses have been performed to assess the influence of the higher order aerodynamic theory on the limit-cycle amplitude of the structure and the dynamic pressure of the flow velocity. Solution procedures to solve the nonlinear panel flutter and large-amplitude free vibration finite-element equations use a linearized updated mode with a nonlinear time function approximation (LUM/NTF) method. Finite-element nonlinear flutter analyses easily account for different boundary support conditions and various system parameters: plate thickness-to-length ratio h/a ; aspect ratio a/b ; lamination angle and number of layers; Mach number M ; flow mass-density-to-panel-mass-density ratio μ/M ; dynamic pressure λ ; maximum-deflection-to-thickness ratio c/h ; and orthotropic material parameter (see the figure). In this figure, E_{11} E_{22} is Young's moduli in the material 1 and 2 directions, respectively, v_{12} is Poisson's ratio for transverse strain, and G_{12} is shear modulus in the material 12 plane. The large-amplitude panel flutter results using the full third-order-piston aerodynamic theory are used to assess the influence of the nonlinear aerodynamic theory on the structural

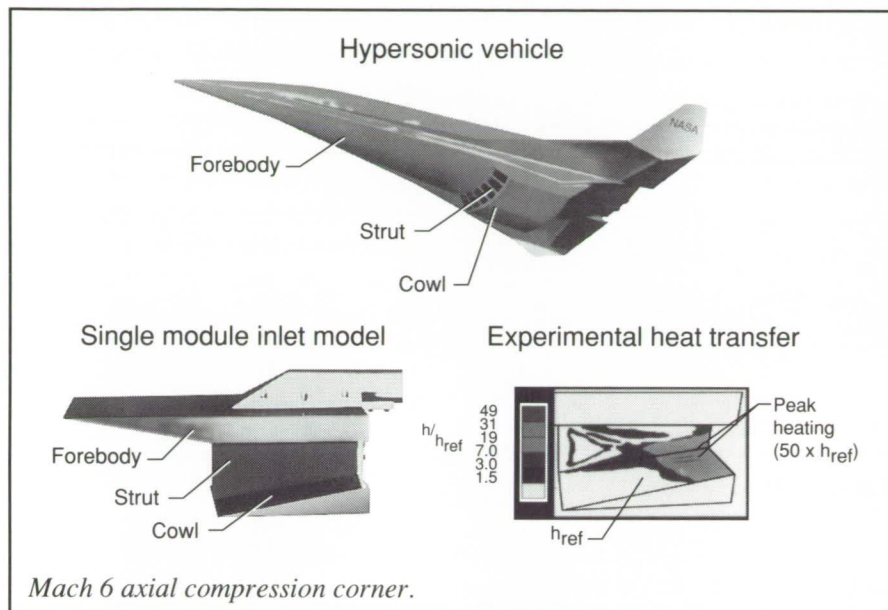
response of composite panels subjected to high-supersonic/hypersonic flow.

(Carl E. Gray, Jr., 47236)
Systems Engineering and
Operations Directorate

Aerothermal Study of Axial Compression Corner With Shock Impingement at Mach 6

At hypersonic speeds, heat loads are more threatening to vehicle safety than are air loads, and they are more difficult to calculate. The ability to accurately calculate heat loads for these conditions is currently beyond the state of the art in computational fluid dynamics (CFD) technology. The objective of this effort was to experimentally define the heating loads for a typical scramjet inlet.

A typical hypersonic vehicle and the wind-tunnel model that simulates a single module scramjet inlet are shown in the figure. The model features an axial compression corner formed by the intersection of the strut and cowl. An oblique shock is generated from the wedge-shaped forebody and impinges on the axial corner. Additional oblique shocks are produced at the cowl and strut leading edges creating a complex three-dimensional flow field. The model was constructed of Stycast ceramic material, which has a low thermal conductivity. The forebody and cowl are wedges of 10° , the strut is a wedge of 5° , and the overall length, width, and height of the model are 18 in. by 10 in. by 6 in. Phase-change paint, infrared-image photography, and oil-flow visualization techniques were used to define the aerodynamic heat loads and the surface flow patterns in the Langley 20-Inch Mach 6 Tunnel. Typical Mach 6 results are presented in



the figure for a Reynolds number of $3.35 \times 10^6/\text{ft}$ and a total temperature of 880°R . The heating rate contours, determined from the phase-change paint data, clearly indicate that shock impingement significantly increases the surface heating rates downstream of the impingement location. The interaction of the shock and the highly viscous axial corner flow produces local hot spots with heating levels about 50 times higher than two-dimensional laminar undisturbed values h_{ref} .

These data provide qualitative information for the designer of the National Aero-Space Plane engine inlets to design corner seals and thermal protection systems. (S. Venkateswaran, L. Roane Hunt, 41370, and David Witte) Structures Directorate

because a cast model can be easily and inexpensively replicated. Slip-casting has been found to provide superior results over other ceramic casting techniques, such as hydraulic casting. One cannot cast monolithic-detailed models, however, using slip-casting state-of-the-art techniques, because individual parts have to be fabricated and glued together. Such assembled models are unacceptable. Both precise model configuration and homogeneous thermal properties are important for heat-transfer code validation experiments. In addition, a disadvantage of these block, or as termed in the industry "flask," molds is the ever-present parting lines that are invariably necessary on or near the leading edges of the model wings, nose tips, and fins for mold separation. These areas are critical for flow boundary-layer control.

A major attribute of the new technique over prior art is that it can provide a detailed ceramic casting using a lost-wax process similar to an investment metal casting with no parting line. A shell mold is used in place of a conventional plaster flask mold for slip casting. It was found that after pouring the slip and obtaining

green strength, the shell mold could be peeled or washed away from the green casting, thus enabling no limit in model configuration and eliminating the requirement for model mold draft which normally limits the casting configuration. (P. Vasquez, 45189) Systems Engineering and Operations Directorate

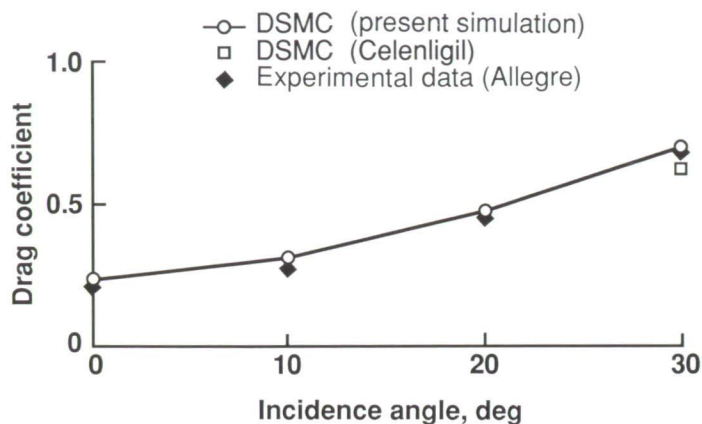
Application of Efficient Direct Simulation Monte Carlo Algorithm to Delta Wing

A new Direct Simulation Monte Carlo (DSMC) computer program has been developed for the simulation of hypervelocity, rarefied flows about three-dimensional bodies of arbitrary geometry. This new program enables rapid problem formulation, setup, and computation for simulations of these complex flows. The program retains all the DSMC physical modeling techniques that have been demonstrated to accurately represent the pertinent fluid physics. The new program utilizes an unstructured computational grid, constructed on a background Cartesian mesh, which enables efficient tracking of molecules in the computational domain. The body surface is defined and stored simply as a list of integers, namely, the tag numbers of the background Cartesian mesh cells which contain body surface elements.

The new program has been applied to the simulation of flow about a delta wing. The figure shows a comparison of results obtained using the new program with experimental measurements made by Allegre and results from an earlier three-dimensional DSMC simulation by Celenligil. The delta wing is 10 cm long, and the free-stream conditions are a Mach number of 20, a Knudsen number of

No Draft, Unique Slip-Cast Wind-Tunnel Models

Casting of ceramic wind-tunnel models is desired over machining



Comparison of computed and experimental drag coefficients for delta wing.

and it required one CPU day on a Silicon Graphics 340D workstation. The present program, together with a set of preprocessor, diagnostic, and postprocessor utilities that have also been developed, shows the potential to become an important engineering tool for the simulation of three-dimensional rarefied flows about vehicles of arbitrary geometry.

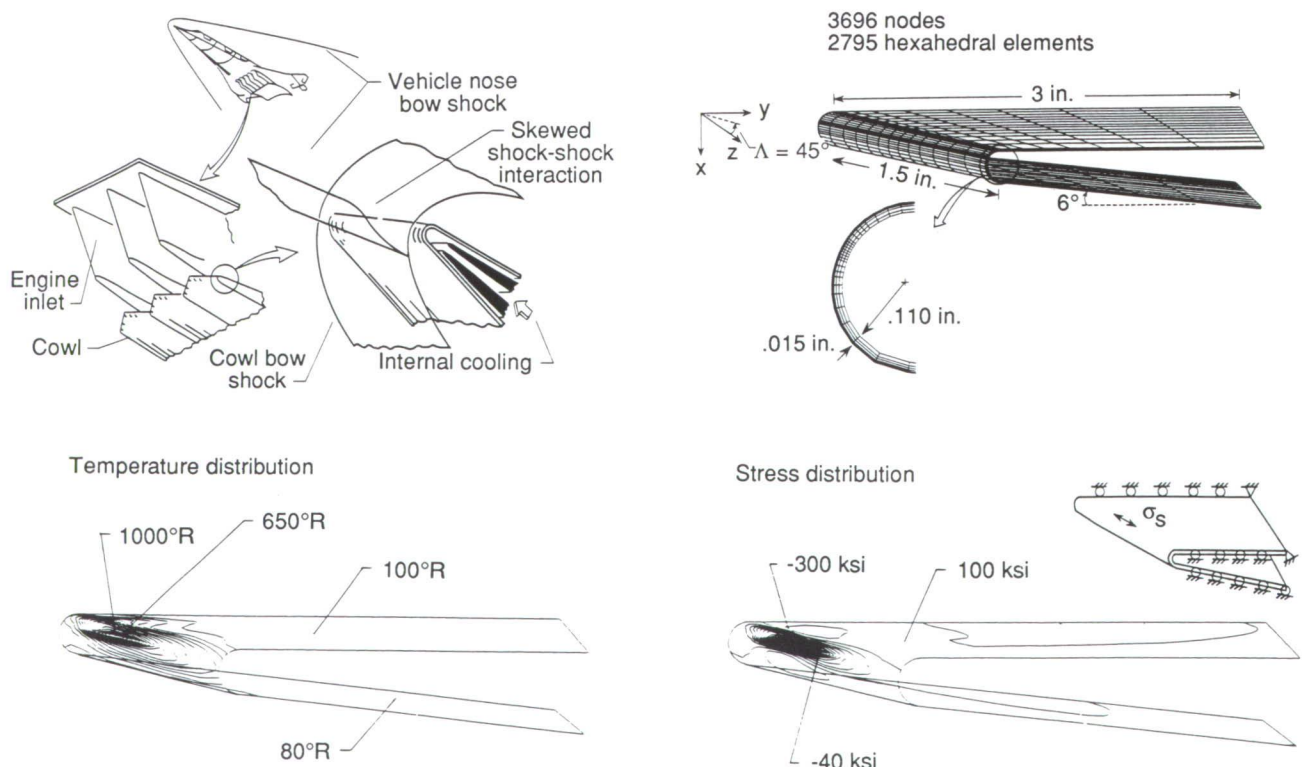
(D. F. G. Rault, R. G. Wilmoth, and G. Bird, 44388)
Space Directorate

Development of Three-Dimensional Nonlinear Flux-Based Thermal Finite-Element Capability

The two-dimensional (2-D) flux-based finite-element method used in

0.016, and a Reynolds number of 1500. Good agreement exists between the present results, the experimental data, and the earlier simulation. The earlier simulation required typical setup times

on the order of several months and computational time of approximately one CPU (central processing unit) day on a CRAY-2. By contrast, the present simulation was set up over a few days,



Three-dimensional flux-based thermal finite element. (Q_{max} is 30 000 Btu/ft²-sec and M is 16.)

the Langley Integrated Fluid-Thermal-Structural (LIFTS) analyzer has been shown to have benefits over conventional finite-element methods. LIFTS has been extended to include a three-dimensional (3-D) flux-based thermal analysis capability that enables the solution of more realistic thermal structures. The objective was to develop a 3-D flux-based thermal finite element that is computationally efficient and compatible with existing structural capability and to investigate the effectiveness of flux-based finite elements in solving realistic thermal structural problems.

Results were verified by comparison with the Engineering Analysis Language (EAL) finite-element solution for academic-type problems. Then the new finite element was used in conjunction with the 3-D flux-based structural analysis capability to predict the thermal structural response of a swept engine cowl leading edge of the National Aero-Space Plane. The copper cowl was analytically subjected to a shock-shock interference heating condition (upper left of figure) which causes a peak heat flux of 30 000 Btu/ft²-sec (flight conditions at $M = 16$). The finite-element model was discretized (upper right of figure) based on the aerodynamic heating distribution to accurately capture thermal gradients. The steady-state temperature distribution predicted from the transient thermal analysis was used as the thermal loading in the quasistatic structural analysis to predict maximum thermal stresses.

The predicted temperature distribution revealed large 3-D thermal gradients (lower left of figure). Comparisons of 3-D and 2-D thermal stresses indicate the need for the more accurate 3-D analyses to predict peak stresses for the swept shock-shock interference heating condition. Predicted stresses (lower right of figure)

using linear theory were excessive and indicate the need for plastic analyses, a stronger material, and/or an improved cooling concept.

(Sandra P. Polesky, 45434, Pramote Dechaumphai, Christopher E. Glass, and A. K. Pandey)

Structures Directorate

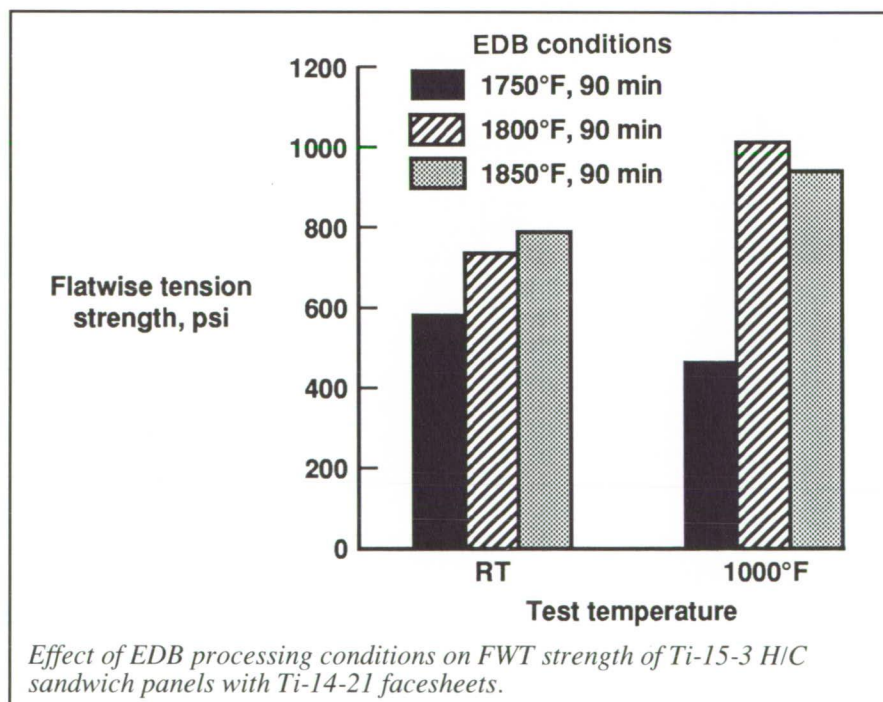
Effect of Processing on Strength of EDB Honeycomb Sandwich Structure

Advanced hypersonic vehicles require the development of lightweight, high-temperature alloys as well as joining processes capable of incorporating these materials into efficient structural components. One class of materials with the potential to meet these objectives is the titanium aluminide (Ti_xAl) intermetallics and fiber-reinforced Ti_xAl composites. Previous work has established the potential of enhanced diffusion

bonding (EDB) as a joint process suitable for fabricating titanium-based honeycomb core sandwich structure. Further development of the EDB process has focused on improving the properties of sandwich structure fabricated from monolithic Ti-14Al-21Nb (Ti₃Al) facesheets and Ti-15V-3Cr-3Sn-3Al honeycomb core.

The figure shows the room and elevated temperature (1000°F) strengths of EDB honeycomb core sandwich panels loaded in flatwise tension (FWT). The FWT test is used to measure the strength of the facesheet/core bond and gives a good indication of the quality of the bonding process. The figure shows that the FWT strength of the EDB honeycomb core sandwich panels is sensitive to processing parameters. For a 90-min exposure, the best room temperature and 1000°F FWT strengths were achieved in specimens processed at 1800°F to 1850°F.

The 1000°F FWT strengths were higher than the room temperature



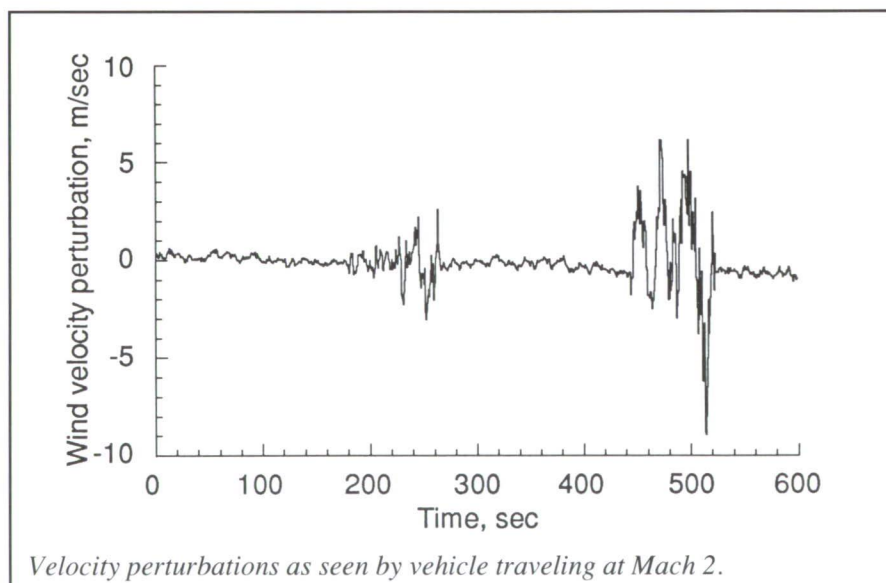
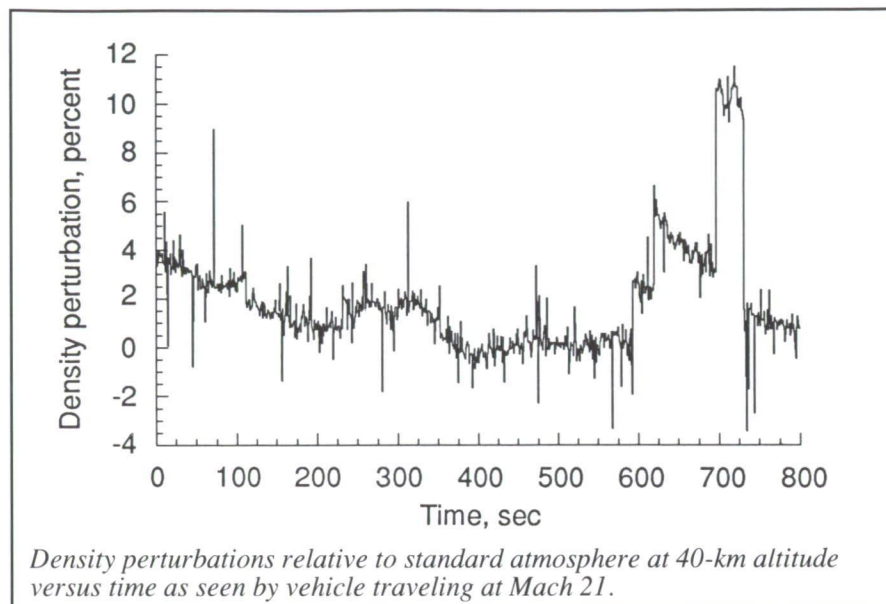
strengths for the 1800°F and 1850°F process variants. The fracture surfaces of the room temperature specimens exhibited failure at the facesheet/core joint interface, while the 1000°F specimens exhibited some degree of honeycomb core fracture. At room temperature, the facesheet/core bondline appears more brittle in nature than at 1000°F, and therefore it may be less fracture resistant. Hence, the 1000°F FWT strengths are higher than the room temperature strengths for the 1800°F and 1850°F process temperatures.

Continued development of the EDB process will focus on refining the bonding parameters to further improve the properties of Ti-15V-3Cr-3Sn-3Al honeycomb core sandwich structure fabricated with monolithic Ti-14Al-21Nb facesheets.

(Eric K. Hoffman, 43127, and R. Keith Bird)
Structures Directorate

Atmospheric Disturbance Model for NASP Applications

The National Aero-Space Plane (NASP) Program faces significant challenges in vehicle system interactions with the flight environment. Both single-stage-to-orbit (SSTO) flight missions and hypersonic flight envelope expansions require a realistic simulation of the environment from the Earth's surface to orbital altitudes for vehicle system development and testing. Additionally, SSTO hypersonic airbreathing vehicles will be required to perform very close to operational limits; therefore, to reduce the performance losses associated with atmospheric uncertainty, a realistic atmospheric disturbance model is required.



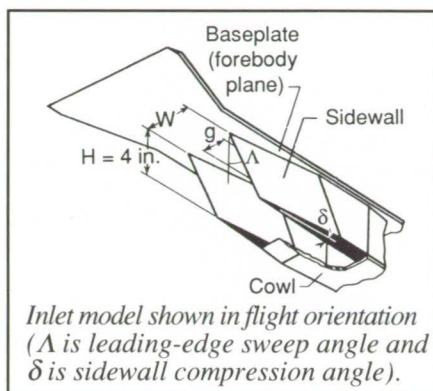
Investigations of current atmospheric disturbance models in use reveal that no single model is capable of satisfying predicted hypersonic vehicle system requirements. Available models either have severe, unacceptable algorithm simplifications to meet computer time constraints or have algorithms that consume gross amounts of core memory or processor time or both, prohibiting on-line closed-loop simulation use. This lack of an efficient disturbance model can

significantly limit development and testing of critical vehicle systems.

In response to this need, a cooperative research effort among Langley Research Center, Dryden Flight Research Facility, and McDonnell Douglas Space Systems Division to develop an atmospheric perturbation model was initiated. The resulting model, based upon the Global Reference Atmosphere Model (GRAM), incorporates new equations for

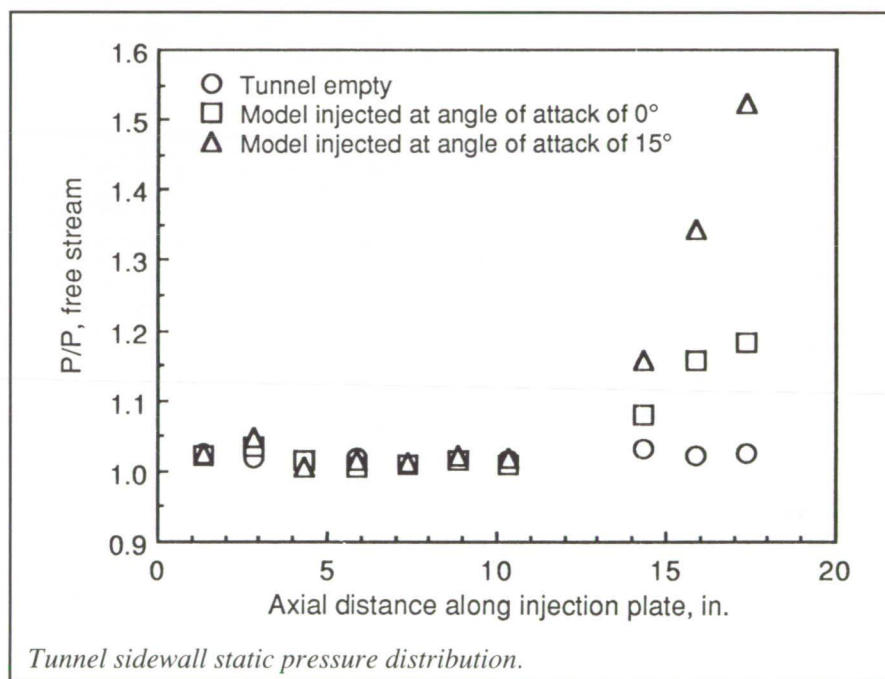
temperature and density (thermodynamics) and wind perturbations, atmospheric and thermodynamic patchiness (regions of alternating light, moderate, and severe perturbations), and an improved statistical, global data base. The model was designed to be computationally efficient by reformulating basic equations and refining executive logic structure.

One of the more significant capabilities of this model is its ability to produce realistic perturbations of atmospheric thermodynamics. For example, the first figure demonstrates density patchiness. Note that density perturbations go from a near-zero level between 400 sec to 600 sec to a 100-sec patch of denser air and finally to a 30-sec patch of air that is even more dense. The second figure shows a typical velocity perturbation time history that is also patchy. The alternating periods of quiescence, moderate velocity fluctuations, and more severe perturbations are typical patchy variations encountered over the flight envelope of hypersonic vehicles. (John D. McMinn and John D. Shaughnessy, 44014) Flight Systems Directorate



possessed 32 static pressure orifices distributed on the forebody plane and sidewalls. Seventeen static pressure orifices on the tunnel wall and three pitot probes on the model monitored the tunnel performance. The wind-tunnel blockage aspects of the effects of contraction ratio (sidewall proximity), cowl location, Reynolds number, and angle of attack were investigated.

Increasing the contraction ratio (moving the sidewalls closer together)



Wind-Tunnel Blockage Tests of Scramjet Inlet at Mach 10

Proper design of primary engine components such as the inlet is necessary to achieve effective propulsion-airframe integration for hypersonic cruise vehicles such as the National Aero-Space Plane (X-30). Based on the results of a computational parametric study, a model of a generic three-dimensional sidewall compression scramjet inlet (see the first figure) has been designed for testing in the 31-Inch Mach 10 Tunnel at Langley Research Center. To increase the

instrumentation density in interaction regions for a highly instrumented model, the model must be made as large as possible. When the cross-sectional area of the model becomes large relative to the inviscid core size of the tunnel, the possibility of tunnel blockage effects must be considered. To assess this possibility, a blockage model (a relatively inexpensive and much less densely instrumented version of the configuration) was fabricated for preliminary testing. Because it was desirable to determine both the effect of the model on the performance of the wind tunnel and if the inlet would start, the model

increased the number of internal shock reflections and, hence, incrementally increased the sidewall pressure distribution. Decreasing the Reynolds number tended to increase the overall compression of the inlet via stronger shocks and stronger shock/boundary-layer interactions. The present configuration was the largest inlet model tested in the 31-Inch Mach 10 Tunnel to date. (The maximum cross-sectional area of the model exceeded 30 percent of the tunnel inviscid core.) For each of the configurations tested, the tunnel remained started following model injection. Based on pitot and tunnel sidewall pressure distributions, no evidence

of tunnel blockage due to the presence or orientation of the model was noted.

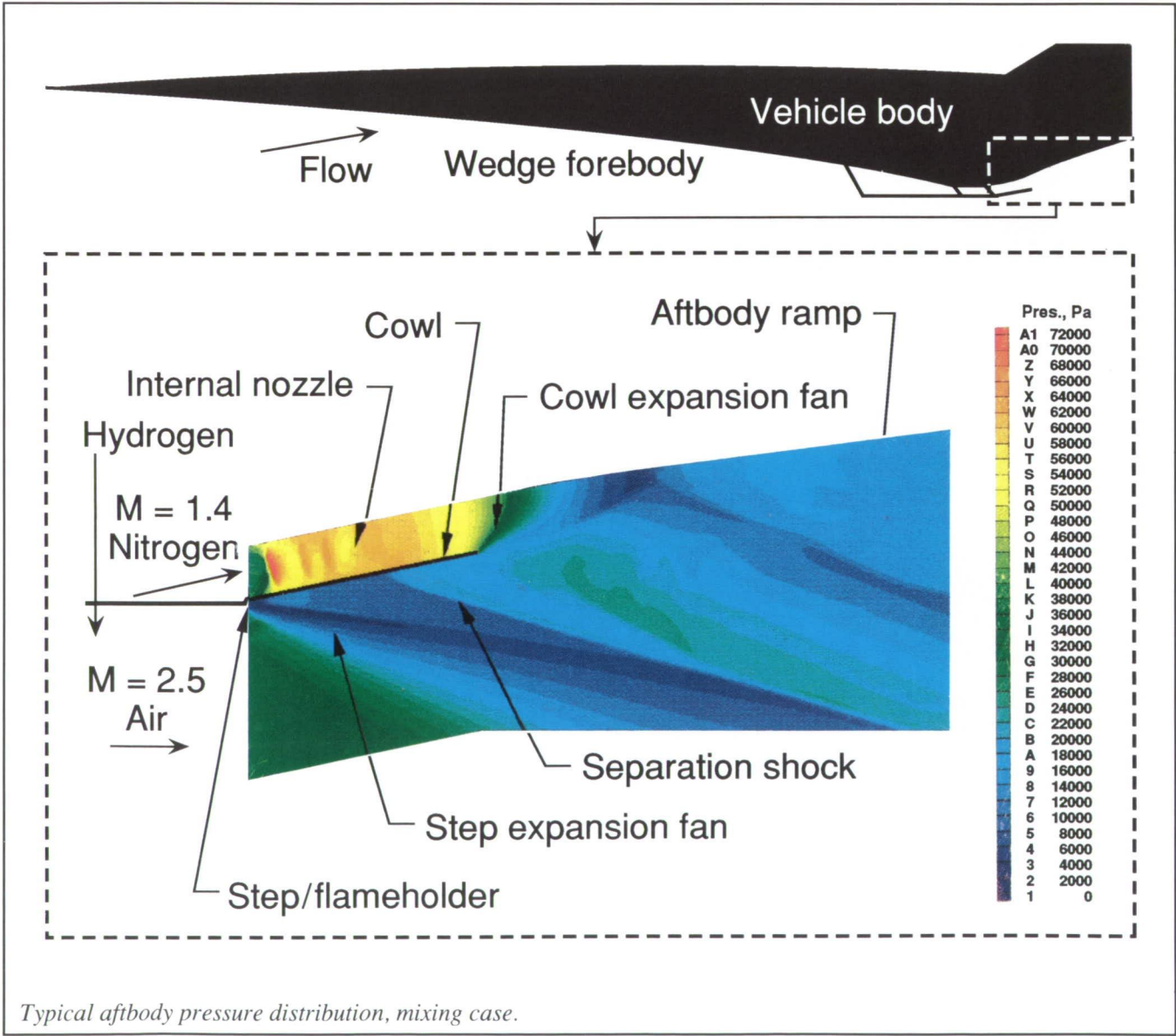
The second figure depicts the axial static pressure distribution on the tunnel sidewall with the tunnel empty, with the model injected at an angle of attack of 0°, and with the model injected at an angle of attack of 15°. The only effect noted was an increased interference of the model support struts (at axial distances greater than 13 in.) when the model was placed at angle of attack. Additionally, the inlet appeared

to start and remain started, based on the 32 static pressure measurements on the baseplate and sidewalls. Since the completion of these tests, a highly instrumented version (256 channels of pressure data) of the configuration has been designed and fabricated to better resolve the internal shock/boundary-layer interactions and their effects on the global performance of the inlet. A concurrent computational fluid dynamics effort has also provided a more detailed accounting of the internal flow physics and a comparison

with experimentally obtained surface static pressures and entrance and exit plane pitot profiles.
(Scott D. Holland, 45248)
Space Directorate

Numerical Study of External Burning Flow Fields

Hypersonic vehicles such as the National Aero-Space Plane (NASP) experience a base pressure drag



problem in the transonic and low supersonic flight regimes. Specifically, the low engine mass capture is insufficient to completely fill the vehicle base. Therefore, studies are being conducted to manipulate the flow field in this region to alleviate this low base pressure problem. One method that is receiving attention is external burning (EB) in which fuel is injected into the external flow, mixed and burned, thus resulting in a pressurized cowl trailing edge.

Under the NASP Government Work Package Number 57, Langley Research Center is providing analysis of external burning environments. A series of computational analyses were performed with the SPARK family of codes for a typical external burning flow field. A representative geometry for external burning was implemented including a normal injector, a step flameholder, and turned up cowl. The complicated physics in this effort include the injection, mixing, ignition, and flameholding of the EB flow and merging of the EB and combustor streams. These solutions provide insight into external burning flows and result in the identification of potential problem areas.

The results indicate that for the geometry analyzed, the region of the flow where external burning was present was very unstable in the presence of a higher pressure engine exhaust. For the streams to mix without separation, a delicate pressure balance was required. The strong pressure gradients at the cowl trailing edge even separated a flow without reaction, as shown in the figure. Also, the external burning flame propagation makes a single, continuous pass through the EB mixing region and burns only the fuel that is mixed. These results suggest that it is essential to operate the engine exhaust in a pressure-matched mode with a variable

nozzle position control and that fuel injection be optimized for complete mixing by the time it reaches the flameholder location.

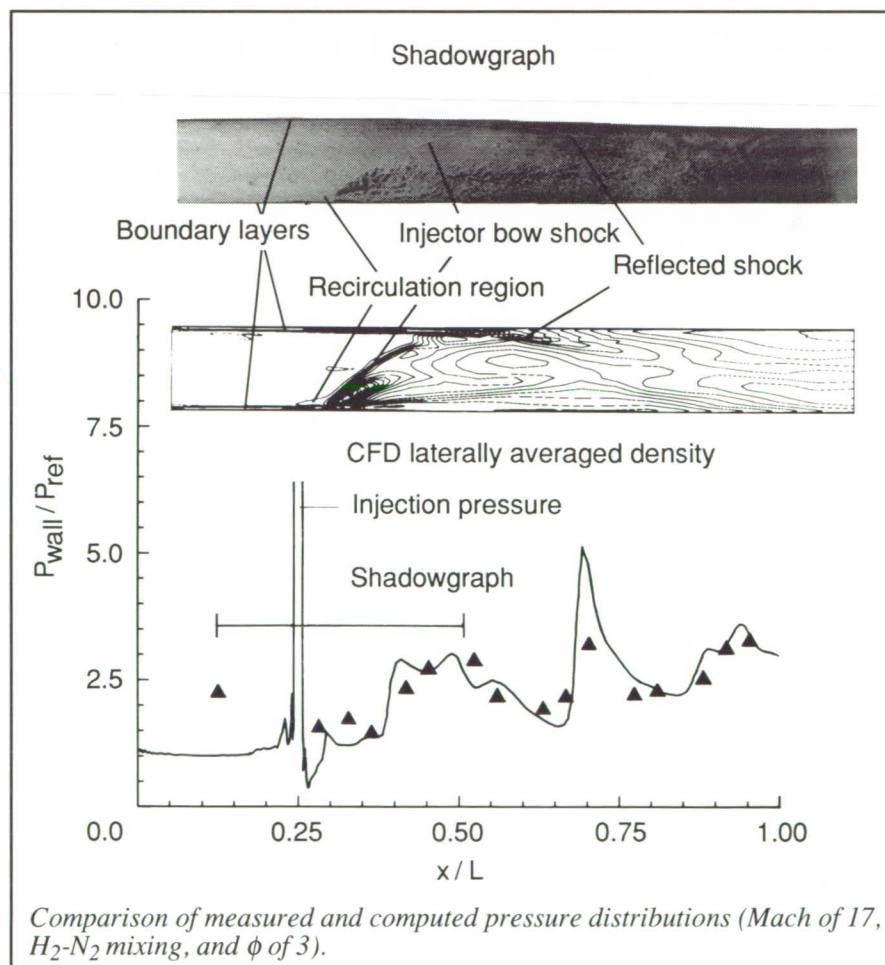
(Robert D. Bittner, 46260)
Aeronautics Directorate

Computational Analysis of Hypersonic Scramjet Combustor Flows

The General Applied Science Laboratories, Incorporated (GASL) HYPULSE facility, formerly the Langley Research Center Expansion Tube, is currently used to provide clean-air, true-enthalpy scramjet

combustor conditions for flight simulations from Mach 13 to 17. Most tests to date have been on simple unit fuel injectors to provide preliminary understanding of combustion phenomena in this high-speed flight regime.

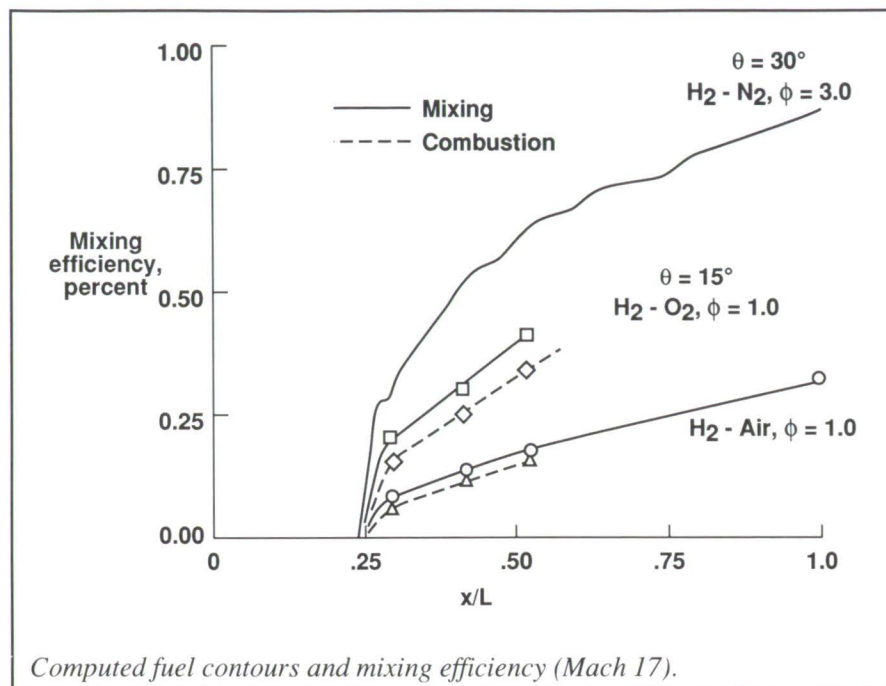
Under the National Aero-Space Plane and NASA Technology Programs, Langley has provided computational support of the GASL HYPULSE combustor testing to accelerate understanding of the combustor flow characteristics. Numerical analysis was performed for tests made with both rectangular and cylindrical semidirect connect combustor models. These solutions were compared to relevant experimental measurements and enabled the mixing characteristics of the injector configurations to be better



Lightweight Coatings Protect Titanium Alloys From Oxidation in Hypersonic Environments

Titanium-based alloys are candidate materials for hot structures and heat shields in hypersonic vehicles because of their low weight and high strength at elevated temperatures. However, the range of conditions in which they can be used is limited by their susceptibility to oxidation at high temperatures. Exposure to oxidizing conditions results in scaling at the surface, which decreases the alloy thickness, and solid solution contamination of the alloy, which causes loss of ductility. Protective coatings that shield the materials from oxidation enable their use at higher temperatures. Existing oxidation-protection coatings are generally quite thick (from 25 μm to 50 μm) and brittle. Thick coatings represent a substantial weight penalty, and a brittle coating may reduce the fracture toughness of the alloy.

Effective coatings must be stable under their projected operating conditions, must not react with the substrate alloy, must stop oxygen transport to the substrate alloy, and must be lightweight. Langley Research Center has used sol-gel processes to develop an ultrathin coating (approximately 5 μm thick) for titanium-based alloys, which reduces their oxidation by a factor of 100. Because low-oxygen diffusivity materials such as SiO_2 and Al_2O_3 tend to react with titanium at high temperatures, the coating design includes multiple layers with a thin reaction barrier layer that separates the alloy from a two-layer diffusion barrier. Because the ultrathin diffusion barrier may contain defects from processing or thermal cycling during service, the outer-most layer is a 0.5- μm -thick glass that becomes molten at high temperatures and provides healing of defects.



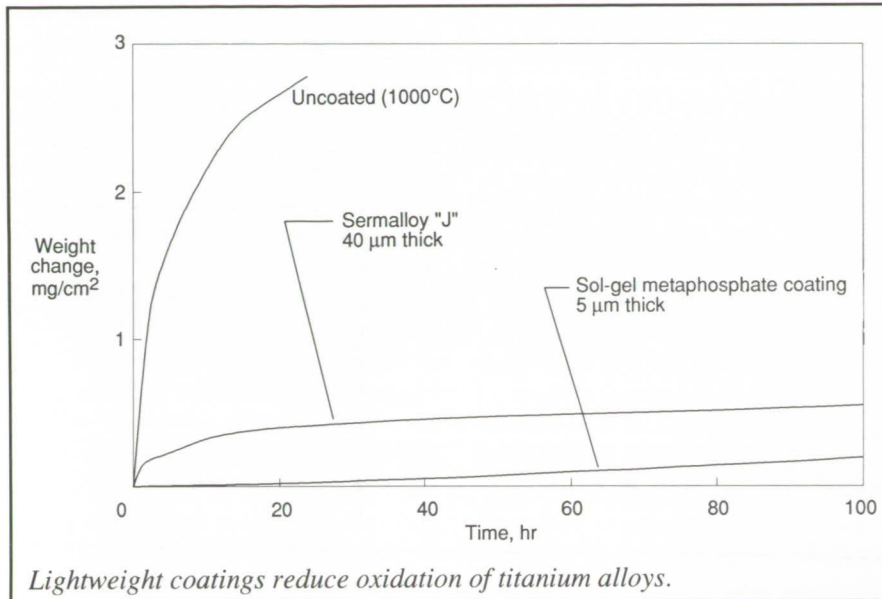
understood. The experimental data available to date are limited to wall pressures, heat flux, and shadowgraphs.

Numerical and experimental results presented in the first figure show excellent agreement for a flush wall sonic hydrogen injector of 30° in a nitrogen flow field (1-in. \times 2-in. \times 28-in. rectangular model). In the upper part of the figure, a shadowgraph is compared with computed lateral density contours to assess the numerical simulation of the actual flow structure. Corresponding non-dimensional wall pressure distribution $P_{\text{wall}}/P_{\text{ref}}$ comparisons are shown as a function of x/L in the lower part of the figure. Fuel distribution, fuel mixing, combustion efficiency, and combustor effectiveness can be determined from these numerical solutions. The second figure illustrates mixing and combustion efficiency for two unit fuel injector geometries, which are flush wall jets of 30° and 15°. These results illustrate some expected behavior, such as faster mixing for the higher angle injector, the higher fuel equivalence ratio ϕ , and

the injection into pure oxygen. Also a slight finite rate chemistry limitation (combustion efficiency relative to mixing efficiency) is observed. These results confirm that high flight Mach numbers have a detrimental effect on fuel mixing. For example, based on an extensive data base for Mach 5 to 7 scramjet combustors, the anticipated combustor exit mixing efficiency for the hydrogen-air solution of 15° is 0.5 (60 percent higher than the 0.3 calculated).

Other studies in progress are evaluation of the difference between cold flow simulation (low velocity) of high (true) enthalpy mixing and performance comparisons of identical fuel injectors at various flight Mach numbers (Mach 5 to 17).

(Robert D. Bittner, 46260, Glenn J. Bobskill, David W. Riggins, and R. Clayton Rogers)
Aeronautics Directorate

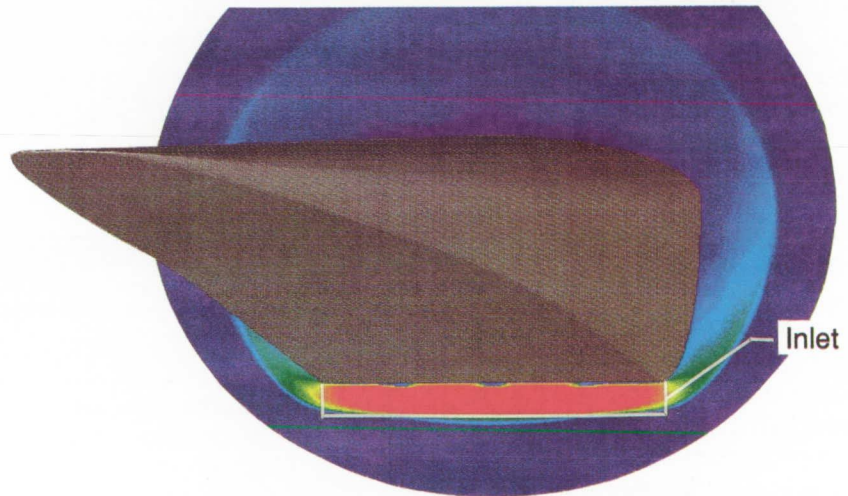


The performance of oxidation protective coatings is judged from static oxidation tests with a thermogravimetric apparatus that measures weight change with time of exposure to oxidizing conditions. The figure shows weight gain for 982°C 100-hr static oxidation tests of Ti-14Al-21Nb (weight percent) samples with no coating, with a Sermalloy "J" coating, and with the Langley-developed sol-gel coating. The Sermalloy "J" coating is a diffusion-type coating that measures approximately 40 µm in thickness. Because it performs very well as an oxidation protection coating, it is included here as a reference for evaluating the much thinner sol-gel coating with respect to oxidation resistance. For the time-temperature conditions investigated here, the multilayer sol-gel coating provides much better protection to the alloy than does the thicker commercial coating. (R. K. Clark, 43513, and K. E. Wiedemann)
Structures Directorate

NASP Forebody Contour Trade Study Benchmark

The purpose of the National Aero-Space Plane (NASP) Contour Trade Study was to select a forebody design that provided maximum inlet performance.

Personnel at Langley and Ames Research Centers teamed with the three NASP airframers to analyze eight forebody designs at several flight conditions (a total of 24 cases) with computational fluid dynamics (CFD) methods. To resolve any uncertainties due to the different CFD codes used or to the postprocessing of results, all participants ran an overlapping or



Participant	Mass capture		Adiabatic kinetic energy efficiency	
	Laminar	Turbulent	Laminar	Turbulent
1	2187.8	2237.8	.9945	.9899
2	2191.6	2253.2	.9932	.9902
Langley	2226.6	2255.6	.9941	.9903
4	-	2234.2	-	.9897
5A	2208.0	2241.6	.9940	.9899
5B	2214.6	2255.8	.9941	.9904
(Max-min)/ave	1.759%	.962%	.128%	.076%

NASP forebody benchmark.

benchmark case. The benchmark results provided the basis for determining bias factors with which the NASP Inlet Design Team adjusted the trade study cases.

Langley used the CFD code CFL3DE to perform computations for the laminar and turbulent benchmarks and several trade study cases. The blunt nose region was computed using the thin-layer Navier-Stokes option, and the forebody region was computed using the parabolized Navier-Stokes option. Integrated performance quantities, such as kinetic energy efficiency and mass capture, were then computed from the CFD solutions.

Comparison of the participants benchmark results (laminar and turbulent) indicated excellent agreement for adiabatic kinetic energy efficiency and mass capture. These integrated results are given in the table in the figure. Other quantities such as forebody lift, drag, and moments were in equally good agreement. However, significant differences were noted in the boundary-layer region. The figure shows density contours at the cowl plane. Accumulation of flow in the boundary layer can be seen at several spanwise locations. This phenomenon varied greatly among the results of the participants. Further analyses have indicated that these differences are primarily due to postprocessing techniques and computational grids chosen for the solution.

One major result of this study was the generation of a high degree of confidence in CFD predictions of external flow fields within the NASP community. In many instances, the variation between numerical performance results is smaller than the known errors in comparable experimental results used for code calibration.

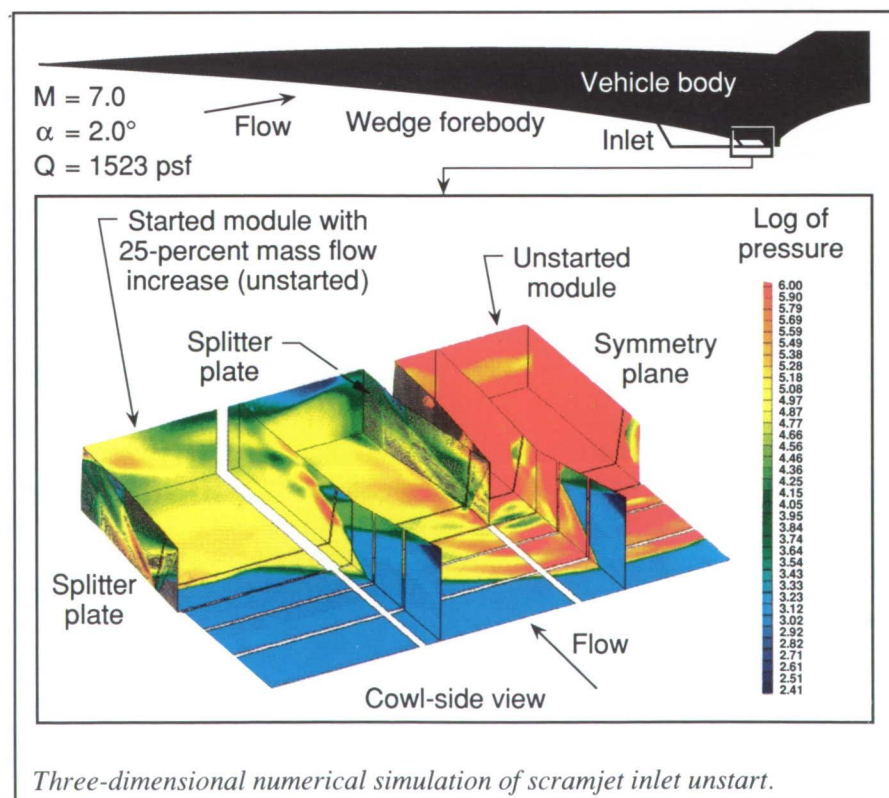
(Arthur D. Dilley, 42288, and Richard W. Hawkins)
Aeronautics Directorate

Scramjet Module-to-Module Interaction Study

Inlet "unstart" is an important issue to be addressed in the design of scramjet propulsion for any hypersonic application, such as the National Aero-Space Plane. If one module unstarts, it will have a large effect on inlet and aerodynamic loads for the entire vehicle, and it may unstart neighboring modules as well. In some design concepts, the modules are separated by very short splitter plates set back in the combustor region of the inlet to reduce drag and corner flow effects. However, short splitter plates also allow much more interaction between the individual modules.

The objective of this study was to computationally unstart a full-scale scramjet engine inlet module and to determine the effect of the unstart on neighboring modules.

The code CFL3D was used in this work. The first step in performing the unstart study was to obtain the two-dimensional (2-D) solution for the entire forebody (modeled as a wedge) and inlet; the solution extended through the engine to the exit of the module region. The 2-D solution within the module region was then used to test possible numerical unstart techniques to be used in the three-dimensional (3-D) simulation. The localized heat addition was chosen over the commonly used practice of specifying a constant back pressure to allow adaptation to the changing mass flow rate through the unstarted module. A specified amount of heat per unit mass flow was added to the governing equations as a source term. During the unstart process, as the mass flow decreases, the amount of heat that is added is reduced; this process then results in a reduced back pressure that more accurately models a true unstart. The next step in the numerical process



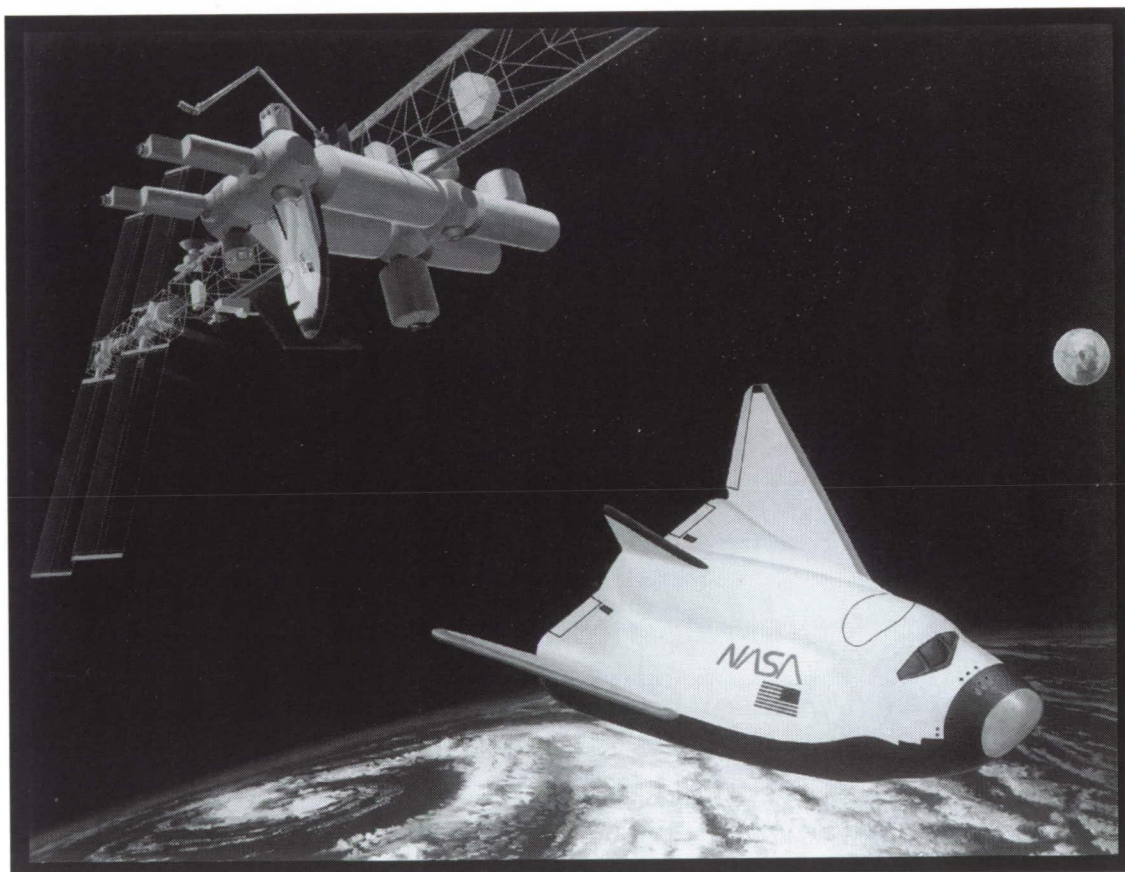
was to obtain a 3-D steady-state solution for a started module and begin the unstart sequence by unstating an adjacent module.

The 3-D simulation was run until the started module showed an increased mass flow of approximately 25 percent (at which point it began to spill mass itself). Because of grid limitations, an additional one-half module width was not added. It can be assumed that continuation of this solution would have resulted in an unstart of the adjacent module followed by a forward movement of the unstart shock to allow spillage over the cowl lip. This process took 32 000 iterations and almost 450 CRAY-2 hours. The final numerical domain consisted of approximately 1.3×10^6 points. The figure shows a sketch of the full-scale forebody and inlet, along with a 3-D, cowl-side view (with the body removed) of the 1 1/2 module solution at the termination of this study.

This computational study has provided a qualitative look at the unstart process for this particular inlet design, and in conjunction with experimental studies, it will help to give a better understanding of inlet unstart in scramjet propulsion systems. The methodology developed for this study will also be useful in future studies and in support of the X-30 flight testing program.

**(Thomas N. Jentink, 46250, and
Arthur D. Dilley)
Aeronautics Directorate**

■ SPACE TRANSPORTATION

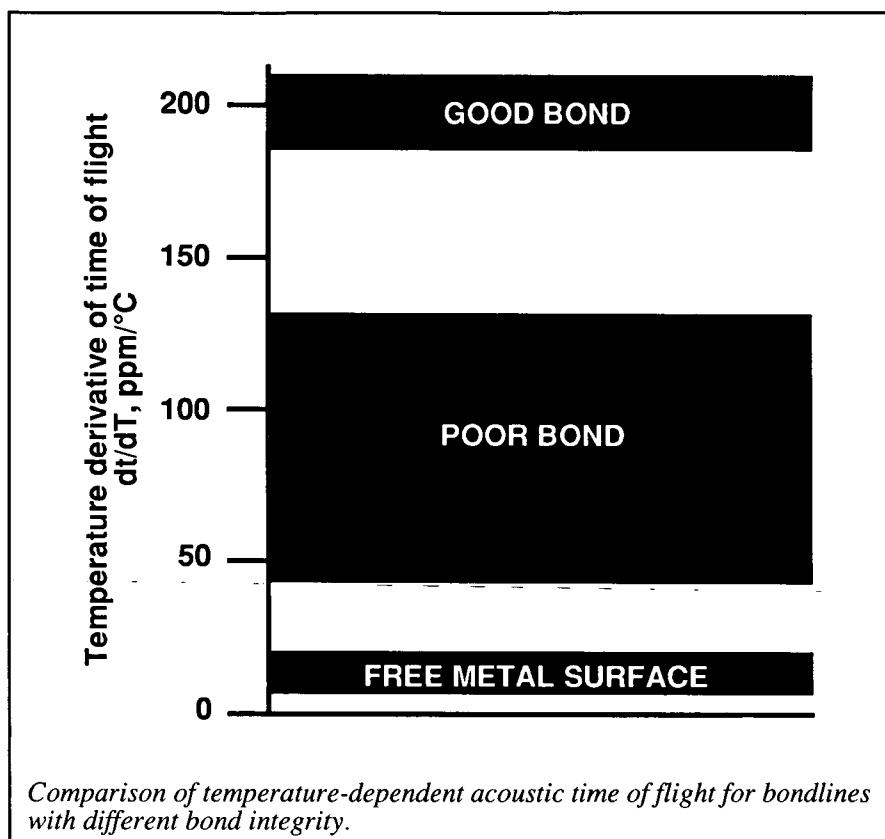


*Provide technology for the
current and evolutionary Space
Transportation System (STS)
and establish the technology
base for future transportation
system developments*

Measurement of Acoustic Property Temperature Derivative at Adhesive Bondline for Determination of Bond Integrity

The integrity of the adhesive bonds in many aerospace structures is critical to their structural performance. In particular, the Space Shuttle Solid Rocket Motor is a bonded structure in which good bonds between the steel case, insulation, and liner are required for adequate structural integrity. As an approach to understand bond integrity measurement, the temperature derivative of the acoustic properties at the interface of adhesively bonded steel/rubber specimens has been measured.

The acoustic properties of materials are well known to be temperature dependent. In addition to the temperature, the state of the stresses in the materials also influences the acoustic properties. In case of an adhesive joint similar to steel/epoxy/rubber, where three different materials exist close by, a change of temperature induces lateral stresses in these materials; this occurs because these three materials may have different linear temperature coefficients of expansions. Therefore, two factors contribute to the changes of the acoustic properties in a bonded material when the temperature is changed. These factors are the temperature dependence of the acoustic properties of materials (the normal temperature effect) and the stress sensitivity of the acoustic properties. The lateral stresses are induced in the bondline region because of temperature



changes. A good bond will be able to sustain such lateral stresses, but a poor bond (or a "kissing bond") will not be able to do so.

Specimens of rubber bonded by epoxy to steel were prepared with varying bond qualities by contaminating the epoxy to different extents. Test results from this process are presented in the figure.

This figure summarizes results for the measurements of the temperature coefficient of the flight time. A bare steel plate exhibits a small dt/dT , a property of the steel itself. A well-bonded interface exhibits a relatively

high dt/dT , as a consequence of the lateral stresses induced by the temperature change in addition to the temperature dependence of the basic materials properties. Poorly bonded specimens exhibit reduced dt/dT , thus indicating less ability of the bond to sustain lateral stresses.

(Al Smith, 44961)
Electronics Directorate

OSEE—Analysis of Surface Contamination Monitor

An optically stimulated electron emission (OSEE) is a physical phenomenon related to the photoelectric effect, in which light impinging on a metallic surface releases electrons that are collected with a positively charged electrode and measured as an electric photocurrent. In OSEE, which is the result of years of development by Marshall Space Flight Center, the light used is an ultraviolet mercury source, and the electrons are collected following their passage through ambient air. This makes OSEE available as a

method for nondestructive evaluation (NDE). OSEE is presently used as a nondestructive monitor of contamination on the Space Shuttle Solid Rocket Motor cases during their refurbishment for reuse.

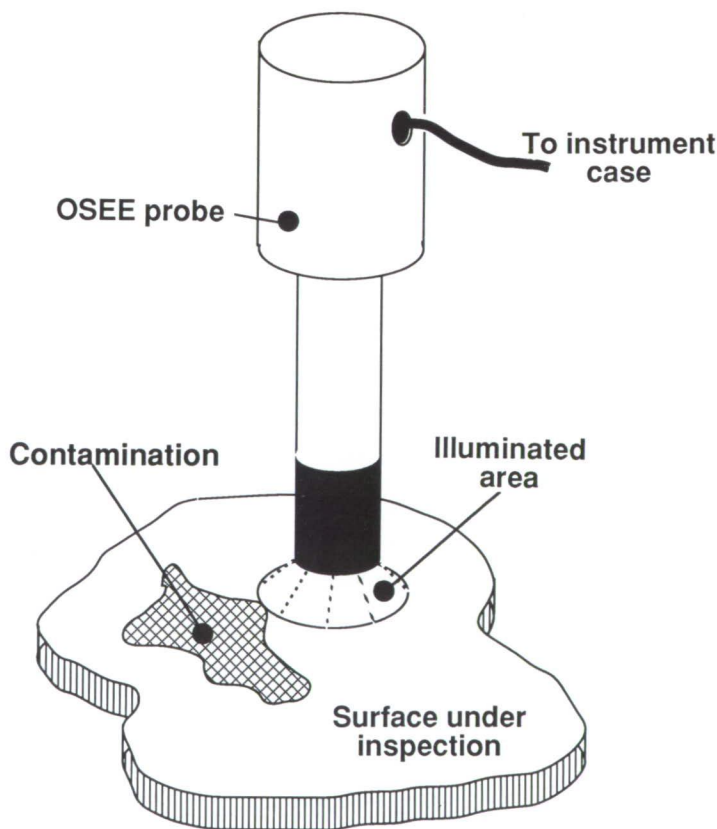
The primary contaminant of concern is the grease used for corrosion protection of the cases. In this work, OSEE was characterized as a photodiode acting in a gaseous environment, and its sensitivity to the grease was identified as a result of absorption of the ultraviolet light at the shortest wavelength (185 nm) emitted by the mercury lamp. The change of the surface work function with small

amounts of the contaminating grease, found to be photoconductive, was shown to dominate the sensitivity of OSEE at very small contaminant thicknesses. Interfering effects due to natural surface work function variations and water vapor were also found, and methods have been suggested by which the NDE inspection of Solid Rocket Motor casings using OSEE may be improved based on the scientific results.

(William T. Yost, 44991)
Electronics Directorate

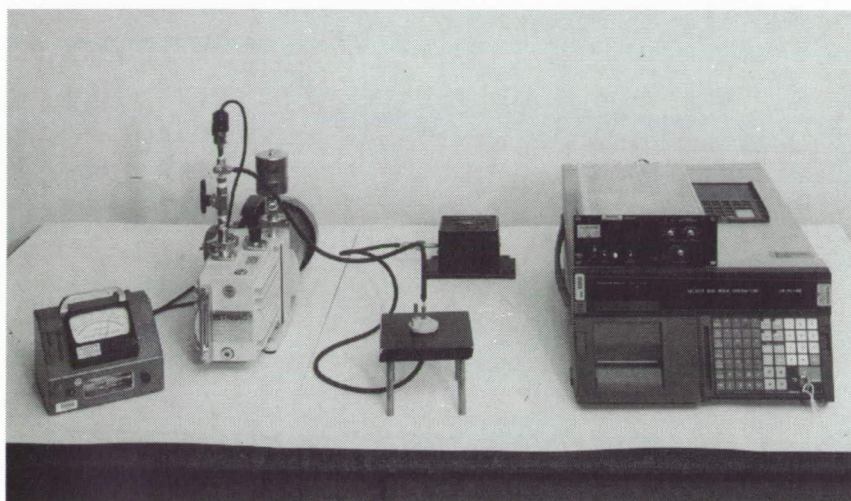
Aerobrake Pressure Port Vacuum Adapter

The Aeroassist Flight Experiment Project will test a new spacecraft heat shield design known as the aerobrake. Models of this concept have been wind-tunnel tested, but no vehicles with this configuration have been flown. There are numerous aerodynamic, thermal, and fluidics uncertainties that can only be resolved by taking actual in-flight data. One experiment onboard the spacecraft will measure the pressure distribution across the asymmetrically shaped aerobrake and gather data for computational fluid dynamics modeling. Because of the high temperatures encountered in aerobraking, the spacecraft structure and instruments are insulated with Space Shuttle tile technology. Pressure distribution measurements are made by penetrating the tile surface at various locations and inserting a high-temperature quartz pressure port attached by a flexible line to an extremely sensitive pressure transducer. Verification of the integrity of the penetration pressure port to transducer assembly is necessary during several stages of spacecraft development, manufacturing, and preflight testing.



Schematic view of contamination inspection using optically stimulated electron emission technology.

ORIGINAL PAGE
BLACK AND WHITE PHOTOGRAPH



Vacuum adapter test setup.

L-91-1434

Testing requires evacuating the test port and transducer assembly after installation. Pressure ports penetrate the tile from the back and are open to the front surface through a hole drilled in the reaction cured glass (RCG) outer layer. A vacuum testing system must be connected to the pressure port from the front side of the heat shield. No marketable device currently exists which will meet the test requirements of the experiment.

A vacuum adapter device has been designed, developed, manufactured, and successfully tested. This device meets the project testing requirements, is portable, affords protection to the delicate RCG opening, may be used in any spacecraft configuration, and is easy to install and remove. The adapter is shown on a tile block in the photograph.

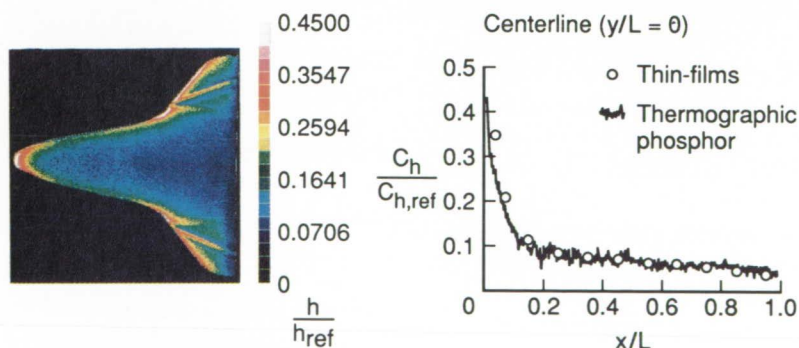
(H. G. Walthall, 45194)
Systems Engineering and
Operations Directorate

Global Heat-Transfer Measurements Using Relative-Intensity Two-Color Phosphor Thermography

A computer program has been developed which quickly and efficiently calculates global heat-transfer rates from relative-intensity two-color phosphor thermography data. This program, called PHOS4, solves the one-dimensional heat conduction

equation at each point on a phosphor image using standard phase-change paint equations with some modifications. The PHOS4 program runs on a 386-based IBM PC, and the results are stored in an image file that can be viewed using standard image processing programs.

In order to determine the validity of the results obtained using PHOS4, a comparison has been made between thermographic phosphor data and thin-film resistance gauge data (which have an accuracy of 5 to 8 percent) obtained from gauges mounted on the windward side of a shuttle orbiter-like configuration. Runs were made with the thin-film model and the ceramic phosphor model set at an angle of attack α of 20° and a free-stream Reynolds number based on model length $Re_{\infty L}$ of 4.2×10^5 in the Hypersonic Facilities Complex (HFC) 31-Inch Mach 10 Tunnel; both models were 10 in. long. As shown, for the case of heating along the centerline of the model, the phosphor data compare very favorably with the thin-film results. (In the figure, M is Mach number, L is body length, y is spanwise distance from the body centerline, x is axial distance from the nose, and $h/h_{ref} = C_h/C_{h,ref}$)



Global heating rates immediately following test

Measurement of global heating rates using thermographic phosphor technique for modified orbiter, M of 10 (air), $Re_{\infty L}$ of 4.2×10^5 , and α of 20° .

L-91-6518

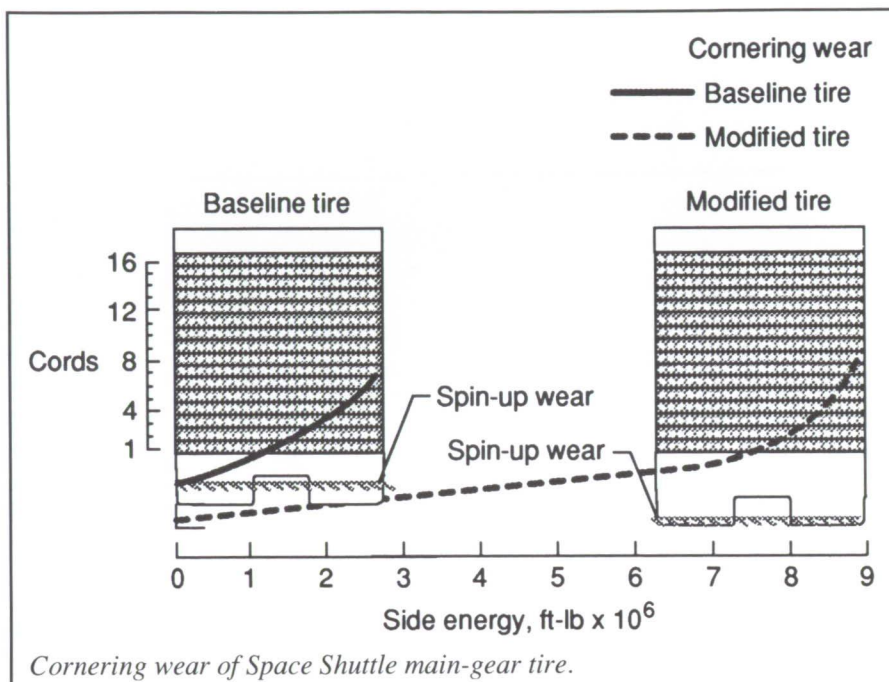
is local heat-transfer coefficient non-dimensionalized by the stagnation point heat-transfer coefficient on a 0.21-in.-diameter sphere.

The fact that phosphor data can be used to obtain heat-transfer results comparable to that of thin films is significant. The technique yields global results versus the discrete readings obtained with thin-film gauges. Also, a phosphor thermography model may be fabricated soon, but by comparison, a well-instrumented thin-film model may take several years to design, fabricate, instrument, and calibrate.

(N. Ronald Merski, 47539)
Space Directorate

Wear Performance of Modified Space Shuttle Main-Gear Tire

The high landing speeds of the Space Shuttle coupled with the highly textured runway surface on the Shuttle Landing Facility have resulted in excessive Space Shuttle main-gear tire wear during landing operations at Kennedy Space Center (KSC). Consequently, considerable interest exists in developing tires with improved wear characteristics. The sketches in the figure show cross sections of the baseline tire and a candidate modified tire. The modified tire has an extra 0.1 in. of undertread rubber to absorb wear. The rubber composition is 65 percent natural rubber and 35 percent synthetic rubber, whereas the baseline tire has a 100-percent natural rubber tread. The spin-up wear on the baseline tire subjected to a 200-knot touchdown on a corduroy runway surface destroys approximately two-thirds of the tread depth, whereas the spin-up wear on the modified tire under identical conditions



destroys only one-sixth of the tread depth as denoted by the spin-up label in the figure. The wear associated with the tire cornering effort is plotted in the figure as a function of side energy. The baseline tire will be worn through six cords (the maximum allowable wear limit) after the tire has dissipated approximately 2.5×10^6 ft-lb of side energy as indicated by the solid line. The modified tire, on the other hand, will be worn to the same limit after it has dissipated more than 8.5×10^6 ft-lb of side energy as denoted by the dashed line. This represents an improvement in tread life for the Space Shuttle orbiter main-gear tire of better than 300 percent over the current baseline tire.

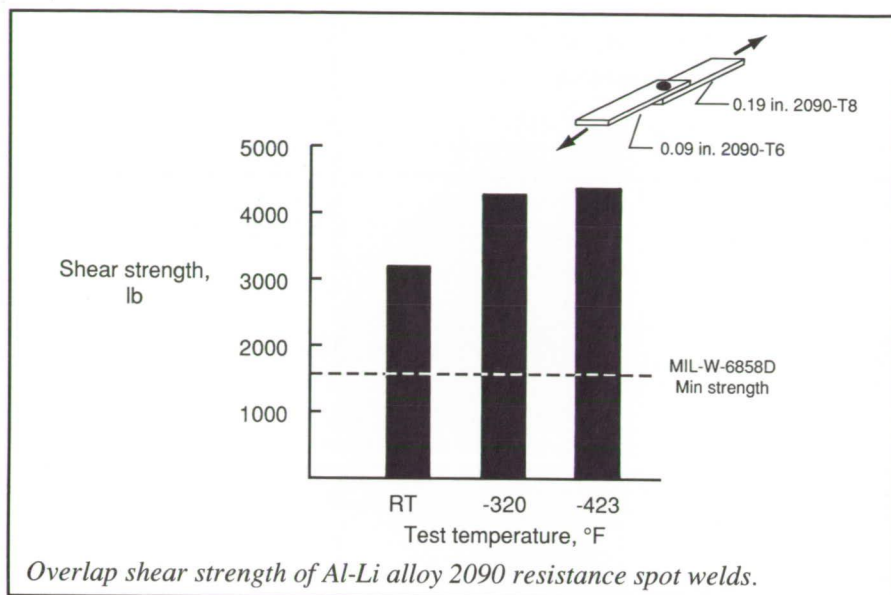
A 15-knot crosswind landing (the current Space Shuttle crosswind limit based on allowable tire wear) will expose each main-gear tire to 2 to 2.5×10^6 ft-lb of side energy. A 20-knot crosswind landing (the original orbiter crosswind limit) will expose each main-gear tire to approximately 4×10^6 ft-lb of side energy. The data in the figure indicate that the modified

tire can easily handle a 20-knot crosswind landing at KSC.

(Robert H. Daugherty and Sandy M. Stubbs, 41309)
Structures Directorate

Resistance Spot Welding of Advanced Aluminum Alloys

Resistance spot welding (RSW) is being considered as a candidate joining method in the built-up structure approach for fabricating cryogenic propellant tanks and dry bay structures in support of the National Launch System (NLS). The built-up structure approach, in which near-net shaped stiffeners are attached to a skin material, has the potential of significantly lowering costs by reducing raw material scrap rate. The scrap rate associated with the Space Shuttle external tank, which is machined from 2-in.-thick aluminum alloy 2219 plate, is approximately 80 percent; the scrap rate for a built-up structure would be



approximately 20 percent. Application of RSW to high-strength, low-density aluminum-lithium (Al-Li) alloys has the potential of further lowering the cost and weight of these structures.

In the RSW process, the work pieces are clamped between two water-cooled electrodes, and a high current is then passed through the work pieces. The heat generated by the resistance of the work pieces to the passage of this current causes them to melt and fuse rapidly, resulting in a high-strength bond. The magnitude and timing of the weld force and weld current are important considerations in developing an optimized resistance welding schedule. RSW is an economical, high-speed process that requires no external gas shielding or consumable materials. In addition, RSW readily lends itself to automation and adaptive feedback control. Resistance spot welding is currently being used to fabricate the stainless-steel fuel tanks of the Atlas-Centaur launch vehicle.

Cleaning and welding procedures have been developed and qualified to resistance spot weld several advanced Al-Li alloys per the requirements of the military handbook MIL-W-6858D.

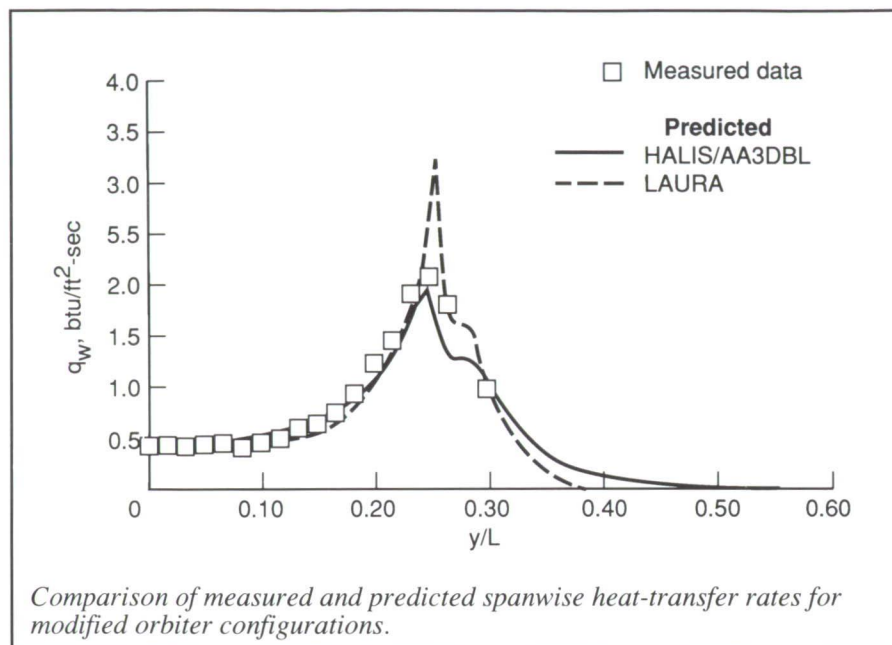
A standard commercial chemical cleaning procedure is sufficient to prepare the materials for welding, and all the Al-Li alloys investigated were readily weldable. The figure shows the overlap shear strength of welds produced between work pieces of Al-Li alloy 2090 of differing thicknesses; these work pieces are representative of a proposed stiffener and skin configuration. The tests were conducted at room and cryogenic temperatures; weld strengths exceeded the MIL-W-6858D requirement for these matrices by 100 to 150 percent at all three temperatures. High-resolution radiography revealed defect-free welds resulting from the optimized weld schedules. (R. Hafley and J. Wagner, 48078) Structures Directorate

Aerothermodynamic Measurement and Prediction for Modified Orbiter at Mach 6 and 10 in Air

Langley Research Center continues to examine new initiatives in Earth-to-orbit space transportation concepts that

will fulfill a variety of anticipated mission needs. Current examples are programs such as the Assured Crew Return Vehicle (ACRV), a vehicle designed to return crew members from Space Station *Freedom*; the Personnel Launch System (PLS), a personnel carrier to low Earth orbit; and the Advanced Manned Launch System, the next U.S. manned space transportation system. These and other programs will benefit from knowledge gained as a result of the comprehensive data base established for the Space Shuttle program. The present study augments the well-established comprehensive data base for the Space Shuttle orbiter while providing additional information concerning the complex three-dimensional windward surface flow field of an orbiter-like configuration. Areas of interest include laminar and transitional heating phenomena and shock/shock interaction phenomena on windward surface heating distributions.

Tests were performed at Mach 6 and 10 in air on a modified orbiter model to obtain detailed spanwise heating distributions over the windward surface; the purpose of these tests was to calibrate computational fluid dynamic codes. (For this code calibration study, the wind-tunnel model was identical to the numerical model of the computer code because the aerolines for the model fabrication on numerically operated machines were supplied by the code.) Heat-transfer rates were inferred from surface temperature-time histories measured with 150 thin-film resistance gauges located at 11 stations along the body length and spaced 0.15 in. apart in the spanwise direction. Global heating distributions were obtained using the relative-intensity two-color thermographic phosphor technique. Angle of attack was varied from 0° to 40° at Mach 6 and 10. Heating rate distributions were predicted with an inviscid/viscous method (referred to as High Alpha



Inviscid Solution/Axisymmetric Analogue for Three-Dimensional Boundary-Layer (HALIS/AA3DBL) code) and a Navier-Stokes solver (Langley Aerothermodynamic Upwind Relaxation Algorithm (LAURA) code) for angles of attack of 30° and 40° and a laminar flow condition at Mach 6.

Results indicate that heat-transfer rates q_w predicted with the AA3DBL and LAURA codes were in good agreement with the measurements for both longitudinal and spanwise locations. An example of these comparisons is presented in the figure for a laminar-flow condition (free-stream Reynolds number of 0.5×10^6) at Mach 6 and an angle of attack equal to 30°. (The data are presented for a spanwise location y/L at 75 percent of the model length.) Global heat-transfer distributions clearly illustrated the complex three-dimensional flow on the aft portion of this configuration. For Reynolds numbers of 0.4×10^6 to 6.0×10^6 based on length at Mach 6, spanwise heating distributions correspond to laminar flow (at the lowest value), fully turbulent flow (at the highest value), and complex transi-

tional flow (at an intermediate value). Streak heating patterns on the aft portion of the configuration were observed at lower angles of attack and are the result of downstream effects of the compression brought about by the discontinuous planform shape and the interaction of the bow shock with the wing shock.

(J. R. Micol, 45250)
Space Directorate

Aerodynamic Characteristics of HL-20/HL-20A Lifting-Body Configurations

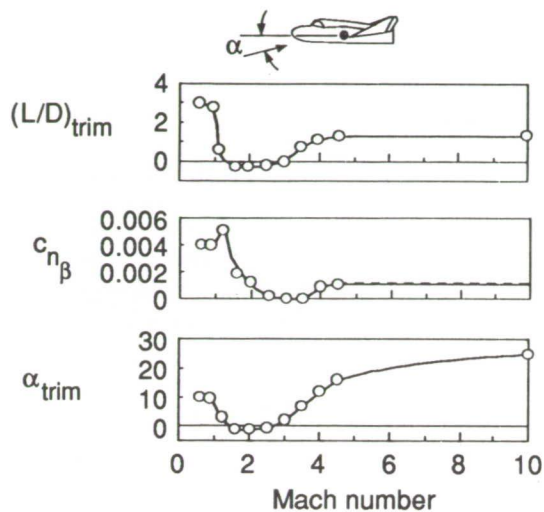
The HL-20 lifting-body shape has been suggested as the vehicle configuration for NASA's Assured Crew Return Capability and Personnel Launch System Programs. Both programs are designed around an entry vehicle with the capability of transporting a crew of 8 to 10 members from Space Station *Freedom*. The HL-20 is a small personnel carrier vehicle approximately 28 ft long with aerody-

namic characteristics similar to those of the Space Shuttle. The vehicle has a low-aspect-ratio body with a flat undersurface and blunt base. Center and outboard flat plate fins are mounted on the upper aft body. The outboard fins are rolled outward 40° from the vertical. Control surfaces are mounted on the outboard fins and aft body.

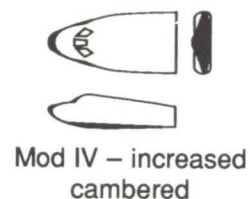
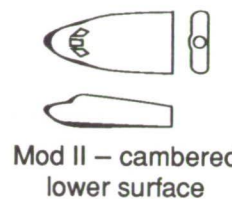
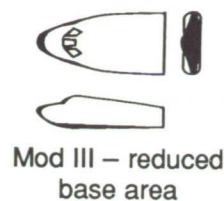
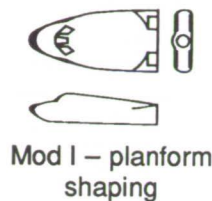
An extensive wind-tunnel test program is under way to define, in detail, the aerodynamics of the HL-20. The HL-20 shape has been "frozen" (and thus is viewed as a baseline) to allow evaluation without configuration variations. A parallel investigation has been undertaken to refine the HL-20. This series of configuration modifications is referred to as the HL-20A (see the upper right portion in the figure). The changes include forebody shaping to minimize drag, negative body camber to increase longitudinal trim angle, reduction in body base area to improve subsonic lift-to-drag ratio, changes in outboard fin dihedral for improved stability and trim, and fin airfoil shape. Tests of the HL-20 and HL-20A have been conducted in six wind tunnels at Langley Research Center and in the Calspan Transonic Tunnel covering a Mach range from 10 to 0.3.

Examples of the results obtained from the study are shown in the figure. The geometry of the HL-20 is presented in the center, and its basic aerodynamics characteristics across the Mach range are presented in the upper left portion of the figure. (The nomenclature is as follows: C_L is lift coefficient; L/D is lift-to-drag ratio; $C_{n\beta}$ is directional stability parameter (yawing moment per degree of sideslip, per degree); and α is angle of attack.) The improved supersonic trim characteristics of the HL-20A are shown in the lower left, and a comparison of the subsonic L/D of the HL-20 (with flat plate fins) and HL-20A is presented in

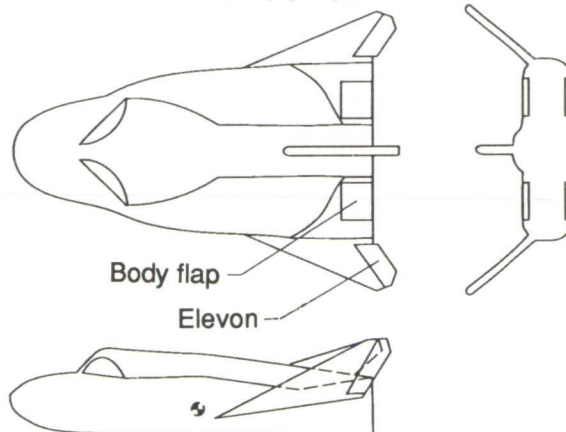
HL-20 aerodynamic characteristics



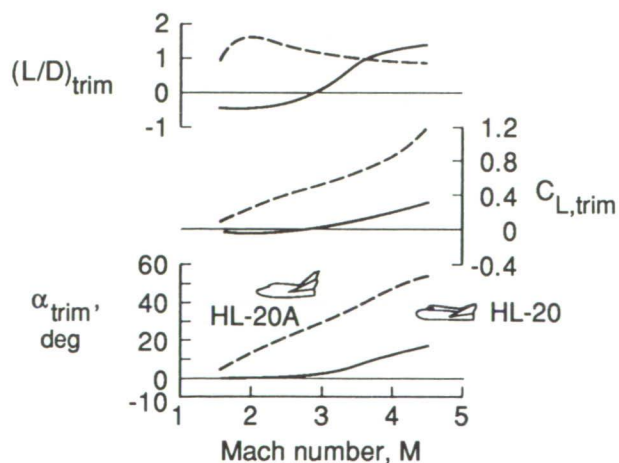
HL-20A body modifications



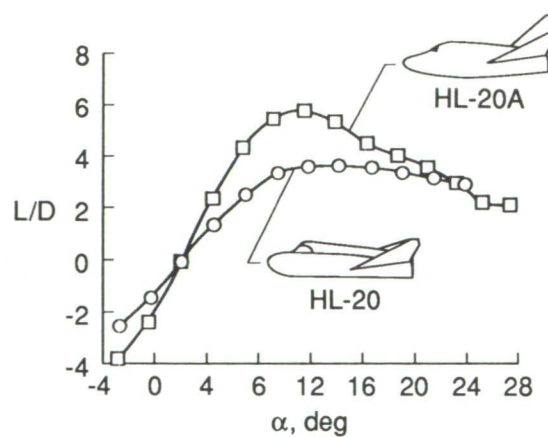
HL-20 3-view



Supersonic enhancement



Subsonic L/D enhancement



Examples of HL-20 and HL-20A wind-tunnel program results.

the lower right. Tests of the HL-20A are continuing over the Mach range to complete the configuration evaluation. (George M. Ware and B. Spencer, Jr., 45246)
Space Directorate

Energetics of Gas-Surface Interactions in Transitional Flows at Entry Velocities

Gas-surface interactions play a critical role in determining the aerodynamic and heat-transfer characteristics of vehicles flying in low-density atmospheres. A study has been performed to provide fundamental information on the molecular details of gas-gas and gas-surface interaction processes in entry vehicle shock layers, both to assist in understanding the physical mechanisms and to provide data that might be useful in designing flight experiments to measure gas-surface interaction behavior.

Direct Simulation Monte Carlo (DSMC) calculations of the flow around a 1.6-m-diameter sphere were performed over an altitude range of 130 km to 90 km for a typical Earth entry at 7.5 km/sec. A five-species air model with up to 23 chemical reactions was used. Velocity and translational energy distributions of gas molecules striking the surface were determined at points around the sphere for each gas species.

Variations of the average energy of gas molecules that strike the stagnation point are shown as a function of Knudsen number (based upon sphere diameter) or corresponding altitude. At 130 km, the average energy approaches that expected for free-molecular flow except for those species, such as N and NO, which are not present in the free stream but are produced through chemical reactions in the shock layer. With decreasing altitudes, the average molecular energy decreases substantially because of the increasing amount of kinetic energy transformed into heat as a result of

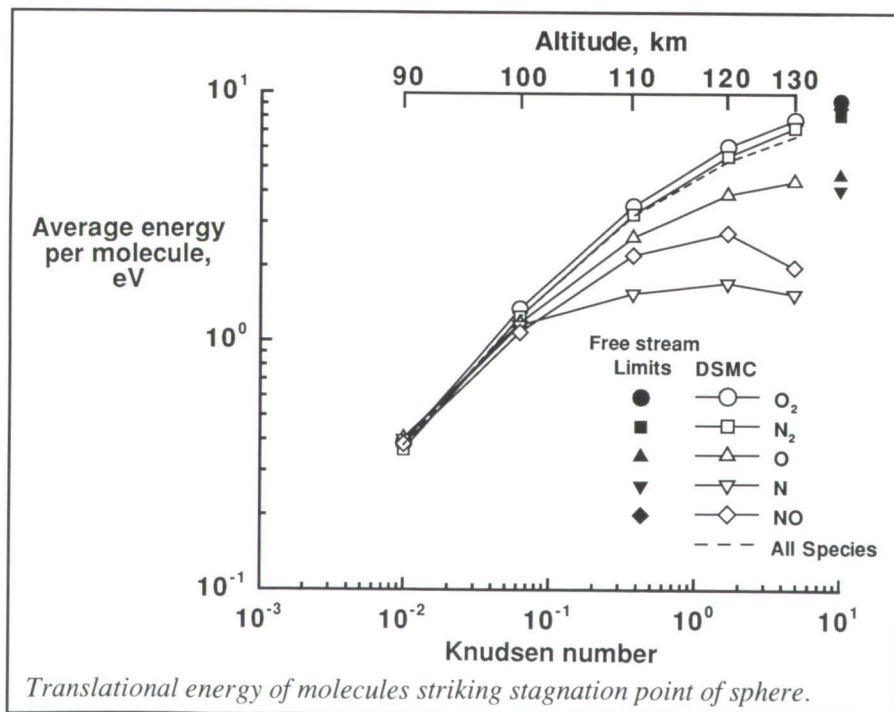
intermolecular collisions. The results also demonstrated that the molecular velocity distributions deviate markedly from those expected for equilibrium processes and even displayed a bimodal distribution at some altitudes intermediate to 130 km and 90 km. The behavior was such that the distributions are not readily explained in terms of simple multitemperature models based on a superposition of equilibrium distributions.

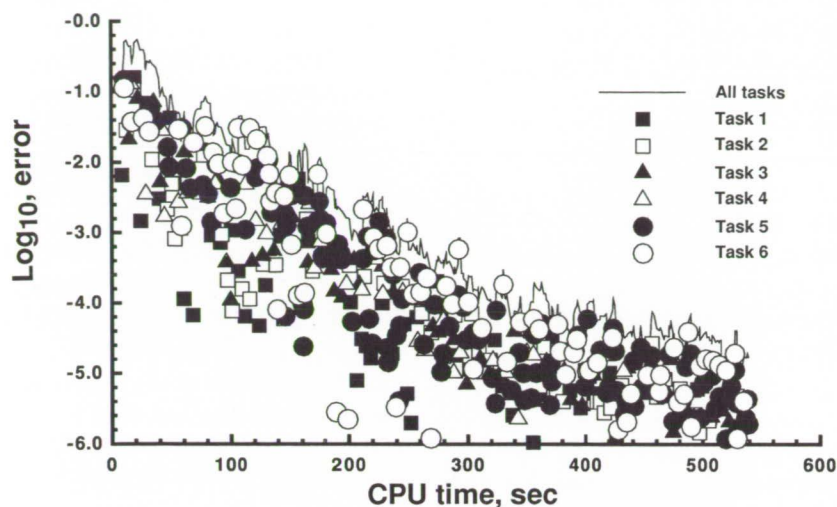
(R. G. Wilmoth, V. K. Dogra, and J. N. Moss, 44368)
Space Directorate

Asynchronous, Macrotasked Relaxation Strategies for Solution of Viscous, Hypersonic Flows

The evolution of the Multiple Instruction-, Multiple Data- (MIMD) stream supercomputer, in which multiple processors may independently and asynchronously execute their own instruction sets, has expanded capabilities for numerical solution of very large, complex problems. The CRAY-2 and CRAY YMP computers support multiprocessing on a DO-loop (microtasking) or SUBROUTINE (macrotasking) level. Macrotasked code has the greater flexibility with regard to parallel, asynchronous execution of large, long-running jobs and dynamic allocation of computational work.

Solutions for hypersonic, thermochemical nonequilibrium flows over aerobreaks have been obtained using as many as eight macrotasks executing asynchronously. Sacrificing synchronization results in no adverse effects on total CPU time required to obtain a solution and reduces turnaround time for a given job. Adaptive partitioning





Convergence histories for six asynchronously executed macrotasks (with adaptive partitioning) for viscous, hypersonic flow problem.

provides further, moderate improvement in required CPU time by moving partition boundaries to concentrate task activity where the contribution to the solution error is highest. The figure shows the convergence history for each of six tasks applied simultaneously and asynchronously to the solution of hypersonic, reacting flow over an aerobrake. The pattern is chaotic because of the lack of synchronization and moving partition boundaries, but the overall trend shows that this solution decreases CPU time and is approximately a factor of 6 times faster in turnaround time than the single-task application.

Simulations of complex entry vehicles require very large memory, sometimes demanding the dedicated use of a supercomputer. The present asynchronous, macrotasking strategy enables utilization of all processors in the dedicated mode, with speedup proportional to the number of processors for coarse grain machines such as the CRAY-2 and CRAY YMP.

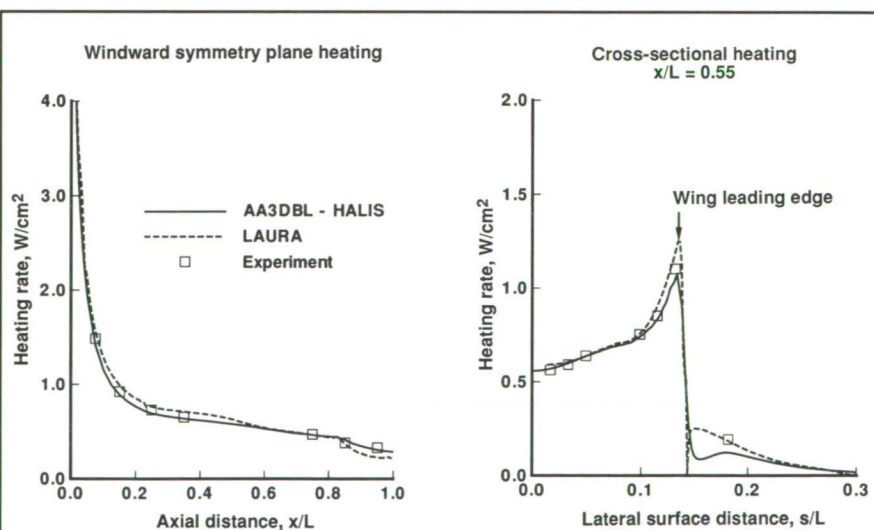
(P. A. Gnoffo, 44380)
Space Directorate

Comparison of Heating Rate Calculations With Experimental Data on Space Shuttle Orbiter at Mach 6

The design of advanced entry vehicles requires accurate prediction of aerodynamic heating rates during entry. In this design process, both engineering and benchmark computer

codes are used. Engineering codes provide reasonably accurate results with very short computer run times, and benchmark codes provide very detailed and accurate solutions but usually require very long computer run times. Before these codes may be confidently applied to vehicle design, they must first be validated by comparison with experimental data.

A study has been performed to assess the ability of an engineering code based on combined inviscid and boundary-layer theory, AA3DBL/HALIS (Axisymmetric Analogue for Three-Dimensional Boundary-Layer/High Alpha Inviscid Solution), and a benchmark Navier-Stokes code, LAURA (Langley Aerothermodynamic Upwind Relaxation Algorithm), to predict heating rates away from the windward symmetry plane and in the vicinity of wing leading edges on vehicles such as the Space Shuttle orbiter at large angle of attack. In support of this study, a new wind-tunnel model of the Space Shuttle orbiter was built, using thin-film gauge technology, which enabled highly detailed heat-transfer measurements, especially away from the symmetry



Heating comparisons on Space Shuttle orbiter (Mach number of 6 and angle of attack of 30°).

plane. This model was tested in the 20-Inch Mach 6 Tunnel.

Calculated results from both codes are in good agreement with the experimental data. These and other similar comparisons demonstrate that the AA3DBL/HALIS and LAURA codes accurately predict the heating over most of the windward surface of winged vehicles such as the Space Shuttle orbiter at a large angle of attack. (H. H. Hamilton II, F. A. Greene, and K. J. Weilmuenster, 44365) Space Directorate

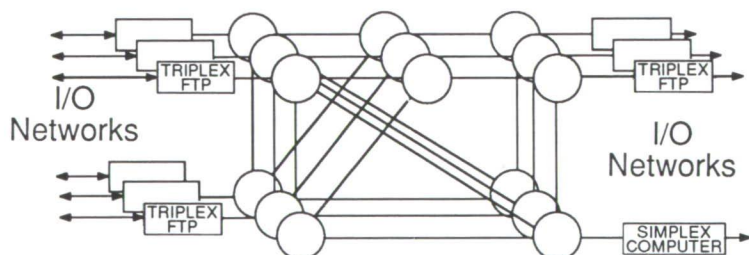
Advanced Information Processing System for Advanced Launch System

Historically, cost and weight considerations have dictated a single-string avionics architecture for expendable launch vehicles; this decision means that a single failure could be catastrophic to a mission, which has been the case in some launch failures. The next-generation launch vehicle avionics suite and its supporting software must extend beyond present switching logic and majority voting techniques to provide cost-effective multiple fail-operational configurations in near real time. A highly reliable computer system architecture is required to meet the low cost and high operational reliability requirements of the Advanced Launch System (ALS).

The goal of the Advanced Information Processing System (AIPS) Program is to develop techniques for achieving semidistributed fault-tolerant computer system architecture designs that are applicable to a broad range of applications with very low failure probability requirements. An example architecture has been designed by the Charles Stark Draper Laboratory, Incorporated, under contract to Langley Research Center. This architecture employs redundant general-purpose computers at processing sites that are interconnected by a fault-tolerant network. The general-purpose computers designed for the AIPS application are termed Fault-Tolerant Processors (FTP), and they may be simplex, duplex, triplex, or quadruplex units based on the reliability requirement of the application program being performed at the processing site.

Objective: devise a fault-tolerant distributed computer system for the advanced launch system to:

- Enhance safety
- Allow launch on demand
- Support autonomy



- Features:
- ADA operating system
 - Fault-tolerant distributed processing sites
 - Fault-tolerant inter-computer network
 - Appropriate function reliability
 - Low fault tolerance overhead
 - Growth capability
 - Redundancy transparent to user

Example AIPS configuration

Candidate Advanced Information Processing System.

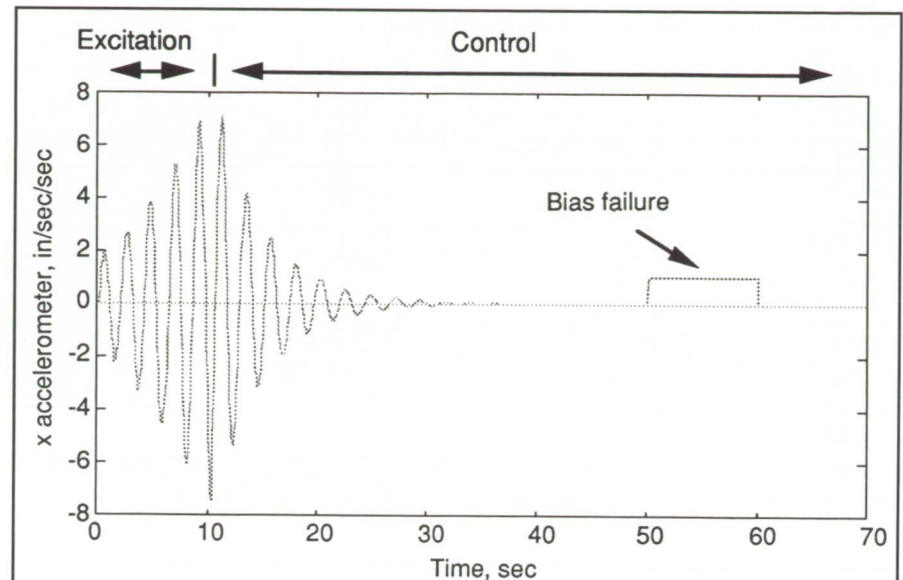
The AIPS for the ALS effort culminated with a demonstration of distributed AIPS operation; this demonstration included multiple fault-tolerant processing sites connected by three fault-tolerant networks such that each fault-tolerant network could independently sustain faults by switching in good links and nodes in response to failures. The demonstration used a configuration of three triplex fault-tolerant processing sites and one simplex (not fault-tolerant) processing site connected by a three-layer I/O (input/output) network. The demonstration consisted of the just-described AIPS configuration running all sites simultaneously but processing only system functions.

(Felix L. Pitts, 46186)

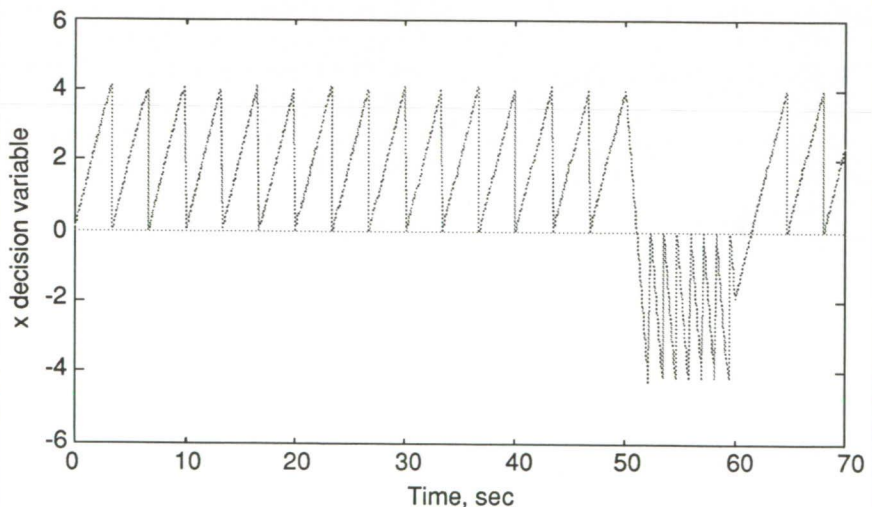
Flight Systems Directorate

Analytic Redundancy Management for Large Flexible Structures

Comprehensive simulation testing of an analytic redundancy management (ARM) approach for on-line component failure detection has been completed on a simulation of the Langley Research Center Spacecraft Control Laboratory Experiment research facility (SCOLE). The SCOLE experimental apparatus is a functional model of the Space Shuttle with a large, flexible, offset-feed antenna cantilevered from the payload bay. This approach uses a single, active, Kalman filter selected from a bank of filters, each element of which was previously designed to accommodate a specific failure condition. Residuals of the active filter are processed through a sequential probability ratio test (SPRT) filter to identify the failure state of the system. Because a failure of a single sensor affects more than one sensor



Accelerometer output generated during SCOLE simulation.



Accelerometer decision variable generated during SCOLE simulation.

innovations (estimated residuals) sequence, an interpreter is required to examine the innovations of the operating filter for the appropriate failure signature and produce the estimate of the failure mode.

The objective of the methodology is to identify component bias failures and reconfigure the control system to accommodate them before significant

performance degradation results. To test the accommodation scheme, bias failures were injected sequentially for 10 sec each to each of three rate sensors and two accelerometers. A typical simulated sensor output is shown in the first figure. During the first 10 sec, the first mode was excited with a sinusoidal input to the torque-wheel actuators. Then, a closed-loop optimal control law was engaged. The

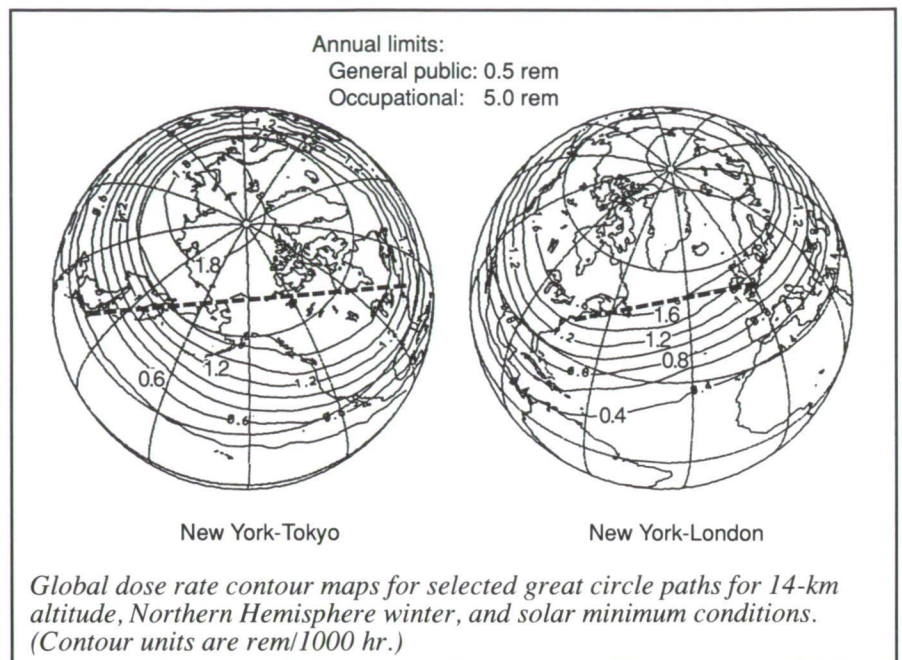
first figure displays the output for the fourth sensor, in which bias was injected during the 50-sec and 60-sec intervals. The second figure displays the associated SPRT decision variable for a positive bias failure. The SPRT decision variable time history reflects the identification of a failure by passing to the negative valued trigger point. Approximately 2 sec after bias injection, system accommodation was accomplished by switching to a Kalman filter designed for the remaining unfailed sensors. Previous bias failures were introduced to the other three sensors during the three preceding 10-sec intervals and also to the fifth sensor during the 60-sec and 70-sec intervals. Inspection of the response in the first figure for those time intervals reveals no adverse effect due to system accommodation via reconfiguration of the Kalman filter.

These results show that bias failures can be detected and recovery can be accomplished on a highly flexible structure using analytic models to establish redundancy between dissimilar sensors.

**(Joram Shenhar and Raymond Montgomery, 46617)
Flight Systems Directorate**

Radiation Exposure Analysis for High-Altitude Aircraft

During the past decade, considerable attention has been given to the cumulative ionizing radiation dose incurred by pilots and crew members of commercial high-altitude aircraft. During the course of a year, the legal annual dose limit prescribed for the general populace (0.5 rem/year) is often exceeded by the aircrew for intercontinental and transcontinental flights, especially for high-latitude,

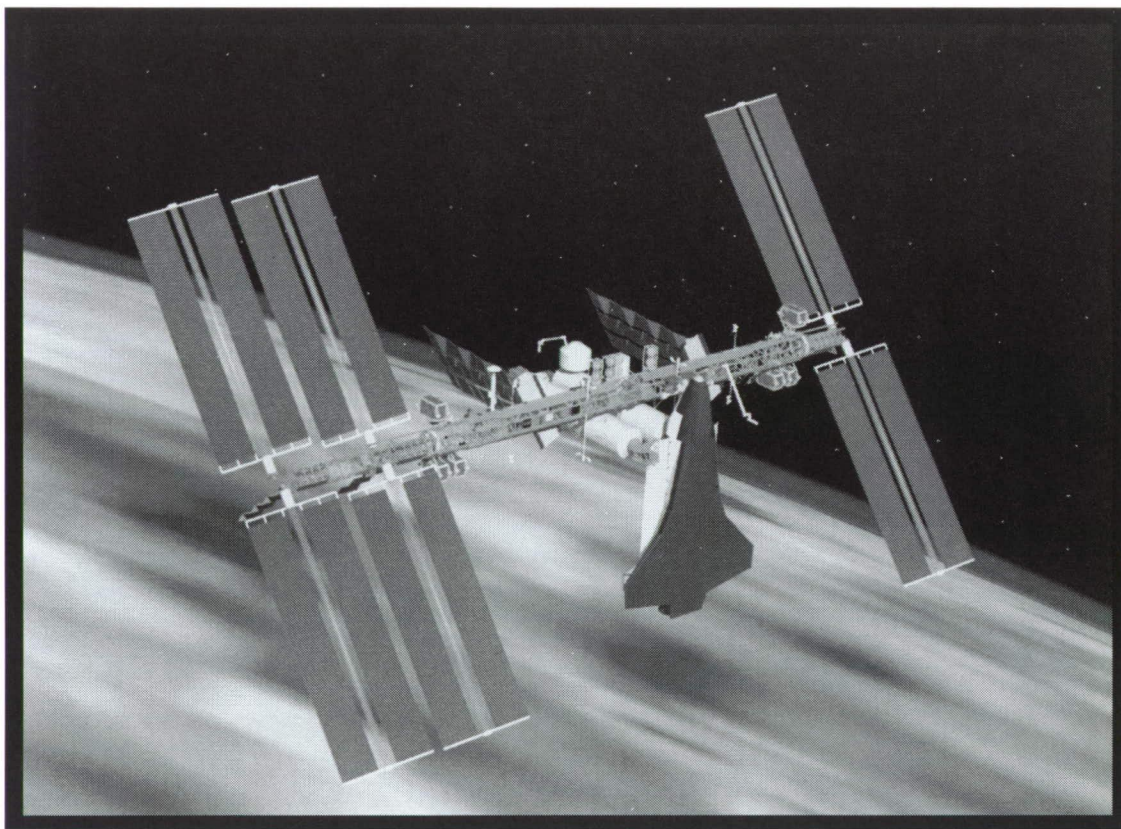


Northern Hemisphere flight paths for which the crew spends approximately 1000 hours per year at altitudes from 11 km to 13 km. At supersonic transport cruise altitudes (16 km to 18 km), dose rates can be several times higher.

The present effort has involved the formulation of a data base for natural background radiation in the upper atmosphere which has been derived from numerous high-altitude balloon and aircraft measurements augmented with computational analyses. A FORTRAN source code has been developed which uses the data base to predict dose rates that depend not only on altitude but also on other pertinent variables (such as geographic location, solar activity levels, and seasonal effects). Climatological atmospheric data obtained from the Langley General Circulation Atmospheric model provide the capability of including both annual variations and Northern and Southern Hemisphere asymmetry effects. The figure shows selected intercontinental great circle routes superimposed on a global contour map of dose rate. It is clear

that for either of these flight paths, 1000 hr per year results in an incurred dose substantially above the legal limit. The present code and associated data base should be valuable to predict potential radiation exposure problems. **(John E. Nealy, 44412, and John W. Wilson)
Space Directorate**

■ SPACE STATION



*Provide technology for the
current and evolutionary Space
Station (including manned and
unmanned space platforms)
and provide the technology
base for future developments*

PRECEDING PAGE BLANK NOT FILMED

ORIGINAL PAGE
BLACK AND WHITE PHOTOGRAPH

Preintegrated Structures for Space Station *Freedom*

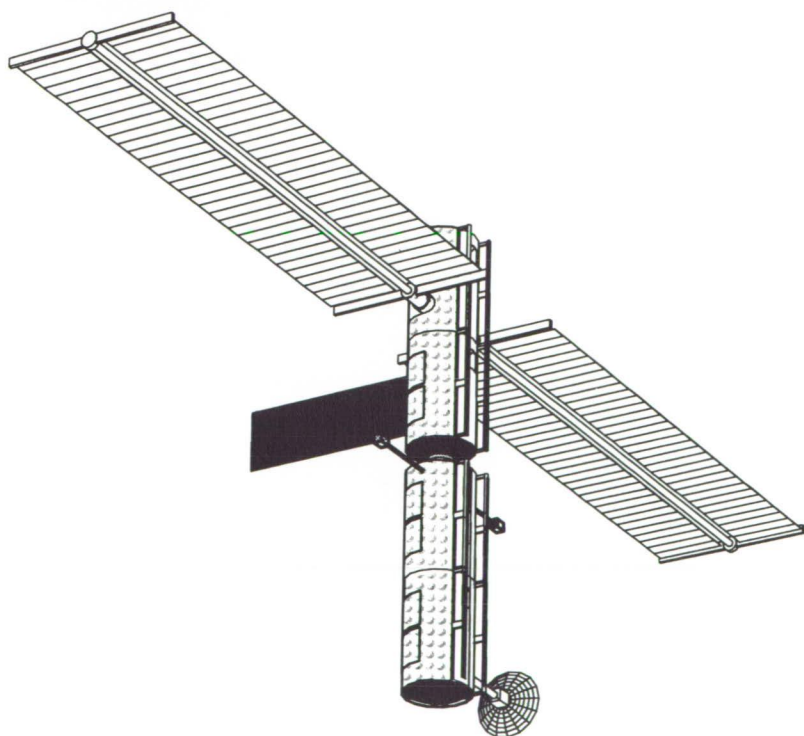
The assembly of Space Station *Freedom* has always presented a significant challenge to its design engineers. Never before had a spacecraft the size of *Freedom* been required to be delivered to orbit in such a comparably small launch vehicle (i.e., the Space Shuttle). This size difference dictated numerous Space Shuttle launches and on-orbit assembly. An in-space construction (erectable truss) approach to assembling *Freedom* was planned; however, Space Shuttle performance decreases, station system

and support hardware mass increases, a more conservative understanding of Space Shuttle packaging and center-of-gravity constraints, increases in flight support equipment (FSE), and large increases in extravehicular activity (EVA) estimates have made it increasingly difficult to launch and assemble *Freedom* with a limited number of Space Shuttle flights. The prime benefit of an erectable space structure (the ability to construct a large spacecraft from a small launch package) was no longer being realized for *Freedom* assembly. In response to these concerns, the Langley Research Center Space Station *Freedom* Office (SSFO) began to study the technical feasibility

of using preintegrated structure in the assembly of *Freedom* with the objective to maximize ground integration and minimize on-orbit integration/verification functions (thus reducing EVA and risk) while maintaining an equivalent number of assembly flights.

The concept for assembling *Freedom* without erectable trusses was investigated assuming a baseline set of Space Station system weights and utilizing an isogrid tube as part of the preintegrated structure. A preintegrated approach combines station primary structure and distributed systems into discreet sections that are assembled and checked out on the ground. The section is then launched as a single structural entity on the Space Shuttle and attached to the orbiting station with a minimum of EVA. A detailed assessment was made of the First Element Launch (FEL) configuration; additional assessments then were made for the rest of the assembly flights based on the FEL-derived information. The feasibility of the preintegrated concept was evaluated with respect to system/structural interfaces, dynamic and thermal loads, assembly manifesting/operations, and station orbital characteristics.

A report containing detailed structural, thermal, and spacecraft characteristic analysis of the preintegrated structure assembly approach was presented to the Space Station *Freedom* Program Director. A detailed assembly analysis showed the preintegrated approach to have significant improvements (with respect to EVA and Space Shuttle lift margin) compared with the then baseline



Stage two of preintegrated structure Space Station concept.

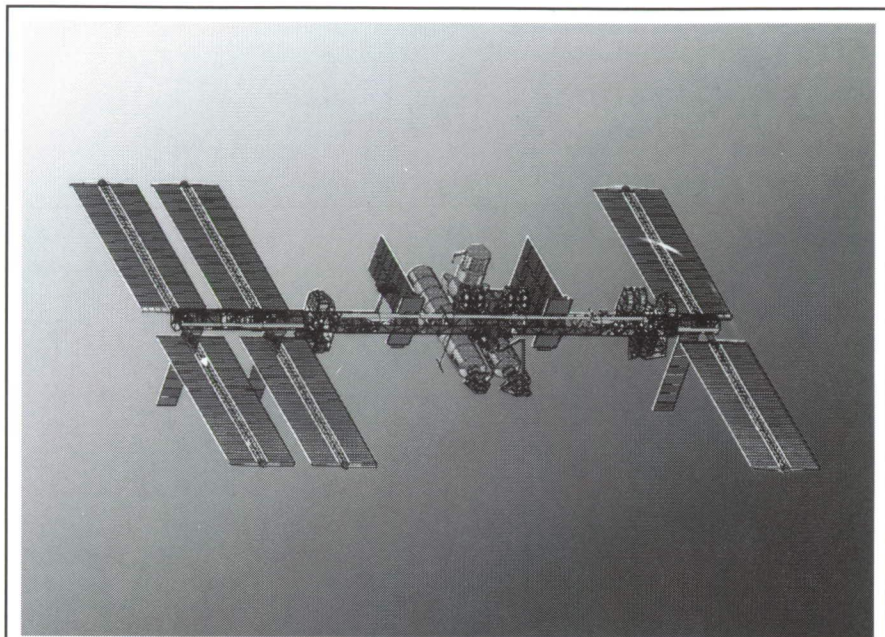
erectable truss based assembly sequence and to maintain an equivalent number of station assembly flights. At the time this study was performed, the *Freedom* program was facing major technical difficulties, thus making the erectable truss based sequence viable because of EVA and Space Shuttle lift constraints. Subsequent to this study, the Space Station program adopted a preintegrated approach to the assembly of *Freedom*.

(Patrick A. Troutman, 41954, and Phil Mutton)
Space Directorate

Restructured Space Station *Freedom* Controllability

In January 1991, the Langley Research Center Space Station *Freedom* Office performed an assessment of the characteristics of the then proposed preintegrated *Freedom* concept. Of particular concern was the relationship between solar array operation and spacecraft controllability. The Man-Tended Configuration (MTC) is required to fly in "arrow" and gravity gradient flight modes that result in a reversal in the way the articular Sun-tracking joints function. One objective of the study was to assess the impact of the joint reversal on MTC. Another assessment involved the asymmetric Permanently Manned Configuration (PMC), which has a third photovoltaic unit on one side of the transverse boom.

Control problems occurred for MTC when the solar arrays were tracking the Sun to produce full power while flying in an arrow or gravity gradient flight mode. At these attitudes, high-rate alpha joint motion may occur during an orbit when the direction to the Sun is nearly parallel to the alpha



Space Station Freedom permanently manned configuration.

joint rotation vector. This motion, in turn, leads to significant variations in configuration inertia, thus invalidating constant inertia control gain derivation assumptions and exerting a disturbance torque on the control moment gyroscopes (CMG) controlled core body. Several modified Sun-tracking techniques were evaluated with respect to producing a controllable MTC requiring no modifications to the CMG control algorithms. A feathered flight attitude produced satisfactory control characteristics, but it reduced available power from 18.75 kW to an average of 8.7 kW. A constrained Sun-tracking strategy was then developed which eliminated the large solar array articular motions and the associated controllability problems while only reducing full power by an average of up to 10 percent. The assessment of PMC indicated that this configuration would utilize almost two-thirds of the CMG momentum storage capability at an orbital altitude of 220 nmi. Large aerodynamic torques resulting from the asymmetric solar array area distribution lead to the large control momen-

tum requirements. Other simulations indicated that the addition of a berthed orbiter utilized nearly all the available CMG capability.

A report was presented to the Space Station *Freedom* Program Director in March 1991. Report recommendations included constraining alpha rotations for MTC in the arrow and gravity gradient flight modes and perhaps developing new non-TEA (torque equilibrium attitude) seeking control laws. Recommendations for PMC included raising the operational altitude or moving to a symmetric configuration as soon as possible. A detailed 6-min computer animation depicting a MTC flight simulation was also produced.

(Patrick A. Troutman, 41954, Michael L. Heck, and Renjith R. Kumar)
Space Directorate

Power Optimal Single-Axis Articulating Strategies

The power required for Space Station *Freedom* is provided by photovoltaic (PV) arrays located on port and starboard articulating structures. Because of the motion of the Space Station along its orbit, variations in orbital geometry with respect to the Sun, and core attitude fluctuations with

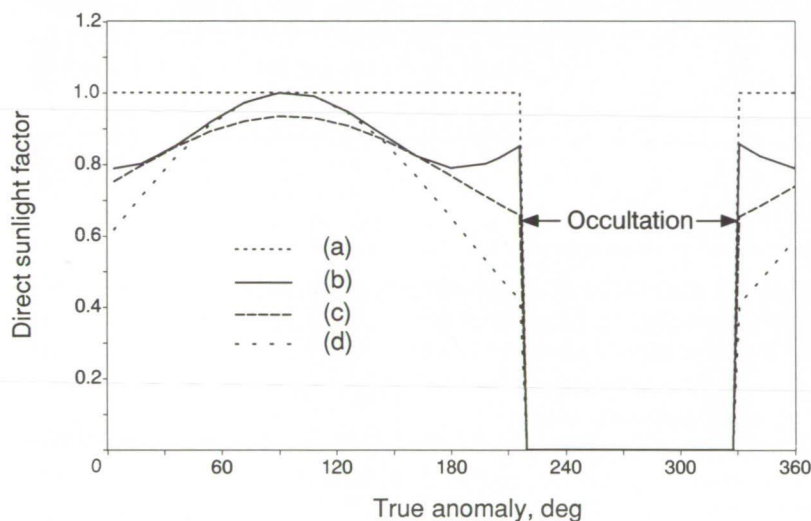
respect to the local vertical local horizontal (LVLH) orientation because of disturbing external torques, the orientation of the PV arrays must be constantly adjusted with respect to the inner core to track the Sun. The physical rotary joints that perform this function are called Solar Alpha Rotary Joints (alpha joints) and Solar Beta Rotary Joints (beta joints). The alpha joints provide a relative rotational motion between the inner core and the

outboard truss. The beta joints perform the PV array orientation adjustment with respect to the articulating port and starboard truss. Power optimal single joint tracking of Space Station *Freedom* was analyzed. The motivation was to eliminate a joint to reduce the cost of the station.

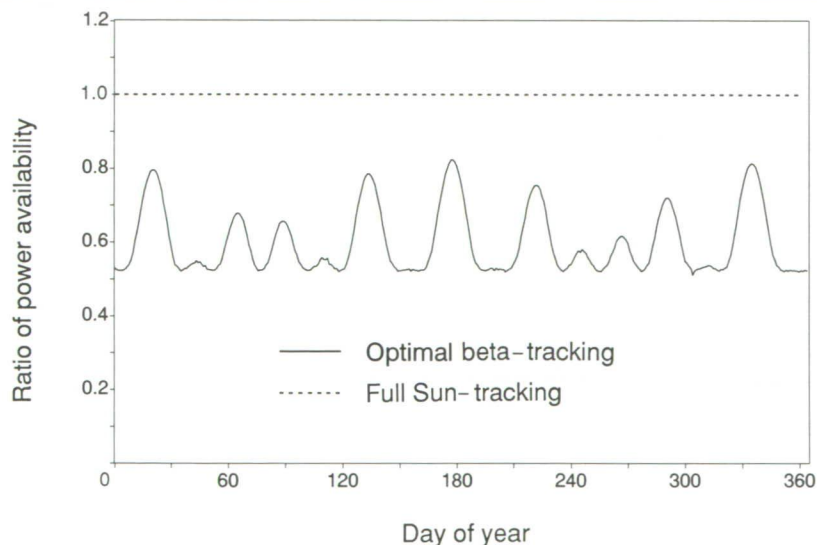
A feathered PV array orientation (in which the array area is perpendicular to the velocity direction) can be continuously maintained when deleting the alpha joint for an LVLH core attitude. Feathered arrays minimize drag, increase orbital lifetime, and decrease atomic oxygen degradation effects on the PV arrays. The power study was performed for both LVLH and non-LVLH station core attitudes. Intra-array shadowing, shadowing thresholds, and power loss from shadowing were also examined. Moreover, power availability with only alpha joints and no beta gimbal degree of freedom was considered for comparison.

Initially, two classes of problems were solved to maximize power availability using beta tracking. The first problem was to evaluate the optimal time-varying beta angle history over an orbit that maximizes the integral of the dot product of the unit vector from the spacecraft to the Sun and the unit vector normal to the active side of the PV array over orbital daylight. The dot product is named direct sunlight factor (dsf) in this study. The second class of problems evaluated a constant optimal beta angle history over an orbit that maximized the same performance index.

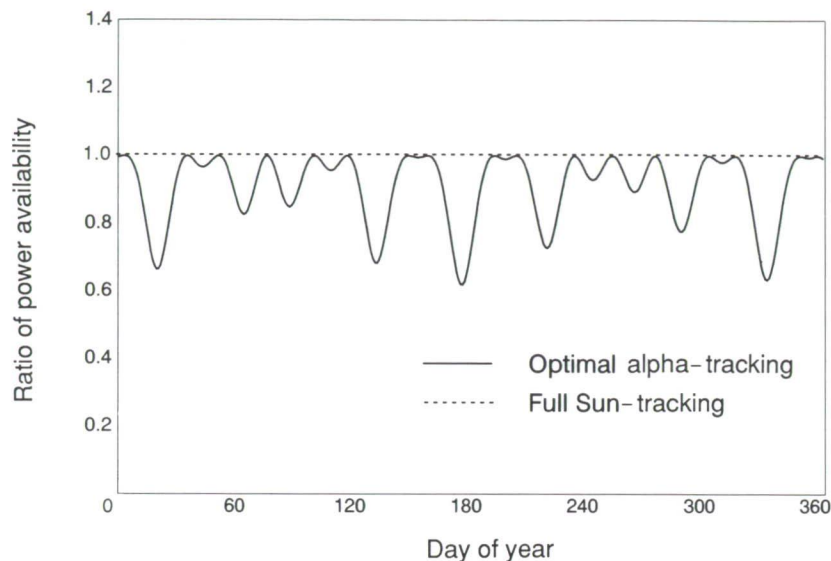
The optimal control problems were formulated as typical Mayer problems, and the solutions were obtained via direct methods using parameter optimization. The first figure shows the variation of the dsf over an orbit on the day of winter solstice at an ascending node of 180°. This variation



Direct sunlight factor.



Ratio of power availability for optimal beta-tracking.



Ratio of power availability for optimal alpha-tracking.

shows the variation of power availability with respect to full Sun-tracking using optimal alpha-tracking over an entire year, assuming LVLH core attitude. This strategy produces an average of about 90 percent of full Sun-tracking power over a year, independent of initial ascending node. On any given day, the power availability may be as low as 62 percent or as high as 100 percent of the full Sun-tracking power. For variations in attitude of the core (as performed for optimal beta-tracking), an additional power loss of 1.5 percent may occur. No power loss because of shadowing occurs for this strategy, assuming that the locked beta angle is at 0° .

(Renjith R. Kumar and Michael L. Heck, 41954)
Space Directorate

corresponds to a maximum solar beta angle, where solar beta is defined as the angle between the Sun-spacecraft line and the plane of the orbit. The core attitude is assumed to be at LVLH. Graph (a) depicts full Sun-tracking using both alpha and beta tracking, which yields a direct sunlight factor of unity during orbital daylight. The plots (b), (c), and (d) show the variation of dsf (with alpha angle locked at 0°) using optimal time-varying beta, optimal constant beta, and solar beta angles, respectively. The percentages of full Sun-tracking power available for the three beta-tracking cases were 87.4 percent, 82.4 percent, and 76.9 percent, respectively. The time-varying optimal beta solution is clearly better than the other two, but it might require large rates at certain orbits to achieve this performance. The optimal constant beta gives a better average performance than the solar beta tracking.

The optimal constant beta-tracking was performed over an entire year. Because of Earth oblateness effects, a nodal regression of approximately $-7.051^\circ/\text{day}$ at an altitude of 220 nm

and orbit inclination of 28.5° was modeled. The second figure depicts the variation of the ratio of available power to full Sun-tracking power over an entire year. The yearly average power was approximately 60 percent of full Sun-tracking power. On any given day, the power availability may be as low as 51 percent or as high as 83 percent of full Sun-tracking power.

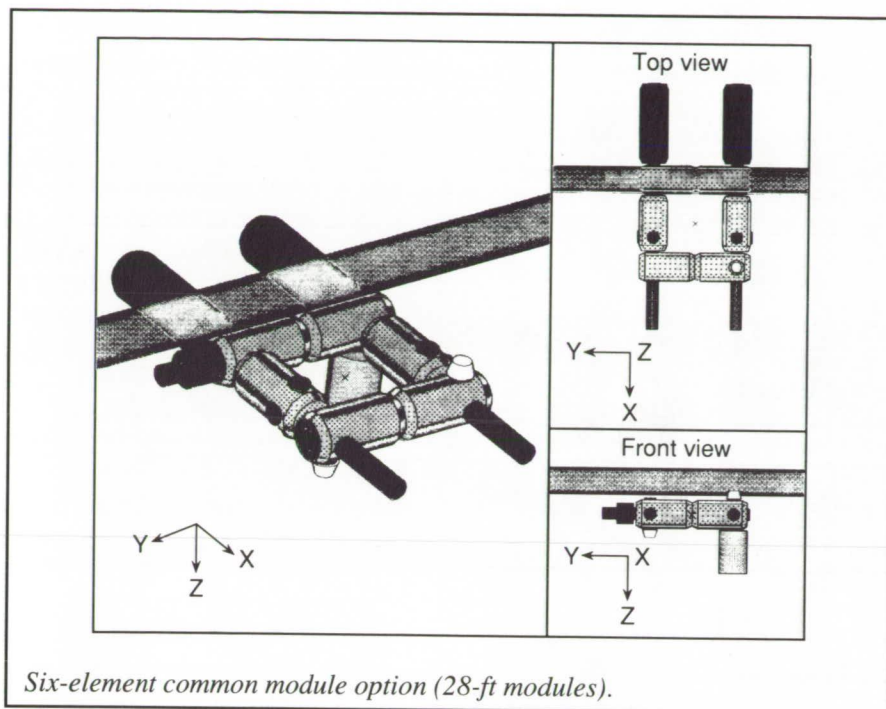
For variations in the core-attitude of $\pm 10^\circ$ in roll and yaw and $\pm 20^\circ$ in pitch, less than 2-percent additional power loss may occur. Intra-array shadowing can cause power reduction, depending on the array geometry and the spacecraft-Sun geometry. A detailed analysis of the intra-array shadowing and the power loss comparisons with full Sun-tracking was made. The actual ratio of available power for configurations with possibility of intra-array shadowing using optimal beta-tracking may be greater than 60 percent of full Sun-tracking with similar shadowing.

For comparison, optimal time-varying alpha-tracking with no beta joints was performed. The third figure

Utilization of Common Modules on Space Station *Freedom*

During the preliminary design review of Space Station *Freedom* elements and subsystems, reductions of cost, weight, and on-orbit integration and verification were shown to be necessary in order to meet program constraints, particularly nominal orbiter payload launch capability. At that time, the baseline station design consisted of four resource nodes and two 44-ft modules. In this study, performed by the Langley Research Center Space Station *Freedom* Office, the viability of a common module that maintains crew and payload accommodation of system racks and user experiments is considered and compared to the baseline design.

Two primary considerations influence the design of the manned



pressurized elements: the size of the modules and the arrangement or configuration pattern. Module sizing objectives included the minimization of the required number of assembly flights necessary to support associated elements and an assessment of the sensitivity to potential changes in the module element weights (e.g., structural weights, rack weights, and flight related support hardware). The number of modules and their length were mandated by the ground rule of maintaining the number of racks in the current baseline program. Configurations consisting of less than five elements provided little or no margin for weight increases, while those consisting of more than six elements required an excessive number of assembly flights and unnecessary duplication of critical systems and structure. Patterns made of five or six primary elements proved to be feasible; however, the latter option could be more efficiently packaged into a fewer number of assembly flights because of the lessening of logistical outfitting requirements.

Module pattern considerations included accommodation of attached elements and international partners, ease of assembly operations, safety concerns including dual egress, and the effect on station flight characteristics and microgravity environment.

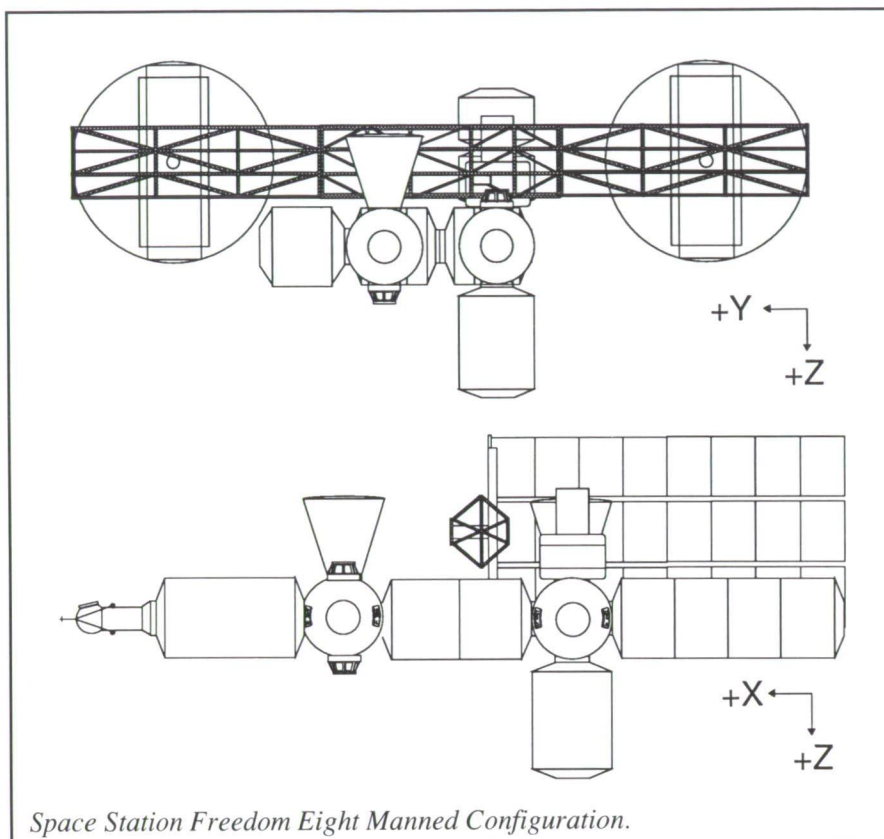
Based on available weight estimates, a module pattern consisting of six 28-ft common elements with three radial and two end ports is shown to be optimal. Advantageous characteristics include a reduction in assembly flights; dual egress from all elements; logical functional allocation; no adverse impacts to international partners; favorable airlock, cupola, Assured Crew Return Vehicle (ACRV), and logistics module accommodation; and desirable flight attitude and control characteristics. The figure shows an isometric view of this pattern. (Marston Gould, 41941, and Dan Mazanek)
Space Directorate

Space Station Module Pattern Evolution

Space Station *Freedom* (SSF) is being designed to serve as a permanently manned platform in space to accommodate growing amounts of supported scientific research and, ultimately, to provide the capability to process vehicles for lunar/Mars missions for the Space Exploration Initiative (SEI). In order to support the evolving requirements of these future missions, the resources available on SSF must expand beyond that of the Permanently Manned Configuration (PMC) baseline space station. One of the most critical resources for the accommodation of user needs is pressurized volume.

The changes made to the baseline program during the restructuring activity of 1990 to 1991, particularly the resizing of the U.S. Habitat and Laboratory modules to 28 ft and the use of the preintegrated truss (PIT), necessitated the reanalyzing of the module pattern evolution. The SSF Advanced Programs Office and the McDonnell Douglas Space Systems Company conducted an extensive study to determine the optimal configuration path at all phases of station evolution. In all cases, it was assumed that the PMC core pattern of U.S. modules and nodes and international modules would be maintained in order to minimally impact the existing program.

The analysis method centered around the gathering of requirements for attached elements, users, and Space Shuttle assembly operations. Combined with physical constraints, a set of all available options were constructed. These options were then ranked according to a set of criteria that were mandated by safety issues, attached payload operations, assembly opera-



tions (such as reach capability of the Space Shuttle and Space Station Remote Manipulator System or RMS), utility impacts, flight characteristics, and user preferences that could be measured in some direct fashion. The criteria were then ranked, and the sensitivity analysis of each was tested to see the effects on the phasing of the module pattern evolution. Finally, a preferred growth path was established for evolution reference configurations entitled Eight Manned Crew Capability (EMCC), Extended Operations Capability (EOC), and Lunar Vehicle Configurations (LVC).
(Marston Gould, 41941)
Space Directorate

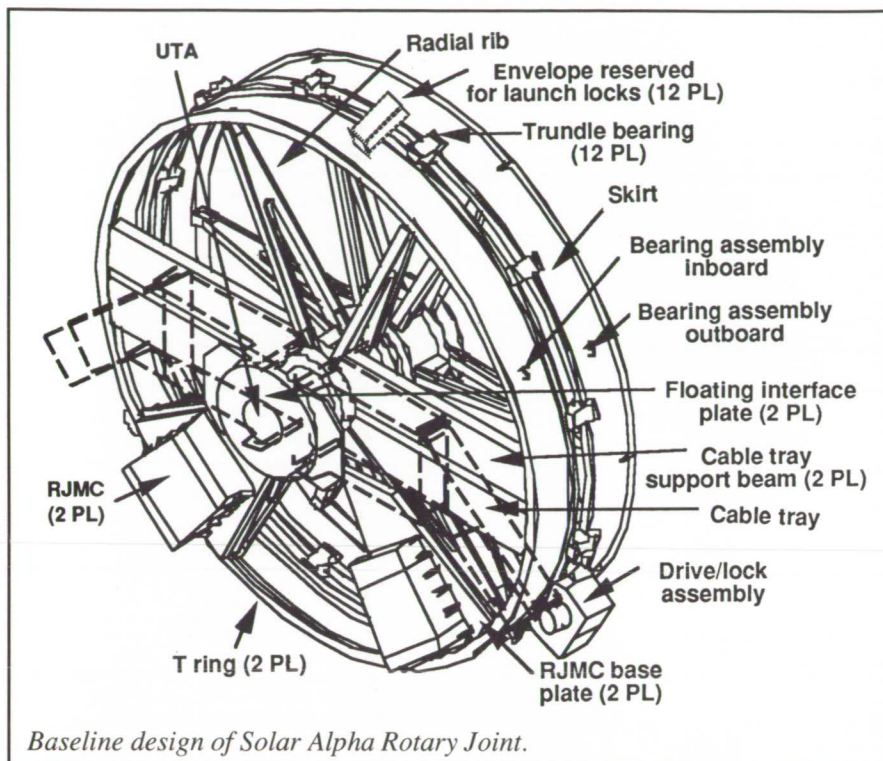
Growth Capability of Solar Alpha Rotary Joint

The design approach currently taken by the Space Station *Freedom* (SSF) Program is one that follows the "go as you pay" philosophy. This approach requires that studies and analyses be performed which assess the ability of the baseline distributed systems and elements to evolve. The Space Station *Freedom* Office/Advanced Programs Office at Langley Research Center is involved with this aspect of the project, as well as defining the evolutionary phases of the station. In support of these tasks, numerous utilization analyses have been performed to determine the resource requirements of potential SSF users. The need for additional electrical power beyond that which is provided by the baseline configuration has been substantiated with each analysis.

The Solar Alpha Rotary Joint (SARJ) provides the vital link between the power generation sources and the load points. The primary function of SARJ is threefold: Sun-tracking rotational movement of the photovoltaic arrays about the alpha axis; structural load transfer between the inboard and outboard truss members; and transfer of 160 V dc power and 1553 bus data across the alpha joint. Langley is currently working with the engineers responsible for the SARJ to assess the baseline design for growth capability. This assessment will determine any margins within the current SARJ design and the feasibility of upgrading the capability on-orbit when an augmentation of the Electrical Power System (EPS) is required.

A growth inertia requirement is a requisite for the design of the drive system. Analysis is under way to determine whether the equipment to be located outboard of the alpha joints during the evolution phase of the station has inertia properties that exceed the capability of the motors. The rotation capability can be enhanced by replacing the drive motors and rotary joint motor controllers (RJMC's) on-orbit. However, the design-limiting factor of this upgrade is the load-carrying capability of the "race" bull gear, which, as an integral part of the bearing assembly structure, is not an orbital replaceable unit (ORU).

The only load path across the alpha joint consists of 12 trundle bearing packages. Replacing the trundle packages on-orbit will allow for greater load transfer, but it could also cause the race ring and skirt to buckle. The possibility of impacting the design of these non-ORU components, to account for increased loads, is currently being studied.



Both data and power are transferred across the alpha joint via the Utility Transfer Assembly (UTA), which is located at the center of the alpha joint. Growth potential for data crossings seems adequate because four data roll rings are allocated as spares. The baseline power transfer capability of the UTA is sufficient from the standpoint of total power across the joint. However, the ability to transfer power is closely related to the EPS architecture. Trade studies are under way which investigate this relationship. Should more roll rings be required during the evolution phase, the UTA designed previous to the 1990 to 1991 restructuring activity would be used as a replacement ORU for the baseline UTA.

A study is under way to identify those scars needed to support the follow-on and evolution phases of the Space Station. For example, the structural capability of the SARJ must be an installed capability so that the addition of structure and growth power

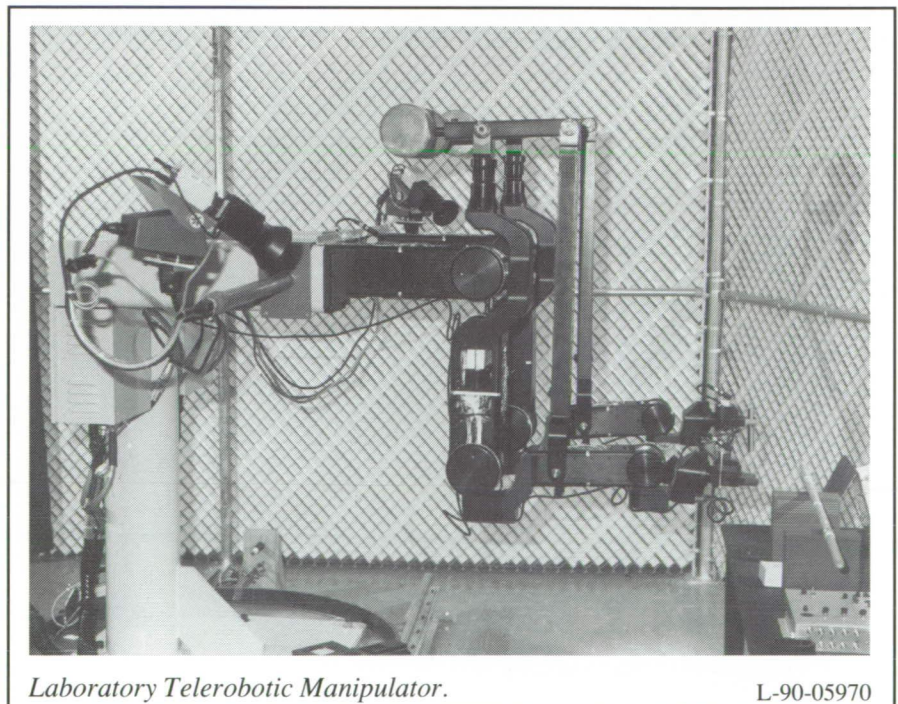
generation equipment outboard of the alpha joints is not precluded.
(Donald W. Monell, 47515)
Space Directorate

Real-Time Optimized Resolved Rate Control of Laboratory Telerobotic Manipulator

Robot arms having more than six joints, or degrees of freedom, are called redundant manipulators. This class of manipulators is desirable for space operations such as construction and satellite servicing because they offer an advantage of more efficient use of a workspace and the ability to reach around obstacles.

Langley Research Center is developing practical methods for motion control of redundant manipulators. A primary facility at Langley for investigating redundant manipulator control is the Laboratory Telerobotic Manipulator (LTM), a seven-jointed robot arm, shown in the figure.

A modified form of resolved rate control used with robots having six degrees of freedom, such as the Space Shuttle's Remote Manipulator System



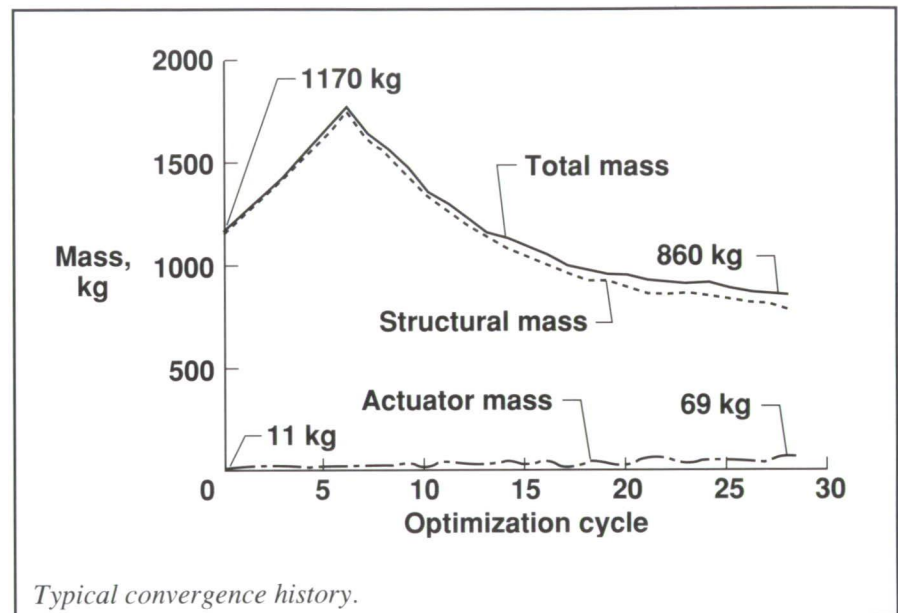
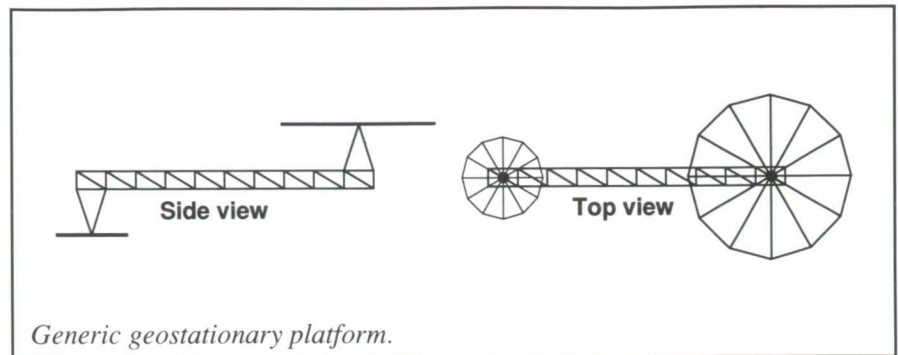
(RMS), has been implemented on the LTM. In resolved rate control, the operator inputs velocity commands to the robot arm from a hand controller. The effect is the same as "flying" the hand of the arm by commanding the hand to move in a selected direction at the desired velocity. The commanded velocity is resolved into joint angle rates (resolved rate control) to move the hand as commanded. With seven joints, an infinite number of joint rotations can produce the same hand velocity, and the computational burden is increased to the point that real-time operation becomes difficult.

Langley has developed an optimized resolved rate control scheme for real-time control of the LTM. The scheme generates a least-squares solution for joint angle rates while optimally trying to configure the arm to satisfy a specified performance criterion of joint angles. The objective is to command the desired hand motion while minimizing joint velocities and satisfying operator specified joint constraints. The scheme also selects the six joints that are optimal for achieving the desired motion, thus reducing the computational burden on the least-squares algorithm. For example, a commanded hand roll produces a desired "screwing" motion, but it can also produce unwanted shoulder rotation. The optimization scheme allows the desired motion to be attained while restricting shoulder rotation.

**(L. Keith Barker, 46694)
Flight Systems Directorate**

Multidisciplinary Optimization of Space Structures

Future NASA missions envision controlled space structures that routinely damp vibrations caused by



payload operations and by spacecraft maneuvers. The preliminary design of these spacecraft is complicated by the coupling between disciplines such as structures, dynamics, and control. For example, changes in the structure impact the control system design by modifying both the plant to be controlled and the characteristics of the expected excitation. At the same time, changes in the control system impact the structural design by modifying the number, mass, and location of actuators.

The preliminary design of a generic geostationary platform (see the first figure) is used to develop controls-structures optimization methods. The goal is to reduce the total mass of the structure and the vibration control

system while satisfying performance constraints on vibration decay rate. The excitation is assumed to be a slow maneuver of 20° accomplished in 10 sec. Three structural design variables (which determine cross-sectional dimensions of truss elements) and 12 control design variables (which determine entries in the rate and position gain matrices) exist. Standard finite-element analysis, optimal control, and mathematical programming routines are coordinated by a new multidisciplinary optimization scheme.

The platform is successfully redesigned so that the mass distribution and dynamic characteristics of the structure enhance the use of rate and position feedback by the control

system. The second figure, a typical convergence history of the optimization process, indicates that a 300-kg reduction in structural mass can be traded for a 58-kg increase in actuator mass. The procedure not only makes a favorable trade of structural mass for control effort but also improves the vibration decay rate as well.

This research demonstrates that an integrated controls-structures optimization method can lead to significant mass savings that would not be revealed by traditional (single discipline) design methods.

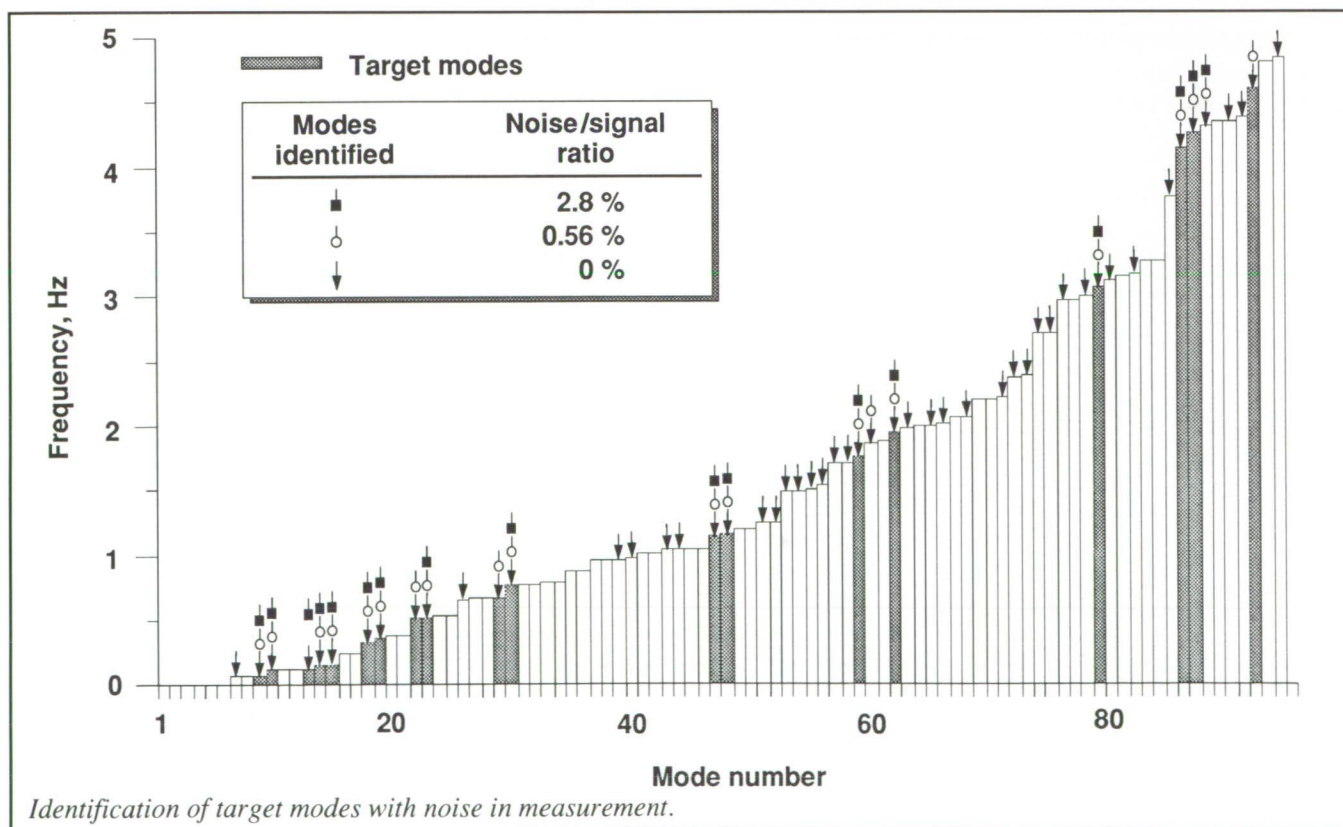
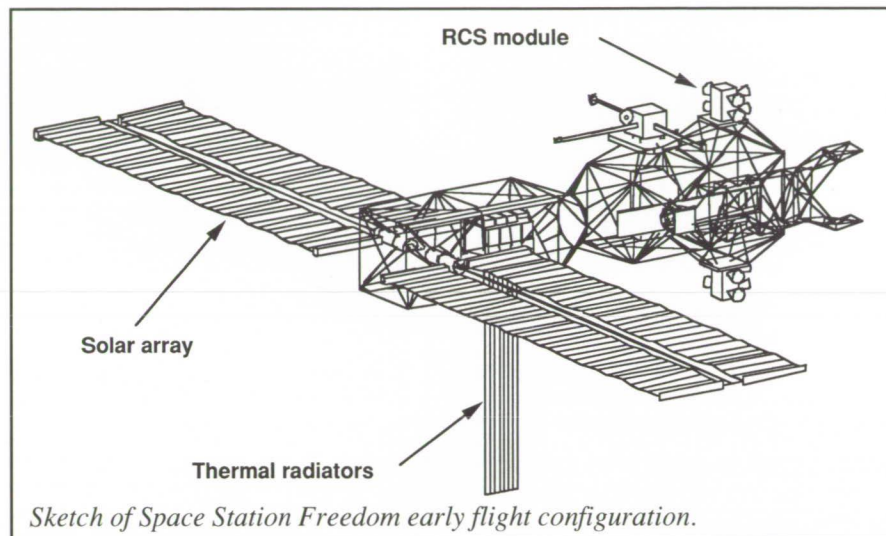
(Sharon L. Padula, 42807)

Structures Directorate

Analytical Simulation Confirms Feasibility of Space Station Modal Identification Experiment

The Modal Identification Experiment (MIE) is a series of planned

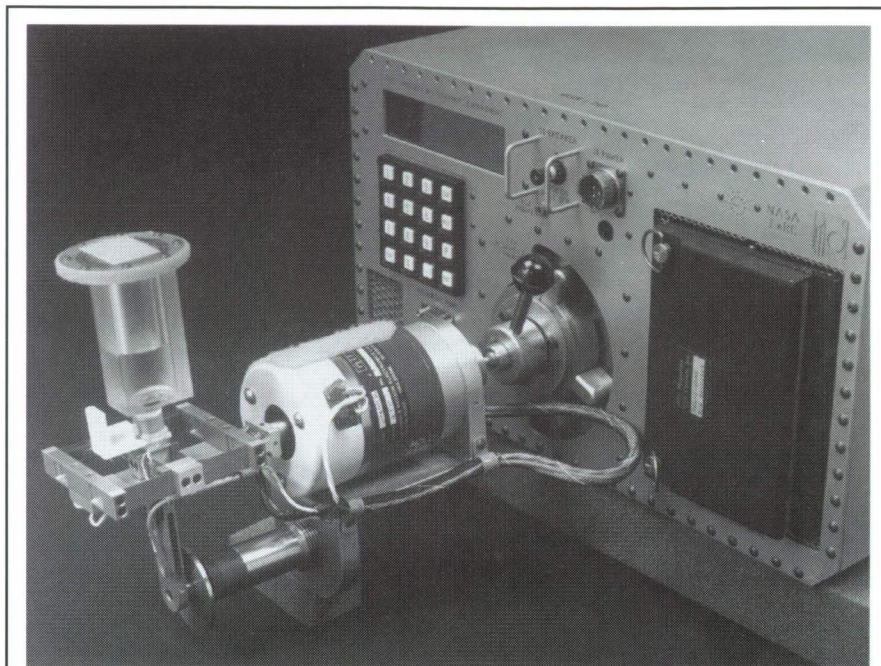
on-orbit modal tests of Space Station *Freedom* and its intermediate flight configurations that occur during the construction process. The first figure shows an early flight configuration of Space Station *Freedom*. Modal information is important because it can



be used to predict structural response and structural loads caused by external disturbances. A complete end-to-end analytical simulation of a modal test of an early flight configuration was performed to assess the feasibility of the experiment. A finite-element mathematical model of the configuration was developed, and 94 undamped natural modes and frequencies below 5 Hz were computed. This modal density is shown by the data in the second figure. Jet firings of the reaction control system (RCS), consistent with a maneuver for reboost, were employed to excite the structural response at various locations. From this analysis, a set of target modes, those that contribute most to the dynamic response of the structure, were defined for MIE measurement. With 19 target modes selected, a limited set of accelerometer locations were assumed, and response information from only these sensor locations was used to extract measured modes.

Simulation results indicated that on-orbit testing, using the RCS jets as excitation devices and a limited number of sensors, would be successful in identifying the target modes even with considerable noise in the measurements. When white noise with levels as high as 2.8-percent noise-to-signal ratio was added to the measurements, 16 of the 19 target modes were successfully recovered. The simulation results confirm that RCS jets will provide sufficient excitation so that the on-orbit MIE is feasible.

**(Paul A. Cooper, Tae Lim, and Zoran Martinovic, 42887)
Structures Directorate**



MODE Experiment Support Module (ESM) with attached Fluids Test Article (FTA) assembly (MODE II).

L-91-9537

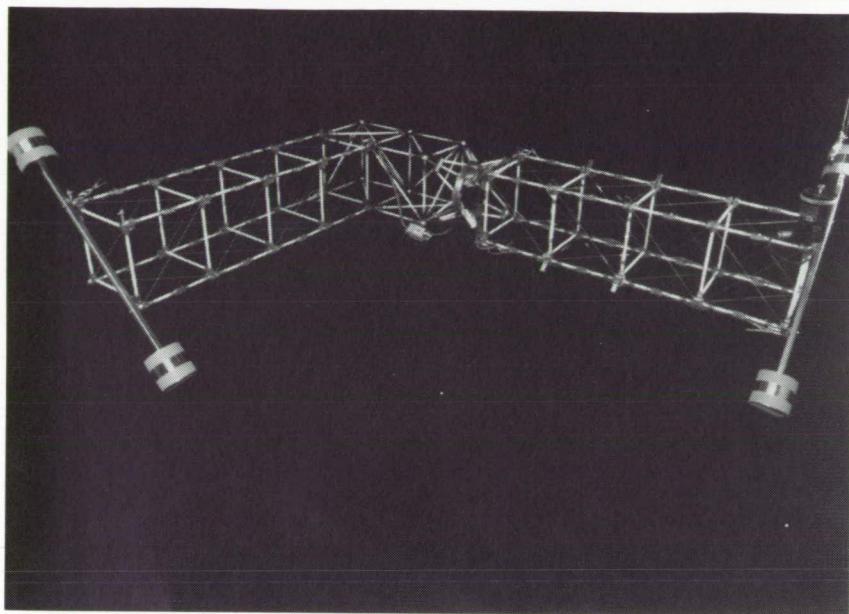
Middeck 0-Gravity Dynamics Experiment

The Middeck 0-Gravity Dynamics Experiment (MODE) is designed to investigate two aspects of nonlinear spacecraft dynamics systems which are altered by the presence or absence of gravity. These two aspects are nonlinear dynamics of jointed truss structures (MODE I) and dynamics of a partially filled fluid tank as it interacts with flexible vehicle motions (MODE II). The engineering science objectives of MODE I are to characterize the fundamental changes in dynamics in 0g because of the absence of gravity on joints; to quantify the changes because of the absence of suspension and gravity load on structural members; and to obtain quantitative data for correlation with numerical models. The engineering science objective of MODE II is to characterize fundamental 0g slosh behavior and obtain quantitative data

on slosh force and spacecraft response for correlation with numerical models.

The MODE hardware has three main components. The Experiment Support Module (ESM) is the electronic brain of the experiment and functions as a semiautonomous test facility. The Fluids Test Article (FTA) consists of a force balance and shaker assembly (attached to the front panel of the ESM) and a small changeable fluid tank to investigate the dynamics of fluid-structure interactions (MODE II). The Structural Test Article (STA) is a hybrid scale, jointed truss structure (a variable configuration), based on the original Space Station *Freedom* transverse boom design, to be used to investigate the open-loop dynamics of four different configurations (MODE I).

Two of the FTA fluid tanks were flown as a Space Transportation System (STS) Precursor Flight Experiment (MODE 0) on the STS-40



MODE I Structural Test Article (STA) (shown in "L" configuration with rotary joint). L-91-9538

Mission in May 1991 for evaluating different techniques to align the fluid and to observe the fluid motion during firings of the Space Shuttle reaction control systems.

Fabrication of the MODE hardware is complete, and all functional, environmental, and certification tests have been successfully concluded. MODE was manifested on the STS-48 Mission (September 1991 launch date) as a middeck locker payload. On-orbit, two mission specialists will attach the test articles to the ESM and conduct MODE operations for a minimum, total period of 20 hours. (Sherwin M. Beck, 41966) Space Directorate

Automated Assembly of Space Structures

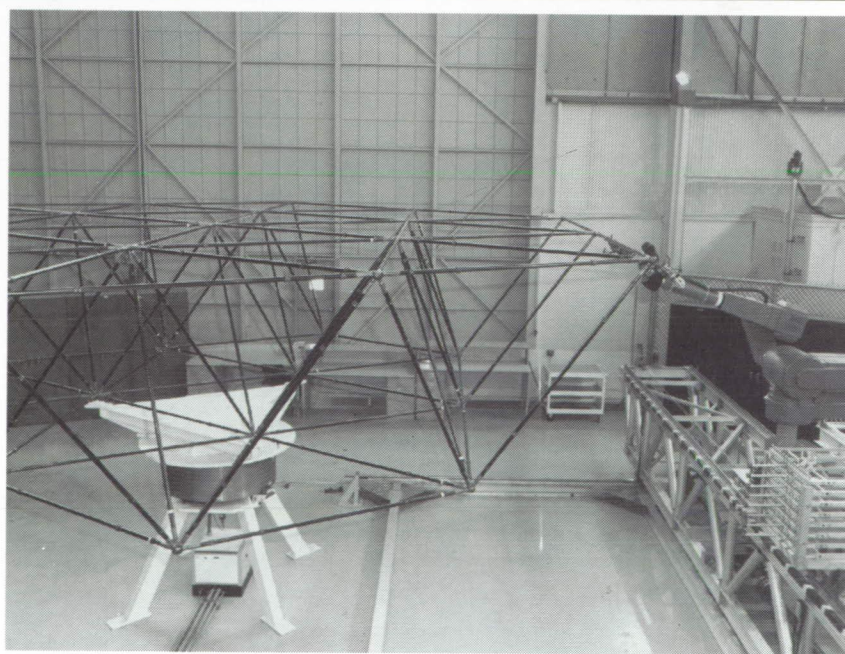
Proposed reusable lunar and Mars vehicles are too large for a single

launch; this fact requires that they be assembled and checked on-orbit. Limited crew resources dictate that alternate assembly methods not dependent on astronaut extravehicular

activity (EVA) must be explored. The Automated Structural Assembly Laboratory (ASAL) has been developed to gain practical experience and develop automation techniques for the assembly of actual truss hardware.

The ASAL facility (shown in the figure) consists of a standard six-degree-of-freedom industrial robot manipulator mounted on an x-y Cartesian translational motion base. The structure being assembled is a planar tetrahedral truss and is mounted on a rotating turntable. The truss hardware has members that are nominally 2 m in length and 2.7 cm in diameter. The two-ring test model has a diameter of 8 m, and the complete structure has 102 struts and 31 nodes.

The system is fully operational in a supervised autonomy mode. This means that operator monitoring and intervention is only required when the automated system encounters a problem it cannot correct. This greatly reduces crew time requirements.



Automated Structural Assembly Laboratory.

L-90-5054

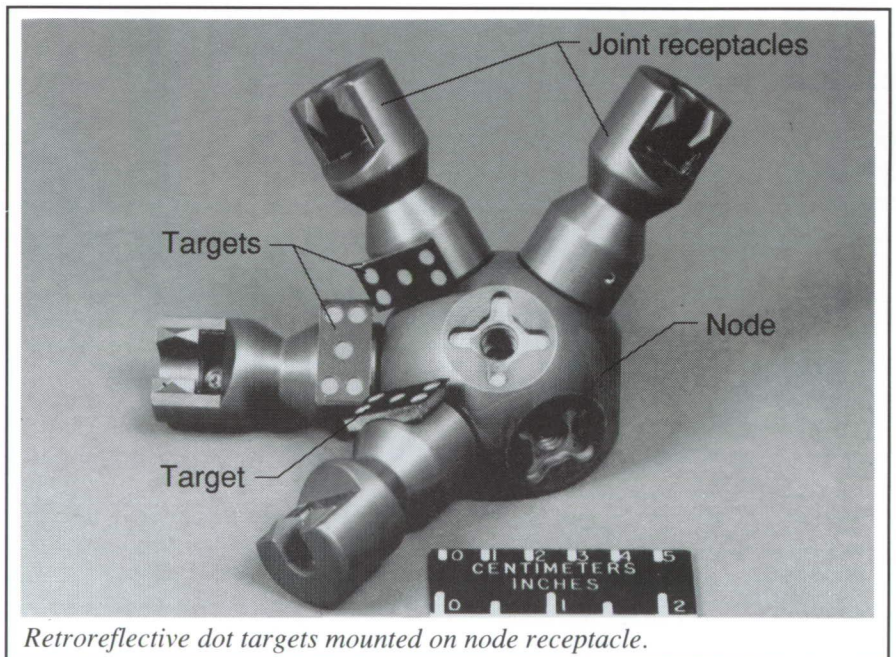
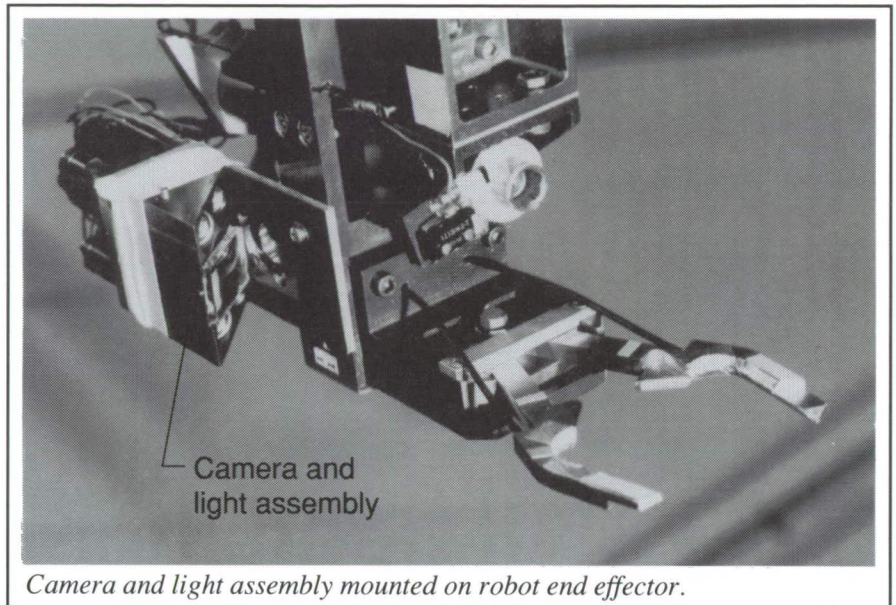
Assembly experience indicates that automated assembly requires 7 min to 8 min per strut with projected improvements to 4 min with system refinements. Ninety-nine percent of the problems encountered are easily corrected by the operator from the console.

The automated system is in the process of being upgraded to include a machine vision capability, an end-effector-mounted microprocessor, and the ability to install panels on top of the structure. Future plans also include the addition of advanced path planning and task sequence planning capabilities. (Marvin D. Rhodes, 43121, and Ralph W. Will)
Flight Systems Directorate

Machine Vision for Automated Structural Assembly

A current research program being conducted at the Langley Research Center Automated Structural Assembly Laboratory is the evaluation of an automated telerobotic assembly system designed to assemble large space truss structures. This system currently relies on "taught" points for structural assembly operations. Reliance on the use of "taught" points for strut capture and installation is neither flexible nor robust enough for space operations. Therefore, work on a machine vision sensor guidance system was initiated to develop and evaluate the capability to locate and guide a robot to a passive target mounted on a strut receptacle.

The hardware portion of this sensor guidance system consists of a miniature Charged-Coupled Device (CCD) camera and light assembly mounted on the robot end effector (first figure) and a target mounted on each node receptacle (second figure). The target, which

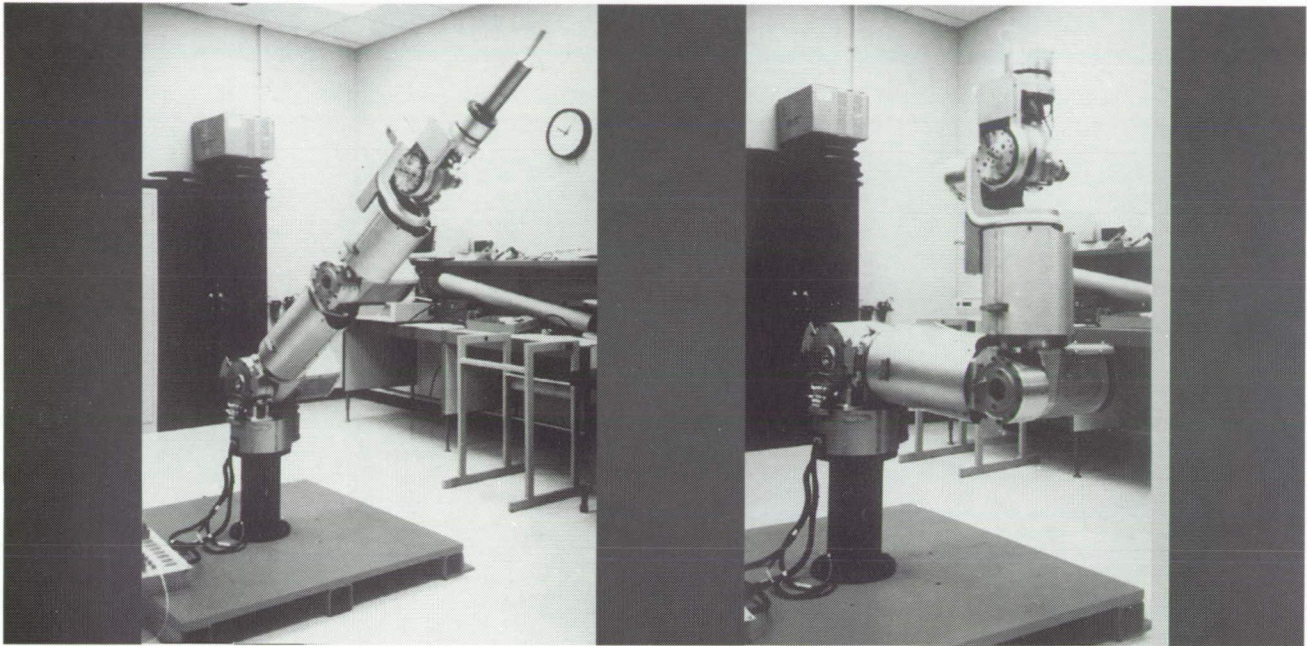


measures approximately 0.5 in. by 1 in., consists of a flat black background with five retroreflective dots. The dots are actively illuminated by five miniature 1.5 V focusable flashlights mounted in the camera assembly. Four of the flashlights, aligned coincident with the camera, provide a concentrated off-axis light source. The fifth, mounted at a right angle to the camera, uses a partially silvered glass beam

splitter that provides a light source directly on the optical axis of the camera. By maintaining light sources as close to the optical axis of the camera as possible, the reflective efficiency of the target dots is maximized.

This vision system hardware provides a standard video image source containing the target. Once

ORIGINAL PAGE
BLACK AND WHITE PHOTOGRAPH



Eight-degree-of-freedom arm position configurations.

digitized, the combination of retroreflective dots and active lighting allows discrimination of the target from background clutter through standard digital image processing techniques such as thresholding, feature centroiding (blobs), and model matching. Threshold, based on a histogram of the image, followed by region centroiding, provides a list of potential target blobs. These blobs are first constrained by size and shape based on the target model and work envelope. Remaining blobs are then formulated into triangles that are subjected to a variety of tests based on geometric properties of similar triangles. Eliminating triangles further reduces the number of candidate target blobs. The remaining five blobs are then sent to a pose estimation algorithm to determine the location, in three-dimensional space, of the target relative to the robot end effector. (Eric G. Cooper, 46674, and P. Daniel Sydow)

Flight Systems Directorate

Kinematics Equations for Control of Redundant ARMII Manipulator

The Advanced Research Manipulator II (ARMII) robot arm, shown in the figure, is a state-of-the-art redundant research manipulator that is well-suited for investigations of space telerobotics applications. Several features distinguish this manipulator from common industrial manipulators: two redundant degrees of freedom, a high payload-to-weight ratio, modular joint design, high joint and link stiffness (with graphite/epoxy composite link material), continuous bidirectional end effector roll, input and output joint position sensing, and spaceflight qualifiable components. A redundant manipulator is one that has more degrees of freedom than the minimum required for general tasks. The ARMII has eight degrees of freedom, and general spatial tasks require six degrees of freedom. The extra freedoms can be used to

optimize various performance criteria, in addition to satisfying commanded motion.

Langley Research Center has two ARMII manipulators for Earth-based experiments and demonstrations of space telerobotic tasks; these manipulators are intended for assembly, maintenance, and repair of Space Station *Freedom* and other missions. With additional hardware, these manipulators are used to validate control methods for compound redundant telerobotic systems and disturbance compensation algorithms.

Kinematic equations for control of the ARMII have been developed. The following problems are solved. First, forward kinematics where the joint angles and rates are given and the Cartesian position/orientation and velocity of the manipulator end-effector are found are solved; the forward kinematics are solved in general redundant form. Then the inverse kinematics where the Cartesian

position/orientation and velocity are given and the joint angles and rates are solved. The inverse kinematic equations involve six equations in eight unknowns for both position and velocity. So, to solve for manipulator positions and velocities the user is required to specify two joint angles and rates at each servo loop, respectively, and then solve each of the six velocity and position equations for the remaining unknowns. This method does not exploit the redundancy in a general manner, but it is better than locking two of the eight joints for all motion.

The solutions just discussed provide the kinematic basis for efficient real-time control of the ARMII manipulator. Research into applied redundancy optimization is required to realize the full potential of these manipulators. This work is currently under way. (Robert L. Williams II, 47690) Flight Systems Directorate

Optical Measurement System for Large-Gap Magnetic Suspension System

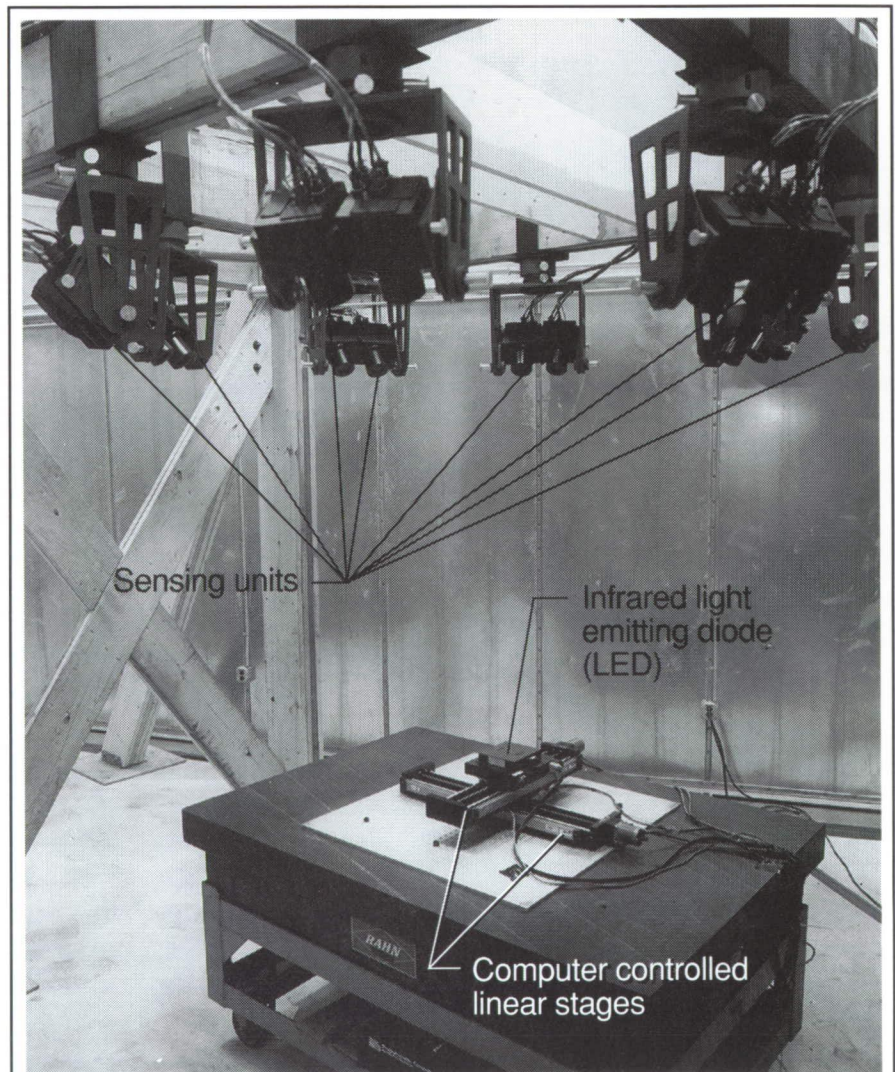
The Optical Measurement System (OMS) is a multisensor, point target tracking system that has been designed, developed, and built for the Large-Gap Magnetic Suspension System (LGMSS). In the OMS, 16 linear Charge-Coupled Device (CCD) cameras image 8 small infrared light-emitting diodes (LED's) embedded in the surface of a magnetically levitated cylinder. Photogrammetric techniques are used to estimate the position and attitude of the cylinder from the measured locations of the projected LED target images in the 16 cameras.

Each sensing unit consists of two cameras, oriented orthogonally, which

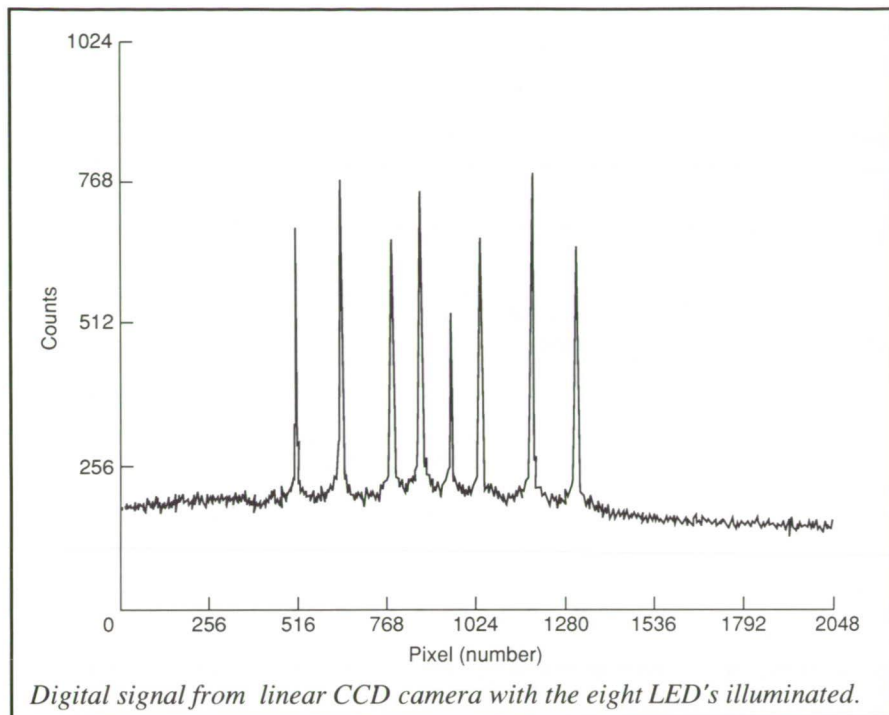
are attached together and to a single mount. In the first figure is a picture of the OMS showing the eight sensing units. (The calibration test setup shown consists of a single infrared LED affixed to two computer-controlled linear stages.) A cylindrical lens, located in front of each sensor, images an LED target as a line on the CCD array. The analog video signal generated by the sensor is converted to a digital signal via a 10-bit analog-to-digital converter. The position of the target image along the array is determined by calculating the centroid of the light distribution using a high-

speed digital signal processor (DSP), a Texas Instruments TMS320C30. Seventeen DSP's exist (one per camera), and there is an additional DSP that is used to perform the final computations required to estimate the position and attitude of the levitated cylinder.

Tests have been conducted on the cameras to determine the signal-to-noise ratios that can be achieved during operation in the LGMSS. A plot of the output from one of the cameras with all eight LED targets illuminated is shown in the second figure. Though devel-



Optical Measurement System for Large-Gap Magnetic Suspension System.



oped for use with the LGMSS, the OMS has potential application to many other areas that require noninvasive position and attitude measurements. (Sharon S. Welch, 46611)
Flight Systems Directorate

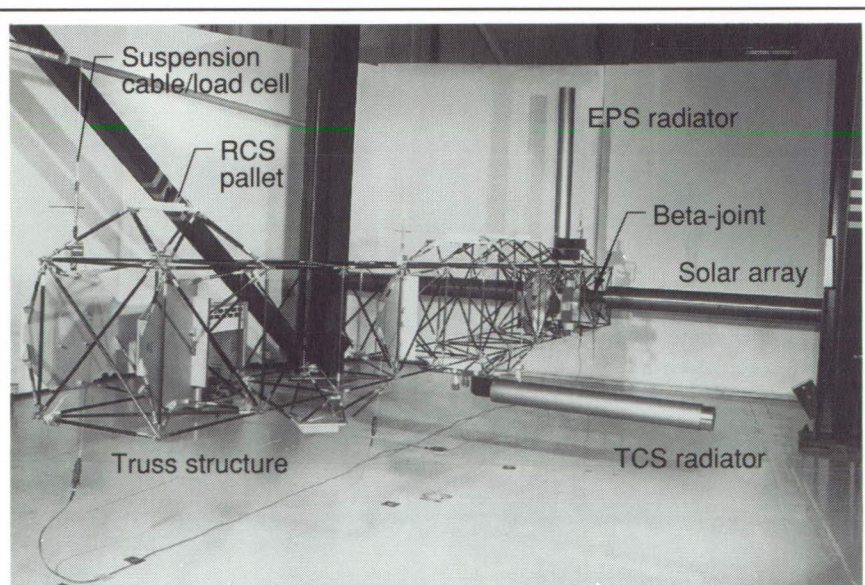
vehicle performance. The use of dynamically scaled models offers an attractive possibility to alleviate these limitations.

A research program for developing scale model technology and associated

ground test and analysis methods for large space truss structures involves a combined in-house and contractual effort. The research has led to the development of an approach for designing hybrid-scale models using realistically scaled hardware with a size suitable for ground testing in existing test facilities. This approach employs classical distorted scaling techniques, used extensively in wind tunnels, to accomplish different scale factors for the truss structure components and payloads. Using this approach, a 1/5:1/10 hybrid-scale model of Space Station *Freedom* has been developed under contract by Lockheed Missiles and Space Company, Sunnyvale, California. The model has the overall size of a 1/10-scale model but the dynamic characteristics of a conventional 1/5-scale model. Space Station *Freedom* was selected as the focus for this research effort because it provides a unique opportunity to obtain flight data on such a complex structure for correlation with ground test predictions.

Dynamic Scale Model Technology for Large Space Truss Structures

The verification of structural dynamic properties for large spacecraft, such as Space Station *Freedom*, represents a significant research challenge. Ground tests of such spacecraft are limited because of their large size and the effects of gravity. Furthermore, flight tests are difficult and costly. Thus, verification is limited to component and subassembly tests, with analytically synthesized results used to predict the fully mated

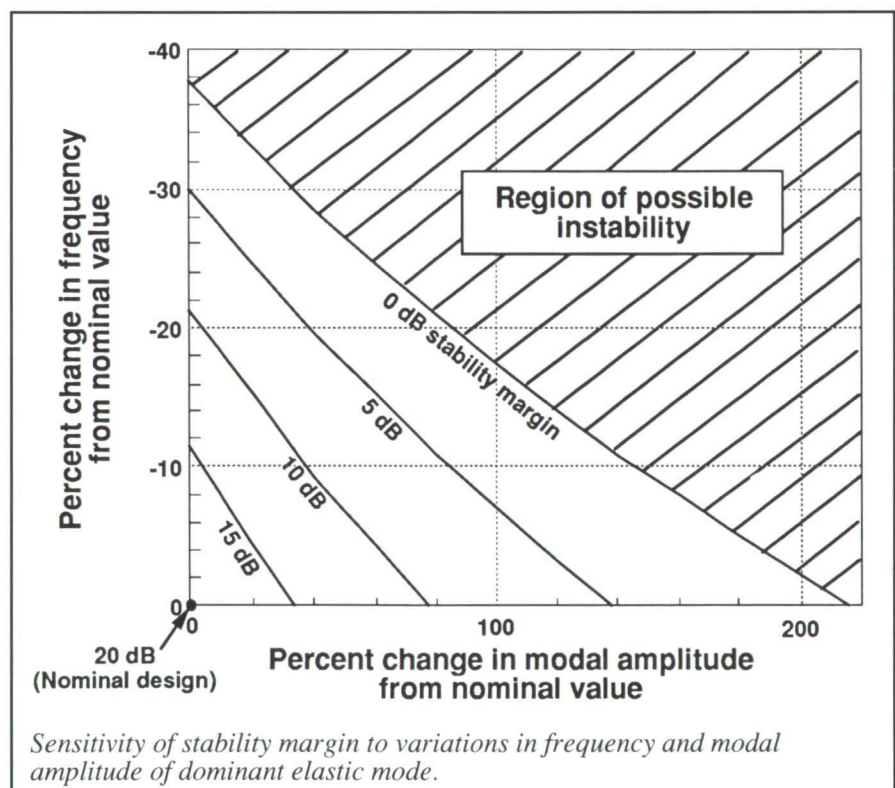
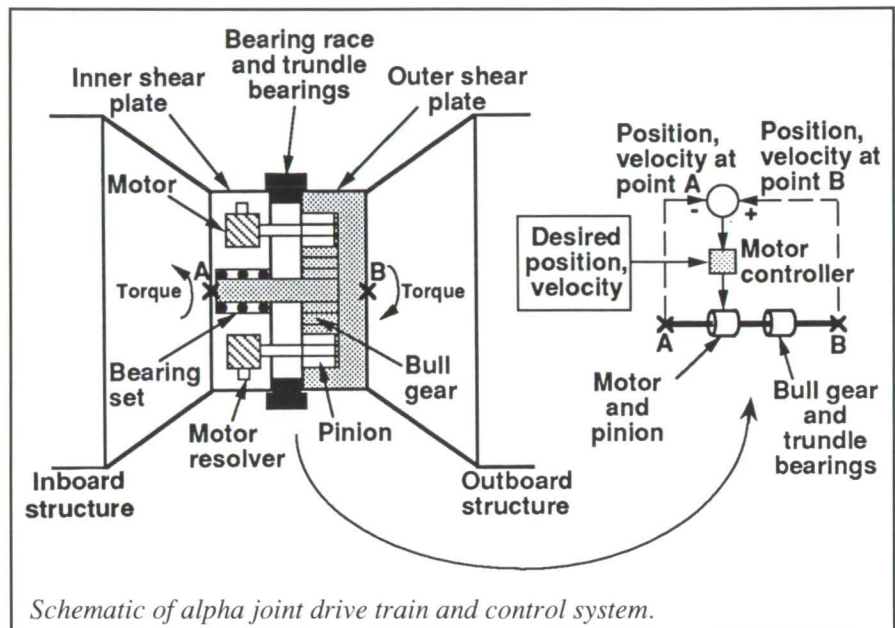


Early configuration hybrid-scale Space Station model suspended for dynamic ground vibration tests; RCS is reaction control system and EPS is electrical power system.
L-90-5794

Model hardware to represent all assembled configurations through flight 15 has been fabricated. All major station structural components were included in the design. Because of the evolutionary nature of *Freedom*, the model components were designed for modular attachment to the truss structure and easy reconfiguration. The model provides a ground test article with challenging dynamic characteristics including closely spaced and low-frequency vibration modes and interactions between flexible component vibrations and global truss vibrations. Shown in the figure is a test article that represents the configuration following the second flight and which is suspended from overhead by cables for dynamic tests. This configuration was selected as the first structure for comparing predictions from component level synthesized data with those obtained from fully integrated testing. Results from test/analysis correlation of this structure will provide updated analysis predictions of larger and more complex configurations. (Paul E. McGowan, 44350) Structures Directorate

Robust Alpha Joint Controller Design

Space Station *Freedom* (SSF) will depend on photovoltaic (PV) solar arrays that track the Sun during orbital daylight to obtain electric power. Solar Alpha Rotary Joints (alpha joints) regulate the relative rotational motion of the outboard structure to the inboard structure (see the first figure). The PV arrays are attached to the outboard structure. The attitude of the inboard structure is maintained while the alpha joint rotates the outboard structure so that the PV arrays track the Sun. A robust alpha joint controller was



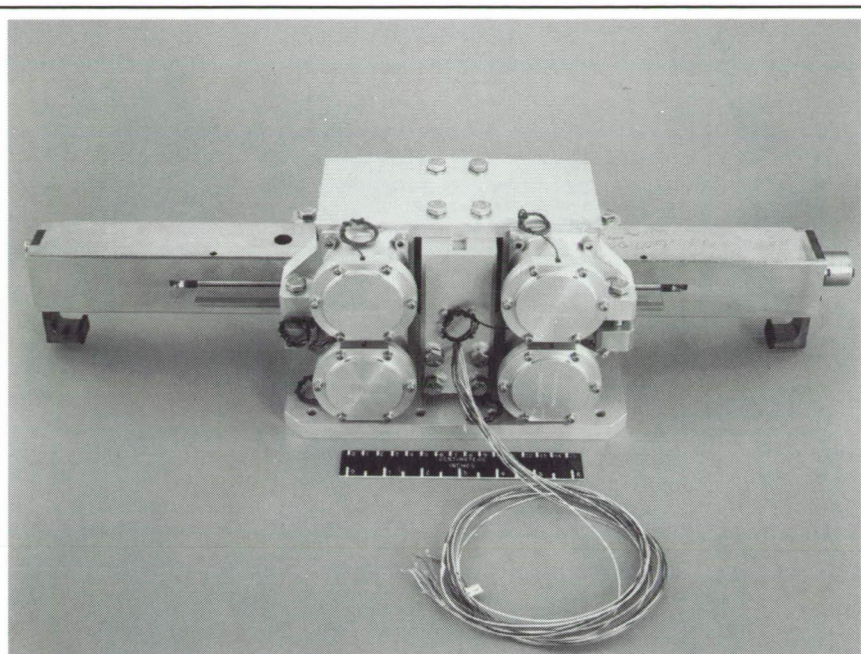
designed for a nominal SSF structural model using an optimization procedure to provide stability robustness to possible structural stiffness and mass changes and to meet transient and steady-state tracking requirements.

The station will not be tested as a complete system before being placed in orbit because it cannot support its own weight on Earth. Modal frequencies and amplitudes will have to be predicted using information from

ORIGINAL PAGE
BLACK AND WHITE PHOTOGRAPH

component tests and analytical models. To investigate how tolerant the alpha joint controller design is to possible errors in the predicted modal frequencies and amplitudes, the change in stability robustness of the nominal design was evaluated as the modal frequencies and amplitudes were varied (see the second figure). The design provides enough stability robustness to tolerate a sizable error in predicted frequency (40 percent) and modal amplitude (200 percent) of the dominant modes. A conservative modal damping of 0.1 percent was employed for this study. The high levels of stability margin suggested in this study for the nominal design are prudently conservative.

(Renjith R. Kumar, Paul A. Cooper, and Tae W. Lim, 42887)
Space Directorate



LPMA prototype assembly number 1.

L-89-4121

Linear Proof Mass Actuator

The Linear Proof Mass Actuator (LPMA) is a friction-driven linear mass actuator developed for the Controls-Structures Interaction (CSI) Program. The LPMA is a unique device capable of damping or exciting oscillations in a space structure or a ground-based test model. The ability to excite oscillations allows for the study of the structure's behavior, whereas the ability to dampen oscillations prevents the structure from incurring structural damage.

The LPMA consists of machined parts toleranced to 0.0002 in., four dc torque motors, an encoder, accelerometer, and controlling hardware and software. The controlling hardware and software allow for frequency inputs between 0 Hz and 50 Hz and several variations of input shapes from step and sawtooth to sinusoidal.

The complex design possesses flexibility to vary motor and mass sizes, stroke length, and software controls. In addition to varying force and acceleration, the actuator is capable of operation in all three orthogonal axes.

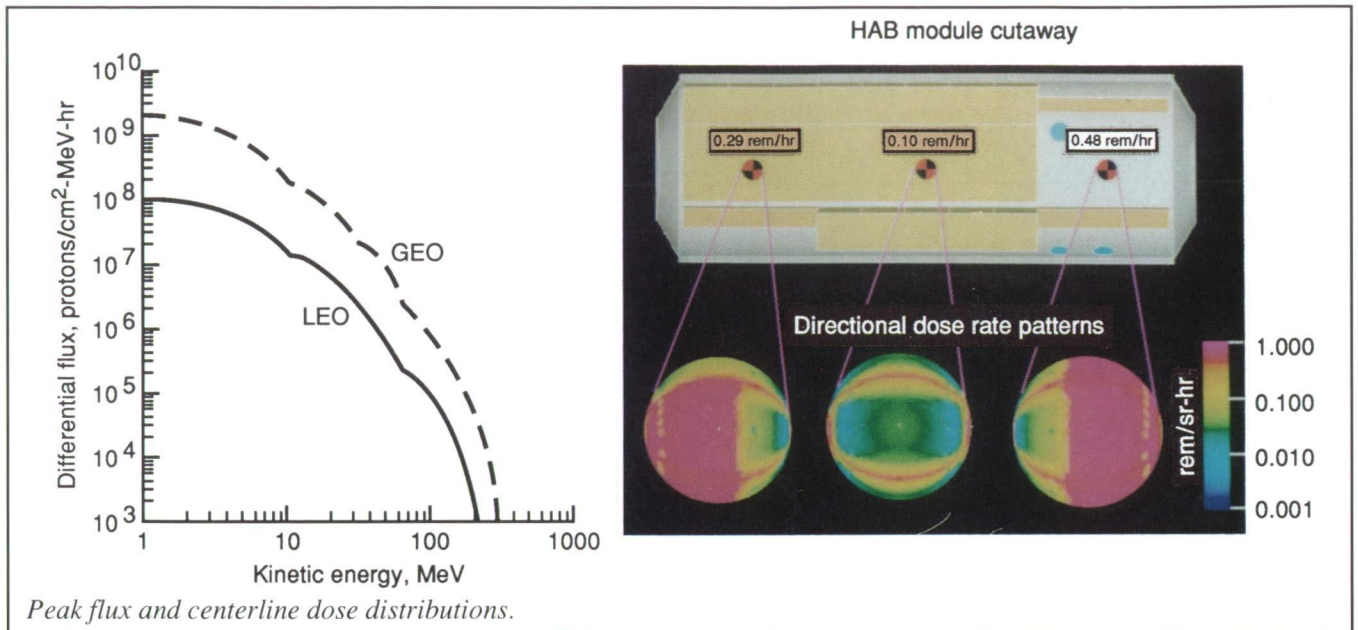
(S. E. Holloway III, 47090)
Systems Engineering and Operations Directorate

Solar Flare Radiation Exposure Analysis for Space Station Freedom Using CAD Techniques

The exposure of Space Station Freedom (SSF) to solar energetic protons from large flares is not expected to be significant under normal conditions because of the shielding provided by the magnetic field of the Earth at low-inclination orbits. However, in the rare case of a large proton flare eruption in combina-

tion with a severe magnetic storm, the geomagnetic field may be perturbed to the extent that flare protons reach the SSF orbit.

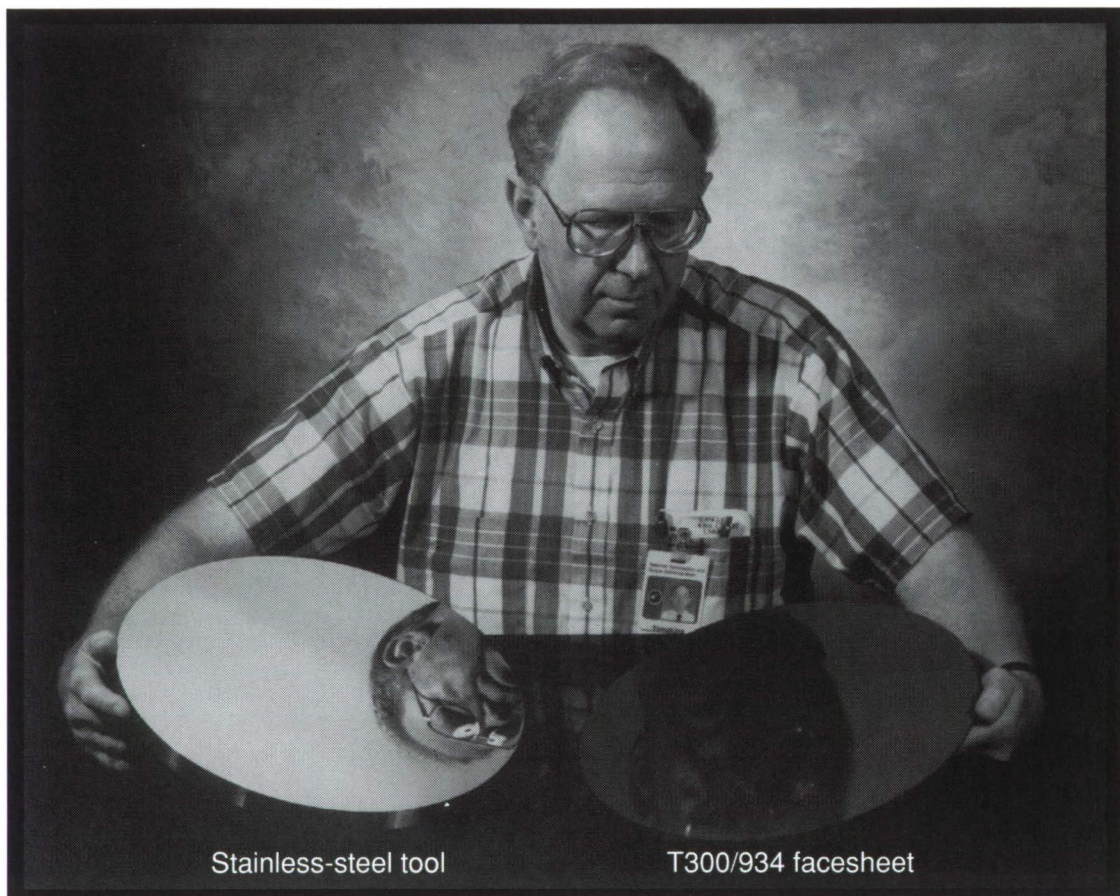
Because present plans may require SSF crews to remain in orbit for extended time periods, the flare/magnetic storm situation has been analyzed for an observed proton flare (October 1989) coincident with a representative large magnetic disturbance. Proton transmission factors were calculated as a function of energy for a 400-km altitude circular orbit (28.5° inclination) by using a computational model of the geomagnetic field altered by an opposing magnetic storm perturbation. The figure shows the flare proton flux spectrum as observed in free space (geostationary orbit altitude, GEO) and the corresponding derived flux at the SSF altitude low Earth orbit (LEO). Radiation dose as a function of material thickness was then obtained from implementation of the Langley Research Center nucleon transport codes. A simplified computer-aided design (CAD) model of the



SSF habitation module was constructed from which the distribution of thickness about given interior points was determined. The final step involved the use of the dose-depth function and the thickness distributions to compute directional and total doses at selected points. The figure depicts the module and the directional dose patterns for three centerline points. The results show the extent to which the midsection of the module provides increased protection. The total dose rates, while several orders of magnitude larger than normal background levels, are not expected to be mission threatening because such high rates would not persist longer than several hours.

(J. E. Nealy, 44412, G. D. Qualls,
and R. M. Boykin)
Space Directorate

■ SPACE TECHNOLOGY



ORIGINAL PAGE
BLACK AND WHITE PHOTOGRAPH

*Provide technology for space
science programs focused on
the planet Earth, the Solar
System, and the Universe*

RT

PRECEDING PAGE BLANK NOT FILMED

Visual Communication

This research in visual communication deals with image gathering, coding, and restoration as a whole rather than as separate and independent tasks. The application of Shannon's communication theory to image coding so far has been limited to the link that connects the output of the image-gathering device to the input of the image-display device. Consequently, past assessments of visual communication have been incapable of mathematically integrating the optical design of image-gathering and image-display devices with the digital algorithms for image coding and restoration.

Shannon's communication theory has been extended to include the characteristics of image gathering and display. Although the mathematics has

become more complex, the increase in complexity is not great enough to prevent a more complete mathematical assessment, and the rewards have been demonstrated to be important. These rewards include a close tie between mathematical analysis and actual performance, improved visual quality from less data, and reduced real-time processing for image coding.

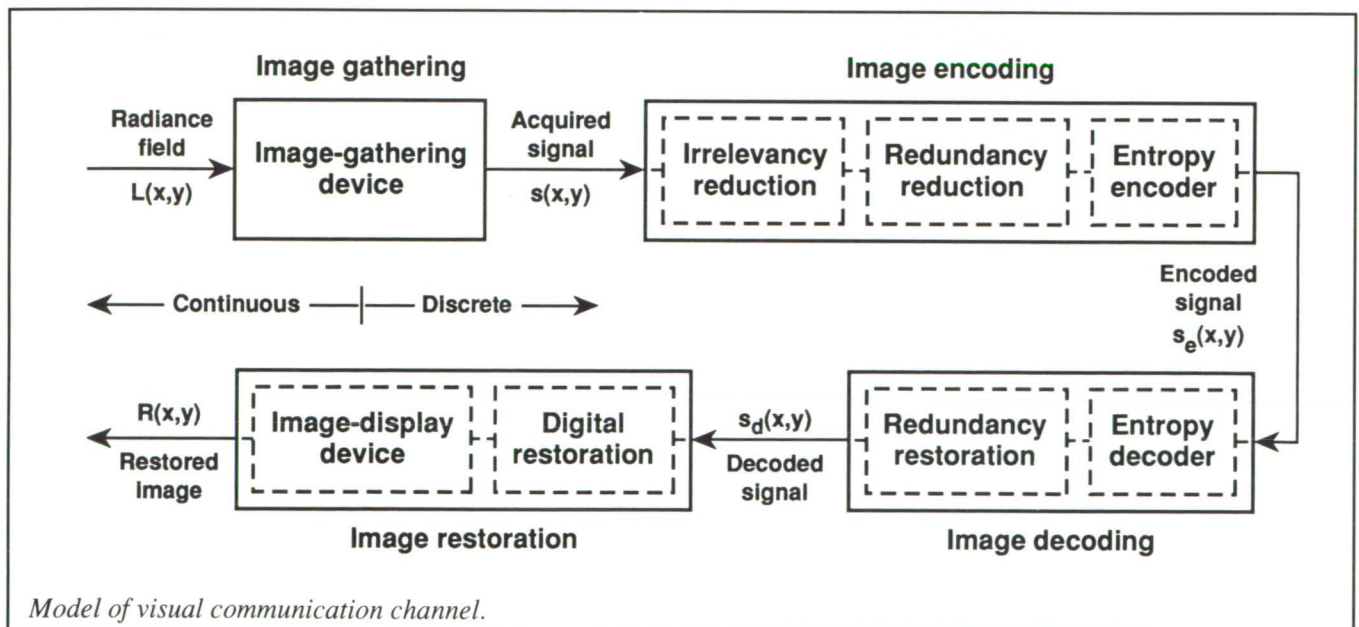
(Carl L. Fales, 41529, and Friedrich O. Huck)

Flight Systems Directorate

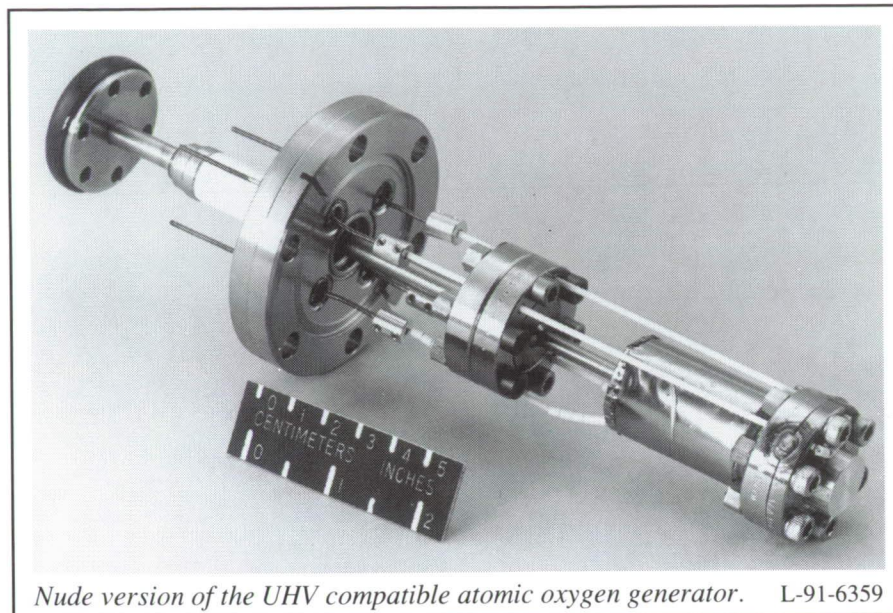
Hyperthermal Atomic Oxygen Generator

The development of an atomic oxygen system that accurately simulates conditions in low Earth orbit

(LEO) for the study of the degradation of materials intended for long-term utilization in orbit has been ongoing for many years with various degrees of success. Only two systems that come close to expectations, however, are currently in existence. One is a Tea laser momentum transfer system, and the other is a negative ion photo detachment system, both developed for accelerated testing. Disadvantages of the aforementioned are that these systems are large, expensive systems that are immobile, require a lot of maintenance and attention, and are not ultrahigh vacuum (UHV) compatible. Thus, they cannot be mounted on existing surface analysis systems or used in concert with other diagnostic systems. Samples have to be sent to these labs for analysis, which, of course, is time consuming, expensive, and, in most cases, scientifically compromising.



Model of visual communication channel.



Nude version of the UHV compatible atomic oxygen generator. L-91-6359

The instrument shown in the figure is a small, UHV-compatible, hyperthermal atomic oxygen generator that can be mounted on any existing UHV analysis system for mechanistic studies. This generator can provide a pure flux (>99 percent atomic oxygen) of ground state (3P) oxygen atoms ($>10^{12}$ atoms $\text{cm}^{-2} \text{s}^{-1}$) with a mean kinetic energy of approximately 5 eV that accurately simulates low Earth orbit. The generation of oxygen atoms is by temperature-controlled diffusion through a silver membrane to convert the molecules into atoms and then the subsequent desorption of the adsorbed atoms at the downstream surface by electron stimulation. The result is an energetic flux of pure atomic oxygen emitted into a UHV environment. The potential applications for this instrument, in addition to the original objective, are many and varied, such as chemical kinetics, surface science, and semiconductor and superconductor development.

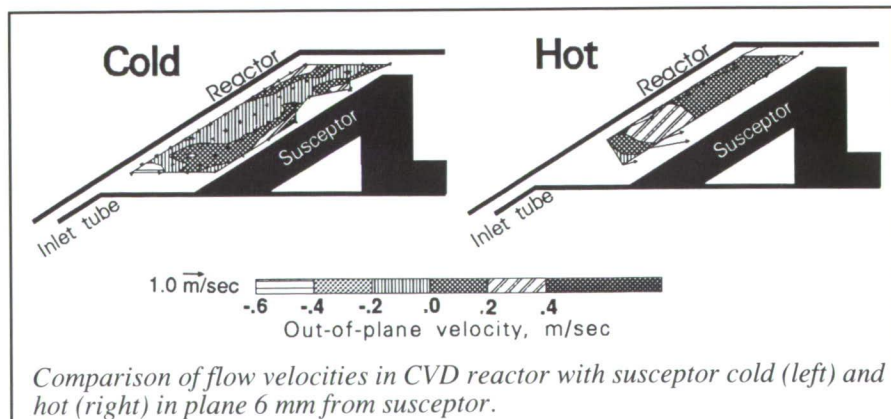
(R. A. Outlaw, 41433)
Space Directorate

Laser Velocimetry Measurements in Nonisothermal Chemical Vapor Deposition Systems

Three-dimensional laser velocimetry (LV) measurements have been successfully made in a chemical vapor deposition (CVD) research reactor under both isothermal and nonisothermal conditions. The reactor studied was a horizontal cylindrical reactor with a flat sloping front plate and an inner diameter of approximately 5 cm. Entry flow was from a tube at the lower edge of the plate oriented

parallel to the front reactor plate. The perpendicular separation between the inner reactor wall and the susceptor was approximately 18 mm. Nitrogen was used as the test gas. For isothermal flow, the reactor was operated at room temperature. For nonisothermal flow, the susceptor was heated to 973 K with RF (radio frequency) heating. Comparing the room-temperature isothermal flow field with the flow field found for the nonisothermal reactor, the effects of temperature could be studied. Data from one such sample plane are shown in the figure.

For the isothermal flow, fluidic switching effects were observed in which pressure fluctuations induced the expanding entry jet to shift position. Flow velocities close to the susceptor were found to be small. For the nonisothermal flow, heating effects stabilized the flow, and no fluidic switching effects were observed. Flow velocities increased significantly close to the heated susceptor, and they are shown on the right half of the figure. This velocity increase is thought to be due to a combination of thermal expansion and thermal buoyancy effects. A plane of data was successfully obtained 6 mm from the hot susceptor. Researchers elsewhere had predicted LV measurements would fail at this distance from the heated susceptor due to thermophoretic effects reducing or eliminating the tracer



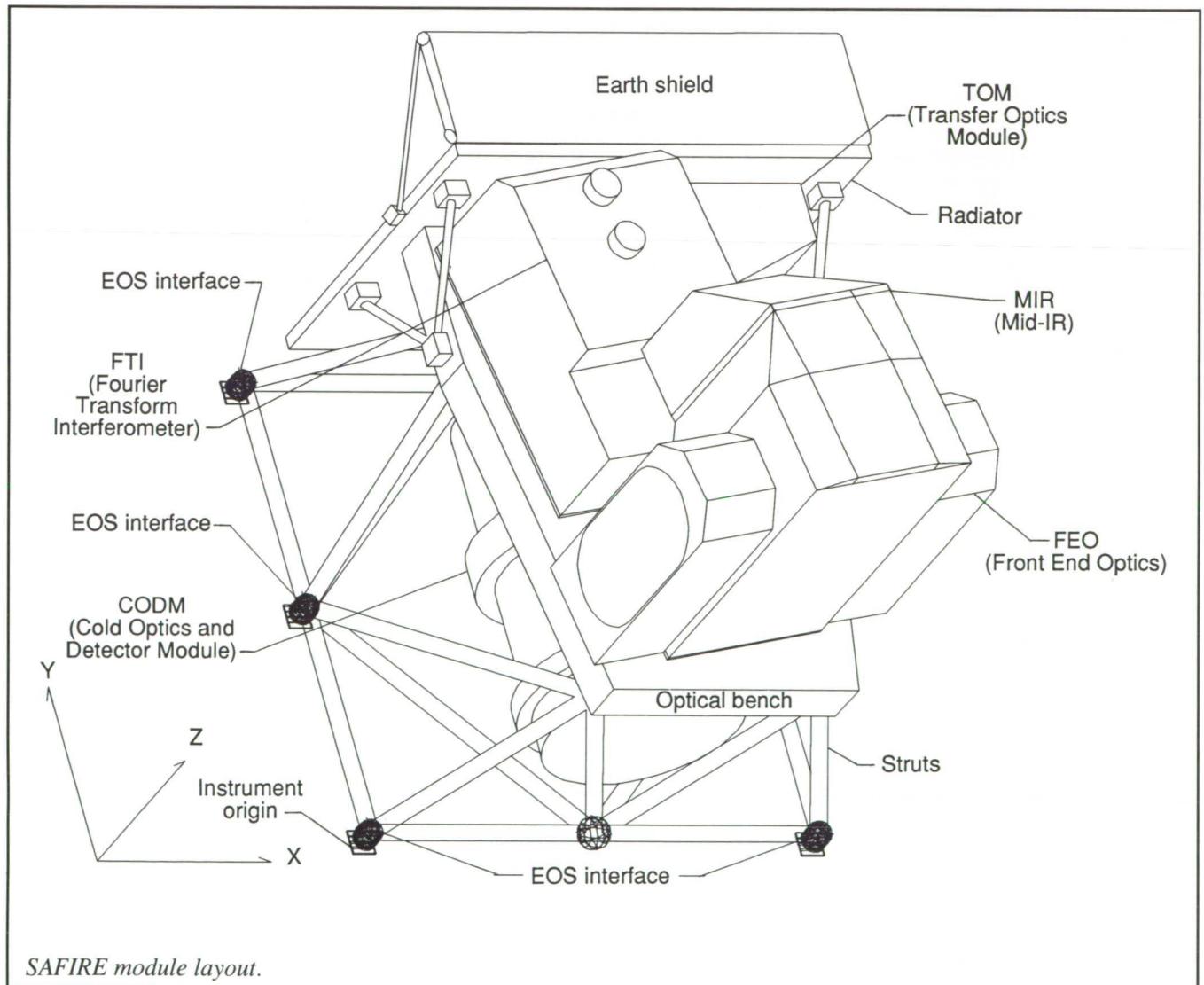
particles necessary for LV measurements. The ability to obtain the data in this effort is attributed to the use of LV techniques based on statistical ensembles of individual tracer particle crossings of the measurement volume at each data location.

(Ivan O. Clark, 41500)
Flight Systems Directorate

Design and Analysis of SAFIRE Instrument

The Spectroscopy of the Atmosphere using Far Infrared Emission (SAFIRE) instrument, which is being developed for the Earth Observing System (EOS) Program, will conduct, for the first time, global measurements of key ozone chemistry constituents in both mid- and far-infrared spectral regions. The conceptual instrument design that meets the EOS platform envelope and interface requirements has been completed and is shown in

the figure. The main structural element is a stable optical bench that supports all the instrument optical and electronic modules. The optical bench is kinematically supported from the EOS platform by a symmetrical truss arrangement of pinned, graphite/epoxy support struts. The optical bench is a sandwich construction with graphite/epoxy facesheets separated by internal ribs and tailored for the design load profile. Structural requirements are to withstand ground handling and launch loads and to maintain optical module alignment throughout the space environment exposure of the EOS



5-year polar orbit. Structural weight was constrained to less than 15 percent of the instrument weight goal or 60 kg.

A detailed MSC/NASTRAN finite-element structural model has been developed which includes the strut arrangement, optical bench, and radiator. A separate structural model of the Cold Optics and Detector Module (CODM), a hybrid cryogenic liquid helium dewar, was incorporated because it was the dominant mass and structural driver. Modal analyses were done to demonstrate that all instrument resonant frequencies were above the 40-Hz EOS platform requirement. Dynamic response studies were performed to evaluate the effect on instrument optical stability of in-flight disturbances from the mechanical cryogenic coolers and other onboard mechanisms. Bench stiffness and strut sizes were optimized for the 17g design load factor. The structural analyses demonstrated that the SAFIRE conceptual instrument can satisfy the EOS platform and instrument structural requirements.

Displacements and stresses because of thermal loads were assessed. The instrument thermal profile was determined using two analytical models. Space environmental effects were calculated by a TRASYS radiation model employing 41 separate surfaces. The radiation loads were input to a 59-node TAK-II instrument model that computed both steady-state and transient thermal profiles at critical source and sink locations in the model. These models demonstrated that a stable instrument thermal profile can be maintained in orbit with passive thermal control techniques while maintaining the required thermal isolation from the EOS platform.

SAFIRE is an international program involving contributions from the United Kingdom, Italy, and France

with the United States responsible for overall instrument integration.

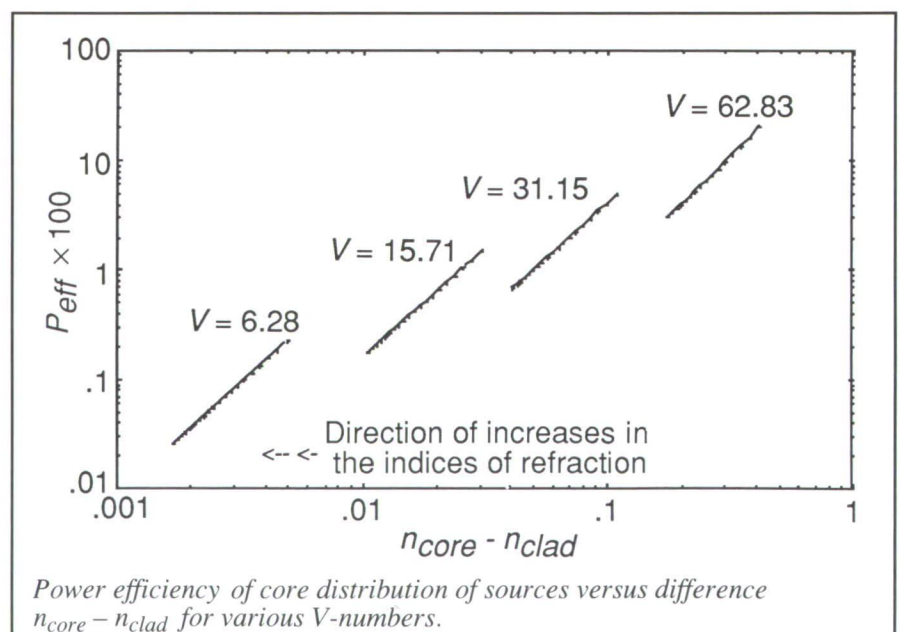
(Robert D. Averill, 47088, Robert W. Moses, and William A. Roettker)
Systems Engineering and
Operations Directorate

Smart Structures Research

Survival in the hostile environment of near-Earth orbit presents unique challenges for smart structures technology. Structures containing organic resin, such as graphite/epoxy, are subject to atomic oxygen degradation. Methods are being investigated for detecting atomic oxygen and monitoring its effects in space structures. Optical fibers that incorporate appropriate reagents, like polyethylene, which fluoresce or chemiluminesce in the presence of atomic oxygen, can be used as a sensor for this atom. Whenever the reagent interacts with atomic oxygen, the resulting chemiluminescence excites the optical fiber and can be detected at the end of the fiber. A computer model was devel-

oped to determine the best configuration for this sensor, a configuration that would allow the highest excitation and, consequently, the highest sensitivity. The result for a luminescent core fiber at four different V-numbers is shown in the figure. The relative amount of light excited in the fiber P_{eff} was plotted against the difference in indices of refraction $n_{core} - n_{clad}$. The values used for the wavelength and core radius were 0.6 μm and 6.0 μm , respectively. The model has used the exact field solution of the electromagnetic vectors in the optical fiber. In consequence, it can be applied for fibers with arbitrary differences in refractive indices. In the figure, the increase in P_{eff} is because of an increase in the difference, $n_{core} - n_{clad}$. The experimental verification of this model is under way.

(Claudio O. Egallon, 44788, and Robert S. Rogowski)
Electronics Directorate



Effects of LDEF Exposure on Polymeric Matrix Composites

A series of graphite-fiber-reinforced epoxy (934 and 5208) and polysulfone (P1700) matrix resin composite materials were exposed for 5 years and 9 months on the Long Duration Exposure Facility (LDEF). On this LDEF flight experiment, the composite specimens were exposed to the full low Earth orbital (LEO) environment of atomic oxygen, solar ultraviolet radiation, thermal cycling, and vacuum. The exposed and control composite materials were in the form of tensile specimens with prebonded fiberglass end tabs.

The figure compares the tensile moduli for the five composite materials evaluated. No major differences are noted between the baseline values (obtained prior to the LDEF launch on April 6, 1984), the ground control composites that remained in reduced humidity storage at Langley Research Center and were tested at the same time as the flight specimens, and the

flight control specimens that flew on the LDEF but were protected from atomic oxygen and solar UV exposure. However, the specimens that flew exposed to the full LEO environment experienced a loss in tensile modulus. These specimens also suffered a loss in thickness ranging from 0.003 in. to 0.005 in., primarily because of surface reactions and erosion caused by atomic oxygen. The decrease in tensile modulus is proportional to this loss in specimen thickness.

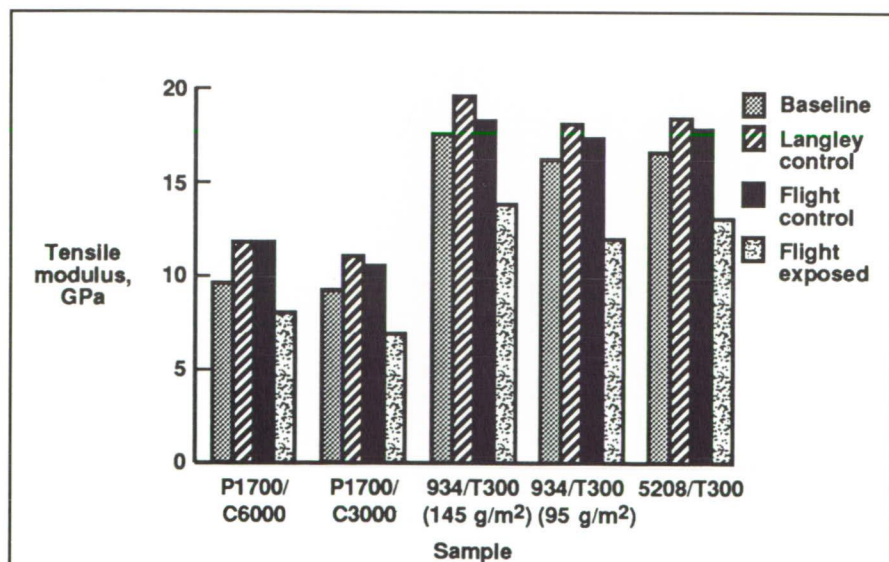
In actual spacecraft applications, a composite material would be flown with some form of coating providing needed thermal control. These flight data reveal that resin matrix composites protected from atomic oxygen and solar UV exposure should perform with no significant loss in mechanical properties for 6-year LEO missions.

(W. S. Slemp, 41334)
Structures Directorate

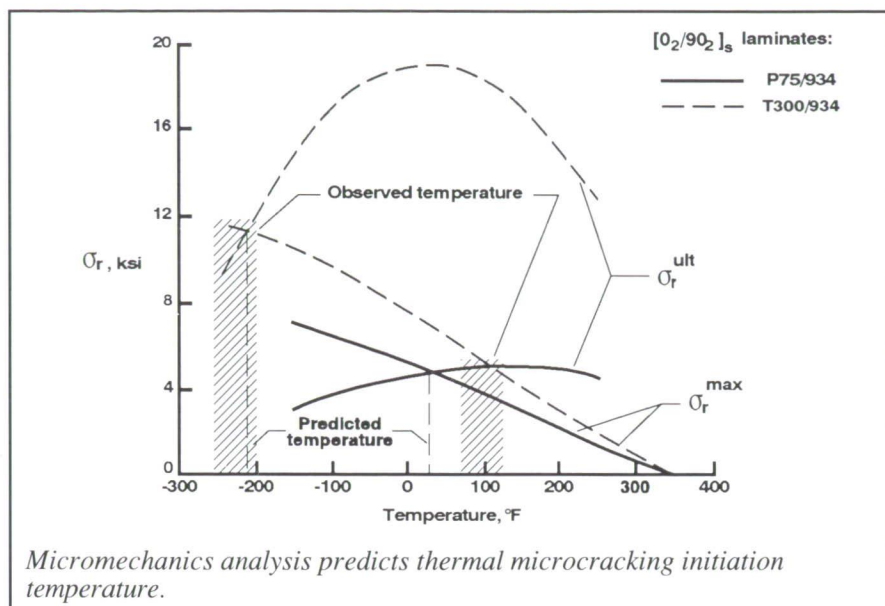
Prediction of Thermally Induced Damage in Composites for Spacecraft Applications

Graphite-fiber-reinforced polymer matrix composites used for spacecraft applications can be subjected to repeated thermal cycling, with cold temperatures as low as -250°F , during orbit. This type of thermal loading can cause damage in composites because of the mismatch in properties between the fiber and matrix and thereby degrade the material's performance. A finite-element-based micromechanics analysis was developed for predicting thermally induced damage in composites and for identifying the performance-critical materials parameters that control damage initiation.

Thermally induced microcrack initiation predictions for $[\text{O}_2/\text{O}_2]_s$ laminates of a 75-Msi modulus P75 graphite fiber and a 30-Msi modulus T300 graphite fiber, both in a 934 epoxy matrix, are shown in the figure. These predictions are based on a micromechanics analysis of the stresses in the fiber, matrix, and at the interface. The microcrack initiation temperatures are predicted by comparing the computed maximum interfacial radial stress σ_r^{max} with the experimentally determined interfacial radial strength σ_r^{ult} computed from measured values of the transverse (i.e., 90°) lamina strength of the two material systems. The predicted microcrack initiation temperatures are in good agreement with the observed initiation temperatures for both material systems. The significant difference between values of σ_r^{ult} for two composites with the same matrix but different fibers (T300/934 and P75/934) illustrates the importance of fiber/matrix bond characteristics. Knowledge of the factors that control thermal stresses and thermally induced damage in composites



Effects of LDEF flight exposure on selected composite materials.



provides a guide for the development of new material systems with reduced microcracking and enhanced durability and performance at the low temperatures encountered in the space environment.
(D. E. Bowles, 43095)
Structures Directorate

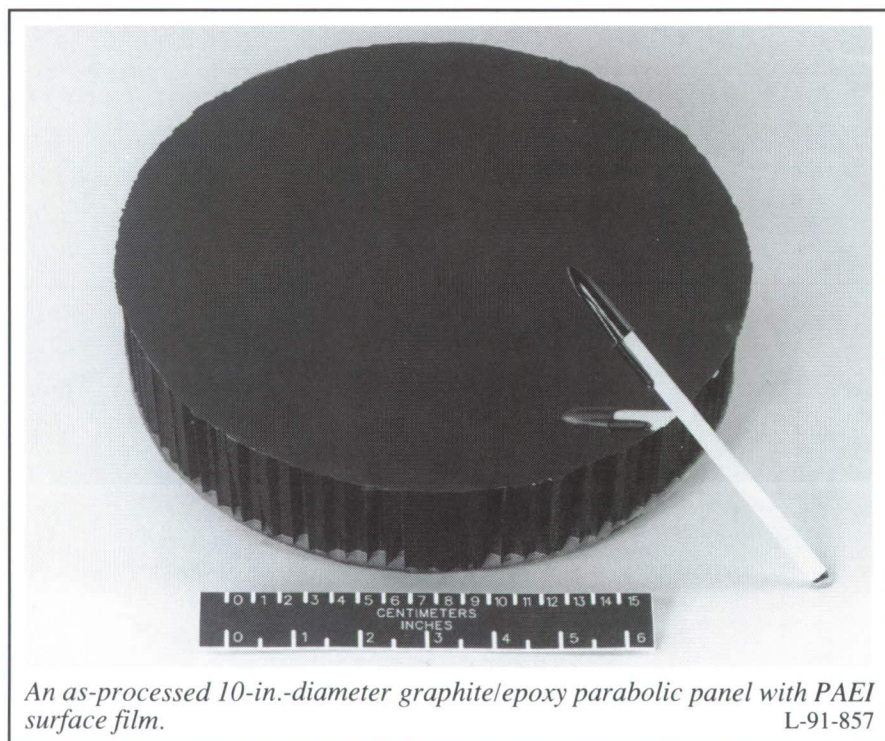
PAEI High-Quality Film for Precision Segmented Reflectors

As part of the Precision Segmented Reflector (PSR) Program, a thermoplastic polymer film (PAEI or poly(arylene ether imidazole)) containing imidazole groups was prepared from novel monomers. One of the goals of the PSR Program was to demonstrate that parabolic panels could be fabricated from graphite/epoxy composites and meet specifications for weight and surface accuracy in their as-molded state without requiring any post-machining or polishing. Precision parabolic composite reflectors (10-in. and 14-in. diam-

eters) were fabricated with the PAEI film as a surface modifier. Imidazole units in the film react chemically with the epoxy and, thereby, provide excellent adhesion to the graphite/epoxy facesheet.

An as-processed panel had a surface smoothness of 1.8 μm root mean square (rms) and an areal weight of 5.7 kg/m^2 , both easily meeting the program goals of 3.0 μm rms and 10 kg/m^2 . The reflector surface was highly specular and exhibited a mirror-like finish when coated with vapor-deposited aluminum and silicon oxide.

The use of high-quality PAEI film eliminated fiber print-through, post-polishing, and the use of mold release agents that can contaminate the reflector surface and contribute to surface roughness. The film is thermally stable, resistant to electron radiation, and adheres tenaciously to the facesheet even when thermally cycled. Films of this type can be used to provide precision surfaces on a variety of graphite/epoxy structures.
(John W. Connell, 44264, and Tim W. Towell)
Structures Directorate



Vibration of Axially Loaded Column With Piecewise Constant Cross Section

It is well known that tapered columns are more efficient compression members than uniform columns and that an approximation to a tapered column can be achieved with a piecewise constant cross section. Unfortunately, even this slight increase in complexity from a column with a uniform cross section results in governing equations for vibration frequency and buckling load that must be solved numerically. The objective was to determine the vibration frequency of a column with piecewise constant cross section under axial load.

Vibration of a mid-span symmetric column with piecewise constant cross section is governed by a fourth-order system of nonlinear equations provided the column has only two different cross

sections as shown in the figure. For generality, the equations were written in terms of nondimensional bending stiffness, length, and lineal density parameters, and numerical solutions were determined for a range of these parameters. The axial load and resulting vibration frequency were normalized to the buckling load P_{cr} and unloaded vibration frequency ω_0 of the column, and this solution was compared to the closed-form expression governing vibration of a uniform column under axial load. As shown in the figure, regardless of the dimensionless length ratio α , bending stiffness ratio β , or lineal density ratio γ , of the column sections, the numerical solution for normalized vibration frequency of the column under axial load is essentially identical to the value determined with the closed-form equation derived for a column of uniform cross section. Therefore, only the buckling load and unloaded vibration frequency of the column

must be determined numerically before the uniform column equation can be applied to determine the vibration frequency of the column under axial load.

The application of tapered columns to large truss structures is impeded by the complexity that vibration and buckling analysis of the members adds to the design process. This study has shown that once the buckling load and unloaded vibration frequency of these members are determined numerically, their vibration frequency under axial load can be evaluated with the closed-form expression derived for uniform columns, thus greatly simplifying the design process.

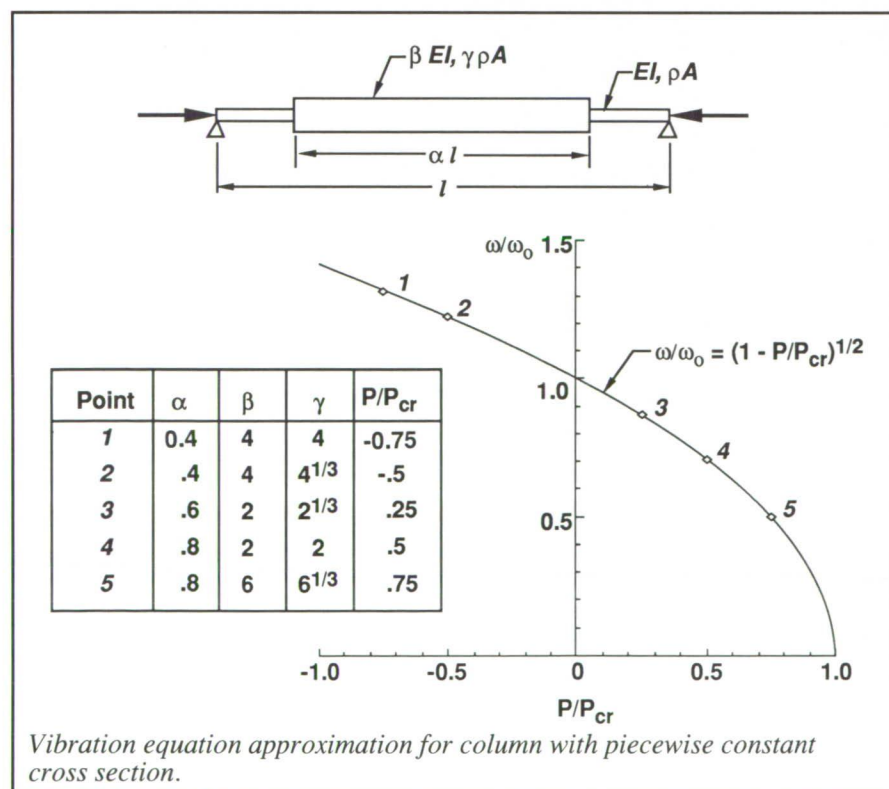
(Mark Lake, 43114)

Structures Directorate

Photogrammetric Surveys Verify PSR Test-Bed Truss Surface Accuracy and Coefficient of Thermal Expansion

High surface accuracy and predictable structural performance are essential to the success of the Precision Segmented Reflectors (PSR) program. The PSR test-bed truss is the first attempt at producing a support structure that meets the demanding requirements of the program. The objective is to determine the surface accuracy and thermal expansion characteristics of the test-bed structure.

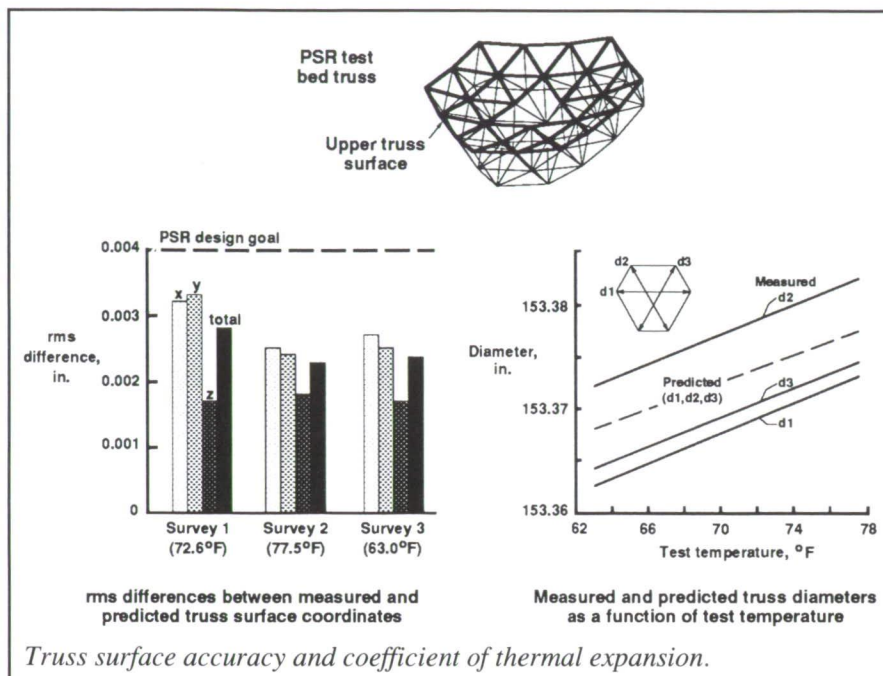
Photogrammetric surveys were conducted at three different temperatures with a large-format photogrammetric camera photographing the truss surface from 24 distinct perspectives. With reflective targets centered on the 27 truss upper-surface nodes, measurements from the photographs along with predictions from finite-element



New Method Controls Thermal Distortion of Space Antenna

Large space antennas demand such accurate surfaces that an active control system may be necessary to limit thermal distortion. Previous control system design methods have not accommodated the time dependence of the distortions because of variable orbital heating and the nonlinear relation between surface distortion and true performance criteria. For example, optimal actuator locations have been selected by minimizing the mean square surface error at the worst position in orbit. Performance at other orbital positions or in terms of radio frequency parameters such as side lobe level or beam efficiency was not evaluated.

This study overcomes these limitations by first developing a new series expansion for the radiation

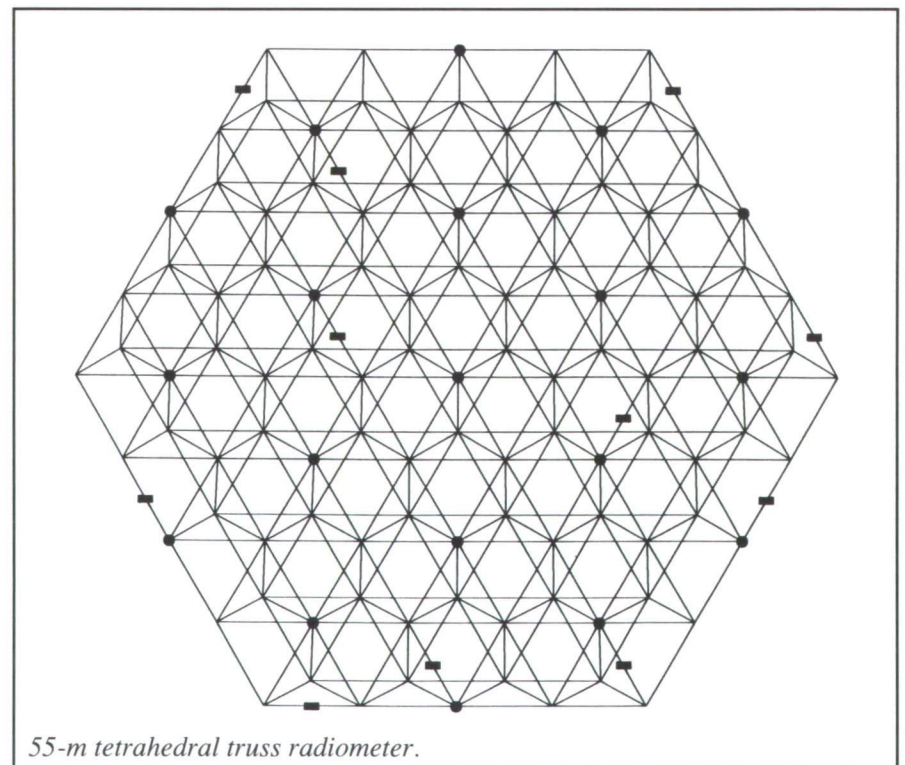


analyses determined truss surface accuracy and coefficient of thermal expansion (CTE). The left side of the figure shows the root mean square (rms) difference between the measured and predicted *x*, *y*, and *z* coordinates of the truss surface nodes for each of the three surveys. For all coordinates the rms differences are less than the PSR design goal of 0.004 in. and are far below the requirement of 0.020 in. The total rms difference (considering *x*, *y*, and *z* coordinates) between the measured and predicted truss surface is less than 0.003 in. The right side of the figure shows truss diameter as a function of temperature. The slope of each line represents the measured rate of truss expansion with temperature, and when divided by the truss diameter it is roughly equivalent to the effective truss CTE. (The predicted truss diameter as a function of temperature is also shown.) The measured CTE (approximately 4.2×10^{-6} in/in/°F) is very close to that predicted by analysis.

The results show that an erectable support truss that meets PSR accuracy goals and which has predictable

thermal expansion characteristics can be reliably manufactured.

(Timothy J. Collins, 43113, and W. B. Fichter)
Structures Directorate

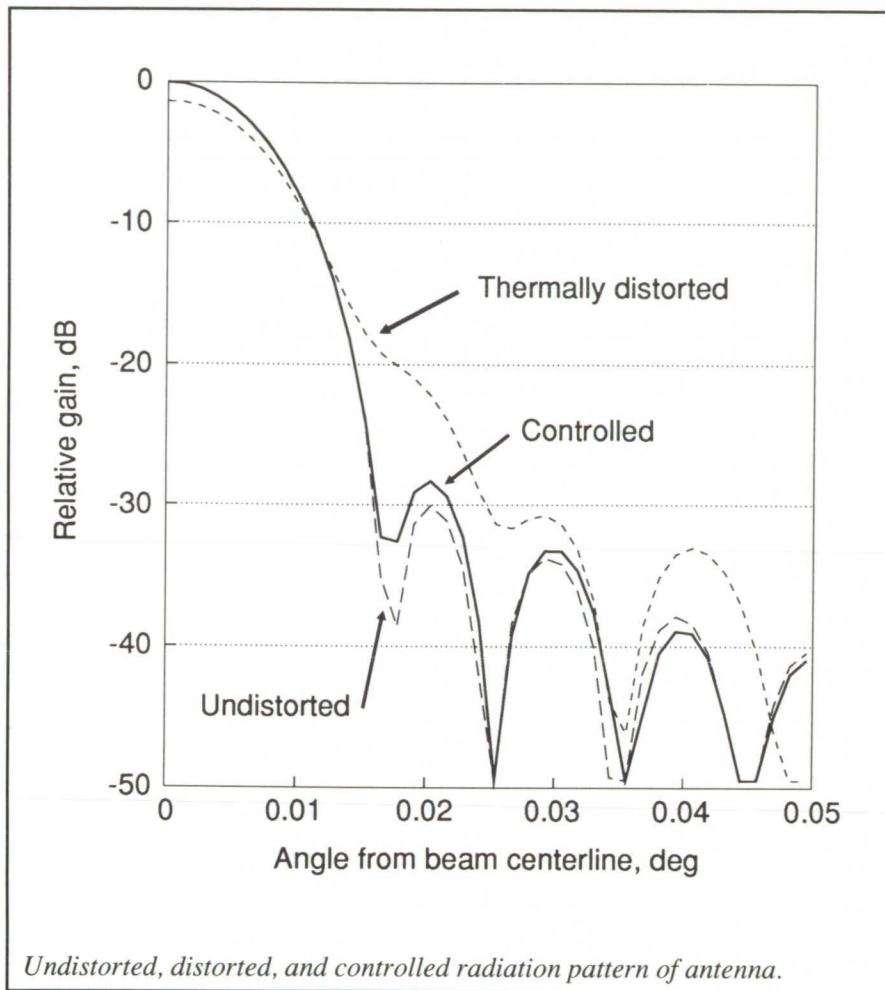


Spaceflight Application of Erasable Programmable Logic Devices

Erasable programmable logic devices (EPLD's) were selected for use on printed circuit boards (PCB's) in several subsystems of Langley Research Center's Lidar In-Space Technology Experiment (LITE). A search of open literature indicates that the selected EPLD's have not previously flown on space flights.

Although the EPLD's are rated as fully compliant to MIL-STD-883C, additional tests were performed to qualify them for LITE. The tests included a 500-hr burn-in, destructive physical analysis, and particle impact noise detection. Results indicated that they are acceptable for LITE, an attached Space Shuttle payload.

Major benefits of EPLD's include increased package density and design flexibility. Limited PCB physical space problems were resolved by using EPLD's to significantly reduce the number of integrated circuits. For example, in one case it was estimated that 15 small- and medium-scale integrated circuit devices and associated traces would have been required to implement the control logic for a serial data interface. However, this function was accomplished with approximately 75 percent of an EPLD, which occupies 1 in² in area. The unused portion of the EPLD is configured such that additional circuitry could be implemented without having to cut traces on the PCB's. This capability allowed design changes without the need to fabricate new PCB's. A total of 36 EPLD's, almost all in different circuit configurations,



Undistorted, distorted, and controlled radiation pattern of antenna.

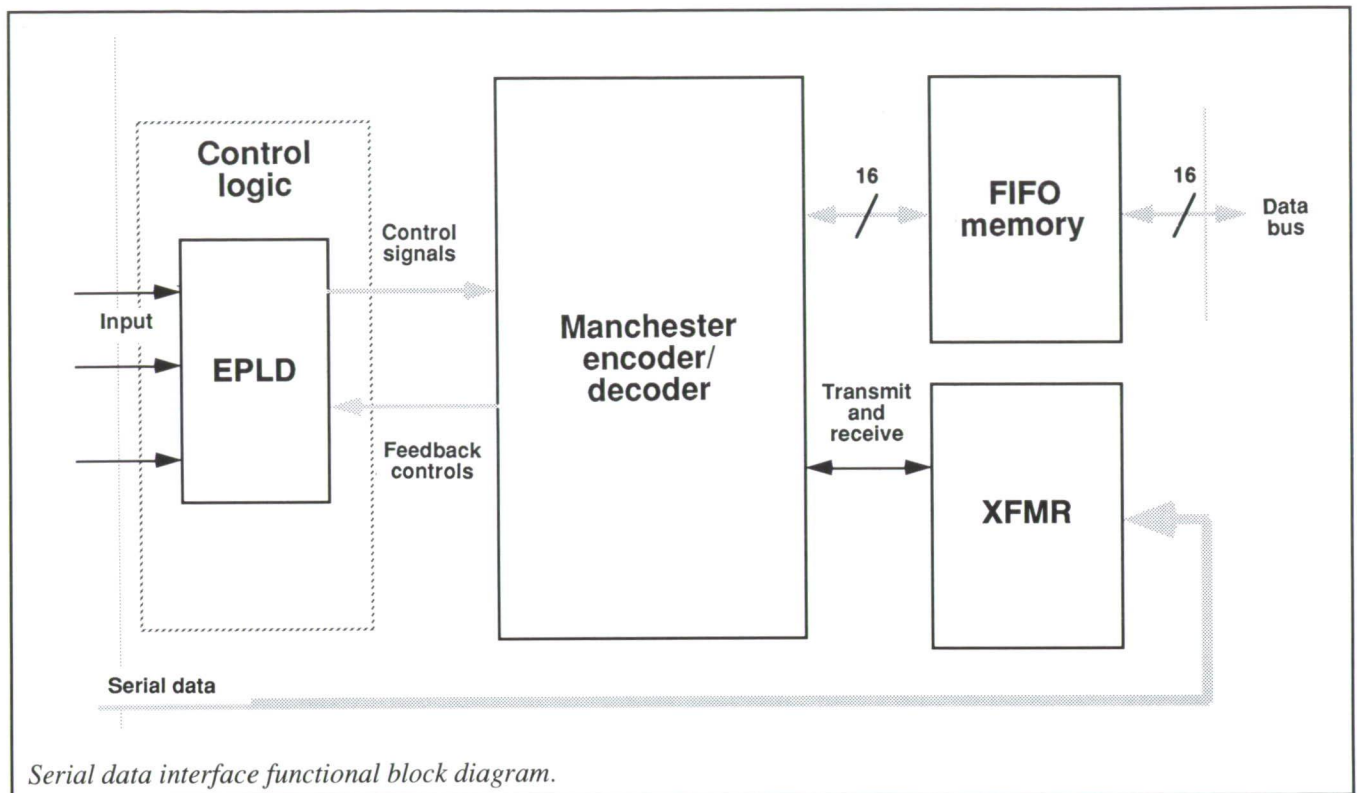
pattern. In this expansion, a quadratic cost function appears quite naturally. Second, the cost is expanded in functions that are orthogonal in space and time. The control system uses a truncated version of this expansion, averaged over an orbit, to include the time dependence implicitly. The orthogonal functions also provide a natural basis set for extrapolating sensor measurements to the entire antenna surface.

Simulations using a 55-m geosynchronous radiometer (shown in the first figure) demonstrate the utility of the method. The ideal pattern (see the second figure) of the undistorted antenna has a well-defined center beam and side lobes below -30 dB. The

thermally distorted pattern has neither important characteristic. The control system, designed by the new method, proved to be very robust to errors in structural materials, thermal properties, and heating conditions. In the worst case, only 11 actuators (rectangles) and 19 sensors (circles) are required to produce an acceptable pattern.

(Robert H. Tolson, 42798)

Structures Directorate



are being incorporated into the LITE electronics.

(D. Rosenbaum, 41800)
Electronics Directorate

Demonstration of Self-Correcting Techniques for Large Antennas

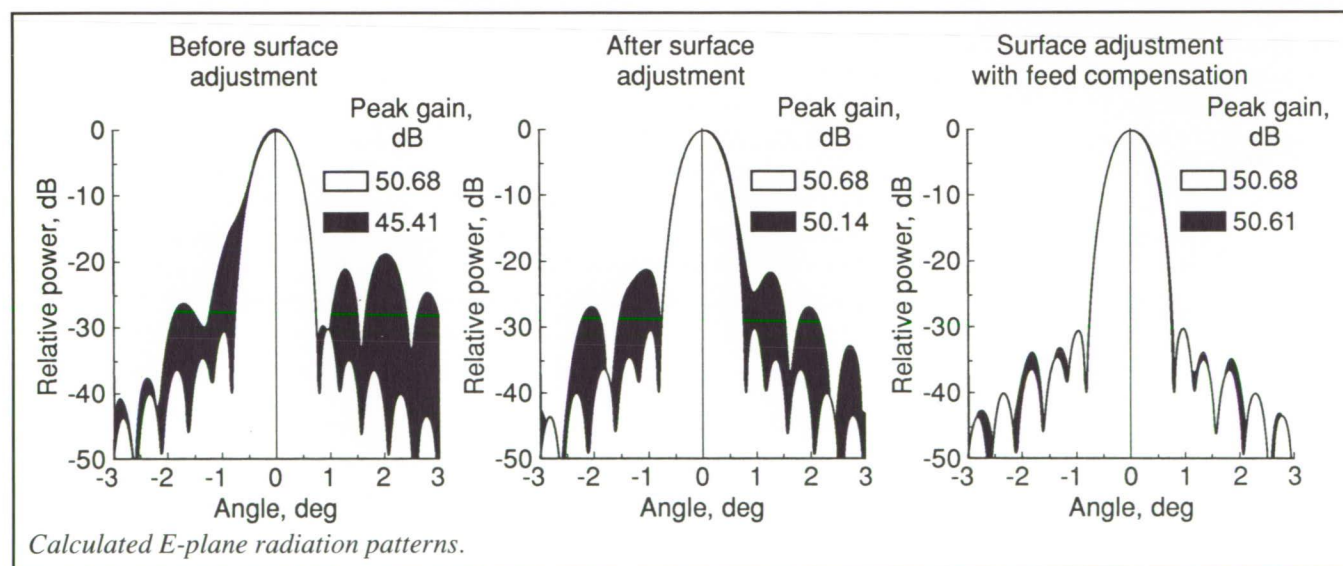
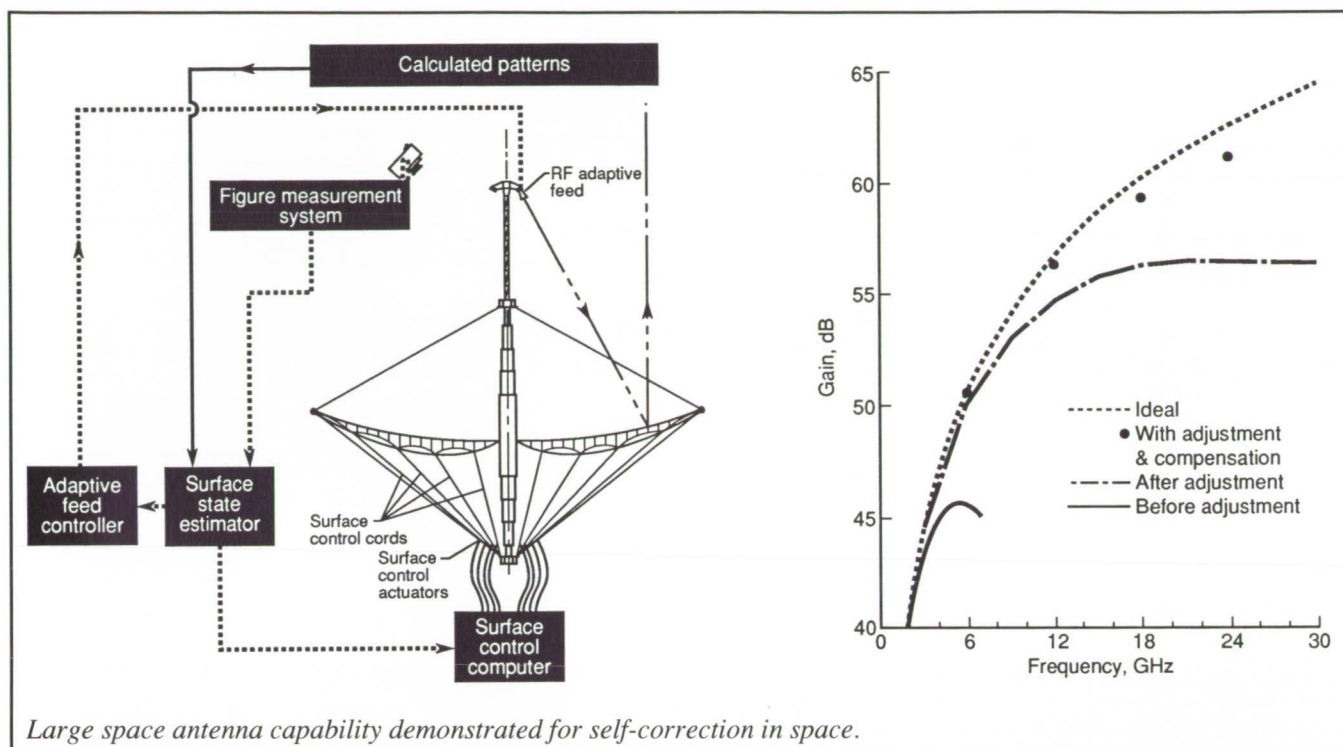
Recent research at Langley Research Center has demonstrated the potential for self-correction by a large deployable antenna for space applications. This work represents the culmination of over 10 years of research with the 15-m hoop-column antenna. In order to accomplish self-correction, optical sensors are used to detect distortions in the antenna reflector; onboard computers then send appropriate commands to perform mechanical adjustments to the surface

and structure. Any residual distortion is compensated for by changes in the antenna feed excitation.

Mechanical correction in space is possible for either solid or mesh antennas for which the adjustment capability of sections of the reflector surface has been incorporated into the design. The 15-m hoop-column antenna is inherently suited for demonstration of this concept. After the antenna reflector is deployed, its surface is shaped by tensioning 24 control cords connected to the back of each quadrant. A computer model that optimizes the reflector shape relative to a design paraboloid through adjustment of the length of the control cords has been developed for this antenna. The adjustment process has been implemented in an automated fashion by installing computer-controlled motors at each of 24 cords to enable adjustment within an accuracy of 0.001 in.

The 15-m hoop-column antenna was deployed in the Langley 16-Meter Thermal Vacuum Facility, and tests were conducted to demonstrate optimization through mechanical adjustment of the antenna. In typical tests, after a few iterations, the surface roughness was reduced to the fabrication limits for this structure, which is approximately 0.060-in. root mean square. The figures illustrate the significant improvement in antenna performance to be expected by automated mechanical adjustment of the antenna surface.

Computer algorithms for feed compensation of reflector surface distortions were used to demonstrate that further improvement in performance is possible beyond the fabrication limits of the antenna. This technique determines the amplitude and phase excitations of multiple antenna feeds that would illuminate the reflector in such a way that the effects



of any residual distortions would be minimized. The figures illustrate that near-ideal antenna performance can be achieved by a combination of mechanical adjustment and feed compensation.

(L. C. Schroeder, 41832, and M. C. Bailey)

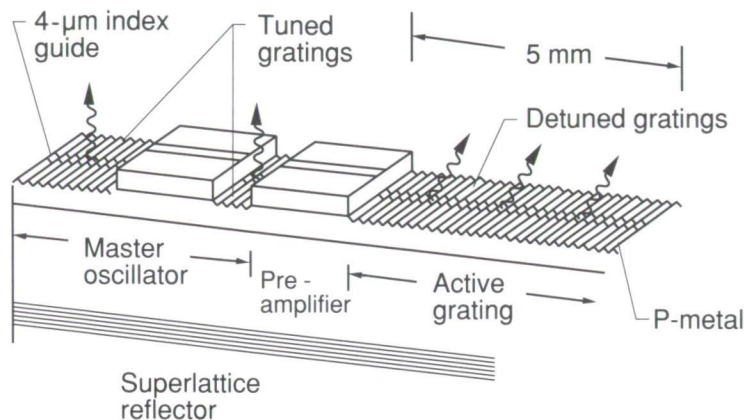
Flight Systems Directorate

High-Power Semiconductor Diode Laser for Optical Communication Applications

The research on high-power semiconductor diode lasers for optical communications is aimed at developing and demonstrating technology

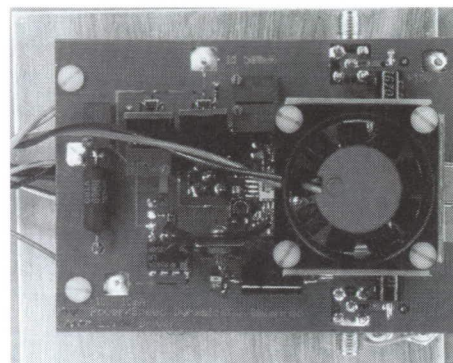
readiness of high-power lasers for NASA's optical communication applications for the next 20 years. The specific objectives to achieve are 0.5 W to 5 W of output power and 0.5 GHz to 4 GHz modulation with single spatial and spectral modes of operation.

MAG-MOPA



High-power semiconductor diode lasers for optical communication.

High-power laser modulator



Shown in the figure is the Monolithic Active Grating-Master Oscillator Power Amplifier (MAG-MOPA) semiconductor diode laser. This device consists of a master oscillator that is a distributed Bragg reflector (DBR) laser with second-order tuned gratings. This DBR laser is first coupled (via a waveguide) to a preamplifier that provides gain for the laser, and then it is coupled into a detuned active grating that also provides gain for the laser and acts as the output coupler for the laser. A superlattice reflector below the device is an integral part of the laser; this device reflects light in phase to the output grating of the laser.

This initial design for a MAG-MOPA has been fabricated and evaluated for output power, spatial characteristics, and modulation. The device operated in the pulsed mode with more than 1.3 W of power output. In the p-side-down, heat-sinked configuration, the laser operated in a continuous wave mode to 0.7 W of power output. The spectral and spatial output characteristics of the laser beam were both single mode.

The high-power laser modulator was designed in-house using GaAs device technology in a current mirror configuration with a dual balanced laser configuration. A second laser was used in the second leg of the current mirror, and its drive characteristics were used to balance and speed up the modulator operation. Without a balanced system, the device operated to 800 MHz with a drive current capability of 1 A. The modulator was demonstrated using a pair of the antiguiding edge emitter phased array lasers.

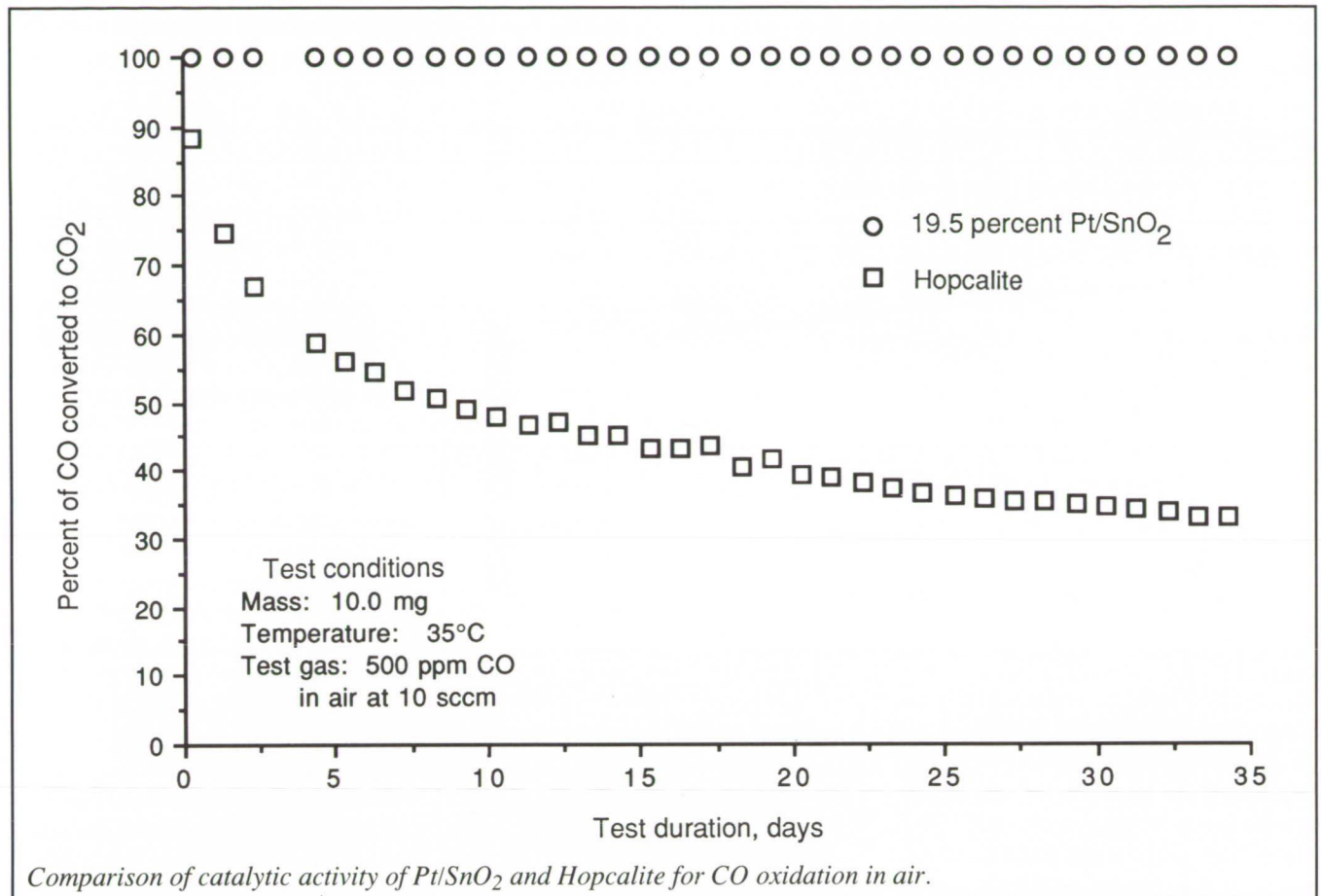
Future work will consist of optimizing the MAG-MOPA semiconductor diode laser for high powers, improving the heat sinking and mounting configuration, and testing and characterizing the modulation characteristics of the laser. The modulation speed of the high-power laser modulator will be increased by the use of a balanced line drive for the two lasers.

**(Herbert Hendricks, 41536)
Flight Systems Directorate**

High-Activity CO-Oxidation Catalyst for Air Purification

Carbon monoxide (CO) is a toxic air contaminant that may accumulate in dangerous quantities in confined environments such as spacecraft, submarines, and underground mines. CO can be removed from such environments by catalytically oxidizing it to nontoxic carbon dioxide (CO₂). The catalyst most commonly used at present for ambient-temperature oxidation of CO to CO₂ in air is the commercial catalyst, Hopcalite.

Another material that can catalyze the oxidation of CO to CO₂ at ambient temperatures is platinumized tin-oxide (Pt/SnO₂), which was originally developed in the United Kingdom and has been significantly improved by research at Langley Research Center. Research on Pt/SnO₂ to date has concentrated mainly on the recombination of stoichiometric CO-O₂ mixtures to regenerate CO₂ in pulsed CO₂ lasers. However, because Pt/SnO₂-catalyzed CO oxidation is enhanced by excess O₂, Pt/SnO₂ should also be a good catalyst for removal of CO in air purification applications.



To demonstrate the catalytic activity of Pt/SnO₂ for CO oxidation in air, its performance was compared to that of Hopcalite under identical conditions in an extended test. Ten-milligram samples of Pt/SnO₂ (19.5 percent Pt by weight) and Hopcalite were placed in a temperature-controlled environment at 35°C and each sample was exposed continuously to a test gas consisting of 500 p/m CO (and 2 percent neon) in air at a flow rate of 10 standard cm³/min for a period of 5 weeks. The amount of CO and O₂ lost and of CO₂ generated was measured periodically with a gas chromatograph with the neon as an inert internal calibration standard.

The results are shown in the figure. The Hopcalite sample achieved an initial conversion efficiency of 88

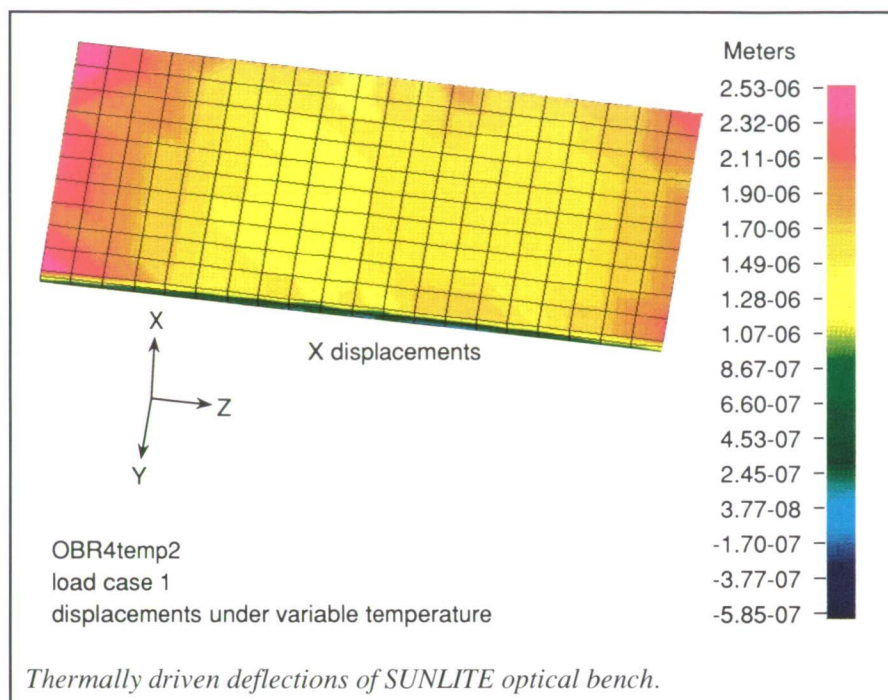
percent that decreased to 32 percent by the end of the test. The Pt/SnO₂ sample achieved complete conversion throughout the entire test. This result clearly indicates that Pt/SnO₂ is a potentially superior catalyst for removal of CO from air.

(David R. Schryer, 44743, and Billy T. Upchurch)
 Electronics Directorate

Integrated Structural/ Thermal Model of SUNLITE Optical Bench

One of the driving requirements for an optical bench, particularly for space applications, is its stability under all

conditions. Accurate predictions of the optical bench deflections are necessary to determine optical performance. On the SUNLITE (Stanford University-NASA Laser In-Space Technology Experiment) project this stability has been accomplished by using a single integrated model for both thermal and structural analysis of the optical bench. The deflections of the bench because of structural loads can be calculated after translating the model from the solid modeling program PATRAN to Engineering Analysis Language (EAL). The thermal response of the optical bench is determined by translating the PATRAN model to the thermal software SINDA-85 for solution. The predicted temperatures are returned to the PATRAN model, and the calculation of thermally driven deflections is performed in EAL.



Postprocessing in PATRAN allows a vivid display of the results as shown in the figure. Animation of the graphical results for both temperatures and deflections yields a better understanding of driving forces in the model and is a valuable debugging tool.

This method allows an exact calculation of the optical bench deflection because of complex thermal distributions as well as gravity loading. Designs can be optimized for maximum deflection. The integrated nature of the process streamlines the modeling and analysis procedure as well as ensuring model continuity between thermal and structural analysis. In the future, this integration hopefully can be extended to the optical analysis as well, with these deflections input directly to an optical analysis model.

(Kelly D. Smith, 47031, and Ruth M. Amundsen)

Systems Engineering and
Operations Directorate

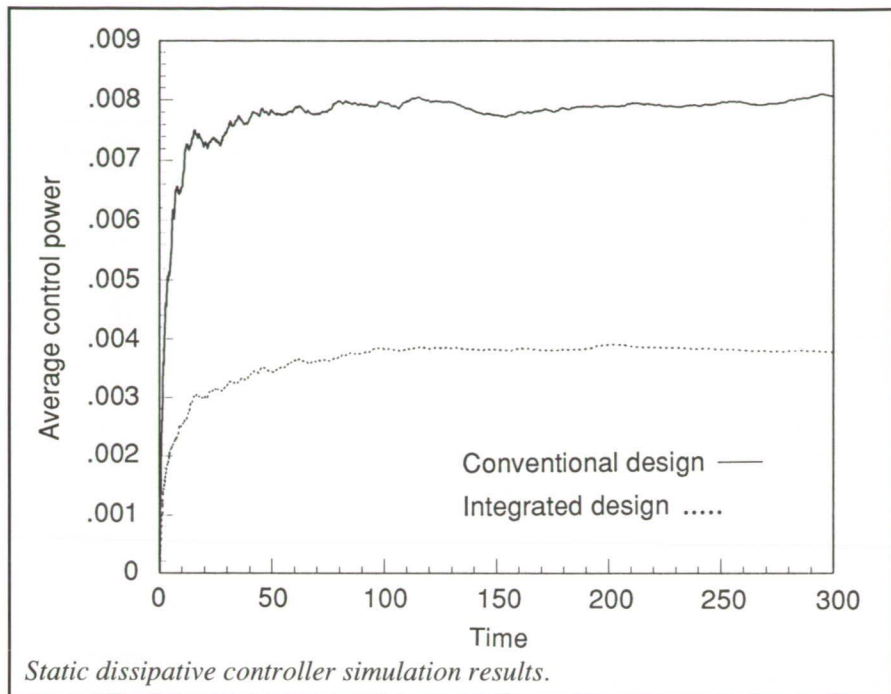
Verification of Integrated Controls-Structures Design of CSI Evolutionary Model

A number of future space missions presently under consideration will utilize large space structures in low Earth and geostationary orbits. To minimize the cost of construction, launch, and operation, these structures should be as light as possible. However, reducing the structural mass tends to increase flexibility, thus making control in attitude and shape with a specified precision extremely difficult. Current spacecraft design practice follows a sequential design approach, wherein the structural design is first performed based mainly on loading considerations. Next, the controller is designed to optimize the performance of the fixed structure. Because the performance of a spacecraft so designed is inherently limited, an integrated design methodology is desired for designing space structures that are optimal in both structural and control design.

An integrated design methodology has now been developed and verified analytically in application to the redesign of the Controls-Structures Interaction (CSI) Evolutionary Model (CEM). The CEM is composed of a 620-in.-long, 62-bay main truss with two horizontal booms and two vertical towers. The structure is suspended from the ceiling by two cables. Control inputs are provided by eight cold-gas thrusters that are collocated with eight accelerometers that provide feedback measurements.

The integrated design problem was posed in the form of a single-objective simultaneous optimization of both the structural and control design variables. A dynamic dissipative controller strategy, which is known for its stability robustness in the presence of unmodeled dynamics and parametric uncertainties, was considered. The structural design variables were chosen as the effective cross-sectional areas of the longerons, battens, and diagonals of seven sections of the structure, while elements of the rate gain matrix and compensator matrices were chosen as the control design variables. In the integrated optimization problem, the steady-state average control power was minimized in the presence of white noise disturbances at the actuator locations, subject to constraints on the line-of-sight pointing error, the total mass of the spacecraft, and bounds on the structural member sizes.

Analytical and simulation results indicate that the integrated design approach can yield an overall design that is substantially superior in performance over the conventional sequential design. This superiority is demonstrated in the figure where it is observed that integrated design achieves the required line-of-sight pointing performance with only one-half the control power needed by the conventionally designed system. Experimental



The control system must maintain stability and performance despite these problems.

Four different state-of-the-art controllers have been designed and implemented; these are the linear quadratic Gaussian (LQG), dissipative (both static dissipative controller or SDC and dynamic dissipative controller or DDC), H-infinity optimal, and high-authority/low-authority controllers (HAC/LAC).

Although stable in simulation studies, early experimental testing of the controllers revealed instabilities because of digital computer implementation and unknown biases that are generally present in the accelerometer signals. These implementation problems were overcome by incorporating a one-step-ahead predictor, antialiasing filter and washout filters for limiting the effects of the bias. The control laws were then tested by applying a disturbance signal for 9 sec and allowing a 1-sec free decay, after which the

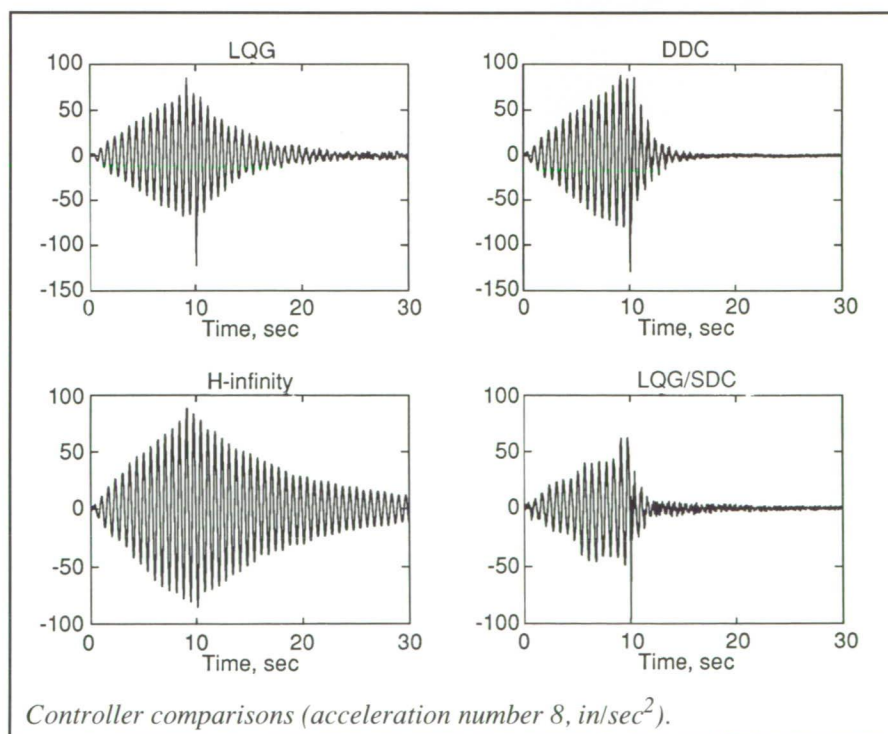
validation of the design is being completed with the fabrication of a new CSI Evolutionary Model that follows the integrated controls-structures design.

(Peiman G. Maghami, 44039)
Flight Systems Directorate

modes; low inherent structural damping (less than 0.5 percent); and inaccuracies in the mathematical model because of limitations that prevent ground tests of a full-scale structure.

Comparison of Controller Designs for CSI Evolutionary Model

The objectives of this research were to design control laws for the CSI Evolutionary Model (CEM) and to implement them experimentally in order to validate various controller design methodologies. The CEM is a 620-in.-long experimental structure with collocated accelerometers and cold gas thrusters. This structure captures many of the drawbacks of large, flexible spacecraft planned for the future, including a large number of significant, closely spaced, elastic



controller was turned on. The responses were then examined to verify agreement with simulation results including the closed-loop damping, which was used as the measure of performance. A 30-sec time history from one of the accelerometers showing excitation, free decay, and control for each of the four control laws is presented in the figure.

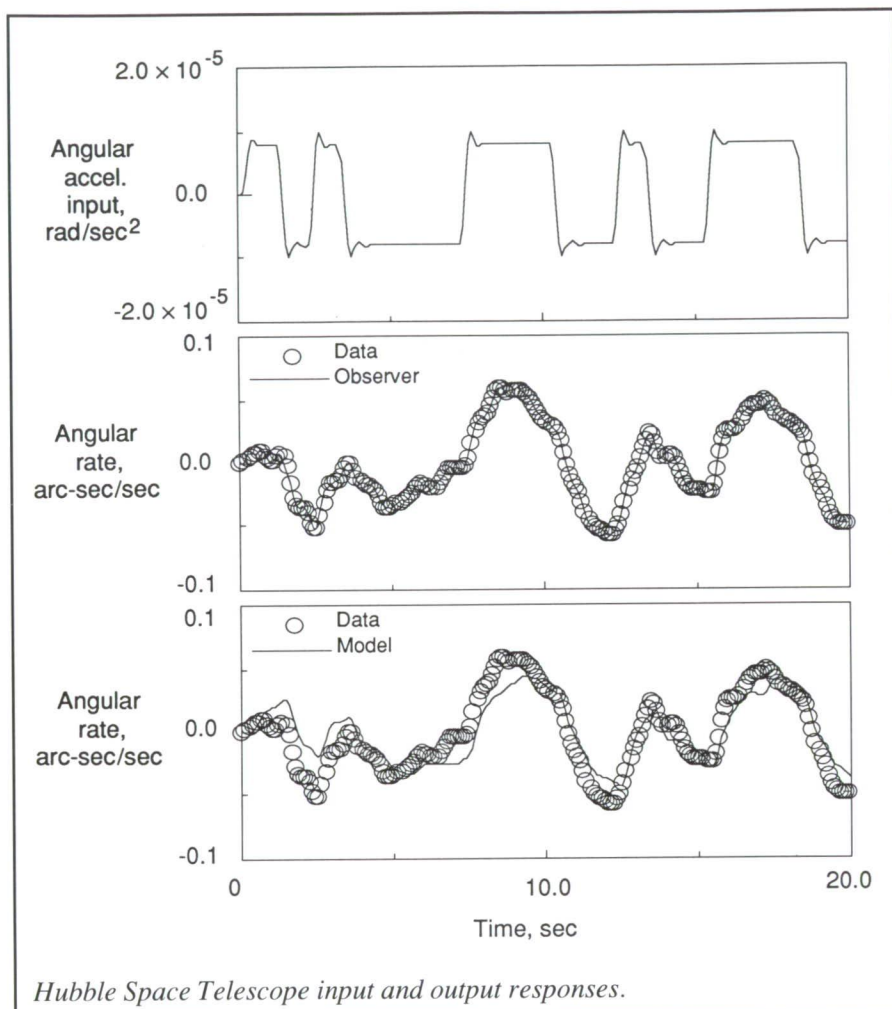
The best performance is given by the dynamic dissipative controller that gave closed-loop damping ratios of 8.5 percent and 14 percent for the first two structural modes respectively, as compared with their open-loop values of less than 0.5 percent. Although the HAC/LAC controller gave slightly better damping, its design was based on several ad hoc design iterations and not on a succinct design methodology. The H-infinity optimal controller gave the smallest damping ratios.

This study underscored the fact that uncertainty modeling and implementation strongly influence the degree of performance attainable in theory and in practice for large, lightly damped structures.

(Kyoung Lim, 44342)
Flight Systems Directorate

Solar Array Vibration Parameters of Hubble Space Telescope Identified From Flight Data

On-orbit vibration can be detrimental to the performance of flexible spacecraft, particularly where precise, stable pointing is crucial. Excessive vibration may be caused by onboard equipment, alternate heating and cooling, or pointing and attitude control forces. Spacecraft attitude control systems can reduce vibration



if the nature of the motions is understood. Unfortunately, gravity effects reduce the ability to determine spacecraft vibration behavior in ground tests. The alternative on-orbit tests require methods to overcome a limited number of measurements and test operations restrictions.

A study was conducted to identify the vibration characteristics of the Hubble Space Telescope from flight data using an advanced system identification technique known as the Observer/Kalman Filter Identification (OKID) method. Vibrations were induced by four torque wheels located on the Spacecraft Subsystem Module (SSM). Pulses combined with sine-sweeps were used as input commands

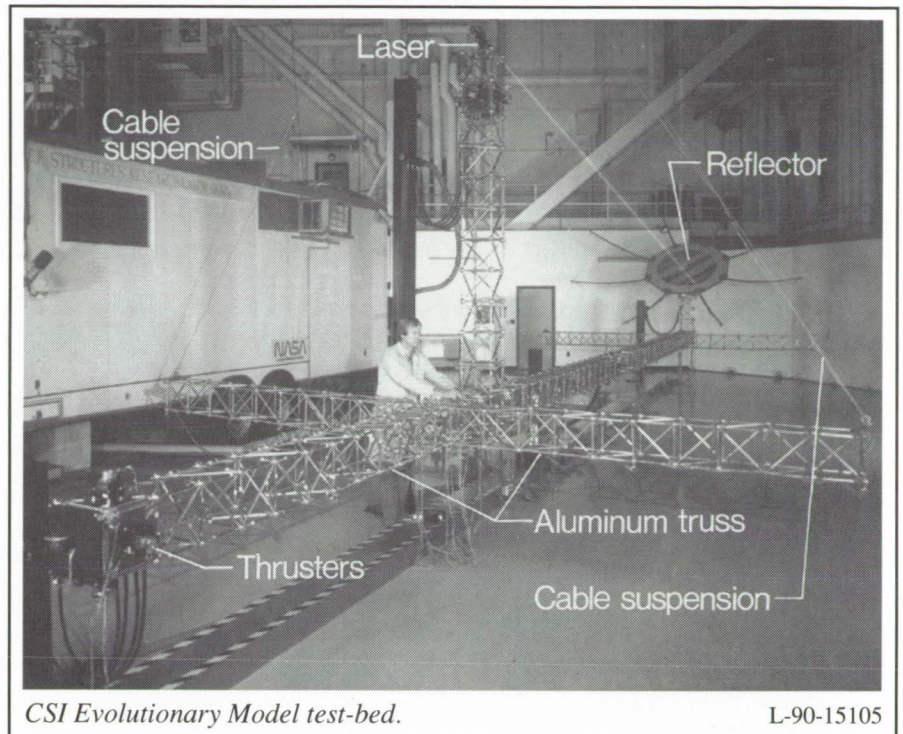
to the torque wheels, and the response data were sampled at 40 Hz. The top plot in the figure shows the first 20 sec of the command signal for the first vehicle coordinate. The experiment was repeated for each vehicle coordinate. Vibration responses were measured by six rate gyros located on the Optical Telescope Assembly, inside the SSM. Poor measurement resolution, 0.005 arcsec/sec relative to a pointing accuracy requirement of 0.007 arcsec/sec, resulted from noisy data.

Three dominant vibration motions were determined: one, at 0.65 Hz (5.5 percent damping), is believed to be in-plane bending of the solar array; a second, at 1.29 Hz (3.5-percent

ORIGINAL PAGE
BLACK AND WHITE PHOTOGRAPH

damping), is coupled solar and membrane motion; and a third, at 2.45-Hz mode (6.9-percent damping), is the motion of a deployment mechanism. Identified damping values are relatively high because of the effects of the attitude control system and of mechanical friction in the solar array masts. Comparison of the observer output with the measured response shows extremely good agreement, thus indicating that the observer is correcting for system uncertainties and nonlinearities. System uncertainties and measurement noise are quantified, and a mathematical model of the system then is extracted. The response of the identified model is shown to compare well with the measured response.

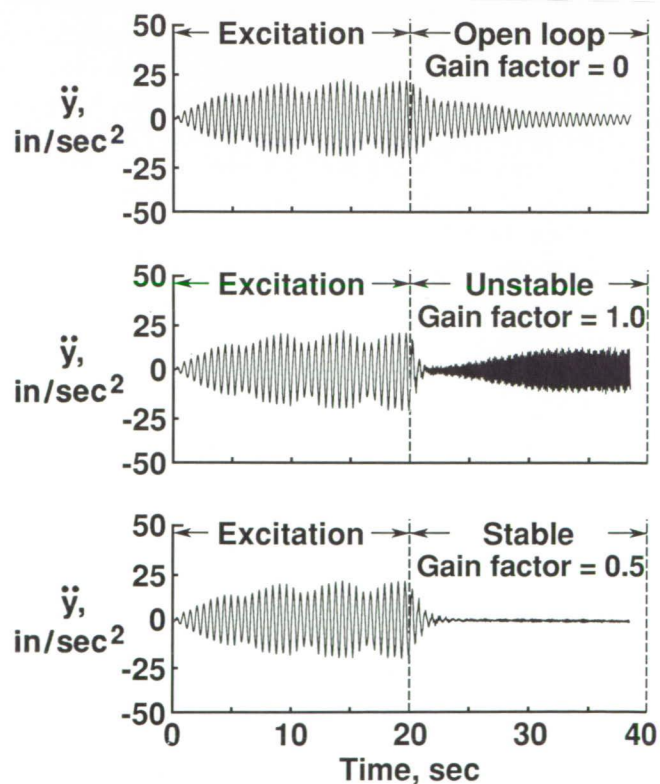
(Jer-Nan Juang, Lucas G. Horta, Keith W. Belvin, and John Sharkey (MSFC), 44351)
Structures Directorate



Control Experiments of CSI Evolutionary Model Test-Bed

A new test-bed, the Controls-Structures Interaction (CSI) Evolutionary Model, has been developed to experimentally evaluate approaches for the control of flexible spacecraft. Initial test objectives are to assess the adequacy of the test facility, to identify dynamic characteristics of the integrated system, and to investigate the performance of various control methodologies. The test configuration simulates the control problems inherent in flexible, multicomponent, science platforms.

The model, shown in the first figure, has five major structural components: a 52.5-ft center truss, a 16-ft-diameter reflector, a 9.2-ft tower that supports a laser, and two 16.7-ft



cross-member trusses. The system is supported from the ceiling by a steel cable harness attached from the cross members to the ceiling. The structure is excited and controlled by using onboard airjet thrusters. Structural response is measured by accelerometers. A feedback control law was designed using the measured accelerations to augment damping of the low-frequency modes. The time history plots show test results for a typical experiment scenario. The structure is excited at the center using two thrusters. The acceleration is measured at the lower left corner. Each sensor output signal is multiplied by a scalar gain factor that varies from 0.0 to 1.0 and is used to prevent excessive response during initial tests of control laws. The top plot in the second figure shows a 20-sec sinusoidal excitation followed by a 20-sec open-loop (free decay) response. The middle plot shows the closed-loop results using a gain factor of 1.0 after the initial excitation. Instability of a high-frequency mode occurs at 7.5 Hz. When the gain factor is decreased to 0.5, a stable closed-loop response is obtained.

(Lucas G. Horta, Anne Bruner, Jeff Sulla, Keith W. Belvin, Kenny Elliott, and Jer-Nan Juang, 44352) Structures Directorate

Results of Phase I CSI Guest Investigator Program

One element of the NASA CSI Program is the Guest Investigator (GI) Program in which industry and academic researchers participate in a research activity in which they use government test-beds to develop and validate integrated control design to meet performance requirements of future space missions. A 2-year activity in the first phase of the GI

Program has recently been completed. During this time, the Phase I GI's and their teams, using ground test facilities at Langley Research Center and Marshall Space Flight Center (MSFC), conducted experiments to validate CSI techniques in system identification and controls development. Five of the research groups developed or enhanced controller techniques, with each group showing a measure of success in controlling the test facility hardware at Langley and MSFC. The controllers ranged from the classical approach to modern control techniques such as μ -synthesis and maximum entropy/optimal projection (MEOP). The objective of demonstrating high-performance active vibration control on realistic large space structures was realized with the most aggressive techniques showing an order of magnitude increase in damping.

The results show that an accurate model of the hardware structure is necessary for controller development; accuracy in modeling sensors, actuators, and system electronics is as important as the modeling accuracy of the structure; and classical single-input/single-output (SISO) provides moderate and sometimes adequate performance and stability with minimum complexity. Other results include that reduced order and decentralized controller design can provide significant performance improvement for some flexible structures, performance requirements should determine the complexity of the controller, and on-line system identification is an essential element for successful integrated design and control of large space structures.

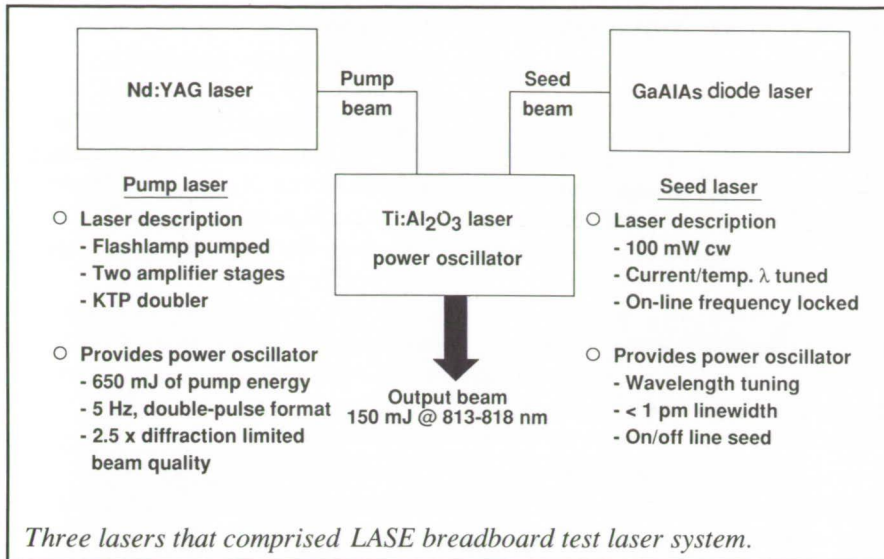
Phase I results have shown that without knowledge of the structural dynamics to be controlled, many of the most accepted control techniques demonstrated only marginally improved performance results. When

these same techniques were integrated with knowledge of the structural dynamics, the results showed considerably better performance, thus proving that controller robustness is no substitute for an accurate model. The advancements made in CSI technology and the newly developed government CSI test-beds are major steps toward making possible the ground validation of integrated control and structure design for future space structures.
(R. Smith-Taylor, 46490) Flight Systems Directorate

Application of Titanium-Doped Sapphire Laser Technology to LASE Project

Research technology for $\text{Ti:Al}_2\text{O}_3$, titanium-doped sapphire lasers, has been applied to the Laser Atmospheric Sensing Experiment (LASE). The LASE lidar instrument will be located in the Q-bay of an ER-2 aircraft and will measure vertical profiles of water vapor and oxygen from altitudes up to 70 000 ft. A $\text{Ti:Al}_2\text{O}_3$ laser will serve as the LASE instruments' tunable laser subsystem (TLS).

With a laboratory breadboard $\text{Ti:Al}_2\text{O}_3$ laser system, demonstrations were made of the capability of the laser to meet state-of-the-art laser performance requirements imposed by the LASE science team. The requirements included 150 mJ energy per pulse, 5 Hz pulse format, <1.0 pm linewidth, >99.0 percent spectral purity, 15 percent stability in energy, 0.25 pm wavelength stability, and tunability from 813 nm to 818 nm. The block schematic shows the lasers that comprised the system used to measure and test the performance of $\text{Ti:Al}_2\text{O}_3$. A Nd:YAG laser provides pump energy at 532 nm to a $\text{Ti:Al}_2\text{O}_3$ power



oscillator that generates the final output pulses. A single-frequency diode laser seeds the power oscillator and controls the final output wavelength and linewidth for the system. The diode output wavelength is current and/or temperature tunable from 813 nm to 818 nm.

Based on the performance of the breadboard test laser system with Ti:Al₂O₃ technology, a flight design for the LASE TLS is currently being built at Langley.

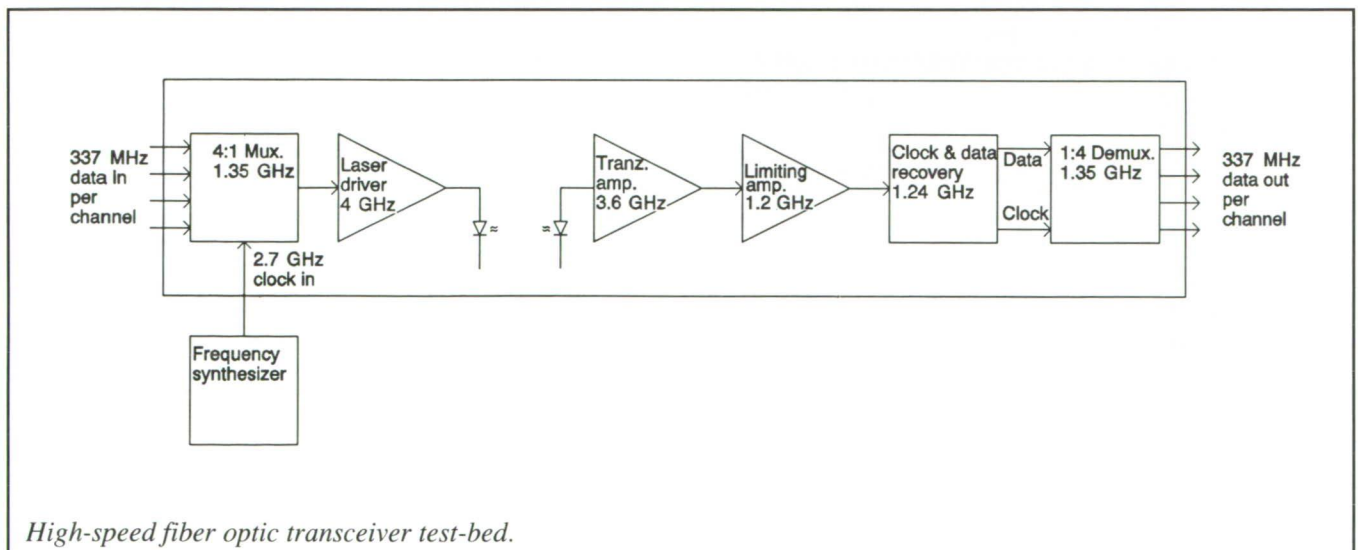
(James C. Barnes, 41637)
Electronics Directorate

High-Speed Fiber Optic Transceiver Description

The high-speed fiber optic transceiver program is aimed at developing and demonstrating transceivers from commercially available integrated circuits, distributed feedback lasers, and p-i-n detectors. Shown in the figure are some of the integrated circuits, distributed feedback lasers, and p-i-n detectors tested and evaluated for use in the overall transceiver design. The block diagram shows

multichannel digital data multiplexed in a 4:1 multiplexer and coupled into a laser driver. The 4-GHz laser drive provides current pulse outputs to drive a semiconductor laser mounted in a high-speed laser package. The laser driver and laser have been mounted onto a strip-line-based, high-speed ceramic printed circuit board that is packaged into a 16-pin dual in-line package. The optical energy, as shown schematically in the center of the figure, is sensed by a p-i-n detector and a transimpedance amplifier, operating at 3.6 GHz. The detector and transimpedance amplifier are mounted and packaged in a similar manner to the laser and laser drive circuit. The remainder of the receiver consists of a limiting amplifier, clock and data recovery circuit, and a 4:1 demultiplexer that again reduces the high-speed data stream into a lower data rate per channel. Initial tests of the analog laser driver and remounted distributed feedback laser together with the p-i-n and transimpedance amplifier portion of the transceiver gave an operating data rate in excess of 3 GBit/sec.

Future work consists of packaging the multiplexer, demultiplexer, and limiting amplifier and combining a



smaller clock and data recovery integrated circuit into a common hybrid package. Higher speed analog and digital integrated circuits will be acquired, evaluated, and tested, thus leading to the development of fiber optic transceivers in the 3-Gbit/sec to 10-Gbit/sec range. Continued re-mounting and redesign of the integrated circuit, laser, and detector packages will be required to increase the overall operational speed of the transceiver.

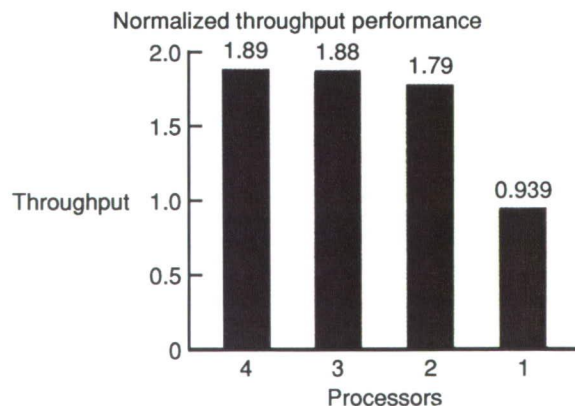
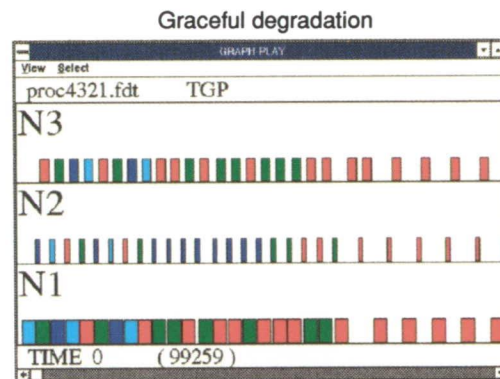
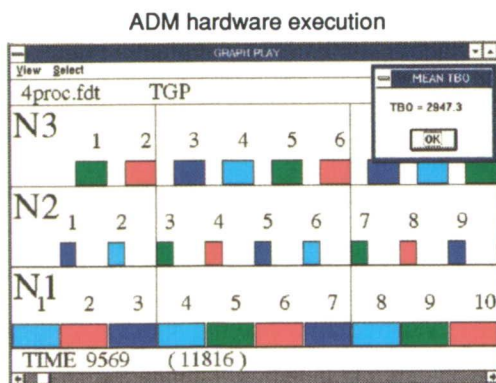
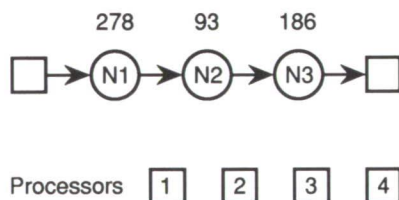
(Herbert Hendricks, 41536)
Flight Systems Directorate

Advanced Multiprocessing Strategy

A new multiprocessing strategy, the Algorithm to Architecture Mapping Model (ATAMM), is being developed to provide automatic and optimum real-time execution of aerospace control and signal processing computations within a data flow based system. A computational problem, such as a flight control algorithm to process sensor data and provide output data for flight control, is represented in a graph format consisting of graph nodes interconnected by data paths. The graph nodes, as illustrated by nodes N1, N2, and N3 in the figure, represent blocks of computer code to perform

desired computations, and the relative time for each node to complete execution is shown above the node. Repetitive data sets are synchronously sampled from sensors to be consistent with the system Nyquist rate. These data sets are passed to the multi-computer. The ATAMM assigns the nodes of the graph to processors in a predictable manner to time-optimize the steady-state generation of the computational results. Intermixed self-testing ensures that only healthy processors receive assignments, and redundant processing may be performed for critical functions.

With the assistance of contractual personnel from both Lockheed Engineering and Sciences Company

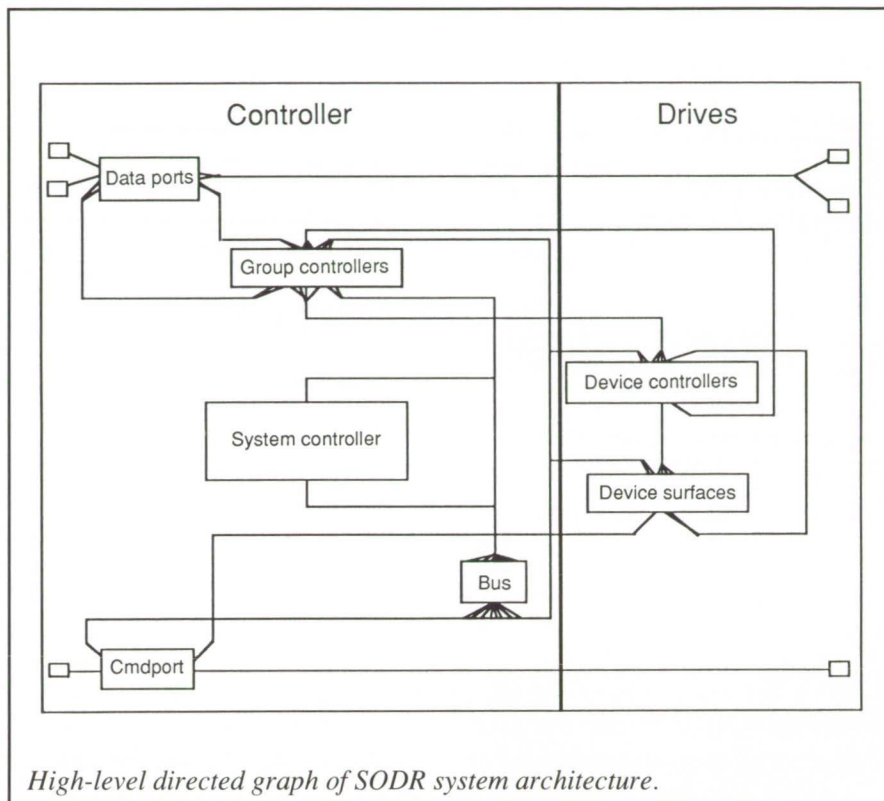


ATAMM-controlled execution of example algorithm graph depicting typical graph play and graceful degradation (three-node graph execution on advanced development model).

and CTA Incorporated, the initial version of ATAMM was implemented on an avionics multiprocessor system. The system was comprised of four identical MIL-STD-1750A processor components that were fabricated in very-high-speed integrated circuit (VHSIC) technology. The ATAMM implementation was tested using the three-node serially connected example graph in the figure. The lower left display in the figure shows the detailed time history of each graph node (including the processor to which it was assigned) as a function of time for data packets one through seven. The actual hardware performance closely paralleled that of the ideal theoretical simulation. The average throughput, or system frequency response, is the reciprocal of the average time between outputs (TBO) of node N3. The measured average TBO of 294.7 time units includes 6 percent overhead compared to the theoretical maximum of 278 time units. Major contributions to operating system overhead in the hardware were wait time associated with interprocessor communications and graph update time.

Continued automatic execution of the graph, or graceful degradation, was also demonstrated as simulated faults were injected and the number of healthy processors decreased from four down to one. Consistent with the theoretical predictions for this graph, throughput changes for the three-node graph were minimal until the number of available processors dropped to one. These multiprocessor tests successfully proved the viability of the ATAMM strategy as a candidate for potential future spaceborne applications. The ATAMM is currently being enhanced to accommodate the simultaneous execution of multiple graphs and statistical variations in the node latency times.

(Paul J. Hayes, 41491)
Flight Systems Directorate



Modeling of Spaceflight Optical Disk Recorder

System modeling and simulation are currently being used in the development of the Spaceflight Optical Disk Recorder (SODR) at Langley Research Center. System modeling involves the concepts of mapping the physical components, functions, and interactions of a system into a computer program. When executed, this program simulates the behavior of the system under study by representing the state changes of the system over time. The SODR is a high-performance, mass data storage system that is based on an expandable, reconfigurable architecture consisting of several rewriteable optical disk drives and an interactive controller. This type of architecture provides versatility and redundancy. The SODR model is implemented with the architecture design and assessment system

(ADAS) software and hardware modeling tool. The SODR model represents all the subsystems of the SODR, as well as the command and data processing environment of the SODR system.

The SODR model consists of several directed graphs. Each directed graph, which is based on a modification of formal Petri nets, is composed of nodes, arcs, and tokens. Nodes represent system components or functions, arcs provide data flow paths, and tokens carry information between nodes. Programs, written with the C programming language, are embedded within the nodes in order to accurately model the details of the system components. Also, each node can contain a lower-level directed graph, thus complex system components can be decomposed into smaller, simpler parts and studied at a greater level of detail. The SODR model provides a cost-effective means to test the

feasibility and performance of various SODR architectures and algorithms, and will be used to determine optimum system specifications and requirements.

(Glenn Hines, 48139)
Electronics Directorate

Solar Dynamic Concentrator Support Truss Enables Replacement of Collector Panels

Construction, growth, and maintenance of an orbiting space station will be accomplished mainly through orbital placement of components. The objective is to structurally modify the baseline solar dynamic concentrator (a component of the solar dynamic power

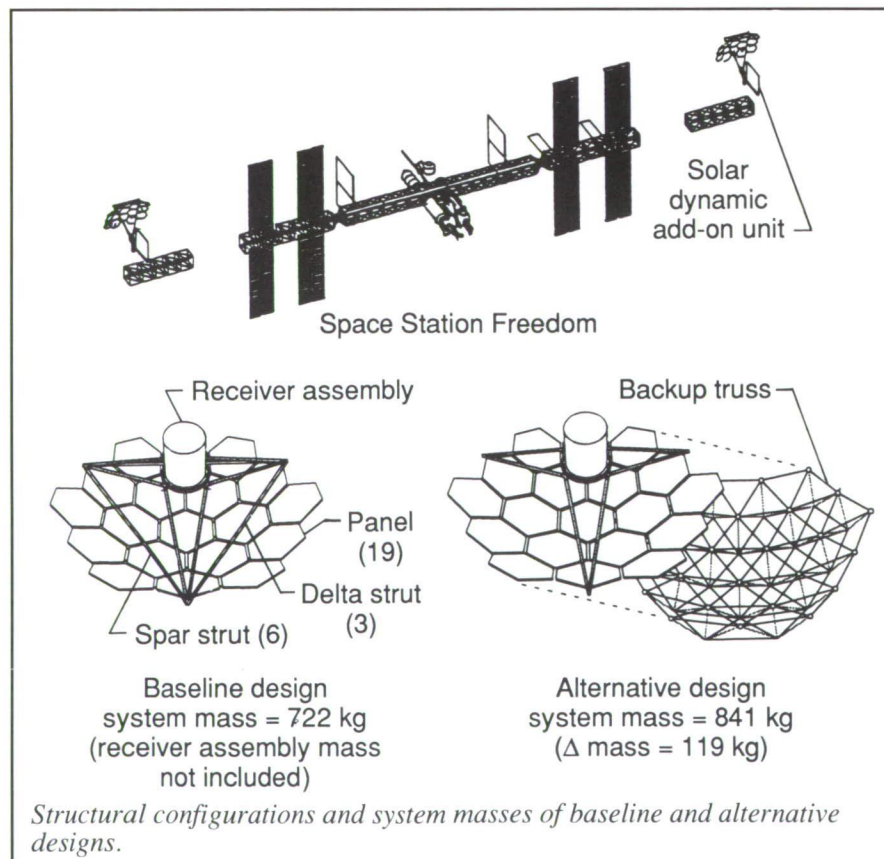
module proposed as the source of growth power for Space Station *Freedom*) to enable orbital replacement of individual collector panels.

Using the technology developed for the design of doubly curved trusses for precision segmented reflectors (PSR's) application in conjunction with the Engineering Analysis Language (EAL) finite-element analysis program, an erectable backup truss structure was designed that can provide the required stiffness and to which the 19 baseline hexagonal collector panels can be independently attached. The geometry of the backup truss was developed such that the node locations on the concave surface of the truss were coincident with the proposed offset parabolic concentrator reflective surface. The truss had a maximum dimension of 18 m, a depth of 3.0 m, and a focal length of 7.8 m. The finite-element

analysis model included the backup truss and the six spar struts that attach the proposed concentrator to the receiver assembly. The mass of the panels was applied discretely as rigid masses at the 27 concave surface nodes.

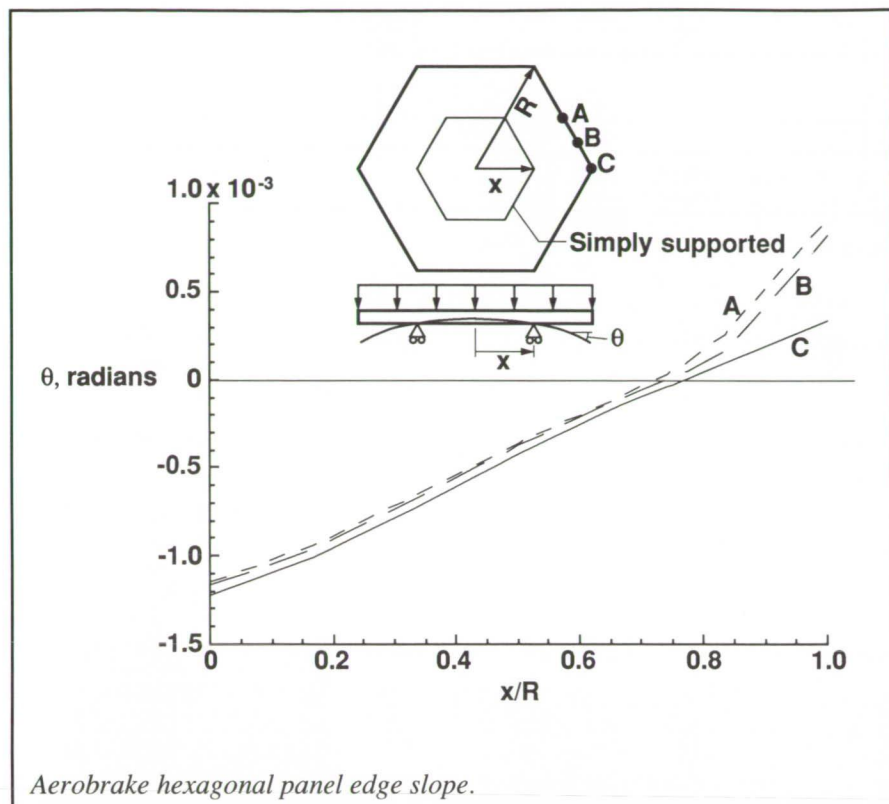
Results indicate that a backup truss of 139 kg could be used with the current baseline design to enable the handling of panels as orbital replacement units (ORU's). Because the backup truss replaces the three delta struts required to stiffen the baseline design, the total added mass is only 120 kg, an increase of 16.6 percent over the baseline concentrator mass (less than 2 percent over the baseline solar dynamic power module mass). The fundamental frequency of the alternative design is 2.01 Hz. The mode shape involves bending of the six spar struts while the truss shows little deformation, thus indicating the potential for further reduction in truss mass.

(Walter L. Heard, Jr., 43123, Harold G. Bush, and Catherine L. Herstrom)
Structures Directorate



Aerobrake Panel Support Concept Results in Zero Slope Along Panel Edge

Aerobrakes for manned Lunar and Mars missions are too large to be launched into Earth orbit fully assembled and thus must be assembled in orbit. Successfully developing concepts for sealing the thermal protection system between adjacent panel edges will be critical if the aerobrake is to be a viable spacecraft component. In one aerobrake concept developed at Langley Research Center, hexagonal heat-shield panels provide



the structural support for the thermal protection system (TPS). The objective of this research was to determine a panel support concept that would result in zero slope along the entire panel edge and thus help maintain panel seal integrity.

A closed-form solution, which gives the out-of-plane deflections and the slopes along a simply supported beam subjected to a uniform pressure loading, was obtained. The slope at the ends of the beam was calculated as the support locations (which were included as a parameter in the beam solution) were varied. The results show that if the two supports are located at distances equal to 0.5 ± 0.289 of the length from one end, the slope at the two ends of the beam will be zero. The results of the beam analysis were used to help define the finite-element mesh for the subsequent hexagonal panel analysis model. A similar support concept for a hexagonal panel (shown

in the figure) places simple supports in a hexagonal ring, resulting in the line of support being equidistant from the panel edge for the entire panel circumference. The radius of the circle that circumscribes the hexagonal supports is denoted by "x," and the radius of the circle that circumscribes the panel is denoted by "R." The hexagonal heat-shield panel features sandwich construction with an aluminum honeycomb core and graphite/epoxy facesheets.

The slopes at three points along the panel edge, because of a uniform applied pressure load, are shown as a function of the support radius in the figure. The results show that locating the panel support at approximately 74 percent of the panel radius results in essentially zero slope along the entire panel outside edge. The support concept developed here, by achieving a zero slope along the entire panel edge, should significantly simplify

the sealing concepts required between adjacent panels.

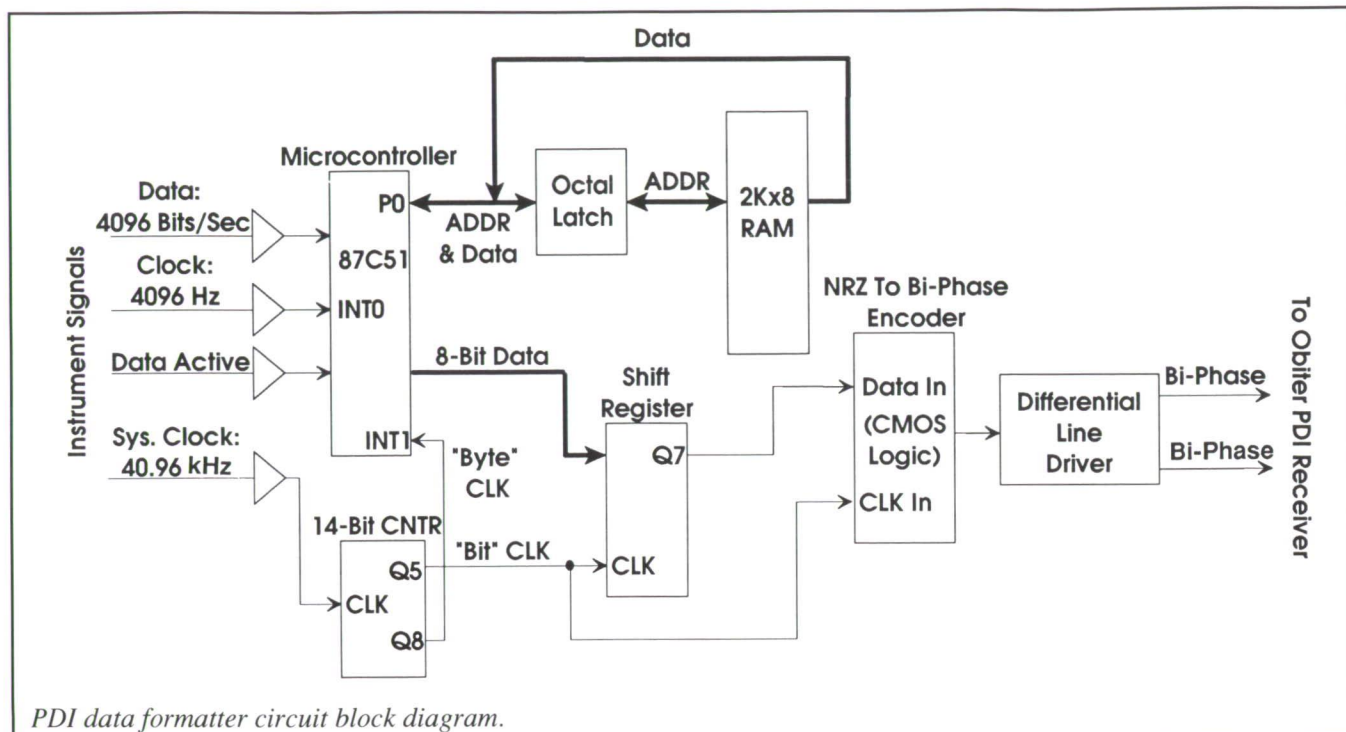
(John T. Dorsey, 43108)
Structures Directorate

Science Data Interface to Space Shuttle Payload Data Interleaver System

Interfacing a scientific instrument on board the Space Shuttle to the orbiter payload data interleaver (PDI) system allows science data to be down linked during flight. A microcontroller-based circuit has been designed for the Measurement of Air Pollution from Satellites (MAPS) experiment to convert instrument science data to a PDI format that meets orbiter electrical interface requirements. This enables quicker turnaround of scientific information with minimal impact on existing hardware.

The PDI data formatter circuit block diagram shows the major components of the circuit. Under interrupt control, the microcontroller periodically acquires a 2-sec "burst" of instrument data and buffers it in random access memory (RAM). The RAM has been initialized to contain an empty template of the PDI format parameters, such as the PDI sync pattern and header information. Incoming data are placed in gaps in this template. Formatted data are produced by sequentially reading the RAM contents, beginning with the first RAM location.

Because the instrument data are available only in bursts and PDI data are required to be continuous, software in the microcontroller causes multiple repeats of the data to be sent to produce a continuous formatted data stream. Instrument-specific signals



are used to ensure synchronization between the PDI formatting circuit and the instrument, with microcontroller software providing out-of-sync detection and correction.

(M. Grant, 43707)

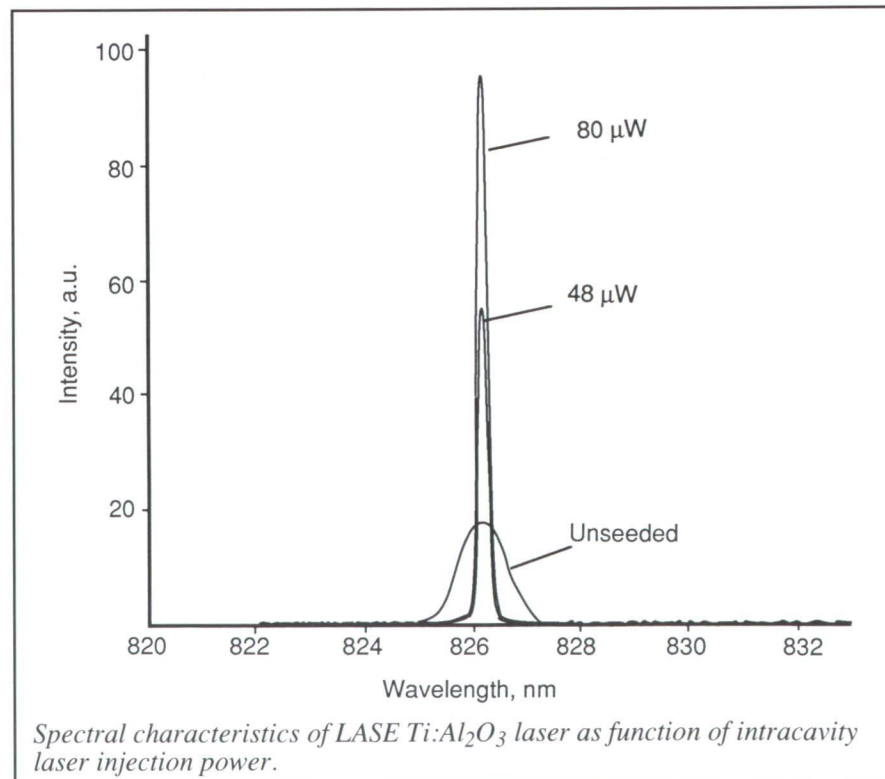
Electronics Directorate

Diode Laser Injection Seeding of LASE Laser

The objective of the LASE instrument is to provide remote sensing of water vapor ($\text{H}_2\text{O}(\text{v})$) distribution from the ER-2 aircraft. For this purpose, the DIAL (differential absorption lidar) technique is used, which requires that the LASE titanium sapphire ($\text{Ti}:\text{Al}_2\text{O}_3$) laser alternately emits energetic (150 mJ) pulses at two wavelengths: one pulse coincident with a $\text{H}_2\text{O}(\text{v})$ absorption line and another pulse off the line. Injection of CW radiation from a 100 mW, single longitudinal

mode, narrow linewidth, semiconductor diode laser into the $\text{Ti}:\text{Al}_2\text{O}_3$ laser cavity provides narrowing of the

titanium sapphire laser pulse bandwidth by more than three orders of magnitude. The figure illustrates the



narrowing of the pulse laser bandwidth as the intracavity seed power is increased. In this figure, the observed line narrowing is limited by the low resolution of the spectrometer. According to measurements made with an etalon, a pulse bandwidth of <0.5 pm was achieved for intracavity seed powers exceeding $80 \mu\text{W}$. This bandwidth is much narrower than an individual $\text{H}_2\text{O}(\text{v})$ absorption linewidth (3 pm to 10 pm) and is thus suitable for LASE DIAL measurements.

Other benefits of a diode laser seed source are its ability to accurately lock the titanium sapphire laser wavelength to the center wavelength of a $\text{H}_2\text{O}(\text{v})$ transition and its ability to rapidly ($<100 \mu\text{sec}$) switch off the absorption line thereby providing the off-wavelength injection at the desired moment. The rapid wavelength switching is attained simply by providing a short

current pulse to the diode laser current. High-accuracy line locking is achieved with ultrahigh-sensitivity FM detection techniques developed at Langley and other laboratories. Locking stability of better than 0.25 pm has been demonstrated while seeding the $\text{Ti}:\text{Al}_2\text{O}_3$ laser.

(L. G. Wang, W. C. Edwards, 41555, G. W. Sachse, J. C. Barnes, and R. V. Hess)

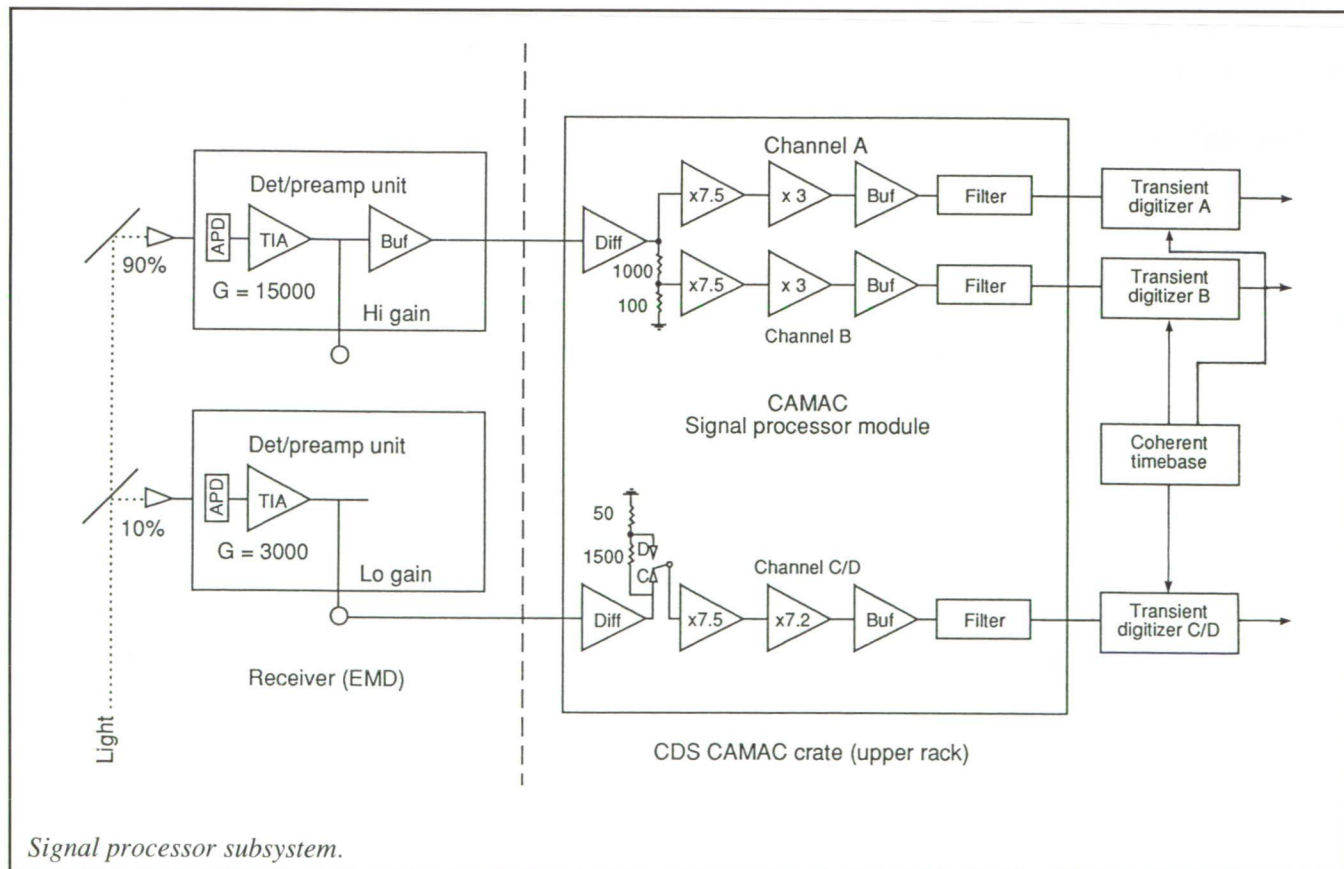
Electronics Directorate

and support electronics for Lidar systems. The Lidar Atmospheric Sensing Experiment (LASE) is one such project under development at Langley Research Center. This instrument will make atmospheric aerosol measurements from an ER-2 aircraft in the mid-1990's. The extremely wide dynamic range and very low noise required in such systems, coupled with the requirement to recover from huge amplifier overload, dictate the need for an overlapping multichannel data acquisition system.

Data Acquisition for Lidar Applications

Increasing sensitivity requirements and the need for very fast recovery from amplifier overload pose challenging problems in the design of detectors

The LASE signal processing subsystem block diagram shows the major components of this system. Signal returns from a titanium sapphire laser are split 9-to-1 and applied to two Avalanche Photo Diode detectors. The output from the high-gain detector is further divided into two overlapping channels to cover the dynamic range



expected from aerosol returns, and it also employs a background subtraction circuit to increase the dynamic range. The output from the low-gain detector is used to measure the high-energy returns expected from clouds and the ground. This channel has a pilot-selectable gain to allow for measurement of ground return from highly reflective surfaces.

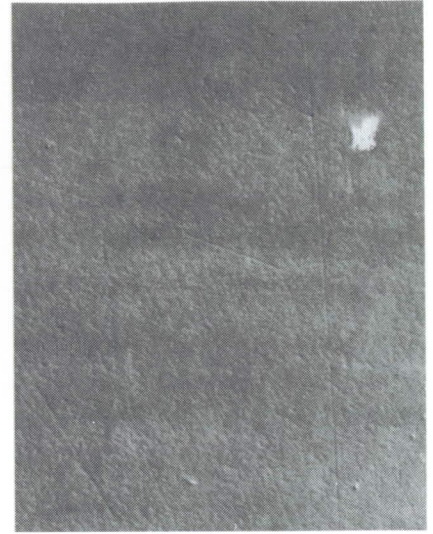
Limiting is employed in each channel of the signal processor module to expedite recovery from overload. Low-pass filters are used to limit noise bandwidth. Three twelve-bit A/D converters are used to digitize return signals prior to formatting and recording. These are synchronized to laser firing by timing and control circuitry (coherent timebase), which also injects a marker into each data stream for on-line and off-line data registration.

(J. Williams, 41888)

Electronics Directorate

Effects of Long-Duration Exposure on UV Optical Components

A set of ultraviolet (UV) transmitting optical windows was flown on the Long-Duration Exposure Facility (LDEF). The vacuum ultraviolet region, 100 nm to 300 nm, was the principal region of interest. Significant surface deterioration occurred on MgF_2 , LiF, and CaF_2 surfaces. The MgF_2 window experienced severe surface degradation on both the surface that was exposed to incident sunlight and the back surface that was in contact with a silicone rubber gasket. Part of the back rough surface layer of the MgF_2 window delaminated and adhered to the silicone gasket. In addition to the surface roughness, small circular areas of translucent



Surface roughness of LiF window resulting from space exposure (LiF flight window, 1000 x (left) and LiF ground control window, 1000 x (right)).

material were deposited and small radial surface scratches are present around the edges of the fluoride windows.

Organic contamination films are present on both surfaces of the optical windows with the heaviest film generally on the back surface. The combination of surface deterioration and organic films resulted in a major to total loss of transmission in the 100-nm to 200-nm spectral region for the fluoride windows. The contamination films, as measured by the 3.4 μm hydrocarbon absorptions, were not as heavy on the Al_2O_3 and SiO_2 windows. The faint brown stain is visually similar on the Al_2O_3 and SiO_2 windows. However, no 3.4 μm hydrocarbon absorptions are present on the SiO_2 window.

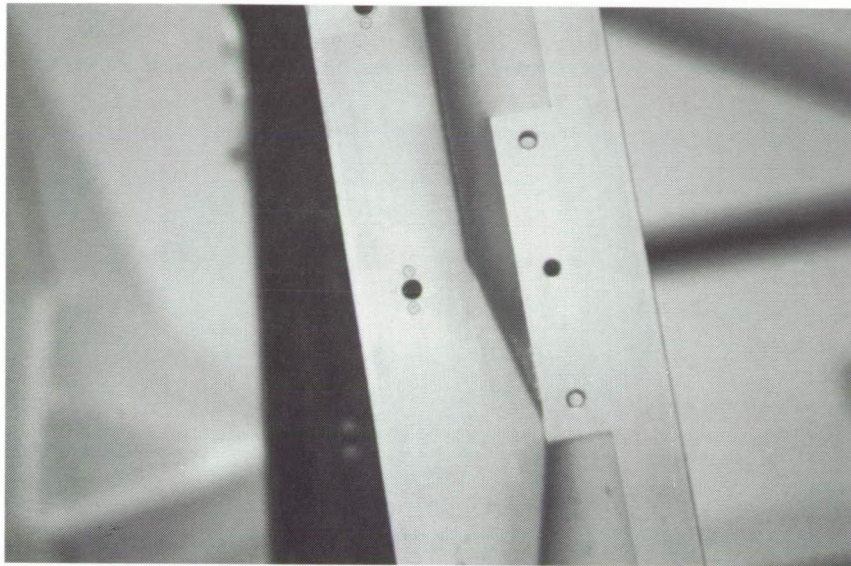
(Gale A. Harvey, 46742)
Space Directorate

Organic Contamination of LDEF

A brown stain of varying thickness was present on most of the exterior surface of the retrieved LDEF. This stain can be easily seen on areas of the deintegrated LDEF which were exposed to sunlight and atomic oxygen. Visual inspections and photographs of the deintegrated LDEF revealed several aspects of the stain. The stain is heavier on the trailing edge than on the leading edge at retrieval. However, the heaviest deposits are on end plate surfaces near vents to the interior. At some of these locations, the organic stain was so heavy it would curl from the rough milled surfaces of the end plates.

The deposits on the end plates were heaviest in the LDEF leading-edge direction, thus indicating that atomic oxygen had severely eroded the stain on the leading-edge longerons and intercostals. The infrared spectra of outgassing residues of thermal control paints used on LDEF are similar to the infrared spectra of the deposits on the

ORIGINAL PAGE
BLACK AND WHITE PHOTOGRAPH



Organic film stain on LDEF intercostal.

end plates. This similarity indicates that much of the strain resulted from bulk (long-term) outgassing of the polyurethane binder of the paints. The presence of silicate in the deposits indicates a subsequent modification by solar ultraviolet and atomic oxygen in addition to the outgassing of thermal control paints used on LDEF.

Organic contamination in several experiment trays differed in $3.4\ \mu\text{m}$ hydrocarbon absorption from the brown stain at the vents from the interior of LDEF. The presence of the brown stain on most exposed surfaces indicates that the return flux of the contaminate molecules was significant on LDEF.

(Gale A. Harvey, 46742)
Space Directorate

Determination of Temperature Anomalies in Space Shuttle Furnace Calibration

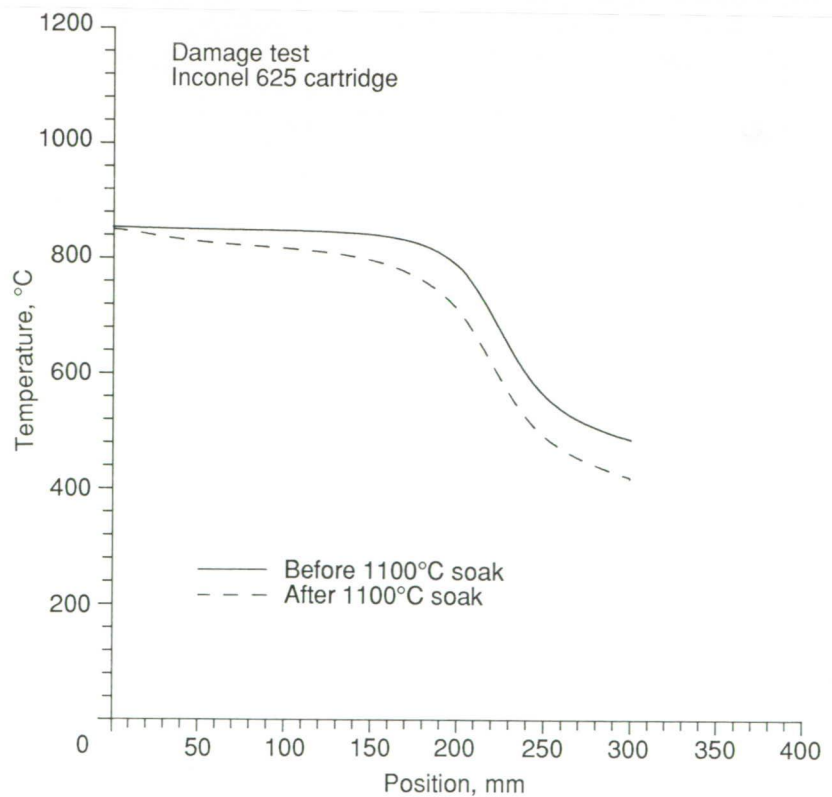
The growth of the alloy compound semiconductor lead tin telluride

(PbSnTe) has been chosen for a microgravity flight experiment in the Advanced Automated Directional

Solidification Furnace (AADSF) on the United States Microgravity Payload (USMP), which is due to be placed aboard the Space Shuttle in 1994. The primary objective of this experiment is to determine the effects of the low-gravity environment on suppressing convective mixing.

Thermal calibration of the AADSF is a vital component of the flight preparation. Calibration with an instrumented sample is necessary to determine the temperature within the ampoule as it traverses through the furnace. These experimental data can then be used as a benchmark for numerical analysis which, in turn, can provide a more detailed thermal description of the isotherms within the sample.

Anomalies were noted in the temperature response when the hot



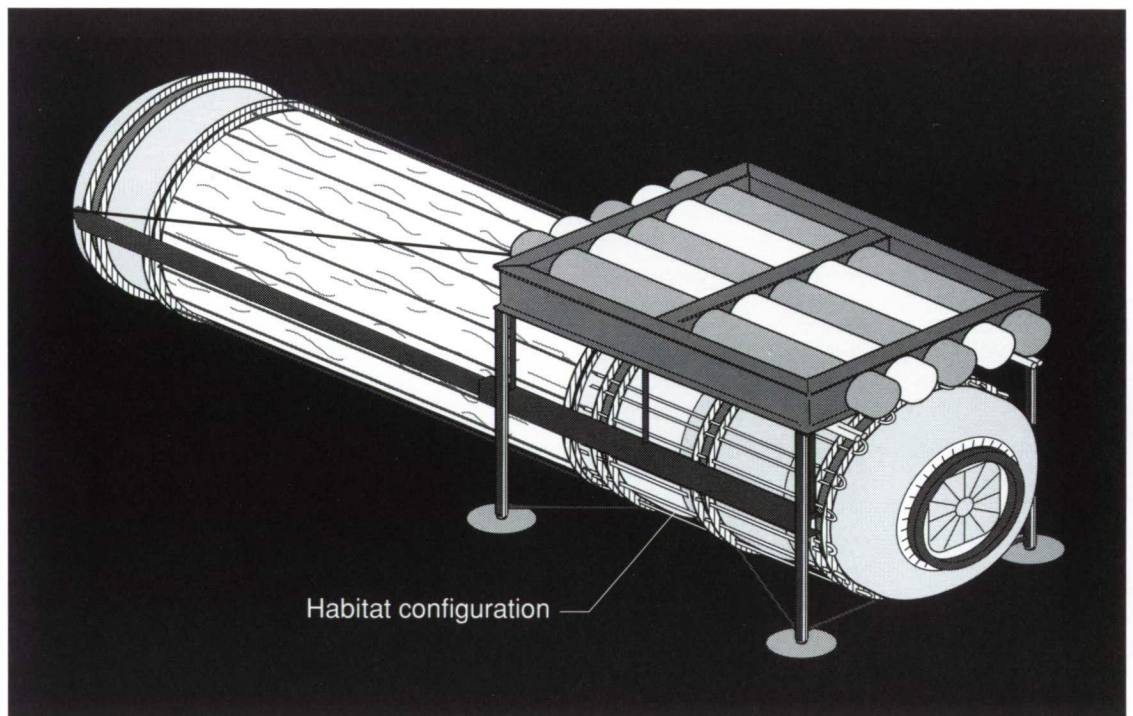
Anomalous thermocouple behavior in AADSF furnace.

zone was increased to 1100°C and the furnace was retested at lower temperatures. The figure shows the results of the lower temperature tests both before and after the calibration sample was taken to 1100°C. Additional tests have shown that Type R (Pt/PtRh) thermocouples, which were protected by a PtRh sheath, were contaminated by the Inconel muffle tube that holds the sample. Type R thermocouples are specified for operation up to 1760°C; hence, the decalibration of impurity transport through the protective sheath was unexpected.

A new calibration sample configuration has been designed which will eliminate these anomalies in the test results.

(Archibald L. Fripp, 41503)
Flight Systems Directorate

■ EXPLORATION

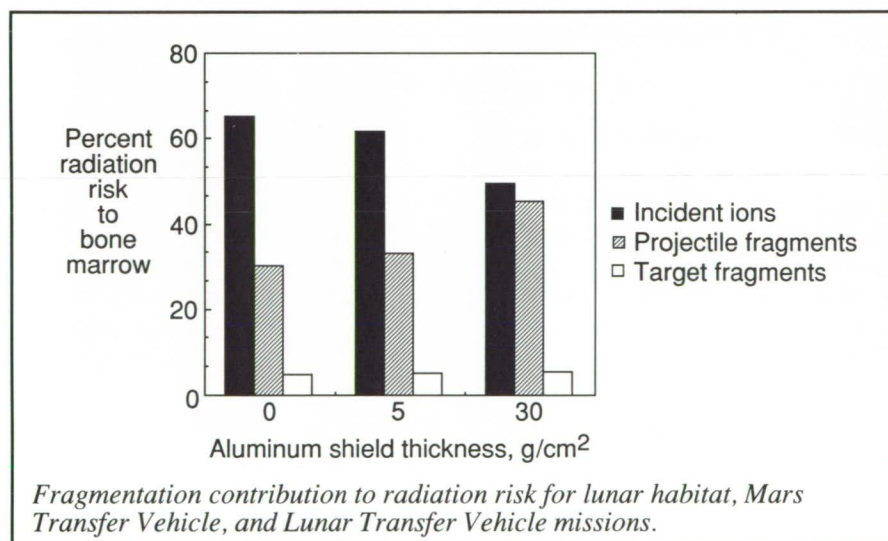


Provide technology for space exploration missions including renewed exploration of the Moon and the establishment of a manned lunar base and piloted missions to explore the planet Mars

Contribution of Galactic Cosmic Ray Ion Fragmentation to Radiation Risk

For several years, a key radiation-exposure issue has been the relative importance of projectile and target fragmentation reactions in producing biological effects from interplanetary galactic cosmic rays. Because the most numerous projectiles are protons, most

This analysis was performed using a realistic solar minimum galactic cosmic ray spectrum as input into the deterministic space radiation transport codes developed at Langley Research Center. The figure shows the calculated exposure to the bone marrow for several (increasing) thicknesses of aluminum shielding. Compared with the target fragmentation contribution, the relative contribution from projectile fragments is 5 to 10 times larger. These



researchers assumed that proton-induced target fragmentation would contribute more to radiation biology than to any other aspect of fragmentation. Our research group disagreed with this assertion and suggested that the largest contribution to astronaut risk would come from high-energy, heavy projectile ions fragmenting against target nuclei and that the target fragmentation in these interactions would be relatively unimportant.

findings are significant because calculations of shielding efficiency and human exposure would be greatly simplified if target fragmentation were the most important nuclear interaction process. Because projectile fragmentation is much more significant, effective shielding of astronauts remains a highly complex issue that demands increased emphasis on high-energy, heavy ion fragmentation.

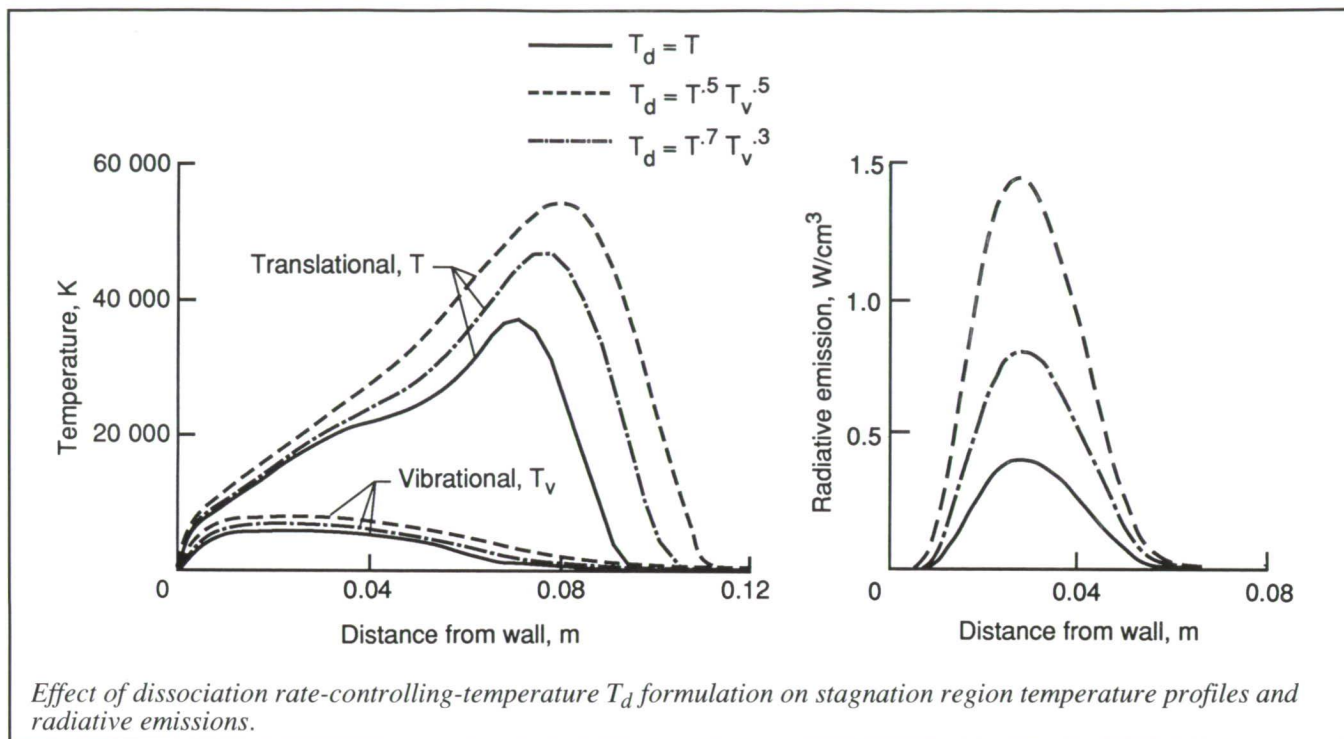
(L. W. Townsend, 41417, J. Wilson, F. A. Cucinotta, and J. L. Shinn)
Space Directorate

Nonequilibrium Radiative Heating and Influence of Energy Exchange Models

Aerobraking as a means of efficiently decelerating space vehicles into the atmosphere of the Earth is currently being proposed for numerous NASA missions. For many of these missions, thermochemical nonequilibrium effects in the shock layer and radiative heating to the heat shield of the vehicle will be significant. Accurate nonequilibrium radiative heating predictions are necessary to define vehicle thermal protection requirements.

Analyzing the aerothermal environment about such a vehicle usually requires separate computational tools for predicting the flow field and the radiation. Each of these tools contains constitutive relations that model the relevant physical processes; however, significant uncertainties exist in the formulation of these models. Obviously, the choice of model formulation in the radiation tool affects the radiative heating prediction. Moreover, the formulations for the energy exchange processes in the flow field tool may also have a profound effect on the radiative heating prediction.

Stagnation point radiative heating predictions for a representative aerobraking flight condition have been generated using flow field solutions obtained with parametric variations of the several energy exchange models. The radiation predictions are from the Langley Optimized Radiative Nonequilibrium code (LORAN) and



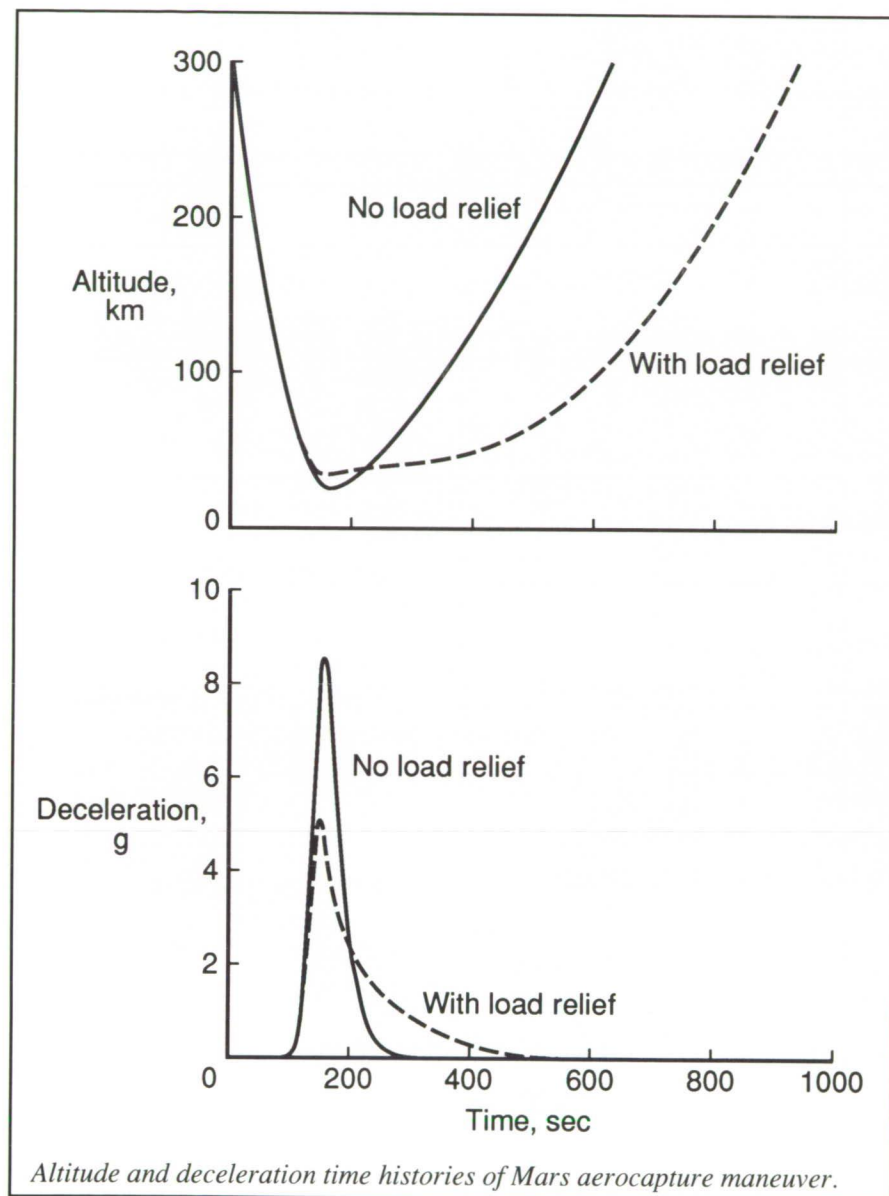
the flow field solutions are from the Langley Aerothermodynamic Upwind Relaxation Algorithm (LAURA). Different formulations of the rate-controlling temperature for dissociation T_d , the vibrational-translational energy exchange cross section, and the energy exchange accompanying dissociation were examined. While perturbations in these models only affect to a small degree the flow field solution, the effect on the radiative heating predictions can be as large as a factor of 4. (L. C. Hartung, R. A. Mitcheltree, and P. A. Gnoffo, 44371) Space Directorate

Adaptive Guidance Algorithm for Manned Mars Aerobraking Vehicles

For a manned Mars aerobraking vehicle, mission success hinges on a successful aerodynamic deceleration

by the vehicle through the Martian atmosphere. This atmospheric passage is designed to provide a transition for the vehicle from an interplanetary trajectory to a captured Mars orbit with the proper characteristics to provide for a subsequent landing and Earth return. A robust, dependable guidance algorithm increases the probability that the vehicle will not be lost or the mission compromised. The guidance algorithm must correct for off-nominal conditions, including errors in interplanetary navigation, mispredicted atmospheric conditions, and mispredicted aerodynamics. In addition, this guidance algorithm must be capable of controlling in-flight constraints, such as maximum deceleration or aerothermodynamic limit. This problem is further complicated by the fact that the lowest cost (minimum mass) vehicles are those with low lift-to-drag ratios L/D . These low L/D vehicles inherently provide low-performance margins that further complicate the guidance algorithm design.

To successfully capture over the range of possible entry conditions, a more robust guidance algorithm than has been used to date (i.e., during the Apollo and Space Shuttle Programs) is required. To meet this requirement, an adaptive guidance algorithm using a predictor-corrector technique has been developed which produces a successful Mars atmospheric passage over a wide range of entry conditions for vehicles with L/D 's ranging between 0.3 and 0.5. A three-degree-of-freedom simulation employing this algorithm has been shown to accurately guide the vehicle through the atmosphere, while providing load relief during a wide range of off-nominal conditions. These off-nominal conditions were composed of variations of atmospheric density profiles (both vertical and horizontal), errors in flight path angle at atmospheric interface, and mispredicted trim angle of attack. In addition, this algorithm was further tasked with the in-flight constraint of a 5g deceleration limit (1g is the acceleration of a body at rest on the surface of the Earth). The



Design Considerations Enabling Low Lift-to-Drag Ratio Aerobrakes for Manned Mars Missions

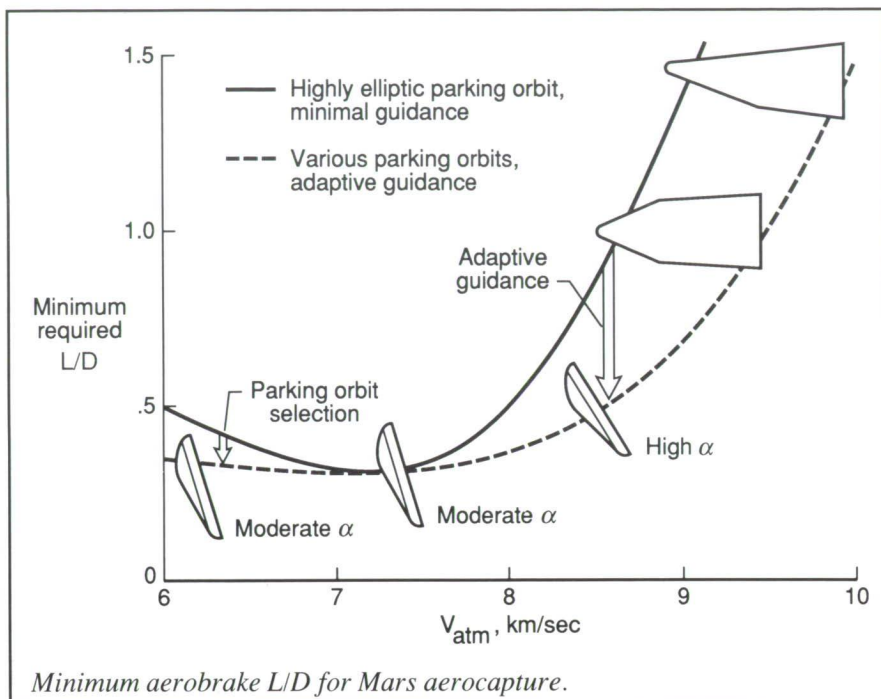
Previous Mars vehicle design studies have demonstrated that the minimum initial mass in low Earth orbit (IMLEO) corresponds to vehicles with low lift-to-drag L/D ratios. However, these low L/D vehicles also have inherently lower mission flexibility (reduced performance margins) than high L/D vehicles. Therefore, a study was conducted to determine the enabling design criteria that would make low L/D vehicles viable.

The study demonstrated that the required Mars aerobrake L/D is a function of Mars atmospheric interface velocity (which typically varies from 6 km/sec to 10 km/sec), prescribed deceleration limit, parking orbit selection, and atmospheric guidance algorithm design. The solid line in the figure shows the minimum L/D , and some corresponding candidate shapes, required for successful aerocapture at Mars as a function of atmospheric interface velocity for a typical set of mission constraints. The lowest L/D vehicle that provides for mission success is 0.3. However, this L/D vehicle is only suitable for an extremely limited velocity range (7.2 km/sec to 7.3 km/sec). This entry velocity range limits the number of potential launch opportunities to only two in 15 years when the Mars entry velocity is left unconstrained during the interplanetary trajectory design and the emphasis is placed solely on identifying minimum mass transfers. By tailoring the parking orbit selection to the entry conditions, as well as using an adaptive guidance algorithm (e.g., a predictor-corrector methodology), the acceptable velocity corridor widens (dashed line) to 6.0 km/sec through 7.4 km/sec. Still, a reduced set of launch opportunities

figure illustrates the load-relief capability of the algorithm, as compared to an open-loop algorithm. The lower deceleration is achieved by rolling the vehicle to stay in the atmosphere longer after peak deceleration is reached. This changes the character of the deceleration history from a peak-type phenomenon to one that is spread out over a longer time. The algorithm has also demonstrated the capability to manage multiple off-nominal effects including load-relief, density waves, and mispredicted aerodynamics.

Because this guidance algorithm has been successful for Mars atmospheric capture, it has been adapted for the Earth return mission also. Two types of Earth return strategies were considered: an aerobraking maneuver into a space station rendezvous orbit and a direct entry with a parachute splashdown.

**(Richard W. Powell, 45506, and Robert D. Braun)
Space Directorate**



results without constraining the Mars entry velocity during the interplanetary mission design. However, when an atmospheric entry velocity constraint is incorporated into the interplanetary trajectory development, the number of opportunities increases to 14 within the same 15 years, with less than a 10-percent increase over the minimum IMLEO.

This study has demonstrated that the successful coupling of the mission design (parking orbit selection and interplanetary trajectory) with an adaptive guidance algorithm is sufficient to demonstrate the feasibility of low L/D aerobrake vehicle concepts (L/D of 0.3). The choice of a low L/D concept provides for design commonality with current lunar mission plans and the Aeroassist Flight Experiment Program.

(Robert D. Braun, 44507, Scott A. Striepe, and Richard W. Powell)
Space Directorate

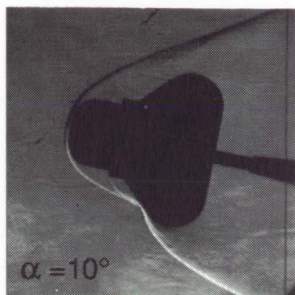
Experimental Aerothermodynamic Characteristics of AFE Engine/Ballute Concept

The project team for the Aeroassist Flight Experiment (AFE) is currently exploring methods to minimize the impact of the Solid Rocket Motor (SRM). Jettison of the SRM is necessary to reduce the weight of the AFE vehicle during the aeropass maneuver to avoid exceeding the limits of the thermal protection system. The initial method of ensuring safe disposal of the jettisoned SRM, through an overly steep atmospheric entry, requires excessive amounts of fuel to return the AFE to the proper trajectory for the aeropass. Alternate methods of disposing of the spent SRM casing which reduce the fuel requirements are being examined. One such proposal incorporates the use of an inflatable drag device, referred to as a ballute, attached to the back of the SRM to provide the necessary entry-trajectory control to ensure splashdown in the ocean.

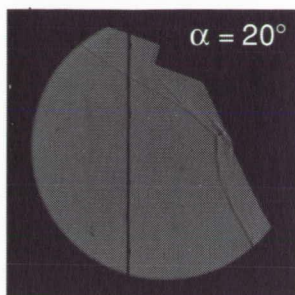
A cursory experimental investigation of the aerothermodynamic characteristics was conducted to examine the viability of the SRM/ballute concept. Shock shapes, surface streamlines, and global temperature distributions were obtained over a range of Mach number, Reynolds number, density ratio, and incidence angle. Tests were conducted in the Hypersonic Facilities Complex, primarily the Langley Hypersonic CF_4 Tunnel and the 31-Inch Mach 10 Tunnel. Shock shapes, interactions, and impingements were determined with the schlieren and shadowgraph techniques; surface streamline patterns were acquired with the oil-flow technique to assist in defining regions of flow separation and reattachment and of shock impingement. Global temperature mappings were obtained using the relative intensity, two-color thermographic phosphor technique as demonstrated in the figure.

The jettisoned SRM will have a center-of-gravity offset that will probably induce a nonzero trim angle; therefore, the primary parameter of interest was the angle of attack α , which was varied from 0° to 40° in increments of 10° . Analysis revealed that the axisymmetric model at zero incidence angle did not experience a shock impingement on the ballute section and that the resulting global surface temperature remained below the SRM nose stagnation temperature. However, at any appreciable incidence angle, impingement of the bow shock on the ballute windward surface resulted in a highly three-dimensional flow field and significantly augmented the local heating. In the worst case, at $\alpha \approx 20^\circ$, shock/shock interaction induced what appeared to be a supersonic jet, which impinged directly on the ballute and resulted in local temperatures on the ballute surface far exceeding the nose stagnation temperature. The aerothermodynamic data

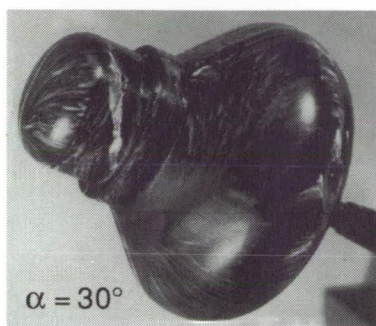
ORIGINAL PAGE
COLOR PHOTOGRAPH



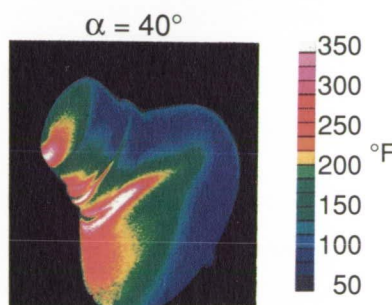
Schlieren

Mach 6 in Hypersonic CF₄ Tunnel

Shadowgraph

Mach 6 in Hypersonic CF₄ Tunnel

Oil-flow

Mach 6 in Hypersonic CF₄ TunnelThermographic phosphor
Mach 10 in air

Examples of ballute test techniques.

L-91-3353

near zero for this configuration to avoid extremely high heating on the inflatable ballute section.

(Scott A. Berry, 45231)

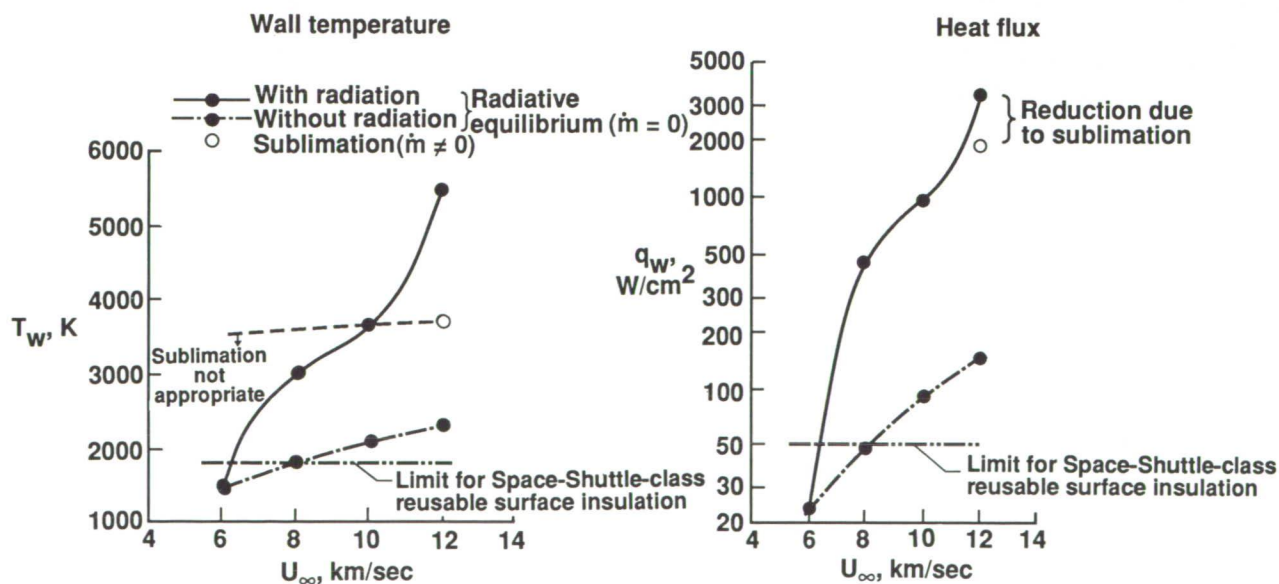
Space Directorate

Viscous Shock-Layer Analysis for Mars Aerobraking Entry

A parametric study of stagnation point heat transfer to vehicles performing high-energy entry and aerobraking in the Martian atmosphere has been performed. This study utilized detailed flow field solutions obtained using the viscous shock-layer equations with coupled radiation and heat shield ablation. The dominant issues addressed were the magnitudes of radiative and convective heating and determination of the flight conditions at which sublimation ablation of the vehicle heat shield would occur. The parameters studied and their ranges of variability were altitude (30 km to 50 km), velocity (6 km/sec to 12 km/sec), and body nose radius

generated by this fast-paced study represent the initial experimental investigation into the viability of a drag

enhancement device for this application. These results clearly show the importance of maintaining a trim angle



Stagnation point heating environment for Martian entry of 23-m nose-radius body at 36-km altitude.

(1 m, 2.3 m, and 23 m). Equilibrium chemistry was assumed in the flow field calculations; comparisons with fully nonequilibrium solutions have confirmed the adequacy of this assumption.

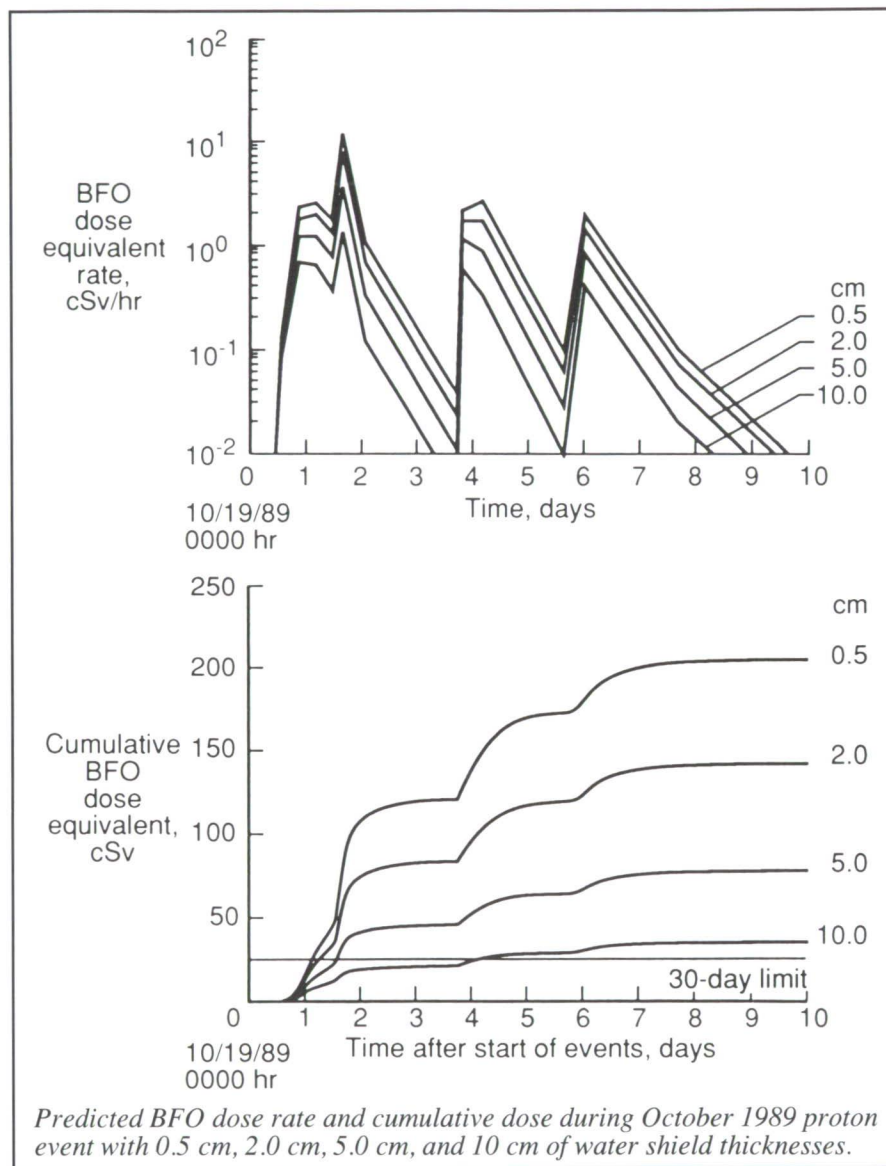
Stagnation point temperatures and corresponding heat fluxes are shown for a nose-radius body of 23 m at an altitude of 36 km over the velocity range considered. The heat-transfer rates were determined assuming radiative equilibrium wall temperature, without ablation ($\dot{m} = 0$). For the 12-km/sec case, the heat flux was also determined for the sublimation wall temperature with coupled ablation injection. As points of reference, the temperature and heating rate limits for Space-Shuttle-class reusable surface insulation (RSI) materials are also indicated.

The results indicate that, for most conditions analyzed, radiation is the dominant component of wall heat transfer. Total heat-transfer rates are greater than the limit for Space-Shuttle-class thermal protection materials, except for velocities of approximately 6 km/sec. Fully coupled carbon-phenolic sublimation ablation occurs only for velocities greater than approximately 10 km/sec; therefore, assumption of sublimation ablation at lower velocities may not be appropriate.

(R. N. Gupta, J. N. Moss, K. Sutton, and K. P. Lee, 44385)
Space Directorate

Exploration Mission Radiation Exposure: Analysis of October 1989 Solar Proton Event

The solar flare that occurred from October 19 to 27, 1989, is the largest observed flare since August 1972, and it was of comparable magnitude. The energetic proton spectral flux data,



monitored in geosynchronous orbit and processed at the National Oceanic and Atmospheric Administration (NOAA)—Boulder Space Environment Laboratory, provides the opportunity for a detailed analysis of exposure rates and cumulative doses that may be incurred by astronauts on exploratory class missions. The utilization of the Langley Research Center nucleon transport codes with the observed proton fluxes as input predicts the time variations of incurred dose throughout the course of the event for selected shield thicknesses.

The figure illustrates some of the results of the analysis in which dose-equivalent rates for a 5-cm tissue layer (sometimes referred to as the BFO or blood-forming organ dose) are given as a function of time. The corresponding cumulative doses for various shield amounts are also shown. The maximum allowed 30-day BFO exposure guideline of 25 cSv (or 25 rem) is exceeded even with a 10-cm water shield as approximately 4 days after flare eruption. As the dose-equivalent rate curves show, dose rates vary by several orders of magnitude during the

course of the event. This indicates that periods of time may exist during the flare when the crew may safely emerge from a sheltered area to perform essential duties. For example, 5-hr to 10-hr periods exist between flare pulses for which the dose rate is approximately 0.1 rem/hr. While an obvious conclusion is that rather heavily shielded storm shelters will be required (at least 13 g/cm² for this flare alone) for long-duration interplanetary missions, the results also indicate the advantages of having active dosimetric instrumentation aboard the spacecraft as indicators of relatively low dose rate intervals during a large flare event. (Lisa C. Simonsen, 44432, and John E. Nealy)
Space Directorate

Aerobrake/SSF Minimum Accommodation Study—Phase II

The aerobrake/Space Station *Freedom* (SSF) minimum accommodation study is a multidisciplinary, three-phase investigation of aerobrake on-orbit assembly and servicing at SSF.

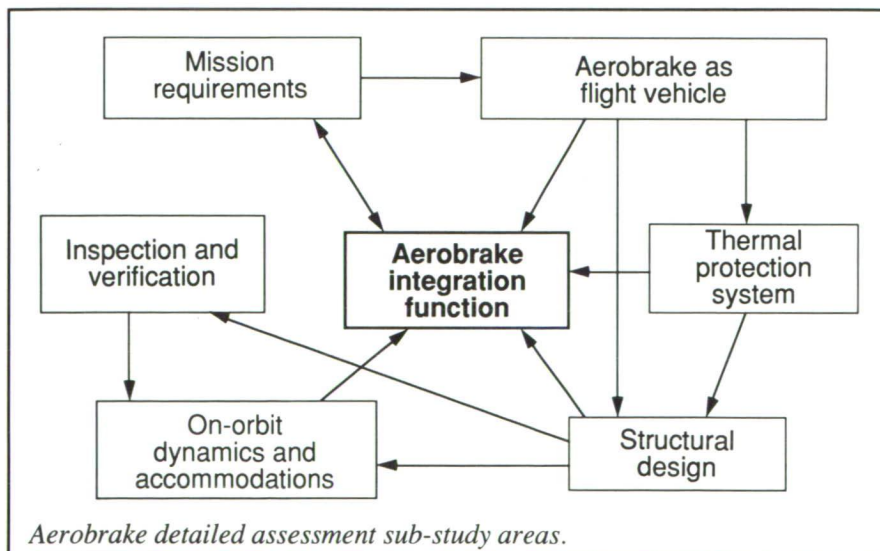
Specifically, the primary objective of the study is to assess what minimum SSF capabilities and facilities are needed to assemble and refurbish a lunar return aerobrake. Secondary objectives are to determine the types of aerobrake design that are useful for extravehicular activity and robotics and to assess the SSF operations and logistics necessary to support assembly and refurbishment of aerobrakes.

The current activities are part two of a three-phase study. The first phase was to consider the feasibility of on-orbit assembly of a lunar return aerobrake at SSF. This phase was successfully completed in October 1990. The second phase (current phase) is a detailed assessment of the lunar return aerobrake and its assembly and refurbishment at SSF. The next, or third phase, will be to consider the design of potential flight experiments that would demonstrate aerobrake assembly and inspection skills and to add to the experience data base for on-orbit assembly of large space structures.

The current study is composed of six sub-study areas. The first of these areas is the Aerobrake as a Flight Vehicle, which provides the initial

conceptual design of the aerobrake considering the aerothermal issues, as well as integration of the aerobrake with the lunar transfer vehicle. The next sub-study area, Thermal Protection Systems (TPS), is tasked with evaluating TPS options as well as application technique development. The third area is the Structural Design sub-study that will be developing detailed structural designs and assembly procedures, as well as conducting structural and thermal analysis of the final design. The fourth sub-study, Inspection and Verification, is tasked with providing vehicle and TPS inspection requirements and techniques. The fifth sub-study area is On-Orbit Dynamics and Accommodations, which is to provide aerobrake assembly sequences, time lines, and hardware requirements, as well as SSF operations and logistics requirements. The final area, Aerobrake Integration Function, is an overall activity that ensures integration and coordination between the sub-study areas. This function is also responsible for the overall management of the study.

The results of this study will better define what the issues are regarding on-orbit assembly of aerobrakes and other large space structures. The study will also provide a starting point for SSF extended capability planning with respect to a reusable lunar transportation system. In addition, the study will provide insight into the development of a reusable, lunar return aerobrake, including a better estimate of aerobrake mass fraction and allocation of mass for the various aerobrake systems. (Stephen Katzberg, 48207, and Dave Haynes)
Space Directorate



Aerobrake Concept Selection and Integration for Lunar Transportation System

As part of an ongoing activity, an aerobrake conceptual design has been selected for a reusable lunar transportation system (LTS) currently being studied at NASA George C. Marshall Space Flight Center. The LTS is based on an aerobraked, single propulsion/avionics (single P/A) stage that also houses a crew module. The objective

for lunar return aerocapture is 0.15) and because some aerobrake components (including the Thermal Protection System) may be common. The aerobrake size was chosen to provide protection for the 25-ft-diameter single P/A and its six RL-10 engines from wake impingement during the aerocapture maneuver. After consideration of the angle of attack required to trim the vehicle (11° at an L/D of 0.15) and the resulting offset of the center of gravity of the single P/A, the aerobrake was sized at 50 ft in diameter with a

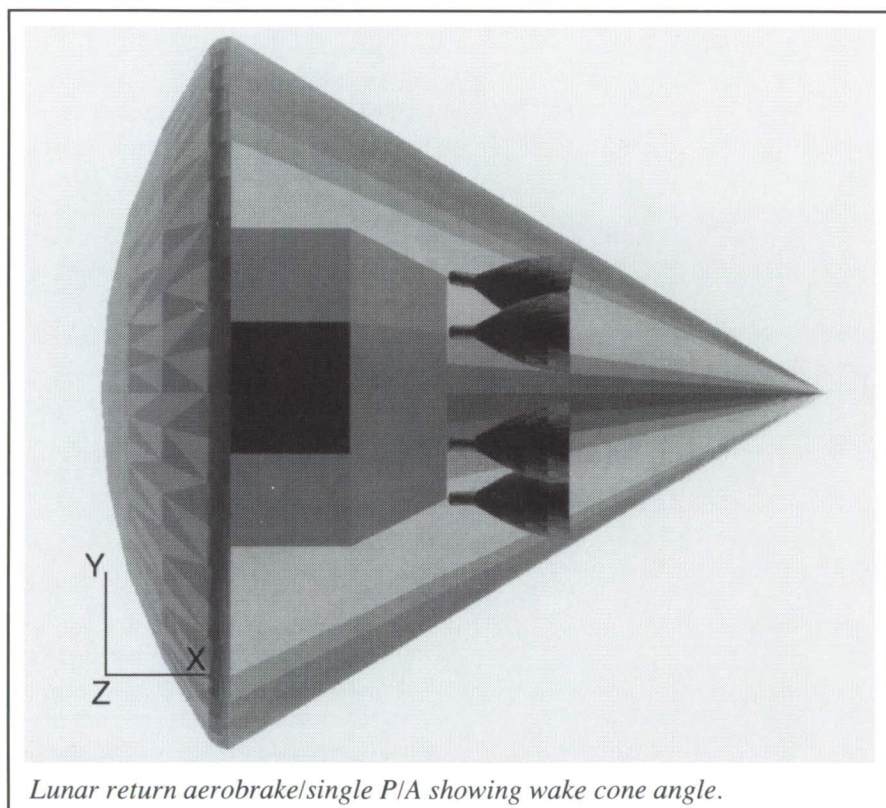
System, the structural design, and techniques for on-orbit assembly of the aerobrake on Space Station *Freedom*.

(Dave Haynes, 48214, and Joe Rehder)
Space Directorate

Manned Lunar Habitat Concepts

The design of initial lunar bases will be based on a compromise between the desired capabilities of the base and the economics of its development and implantation. To achieve this compromise, the design will be simple, make use of existing technologies, require the least amount of lunar surface preparation, and minimize crew activity. Three concepts for an initial habitat capable of supporting a crew of four for 28 to 30 days have been studied. Two concepts are based on using Space Station *Freedom* structural elements modified for use in a lunar-gravity environment. The third concept is based on an earlier technology base of expandable modules.

The expandable concept offers significant advantages in launch mass and packaged volume reductions. Designing a transport spacecraft lander appears feasible, which, once landed, can serve as a habitat and a standoff for supporting a regolith environmental shield. The figure shows the expandable (Concept 3) habitat and the spacecraft lander configuration details after expansion on the lunar surface. A permanent lunar base habitat supporting a crew of 12 for an indefinite period can be created by using multiple initial habitats. No compelling need exists to establish an entirely different structure with a

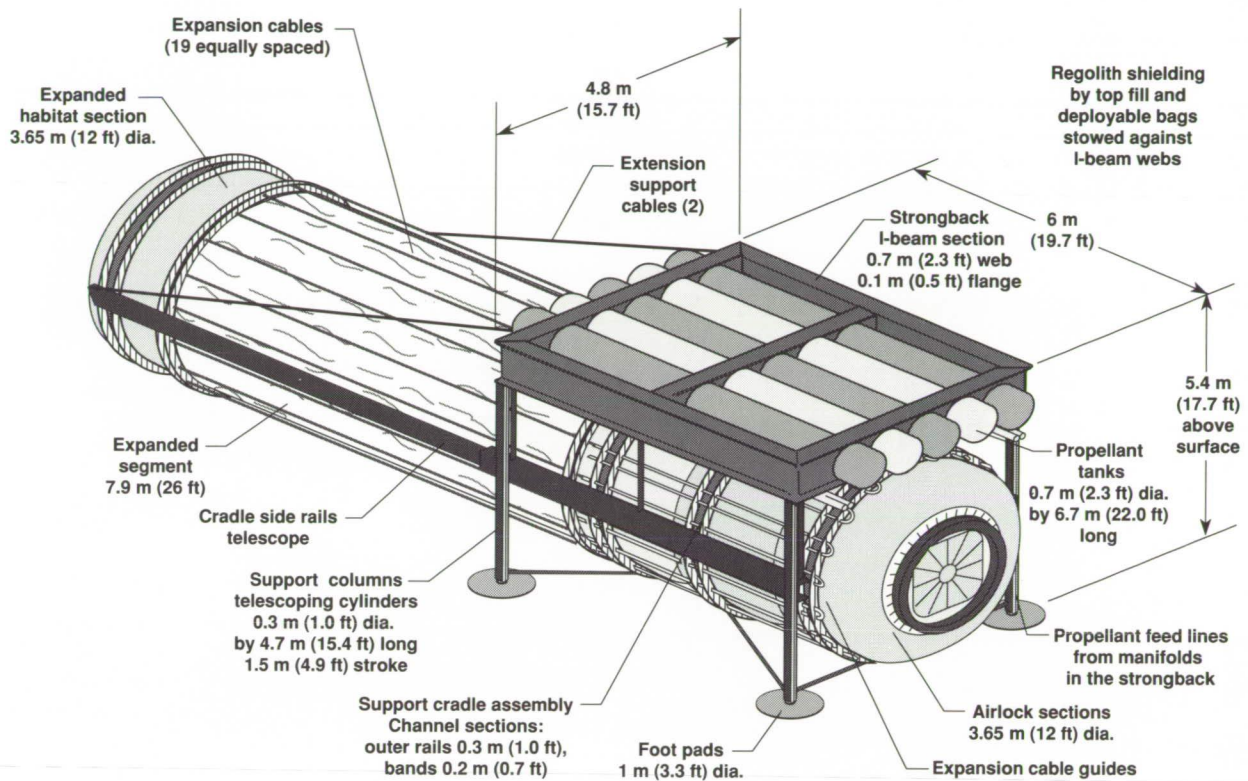


of this part of the overall study activity is to select a credible aerobrake design that can withstand the rigors of lunar return aerocapture, protect the single P/A from loads, heating, and wake impingement, and is reusable.

A spheroid-shaped aerobrake was selected for the concept because it has adequate aerodynamic performance (the nominal lift to draft (L/D) required

radius of curvature of 45 ft. In addition, the aerobrake has a radius skirt of 2 ft on the periphery for additional wake clearance.

This aerobrake/single P/A concept will be used in ongoing activities to assess on-orbit assembly, checkout, and basing questions. The concept will also be used to further detail the requirements of the Thermal Protection



Concept 3 habitat configuration details after expansion on lunar surface.

larger volume and with an increased
implantation complexity.

(Warren D. Hypes, 45751, Robert L.
Wright, and Marston J. Gould)
Space Directorate

■ GLOBAL CHANGE



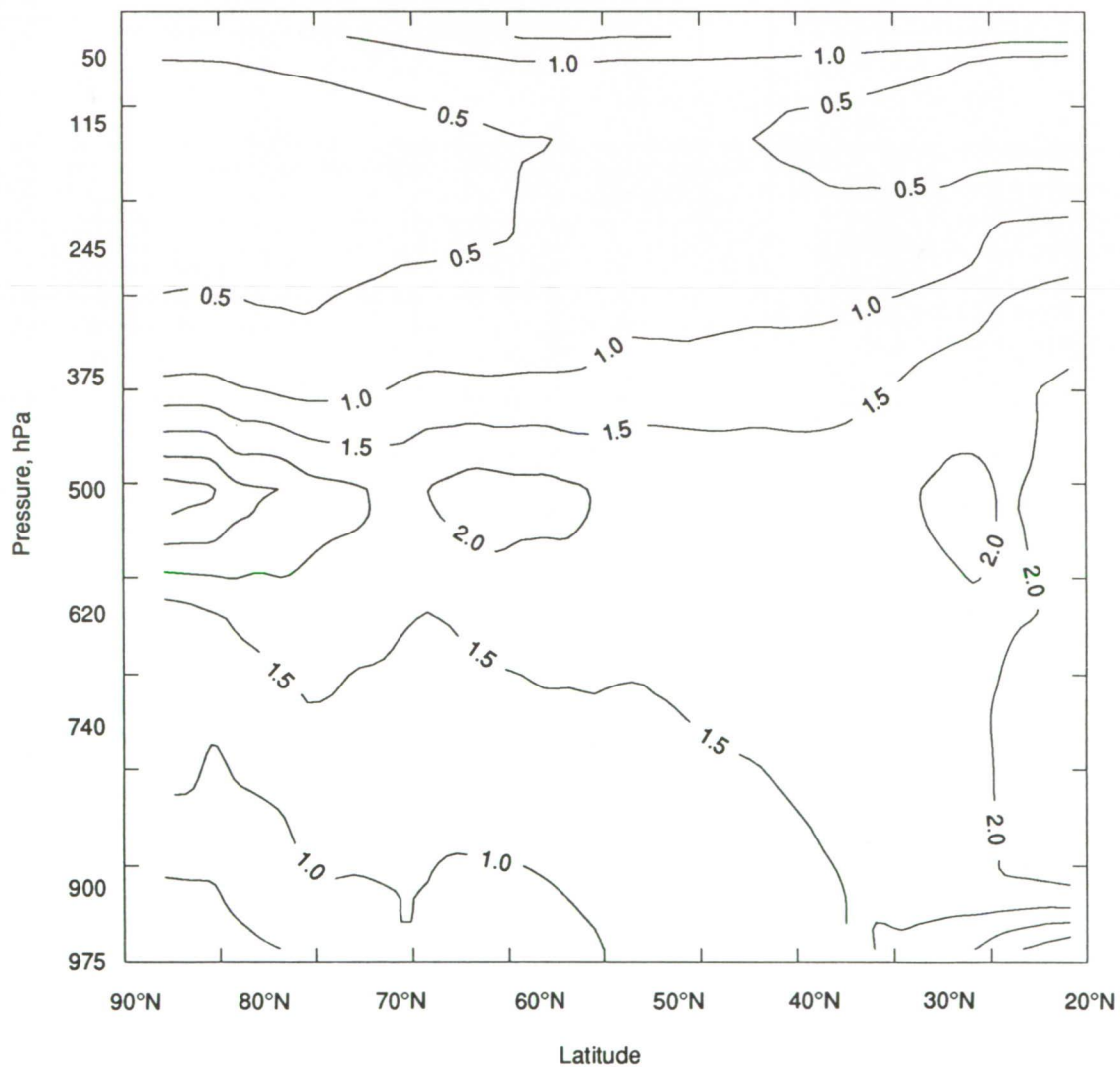
*Establish the scientific basis for
national and international
policymaking relating to natural
and human-induced changes to
the global Earth system*

Radiation Budget of Atmosphere in Thermal Infrared Wavelengths

The radiation budget of the atmosphere in thermal infrared wavelengths

is a major determinant of the surface temperature, the general circulation, and the hydrological cycle. Changes in the vertical profile of the thermal infrared fluxes by increases in the concentration of greenhouse gases constitute the basic physical forcing

of global warming. The vertical profile of thermal infrared fluxes can be computed as a function of temperature, trace gas concentration, and cloud properties. Most of the error in a computed vertical flux profile of the present atmosphere is generated by



Atmospheric thermal infrared flux divergence (expressed as cooling rate in degrees per day) for January 1986.

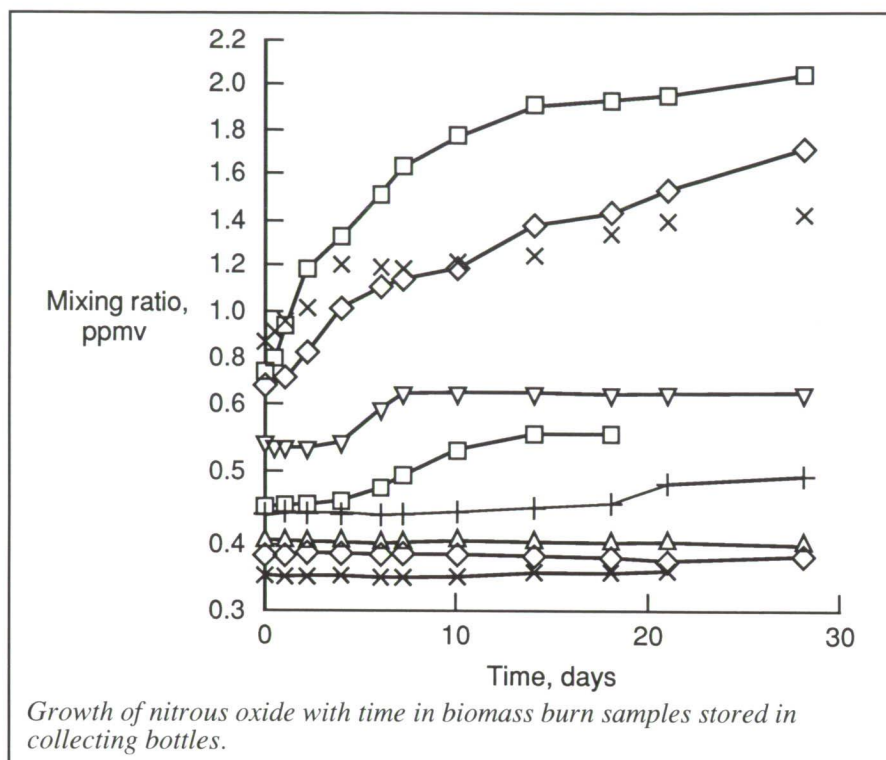
uncertainties in the cloudiness. Here, the vertical profile of thermal infrared fluxes has been computed with a radiative transfer code using newly available cloud retrievals from the International Satellite Cloud Climatology Project (ISCCP). The ISCCP uses radiometric data from both geostationary and Sun-synchronous operational meteorological satellites.

In the figure, which shows data collected in the Northern Hemisphere for January 1986, the vertical profile of flux divergence in thermal infrared wavelengths is expressed as an atmospheric cooling rate (K/day). The atmosphere, which is warmed by the condensation of water aloft and by sensible heating from the surface below, is generally cooled in thermal infrared wavelengths. Clouds generate a cooling rate maximum of 2 K/day at 500 hPa, approximately 5 km above the surface. A data base of such profiles is now being used in studies of radiation and general circulation interaction. Preliminary intercomparisons of the computed fluxes with Earth Radiation Budget Experiment top-of-the-atmosphere observations are favorable.

(Thomas P. Charlock and G. Louis Smith, 45687)
Space Directorate

Biomass Burning and Production of Nitrous Oxide

Nitrous oxide is an important constituent of the atmosphere which is increasing with time. Nitrous oxide is responsible for approximately 65 percent of the global chemical destruction of stratospheric ozone. In addition, nitrous oxide is a greenhouse gas whose decreasing concentration will lead to global warming. Microbial metabolic processes of nitrification and



denitrification are believed to be the major global sources of nitrous oxide, with important production contributions coming from biomass burning. However, Langley Research Center measurements of biomass burning emissions suggest the presence of a chemical artifact that leads to the growth of nitrous oxide in collecting bottles (see the figure). A similar artifact was detected in samples of fossil fuel emissions stored in collecting bottles.

To quantify the actual production of nitrous oxide in the burning of biomass, Langley researchers obtained the first real-time, in situ measurements of nitrous oxide during a boreal forest fire in Ontario, Canada, in July 1990. These measurements indicate that only minute concentrations of nitrous oxide are produced during biomass combustion and that the previous high levels reported most probably resulted from growth of nitrous oxide in the collecting bottle. These results suggest that a significant global source of nitrous

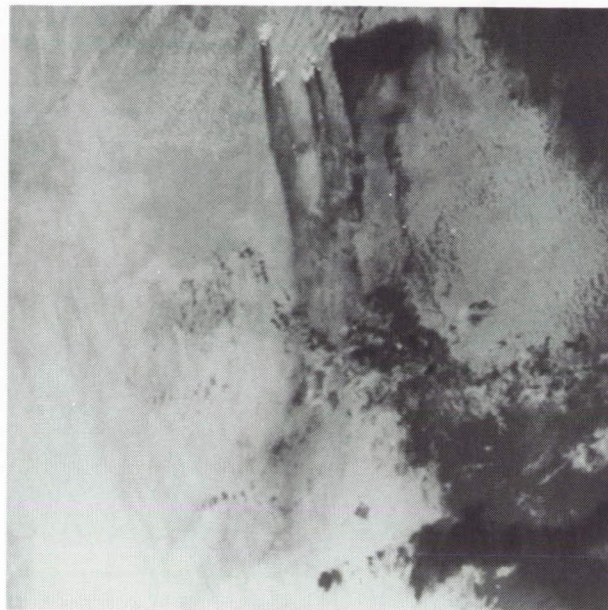
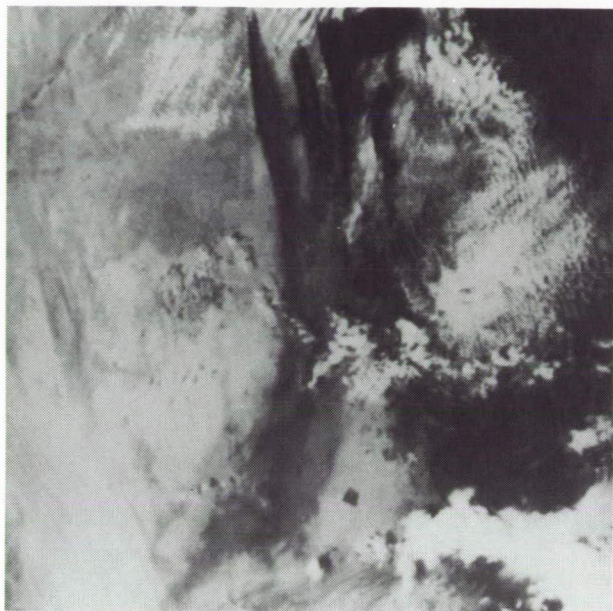
oxide has yet to be identified and/or that a known source or sources may have been significantly underestimated. A paper on this research was the cover story in *Nature* magazine (February 21, 1991).

(Wesley R. Cofer III, 45835, Joel S. Levine, and Edward L. Winstead)
Space Directorate

Gaseous and Particulate Emissions From Kuwaiti Oil Fires

The World Meteorological Organization (1991) report on the Kuwaiti oil fires begins "The World is facing a unique, man-caused environmental pollution on an order never before experienced. The 500 or more burning oil wells in the Kuwaiti oil fields ... represent an unprecedented threat to the environment..." To assist in the international assessment of the Kuwaiti

ORIGINAL PAGE
BLACK AND WHITE PHOTOGRAPH



Satellite image of Kuwaiti oil fire smoke plume on left (NOAA-11 AVHRR Channel 1: $0.58\ \mu\text{m}$ to $0.68\ \mu\text{m}$) and the actual fires as white dots on right (NOAA-11 AVHRR Channel 3: $3.55\ \mu\text{m}$ to $3.93\ \mu\text{m}$) for February 21, 1991.

oil fire pollution, Langley researchers have concentrated on two areas: estimates of the carbon dioxide, carbon monoxide, and carbon particulates produced by the burning oil, and satellite imagery of the fires and their smoke plumes. Six million barrels of petroleum are estimated to be burning each day in Kuwait; this figure corresponds to 920 000 tons of petroleum per day. Langley calculations indicate that the burning of this quantity of petroleum produces, on a daily basis, approximately 2.6 million tons of carbon dioxide (CO_2), 184 000 tons of carbon monoxide (CO), and 24 000 tons of carbon particulates. These numbers correspond to approximately 3 percent of the global annual emissions of CO_2 and CO and about 0.5 percent of the global annual emissions of carbon particulates. The estimates suggest that the Kuwaiti oil fires will not significantly impact the global budgets of these three atmospheric carbon species. The real concern appears to be the nature and magnitude of emissions of other trace carbon and nitrogen, hydrogen, and sulfur com-

pounds and their local and regional environmental impacts. Near-source measurements of the emissions of these trace gases, which have not been obtained to date, are critically needed.

Satellite imagery has proved to be a very powerful tool to study the spatial and temporal distribution of the fires and their smoke plumes. In this analysis, researchers have utilized measurements obtained with the five-channel Advanced Very High Resolution Radiometer (AVHRR) aboard the NOAA-11 meteorological satellite. Satellite images obtained on February 21, 1991, show the distribution of the smoke plumes (AVHRR Channel 1: $0.58\ \mu\text{m}$ to $0.68\ \mu\text{m}$) and the location of the fires themselves as white dots (AVHRR Channel 3: $3.55\ \mu\text{m}$ to $3.93\ \mu\text{m}$). The techniques to estimate the gaseous and particulate emissions from the Kuwaiti oil fires were originally developed at Langley to study global biomass burning.

(Joel S. Levine, 45692, Donald R. Cahoon, Jr., and Wesley R. Cofer III)
Space Directorate

Cloud-Pumping Theory and Global Simulation of Pollution

Cumulus clouds transport pollutants upward from the boundary layer of the Earth and release them at various heights in the troposphere. This process, which is called cloud pumping, is illustrated in the first figure. The transport process is much faster than atmospheric eddy diffusion, which operates in the absence of such clouds. Because most trace chemical species have longer lifetimes at higher altitudes, a small amount of cloud pumping can have a large effect on the vertical distribution of pollutants and the subsequent atmospheric chemistry.

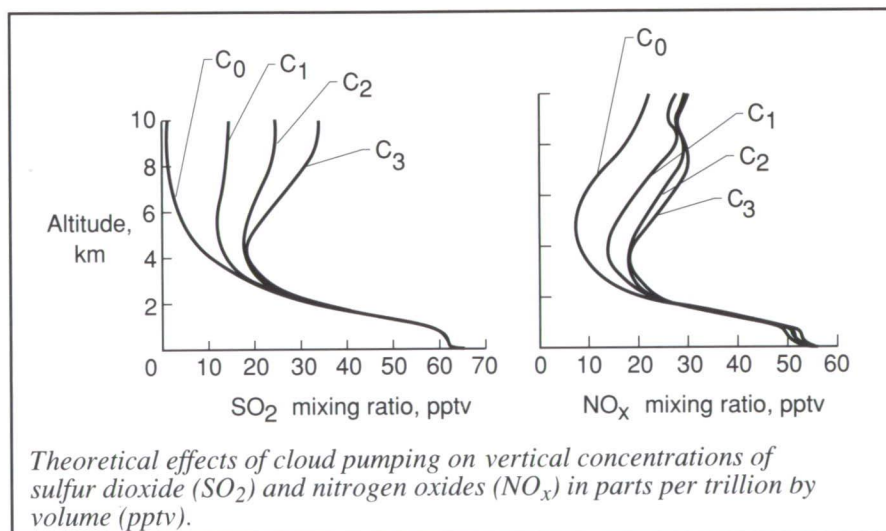
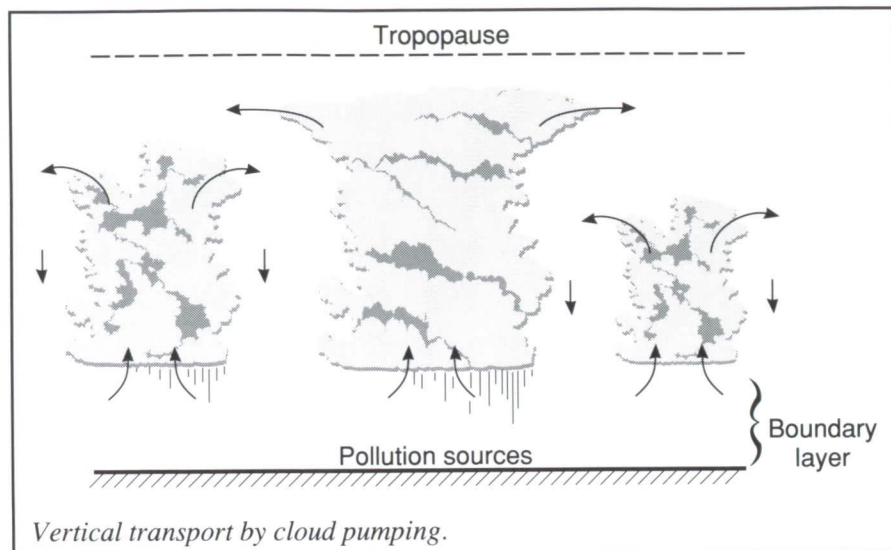
To include the effects of cloud pumping in a one-dimensional model, researchers derived and added transition probability terms to the eddy diffusive transport equation for trace species. The theoretical basis is that for every air parcel in the boundary layer, a probability per second (determined

Long-Term Monitoring of Clouds by Lidar

Clouds are recognized as having a major influence on the global radiation budget, and their effects currently constitute the largest uncertainty in models of global warming. A small depolarization lidar system, consisting of a 140-mJ Nd:YAG laser operating at 532 nm and a receiver with an 8-in. aperture, has been developed at Langley Research Center for long-term monitoring of cloud heights and optical properties. This system has been operated several times per week since 1989, normally at times coincident with overpasses of the Advanced Very High Resolution Radiometer instruments on the NOAA-10 and NOAA-11 satellites so that the lidar data base can be used as ground truth for satellite cloud retrieval methods.

The lidar data are routinely analyzed to determine cloud base and top heights and the profile through the cloud of depolarization ratio, which is an indicator of scattering particle type. For example, backscatter from molecules or aerosols in the atmosphere produces little, if any, depolarization. Backscatter from clouds, however, can result in significant levels of depolarization. In dense water clouds, the depolarization is because of multiple scattering, while in cirrus clouds, which have much lower particle concentrations, the depolarization is because of the irregular shapes of the ice crystals composing the clouds. Since depolarization is, on the average, higher than that from multiple scattering, the degree of depolarization can be used to discriminate ice clouds from water clouds.

As an example of the statistics being compiled by this instrument, the figure displays frequency-of-occurrence histograms of cloud base



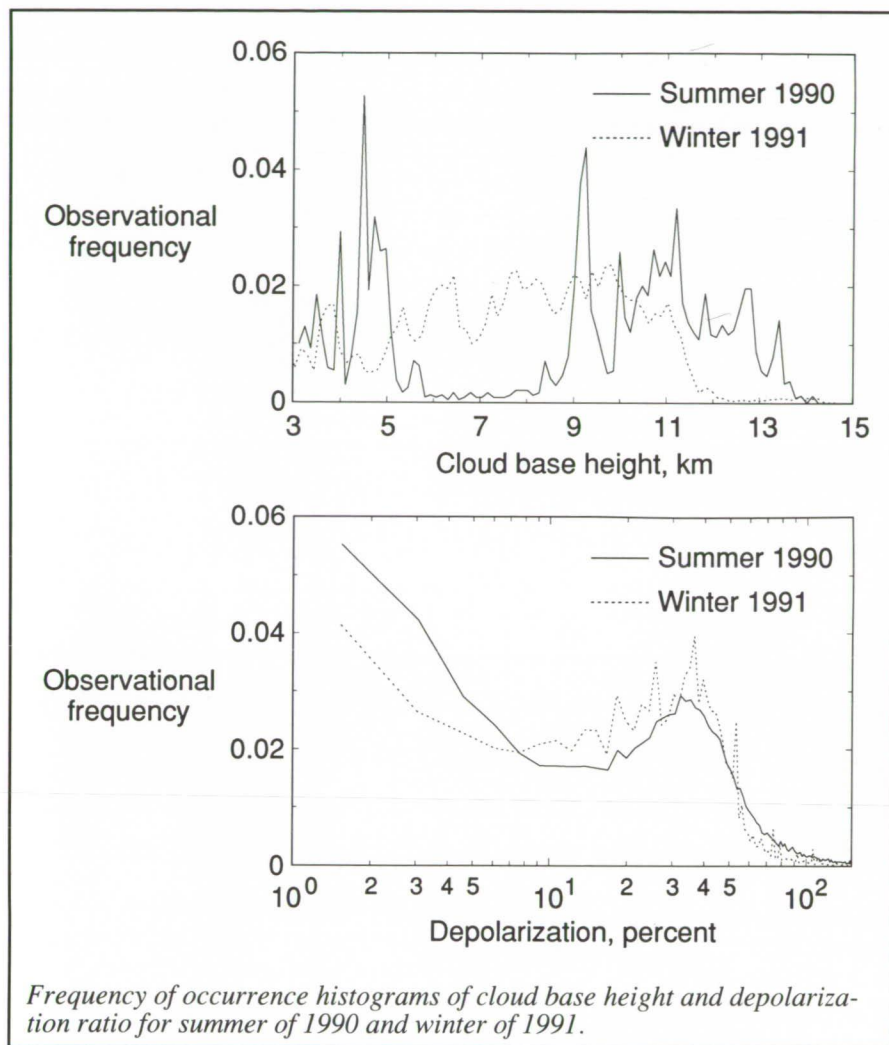
from measurements) exists that the parcel will be cloud-pumped to a higher layer. The resulting theory is mathematically complete and computationally very efficient. The model included 81 species undergoing 225 photochemical reactions, and the results are generally supported by available data.

The theoretical effects of cloud pumping on the vertical profiles of sulfur dioxide (SO_2) and nitrogen oxides (NO_x , a combination of NO and NO_2), which are all precursors of acid rain, are shown in the second figure. The curves labeled C_0 represent pure

eddy diffusion with no cloud pumping. The curves labeled C_1 , C_2 , and C_3 represent increasing amounts of cloud pumping observed in the atmosphere.

The National Center for Atmospheric Research (NCAR) has selected the Langley cloud-pumping theory for inclusion in its three-dimensional tropospheric photochemical model. This model will be used to simulate pollution and tropospheric chemistry on a global scale.

(Robert C. Costen, 41413, Geoffrey M. Tennille, and Joel S. Levine)
Space Directorate



height and depolarization ratio measured within clouds for two 3-month periods, the summer of 1990 and the winter of 1991. Data acquired below 3 km were not analyzed; thus, statistics for low-altitude stratus and cumulus clouds are not included in the figure. The distributions of both cloud base height and depolarization are seen to have seasonal dependencies. Many more cloud bases are found above 12 km in summer than in winter because of the greater height of the tropopause during summer. Cloud bases tend to be found either below 5 km or above 9 km during the summer, while cloud bases are more evenly distributed during winter. The

figure shows statistically significant differences between winter and summer in the distributions of depolarization ratio. These differences can be attributed to seasonal variations in cloud type and morphology. For example, water clouds are more prevalent in summer than winter because of higher atmospheric temperatures, higher humidity, and more intense convection during summer. The higher frequency of depolarization ratios that are less than 10 percent during summer is because of the greater prevalence of water clouds. (David Winker, 46747)

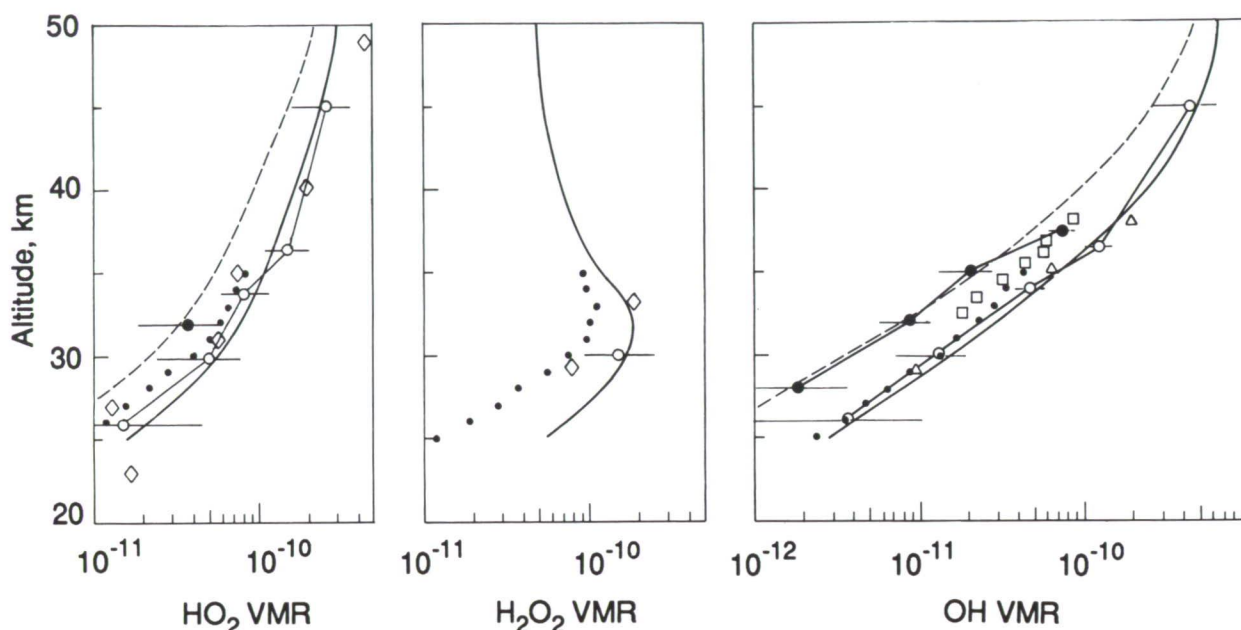
Space Directorate

Spectroscopic Measurement of HO₂, H₂O₂, and OH in Stratosphere

The presence of the HO_x (OH, HO₂, H, and H₂O₂) family of gases in the stratosphere has been recognized to be an important factor affecting ozone production and loss rates both directly and indirectly, through reactions with gases in the O_x, ClO_x, and NO_x families.

Far-infrared emission spectra (90 cm⁻¹ to 180 cm⁻¹) have been obtained with a high-resolution Fourier transform spectrometer on a balloon-borne platform floating at approximately 38 km. The experiment was launched from the National Scientific Balloon Facility, Palestine, Texas, on June 20, 1983 (Carli et al., 1984). From these emission spectra, three important HO_x components (OH, HO₂, and H₂O₂) have been detected simultaneously, and concentrations of these species have been obtained for the stratosphere. The retrieved profiles of HO₂, H₂O₂, and OH have uncertainties in the range from 20 to 50 percent and are compared in the figure with other experimental results and also with theoretically predicted values for similar conditions of latitude and solar zenith angle (i.e., for afternoon, local time between 13:00 and 17:00; for sunset, local time between 17:00 and 19:30). The retrieved values agree well with other individually measured concentrations.

The symbols in the figure are for HO₂, o (this work for afternoon data), • (this work for sunset data), ◇ (Traub et al., 1990), • (Stimpfle et al., 1990); for H₂O₂, o (this work), ◇ (Chance and Traub, 1987), and • (Wennberg et al., 1990, inferred steady-state values using measured distributions of OH and HO₂ by Stimpfle et al., 1990); and for OH, o (this work for afternoon data), • (this



Comparisons of reported distributions of HO_2 , H_2O_2 , and OH for similar conditions (for afternoon if not indicated otherwise).

work for sunset data), Δ (Carli and Park, 1988), \square (Heaps and McGee, 1985), and \bullet (Stimpfle et al., 1990). Theoretical predictions by Natarajan (private communication, 1991) are shown as - for afternoon and -- for sunset. This work has been a collaboration with B. Carli of IROE-CNR, Italy. References include Carli et al.: *Int. J. IR and Mm Waves*, vol. 4, 475-488, 1984; Carli, B. and J. H. Park: *J. Geophys. Res.*, vol. 93, 3851-3865, 1988; Chance, K. V. and W. A. Traub: *J. Geophys. Res.*, vol. 92, 3061-3066, 1987; Heaps, W. S. and T. J. McGee: *J. Geophys. Res.*, vol. 90, 7913-7922, 1985; Stimpfle et al.: *Geophys. Res. Lett.*, vol. 17, 1905-1908, 1990; Traub et al.: *Science*, vol. 247, 446-449, 1990; and Wennberg et al.: *Geophys. Res. Lett.*, vol. 17, 1909-1912, 1990.

This experiment is the first time that three constituent concentrations

have been determined from a single experiment.

(Jae H. Park, 45811)

Space Directorate

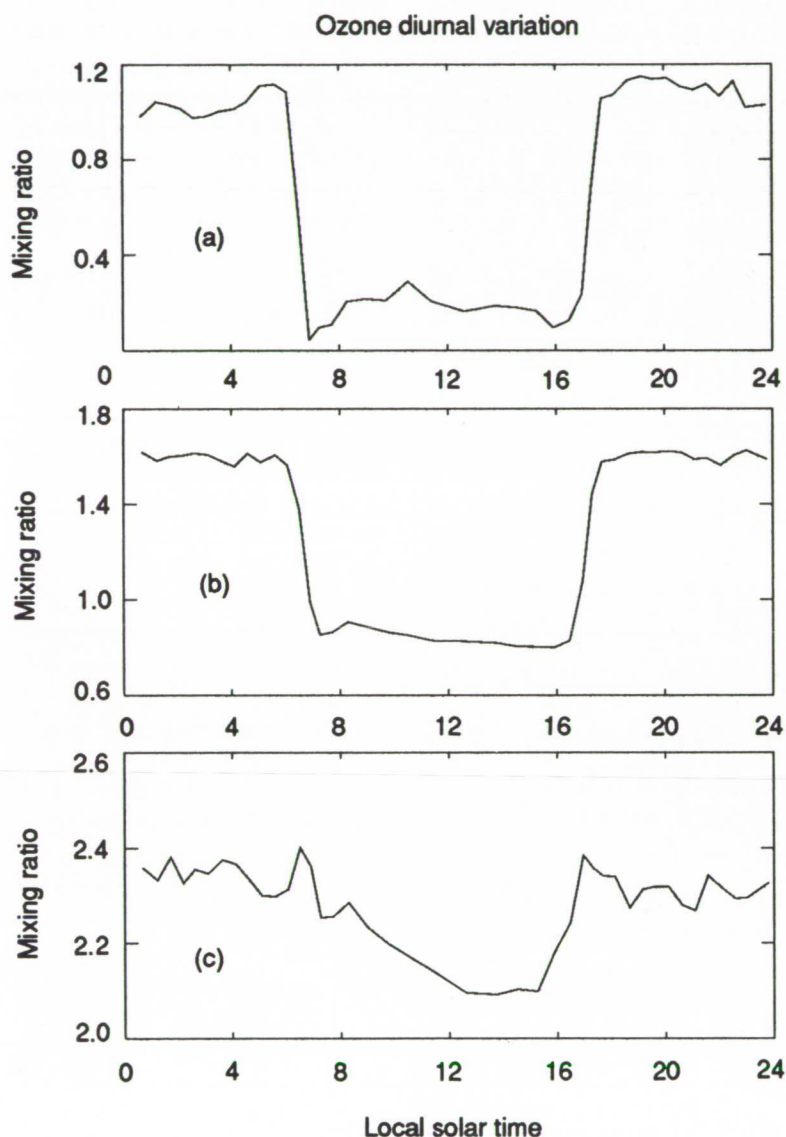
Diurnal Variation of Ozone in Middle Atmosphere

In the upper stratosphere and mesosphere, the ozone concentration undergoes a substantial diurnal cycle, the magnitude and details of which are dependent on the rates of various chemical and photolytic reactions, as well as the concentrations of O , H_2O , and other molecules. Thus, observations of the diurnal variation may provide important constraints on chemical models of the upper atmosphere. For technical reasons, however,

only a few such observations have been made previously, and those are of relatively low quality.

A microwave spectrometer has been monitoring ozone in the stratosphere and mesosphere at the Table Mountain Facility of the Jet Propulsion Laboratory (JPL) since July 1989. This instrument is a part of the Network for Detection of Stratospheric Change (NDSC), which is presently under development.

The microwave technique is the only ground-based means of obtaining ozone profiles around-the-clock. Profiles are retrieved every 20 min from 20 km to 70 km; the resulting data set is, thus, ideally suited to study diurnal changes in ozone. The figure shows the diurnal cycle of ozone at various altitudes, averaged over the month of December 1990. These data



Ozone mixing ratio at Table Mountain as function of local solar time at (a) 70 km, (b) 60 km, and (c) 50 km, averaged over December 1990.

are the highest quality observations of this cycle made to date, and they are being used to assess a state-of-the-art photochemical model.

The instrument, which was designed and built by Millitech Corporation, is being operated under a collaborative arrangement involving Langley Research Center, the University of Massachusetts, and JPL. Data analysis

and software development are done at Langley.

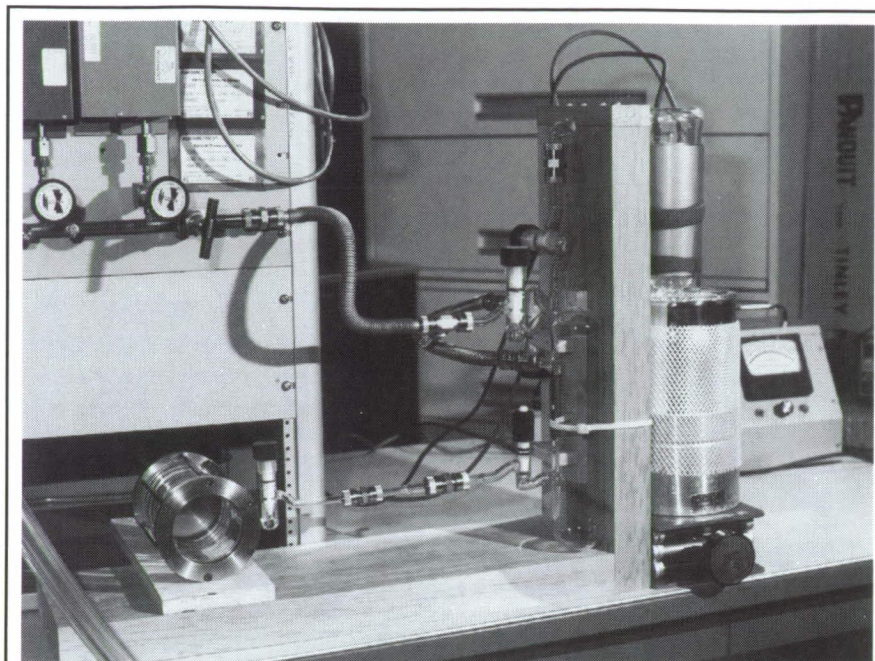
**(Brian J. Connor, 45698)
Space Directorate**

Simple Method for In Situ Production of High-Purity Ozone

A simple, inexpensive, and efficient method for producing high-purity ozone has been developed and used extensively at Langley Research Center in laboratory studies of high-resolution infrared absorption spectra of ozone and in the HALOE (Halogen Occultation Experiment) gas response tests. The ozone generator shown in the figure has been used for in situ production of ozone and filling of an absorption cell directly without intermediate storage or transport. Because concentrated ozone is unstable and can explode upon mechanical or thermal shock, great care must be exercised during its generation and use.

The ozone generator illustrated is an evacuative double-walled Pyrex U-tube (0.5-cm annular space), approximately 30 cm long, with a 7.5-cm outer diameter and a 0.25-cm wall thickness. The metal foil electrodes in contact with the external surfaces of the U-tube are connected to a 10-kV transformer. A silent electrical discharge is produced between the electrodes by applying high voltage. A Pyrex absorption cell with Teflon stem valve and potassium chloride windows and a gas-handling manifold with pressure-monitoring instrumentation are also shown in the figure. The generator is enclosed in a protective plexiglass safety shield during use.

Ozone generation is initiated after introducing a desired quantity of high-purity oxygen into the system. The liquid-nitrogen-filled dewar is slowly raised until the tops of the electrodes are immersed. The liquid nitrogen level should be maintained at the top of the electrodes. Voltage applied to the electrodes can be regulated by a



Ozone generator as used in HALOE gas response test.

L-88-12141

Variac. An electrical discharge is applied for a duration according to the amount of ozone desired. During the discharge, ozone will be produced and collected as a liquid on the inner walls of the U-tube. A 30-min excitation at approximately 8 kV will yield a few cubic centimeters of liquid ozone. When the desired amount has been produced, the high voltage is turned off. The ozone is purified by pumping the excess oxygen gas from the system while the ozone remains liquid. The liquid ozone is converted to high-purity gas by slowly removing the LN₂ dewar. Special care should be taken that the changes in temperature and pressure occur very gradually and that the ozone generator system is not mechanically shocked.

After use, the system is flooded with dry nitrogen to dilute the ozone for pumpout. Ozone deterioration within the absorption test cell can be minimized by preconditioning the cell with ozone for several hours.

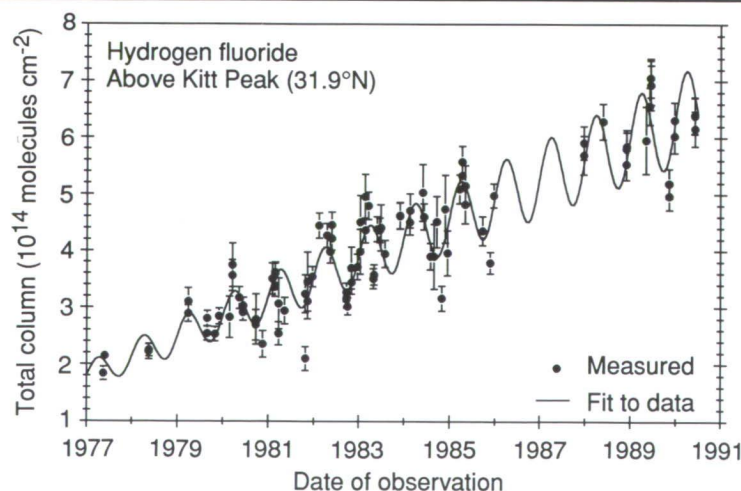
(M. D. Venkataraman, 45521, C. T. Solomon, and M. A. H. Smith)
Space Directorate

Long-Term Trends of Hydrogen Fluoride and Hydrogen Chloride

Hydrogen fluoride (HF) and hydrogen chloride (HCl) have long been recognized as key molecules for monitoring anthropogenically produced changes in the composition of the upper atmo-

sphere of the Earth. Hydrogen fluoride originates in the upper atmosphere almost entirely from the photodissociation of man-made halocarbons, primarily CCl₂F₂ (CFC-12) and CCl₃F (CFC-11). Hydrogen chloride is also a byproduct of halocarbon photolysis, but in contrast to HF, significant natural sources of HCl exist.

To measure the long-term changes in atmospheric HF and HCl, infrared spectral features of the two gases have been analyzed in high-quality solar spectra recorded since 1977 from Kitt Peak, a high-altitude observatory in southern Arizona. A multilayer, nonlinear least-squares spectral fitting procedure and a consistent set of spectroscopic line parameters have been used in the retrievals. The results for HF are shown in the figure. Over the 13-year observing period, the HF total column increased by a factor of 3.2; the corresponding HCl increase was a factor of 1.8. The long-term increases of both gases are superimposed on a seasonal cycle with an early spring maximum and an early fall minimum. In addition, short-term changes in the HF and HCl total columns have been identified. The fluctuations of the two gases are highly correlated and are believed to be caused by meridional transport in the lower stratosphere.



Kitt Peak HF measurements and best-fit to data.

The measurements have been compared with model-calculated total columns derived from the emission histories and photo-oxidation rates for the source molecules. These calculations (performed by collaborators at Atmospheric and Environmental Research, Incorporated) reproduce the measurements (including the long-term trends and seasonal cycles) to close to measurement errors; this suggests that the overall chemistry of HF and HCl is well-understood. (Curtis P. Rinsland, 42699) Space Directorate

Effects of African Fires on Southern Hemisphere

A satellite data analysis technique developed at Langley Research Center has revealed large amounts of ozone pollution (i.e., smog) emanating from Africa. This technique makes use of the differences in ozone measurements obtained from the Total Ozone Mapping Spectrometer (TOMS) and the Stratospheric Aerosol and Gas Experiments (SAGE) to infer the

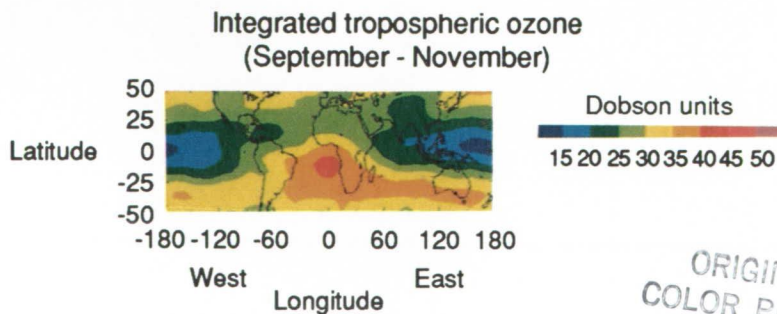
amount of ozone present in the lower portions of the atmosphere (the troposphere). The distribution of tropospheric ozone during Southern Hemisphere spring (September to November) reveals high levels of ozone being carried by the easterly trade winds, where the highest concentrations of ozone are found over the southern tropical Atlantic Ocean. Eventually, this ozone reaches the middle and upper troposphere (15 000 ft to 60 000 ft), where the winds are primarily from the west. The resultant



As seen from an airplane
over Botswana



As seen from Space Shuttle
over Mozambique



As seen from an analysis of global pollution from satellites

Views of African fires (top) and integrated tropospheric ozone distribution (bottom).

L-91-5773

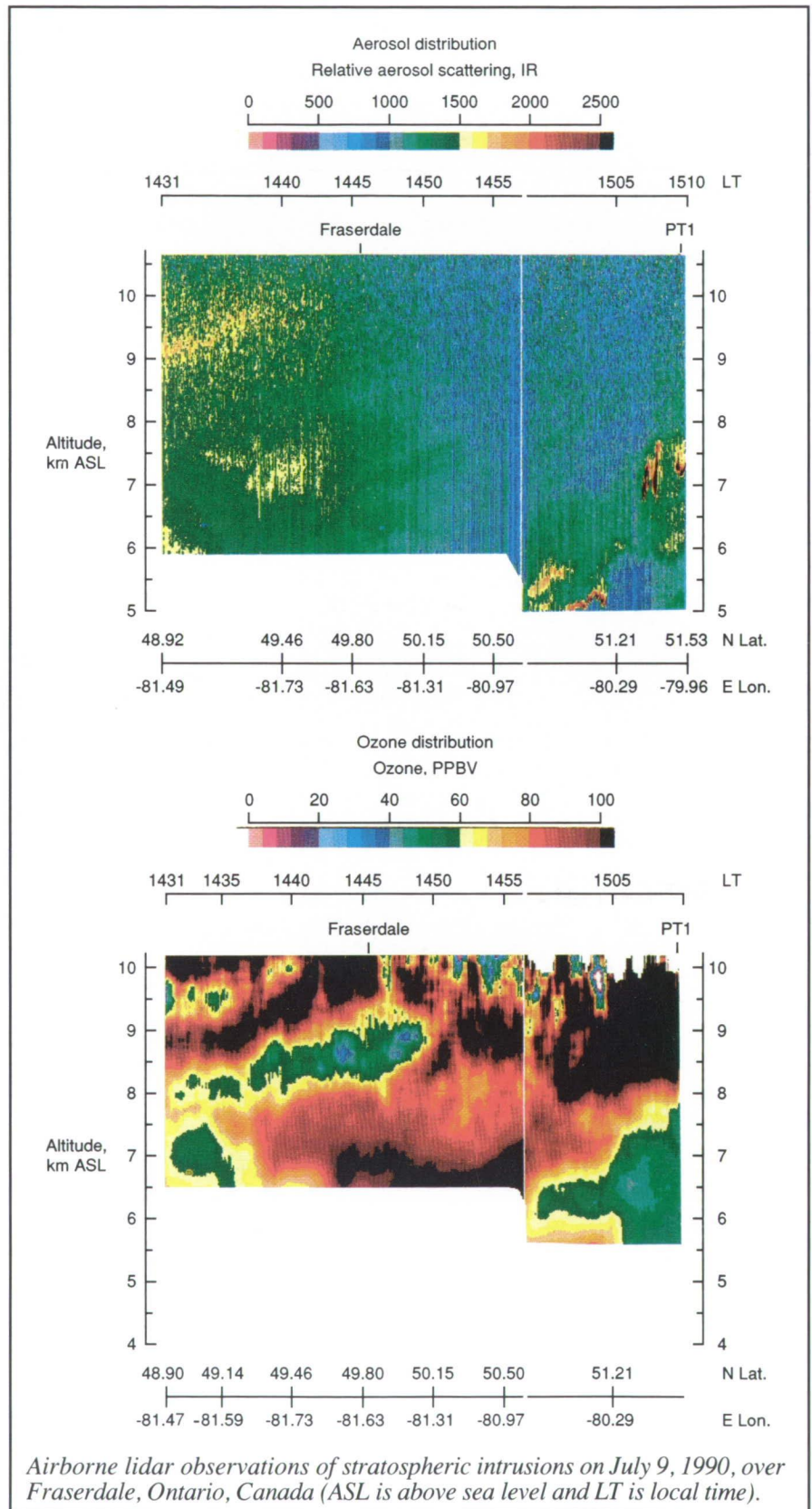
ORIGINAL PAGE
COLOR PHOTOGRAPH

plume shows that the elevated ozone concentrations are transported past Australia.

The cause of this pollution is the widespread use of fire which has been traditionally used by farmers and tribesmen to clear the land. The Botswana fire (shown in the figure) burned for more than 1 week in September 1989, and the fire front eventually extended to more than 60 miles. The top panels of the figure show two different views of fires in Africa. One view was obtained from an airplane and the other from the Space Shuttle. The global impact from these fires, which are a seasonal occurrence and generally are most pronounced in September and October, can be seen in the lower panel, which shows that the pollution generated from these fires can be identified by the orange plume extending past Australia. The smoke from the plumes of these fires observed from the Space Shuttle *Challenger* in October 1984 could be identified for hundreds of miles. A comprehensive field mission using the NASA DC-8 is planned for September 1992 to investigate the chemistry and the global impact of this pollution source from Africa. (Jack Fishman, 42720)
Space Directorate

Airborne Lidar Investigation of Ozone and Aerosols Over Canada

During the 1990 NASA Atmospheric Boundary Layer Experiment (ABLE-3B), an airborne lidar system was used to investigate the summer-time distributions of ozone and aerosols over the lowland and boreal forest regions of eastern Canada. Ozone and aerosol measurements were simultaneously made with the lidar system above and below aircraft to

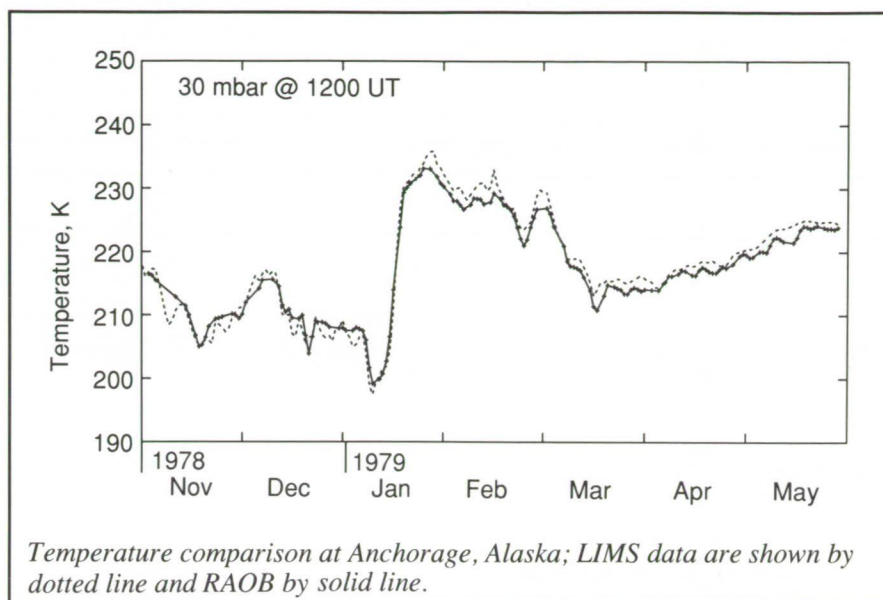


observe the large-scale variability of the atmosphere from near the surface to above the tropopause (typically at approximately a 10-km altitude). Based on the lidar measurements, seven types of air masses were identified in the ABLE-3B data: stratospheric intrusions, convective outflows, low ozone cases, young plumes from fires, aged plumes from fires, urban/industrial pollution, and background (unperturbed) air. Each of these air mass types had distinct characteristics that distinguished it from the others.

Numerous stratospheric intrusions were observed with the lidar. Evidence was found that the effect extended well down into the lower troposphere with enhanced ozone (>50 percent above background) and low aerosol scattering. The figure shows an example of a strong stratospheric intrusion observed on the first flight from North Bay, Ontario, to the Hudson Bay region. The aerosol distribution (top of figure) shows low aerosol scattering in high ozone regions (>80 parts per billion by volume (ppbv)) which extends from the stratosphere down to below an altitude of 6.5 km. The downward transport of stratospheric air into the troposphere was found to be the dominant factor in determining the ozone distribution in the troposphere over this region. This finding is similar to that for the ABLE-3A field experiment conducted over Alaska during the summer of 1988. In contrast to the ozone, the aerosol distribution was influenced by plumes from fires in Canada and the natural source of surface aerosols from the boreal forest and tundra regions.

(Edward V. Browell, 41273)

Space Directorate



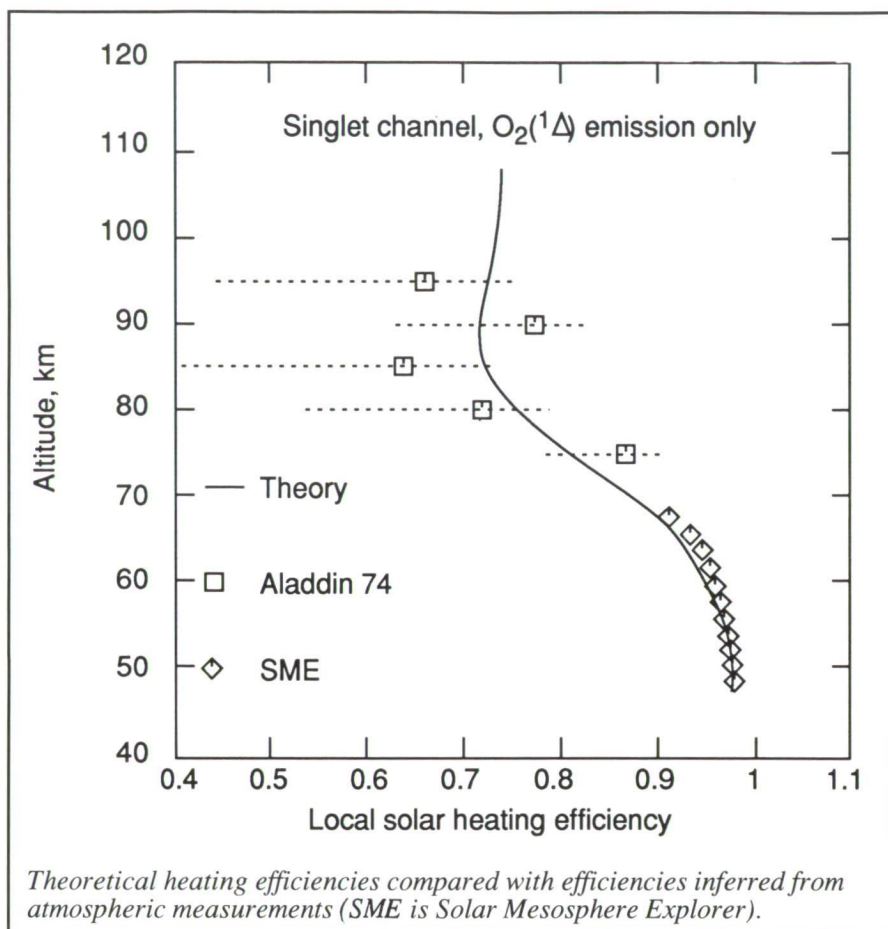
Accuracy of Nimbus 7 LIMS Temperatures in Arctic Stratosphere

The Nimbus 7 Limb Infrared Monitor of the Stratosphere (LIMS) experiment obtained near-global distributions of temperature in the stratosphere from late October 1978 through May 1979. Those temperature profiles were also used in the retrieval of the LIMS species (ozone, water vapor, nitric acid, and nitrogen dioxide). Distributions of these species are of interest particularly in the polar lower stratosphere, where chemical processes can cause reductions in ozone for some seasons. Because temperature bias errors can affect the retrieved species profiles, the LIMS temperatures must be accurate. Temperature time series comparisons between LIMS and radiosonde observations (RAOB) have been conducted for 22 stations poleward of 60° north latitude. For example, the figure shows a time series for Anchorage, Alaska, at 1200 Universal Time (UT) and for the 30-mbar pressure-altitude (approximately 23 km). The LIMS data were constructed from the

LIMS Map Archival Tape (LAMAT) product, and the RAOB data were available on a daily basis. The RAOB data at Anchorage are missing for some days in early November and December. In general, the LIMS data represent well both the magnitude and variation of temperature, particularly the increase of 30° near January 10, 1979.

Monthly statistics of the daily temperature comparisons have been generated for the 22-station sample and at each of five pressure levels in the lower stratosphere. When averaged over the 7 months, mean differences are within ± 1.3 K from 100 mbar (near 16 km) through 30 mbar; root mean square differences are less than 2.7 K. Systematic errors in the RAOB results are on the order of 0.5 K to 1.0 K. These findings indicate that accurate, satellite-derived temperature profiles can be obtained with the limb-infrared technique with relatively high vertical resolution and that the LIMS species data set is free from any significant temperature bias errors in the Arctic. (Ellis E. Remsberg, 45823)

Space Directorate



assumed to be converted to heat (i.e., 100-percent heating efficiency). However, detailed calculations of the disposition of the energy of the excited photolysis products demonstrate that substantial energy loss occurs because of radiative emission from the product $O_2(^1\Delta)$ and to energy transfer processes involving $O(^1D)$, which ultimately generates excited O_2 species. This energy loss results in a significant decrease in the heating efficiency (and, therefore, in the heating rates) over those presently calculated in models of the mesosphere and lower thermosphere. Calculated heating efficiencies have also been compared with atmospheric measurements from which the heating efficiency can be inferred, and favorable agreement has been obtained (as shown in the figure).

(Martin G. Mlynczak, 45695)
Space Directorate

Polar Stratospheric Cloud Climatology From SAM II

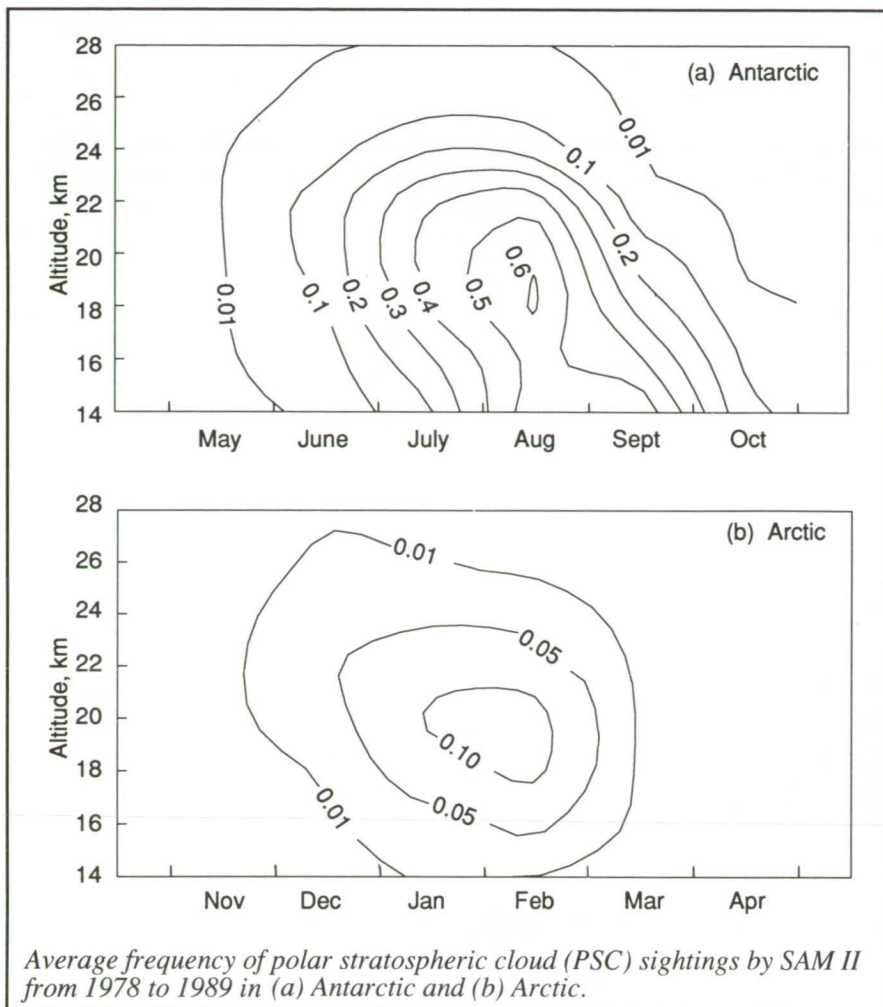
Data from recent field and laboratory experiments, as well as theoretical calculations, have demonstrated convincingly that polar stratospheric clouds (PSC's) play critical roles in the formation of the springtime Antarctic ozone hole. The surfaces of PSC particles catalyze heterogeneous chemical reactions that liberate active (ozone-destructive) chlorine radicals from benign reservoir species. Formation of the clouds also perturbs the local budget of odd nitrogen, compounds that must be present in order to reform the benign reservoirs and shut off the ozone destruction cycle. This perturbation to the odd nitrogen supply is effectively irreversible if the PSC particles grow large enough to undergo significant sedimentation.

Efficiency of Solar Heating in Middle Atmosphere

The conversion to heat of solar ultraviolet radiation absorbed by ozone (O_3) is a primary source of heat in the terrestrial mesosphere and lower thermosphere (50 km to 110 km). A portion of the solar photon energy is required to break the chemical bonds of O_3 , leading to photolysis. Some heating occurs as the residual energy (i.e., the difference between the energy of the initial photon and the energy required to produce ground-state products) is converted to kinetic energy of the photolysis products (atomic oxygen and molecular oxygen). The products, in turn, collide with other species, and the atmosphere rapidly reaches a new equilibrium kinetic

temperature. However, not all of the residual energy is directly converted to heat. Some of the residual energy initially resides as internal energy of electronically excited photolysis products, namely $O(^1D)$ or $O_2(^1\Delta)$. The internal energy of the excited products may be converted to heat during collisions with other species, may be radiated spontaneously, or may be transferred to other species that may then radiate or be quenched. The radiated energy is largely lost to space. The ultimate disposition of the internal energy of the photolysis products thus determines the magnitude of the local heating.

Radiative emission from and energy transfer processes involving these metastable photolysis products have not been previously considered. The entire residual energy has been



Observations from 1978 to 1989 by the Stratospheric Aerosol Measurement II (SAM II) sensor aboard the Nimbus 7 satellite have been analyzed to produce a decadal average climatology of PSC's in both the Antarctic and Arctic. The figure shows that interesting differences exist in the frequency of cloud sightings between the two polar regions. Antarctic PSC sightings normally begin in late fall (May) at altitudes above 20 km and in early winter at lower altitudes. Average sighting frequency at all altitudes increases during the winter, reaching a seasonal peak of approximately 60 percent near 18 km in August. The frequency falls sharply at higher altitudes after August, but there are many

sightings from 14 km to 18 km in late winter and early spring (September and October), the time period during which the ozone hole forms. In contrast, relatively few Arctic PSC's are sighted in December, and even in the most favorable months (January and February), the peak sighting frequency is only approximately 10 percent. Essentially no PSC's are sighted in the Arctic in late winter and early spring. The relative persistence of PSC's in the Antarctic demonstrates that seasonal temperatures are colder there and that, on average, the southern polar vortex is stronger than its Arctic counterpart and maintains its integrity well into spring. (Lamont R. Poole, 42689) Space Directorate

Stability of ERBE Scanner Measurements

The goal of the Earth Radiation Budget Experiment (ERBE) is to provide a data set to study the regional, zonal, and global radiation properties of the Earth at daily, monthly, seasonal, and annual time scales. This radiation data set must be highly accurate in order to detect and understand the often small, yet important global climate changes. All of the ERBE instruments were extensively calibrated and characterized in ground test facilities, and onboard calibration systems were included to recalibrate the sensors in flight. However, in-flight calibration systems can also fail, degrade, or become unusable for numerous reasons, and their applicability is often questionable because they are usually activated in special calibration sequences (as were the ERBE scanners) which are substantially different from their normal Earth-viewing modes.

One method of determining the long-term stability of ERBE radiometers is to make interannual comparisons of measurements from regions that are believed to be relatively stable. Clear-sky scanner measurements from surfaces such as deserts, oceans, and polar snow, which have different spectral characteristics, were analyzed. The most applicable area included 30° north to 30° south latitude (one-half the surface of the Earth). In the table (see the figure), the monthly, clear-sky, reflected shortwave (0.3 μm to 5 μm) and emitted longwave (5 μm to 50 μm) fluxes for the first 2 years of the Earth Radiation Budget Satellite (ERBS) and NOAA-9 operations are listed. The first year was from February 1985 through January 1986, and the second year was from February 1986 through January 1987. Most of the monthly differences were less than 1 W/m^2 , and

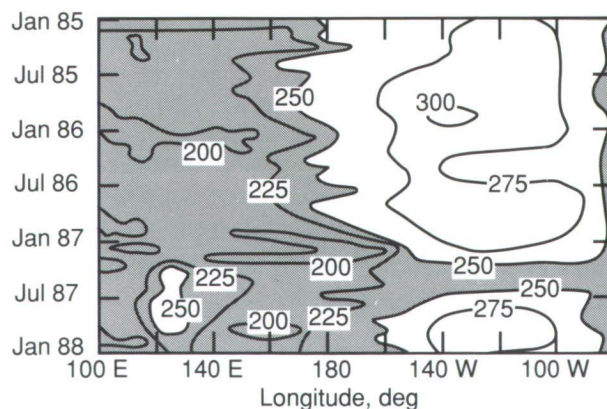
ERBE Observations of 1987 El Niño Event

Satellite measurements from ERBE are providing key data on the interannual variability of the climatic system of the Earth. The variation of longwave radiation measured over the equatorial Pacific Ocean is shown in the figure for 1985 through 1987. These results indicate that significantly lower values of longwave radiation were observed over the central and eastern Pacific in 1987 than in 1985 and 1986. The lower values reached during this time period are because of increased cloudiness associated with the warmer than normal sea-surface temperatures. These abnormally high sea-surface temperatures are caused by a phenomenon called El Niño, in which there was a movement of low atmospheric pressure from the western to central Pacific, coinciding with relaxed trade winds and heavy rainfall. The El Niño event observed by ERBE caused the jet stream to move northward over the United States, thus resulting in a major drought over the mid-western United States in 1988. (Edwin F. Harrison, 45663) Space Directorate

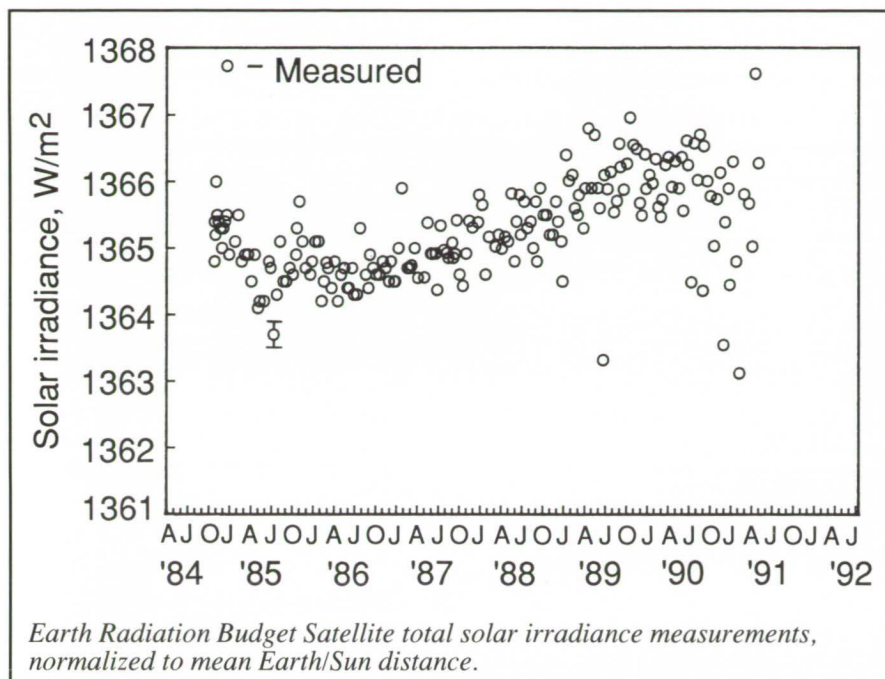
	Shortwave, W/m ²		Longwave, W/m ²	
Month	First year	Second year	First year	Second year
February	53.16	52.33	286.3	285.6
March	55.00	55.05	287.4	287.9
April	52.83	52.25	288.2	286.3
May	53.18	52.45	288.6	286.7
June	50.19	50.43	287.6	287.0
July	50.14	50.23	286.2	286.3
August	51.90	51.57	288.0	287.0
September	52.69	52.06	287.7	286.6
October	53.02	52.35	288.0	287.3
November	51.79	52.43	287.0	287.1
December	51.77	52.09	286.8	286.5
January	53.32	53.17	288.1	287.4
Annual	52.42	52.20	287.5	286.8

ERBE clear-sky shortwave and longwave fluxes for 30°N to 30°S during first 2 years of operation.

the annual differences were 0.2 W/m² and 0.7 W/m² for the shortwave and longwave fluxes, respectively. Results for the other target sites were similar. It is concluded that measurements from the ERBE scanners were stable to within several tenths of a percent during their first 2 years of operation. (W. Frank Staylor, 45680) Space Directorate



Monthly variability of longwave flux (W/m²) derived from ERBE (latitude of 5°N to 5°S).



Systematic Variability in Total Solar Irradiance

The incoming total solar irradiance is the primary energy source for the Earth/atmosphere climatic system. Long-term increases or decreases in the solar irradiance can cause significant changes in the temperature of the Earth. The Earth Radiation Budget Experiment solar monitors are being used to define long-term changes in the mean value of the total solar irradiance (1365 W/m^2). These monitors were placed into orbit aboard the Earth Radiation Budget Satellite (ERBS) and the National Oceanic and Atmospheric Administration (NOAA) 9 and 10 spacecraft platforms during October 1984, December 1984, and September 1986, respectively.

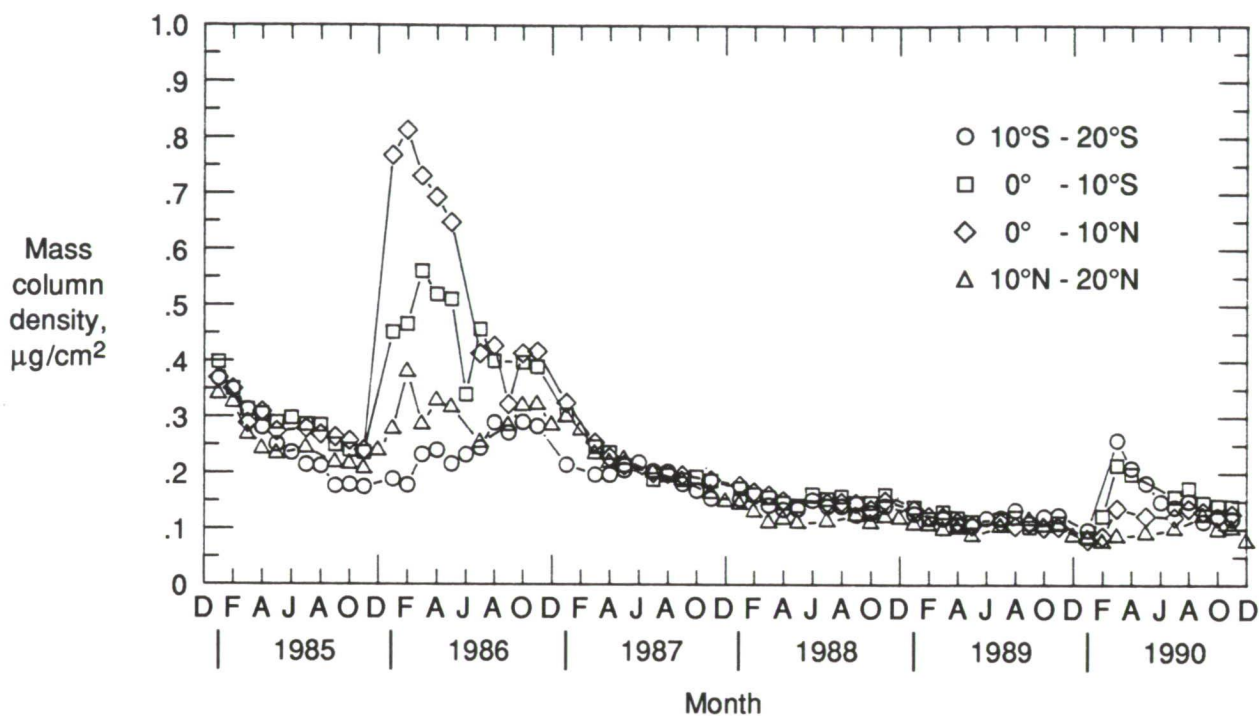
Measurements from the ERBS monitor for the 1984 to 1991 period are presented in the figure. Measurement precision is 0.01 percent (as indicated by the error bar). The low isolated irradiance values correspond to days in which large numbers of

sunspots were present on the solar disk. The irradiance systematically decreased before 1986, increased between 1986 and 1989, and decreased again after late 1989. These systematic trends were caused by the 11-year cycle of solar magnetic activity. Between 1986 and 1989, the irradiance rose approximately 0.1 percent. Between 1978 and 1986, earlier spacecraft experiments revealed a 0.1-percent decline in the irradiance. Comparisons between the 1978 to 1991 observed irradiance and global surface temperature changes should define the actual impact of solar variability upon the climate of the Earth during the 1980's. The solar irradiance is expected to reach minimum levels in 1997 when the solar magnetic activity is forecast to be at a minimum. Differences between the observed 1986 and the forecasted 1997 irradiance minima may be used to identify additional irradiance variability with periods greater than 11 years. (Robert B. Lee III, 45679) Space Directorate

Mass Loading of Stratospheric Aerosols

In sufficient quantities, such as those present following a major volcanic eruption, stratospheric aerosol particles can impact the climate of the Earth by reflecting incoming sunlight back to space. Also, recent laboratory experiments show that the particle surfaces can efficiently promote heterogeneous chemical reactions that reduce the supply of gaseous odd nitrogen radical species and, hence, indirectly increase the potential for halogen-catalyzed ozone destruction. Data obtained from balloon-borne in situ particle sensors launched at Laramie, Wyoming, indicate that the total mass of background stratospheric aerosols has increased in the past 10 years. Furthermore, sulfur emissions from the subsonic jet fleet may be responsible for the increase, and future increases may be even more severe because of emissions from the proposed high-speed aircraft. In order to examine the trend of background stratospheric aerosols from a more global perspective and to assess the effect of natural and anthropogenic sources on the aerosol mass loading, aerosol extinction and water vapor density data obtained by SAGE II have been analyzed.

The temporal variation of the estimated aerosol mass column density for latitude bands of 10° in the Tropics is shown in the figure. The effects of the eruptions of the volcanoes Ruiz (4.89°N and 75.37°W) in November 1985 and Kelut (7.93°S and 112.31°E) in February 1991 are obvious. By integrating the estimated aerosol mass column density over the globe, the eruptions of Ruiz and Kelut were found to eject at least 5.6×10^5 and 1.8×10^5 tons of material into the stratosphere, respectively. The former value is nearly equal to the global mass



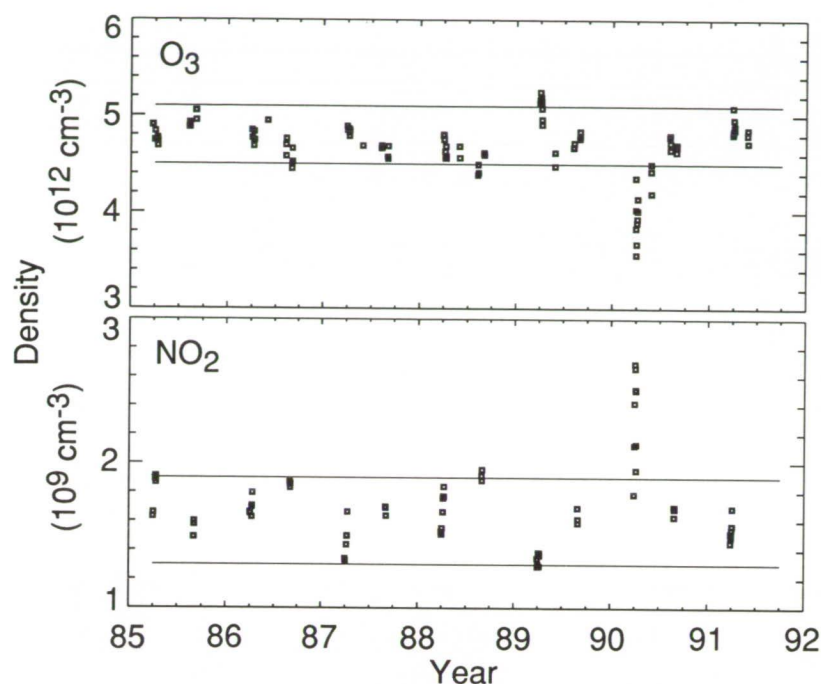
Estimation of stratospheric aerosol mass column density from SAGE II measurements.

loading of background aerosols in 1979, which was estimated from data obtained by the orbiting SAGE I sensor to be 5.7×10^5 tons. In the present study, the global mass loading in 1989 was found to be 7.5×10^5 , thus indicating a 30-percent increase over the decade. The amount of sulfur emissions expected from the proposed High-Speed Civil Transport fleet was found to be comparable to the sulfur contained in present-day background aerosols in latitude corridors where most commercial flights are expected to take place. (Glenn K. Yue, 42678)
Space Directorate

Observation of Stratospheric Response to Solar Proton Events

High-energy ionizing protons generated by solar flares have long been known to affect the atmosphere of the Earth. The shower of secondary electrons created by the protons eventually results in the increased production of radicals such as HO_x and NO_x . These radicals then proceed to destroy ozone through the normal chemical cycles. While changes in mesospheric ozone because of the altered HO_x chemistry have been both predicted and observed, changes in O_3 and NO_x in the lower stratosphere have not been previously observed.

During late 1989, several large solar flares with accompanying solar proton events (SPE) occurred on a scale not seen since August 1972. Models predicted long-lived, measurable changes to the stratospheric ozone and NO_2 . The Stratospheric Aerosol and Gas Experiment (SAGE II) sensor has made global measurements of ozone and nitrogen dioxide since October 1984. The first 6 years of SAGE II data provide an adequate sample for the assessment of the climatology and interannual variability of these species, and they are presented in the figure. The data have been deseasonalized by using the SAGE II coverage, which repeats, to within a few days, from year to year. A typical month can be obtained by taking the average of the 6 years of data for that month. Once the data are



6-year deseasonalized time series of ozone (top panel) and nitrogen dioxide (bottom panel) at altitude of 21.5 km as measured by SAGE II for latitudes near 70°N.

deseasonalized, all that remains is the interannual variability. Except for the spring of 1990, the deseasonalized data display an interannual variability about the mean of ≈ 5 percent for O_3 and ≈ 20 percent for NO_2 (as depicted by the pairs of horizontal lines in the figure). The April 1990 values are well outside the interannual variability, even at the three-sigma level. At the location of 70°N, the NO_2 has increased by 70 percent, while the ozone has decreased by 25 percent.

Photochemical models using the observed proton energy spectra and fluxes predict that by the beginning of April an increase in NO_2 in excess of 20 percent and a corresponding decrease in O_3 approaching 10 percent would exist at the high northern

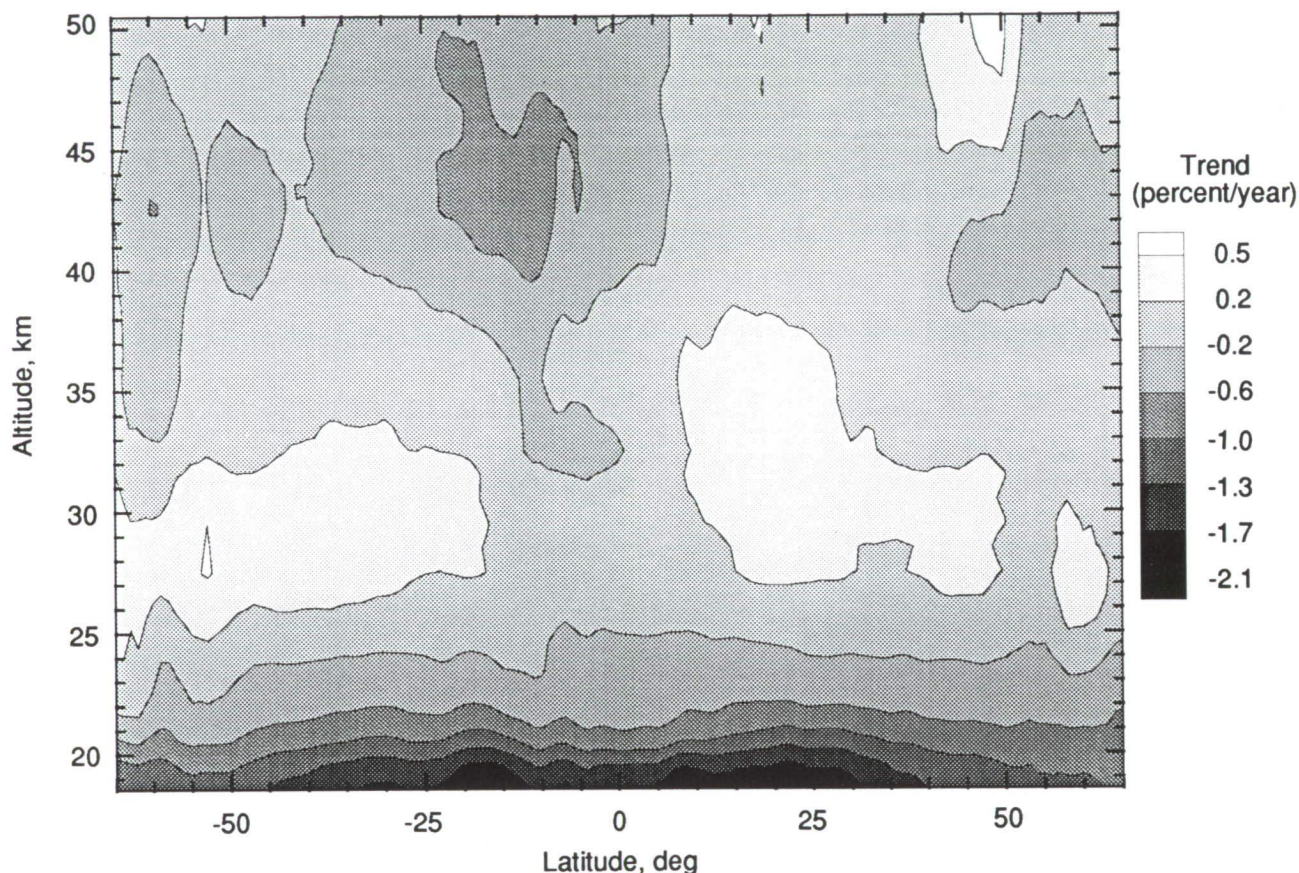
latitudes. The SAGE II measurements qualitatively support the model predictions, but several important differences exist. While models predict that the peak effects would be found slightly above 30 km, SAGE II found them to be at 21 km and to have a larger amplitude than predicted. If the actual SPE contained significant fluxes at energies above the upper limit of the available measurements, the actual production of NO_x would have been greater and would have occurred even lower in the atmosphere.

(Joseph M. Zawodny, 42681)
Space Directorate

Global Ozone Trends From SAGE I and SAGE II Measurements

The springtime Antarctic ozone hole, which is caused largely by chlorine-catalyzed chemical ozone destruction, serves as a dramatic illustration of the rather sudden and unexpected deleterious effects human activities can have on our environment. The discovery of the hole during the mid-1980's has heightened concern over the possibility of decreasing ozone levels, not only in the relatively isolated Antarctic but also on a global scale. A recent analysis has combined data sets from the SAGE I and SAGE II satellite instruments, which span a 12-year period from 1979 through early 1991, to estimate global stratospheric ozone trends over that time period.

The figure shows, as a function of latitude and altitude, ozone trend estimates derived from a linear regression/time-series analysis that accounted for (and removed) cyclic components (annual, semi-annual, and quasi-biennial) of the ozone variability. The residual linear trends, expressed in units of percent per year, indicate that ozone is both increasing and decreasing in the stratosphere. However, the trends are statistically significant in only a few regions. Significant decreases have occurred in a region centered at 43 km over the southern tropical latitudes, while increases have occurred from 28 km to 32 km over the mid-latitudes. Relatively large ozone decreases have occurred over essentially all of the lower stratosphere. Because a large fraction of the total ozone column is contained in the lower stratosphere, these results translate to a significant negative trend in column ozone content



SAGE I and II stratospheric ozone trends (1979 to 1990).

over mid- to high latitudes during the past decade.

(William P. Chu, 42675)

Space Directorate

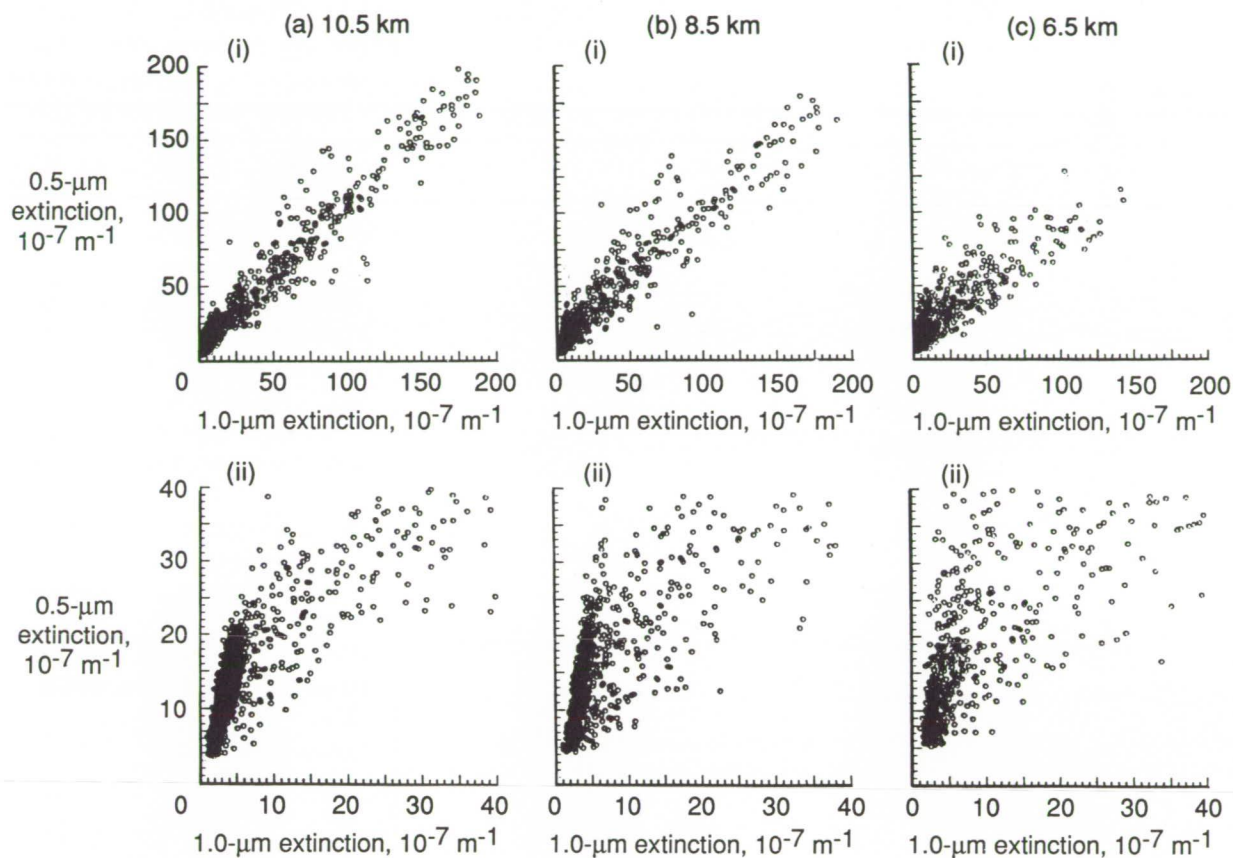
Measurement of Tropospheric Aerosols From Space Using Solar Occultation Techniques

The SAM II, SAGE I, and SAGE II series of solar occultation experiments were designed for the measurement of

stratospheric aerosols and gases. In the absence of high-altitude clouds, tropospheric measurements are also possible. Such tropospheric measurements are often contaminated by small patches of optically thin clouds along the optical path from the Sun to the satellite instrument. The use of measurements made at two wavelengths ($0.525\ \mu\text{m}$ and $1.02\ \mu\text{m}$) has made it possible to separate attenuation due to aerosol from that due to thin clouds.

The figure shows a scatter plot of extinction at $0.525\ \mu\text{m}$ versus that at

$1.02\ \mu\text{m}$ for 3 months of global data at different altitudes. In order to emphasize certain features, the same data are shown on two different scales in sections (i) and (ii) of the figure. Aerosol data, uncontaminated by clouds, are found to be within the dense linear concentrations of data points near the origin, where the $1.0\text{-}\mu\text{m}$ extinction is less than $10 \times 10^{-7}\ \text{m}^{-1}$. Cloud-contaminated data are found to be in the other parts of these diagrams, in particular within the linear cluster of higher extinction values where the extinction is approximately the same at the two wavelengths.



SAGE II data at different altitudes for period September to November 1989, including all latitudes between 80°S and 80°N. Each pair of panels, (i) and (ii), shows same data subset but with different axial scales.

Validation studies have recently been carried out which confirm this subdivision of the data set, and work is currently in progress to use the satellite data to produce global maps of tropospheric aerosol extinction.

(M. P. McCormick, 42669)

Space Directorate

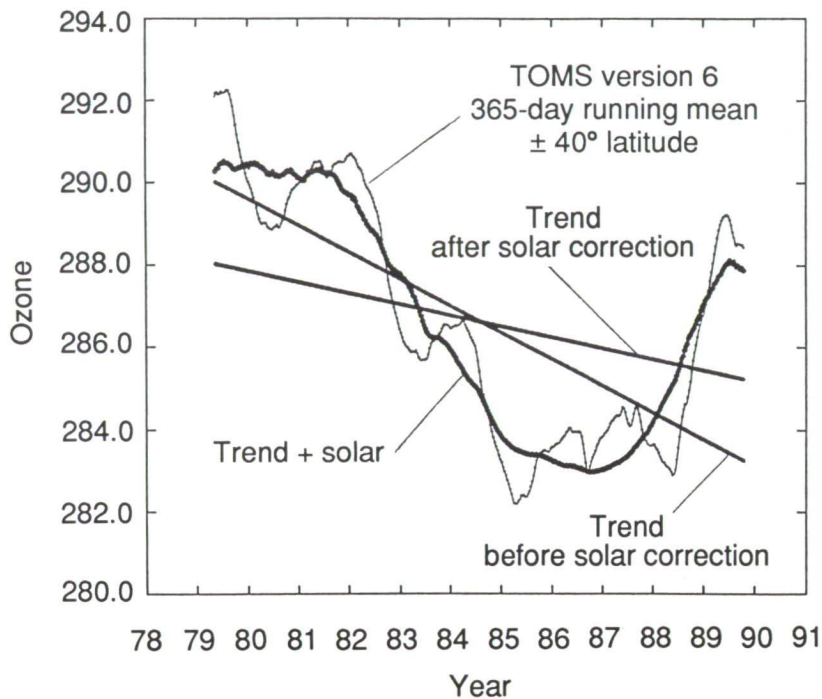
Anthropogenic Trends and Solar Effects on Total Column Ozone

In order to isolate anthropogenic trends in global ozone, the natural atmospheric changes associated with

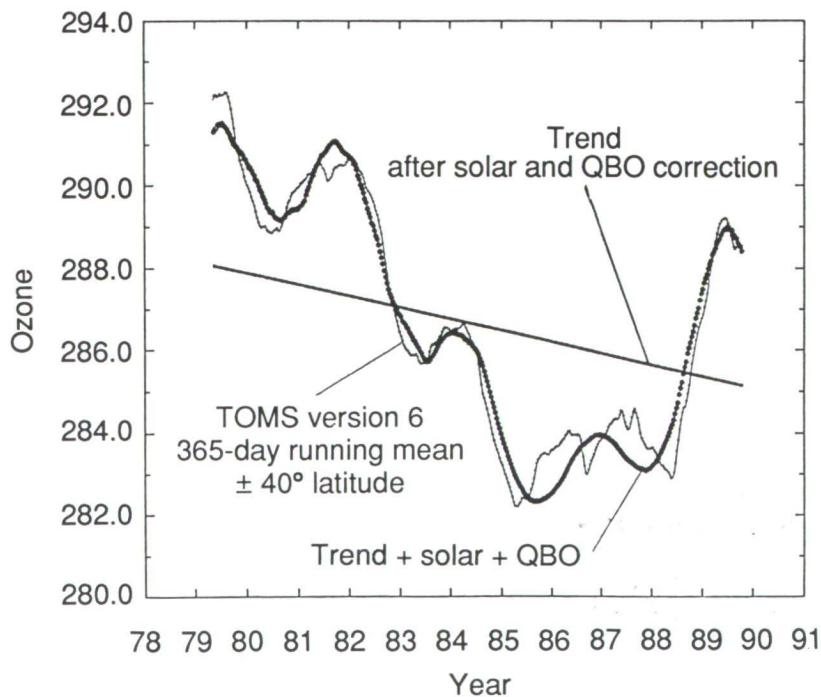
the 11-year cycle of solar ultraviolet (UV) variations must be accurately taken into account. This is very difficult because statisticians need at least 10 solar cycles to clearly isolate the atmospheric response to 11-year solar variations, but satellite data are available for less than two such cycles. In the approach developed here to circumvent this problem, the ozone response to numerous 27-day solar rotation cycles is determined to good statistical accuracy and then, adjusting for the theoretical difference between short- and long-term responses, the 11-year response is estimated.

Ozone/UV studies were performed using two data sets in which long-term instrument drifts had been removed: a

280-nm solar UV index and the recently released Nimbus 7 Total Ozone Monitoring Spectrometer (TOMS) Version 6 total column ozone data. The short-term response of total column ozone to solar UV variations was discovered to be unexpectedly strong (by a factor of 2). The figures show the variations in the 365-day running mean of total column ozone averaged between $\pm 40^\circ$ latitude over 11 years. The first figure also shows the estimated ozone response to 11-year solar UV variability, taking into account the observed strong ozone response to short-term solar variations and the theoretical difference in relative amplitude between short-term and long-term responses. The estimated strong 11-year variation (labeled



Observed ozone variation compared with estimated response to 11-year solar cycle (trend plus solar) and trend before and after solar correction.



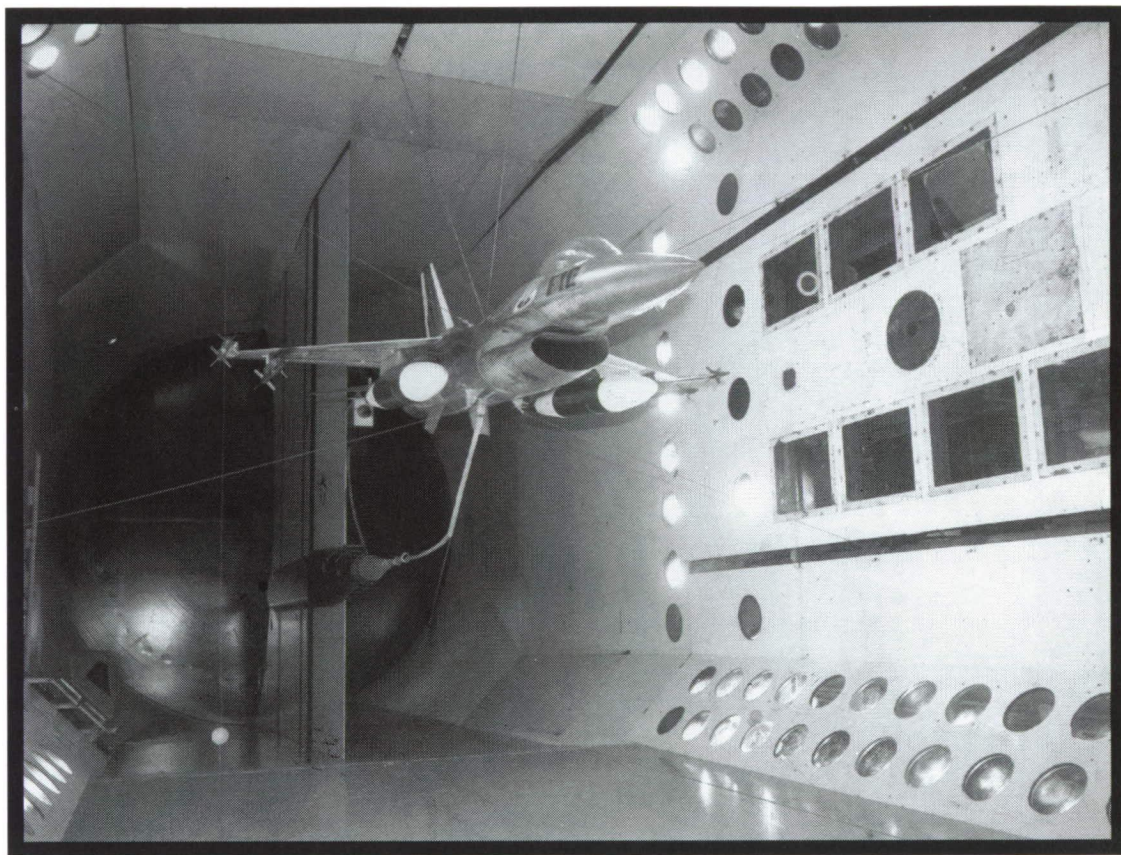
Observed ozone variation compared with estimated response to trend plus solar plus quasi-biennial oscillation and corresponding trend.

Trend + solar in the figure) is in accord with the observed variations. The linear ozone trends show a 2-percent decline during the 1980's when solar effects are ignored, but only one-half that decline when solar effects are properly taken into account. In the second figure, the quasi-biennial oscillation (QBO) in ozone is taken into account in addition to solar effects. This results in an improved estimate of the observed ozone variations, but gives approximately the same linear trend as after the solar correction. Thus, a technique has been developed to accurately estimate the ozone response to 11-year solar variations taking into account the response to 27-day variations; this technique, in turn, allows substantial improvements in long-term trend estimates.

(Gerald M. Keating, 45804, G. Brasseur, L. S. Chiou, and N. C. Hsu)

Space Directorate

■ FACILITIES



ORIGINAL PAGE
BLACK AND WHITE PHOTOGRAPH

*Develop, maintain, and
operate national facilities for
aerospace research and for
industry and Department of
Defense development support*

PRECEDING PAGE BLANK NOT FILMED

Reduction of Tire Characterization Test Time by Variable Yaw System

Because of the unique capabilities of the Aircraft Landing Dynamics

Facility (ALDF), many challenging test programs that are otherwise difficult or impossible to conduct safely elsewhere are scheduled at the facility. Thus, attempts to streamline test programs result in increased productivity. A variable yaw system,

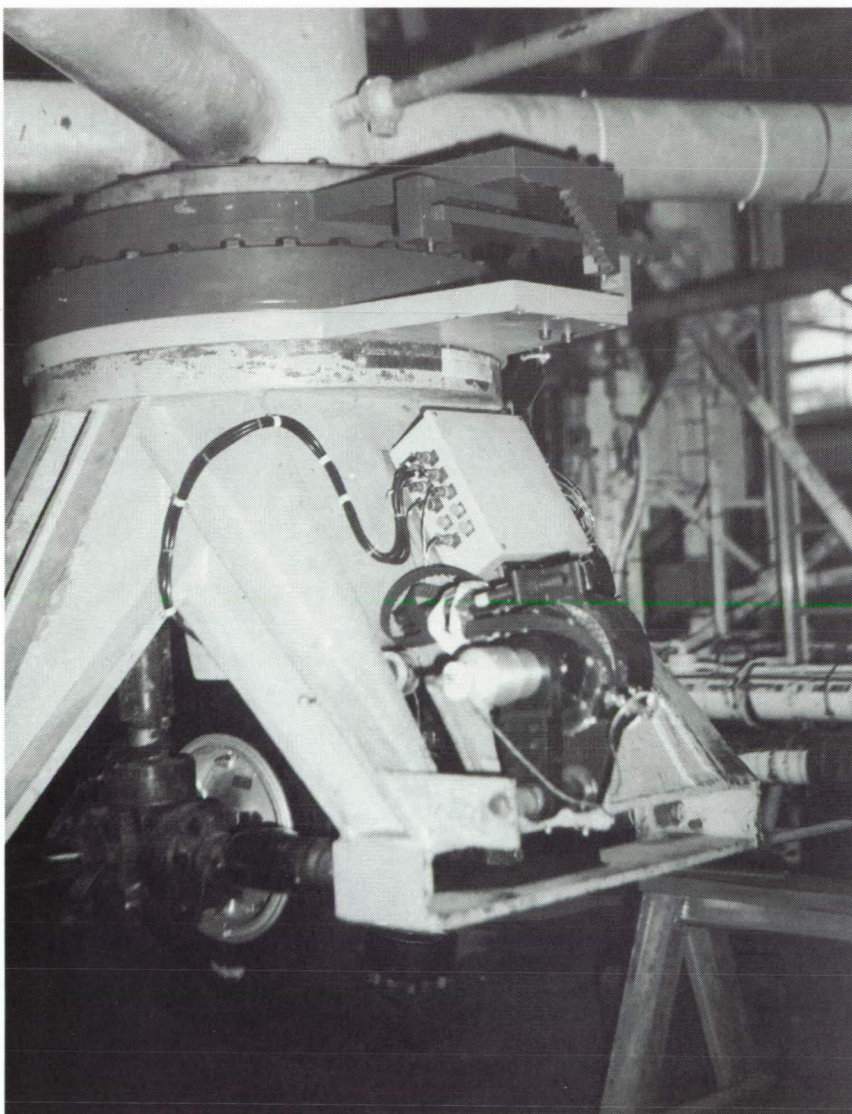
shown in the figure, was designed and installed on the ALDF test carriage to permit a range of yaw angles to be tested during a single run. Prior to this, only a single yaw angle was used during a test run. The variable yaw system allows yaw angle to vary from 0° to 16° or anywhere between, and it also allows for static yaw capability as before.

Initial tests with the variable yaw system were aimed at evaluating how high a yaw rate was possible while not compromising the quality of side force data compared to a fixed yaw angle. These tests showed that yaw rates as high as 5° per second were satisfactory. A typical set of tire characterization tests may involve five or six yaw angles and three to four vertical loads. Because yaw angle used to be fixed during tests, five or six runs would be needed to characterize the cornering behavior of the tire. Use of the variable yaw system with fixed vertical load accomplishes the same objective with only three or four runs for each test surface. Thus, this system can reduce test time by up to 40 percent during certain test programs.

(Robert H. Daugherty, 41309)
Structures Directorate

Statically Unstable Model on Cable Mount System

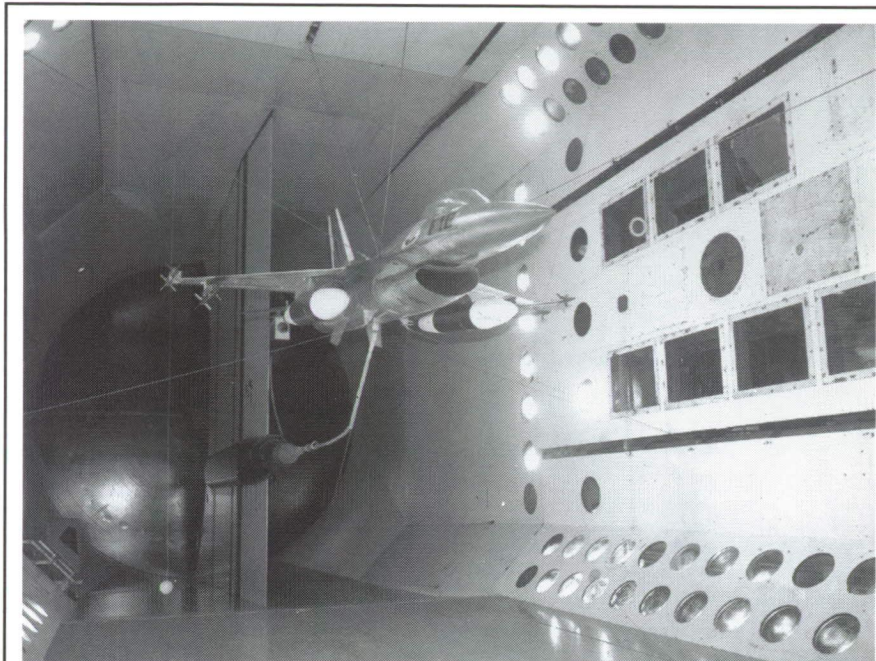
Fighter aircraft configurations have been tested for flutter clearance in the Transonic Dynamics Tunnel (TDT) most often by using cable-mounted statically stable, scaled-aeroelastic



Variable yaw device.

L-90-09221

ORIGINAL PAGE
BLACK AND WHITE PHOTOGRAPH



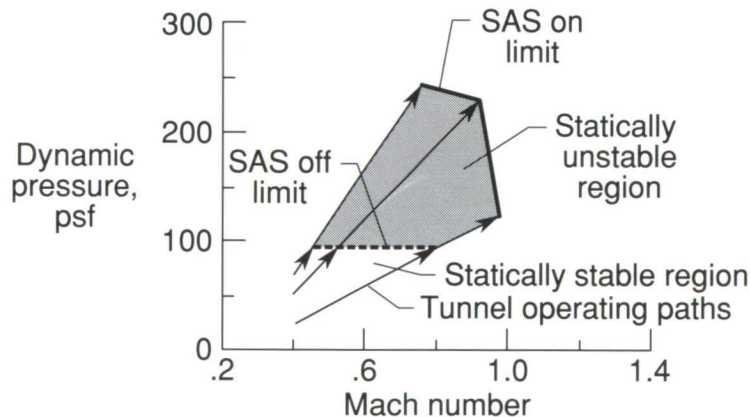
Aeroelastic model of advanced fighter aircraft.

L-86-1685

onboard hydraulic system. These systems were implemented in a full-span aeroelastic flying model that was designed and constructed to represent an advanced fighter aircraft. Statically stable and unstable test conditions were achieved with a movable mass system within the model which allowed the center of gravity to vary over a wide range (12 percent) of mean aerodynamic chord. Rate gyros were mounted in the model to provide pitch and roll inputs to the SAS. Analog control systems were designed to command the individual horizontal tail surfaces using pilot trim inputs, the horizontal tail position, and gyro feedbacks.

The model was first flown on the cable mount system with the movable mass forward to provide the most static stability. Flying characteristics were evaluated both with and without the SAS engaged. The SAS improved the flight-handling characteristics, allowing the model to be flown up to a Mach number of 1.1. The model was then flown with the movable mass in the rearward, more unstable position. The shaded region in the second figure represents the increase in the test envelope achieved with the use of the SAS with the movable mass in rearward positions. Testing up to dynamic pressures of 250 psf was possible with the SAS on. The dashed line indicates the test limits without the SAS. Open-loop measurements determined the model would have been statically unstable at dynamic pressures above 100 psf.

(Michael H. Durham and Donald F. Keller, 41262)
Structures Directorate



Increased test envelope with stability augmentation.

models such as the one shown in the first figure. However, some current and many newer fighter aircraft are designed to fly with reduced or negative static stability to improve performance and combat maneuverability. As a result, accurately scaling the aeroelastic characteristics of statically unstable aircraft with statically stable aeroelastic flying models is becoming more difficult.

Therefore, a new method for testing statically unstable flying models was developed and demonstrated in the TDT.

This new method for testing statically unstable aeroelastic flying models uses an onboard active control stability augmentation system (SAS) to provide pitch and roll stability. The required horizontal tail surface actuation was accomplished using an



New signal conditioner cards.

L-90-13802

TDT Data Acquisition System Improvements

Testing of aeroelastic research models involves acquiring large volumes of data from many different sensors and then analyzing the data in near real time to acquire information needed to guide continuation of the testing. The objective of improving the data acquisition system at the Transonic Dynamics Tunnel (TDT) was to provide the test engineers with the tools needed to meet these near-real-time data analysis and display requirements and thus increase the efficiency and safety of testing.

In the hardware area, two significant modifications were made to the analog/digital interface system. First, the instrumentation signal conditioning cards, shown in the figure, were modified to provide a more convenient means for adjusting instrument excitation voltages and for setting the values of shunt calibration resistors. These modifications significantly

reduce the time required for initial instrumentation setup and for daily adjustments. Second, buffer amplifiers were added to eliminate drift between analog and digital signals, thus eliminating the need for frequent adjustments of the analog signal levels. Several significant improvements were also made in the applications software area. Two subcritical damping analysis techniques, called Moving Block and Randomdec, were added to the data acquisition system for real-time data analysis purposes. The Moving Block analysis method for determining system damping is particularly useful for evaluating dynamic response and aeroelastic stability characteristics during testing of helicopter rotor systems. The Randomdec subcritical damping technique is used for aeroelastic stability testing of airplane models. Other noteworthy improvements were the addition of tunnel test condition information to video tape recordings of model motions and the acquisition of several new user interface terminals that provide 40 pages of nonvolatile memory capability,

thus decreasing down time associated with recovery from failure in other system components.

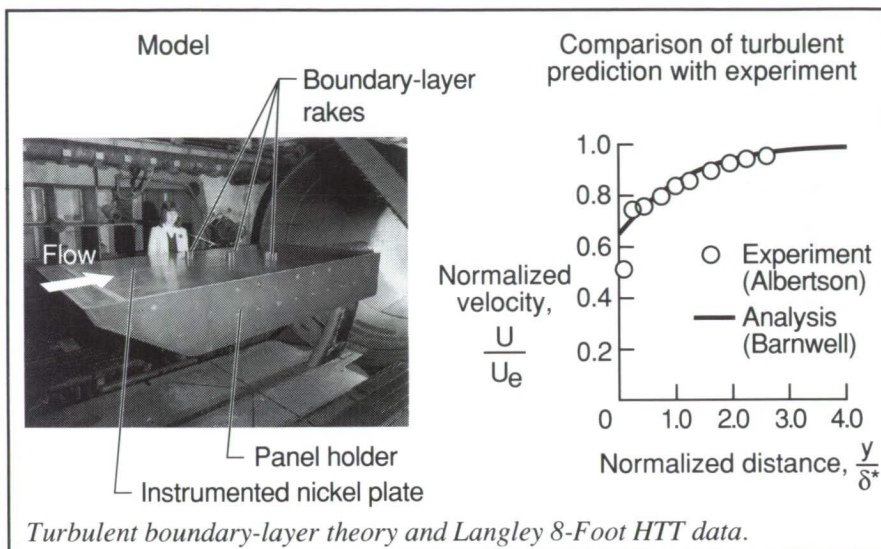
These hardware and software changes have provided significant improvements to the operational efficiency of the TDT data acquisition system and/or have provided the test engineers with significant added data acquisition, display, and analysis capabilities, thus improving data quality and providing for more efficient wind-on testing.

(David C. Rosser, Jr., 41249)
Structures Directorate

Compressible Turbulent Boundary-Layer Predictions Use Langley 8-Foot HTT Data

An experimental study was conducted in the Langley 8-Foot High-Temperature Tunnel (8-Foot HTT), which provides high-temperature Mach 7 flow by burning a mixture of air and methane in a combustor. The nominal total temperature for the study was 3300°R, which produced a wall temperature ratio of 5.4. Previous compressible boundary-layer experiments have achieved temperature ratios only up to 3.2. The objective is to compare experimental, naturally developing boundary-layer data from the 8-Foot HTT study with an existing closed-form solution for nonadiabatic compressible equilibrium turbulent flows.

In the experimental study, the model (left side of the figure) consisted of a hydraulically smooth flat plate measuring 9.7 ft long and 4.3 ft wide, which was instrumented with pressure orifices, coaxial thermocouples, and boundary-layer rake assemblies. The model was inclined to the flow to increase the local Reynolds number,



producing boundary-layer edge Mach numbers between 4.9 and 6.4. The local Reynolds number, based on boundary-layer edge conditions and plate length, ranged from 8×10^6 to 39×10^6 .

The closed-form approximate solution to the compressible boundary-layer equations was derived with a defect stream function formulation, is applicable to nonadiabatic equilibrium turbulent boundary layers with small crossflow, and can be applied to attached boundary-layer flows in the incompressible to supersonic range with the additional restriction that hypersonic-range boundary layers have small pressure gradients. A typical experimental velocity distribution is compared on the right side of the figure with the analytic solution. The velocity U has been normalized with the boundary-layer edge velocity U_e and plotted with the distance from the wall y normalized with the boundary-layer displacement thickness δ^* . Both the data and the analytic solution show good agreement except for a small excursion in the data near the wall.

The experimental study has provided new equilibrium compressible boundary-layer high-temperature data that have been useful in

validating a new boundary-layer solution technique.
(Cindy W. Albertson, 41371, and Richard W. Barnwell)
Structures Directorate

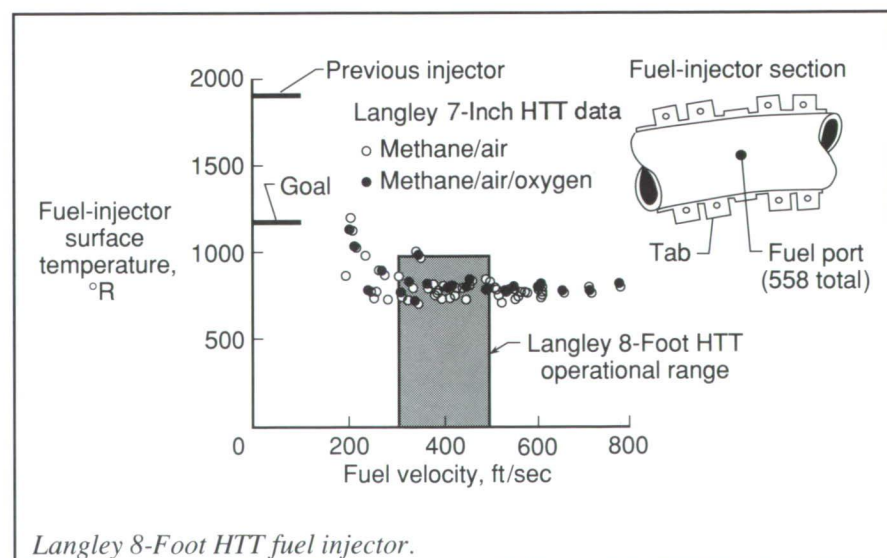
Improved Fuel Injector for Langley 8-Foot HTT Developed

The objective of this effort was to develop a stable fuel injector for the

Langley 8-Foot HTT combustor to operate for the methane/air mode and the new methane/air/oxygen mode. This mode is required for scramjet testing and to maintain fuel-injector surface temperatures of 1200°R or less to prevent thermal fatigue, which causes cracks in the fuel injector.

To meet the schedule and cost constraints of the in-progress 8-Foot HTT construction of facility project, the approach was to modify the existing fuel injector and to evaluate concepts based on thermal loads (surface temperature $<1200^\circ\text{R}$) and flame stability by testing full-scale segments in the Atmospheric Combustor and the Langley 7-Inch High-Temperature Tunnel (7-Inch HTT), which is a 1/12-scale pilot facility for the 8-Foot HTT.

The result is a unique lifted-flame fuel injector that provides stable flames and exceeds the surface temperature goal over the entire operational range of the 8-Foot HTT for both the methane/air and the methane/air/oxygen modes. Fuel velocities >200 ft/sec met or exceeded the maximum surface temperature goal (but at the expense of flame stability). Flame blowout generally occurred at



approximately 300 ft/sec. It was found that 1/8-in. tabs (see the figure inset of the fuel-injector section) increased flame stability from 300 ft/sec to at least 800 ft/sec in the 7-Inch HTT by creating multiple vortices and by recirculating hot, partially reacted species at the base of the lifted flame. The hole in each tab provides air convective cooling and prevents flame "splash." The very small rearward-facing step, in line with the fuel port, helps increase the strength of the surface vortex. The modified injector was operated in the Atmospheric Combustor with fuel velocities up to 1000 ft/sec and at air velocities 10 times the design value of 5 ft/sec, demonstrating high stability.

The modification resulted in 1000 fewer fuel ports than the original attached-flame fuel injector, lower structural temperatures ($<850^{\circ}\text{R}$)

which significantly increase the predicted life of the component and minimize the possibility of fuel-injector cracking, and flame stability that essentially eliminates the potential for flameout.

(Richard L. Puster, 41390)

Structures Directorate

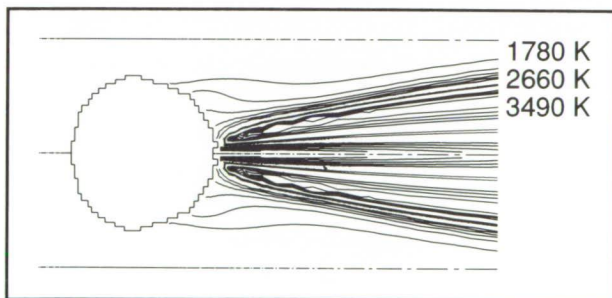
Convective Temperatures and Heat-Transfer Coefficients on Spray Bar of Langley 8-Foot HTT

The determination of the most important parameters needed to compute the thermal stresses, the heat-transfer coefficients, and the convective temperatures on the spray bar of the Langley 8-Foot HTT were the main

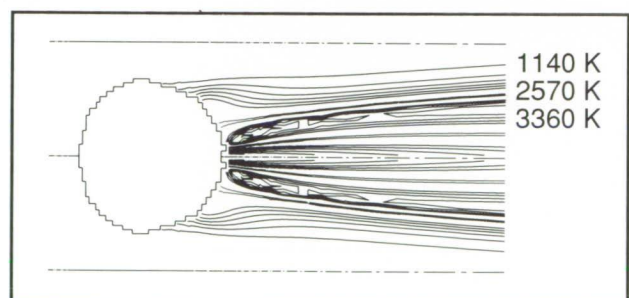
objectives of the design verification analysis. The temperature fields considered are generated during the combustion process in the Lox Mode, which is air enriched to approximately 47 percent by mass in oxygen concentration.

The spray bar consists of 15 concentric rings of 1/2-in., 3/8-in., and 1/4-in. pipes located in a vertical plane. The fuel is injected through 860 orifices of 0.052-in. diameter distributed on the pipes.

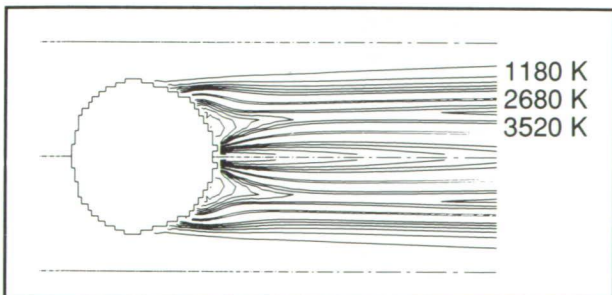
The Fluent computer code and well-known empirical equations, such as Churchill, Berstein, and Petukhov equations, were the two methods followed to compute the heat-transfer coefficient. The same code, together with experimental data, determined the convective temperatures around the spray bar. Two-dimensional, three-dimensional, steady-state and transient,



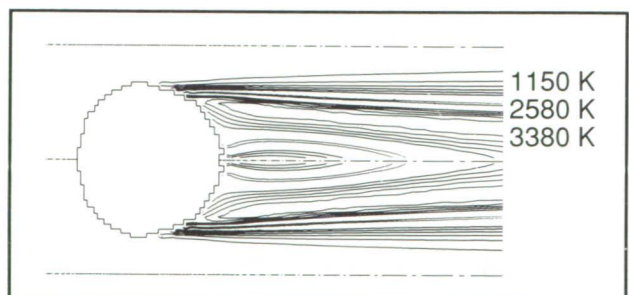
2-D time step 30, 64 m/sec



2-D time step 73, 25 m/sec



2-D time step 91, 8 m/sec



2-D time step 110, .001 m/sec

Two-dimensional transient conditions fuel velocity 91.4 m/sec to 0.01 m/sec in 0.7 sec.

two- and three-step reaction, low- and high-fuel velocity cases were evaluated using Fluent.

The figure shows the development of the temperature field around the spray bar during the transient solution. This case studies the effects of the fuel velocity variation from 91.4 m/sec to 0.01 m/sec in 0.7 sec. It shows that at a high velocity the flame is practically lifted and as the fuel velocity is reduced the flame is attached toward the spray bar.

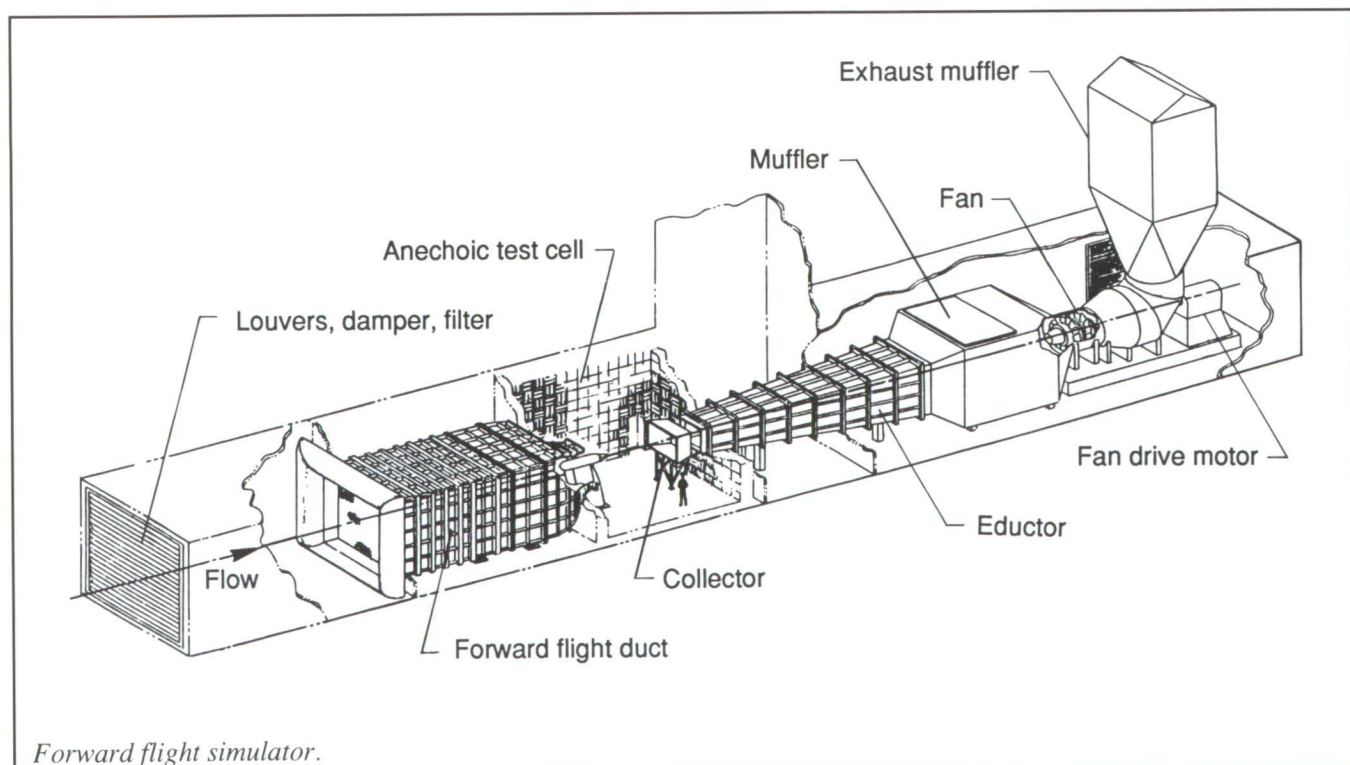
The main conclusions are that Fluent predicts higher (conservative) convective temperatures than experimental data at shutdown conditions and that the heat-transfer coefficients calculated by the empirical equations are acceptable.

(Marco A. Egoavil, 47247)
Systems Engineering and
Operations Directorate

Langley Jet Noise Laboratory Forward Flight Simulator

As a major effort to develop innovative methods of jet noise suppression for the High-Speed Civil Transport (HSCT), a low-speed, aeroacoustic wind tunnel is being designed with a propulsion model to simulate aircraft forward-speed effects on supersonic jet noise. The wind tunnel is being designed to rigorously define takeoff community noise levels with full parameter simulation using noise suppression concepts between 1/8 and 1/10 scale. The nonreturn aeroacoustic tunnel is designed as an open jet suck-down tunnel with minimum and maximum velocities of 35 ft/sec and 350 ft/sec. The 4.5 ft by 4.5 ft forward flight nozzle with an area contraction ratio of 11 to 1 exhausts into an anechoic test chamber. The test chamber and nozzle-to-collector distance is sized to permit a 90° acoustic view of the propulsion model.

The wind tunnel is powered by a two-stage axial flow fan, which is driven by a 4000-hp motor and controlled by a variable-speed drive. The fan blade pitch is manually adjustable. Acoustically treated baffles are used downstream of the diffuser to control fan noise emission into the test chamber. An acoustically treated muffler is also used downstream of the fan to manage noise that is radiated external to the tunnel. The propulsion model is capable of burning either propane or hydrogen fuel to jet total temperatures of 2500°R with nozzle pressure ratios of 11 to 1. The water-cooled model supports dual-stream flow with externally mounted lined ejectors of either round or rectangular nozzle geometry. The 12-in.-diameter model contains a single component balance for initial performance assessment. Completion of construction is expected in November 1992.
(John M. Seiner, 46276, and James C. Manning)
Structures Directorate



Space Structures Research Laboratory Placed Into Operation

Many future NASA space mission concepts envision very large, multi-function, multimission spacecraft for observation of the Earth environment and exploration of the Solar System. These spacecraft will probably have multiple sensors and instruments with very precise pointing and disturbance rejection requirements. Low structural frequencies characteristic of large spacecraft and high-gain control systems needed to meet pointing requirements may lead to controls-structures interactions that could seriously degrade the performance of the spacecraft.

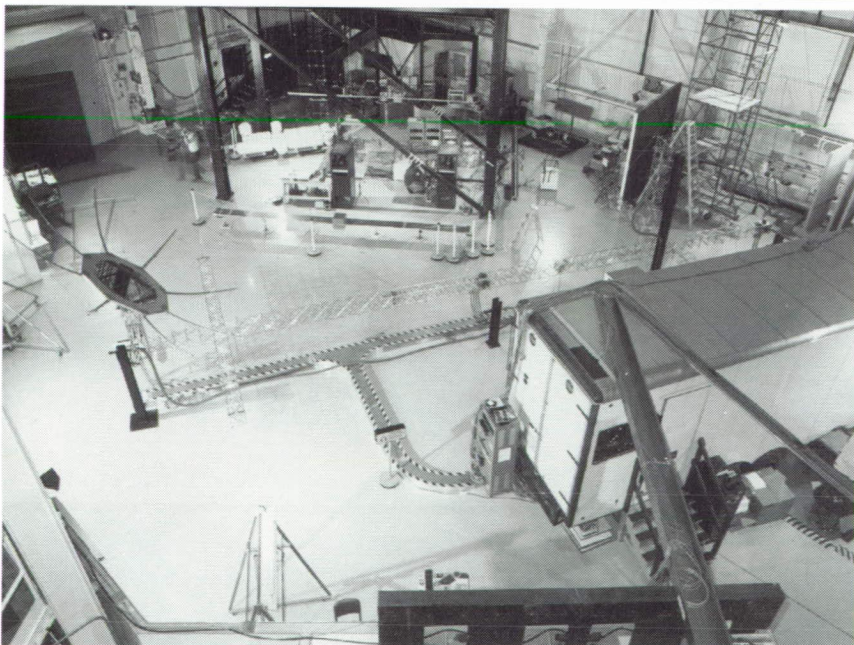
Research is currently being conducted to define, develop, and validate structural dynamic and controls-structures interaction analysis and testing methods. Experimental validation of the methods, using realistic scaled or full-size structural hardware,

is critical. To support experimental validation, a new Space Structures Research Laboratory (SSRL) has been brought on line for structural dynamics and controls testing. Initial test models include a 1/10-size scale model of Space Station *Freedom* (SSF) and a 55-ft-long Controls-Structures Interaction Evolutionary Model (CEM).

The SSRL is an approximately 80-ft by 80-ft by 80-ft high-bay area in Building 1293. The high-bay area was modified to include a 10-ton work platform at the 73-ft level for cable suspension of test models and a separate 60-ft-high gantry for isolated suspension of the 1/10-scale SSF model. A trailer was positioned in the SSRL to serve as a control room for controls-structures interaction testing. The control room has state-of-the-art data acquisition and control capabilities including multichannel instrumentation, analog/digital and digital/analog conversion equipment, and links to real-time control computers.

The SSRL is a unique facility for dynamics and controls-structures interaction testing of large spacecraft systems. The facility provides the height necessary to properly suspend models to reduce the effects of gravity; it also provides the space necessary for simultaneous testing of large structural test articles over long periods of time and provides state-of-the-art data acquisition and control equipment for experimental validation of analysis methods.

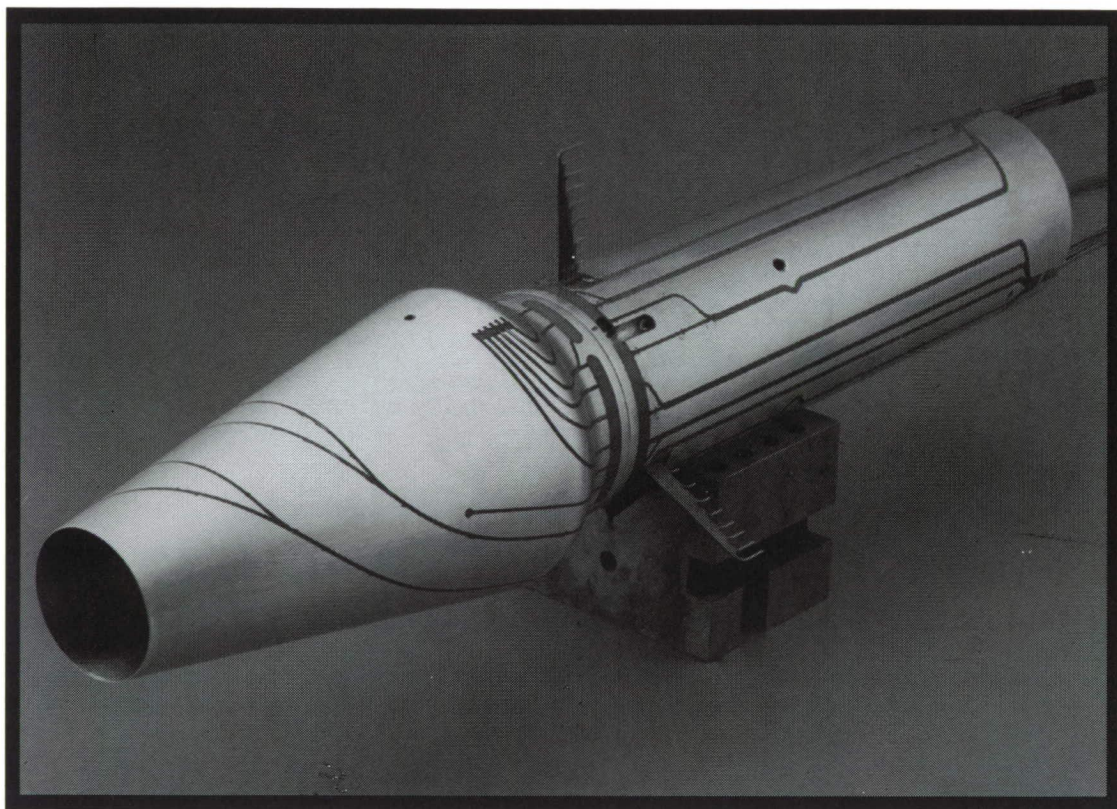
(Robert Miserentino, Keith Belvin, and Paul McGowan, 44318) Structures Directorate



Space Structures Research Laboratory.

L-91-07450

■ TECHNOLOGY UTILIZATION



*Facilitate the transfer of
aerospace-generated technology
to the public domain*

X-Ray Spectroscopy of Contact Lens Polymers

The free volume fraction in contact lens polymers has previously been demonstrated to be a critically important indicator of their suitability for eye wear. However, Positron Lifetime Spectroscopy (PLS) is the only technique currently available for measuring free volume fraction in polymers. PLS, although elegant, is a complex technique for routine use in an industrial laboratory. Free volume fraction has been hypothesized to affect the linear attenuation coefficients of low-energy X rays in contact lens polymers. The higher the free volume fraction in the polymer, the lower will be its linear attenuation coefficient for the selected X rays.

This hypothesis has now been tested in five contact lens polymer specimens. First, linear attenuation coefficients for $\text{Cd}^{109}/\text{Ag}^{109}$ X rays

were measured in several samples of each type of specimen. The difference between μ_{max} and μ_{min} values ($\Delta\mu$ (experimental)) was then determined for each specimen. Next, free volume fractions were measured in the same samples of each specimen. The $\Delta\mu$ (calculated) was then obtained by attributing the entire difference in the linear attenuation coefficients to the difference in free volume fractions in the polymer samples. The values of $\Delta\mu$ (experimental) and $\Delta\mu$ (calculated) are summarized in the figure for all the samples tested. Clearly, the agreement between the two sets of values is reasonably good. This good agreement indicates that soft X-ray linear attenuation coefficients of the polymer specimens can be used as their quality monitor. Specimens with lower linear attenuation coefficients have higher free volume fraction and are, consequently, more suitable for eye wear. (Jag J. Singh and Chih-Ping Shen, 44760)

Electronics Directorate

Carbon-Carbon Piston Development

Pistons used in two- and four-stroke cycle engines must reliably endure a high-pressure and high-temperature cyclic environment. The most common piston materials are steel and aluminum. Pistons made of steel alloys have relatively high mass and high strength, whereas pistons made of aluminum alloys are lower in mass and in strength. Special high-temperature ceramic coatings known as thermal barrier coatings (TBC) have been applied to the crown areas of pistons to improve engine thermal performance by minimizing heat losses during the combustion process. However, excessive thermal stresses can result because of differences in coefficients of thermal expansion between the metallic piston and the TBC. These stresses can cause the coating to debond and/or crack. A high-temperature composite material called carbon-carbon is being considered for fabricating high-temperature pistons. Carbon-carbon materials are currently used on many high-temperature aerospace applications such as wing leading edges, brakes, heat shields, and rocket engine nozzles. A piston manufactured from carbon-carbon is potentially lighter and stronger than an equivalent aluminum piston and can withstand significantly higher operating temperatures than a steel piston.

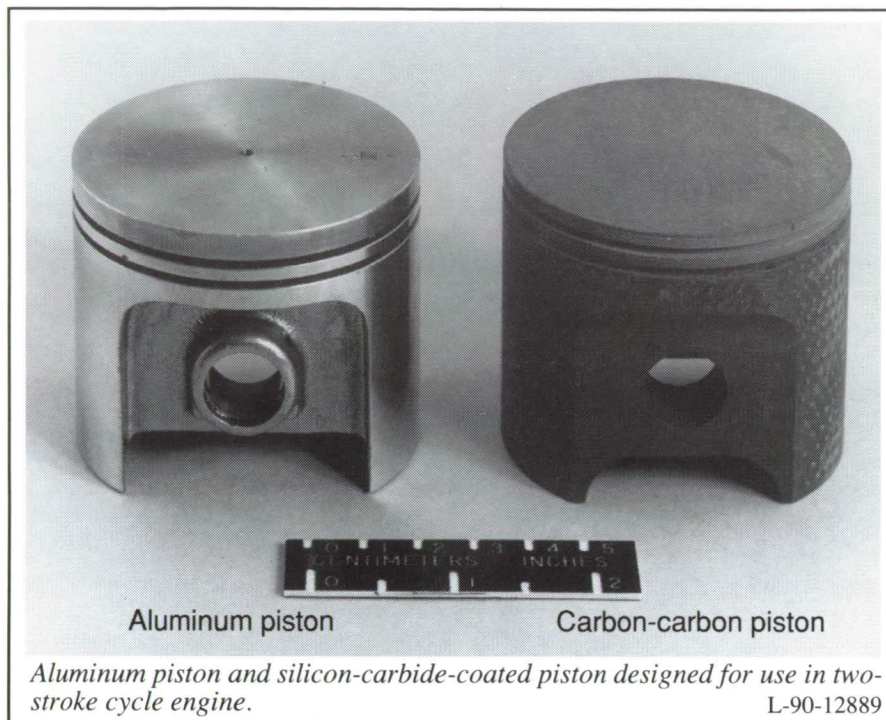
Langley Research Center and the U.S. Army are working together on a joint program to develop carbon-carbon pistons for use in a drone

Contact lens specimens	$\Delta\mu, \text{cm}^{-1}$	
	Experimental *	Calculated +
Paraperm-O ₂	0.0150 ± 0.0076	0.0152 ± 0.0076
Paraperm-EW	0.0392 ± 0.0089	0.0426 ± 0.0090
Fluoroperm-30	0.0140 ± 0.0083	0.0168 ± 0.0083
Fluoroperm-60	0.0203 ± 0.0088	0.0211 ± 0.0088
Fluoroperm-92	0.0134 ± 0.0092	0.0134 ± 0.0092

* The errors on $\Delta\mu$ (experimental) are entirely of statistical origin.

+ The errors on $\Delta\mu$ (calculated) include the statistical errors on μ_{min} and experimental errors on free volume fraction values.

Comparison between experimental and calculated values of $\Delta\mu$ for contact lens samples tested.



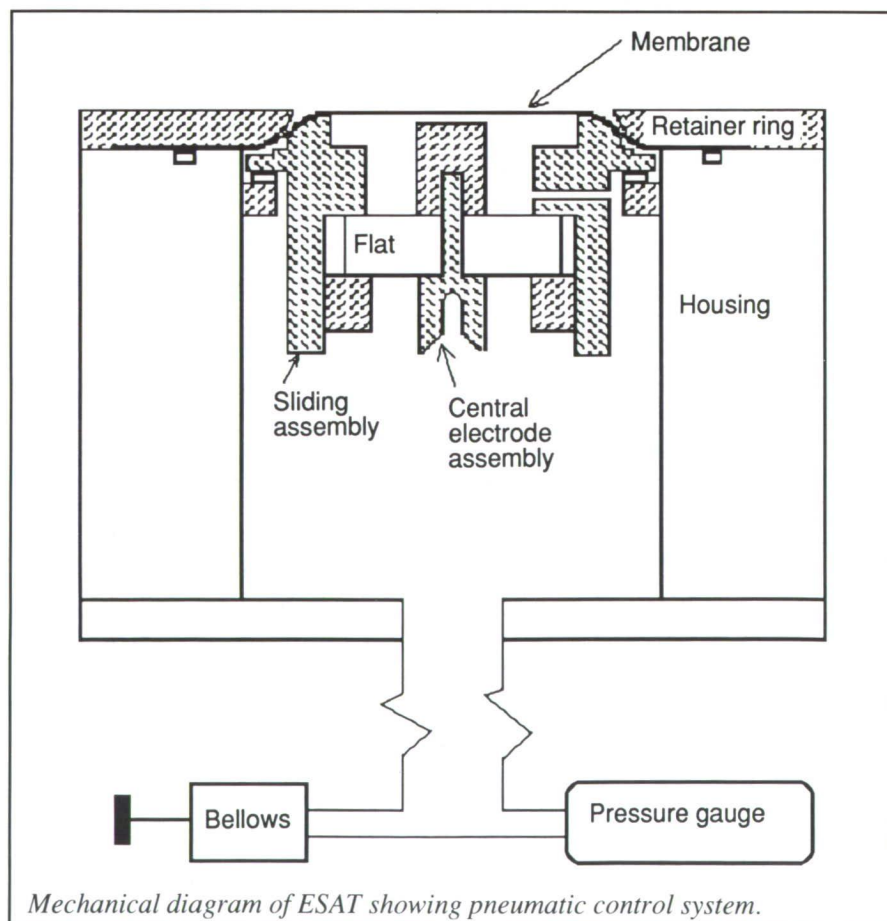
coated crown indicate that the use of a carbon-carbon piston in place of an aluminum piston results in higher cylinder head and exhaust gas temperatures, higher engine r/min for a given fuel/air mixture, and greater torque output. Carbon-carbon and aluminum piston performance tests in a four-stroke cycle engine will begin upon completion of the two-stroke cycle engine tests. (Mark P. Gorton, 45422, and John L. Shideler)
Technology Utilization Program

Ultrasonic Dosimetry

As ultrasonic devices find more widespread applications in medicine, medical experts have noted that patient

aircraft engine. Various piston configurations, with and without sealing rings and oxidation-resistant coatings, have been fabricated using several carbon fiber architectures and densification processes. Two manufacturing methods, hand lay-up and knitting, are being developed for fabricating the carbon-carbon pistons. Several carbon-carbon pistons have been fabricated using a hand lay-up process. However, a knitted carbon-fiber preform has the potential to improve cost effectiveness, and a process for knitting a preform is being developed through a cooperative effort between Langley and Clemson University. Three U.S. patents related to the fabrication of carbon-carbon pistons have been granted: Patent numbers 4,683,809, 4,736,676, and 4,909,133.

Carbon-carbon and aluminum pistons such as those shown in the figure are being tested in a single-cylinder, air-cooled, two-stroke cycle engine. Preliminary results from tests of a carbon-carbon piston having two sealing rings and a silicon-carbide-

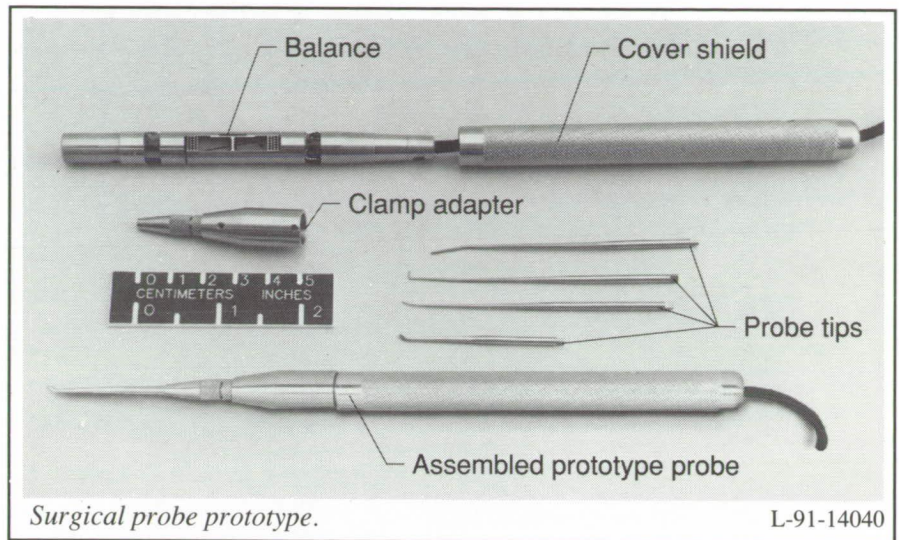


dosage may be biologically significant, especially at very high dosage levels. The quantitative determination of ultrasonic dosage, however, has been a problem for some time. A technique to measure the absolute particle displacement amplitude of an ultrasonic wave using a broadband device called an electrostatic acoustic transducer (ESAT), invented at Langley Research Center, is being developed for this application. Using properties of the propagation medium combined with measurements based on the ESAT, ultrasonic energy flux can be calculated; it is possible to determine the conversion of applied electrical power to ultrasonic energy flux of ultrasonic transducers used in medical applications.

The system works in the following way. Referring to the diagram, a back pressure is applied to the system interior of the ESAT until a gap spacing between the central electrode and the membrane is set up at an appropriate value (approximately $10\text{ }\mu\text{m}$) with the ESAT positioned at its operating level in the liquid. With the central electrode possessing a d.c. voltage bias, an ultrasonic wave, generated by a transducer under calibration, impinges on the membrane. An a.c. voltage output is generated at the central electrode. By measuring the amplitude of the output voltage, the amplitude of the ultrasonic wave can be determined to an accuracy of typically 1 to 2 percent. The ultrasonic amplitude is used to calculate the energy flux to an accuracy of typically 2 to 4 percent.

(William T. Yost, 44991, and John H. Cantrell)

Electronics Directorate



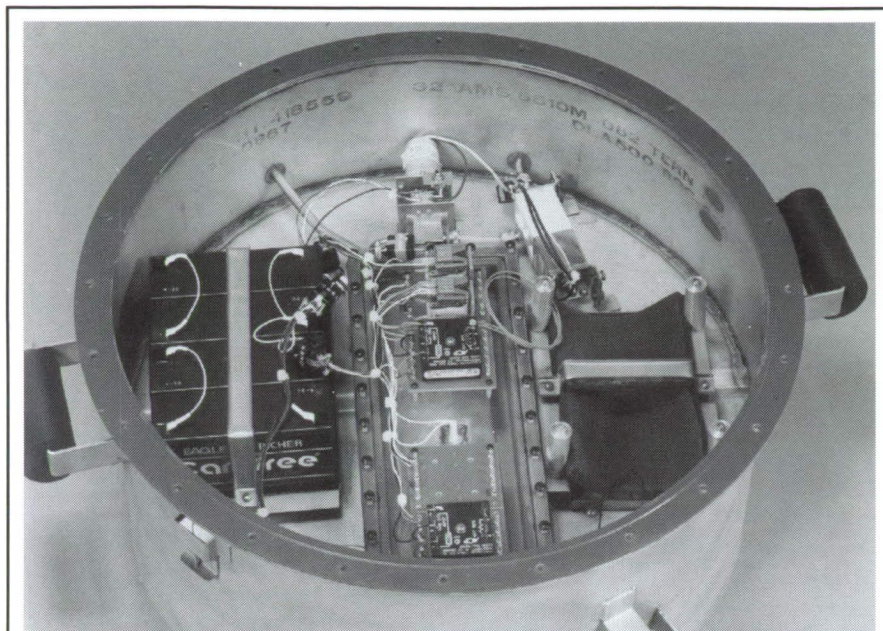
Surgical Force Detection Probe

A precision electro-mechanical instrument is being developed at Langley Research Center which allows the detection and documentation of the forces and moments applied to human tissues during surgery under actual operating room conditions. The pen-shaped instrument, which measures approximately 1/2 in. in diameter and 6 in. in length, consists of three components: a cover shield, a simplified aerodynamic balance, and a tip with an interchangeable scalpel. The simplified aerodynamic balance, developed for wind-tunnel applications at Langley during the last three decades, has a strain-gauged beam section to measure the normal and axial forces and roll moment transmitted through the surgeon's hand to the human tissue during surgery. The full-scale loads of the two forces are approximately 1 lb. The instrument drives a PC-based data system that includes signal conditioning, data acquisition, and graphics display. The overall accuracy of the instrument is better than 1 percent full scale.

The ability to detect the forces applied to human tissue during surgery under actual operating room conditions would allow documentation of the usual forces applied during routine surgical procedures. Such documentation has never been reported. This ability would also allow comparison among experienced surgeons and those in training. Such data may provide feedback that could be effectively used during residency training. When used in conjunction with interoperative neurological monitoring, this ability will allow correlation of specifically applied forces to monitored nerves that are responsible for nerve injury. These data may lead to new concepts in nerve dissection which improve surgical outcome.

Note that the scalpel can easily be replaced by a pen to convert this device into an instrumented writing tool. Such a tool can be used to monitor the steadiness of handwriting which may be useful to check for soberness in the law enforcement field.

(P. Tcheng, 44717, Charles Scott, and Paul Roberts, 44704)
Electronics Directorate



Internal view of semicontinuous flow rate logging seepage meter. L-91-7461

Remote Semicontinuous Flow Rate Logging Seepage Meter

Considerable research has been devoted to qualitatively and quantitatively defining material input into coastal waters; however, this effort has primarily focused on point and nonpoint source surface runoff contributions. Recent evidence suggests that advective transport mechanisms of solutes is significant in many coastal regions. Advective transport mechanisms include: elevated upland hydraulic head (i.e., ground water intrusion), convective flows caused by thermal and salinity density differences in water, sedimentation, benthic boundary currents, spatial variations in sea state, and benthic macrofaunal irrigation. Implications of such transport mechanisms are geologically and biologically important.

Current methods to directly assess ground water discharge and associated solute fluxes are limited to manually operated seepage meters. These efforts are limited by manpower and safe diving conditions. Langley Research Center

and Virginia Polytechnic Institute and State University have jointly designed and developed a remote semicontinuous flow rate logging seepage meter.

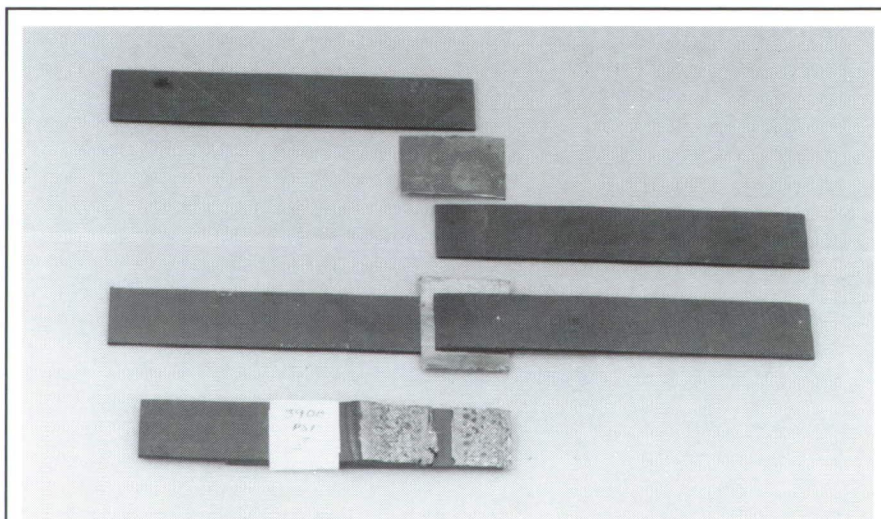
Ground water seeps into coastal waters at a very low flow rate with a low head pressure. (Typical flow rates are from 0 L to 2 L per hr with 10-mm to 150-mm head pressure.) No instruments currently exist that can measure

flow rates under these conditions. The semicontinuous flow rate logging seepage meter operates remotely with batteries and collects water in a plastic bag. When the bag is filled to a predetermined volume, a proximity switch initiates an electrically operated cycle that momentarily stops sampling and pumps a calibrated volume of water out of the bag, logs the cycle date and time, and resets to the sample mode. Considerable interest in this equipment has been expressed by several environmental organizations, and extensive usage nationally and internationally is anticipated. A patent disclosure has been prepared.

(H. G. Walthall, 45194)
Systems Engineering and
Operations Directorate

Ceramic Susceptor for Induction Bonding of Metals, Ceramics, and Plastics

A thin (0.005-in.), flexible ceramic susceptor (carbon) has been developed to join ceramics, plastics, metals, and combinations of these materials using a unique induction heating process.



Ceramic (carbon) susceptor for induction bonding of composites. L-90-6328

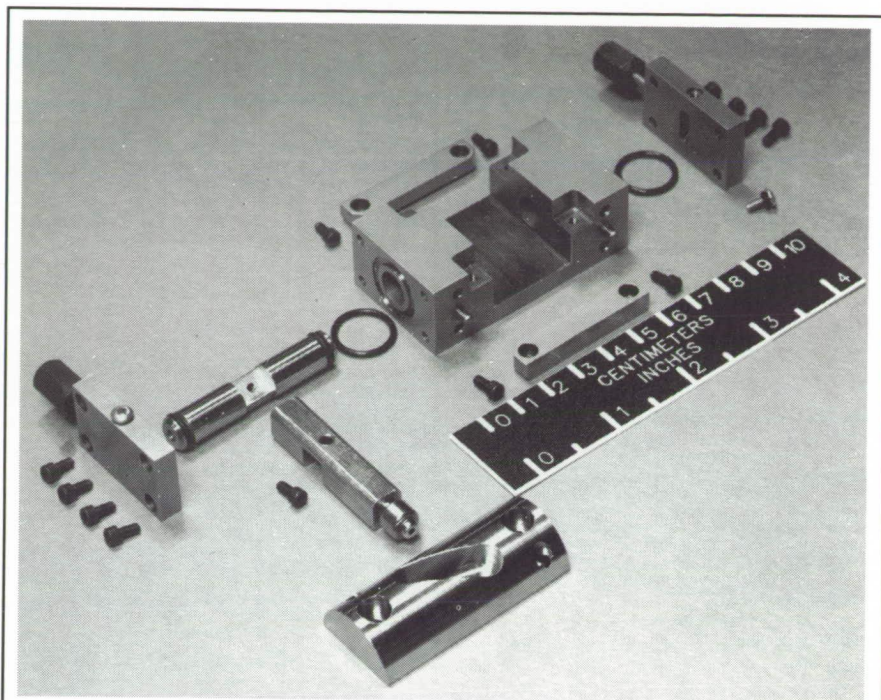
ORIGINAL PAGE
BLACK AND WHITE PHOTOGRAPH

Bonding times for laboratory specimens comparing state-of-the-art technology to induction bonding have been cut by a factor of 10 to 100 times. This novel type of carbon susceptor allows for applying heat directly and only to the bondline without heating the entire structure, supports, and fixtures of a bonding assembly. The ceramic (carbon film) susceptor produces molten adhesive or matrix material at the bond interface. This molten material flows through the perforated susceptor producing a fusion between the two parts to be joined, which in many instances has proved to be stronger than the parent material. Bonding can be accomplished in 2 minutes on areas submitted to the inductive heating. Because a carbon susceptor is used in bonding carbon-fiber-reinforced plastics and ceramics, no radar signature of return exists, making it an ideal process for joining advanced aerospace composite structures. (R. L. Fox, 45468)

Systems Engineering and Operations Directorate

Benchmark Active Controls Model Actuator

A miniature hydraulic actuator capable of transmitting linear actuator motion to rotational motion of a generic control surface has been designed for the Benchmark Active Controls Model. Because of space constraints and the torque requirements of an oscillating control surface at frequencies up to 50 Hz, a new actuation system was developed to meet research objectives. To validate the design, a prototype actuation system was designed and fabricated and is currently being evaluated for load limits and dynamic characteristics.



Disassembled servo and helical drive insert.

L-91-5050

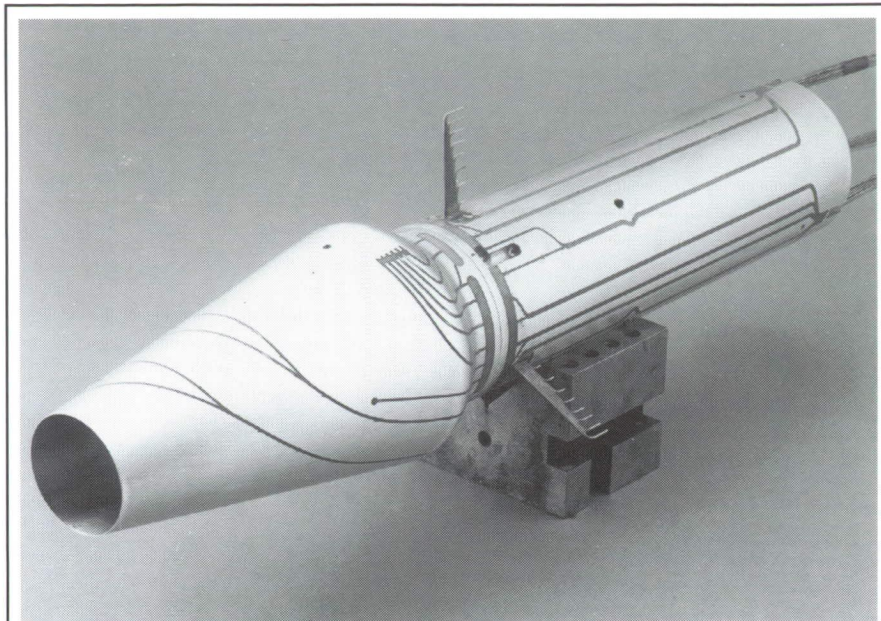
The prototype system consists of the hydraulic actuator, a flap simulator with variable mass moment of inertia, and a test-bed for mounting the hardware. The linear motion of the miniature actuator is converted to rotary motion for control surface actuation through an insert with a high-precision helical trough. This insert is incorporated into the actuated control surface as part of its leading edge. Minimal tolerance buildup in the system is required in order to reduce the free play between individual components. All surfaces with relative motion are coated with a nickel alloy plating (NEDOX) to improve surface hardness (R_c 63 to 67) and lubricity, thus decreasing wear. The actuator is driven hydraulically with a maximum operating pressure of 1000 psi. Miniature pressure transducers capable of monitoring servo loads are incorporated into the servo body. The overall dimensions of the actuator are 3.09 in. by 1.38 in. by 0.88 in.

Current evaluation of the actuator has revealed its capability of short-throw/high-frequency control surface deflections ($\pm 5^\circ$ at 40 Hz to 50 Hz) and long-throw/low-frequency deflections ($\pm 15^\circ$ at 5 Hz to 10 Hz). Further testing will be conducted to determine component wear characteristics at sustained high-frequency control surface deflections. The actuator design will be incorporated into a transonic flutter model with an active trailing-edge flap and two active spoilers for testing in the Langley 16-Foot Transonic Dynamics Tunnel. (Michael R. Sorokach, Jr., 47143)

Systems Engineering and Operations Directorate

CAD Interface Programming to Aid Model Fabrication

The conflicting requirements of a high degree of instrumentation, quality



Typical core cowl and core assembly after tube installation.

L-91-6316

surface finish, and easy interchangeability resulted in a new fabrication method for routing pressure tubing in a body of revolution. For the Dual-Flow High Bypass Ratio Nozzles, several computer programs were written using the GRAPL-IV interface language to computer aided design/computer aided manufacturing (CAD/CAM) software ANVIL-5000. These programs allow a user to graphically project 2-D curve definitions precisely around a body of revolution. These curve definitions are output in a form readable by a Wasino numerically controlled (NC) lathe with third-axis milling capability. This process allows the lathe operator to cut complex grooves around the body of revolution while accurately controlling the depth.

This method has shown to be a promising approach. The programming and machining times are less than more traditional fabrication methods. The final surface finish is very good because grooves are narrow and easily faired. The tube installation is simplified because curvature can be gentle

and tubes can be routed directly to interface locations.

(Christopher M. Cagle, 47140, and Melinda F. Cagle)
Systems Engineering and Operations Directorate

■ CONTRIBUTING ORGANIZATIONS

Aeronautics Directorate

The Aeronautics Directorate, which is composed of approximately 350 scientists and engineers engaged in basic and applied research in the various aeronautics disciplines, includes research wind tunnels, aircraft, and computers with a replacement value exceeding 1 billion dollars. The directorate is organized into four research divisions, a hypersonic technology office, and a facilities planning office, which conduct aeronautical research to advance the state of the art throughout the complete aerodynamic speed range.

The research divisions of the Aeronautics Directorate form a team whose mission is to develop advanced technology for future civil and military aircraft. Each division plays a unique role through application of wind-tunnel testing, flight experiments, theoretical research, and computational efforts to advance the state of the art in aeronautics. The Advanced Vehicles Division conducts multidisciplinary advanced aeronautical vehicle studies to assess the benefits of discipline research advances and to identify potential new research thrusts. The Applied Aerodynamics Division conducts research on subsonic through hypersonic aerodynamics including propulsion integration using computational fluid dynamics techniques and a variety of wind tunnels including the 14- by 22-Foot Subsonic Tunnel, the National Transonic Facility, the 16-Foot Transonic Tunnel, and the Unitary Plan Wind Tunnel. The Flight Applications Division utilizes the Langley

30- by 60-Foot Tunnel, 20-Foot Vertical Spin Tunnel, and research aircraft to conduct experiments that complement the ground-based research efforts of other organizations at the Center with an emphasis on flight experiments, flight dynamics, and aviation safety. The Fluid Mechanics Division conducts theoretical, computational, and experimental research to advance the state of knowledge in fluid mechanics as it applies to the design of advanced aircraft and missiles across the speed range and to hypersonic propulsion systems. The Hypersonic Technology Office coordinates broad-scope hypersonic vehicle research and technology programs including those involving the National Aero-Space Plane (NASP).

The extremely successful Boeing 757 hybrid laminar-flow control flight experiment exceeded expectations, and flight results provided industry with confidence toward application. The first full-scale Reynolds number data in a wind tunnel were successfully measured on a transonic transport configuration in Langley's cryogenic National Transonic Facility. Supersonic Low-Disturbance Pilot Tunnel test results demonstrated the means to achieve laminar-flow conditions on supersonic swept-wing leading edges. The results of a vortex flap applied to the Langley F-106 airplane demonstrated dramatic performance benefits for transonic fighter aircraft maneuvering conditions; these results are potentially applicable for improving low-speed climb performance and noise characteristics of High-Speed Civil Transport (HSCT) configurations. The supersonic lift and drag

characteristics of the Langley baseline HSCT configuration were successfully predicted with an improved, Langley-developed, thin-layer Navier-Stokes three-dimensional (TLNS3D) code.

Electronics Directorate

The Electronics Directorate is responsible for planning, directing, and evaluating research and applications programs in the areas of measurements and computer science which will benefit the Center's aerospace activities. This directorate also manages the Center's instrumentation, data acquisition, and data processing resources through the four divisions, each of which has specific support functions.

The Analysis and Computation Division is responsible for the development and application of mathematical and computer theory to the solution of computational problems arising from theoretical and experimental aerospace research activities performed at Langley Research Center. Additional responsibilities include conception, design, implementation, and management of advanced centralized data processing systems, flight software systems, flight simulators, and advanced communications and networking technology.

The Instrument Research Division provides instrumentation and measurement for experimental aerospace research activities performed at Langley, with primary responsibility for the

instrumentation of ground-based facilities. This division conducts research in instrument areas in which present measurement capabilities are deficient. Additional responsibilities include providing computer-based data acquisition and control systems, developing and maintaining measurement standards, calibrating and repairing instruments, and managing an instrument pool.

The Flight Electronics Division is responsible for the development and application of electronic and electro-optical systems for aerospace flight and flight-related projects. This division conducts research and development programs in electronics, optics, lasers, and related disciplines to provide measurement, communication, and data processing systems.

The Projects Division is responsible for the management of Langley's participation in major NASA projects. These projects include atmospheric sensing instruments (CERES (Clouds and the Earth's Radiation Energy System); SAGE III (Stratospheric Aerosol and Gas Experiment); and SAFIRE (Spectroscopy of the Atmosphere Using Far-Infrared Emissions)) and the development of NASA's first spaceflight lidar (laser-radar), the Lidar In-Space Technology Experiment (LITE).

The accomplishments of the Electronics Directorate over the past year are as diverse as the directorate itself. Significant advances have occurred in applied research for remote sensing of the Earth's atmosphere and nonintrusive diagnostic measurements for Center-wide ground facilities. Some examples of these advances include an efficient multitasking solution of linear systems on the CRAY-2 and CRAY YMP supercomputers, the application of titanium-doped sapphire laser technology to differential absorption lidar for atmo-

spheric measurements, the application of thermal nondestructive evaluation (NDE) techniques to locate lap joint bond deficiencies in the Aging Aircraft Program, and the application of neural networks for the detection of these disbonds.

Flight Systems Directorate

The Flight Systems Directorate, which consists of three research divisions and two project offices, conducts basic research and development in the broad, multidisciplinary areas associated with aerospace flight systems. This includes systems hardware and software architecture concepts and design guidelines, validation and verification methods for reliable flight control systems, advanced flight deck research, advanced airborne systems technology, aircraft operating procedures, fundamental electronics research, automation and robotics technology, and aircraft and spacecraft guidance and control system design methods, guidelines, and criteria. A special multidirectorate, multicenter research activity addressing controls-structures interaction (CSI) issues associated with large flexible space systems is also managed and participated in by directorate personnel.

In the past year, the Flight Systems Directorate accomplished a number of significant technical objectives in a wide range of technical areas. Of special note were the continued activities associated with the NASA/FAA (Federal Aviation Administration) Airborne Wind Shear Detection and Avoidance Program. This year a major wind shear accomplishment was the continued development and successful flight testing, in the Transport Systems Research Vehicle (B-737), of two (Doppler radar, infrared) of the three major candidates for an airborne sensor

that may provide early detection of wind shears. Also of note was the validation, using actual accident data, of the artificial intelligence based fault detection, monitoring, and recovery recommendation system known as Faultfinder. (Faultfinder received a Research and Development (R&D) 100 Award this year recognizing it as one of the 100 most innovative research accomplishments for the year.) In the human engineering methods area, novel techniques using brainmapping analysis to identify states of awareness of pilots were developed, and a multiattribute task battery was established for use in studying a pilot's strategic behavior, work load, and complacency while flying an aircraft. Also completed were several investigations related to the basic guidance and control of supersonic and hypersonic vehicles. Work continued on the development of automated assembly techniques and other telerobotics technology associated with in-space operations. The CSI program research accomplished this past year included testing different controller designs on the CSI Evolutionary Model (CEM) and the completion and verification of an integrated controls-structures design of the CEM. This year also marked the end of Phase I of the CSI Guest Investigator (GI) program that supported university and industry researchers and provided CSI test facilities on which they could test their control systems design techniques. Phase II of the GI program was also initiated this year.

Space Directorate

The Space Directorate is primarily responsible for research in atmospheric sciences, advanced transportation systems, and energy conversion for space applications. In addition, this

directorate is the focal point for conceptual design activities for large space systems technology, Space Station *Freedom*, the Space Exploration Initiative, and the Aeroassist Flight Experiment.

Continuing a role in the development of the Personnel Launch System (PLS), the Space Systems Division has established the technical feasibility of its lifting-body configuration, the HL-20, as a candidate for the PLS. In addition, the HL-20 was determined to be a technically viable, cost-effective candidate for both the Assured Crew Return Capability and Personnel Launch System applications. A full-scale mockup was fabricated, outfitted, and utilized for flight-crew fit analysis, egress and ingress studies, and pilot landing visibility assessments. Results from these assessments showed that the HL-20 volume was satisfactory and adequate pilot vision during landing was achievable with slight modifications to the nose of the vehicle. The aerodynamic data base developed over the entry regime was implemented in the moving base simulator and resulted in verification of Level II handling quality for the HL-20 during landing with the increased subsonic L/D of 4.3. Design approaches were completed which simplify manufacturing and provide accessibility for maintenance and streamlined operations. Design, development, test, and evaluation cost estimates were determined, and life-cycle cost estimates show the lifting-body concept is cost competitive compared with lower lift-to-drag ratio concepts for both the Agency Assured Crew Return Capability requirement and any future requirements for the Personnel Launch System.

Several important experiments designed to provide new insights into chemical and dynamical process in the atmosphere were accomplished by the Atmospheric Sciences Division. The

Global Tropospheric Experiment (GTE), which was conducted in the northern latitudes of Alaska and Canada, characterized emissions from wetlands and demonstrated that they are a major contributor to the global methane budget. Additional field experiments characterized emissions from biomass burning and determined that it is a major source of environmentally significant gases. These experiments also demonstrated that biomass burning is not an important source of nitrous oxide and that previous measurements of nitrous oxide could be in serious error. An analysis of historical solar spectral data was completed which determined that large increases in environmentally significant traces gas have occurred.

The analysis of spectroscopic data revealed that hydrogen fluoride increased by a factor of 3.2 over the past 13 years during which time hydrogen chloride increased by a factor of 1.8. Significant improvements were made in the quality of the simulations of stratospheric chemical and dynamical process in the Langley 3-D global circulation model. A formulation for self-consistent treatment of heterogeneous chemistry in polar regions was developed which permits study of polar ozone depletion including dilution effects over an annual cycle in the Arctic and Antarctic regions. Ozone data from the Stratospheric Aerosol and Gas Experiment satellite instruments, SAGE I and SAGE II, were combined to estimate trends in stratospheric ozone over the time period from 1979 to 1991. Relatively large ozone decreases occurred over almost all of the lower stratosphere resulting in a significant negative decadal trend in ozone column content over mid- to high latitudes. Analysis of the data from the Earth Radiation Budget Experiment (ERBE) satellite instruments demonstrated that clouds have a net cooling

effect in all seasons, an important finding for the climate modeling community. Also, the complete development of the 1987 El Niño event was detected from the analysis of 3 years of ERBE data.

The Space Station *Freedom* Office (SSFO) participated in several key studies related to the restructure of Space Station *Freedom* (SSF) including module pattern options and preintegrated truss options. These studies had a major impact on the Agency's restructure plan and led to the incorporation of the shorter pressurized modules and the preintegrated truss, cornerstones to the restructure effort. In addition, the Crew and Equipment Translation Aid (CETA) was designed, developed, constructed, and successfully operated by the crew of STS-37 to demonstrate methods and techniques for the translation of crew and equipment on SSF.

The Space Exploration Initiative Office defined a simple, cost-effective aerobrake vehicle facility for SSF that resulted in the generation of an aerobrake reference configuration as a baseline for continued evaluation. Also, alternative concepts were developed for lunar habitats, including innovative regolith handling and descent and landing systems.

Structures Directorate

The Structures Directorate conducts basic research and develops technology in the areas of advanced aerospace materials and structures, structural loading, dynamics and aeroelasticity, noise generation by aircraft propulsion systems and its interaction with structures, and methodologies for interdisciplinary design, optimization, and vibration control. This technology development is directed toward

reduction in both weight and cost of aircraft and space structures along with an increase in their reliability and service life.

Research results from the Materials Division include determining the effect of processing parameters on the strength of enhanced diffusion-bonded honeycomb core sandwich structure. A lightweight coating that protects titanium alloys from oxidation in a hypersonic environment and procedures for resistance spot welding of advanced aluminum alloys have been developed. A fabricated powder-metallurgy aluminum-alloy dispersion-hardened sheet has demonstrated useful stability at 600°F. The influence of postforming processing on the tensile properties of superplastic Al-Li alloys has been determined, and toughened matrix composite materials have been evaluated. The effects of space exposure of polymeric matrix composites have been evaluated from satellite Long Duration Exposure Facility samples returned to Earth. Thermally induced damage in composites has been predicted for spacecraft applications, and knitted/stitched composites have demonstrated improved damage tolerance.

A code (VISCOPLY) which analyzes thermomechanical fatigue of unidirectional titanium metal-matrix composites and an analysis method that predicts local delaminations from matrix cracks in laminated composites have been developed. In addition, research included a fracture mechanics analysis of cracks extending from rivets which is applicable to multiple site damage (MSD). A mechanics model for textile preforms composites and a high-quality film of poly(arylene ether imidazole) (PAEI) have been developed for the Precision Segmented Reflector (PSR). A series of tough, high-modulus, semicrystalline amide polyimides have been prepared from amide diamines.

Research results from the Structural Mechanics Division include identification of failure modes for composite laminates with a hole and subjected to four-point bending. Structural efficiency has been determined for optimized graphite-thermoplastic panels. Computer programs have been developed for structural element sizing and structural weight prediction (EZDESIT) and for three-dimensional nonlinear flux-based thermal finite elements. Research in advanced reduced-basis methods has resulted in reduced computational requirements for linear, transient structural analysis. Curved beams have been made from long discontinuous fiber (LDF). Blade-web intersection characteristics have been found critical for graphite/epoxy Y-stiffened panels. An aerobrake panel support concept has been developed that results in zero slope along the panel edge as well as a support truss that enables orbital replacement of collector panels for solar dynamic concentrators. Photogrammetric surveys have verified the desired surface accuracy, and coefficient of thermal expansion characteristics have been obtained for the Precision Segmented Reflector (PSR) test-bed. Analysis has also occurred for the vibration equation of a uniform column under axial load through piecewise constant cross section. Adaptive analysis procedures have been demonstrated for the nonlinear response of composite panels.

A new eigensolver has been developed that reduces supersonic-hypersonic flutter analysis time by two orders of magnitude, and a nonlinear finite-element analysis was found to accurately predict strain in stiffened composite panels. An aerothermal study of the axial compression corner with shock impingement at Mach 6 was demonstrated, and predictions were made of a compressible turbulent boundary layer using data acquired in

the Langley 8-Foot High-Temperature Tunnel. An improved fuel injector was developed for this tunnel.

The Structural Dynamics Division has determined the cornering properties of bias-ply, H-type, and radial aircraft tires. The wear performance of a modified Space Shuttle main-gear tire was obtained, and a variable yaw system installed on the Aircraft Landing Dynamics Facility carriage reduced tire characterization test time. The effect of floor location on the response of a composite fuselage frame was determined, and an optimization scheme was used to obtain maximized gust loads for nonlinear aircraft. Sensitivity analysis of aeroelastic response was performed. Finite-difference meshes for solution of transonic small disturbance equations were developed, and active control of delta wing rocking motion was simulated using CFD (Computational Fluid Dynamics). Spatial adaption procedures were developed for accurate unsteady flow analysis. The CAP-TSD computer code was used to predict HiSAIR vehicle airloads, and a knowledge-based tool was applied to understand HiSAIR data flow.

An additional research result from the Structural Dynamics Division includes development of an approach for modeling the nonlinear aerodynamic response for aero-servoelastic analysis and design. Flutter has been actively suppressed using piezoelectric ceramic actuators. Multi-input/multi-output, multiple function digital control has been demonstrated in the Active Flexible Wing (AFW) Program. An NACA 0012 airfoil has been tested as part of the benchmark model test program to obtain aeroelastic data for code development, evaluation, and validation. Transonic shock-induced dynamics of a flexible wing have been studied, and aileron buzz characteristics have been examined for several NASP

wing configurations. The data acquisition system of the Transonic Dynamics Tunnel (TDT) has been improved. A new cable mount method has been developed for testing statically unstable models in the TDT, and the effect of thermal gradients on structural vibration frequencies has been evaluated. An assessment of the DAMVIBS program has been completed with Government and industry participation.

An extension-twist coupling concept has been demonstrated on a rotor model, and trail-rotor model flutter characteristics have been studied experimentally. An analytical simulation has confirmed the feasibility of a Space Station modal identification experiment. Dynamic scale model technology for large space truss structures has been demonstrated, and control experiments of a CSI evolutionary model test-bed have been initiated. Flight data from the Hubble Space Telescope have been used to identify the solar array vibration parameters, and the multidisciplinary optimization of space structures has shown that a significant mass savings is possible. A new method to control thermal distortion of a space antenna has been simulated, and the Space Structures Research Laboratory has been placed into operation.

The Acoustics Division demonstrated interior noise control using piezoceramic actuators. Active adaptive control was applied to an axial flow turbofan engine to reduce noise, and a computer program was developed to predict jet noise for a High-Speed Civil Transport. The prediction of subjective response to sonic booms was studied. Sonic boom shaping was found to control subjective boom loudness, and atmospheric turbulence was found to increase sonic boom rise time. The effect of nonaxial inflow on propeller noise was evaluated. A frequency-based approach to

prediction of dynamic stress intensity was developed. The dynamic response of initially deformed composite plates was studied using finite elements, and acoustic radiation damping in subsonic flows was studied. The acoustic characteristics of the XV-15 tilt-rotor aircraft with an advanced technology blade were measured in hover. The effect of higher harmonic control on the directivity and level of rotor impulsive noise was studied in the German-Dutch Wind Tunnel (DNW). Predictions from a noise prediction code for blade-vortex interaction noise were validated with data from the DNW tunnel. A forward flight simulator is being added to the Langley Research Center Jet Noise Laboratory. The acoustic characteristics of a supersonic elliptic nozzle were evaluated.

The Structures Technology Program Office is studying the influence of load and component interactions on the failure of the Technology Integration Box Beam during tests to ultimate load. Global stitching has been selected for demonstration as a low-cost composite wing structure. A design-build-team approach to the design of a large aircraft composite fuselage structure indicates both cost and weight savings compared with metallic baseline structural concepts.

Systems Engineering and Operations Directorate

The prime function of the Systems Engineering and Operations Directorate is to support the ongoing aeronautic and space research at Langley Research Center. This directorate is organized into five divisions and two offices with specific support functions in a wide variety of engineering and technical disciplines. Systems Engineering is

responsible for the design, development, analysis, and test of aerospace hardware and wind-tunnel models. Facilities Engineering is responsible for the design, construction, and modification of institutional and research facilities and hardware. Fabrication produces hardware, components, and systems for aerospace projects and research facilities. Operations Support provides maintenance services and operates the wind tunnels and research equipment and facilities. Systems Safety, Quality, and Reliability ensures the integrity of hardware and facilities and manages the environmental health programs, the Facilities Program Development Office, and the 8-Foot High-Temperature Shakedown Project Office.

Because of the unique requirements of some of the research performed at the Center, engineers and technicians are involved in applied research in solving engineering and fabrication problems. These problems relate to the design and fabrication of hardware and software necessary to provide the various components and experimental systems requested by the researchers.

This year the directorate made major strides in developing unique analytical tools to aid in the analysis of flutter in hypersonic flow, structural properties of sensitive space instruments, effects of thermal disturbances on optical benches, and thermal properties of a principal element in the Langley 8-Foot High-Temperature Tunnel. Several devices were designed and fabricated to assist in the collection of pressure distribution on an aerobrake, to actively control spoilers and flaps on wind-tunnel models, and to control or excite large space structures. Special fabrication techniques were developed for induction bonding composite materials, producing thin-film heat-transfer arrays, providing leading-edge porous skins for tunnel models,

manufacturing high-temperature thermoplastic prepreg, and routing intricate pressure tubing in tunnel models.

Technology Utilization

One of the Congressionally mandated responsibilities of NASA is to promote economic and productivity benefits to the Nation by facilitating the transfer of aerospace-generated technology to the public domain. NASA meets this objective through its Technology Utilization Program, which provides a link between the developers of aerospace technology and those in either the public or private sectors who might be able to employ productively the technology. The *NASA Tech Briefs Journal*, which has more than 190 000 subscribers, has been an effective method of announcing new technology generated by NASA.

Another important facet of the NASA Technology Utilization Program is its applications engineering projects, which involve the use of NASA expertise to redesign and reengineer aerospace technology to solve the problems delineated by federal agencies or other public-sector institutions. Applications engineering projects originate in various ways; some stem from requests for NASA assistance from other government agencies and some are generated by NASA engineers and scientists who perceive possible solutions to public-sector problems through the adaptation of NASA technology. Additionally, NASA employs a multidisciplinary applications team that maintains a liaison with public-sector agencies, medical and public-health institutions, professional organizations, and academia to uncover significant problems in diverse fields such as

health care, public safety, transportation, environmental protection, and industrial processes that might be amenable to solution by the application of NASA technology.

A Technology Utilization applications engineering project is considered successful when the technology developed under the project is used or is manufactured for the market.

To help obtain secondary uses of Langley technology, public awareness of Langley innovations is promoted by the Technology Utilization Office. One such method is the entry of Langley candidate items into the Research and Development (R&D) 100 competition. The prestigious R&D 100 Award is presented annually to the 100 most significant technological advancements selected from candidate items received worldwide. Langley received two R&D 100 Awards in 1991 for the Faultfinder and for the Thermoset Impedance Monitoring Control System (TIMACS). Faultfinder provides pilots information for the monitoring, diagnosis, and recovery from engine and hydraulic system component faults. TIMACS is a process control apparatus used to monitor impedance changes of thermosets in manufacturing.

REPORT DOCUMENTATION PAGE			Form Approved OMB No. 0704-0188	
Public reporting burden for this collection of information is estimated to average 1 hour per response, including the time for reviewing instructions, searching existing data sources, gathering and maintaining the data needed, and completing and reviewing the collection of information. Send comments regarding this burden estimate or any other aspect of this collection of information, including suggestions for reducing this burden, to Washington Headquarters Services, Directorate for Information Operations and Reports, 1215 Jefferson Davis Highway, Suite 1204, Arlington, VA 22202-4302, and to the Office of Management and Budget, Paperwork Reduction Project (0704-0188), Washington, DC 20503.				
1. AGENCY USE ONLY (Leave blank)	2. REPORT DATE February 1992	3. REPORT TYPE AND DATES COVERED Technical Memorandum		
4. TITLE AND SUBTITLE Research and Technology 1991 Langley Research Center		5. FUNDING NUMBERS		
6. AUTHOR(S)				
7. PERFORMING ORGANIZATION NAME(S) AND ADDRESS(ES) NASA Langley Research Center Hampton, VA 23665-5225		8. PERFORMING ORGANIZATION REPORT NUMBER L-17018		
9. SPONSORING/MONITORING AGENCY NAME(S) AND ADDRESS(ES) National Aeronautics and Space Administration Washington, DC 20546-0001		10. SPONSORING/MONITORING AGENCY REPORT NUMBER NASA TM-4331		
11. SUPPLEMENTARY NOTES				
12a. DISTRIBUTION/AVAILABILITY STATEMENT Unclassified-Unlimited Subject Category 99		12b. DISTRIBUTION CODE		
13. ABSTRACT (Maximum 200 words) The mission of the NASA Langley Research Center is to increase the knowledge and capability of the United States in a full range of aeronautics disciplines and in selected space disciplines. This mission will be accomplished by performing innovative research relevant to national needs and Agency goals, transferring technology to users in a timely manner, and providing development support to other United States Government agencies, industry, and other NASA centers. This report contains highlights of the major accomplishments and applications that have been made during the past year. The highlights illustrate both the broad range of the research and technology (R&T) activities at NASA Langley Research Center and the contributions of this work toward maintaining United States leadership in aeronautics and space research. For further information concerning the report, contact Dr. Michael F. Card, Chief Scientist, Mail Stop 105-A, NASA Langley Research Center, Hampton, Virginia 23665, (804) 864-6062.				
14. SUBJECT TERMS Research and technology; Aeronautics; Space; Structures; Materials; Electronics; Flight systems; Technology utilization; Engineering; Aerodynamics			15. NUMBER OF PAGES 286	
			16. PRICE CODE A13	
17. SECURITY CLASSIFICATION OF REPORT Unclassified	18. SECURITY CLASSIFICATION OF THIS PAGE Unclassified	19. SECURITY CLASSIFICATION OF ABSTRACT	20. LIMITATION OF ABSTRACT	

NSN 7540-01-280-5500

Standard Form 298 (Rev. 2-89)
Prescribed by ANSI Std. Z39-18
298-102

NASA-Langley, 1991

PRECEDING PAGE BLANK NOT FILMED